A STUDY OF THE TURBULENT WAKE OF AN AIRFOIL IN AN AIR STREAM WITH A 90^{o} CURVATURE USING HOT-WIRE ANEMOMETRY AND LARGE EDDY SIMULATION

A thesis submitted for the degree of Doctor of Philosophy

By

Ehsaan Farsimadan

School of Engineering and Design, Department of Mechanical Engineering, Brunel University

August 2008

For my mother and father...
Thank you for giving me the opportunity to get this far

Abstract

The broad aim of the work presented in this thesis is to investigate the wake of an airfoil under the combined effects of streamwise curvature and pressure gradient. This was accomplished by an experimental investigation using hot-wire anemometry and large eddy simulation (LES). The wake was generated by placing a NACA 0012 airfoil in a uniform stream of air, which is then subjected to an abrupt 90^o curvature created by a duct bend.

The experimental work was conducted in a subsonic open-return type wind tunnel. The test section measured 457 mm × 457 mm in cross-section and consisted of a 90^o bend with radius-to-height ratio of 1.17. The symmetrical airfoil was of chord length (c) 150 mm, and its trailing edge was located one chord length upstream of the bend entry. The effects of airfoil angle of attack and mainstream velocity on the mean velocity and turbulence quantities of the near-wake were examined. In addition, the mean velocity and turbulence intensity profiles of the boundary layer on the upper surface of the airfoil were measured.

In the numerical investigation, the three-dimensional, incompressible turbulent flow in the duct was computed using the finite volume method. The effect of modelling parameters, namely, grid resolution and sub-grid scale (SGS) model were studied. Three different sub-grid scale models were employed, namely, the classical Smagorinsky, its dynamic variant (DSMG) and the dynamic kinetic energy transport. The effect of grid resolution was assessed by conducting simulations with the DSMG model on three different grids. The first two grids incorporated the full spanwise extent of the duct ($3c$), and the third grid comprised a reduced spanwise segment ($0.5c$) with periodic conditions set in the spanwise direction. A bounded central differencing scheme was employed for the discretization of the convection terms. The temporal discretization was by a second-order implicit method that incorporated a forward difference approximation. The performance of LES in depicting the experimental flow was assessed and compared with the results predicted by the Reynolds Stress Model.

The experimental profiles at zero angle of attack revealed the differing effects of curvature on the mean and turbulence quantities in the inner-side and outer-side of the wake. The spanwise distributions of mean velocity and turbulence intensity, in the near-wake, indicated variations with identifiable peaks and troughs which corresponded to the presence of streamwise vortices in the wake. The spanwise variations were larger on the inner side of the wake and significantly reduced on the outer side. The results showed that close to the trailing edge, the

dominant effect on the wake was from the airfoil boundary layer, whereas one chord length downstream of the trailing edge, it was the effect of curvature and pressure gradient from the duct which was dominant.

The results from the numerical study showed the advantages of LES over Reynolds-averaged Navier-Stokes methods in predicting separation on the convex wall of the bend on relatively coarse grids, but also shortcomings in the prediction of the wake parameters. The dynamic variants of the SGS models were more accurate in predicting the flow in the wake. On a considerably finer grid with near-wall airfoil grid spacings of $\Delta x^+ < 80$, $\Delta y^+ < 0.5$, and $20 < \Delta z^+ < 50$, LES resulted in much improved comparisons with the experimental data. The improved prediction of the wake parameters was attributed to the improved simulation of the boundary layers on the upper surface of the airfoil. However, the effect of the reduced spanwise extent resulted in a lack of prediction of separation on the convex wall of the duct.

Contents

Page

Acknowledgements

I would like to thank my supervisor Dr. M. R. Mokhtarzadeh-Dehghan for his continued support, encouragement, reading and correction of the thesis, supervision of the work and the advice provided over the course of the study. These contributions have served to significantly improve the presentation quality and standard of the thesis. Also, thanks to my second supervisor Dr. Xi. Jiang for his helpful discussion and advice during the programme of research.

I am grateful to the head of research, Professor. L. Wrobel for offering me the position as a research student in the School of Engineering and Design, and the financial support from Brunel University.

I would like to thank the technicians and administrative staff of the Mechanical Engineering Department, particularly Mr. Kevin Robinson for the support of the experimental work, and Mr. John Morse in the support and maintenance provided for the COMPUSYS cluster used in the numerical work.

Special thanks to Mr. Graham Hassall and Robert Jaryczewski from DANTEC Ltd for their kind visits and technical support with respect to the use of the hot-wire anemometry system employed in the experimental investigation.

I am deeply grateful to my mother Dr. Farkhondeh Farsimadan, my father Mr. Nourhmohamad Farsimadan, my sisters Golshan, Mona and Elaahe, and my wife Sara, for their invaluable support and encouragement during my PhD studies.

Last, but not least I would like to acknowledge my colleague, Mr. Syoginus Aloysius in the School of Engineering and Design, with whom I have had the pleasure of working alongside.

Declaration

The work presented in this thesis has not been previously submitted for a degree or other qualification of any university or institution.

Nomenclature

A	King's law constant, Cross-sectional area, Constant
$A^{'}$	Modified King's law constant
A	WW wall function constant
A_t , A_ε	Constant in the two-layer zonal model
a	Matrix coefficient
$\overline{ab}, \overline{a'b'}, \bar{a}\bar{b}$	Terms from the ensemble rule of averaging for two properties a and b
B	King's law constant, Constant
B	WW wall function constant
$B^{'}$	Modified King's law constant
b	Wake width, Mass flow rate into a cell
b'	Wake half-width
C	Dimensionless constant, Convective term
C_o, C_1, C_2, C_n	Calibration constants of the nth order polynomial,
C_1, C_2, C_3, C_4	Turbulence model constants
C_{ij}	Convection term in the pressure strain equation of RSM, Cross stress tensor representing the interactions between the large and small scales in LES
C_μ	$k-\varepsilon$ model constant
C_D	$k-\varepsilon$ model constant
C_f	Friction coefficient
C_l	Constant in the two-layer zonal model
C_w	Heat capacity of the wire
C_s	Smagorinsky-Lilly constant
C_k	Dynamic parameter in DKET model
C_ε	Dynamic parameter in DKET model
C_v	Smagorinsky-Lilly parameter
C_p	Pressure coefficient
c_s	Dynamic parameter in DSMG model
c	Airfoil chord length, Constant
D_h	Hydraulic diameter
D	Cross-sectional width

D_i	Diffusion coefficient
D_{ij}	Turbulent diffusion term in RSM transport equation
d	Diameter, Distance
E	Output bridge voltage, Square of the error
E	Log-law constant
E_{AD}	Analogue to digital input voltage range
E_{corr}	Temperature corrected bridge voltage
e_{ij}	Rate of strain tensor in the eddy viscosity hypothesis
F_i	Convective mass flux
f	Under-relaxation factor
f_o	Reference scale frequency
$\overline{G}(r)$	Grid filter function
$\tilde{G}(r)$	Test filter function
g	Gravitational acceleration
H	Duct height
h_i	Duct half-height
h	Thickness, Heat transfer coefficient
I	Current
K_o	Kolmogorov constant
K_{test}	Subtest scale turbulence kinetic energy
k	Turbulence kinetic energy
k_{sgs}	SGS turbulence kinetic energy
k_1	Yaw coefficient
k_h	Pitch factor coefficient
$\vec{L}$	Periodic length vector
L_{ij}	Leonard stress tensor representing the interactions between the large scales
M_{ij}	DSMG model parameter
N_x, N_y, N_z	Number of nodes in the streamwise, normal and spanwise directions
n	King's law constant, Resolution of the data acquisition board, Normal direction
N	Number of samples, Number of harmonic functions representing the turbulence spectrum

O_{ij}	Rotation term in RSM transport equation
$\mathbf{P}_k$	Shear production of k in the $k-\varepsilon$ model and DKET model
P	Pressure
P_a	Ambient pressure
P_o	Reference ambient pressure
$\overline{P}$	Time-averaged/ spatially filtered pressure
$\tilde{\overline{P}}$	Test filtered pressure
P_{ij}	Shear production term in RSM transport equation
P^*	Guessed pressure
P^{**}	Correct pressure field
P'	Pressure correction
$\tilde{p}$	Periodic pressure
p'	Fluctuating pressure
$\dot{Q}$	Rate of heat transfer to the surroundings
Q_i	Thermal energy stored in the wire
Re	Reynolds number
R	Radius of curvature, Universal gas constant
R_w	Wire resistance
R_1, R_2	Bridge top resistance
R_3	Bridge overheat resistance
R_{ij}	Reynolds stress tensor, $\overline{u_i' u_j'}$
R_ϕ	Scaled residual for a single computational cell
R_C	Unscaled residual for the continuity equation
r	Length
$\vec{r}$	Position vector
S	Source term
$\overline{S}$	Spatially filtered local shear
$\overline{S}_{ij}$	Rate of strain tensor for the resolved scales
$\tilde{\overline{S}}_{ij}$	Test filtered rate of strain tensor $\overline{S}_{ij}$
SR	Sampling rate
s	Streamwise coordinate

T	Time interval
T_{ij}	Subtest scale stress associated with the larger resolved scales
T_a	Ambient temperature
T_{cal}	Ambient temperature of air during calibration
T_w	Temperature of the wire
t	Time
U_o	Mainstream velocity
U_e	Effective cooling velocity
U_{cal}	Calibration velocity
$Urms$	Streamwise turbulence intensity, $\sqrt{\overline{u'^2}}$
U_i, U_j, U_k	Velocity tensor
$\overline{U}_i, \overline{U}_j, \overline{U}_k$	Time-averaged/ spatially filtered velocity tensor
$\tilde{\overline{U}}_i, \tilde{\overline{U}}_j, \tilde{\overline{U}}_k$	Test filtered velocity tensor
$\boldsymbol{U}$	Velocity vector
U, V, W	Instantaneous velocity component in the x-, y- and z- directions
$\overline{U}$, $\overline{V}$, $\overline{W}$	Time-averaged/ spatially filtered velocity components in the x-, y- and z-directions
U_N, U_T, U_Z	Velocity components in normal- tangential- and spanwise-directions of the hot-wire sensor
U_1, U_2	Velocity components in probe coordinate system
U^*	Guessed velocity
U^{**}	Correct velocity field
U'	Velocity correction
U_1	Resolved tangential velocity at the centroid of the first cell from the wall
u_τ	Friction velocity
u^+	Non-dimensional velocity
u', v', w'	Fluctuating velocity component in x-, y- and z- directions
$\overline{u'^2}$, $\overline{w'^2}$, $\overline{v'^2}$	Time-averaged fluctuating velocity component x-, y- and z- directions
$-\overline{u'v'}$	Turbulence shear stress
$-\overline{u'w'}$	Turbulence shear stress
V	Volume

Vrms	Normal turbulence intensity, $\sqrt{\overline{v'^2}}$
$-\overline{v'w'}$	Turbulence shear stress
Wrms	Spanwise turbulence intensity, $\sqrt{\overline{w'^2}}$
w_o	Maximum velocity defect
X	Streamwise distance from station 1
X_o, Y_o, Z_o	Reference cartesian coordinates
x, y, z	Cartesian coordinates
x', y'	Cross-wire probe axes
Y_a	Normal distance from the upper surface of the airfoil
y^+	Non-dimensional normal distance from the wall
y_1	Normal distance from the wall to the first grid point

Greek symbols

δ_o	Boundary layer thickness at the start of curvature
δ	Boundary layer thickness
δ_2	Momentum thickness
δ_{ij}	Kronecker delta
δ_x	Distance between cell nodes
δ_P	Width of the cell P (δ_W and δ_E for the width of cell W and E, respectively)
Γ	Diffusion coefficient
ε	Rate of dissipation of turbulence kinetic energy
ε_{ij}	Rate of dissipation term in RSM transport equation
ε_{sgs}	Rate of dissipation of sub-grid scale turbulence kinetic energy
ε_{test}	Rate of dissipation of subtest scale turbulence kinetic energy
α	Airfoil angle
α_{tot}	Total relative uncertainty
α_i	Relative uncertainties associated with the experimental setup
α_{Pcal}	Relative uncertainty of velocity calibrations with the streamline calibrator
α_{Rcal}	Relative uncertainty of velocity calibrations conducted in the wind tunnel
α_{Tcal}	Relative uncertainty from tunnel calibration
α_{lin}	Relative uncertainty associated with the curve fitting error

α_{pos}	Relative uncertainty due to probe misalignment (α_{Spos} for a single probe and α_{Rpos} for the rake)
α_{Hpos}	Relative uncertainty associated with the alignment of the rake housing
α_{A}	Relative uncertainty in the airfoil alignment
α_{Stemp}	Relative uncertainty in sensor temperature due to changes in the ambient temperature
$\alpha_{\rho temp}$	Relative uncertainty due to changes in air density with temperature
α_{P}	Relative uncertainty due to changes in ambient pressure
$\alpha_{A/D}$	Relative uncertainty as a result of the A/D board resolution
α_{ij}	DSMG model parameter
θ	Uncertainty angle
θ	Variable in QUICK scheme, Flow angle
$\overline{\theta}$	Mean angle between hot-wire sensor and x-axis
Δx	Length interval
Δx^+, Δy^+, Δz^+	Non-dimensional wall units in the streamwise, normal and spanwise directions
Δt	Time-step
Δh_w	Pressure difference
ΔT	Temperature difference
$\overline{\Delta}$	Grid filter width
$\tilde{\Delta}$	Test filter width
ρ	Density
ρ_a	Density of air
ρ_w	Density of water
μ	Dynamic laminar viscosity
μ_t	Dynamic turbulent viscosity
τ_w	Wall shear stress
τ_{ij}	Viscous stress component
$\overline{\tau}_{ij}$	Time-averaged viscous stress component
ϕ	Variable parameter
$\overline{\phi}$	Time-averaged value of a variable ϕ

ϕ'	Fluctuating part of variable ϕ
$\overline{\phi'}$	Time-averaged value of the fluctuations ϕ'
ϕ_{ij}	Pressure strain interaction term in RSM transport equation
ℓ	Length scale (ℓ_t and ℓ_ε in the two-layer zonal model)
ℓ_s	Smagorinsky length scale
υ	Velocity scale
μ_{eff}	Effective viscosity
σ_k	Turbulent Prandtl number in k -transport equation
σ_ε	Turbulent Prandtl number in ε -transport equation
σ_{ij}	SGS stress tensor
$\tilde{\sigma}_{ij}$	Test filtered SGS stress tensor
κ	von Kàrmàn constant
β_{ij}	DSMG model parameter
β	Pressure gradient
v	Kinematic viscosity
ω_k	Angular velocity
ω_x, ω_z	Streamwise and spanwise vorticity component

Subscripts

a	Ambient conditions
CD	Central-difference
i, *j*, *k*	Tensor notation
k	Turbulence kinetic energy
nn	Nearest neighbour
o	Reference value
P	Current point or node
t	Turbulent flow condition
UP	Upwind
W	West node of a control volume (*E* for east node)
w	wire, water, west face of a control volume (*e* for east face)

Superscripts

/	Correction, Fluctuation
+	Non-dimensionalized variables

Acronyms

A/D	Analogue to digital
BNC	Bayonet Neill-Concelman
CC	Constant current
CCA	Constant current anemometry
CFD	Computational fluid dynamics
CFL	Courant-Friedrichs-Lewy
CGNS	CFD General Notation System
CPU	Central processing unit
CT	Constant temperature
CTA	Constant temperature anemometry
DC	Direct current
DSMG	Dynamic Smagorinsky model
DKET	Dynamic kinetic energy transport model
DNS	Direct numerical simulation
LDA	Laser Doppler anemometry
LES	Large eddy simulation
LESFOIL	Large eddy simulation of flow around an airfoil
NACA	National Advisory Committee for Aeronautics
ONERA	Office National d'Etudes et de Recherches Aérospatiales
PIV	Particle image velocimetry
QUICK	Quadratic Upwind Interpolation for Convective Kinetics
RANS	Reynolds-averaged Navier-Stokes
RMS	Root mean square
RSM	Reynolds stress model
RFG	Random flow generation
RAM	Random access memory
SGS	Sub-grid scale
SIMPLEC	Semi-Implicit Method for Pressure Linked Equations
SMG	Smagorinsky model
SSS	Statistically steady state

URF	Under-relaxation factor
TKE	Turbulence kinetic energy
WALE	Wall-adaptive local eddy-viscosity
WW	Werner and Wengle

Chapter 1

1. INTRODUCTION

1.1. Background

Turbulent flows that develop without the direct influence of a solid wall can be described as free turbulent flows. These are among the simplest turbulent flows encountered in engineering applications, of which examples include mixing layers, jets and wakes. A mixing layer forms when two fluids moving at different speeds but in the same direction come into contact. The discontinuity between velocity streams gives rise to the formation of a turbulent mixing layer further downstream. A jet forms when a fluid is issued from a small opening such as a nozzle into the surrounding fluid. The velocity within a jet is higher than the surrounding fluid. A wake forms behind a body placed in a fluid stream, when the boundary layers on the upper and lower surfaces of the body come into contact past the trailing edge (Figure 1.1). The local velocity in the wake is smaller than that of the mainstream velocity, and due to the mixing and entrainment of the surrounding fluid into the wake, the wake spreads in the cross streamwise direction as the distance from the body is increased. The formation of the wake is a consequence of the upstream airfoil boundary layers.

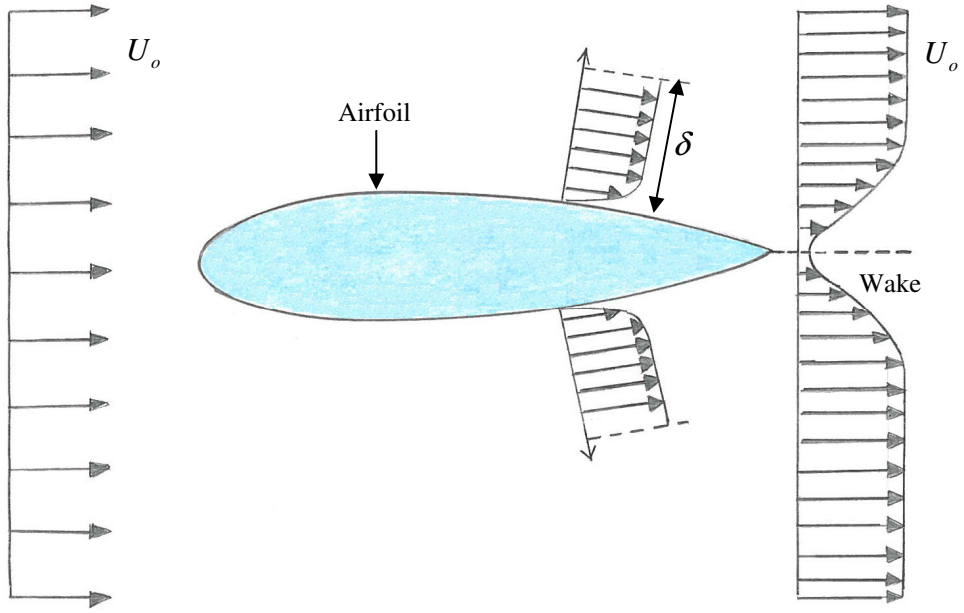

Figure 1.1: The formation of a wake past an airfoil

Flow separation from a solid body forms one of the most fundamental processes in fluid dynamics. The separation of a steady two-dimensional laminar boundary layer was first

explained by Prandtl (1904). Prandtl described flow separation as a result of the boundary layer formation. Within the boundary layer viscous effects are dominant, but in the freestream region viscosity is negligible. The flow is retarded by wall friction and positive pressure gradient effects, while the boundary layer thickness grows with increasing streamwise distance. If the fluid has insufficient momentum to continue it will be brought to rest. At some point the viscous layer departs from the wall (the streamline nearest to the wall breaks away from the body) and the boundary layer separates. The persistence of an adverse pressure gradient will cause reversed flow further downstream. Boundary layer separation is accompanied by a thickening of the rotational flow region near the wall. Downstream of the separation point the shear layer may pass over the region of re-circulating fluid and reattach to the body surface, or a wake may form, where the boundary layer never reattaches to the body.

The present investigation considers the prediction and measurement of both boundary layers and wakes, using an advanced numerical method and experimental technique. In section 1.2 the main characteristics of curved turbulent shear layers are described. Also detailed in this section are the applications and motivations for the present work. Section 1.3 presents an overview of the research that outlines the common practices and the previous work carried out in the context of the present research. The aims, objectives and research contributions are presented in section 1.4. The final part of this chapter gives an outline of the thesis.

1.2. Curved turbulent shear layers

Flows subjected to curvature can be described as complex turbulent flows (Bradshaw, 1976). Boundary layer separation from curved surfaces, and curved wakes, are prime examples of complex turbulent flows.

1.2.1. Boundary layer separation from curved surfaces

Most flows in practical engineering applications involve separation. As stated earlier Prandtl (1904) defined two regions in the fluid flow over a solid surface. The first being the inviscid region, that comprise the main part of the flow, and the second, the thin region near the wall where flow is viscous (i.e. the boundary layer). The development of flow in a boundary layer depends on the distribution of pressure on the walls. If the pressure decreases in the direction of the flow (favourable pressure gradient) then the boundary layer remains attached. On the other hand an increase in pressure in the direction of the flow (adverse pressure gradient) can

cause separation of the boundary layer from the body surface. Figure 1.2 presents the time-averaged characteristics of a laminar separation bubble, courtesy of Horton (1967).

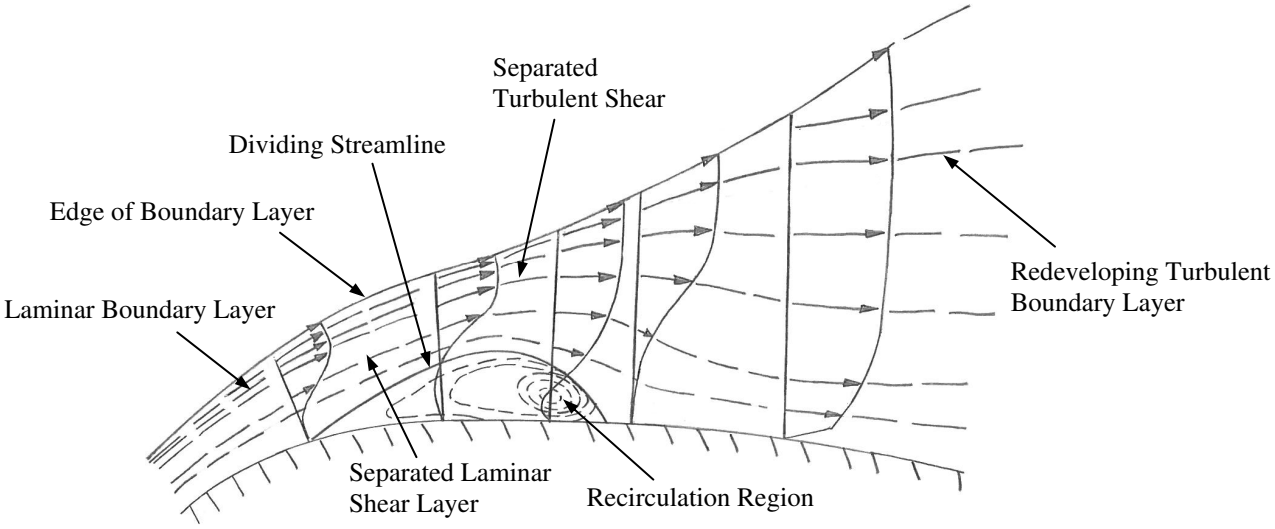

Figure 1.2: Time-averaged characteristics of a laminar separation bubble, Horton (1967)

The laminar shear layer separates from the curved surface at the point where velocity gradient is zero. According to the flow visualization and hot-wire experiments of Brendel and Mueller (1988) and LeBlanc et al. (1987), just beyond this point, the fluid exhibits steady flow behaviour. In the recirculation region, flow is reversed, characterized by the presence of negative velocity in the near wall. The dividing streamline forms a closure between the flow inside and the flow outside the separation bubble. As shown in Figure 1.2, the unsteady shear layer reattaches downstream of the bubble and a turbulent boundary layer starts to develop. For flow over an airfoil, at high Reynolds numbers, typically $\mathrm{Re} > 1\times10^{6}$, laminar to turbulent transition on the curved surface occurs at the onset of adverse pressure gradient (Gad-el-Hak and Bushnell, 1990). At lower chord Reynolds numbers, depending on the surface curvature, and hence the severity of the adverse pressure gradient, laminar separation may take place prior to transition. For sufficiently low Reynolds numbers the separated flow does not reattach to the surface. In the intermediate range of Reynolds numbers, $10^{4} < \mathrm{Re} < 10^{6}$, transition can take place in the wake past the trailing edge.

1.2.2. Wakes

Chevray and Kovasznay (1969) conducted the first extensive experimental study of the wake of a thin flat plate. The importance of wake flows behind streamlined bodies, such as an airfoil or flat plate, has led to considerable research on wakes. The following part describes the main characteristics of the wake of a flat plate. Ramaprian et al. (1982) found that the asymptotic stage (far-wake region) is at a distance of $x/\delta_2 \geq 350$, where δ_2 is the boundary layer

momentum thickness and x is the streamwise distance from the trailing edge. Alber (1980) divides the region between the far-wake and the trailing edge of the body into two regions, the near-wake and the intermediate-wake region, as indicated in Figure 1.3.

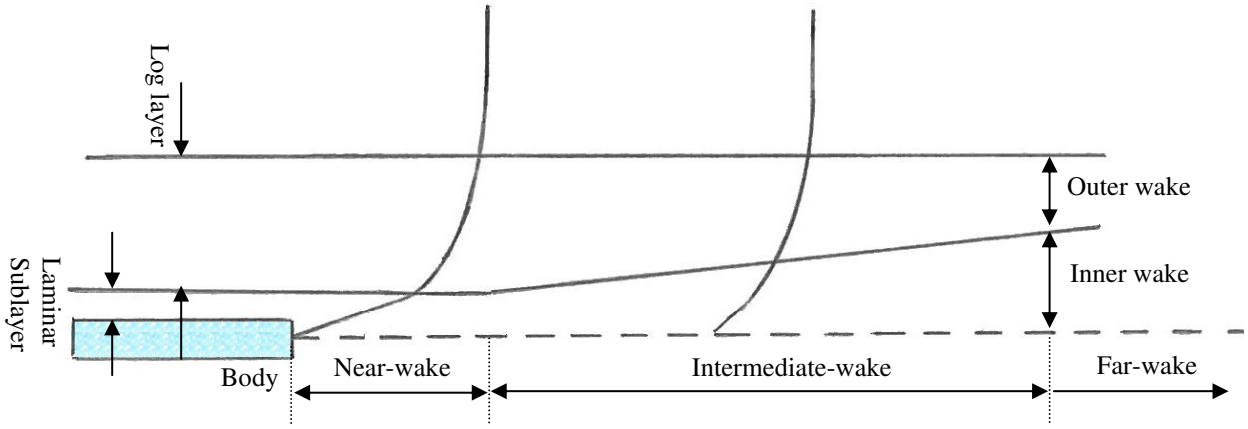

Figure 1.3: The wake regions of a flat plate, Alber (1980)

The length of the near-wake was reported to be about ten laminar sublayer thicknesses, measured from the trailing edge past the flat plate. Ramaprian et al. (1982) reported the near-wake to extend to $x/\delta_2 = 25$. In the intermediate-wake region $(25 \le x/\delta_2 \le 350)$ the turbulent inner layer grows into the initial logarithmic layer of the boundary layer formed on the body. The wake develops as a free turbulent flow in this region, and Alber (1980) reported the length of this region to be approximately ten initial boundary layer thicknesses.

There have been a large number of studies concerned with straight wakes. In practice, however, a turbulent wake may be subjected to extra rates of strain due to streamwise curvature and pressure gradient. The work of Ramjee and Neelakandan (1990), Tulapurkara et al. (1994), Weygandt and Mehta (1995), and more recently Piradeepan and Mokhtarzadeh-Dehghan (2005), have shown that the mean and turbulence quantities are significantly affected by these extra rates of strain.

1.2.3. Applications and motivations for research

The present research is motivated by the needs of industry, such as aerospace, turbomachinery, and building services industries. The experimental and numerical studies of curved wakes are particularly important because of the numerous applications in the aircraft industry. The wake produced by the main airfoil section in a multi-element airfoil, during high lift conditions, under the combined effects of curvature and pressure gradient, interacts with the flow over the trailing edge flaps. Therefore, one seeks to achieve a better understanding of the flow around

an airfoil in the high lift condition. The research into curved wakes is also of interest to the field of turbomachinery. It is well known that the wake generated by the blade of an impeller or diffuser is influential on the boundary layer behaviour and the heat transfer characteristics of the blades positioned downstream of the wake. The impact that this presents on the efficiency of the turbomachine has led to the development of advanced numerical modelling techniques that require validation with experimental data in basic configurations. Curved wakes are also common in bends with guide vanes, heat exchangers and the intake of an aircraft engine.

Boundary layer separation is important to the performance of air, land or sea vehicles, and turbomachines. The large energy losses associated with boundary layer separation means that the performance of many practical devices is dependent on the separation location. It is commonly known that if separation is postponed, drag is reduced, stall is delayed, lift of an airfoil at high angles of attack is enhanced and the pressure recovery in a diffuser is improved. The research into separation phenomenon is beneficial in the design of propellers, windmills, helicopters, and axial flow compressors. The present motivation in the aerospace industry, in relation to the design of an aircraft, is to reduce the engine power and noise at take-off, to shorten the run ways, and to reduce the approach speed. Within the building services industry curved turbulent flows take place in heat exchangers, ventilation ducts, and air-conditioning systems. In these applications heat transfer properties are directly affected by the air flow, separation, and the development of secondary flow in the duct.

The broad aim of the present research is to seek a better understanding of the complex turbulent flows, and, therefore, to initiate the design of more efficient energy saving devices.

1.3. Overview of the research

As was stated earlier, flows subject to curvature are complex flows. A lack of understanding of the effects of curvature has consequences in modelling such flows. A range of experimental techniques and numerical methods have been used to study complex turbulent flows. The majority of the earlier studies were experimental and often involved the insertion of a body in a wind tunnel coupled with the appropriate measurement tools. The advancement of computer technology has led the way for the development of numerical models which have been used to study more intricate flow details. Computational fluid dynamics (CFD) has attracted the attention of the engineering and design industry. The method has become widely accepted as a

design and visualisation tool that can be used to confirm compliance of a system or a product with the relevant standards.

Among the experimental techniques, constant temperature anemometry (CTA), laser Doppler anemometry (LDA) and particle image velocimetry (PIV) are all valid techniques. The choice of the experimental method is dependent on the availability of the equipment, cost, the type of measurement, and the level of precision required. The methods of PIV and LDA are both non-intrusive laser optical techniques that can be used for the measurement of velocity, turbulence, and temperature. On the other hand CTA is a point measurement technique, appropriate for the measurement of flows with very fast fluctuations at a point, where flow structures down to the order of one-tenth of a millimetre can be resolved.

The available numerical methods, namely the Reynolds-averaged Navier-Stokes (RANS) technique, large eddy simulation (LES) and direct numerical simulation (DNS), rely heavily on the experimental data as input for boundary conditions and for validation. Over the last two decades, the models within the traditional RANS approach have developed significantly and become sufficiently robust to enable an accurate prediction of a wide range of turbulent flows. Consequently, this method has been incorporated into commercial CFD packages, such as FLUENT, and is used to study practical flows and large-scale problems. However, it is well known that RANS has its shortcomings, especially in the prediction of unsteady separation and complex turbulent flows that are affected by curvature.

More recently, with the availability of increased computer memory, power and storage, research has enabled the development of advanced numerical methods such as LES and DNS, although, to some extent, these advanced techniques are often associated with academic problems and are still undergoing validation and development for more general applications. LES has its advantages, in that it can predict flow separation successfully, in situations where large scale structures play a major role. Furthermore, with implementation into CFD codes, the method has been used to highlight the limitations of RANS methods in predicting such flows. The main disadvantage of these higher order methods is the time and cost associated with obtaining a converged solution. This is especially the case with DNS, which is at present limited to simple geometries and low Reynolds numbers. In the industry the common practice is to adopt the RANS method due to the relatively low computer memory requirement, power and turn-around time for simulations. However, the expectation is that, with further development, LES will eventually replace RANS as the preferred prediction tool in industry.

The present numerical investigation assesses the capabilities of LES methods in the prediction of complex turbulent flows. The experimental investigation provides data for direct validation of the simulations.

1.3.1. Outline of the previous work

Before a detailed review of the previous experimental and numerical works is presented in Chapter 2, a brief overview of the most important publications in the context of the present research is first presented here. The majority of research over the past two decades has considered two-dimensional straight wakes. The growing interest in the development of turbulence models to predict curvature and pressure gradient effects on a wake has motivated further research in this area, and led to an increase in published experimental data on curved wakes. Most of these works consider the wake of a cylinder or an airfoil at zero angle of attack. The combined effects of curvature and pressure gradient on the wake of bluff bodies have been reported by numerous researchers, namely, Savill (1983), Nakayama (1987), Tulapurkara (1995), Stark et al. (1999), and John and Schobeiri (1996). The wake of a NACA 0012 airfoil subject to curvature and pressure gradient has been studied by several researchers including, Ramjee et al. (1988), Ramjee and Neelakandan (1990), Tulapurkara et al. (1994) and Weygandt and Mehta (1995). More recently, Piradeepan (2002) studied the flow configuration shown in Figure 1.4, which is also the configuration adopted in the present study.

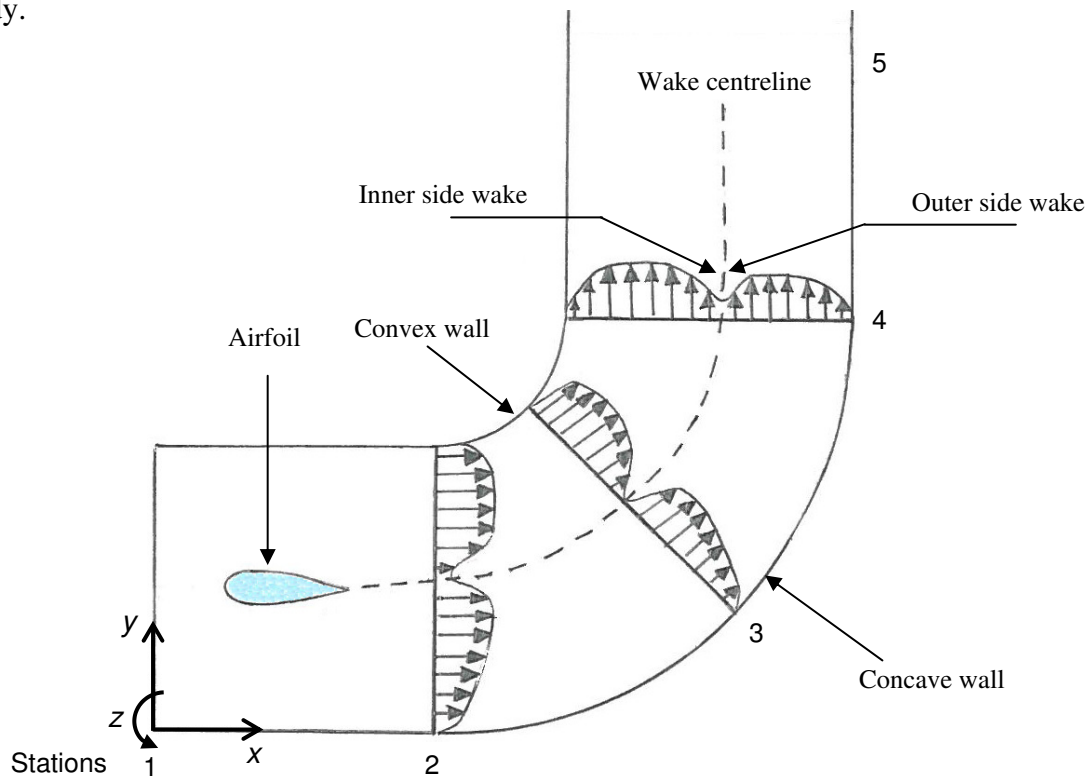

Figure 1.4: The wake of an airfoil developing in a bend.

The duct shown in Figure 1.4 consisted of five measuring stations. The airfoil was placed in the upstream straight section, between stations 1 and 2. Piradeepan (2002) measured the mean and turbulence quantities at each measurement station for the wake developing under the effects of streamwise curvature and pressure gradient, as shown in Figure 1.4. The effect of increased mainstream velocity on the wake was also considered. Findings were generally in agreement with previous researchers, for the effect of curvature on the wake, that is, enhancement of turbulence on the inner side and its suppression on the outer side. The inner- and outer- side regions of the wake correspond to the regions between the centre line of the wake and the convex and concave walls, respectively. Some quantitative differences were reported in the profiles, compared to Tulapurkara et al. (1994), which were attributed to the state of the boundary layers on the airfoil.

Numerical studies on curved wakes are fewer than experimental ones. The majority have adopted the RANS method. Rhie and Chow (1983) computed the turbulent flow past airfoils with and without trailing edge separation. Their results highlighted the requirement of better turbulence models over the standard $k-\varepsilon$ model in the computation of flows with separation. Narasimhan et al. (1991) and Tulapurkara et al. (1996) carried out investigations in the curved wake of an airfoil using the standard $k-\varepsilon$ model. These computations were able to capture the asymmetry in the mean velocity profile. Differences between turbulence quantities and experimental data were related to the weaknesses of the $k-\varepsilon$ model and its inadequate response to curvature and pressure gradient. In the above studies, the experimental data at trailing edge of the airfoil was used to prescribe the inlet condition. Piradeepan (2002) computed the three-dimensional flow domain in Figure 1.4, as occurred in the experimental investigation, using several RANS turbulence models. In these simulations mean velocity and turbulence quantities measured upstream of the airfoil were used to define the inlet boundary conditions. This method allowed the wake to develop from the boundary layers on the airfoil, thus testing further the performance of turbulence models in the prediction of complex turbulent flows. The results in the wake indicated qualitative agreement between numerical and experimental data. Quantitative differences were found to originate from the difficulties in modelling the laminar boundary layer and the transition on the airfoil. Further discrepancies were evident on the convex wall in the region were separation had occurred.

As stated earlier LES is an advanced numerical technique that can be used for the prediction of complex turbulent flows. In LES the large and medium scales of the flow are fully resolved, whereas the effect of the unresolved scales is modelled. The method falls between the fully

modelled approach of RANS and the fully resolved scheme of DNS. Studies concerning LES of flow past an airfoil have focused mainly on straight wake or high angle of attack configurations. The high lift configuration of the Aerospatiale A-airfoil has been investigated by several researchers, namely, Dahlström and Davidson (2000), Fröhlich and Mellen (2001) and Mary and Sagaut (2002). In these studies LES has been used to compute the flow around the airfoil at an angle of 13^o for high Reynolds numbers of the order $\mathrm{Re} = 2\times10^6$. The understanding from these studies is that successful simulations of high Reynolds number airfoil flows at near-stall angles of attack are only possible when a very fine near-wall grid resolution is adopted, especially in the spanwise direction. In most cases this was achieved by a reduced spanwise extent. Other researchers have considered the computation of flow over airfoils at lower Reynolds numbers $(\mathrm{Re} = 1\times10^5)$. Jovičić and Breuer (2004) used LES to predict the wake past an airfoil at an angle of attack of 18^o. The flow separation around a NACA 0012 airfoil inclined at an angle of 4^o was computed by Shan et al. (2005) using DNS. More recently, Marsden et al. (2006) presented large eddy simulations of flow around the NACA 0012 airfoil at zero angle of attack. There are very few LES publications that have focused on the wake past streamline bodies, and even fewer on the wake of an airfoil. In fact, to date, there exist no known publications on LES of curved wakes.

There have been a number of recent publications concerning LES of flows in strongly curved ducts. These include the work of Breuer and Rodi (1994), and that of Guleren and Turan (2007) on LES of turbulent flow through a duct with a 180^o bend. Furthermore, Lund and Moin (1996), Hébrard et al. (2004), and Lopes et al. (2006) have conducted similar investigations in *S*-shaped ducts. These studies have indicated that the favourable and adverse pressure gradients in concave and convex curvatures result in significant changes to the profiles of Reynolds stresses. The presence of streamwise vortices on the concave wall and the development of secondary flows have also been reported in these simulations. In general, LES in comparison to RANS is better suited for predicting concave wall boundary layer flows. The RANS models based on the linear Boussinesq relationship between Reynolds stresses and mean velocity gradients fail to capture the streamwise vorticity mechanisms.

1.3.2. Outline of the present work

There is a continuation between the present research and the work of Piradeepan (2002). In comparison with Piradeepan's work, the present study focuses closely on the near-wake region up to one chord length downstream of the trailing edge. The structure of the near-wake under

the influence of curvature and pressure gradient is studied for different airfoil angles of attack, using a more probing experimental technique. Additionally, the airfoil boundary layer is also measured. The motivation behind the experimental investigation is to provide validation data for the numerical study of curved wakes with large eddy simulation, and to further identify the effects of airfoil angle of attack and streamline curvature on the near-wake.

In the numerical part of this investigation LES is used to compute the experimental flow according to the configuration shown in Figure 1.4. Through this, the aim is to assess the capabilities of LES in overcoming the previous inaccuracies reported in RANS simulations by Piradeepan (2002), and to evaluate the performance of the large eddy simulations in the different flow regimes, through comparisons with the experimental data. The simulations presented here consider the curved wake of the airfoil, its boundary layer as well as the flow through the duct with a 90^o bend. The inlet boundary condition is placed upstream of the airfoil, to evaluate the quality with which the laminar boundary layer is resolved using LES, and the downstream effect placed on the wake. This approach is considered to be more practical and will thus yield more realistic information on the capability of LES in predicting complex turbulent flows. LES modelling parameters, namely, the SGS model and grid resolution are investigated. Several features are examined, including the mean and turbulence quantities in the wake, vortical structures and their development in the near-wake, and flow separation on the walls of the duct. Some of these results have already been presented in a recent publication by Farsimadan and Mokhtarzadeh-Dehghan (2008), where the performance of LES in depicting the experimental flow is assessed and compared with the results predicted by the Reynolds Stress Model (RSM). This paper is attached in Appendix I.

1.4. Project aims, objectives and contributions to knowledge

The main aim of the work is to gain a better understanding of the development of the turbulent near-wake of an airfoil under streamwise curvature. To achieve this aim, an extensive experimental and numerical investigation, using hot-wire anemometry and large eddy simulation, was carried out. Using a NACA0012 airfoil as the wake generating body and a 90^o duct bend to produce the curvature, the specific objectives were to:

Experimentally with hot-wire anemometry

- Measure the mean velocity and turbulence quantities at a series of locations in the near-wake.

- Assess the effects of the angle of attack on the near-wake development.

- Study the three-dimensional structure of the wake, and the sensitivities to angle of attack and mainstream velocity.

- Measure the boundary layer development on the airfoil.

Numerically with large eddy simulation

- Compute the flows studied and compare these results with those obtained experimentally.

- Investigate the contributions of the modelling parameters, namely, sub-grid scale models and grid resolution to the quality of the results.

To fulfil the experimental objectives, hot-wire anemometry was employed to obtain the mean velocity and turbulence stresses in the normal and spanwise directions at a series of locations in the near-wake, up to one chord length downstream of the trailing edge. Tests were carried out at a mainstream velocity of 10 m/s for airfoil angle of attack α = -6^o, -4^o, -2^o, 0^o, 2^o, 4^o and 6^o. In addition pressure measurements were carried out to obtain the distributions of static pressure on the upper and lower surfaces of the airfoil for the different angles tested. To study the airfoil boundary layers leading to the wake, profiles of mean velocity and turbulence intensity were taken in the normal direction, at several streamwise locations ranging from the mid-chord to the trailing edge.

The objectives of the numerical investigations were accomplished by computing large eddy simulations of the three-dimensional flow field as occurred experimentally. Qualitative features of the flow in the duct, as resolved by LES, such as the vorticity field and the occurrence of separation were also examined. The results from the large eddy simulations were compared to those predicted by the RANS method, the present experiments and the available experimental data of Piradeepan (2002). The performance of the SGS models, namely, the Smagorinsky model, its dynamic variant and the dynamic kinetic energy transport model, in conjunction with changes in the grid resolution were evaluated.

The following part details the contributions to knowledge.

- The test case is original, and the work presented is the first of its type to consider LES of curved wakes in such a configuration.

- The research assess the current capabilities of LES in computing wakes subjected to curvature and pressure gradient, and makes recommendations for numerical modelling improvements to be incorporated into the FLUENT CFD code for the prediction of such flows.

- The work examines the effect of streamwise curvature on the wake and the sensitivity of the wake to the development of the airfoil boundary layer, and describes the physical flow phenomena, through a series of numerical and experimental investigations, the latter of which also considers the effect of airfoil angle of attack.

- The experimental investigations in the curved duct provide further data for the future validation of CFD codes with respect to complex turbulent flows.

1.5. Outline of the thesis

The thesis comprises eight chapters. Chapter 1 is an introduction to the present work and research objectives. Chapter 2 presents a review of the literature, and is divided into sections covering the previous work on wakes, airfoil boundary layers, and flow in curved ducts. The experimental setup, methodology and instrumentation are described in Chapter 3. In Chapter 4, governing conservation equations, numerical modelling techniques, and discretization schemes are presented. Computational details such as boundary conditions, grid resolution, computer power, time and memory used for the numerical work are presented in Chapter 5. The experimental results and findings are presented in Chapter 6, whereas the discussion of the numerical results and comparison with experimental data are presented in Chapter 7. In Chapter 8, the conclusions and recommendations for further work are presented.

Chapter 2

2. LITERATURE REVIEW

2.1. Introduction

This section presents the background of the earlier work concerning flow over airfoils, the curved wake of streamlined and bluff bodies, and flow in curved ducts. The review is divided into three main sections. Section 2.2 details previous research concerning straight and curved wakes. This section is subdivided into experimental and numerical works. The studies of curved wakes are much fewer than that of straight wakes; this literature survey therefore considers those works that are most relevant to the present research. This is followed by section 2.3 which details the works on flow over streamlined bodies, and section 2.4 which is a review of the studies on flow through curved ducts. Section 2.5 presents the summary and conclusions, establishing the salient points from the review. The main focus of this review is on airfoil boundary layer separation and the generation of turbulent wakes past streamlined bodies.

2.2. Straight and curved wakes

2.2.1. Experimental investigation of turbulent wakes

Curved wake of bluff bodies

The works of Savill (1983), Koyama (1983) and Nakayama (1987) formed the early experimental investigations into the combined effects of curvature and pressure gradient on the wake of bluff bodies. Savill (1983) investigated the wake of a circular cylinder directed round a 90^{o} bend using hot-wire anemometry. The measured profiles of the mean and turbulence intensities indicated a strong influence of streamwise curvature on the wake. Data was presented for the duct central plane only and no spanwise variations of quantities were presented. Koyama (1983) studied the stabilizing (concave) and destabilizing (convex) effects of streamline curvature on laminar and turbulent wakes behind a circular cylinder. Instantaneous smoke streak line patterns and comparisons of mean velocity and turbulence intensity profiles in the straight and curved wakes were presented. Results indicated that the

development of the turbulent wake is promoted on the convex side and suppressed on the concave side. The secondary flow effects which arise as a result of the pressure gradient force acting towards the centre of the curvature and the centrifugal force due to streamwise curvature, contributed to the suppression of the wake on the outer side. Nakayama (1987) studied the wake of a circular cylinder of diameter 1.6 mm with Reynolds number Re = 1550 subjected to a mild pressure gradient and streamwise curvature. It was found that turbulence quantities such as Reynolds shear stress are strongly influenced even by mild curvature and mild pressure gradient.

Ramjee and Neelakandan (1989) investigated the wake of bluff bodies such as rectangular and circular cylinders. Comparisons of turbulence quantities were made for curved and straight wakes. The results showed that the profiles of mean velocity were asymmetric about the centre line of the duct. It was concluded that the velocity defect of the curved wake was larger than that in the straight wake.

The combined effects of curvature and pressure gradient on the wake of a bluff body were studied by Tulapurkara et al. (1995). Their results showed that curvature makes the wake asymmetric and the half-width of the wake is larger on the inner side of the curved wake compared to the outer side. This finding was in agreement with those of Ramjee and Neelakandan (1989). Tulapurkara et al. (1995) further suggested that the presence of pressure gradient contributed to greater wake growth and velocity defect. The decay of velocity defect was not significantly affected by curvature but more so by pressure gradient which reduced the rate of decay of velocity defect. It was concluded that the presence of both curvature and pressure gradient enhanced further the asymmetrical nature of the wake.

Schobeiri et al. (1995, 1996) investigated the wake of a cylindrical rod in a curved channel under zero streamwise pressure gradient. In John and Schobeiri (1996) a similar work was carried out but with a positive pressure gradient. Their results showed that the rate of decay of velocity defect was slower than in the case of curved wake development with zero streamwise pressure gradient. In agreement with Tulapurkara et al. (1995), the growth of the wake width was faster for positive streamwise pressure gradient.

Straight and curved wake of an airfoil

Viswanath et al. (1980) conducted an experimental investigation of the symmetric and asymmetric trailing edge flow past an airfoil-like flat plate of chord 928.9 mm and thickness 25.4 mm, at high Reynolds numbers ($9\times10^6 < Re < 6\times10^7$). A flap located on the rear side of the plate was deflected downwards by 6.25^o to impose a pressure gradient on the developing upper surface boundary layer which resulted in an asymmetric wake. The symmetric case was also computed using eddy viscosity models. The numerical solutions yielded results of comparable quality for the mean velocity and turbulence profiles for the symmetric case, showing the increased effect of viscous interaction in the trailing edge as the Reynolds number is increased. In the asymmetric case the streamwise development of the mean velocity in the near-wake was more in the upper part of the flow. The profiles of turbulence shear stress and turbulence kinetic energy were more pronounced on the upper side.

The near wake of a NACA 0012 airfoil of chord length 200 mm and span 1100 mm was investigated by Hah and Lakshminarayana (1982). Experiments were conducted at a freestream velocity of 30 m/s, corresponding to the chord Reynolds number $Re = 3.8\times10^5$. Hot-wire anemometry was used to measure the mean velocity and turbulence quantities at several centre span locations in the near-wake of the airfoil. The incidence angle of the inlet flow was set at 3^o, 6^o and 9^o, to enable comparison of the asymmetric and symmetric wakes. It was found that the decay rate of the mean velocity defect at the wake centre decreased when the incidence angle was increased. The asymmetrical property within the wake became symmetric at one chord length downstream of the trailing edge. The streamwise curvature arising from the non-zero incidence angle substantially affected the profiles of mean velocity and turbulence quantities, resulting in an increase in turbulence kinetic energy and turbulence shear stress on the upper side, and a decrease on the lower side. The wake of the symmetrical airfoil was also predicted using turbulence models. It was concluded that modifications need to be made to the turbulence closure models to take into account the effect of streamwise curvature.

The development of an airfoil wake in a straight duct and two curved ducts of different radii of curvature (R = 350 mm and R = 700 mm) was investigated by Ramjee et al. (1988). A NACA 0012 airfoil of chord length 100 mm was placed in the straight section of length 600 mm. The freestream velocity in the test section was 15 m/s. At entry to the duct the values of curvature parameter, b/R (b is the wake width), were 0.0286 and 0.0143 for R = 350 mm and R = 700

mm, respectively. The results showed that the mean velocity profile of the wake was asymmetric and that the velocity defect and wake width was larger in curved ducts than in straight ducts. The streamwise intensity was enhanced on the inner side compared to the outer side. The inner side represents the region between the wake centre line and the convex wall, and the outer side represents the region between the wake centre line and the concave wall. Turbulence shear stresses were not measured in the experiments.

In Ramjee and Neelakandan (1990) a more extensive study was carried out using a NACA 0012 airfoil, a square cylinder (side length 4 mm) and a rectangular cylinder (height 2.5 mm and length 8 mm). A setup similar to that of Ramjee et al. (1988) comprising, a straight duct, and two curved ducts was adopted. A trip wire of diameter 0.8 mm was attached along the span on the upper and lower surfaces of the airfoil at 0.3c from the leading edge, where c is the chord length. Tripping the boundary layer promoted the development of the turbulent wake beyond the trailing edge. Comparisons were made to the earlier work of Ramjee and Neelakandan (1989) on bluff bodies. The maximum velocity defect was larger in the curved wakes than in straight wakes. In the curved wake experiments, the half-width of the wake on the inner side was greater than the half-width on the outer side. The turbulence shear stress was increased on the inner side of the curved wake and reduced on the outer side, compared to that of the straight wake. Comparisons were made for the variation of turbulence shear stress in the wake of the square cylinder, rectangular cylinder and that of the airfoil. The results showed a greater peak in the cylinder wake than in the wake of an airfoil.

Tulapurkara et al. (1994) investigated the development of a wake in the presence of both curvature and pressure gradient. Curved and straight ducts similar to those used by Ramjee et al. (1988) were used. Additionally, a curved diffuser with an area ratio of 1.74 and turning angle of 60^{o} was employed; in this case the curved wake was subjected to both curvature and pressure gradient. The boundary layer over a NACA 0012 airfoil (c = 100 mm) was tripped at 30% of the chord length and experiments were conducted for a freestream velocity of 15 m/s. The presence of an adverse pressure gradient caused slower decay of the velocity defect. It was found that the half-width of the wake was increased on the inner side and decreased on the outer side. They concluded that the effect of curvature was to make the Reynolds stresses and turbulence kinetic energy profiles more asymmetric with increasing streamwise distance. The additional presence of an adverse pressure gradient increased the extent of the wake asymmetry.

The mean velocity and turbulence properties at the trailing edge of an NLR 7702 airfoil (chord length 600 mm) were presented by Absil and Passchier (1994). Their aim was to attain flow data for the development of turbulence models. The airfoil was placed inside a low turbulence tunnel at an angle of 4^o to the flow (trailing edge down). Measurements were conducted for a chord Reynolds number Re = 1.47×10^6. The merging of the upper and lower surface boundary layers formed a highly asymmetric wake where the half-width of the wake was increased on the upper side compared to the lower side. The profiles of mean velocity and Reynolds stresses were also further enhanced on the upper side of the wake compared to the lower side. The wake became more symmetric with increased distance from the trailing edge. The main characteristic features of the leading edge separation bubble were detected from the airfoil surface pressure distributions.

Huang and Lin (1995) investigated experimentally the vortex shedding from a finite NACA 0012 wing at low Reynolds numbers. The airfoil was of chord length 60 mm and span length 300 mm. The flow over the wing was subjected to boundary layer and wing tip effects. Smoke wire and surface oil flow techniques were used to visualise flow patterns and evolution of vortex shedding. Chord Reynolds numbers in the range $3000 < Re < 80000$ were investigated for several angles of attack. In these experiments, separation was observed near the trailing edge. The location of the separation point moved towards the leading edge with increased angle of attack. At $\alpha = 7^o$ for Re = 3195 no reattachment was observed and the presence of unsteady flow structures in the near-wake region was noted, where vortices were reported to shed alternatively from the upper and lower shear layers developing from the trailing edge. At higher angles of attack, the mixing and fluctuations were stronger in the separated flow region, with paired structures developing in the near-wake. For small angles of attack no separation was reported.

Weygandt and Mehta (1995) studied the three-dimensional tripped and untripped structure of straight and mildly curved flat plate wakes at a Reynolds number Re = 28000. The flat plate was approximately 3100 mm long. The curved test section was of mean radius R = 3050 mm giving $b/R < 2\%$. The boundary layers were tripped on both sides of the plate using a 1.5 mm diameter round wire located 18 mm upstream of the trailing edge. The results confirmed the sensitivity of wake structure to initial conditions. The untripped wakes were three-dimensional in the near field with large spanwise variations observed in the wake velocity defect and Reynolds stresses. These features decayed in magnitude with increased streamwise distance. Counter-rotating streamwise vortices were observed on both sides of the untripped wake. In

the straight case, streamwise vortices decayed at the same rate on both sides of the wake. The effect of curvature was to reduce the decay of streamwise vorticity on the inner side of the wake compared to the outer side. The wake from the tripped case appeared to be two-dimensional, where no significant spanwise variations were present; streamwise vorticity was not indicated in either straight or curved wake measurements. In the untripped wakes a smaller maximum velocity defect was measured, and considerably larger magnitudes were reported in the profiles of normal and turbulence shear stress, compared to the tripped case. The effects of curvature on the wake half-width were consistent with the previous findings of Ramjee and Neelakandan (1989, 1990) and Nakayama (1987). Curvature imposed asymmetry in the profiles of Reynolds stresses with enhanced stress levels on the inner side and suppressed levels on the outer side. They concluded that the three-dimensional structure of the untripped wake and the streamwise development of both tripped and untripped cases were significantly affected by mild curvature.

Stark et al. (1999) investigated the curved turbulent near-wake region of a flat plate of chord length 600 mm and width 18 mm. The effects of curvature and pressure gradient were studied systematically. Boundary layers were tripped at $0.06c$ from the leading edge. These experiments showed accurately the known wake characteristics such as the increase in Reynolds stresses and the higher spreading rate on both sides of the wake due to adverse pressure gradient.

Piradeepan (2002) carried out experimental and numerical investigations of a turbulent airfoil wake. Experiments were conducted in a subsonic wind tunnel consisting of a straight section and a 90^{o} duct bend (see Figure 1.4). The tunnel test section had a square cross section 457 mm × 457 mm and the bend incorporated a radius to height ratio of $R/H = 1.17$. The airfoil was placed one chord length upstream of the bend, which had a concave and convex radii of curvature 764 mm and 307 mm, respectively. The experimental findings were reported in Piradeepan and Mokhtarzadeh-Dehghan (2005). Measurements of mean and turbulence quantities in the wake of a NACA 0012 airfoil (chord length 150 mm) were made using hot-wire anemometry. Three mainstream velocities 10, 15 and 20 m/s were tested. The formation of an asymmetric wake, about the wake centre line, was reported. Increasing the mainstream velocity, reduced the half-width of the wake on the inner and outer sides, but resulted in an increase in maximum velocity defect and an increase in the magnitude of Reynolds stresses. These findings were in agreement with previous experiments on curved wakes. However, Piradeepan and Mokhtarzadeh-Dehghan (2005) reported less pronounced double peak profiles

of streamwise and spanwise intensity as well as a smaller maximum velocity defect compared to Tulapurkara et al. (1994) and Ramjee and Neelakandan (1990) who both employed turbulence tripping. Weygandt and Mehta (1995) attributed the less distinguishable double peaks in the untripped cases to the existence of streamwise vortices and large spanwise variations which were known to wash out the double peaks. In the tripped wakes of Weygandt and Mehta (1995) spanwise variations were not present resulting in more pronounced double peaks. The untripped nature of experiments in the study of Piradeepan (2002) was used to explain the differences observed compared to previous research.

Airfoil boundary layer and wake development at low Reynolds numbers were investigated by Yarusevych et al. (2004), experimentally. Experiments were performed in a low turbulence wind tunnel for different Reynolds numbers and angles of attack. A NACA 0025 airfoil of chord length 300 mm was used. Laminar boundary layer separation was detected in all cases. The streamwise location of transition was identified with the position of the largest peak in turbulence intensity. For high Reynolds numbers ($\alpha = 5^o$, Re = 150×10^3), the maximum turbulent fluctuations were recorded at $x/c = 0.72$, where the separated shear layer reattached to the surface of the airfoil resulting in the formation of a separation bubble. At the lower Reynolds number ($\alpha = 5^o$, Re = 100×10^3), transition to turbulence occurred at approximately $x/c = 0.62$ and the separated shear layer failed to reattach, resulting in the formation of a wider wake.

Subaschandar (2005) presented hot-wire measurements in the turbulent near-wake behind an infinitely swept flat plate. The aim was to gain a better understanding of the three-dimensional turbulent near-wake development. The boundary layer on the plate was tripped to promote a fully turbulent boundary layer at the trailing edge. Measurements were carried out at a chord Reynolds number of 1.4×10^6. Comparisons were made to the experiments of Chevary and Kovaznay (1969) and Ramaprian et al. (1982) which were concerned with the two-dimensional wakes of unswept flat plates. The profiles of streamwise velocity in the near-wake resembled those observed in the two-dimensional cases. The variation of the half-width of the wake in the streamwise direction was similar to the two-dimensional cases. However, the far-wake structure was not achieved, that is, the profiles of the normal stresses were different from each other even at the downstream locations. According to Ramaprian et al. (1982), in the far-wake, the non-dimensionalized turbulence quantities should be nearly equal to each other.

Zhang et al. (2004) first investigated the effects of surface roughness on the wake structure of symmetric turbine airfoils at different freestream turbulence intensity levels. Zhang and Ligrani (2004) further described the effects of freestream turbulence and surface roughness on the aerodynamic performance of a symmetrical airfoil. In another study, Zhang and Ligrani (2006) considered the influence of surface roughness and freestream turbulence intensity on the wake structure downstream of a cambered turbine airfoil. The airfoil (chord length 72.7 mm) was placed inside the bend section of a wind tunnel where a flow turning angle of 62.75^{o} was imposed. The resulting wake developed in a straight section downstream of the bend. Tests were conducted at chord Reynolds number $Re = 4 \times 10^5$. Airfoils with different surface roughness properties were employed; these ranged from a smooth surface to one with a large sized roughness. Measurements of wake turbulence quantities were taken at one chord length downstream of the airfoil. In comparison to the symmetrical airfoils, an asymmetry was present in the wake profiles measured downstream of the cambered airfoil. The wake resulting from the upper surface was thicker than that developing from the lower surface. This asymmetry in the profile was attributed to the different growth rates and development of boundary layers on the upper and lower surfaces of the cambered airfoil. The cambered airfoil presented profiles with larger wake velocity defect, increased wake width and enhanced turbulence, when compared to the symmetrical airfoils studied in Zhang et al. (2004) and Zhang and Ligrani (2004), for the same experimental conditions. It was reported that an increase in surface roughness resulted in a larger wake defect and higher turbulence intensity levels. The wake profile of symmetrical airfoils was found to be more sensitive to surface roughness than cambered airfoils. They concluded that the thickening of the boundary layers by the roughness elements and increased separation region near the trailing edge led to a greater momentum dissipation in the wake and larger low frequency vortices.

More recently, El-Gammal and Hangan (2008) investigated the wake dynamics of an airfoil with a blunt and divergent (curved) trailing edge, using hot-wire anemometry. The model was of chord length 1220 mm and span length 1220 mm, and experiments were conducted in an open-return type wind tunnel. Simultaneous multi-point hot-wire measurements were carried out in the near- and intermediate-wake regions. In the near-wake the profiles of mean velocity and turbulence intensity were asymmetric, where the turbulence production levels on the lower side of the wake were higher than those on the upper side. This was attributed to the streamline curvature effect caused by the divergent trailing edge. The freestream turbulence intensity levels were found to have a significant effect on the shape of the turbulence profiles. An increase in freestream turbulence intensity resulted in an acceleration of the development

of the wake towards the asymptotic far-wake stage. Spanwise variations were measured in the distribution of the mean velocity and turbulence intensity, which were attributed to the passage of organised streamwise vortical structures. The peaks and troughs that characterised these spanwise variations were out of phase on the upper and lower sides of the wake, corresponding to the periodic pattern of the vortices in the spanwise direction. Furthermore, the variations were more pronounced on the lower side of the wake, due to the effect of streamline curvature on this side. In the downstream region the variations were less pronounced, but spanwise periodicity was still observed in the profiles. The results were in good agreement with previous studies on the three-dimensional structure of wake flows (Weygandt and Mehta, 1995). They conclude the statistical spanwise distribution of the peaks and troughs to be independent of the freestream turbulence intensity levels and airfoil angle of attack.

2.2.2. Numerical investigation of wakes

Rhie and Chow (1983) studied numerically the turbulent flow past an airfoil. A finite volume numerical method was used for the solution of the steady two-dimensional incompressible Navier-Stokes equations. The main aim of their work was to compute the flow past a NACA 0012 airfoil at $\alpha = 0^o$, 6^o and a NACA 4412 at $\alpha = 13.87^o$. To validate the $k-\varepsilon$ model, comparisons were made with the experiments of Hah and Lakshminarayana (1982), Gregory and O'Reilly (1970) and Coles and Wadcock (1979). The computations for flow past the NACA 0012 airfoil at chord Reynolds numbers of Re = 2.8×10^6 and Re = 3.8×10^5 indicated no separation, although the increase in angle of attack resulted in a thicker viscous layer on the upper surface. For the NACA 4412 airfoil at chord Reynolds number Re = 1.5×10^6, the presence of a separation bubble near the trailing edge was apparent. In these results discrepancies were noted in the profiles of the mean velocity and turbulence shear stress when compared to the experimental data. They concluded that for the simple flow with no separation, the $k-\varepsilon$ model predictions provided good agreement with the experimental data. However, with the presence of separation, the $k-\varepsilon$ model computations tended to yield poorer representation of the flow.

Narasimhan et al. (1991) predicted the wake of a NACA 0012 airfoil in a curved duct. These computations adopted the standard $k-\varepsilon$ model with the model constant C_μ being dependent on the local curvature. The numerical solution was based on the finite volume method. The experimental data obtained at the trailing edge of the airfoil were used as the inlet boundary

conditions, where the profiles of streamwise velocity, turbulence kinetic energy k and its rate of dissipation ε were defined. Features such as the increase in half-width of the wake on the inner side compared to the outer side and the asymmetrical nature of the mean velocity profile were in agreement with experiments of Ramjee and Neelakandan (1989, 1990) and Ramjee et al. (1988). Although the $k-\varepsilon$ model captured the asymmetry in the profiles of Reynolds shear stress and mean velocity, the predicted peak values did not match the experimental values from Ramjee and Neelakandan (1990). It was concluded that the $k-\varepsilon$ model was capable of capturing curved wake characteristics satisfactorily. Adjusting the model constant by making it dependent on local curvature resulted in improved agreement on the inner side but slightly worsened it on the outer side.

The finite volume method with the standard $k-\varepsilon$ model was used by Tulapurkara et al. (1993) to compute the asymmetric wake of an airfoil in turbulent incompressible flow. Comparisons were made with the experiments of Ramaprian et al. (1981). The trailing edge of the airfoil was treated as the inlet to the flow domain. These computations indicated that the shift in the point of minimum velocity in the wake (wake centre) was sensitive to the value of normal velocity defined at the trailing edge (inlet). Tulapurkara et al. (1993) concluded that making the model constant C_μ a function of streamwise curvature had a marginal influence on the results, a finding which was also reported by Narasimhan et al. (1991). Leschziner (1993) related the weakness of the standard $k-\varepsilon$ model to its inadequate response to streamwise curvature and adverse pressure gradient, where modifications to the model constants were recommended.

The wake of an airfoil (NACA 0012) subjected to the effects of curvature and pressure gradient was predicted numerically by Tulapurkara et al. (1996). The inlet boundary and initial conditions were implemented as in Narasimhan et al. (1991). To improve the performance of the $k-\varepsilon$ model, modifications were made to the model constant C_μ based on the curvature parameter and the ratio between the production of turbulence kinetic energy to its rate of dissipation (Leschziner, 1993). The results for the modified $k-\varepsilon$ model were in good agreement with experimental data of Tulapurkara et al. (1994), in accurately predicting the mean velocity profiles and wake parameters. It was concluded that the scheme was able to capture the asymmetry in the profiles of turbulence kinetic energy and Reynolds shear stress. In the light of some differences between experimental and computed values, the use of higher order models such as the Reynolds stress model was recommended for more accurate predictions.

Mokhtarzadeh-Dehghan and Piradeepan (2006) present the numerical findings of the investigation into the curved wakes described by Piradeepan (2002). Numerical predictions of a turbulent curved wake were carried out with several RANS methods, namely, the standard $k-\varepsilon$, RNG $k-\varepsilon$, Realizable $k-\varepsilon$, and the Reynolds stress model (RSM). The wake was generated by placing a NACA 0012 airfoil in a uniform stream of air at 10 m/s, which was then subjected to an abrupt 90^{o} curvature created by a duct bend, as shown in Figure 1.4. The inlet to the domain was placed at one duct height upstream of the bend, where experimentally measured profiles of the mean and turbulence quantities were defined. The flow domain consisted of 676,000 cells and the full spanwise extent of the duct was represented by 42 cells. The nearest cells to the airfoil were situated within the viscous sublayer $y^{+} < 2$. On the bend walls the resolution deteriorated to $y^{+} \approx 100$. A two-layer zonal wall model was applied. The experimental study of the flow in the bend (Piradeepan and Mokhtarzadeh-Dehghan, 2005) reported intermittent separation and reattachment on the convex wall between stations 4 and 5 (station 4 was at the end of the convex curvature and station 5 further downstream), which resulted in an increase in turbulence quantities in the vicinity. Discrepancies were evident between numerical predictions and experiments in regions where separation had occurred. A main source of discrepancy was a lack of prediction of separation on the convex wall of the 90^{o} duct. This was highlighted in the pressure distribution computed on this wall and the prediction of turbulence quantities at station 5.

At the upstream stations (2, 3 and 4), Mokhtarzadeh-Dehghan and Piradeepan (2006) reported qualitative agreement between numerical and experimental data. Noticeable differences were evident when the exact values of certain parameters were compared. The computed wake width and the maximum velocity defect were larger in comparison to the experiments. The quantitative differences between predictions and experiments in the wake were found to originate from the differences on the airfoil, and attributed to the difficulties in modelling the laminar boundary layer near the leading edge of the airfoil and transition to turbulence near the trailing edge. The effect of curvature was computed correctly by all models. The results obtained with RSM showed better agreement with the experimental data. In their conclusions they highlighted that the prediction of the boundary layer on the airfoil was important in obtaining an accurate prediction of the wake.

2.3. Separation of flow over streamlined bodies

Pauley et al. (1990) and Ripley and Pauley (1993) performed numerical computations of two-dimensional laminar boundary layer separation on a flat plate, under the effects of curvature and pressure gradient. For a weak adverse pressure gradient they observed a separation region containing a steady closed separation bubble. For stronger adverse pressure gradients, the computations indicated a periodic vortex shedding. The computed time-averaged surface pressure distributions indicated a region of nearly constant pressure followed by an abrupt rise in the surface pressure just before the reattachment.

Lin and Pauley (1996) studied the unsteady boundary layer separation from the curved surface of an Eppler 387 airfoil numerically at low Reynolds numbers. The effects of Reynolds number and angle of attack on the evolution of vortical structures were investigated. A C-type mesh was used with 425 grid points wrapped over the airfoil, and 101 points normal to the airfoil. Their 2D domain stretched 15 chord lengths in all directions. Reynolds numbers $Re = 6 \times 10^4$, 1×10^5, 2×10^5 and angles of attack $\alpha = 0^o$, 4^o, 7^o were considered. Increasing the Reynolds number reduced the extent of the separation region, and moved the separation point downstream. Increasing the angle of attack moved the separation point upstream and shortened the extent of the separation bubble. The computed surface pressure distributions showed a region of nearly uniform pressure followed by a sudden increase in pressure just before the reattachment.

Boundary layer development and transition with large leading edge roughness was investigated experimentally by Kerho and Bragg (1997). The study was performed on a NACA 0012 airfoil (chord $c = 533.4$ mm, $\alpha = 0^o$), for a smooth model, and a series of airfoils incorporating different surface roughness. Tests were carried out in the straight section of a subsonic open-return type wind tunnel. The location of transition was identified by the sudden growth in turbulence intensity on the surface of the airfoil, and the changes in the shape of the velocity profile. For the smooth airfoil at $Re = 7.5 \times 10^5$, the transition point was located between $x/c = 0.7$ and 0.8. At the higher Reynolds number of 2.25×10^6, the location of the transition point had moved upstream to $x/c = 0.5$. For the rough surface airfoil at $Re = 1.25 \times 10^6$, the velocity profile indicated the occurrence of transition at $x/c = 0.05$, although a fully developed turbulent profile was not achieved until $x/c = 0.4$. The length of the transitional region was considerably shorter for the smooth model, compared to the corresponding surface roughness cases. It was concluded that the roughness induced boundary layers did not reach a

fully developed turbulent state as rapidly as previously thought. The experimental study of Zhang and Ligrani (2006) reported a larger velocity defect and higher turbulence intensity levels in the wake of an airfoil with surface roughness, in comparison to a smooth model. Kerho and Bragg (1997) did not present data for the wake, however the boundary layers developing in the roughness induced cases were thicker than those developed on the smooth model.

Conway et al. (2000) studied the flow through the blades of a swirl generator using LES. The flow between the upper surface of one blade and the lower surface of another blade was considered. Structured grids were set-up to represent a simplified geometry of the blade with uniform infinite span. Periodic boundary conditions were applied in the spanwise direction. No-slip conditions were set at the blade surfaces. The Reynolds number of the flow based on the blade chord length was 100,000. Simulations were conducted at the blade tilt angles 0^o and 15^o. The contours of vorticity and the distribution of mean skin friction coefficient on the upper and lower surfaces of the blade were used to identify features associated with separation and transition. The boundary layer exhibited transition from an initially laminar flow to a turbulent flow characterised by the stretching and deformation of spanwise vortices on the surfaces of the blade. Streamwise vortical structures were computed between the blades. These were characterised as Görtler instabilities (Saric, 1994), known to be an important factor in transition to turbulence. The presence of streamwise vorticity was related to the blade surface curvature and the centrifugal instability due to the concavity of the blade.

Wang and Moin (2000) computed LES of the trailing edge flow past a flat strut with a circular leading edge and an asymmetric sharp bevelled trailing edge. The streamlined body was parallel to the flow ($\alpha = 0$). A chord Reynolds number of 2.15×10^6 was considered which was based on the strut chord length $c = 21.125h$, where h is the thickness of the strut. The dynamic SGS model described by Germano et al. (1991) and Lilly (1992) was used. To reduce the computational cost, Wang and Moin (2000) conducted simulations in a domain containing the aft section of the strut and the near-wake, extending $0.5h$ in the spanwise direction. The inlet was prescribed $8h$ upstream of the trailing edge, where a turbulent boundary layer was used to describe the inflow condition. The grid contained more than 7 million cells where the maximum spacing expressed in wall units were $\Delta x^+ = 62$, $\Delta y^+ = 2$ and $\Delta z^+ = 55$. A no-slip condition was used at the wall. In general the computed profiles of mean velocity and fluctuations compared well with the available experimental data from Blake (1975). The discrepancies observed at the station close to the trailing edge were attributed in part to the

small spanwise extent of the computational domain, as well as the possibility of experimental uncertainties in the separation region near the wall. It was recommended that simulations should be conducted with a larger spanwise extent, to achieve better comparisons with the experiments.

The effectiveness of wall modelling in conjunction with LES for the turbulent boundary layer past an asymmetric trailing edge was assessed by Wang and Moin (2002). The flow configuration of their previous study was considered. The mesh was coarsened resulting in a 90% reduction in CPU time compared to the study of Wang and Moin (2000). The grid was designed to resolve the flow scales in the outer layer of the boundary layer. There was general agreement with the experimental data (Blake, 1975) for the profiles of velocity and RMS fluctuations on the upper surface of the plate and in the wake. They concluded that the use of advanced wall models in conjunction with LES can reproduce solutions at a drastically reduced computational cost, in particular in relation to the unsteady separations near the trailing edge.

Yang and Voke (2001) studied boundary layer separation and transition on a flat plate with semicircular leading edge using LES with a dynamic SGS model. The Reynolds number based on the semicircular leading edge diameter was Re = 3450. The domain extended $2d$ in the spanwise direction, where d is the leading edge diameter. The outflow boundary was placed $9.5d$ downstream of the leading edge of the plate. The mesh sizes close to the wall were in the range $10 < \Delta x^+ < 30.5$, $\Delta y^+ = 1$, and $\Delta z^+ = 9$. The time-step used in the simulation was $0.005d/U_o$. The curvature at the leading edge resulted in the formation of a separation bubble, the extent of which including the reattachment point were computed correctly. There was good agreement between the simulated results and available experimental data for the mean streamwise velocity and RMS fluctuations. Some discrepancies existed near the wall in the vicinity of the separation bubble, where a higher U-fluctuation was computed in the profile. Near the leading edge the streamwise velocity profile in the spanwise plane was observed to be flat, indicating a two-dimensional flow. Instabilities in the shear layer resulted in the formation of spanwise vortices. Peak valley wave structures were observed in the spanwise distributions of mean streamwise velocity which were attributed to the formation of longitudinal vortices. Peaks formed when the fluid with larger streamwise velocity was pushed down from the layer above, and valleys when the fluid with lower velocity was pushed up from the layer below. It was concluded that it took a considerably long distance for the turbulent boundary layer to develop and the logarithmic law to be established.

The LESFOIL project (1998-2003) was set-up to assess the feasibility of large eddy simulation in calculating the flow around an Aerospatiale A-airfoil (Davidson et al., 2003). The main aim of the project was to establish the common findings on the use of LES. Within the programme, the high lift configuration of the airfoil at an angle of attack $\alpha = 13.3^{o}$ and chord Reynolds number 2.1×10^{6} was studied by numerous researchers using large eddy simulation; Dahlström and Davidson (2000), Weber and Ducros (2000), Fröhlich and Mellen (2001) and Mary and Sagaut (2002). The specific objectives were to evaluate parameters used in SGS modelling, near wall treatment and numerical methods. In these studies comparisons were made with the experiments of Huddeville et al. (1987) and Gleyzes (1989), conducted at ONERA in two different wind tunnels.

Dahlström and Davidson (2000) used the standard Smagorinsky model to compute the high lift configuration of the Aerospatiale A-airfoil. Computations were carried out on two different C-grid meshes. The first grid was of spanwise extent $0.03c$ with maximum cell sizes on the upper surface of the airfoil in non-dimensional wall units Δx^{+}, Δy^{+}, Δz^{+} = (1200, 20, 130), respectively. The second grid had a spanwise extent of $0.08c$ with the corresponding resolutions Δx^{+}, Δy^{+}, Δz^{+} = (600, 40, 350). Periodic conditions were set in the spanwise direction throughout the flow domain. Computations were conducted using no-slip and wall functions. A time-step of $\Delta t = 3 \times 10^{-4} c/U_o$ was employed. The results showed that none of the simulations predicted separation satisfactorily. The cases with wall functions were found to give better results in comparisons with available experimental data, and were seen to compensate for the low resolution in the spanwise direction. It was concluded that the transition process and the behaviour of the SGS needed further examination. In a wall resolved LES the first node should be located well below $y^{+} < 2$ to resolve the velocity gradients close to the wall (Piomelli and Chasnov, 1996). The energy producing structures in the near wall region can be captured in a wall resolved LES if the size of the cells close to the wall satisfy $50 < \Delta x^{+} < 150$, $\Delta y^{+} < 4$ and $15 < \Delta z^{+} < 40$. In the study of Dahlström and Davidson (2000) a wall resolved LES was not conducted due to immense computer power required. They highlighted the significance of resolving the approaching laminar boundary layer, and the importance of spanwise resolution in the simulations.

In the study by Weber and Ducros (2000) a C-mesh with less than one million cells was used in the large eddy simulations of the Aerospatiale A-airfoil in the high lift configuration. A spanwise extent of $0.036c$ was adopted with 30 cells in the spanwise direction. The streamwise spacing on the upper surface of the airfoil was in the range $30 < \Delta x^{+} < 900$, and the first cell

normal to the wall was located at $y^+ = 2$ over the majority of the airfoil. Due to the rapid changes in the flow field, their grid experienced a change in the spanwise resolution from $\Delta z^+ = 180$ to $\Delta z^+ = 12$ between $x/c = 0.15$ and $x/c = 0.9$, respectively. A no-slip condition was used at the wall and periodic boundary conditions were set in the spanwise direction. A time-step of $\Delta t = 1.8 \times 10^{-4} c/U_o$ was employed in the computations. Visualisation of the flow field indicated the growth of turbulent structures near the trailing edge. None of the simulations could satisfactorily predict trailing edge boundary layer separation, with sufficient reversed flow. Features such as the adverse pressure gradient and flow retardation were captured. A laminar separation bubble was reported, with detachment at $x/c = 0.12$ and reattachment at about $x/c = 0.83$. The discrepancies between LES and experimental results raised questions about the resolution and suitability of their mesh for the simulation. The influence that the spanwise resolution had on the results and the importance of resolving the upstream boundary layer were emphasized in their conclusions.

Fröhlich and Mellen (2001) considered a similar test case. A C-grid was setup with spanwise extent of $0.06c$. The dynamic Smagorinsky SGS model was employed. As with the previous studies, it was emphasized that resolving the attached upstream boundary layer would require a fine grid for the high Reynolds number considered. The strategy here was to incorporate the Werner and Wengle (WW) wall functions (Werner and Wengle, 1991) and model the attached boundary layer instead of resolving it. The grid spacing in wall units indicated average magnitudes of $\Delta x^+, \Delta y^+, \Delta z^+ = (100, 10, 40)$. Computations were performed with a time-step $\Delta t = 1 \times 10^{-4} c/U_o$. The simulations did not detect a laminar separation bubble, that is, friction coefficient did not become negative near the leading edge. Their initial computations yielded unrealistic transitional behaviour. Modelling adjustment were made in the vicinity of the transition point to improve predictions of streamwise velocity, fluctuations and separation at the trailing edge.

In the study by Mary and Sagaut (2002) the aim was to assess the contributions of spanwise resolution, spanwise extent and SGS modelling on the quality of the large eddy simulations of flow over the Aerospatiale A-airfoil. The selective mixed-scale model was used for the SGS contributions. On the upper surface, transition was known to occur naturally due to the presence of an adverse pressure gradient. A fully three-dimensional mesh was designed close to the airfoil, within the turbulent boundary layer and the wake, while a large two-dimensional zone was prescribed outside the boundary layer where the flow was inviscid. Grids of different spanwise extent were considered, the finest grid extended $0.012c$ in the spanwise direction

with wall spacing Δx^+, Δy^+, Δz^+ = (60, 2, 25). The grid resolutions near the airfoil more than satisfied the recommendations for wall resolved LES. A no-slip condition was prescribed at the walls. Periodic conditions were defined in the spanwise direction and a time-step of $\Delta t = 3.3 \times 10^{-5} c/U_o$ was used. The results indicated a sensitivity to mesh resolution and not so to the particular SGS model used. In all simulations the presence of a laminar separation bubble was observed at $x/c = 0.12$ with reattachment occurring immediately after this region. On the grid with the smaller spanwise extent, separation was over-estimated and turbulent fluctuations at the trailing edge were over-predicted. The results from the simulations with the largest spanwise extent and highest spanwise resolution provided the best comparisons with the experimental data. They concluded that spanwise extent of the domain and the spanwise resolution are important in the accuracy of the simulation.

The findings of the above series of work (LESFOIL project: Davidson et al., 2003) concerning LES of the Aerospatiale A-airfoil in a high lift configuration were summarised by Mellen et al. (2003). In the assessment of different pressure-correction-based solution methods, it was found that SIMPLEC and PISO were equally useful in terms of reducing CPU time. The pure central-differencing scheme gave rise to unphysical oscillations all over the computational domain, especially at high Reynolds numbers with poor grid resolution. In most cases this scheme was blended with a bounded second-order upwind scheme to suppress any unphysical oscillations. To accurately capture the transition process, a near wall mesh resolution of the order $\Delta x^+ = 100$, $\Delta y^+ = 2$ and $\Delta z^+ = 20$ was required. In most cases, the investigators reduced their spanwise extents to achieve this requirement. It was found that a significantly reduced spanwise extent can enhance the two-dimensionality of the downstream flow with increased fluctuations near the wall (Mary and Sagaut, 2002). The studies indicated that for a successful simulation of transitional flow, the leading edge separation bubble and trailing edge separation must be resolved. The general understanding was that grid resolution and mesh criteria were dominant factors in determining the quality of the results, whereas the SGS models played a secondary role in comparison. The no-slip condition required a sufficiently fine resolution near the wall. To reduce the computational time and cost, the use of wall functions with coarse near-wall grids was assessed. These studies found that the wall function method and such meshes performed well in the attached boundary layer regions, whereas their ability to resolve trailing edge separation was limited. In order to predict features of flow separation, however, the non-dimensional near-wall-to-node distance tended towards the resolution required for the imposition of a no-slip condition ($\Delta y^+ < 10$). Mellen et al. (2003) concluded that LES of flow over airfoils in high lift conditions and high Reynolds number configurations can only be

successful when a fine grid resolution is adopted, in such a way to resolve near wall turbulent structures.

Temmerman et al. (2003) reported that the application of a no-slip condition coupled with poor streamwise resolution on a wall where separation is known to occur can yield substantial errors even if the wall nearest grid nodes are located within $5 < y^+ < 15$. They suggested that on finer grids LES is weakly sensitive to SGS modelling and that the grid resolution parameters are critical in flows involving separation from curved surfaces such as airfoils and blades.

Komurasaki and Kuwahara (2004) presented the results of large eddy simulations of subsonic flow around a NACA 0012 airfoil at a Reynolds number 1×10^6. The no-slip condition was applied at the surface of the airfoil and the periodic condition was introduced in the spanwise direction. An O-grid was adopted with $129 \times 65 \times 65$ grid points. No explicit SGS model was employed, instead a high-order upwind difference scheme was used to discretize the convection terms. Angles of attack in the range $8^o < \alpha < 16^o$ were adopted. There was good agreement between the computations and the available experimental data of Abbott and Von Doenhoff (1959). Their conclusions put emphasis on the fact that the flow structures that caused stall and the characteristic leading edge separation were simulated without the use of an explicit SGS turbulence model.

The majority of previous work concerning LES of airfoil flows at large angles of attack and high Reynolds numbers, found that in most cases the important flow properties could not be resolved. This was mainly due to the application of a Reynolds number of the order 10^6, which reduced the size of flow structures in time and space. Jovičić and Breuer (2004) predicted the turbulent flow past a NACA 4415 airfoil at an angle of attack $\alpha = 18^o$ for a lower chord Reynolds number $Re = 1 \times 10^5$. The dynamic Smagorinsky SGS model was used, with a no-slip boundary condition applied at the wall. The grid used extended one chord length in the spanwise direction and the cell sizes satisfied $\Delta y^+ \approx 0.5$ over most of the airfoil surface. To resolve the time scales, a time-step of $\Delta t = 1 \times 10^{-4}\, c/U_o$ was employed. Periodic boundary conditions were set in the spanwise direction. Simulations captured the characteristics of flows at high incidence angles. The attached laminar shear layer emerging from the leading edge was observed. The presence of an adverse pressure gradient due to surface curvature led to flow separation before $x/c = 0.04$. The shear layer reattached shortly after $x/c = 0.11$ and a separation bubble of time-averaged length $0.09c$ and maximum height $0.005c$ was formed.

Downstream of the bubble a turbulent boundary layer developed, which remained attached for about 60% of the chord length, after which it separated forming a large recirculation region in the vicinity of the trailing edge. The numerical results were successfully validated with the experimental data from Kindler et al. (2003).

Direct numerical simulation of flow separation around a NACA 0012 airfoil was conducted by Shan et al. (2005). The airfoil was placed at an angle of attack $\alpha = 4^o$ and the chord Reynolds number was 1×10^5. A C-type grid was constructed with a spanwise extent of $0.1c$. The grid points were uniformly distributed in the spanwise direction and clustered near the airfoil surface in the wall normal direction. The grid spacing in wall units were defined by $\Delta x^+ < 13$, $\Delta y^+ < 1$, and $\Delta z^+ < 15$. A no-slip condition was applied on the surface of the airfoil and spanwise periodic conditions were defined. The time-step employed was $\Delta t = 8.35 \times 10^{-5}\, c/U_o$. A recirculation zone was identified, with flow separation near $x/c = 0.19$ and reattachment at $x/c = 0.68$. The time-averaged length of the separation bubble was estimated to be approximately $0.49c$. The profiles of mean pressure coefficient and skin friction coefficient on the surface of the airfoil were used to discern the flow transition to turbulence. A sudden decrease in friction coefficient C_f near $x/c = 0.63$ indicated the occurrence of transition, and the recovery of C_f to positive values at $x/c = 0.68$ was attributed to the reattachment. The development of vortical structures in the shear layer and the breakdown to turbulence were captured in the simulations.

Marsden et al. (2006) presented large eddy simulations of flow around a NACA 0012 airfoil at Re = 500,000 and zero angle of attack. A high-order numerical procedure was used to resolve the Navier Stokes equations. Their computational domain consisted of 12.3 million cells, extending one chord length in the z-direction and $0.5c$ beyond the trailing edge. The spanwise extent of the domain was represented by approximately 45 cells. The grid spacing near the surface of the airfoil in wall units were $\Delta x^+ \approx 20$, $\Delta y^+ \approx 2.5$, and $\Delta z^+ \approx 20$. A no-slip condition was applied at the walls and periodic boundary conditions were set in the spanwise direction. The boundary layers were initially laminar and transition to turbulence took place along the second-half of the airfoil. The location of the transition point was determined by observing the contours of streamwise RMS fluctuations and the distributions of skin friction coefficient on the airfoil. Lee and Kang (1998) found experimentally the transition zone for a NACA 0012 airfoil at zero angle of attack and Reynolds number 600,000 to be located between $x/c = 0.62$ and $x/c = 0.78$. The computational results showed that the transition was well captured, and for Re = 500,000, the transition zone was located between $0.54 < x/c < 0.72$. Good agreement was

achieved between experiments and computations for the profiles of velocity, turbulence intensity, skin friction and mean pressure coefficient.

2.4. Flow through curved ducts

There is an extensive amount literature with reference to flow through curved ducts. Mokhtarzadeh-Dehghan and Yuan (2002) have reviewed the majority of the experimental studies in this area, and thus the following part focuses on the most relevant aspects to the present study.

The boundary layer that develops on a concave surface is known to lead to the formation of longitudinal vortices. These vortices are very different from the counter-rotating vortices that characterise secondary flows. Taylor Görtler vortices (Saric, 1994) form as a result of the centrifugal instability associated with concave curvature, and possess a counter-rotating property that can be strong enough to induce changes in the boundary layer, statistically. The increase in the three-dimensionality due to the formation of streamwise vortices results in an increase in turbulence and wall friction. The experimental studies of Barlow and Johnston (1988), and Hoffman et al. (1985) on the effect of concave curvature on turbulent boundary layers have shown that even a small curvature can significantly affect the flow development. The effect of concave and convex curvature are very different on the flow, the concave surface has a destabilizing effect on the boundary layer and results in an enhancement of turbulence, whereas the convex surface has a stabilizing effect and results in a decrease in turbulence.

Breuer and Rodi (1994) used LES to compute the turbulent flow through a straight duct (at Re = 44100 and Re = 56690) and a duct with a 180^o bend (Re = 56690). Due to the difficulties in resolving the near wall region at high Reynolds numbers, the wall function method was employed. For the lower Reynolds number, LES results were in good agreement with available DNS and other LES data. Discrepancies were evident for the high Reynolds number simulations. They concluded that LES captured the main features of the flow such as the secondary flow behaviour.

Large eddy simulation of a concave wall boundary layer with the dynamic SGS model was carried out by Lund and Moin (1996). The radius of curvature was $18.1\delta_o$ (where δ_o is the boundary layer thickness at the location where the curvature begins). The concave curvature measured $24\delta_o$ along the arc and ended at the 75^o station where the outflow boundary was

defined. The momentum thickness Reynolds number at the beginning of the curvature was 1300. The domain extended $10\delta_o$ upstream of the curvature, $3\delta_o$ in the normal direction, and $2\delta_o$ in the spanwise direction, where periodic conditions were employed. The grid nodes were spaced uniformly in the streamwise and spanwise directions, but stretched in the normal direction so that a finer resolution was achieved near the concave wall. The near wall grid spacing in wall units at the start of curvature were $\Delta x^+ = 50$, $\Delta y^+ = 1$ and $\Delta z^+ = 16$. The results compared well with the experiments and predicted accurately the changes in the profiles of the mean and turbulence statistics that resulted from the destabilizing effect of concave curvature, and the transition from a flat wall to a concave surface. The peak value of Reynolds stresses increased along the curved section and a bulge developed in the profiles for $0.2 < y/\delta < 0.8$. Quantitative differences between LES and experimental data in the Reynolds stress profiles were attributed to the inadequate inflow conditions, which were generated with simulations of flat plate boundary layers. Large scale Taylor-Görtler vortices were computed in the simulations that adopted a more experimentally representative set of inflow data. However, the simulations with inlet data, taken from the computations of a spatially evolving boundary layer, produced weaker, less developed secondary flow patterns. Lund and Moin (1996) concluded that the definition of the upstream flow can exert significant influence on the development and amplification of the secondary flow structures in concave wall turbulent boundary layers.

Mokhtarzadeh-Dehghan and Yuan (2002) presented measurements of mean velocity and turbulence quantities in the developing turbulent boundary layers on the concave and convex walls of the 90^o bend shown in Figure 1.4. Experiments were conducted using hot-wire anemometry, in the subsonic blower wind tunnel, which is also used in the present investigation. The mainstream velocity was 12.3 m/s at station 1 (457 mm upstream of the bend) corresponding to a flow Reynolds number of $Re = 3.7 \times 10^5$. The profiles of mean and turbulence quantities were investigated for the four stations on the concave and convex walls. The Clauser chart method applicable to turbulent boundary layers and based on the logarithmic law of the wall was used to determine the local wall shear stress. In the flat section upstream of the bend, the presence of an adverse pressure gradient on the concave wall resulted in a decrease in friction coefficient. Further downstream on the concave wall, the effect of curvature overcame the opposite effect of positive pressure gradient and resulted in an increase in C_f. On the convex curvature the presence of a favourable pressure gradient resulted in an increase in wall friction over the first 45^o of the bend. The range of y^+ values over which the logarithmic law was applicable, varied considerably along the concave and

convex walls of the duct. The concave curvature resulted in the enhancement of turbulence quantities, whereas a reduction in turbulence was observed near the convex wall. In the region of adverse pressure gradient and intermittent separation between stations 4 and 5 on the convex wall, turbulent fluctuations increased considerably compared to the levels seen on the concave wall. The investigators reported the presence of organised wavy patterns in the spanwise distribution of the profiles of mean velocity and turbulence intensities on the concave wall. These patterns were characterised by peaks and troughs, taken to be as a result of up-flow and down-flow motions from longitudinal vortices. The spanwise variations near the concave wall were found to increase at stations 2 and 3.

Hébrard et al. (2004) investigated with LES the effect of curvature in turbulent duct flow. The case of an *S*-shaped duct was considered exhibiting both convex and concave curvatures. Simulations were performed at a Reynolds number of 6000 based on the bulk velocity in the duct and the hydraulic diameter D_h. No-slip boundary conditions were imposed at the upper, lower and side walls. The computational domain extended $15D_h \times D_h \times D_h$ in the streamwise, normal and spanwise directions, respectively. At the inlet, the first grid point near the wall was located at $y^+ = 1.8$. In the straight section near the inlet, weak counter-rotating vortices were observed at the four corners of the duct and the mean flow was directed towards the upper wall (convex wall) at the mid-plane. A decrease in friction coefficient on the concave wall, near the inlet, was attributed to the radial pressure gradient that pushed the fluid away from the concave wall. In the curved section, the radial pressure gradient promoted an upward current near the side walls of the duct towards the convex wall, meanwhile the centrifugal effect induced a flow towards the concave wall at the mid-plane. This resulted in an increase in friction coefficient further downstream on the concave wall. The formation of large counter rotating vortices near the convex wall was reported. The evolution of skin friction coefficient on the walls of the duct was in agreement with the experimental results of Bandyopadhyay and Ahmed (1993). The profiles of turbulence kinetic energy were enhanced near the concave wall and suppressed near the convex wall. It was concluded that the presence of radial pressure gradient between the concave and convex surfaces of the duct modified significantly the mean flow in the duct, through secondary flow effects that resulted in the formation of counter-rotating streamwise vortices near the convex surface, and increased turbulence production near the concave surface.

Lopes et al. (2006) considered LES of the flow in an *S*-shaped duct. The flow Reynolds numbers based on the duct half-height and the freestream velocity, were 13,800 and 30,800.

The *S*-shaped duct consisted of an initial flat section, two curved sections, and another flat section in the downstream. The curved sections comprised a concave-to-convex curvature (lower wall) and a convex-to-concave curvature (upper wall). Each section was 504 mm long and the radii of the curved sections were 504 mm. The distance between the upper and lower walls was 102 mm and the spanwise width of the domain was πh_i, where h_i is the duct half-height. The dynamic SGS model of Germano et al. (1991) was employed. The near-wall grid sizes based on the local wall shear stress were in the range of $\Delta x^+ < 60$, $\Delta y^+ < 2$ and $\Delta z^+ < 30$. A no-slip condition was imposed at the walls. Comparisons were made with the experiment of Bandyopadhyay and Ahmed (1993). There were some notable differences between the numerical model and the experiments, in that the spanwise periodic conditions defined in the LES replaced the side walls in the wind tunnel experiments. In addition, the Reynolds numbers considered in the numerical study were lower and, therefore, only qualitative comparisons could be made with the experimental data. The results showed significant asymmetry in the velocity profiles developing through the duct which was attributed to the effect of curvature and pressure gradient. The adverse pressure gradient experienced by the flow on the concave curvature resulted in significant amplifications in the profiles of turbulence kinetic energy and Reynolds stresses in the near wall vicinity. The Taylor-Görtler vortices which were observed near the concave wall were found to contribute significantly to the turbulence production. The favourable pressure gradient on the convex wall resulted in a significant decrease of the Reynolds stresses and the turbulence kinetic energy. Findings were consistent with the numerical studies of Lund and Moin (1996) and Hébrard et al. (2004). However, the computed pressure coefficient was higher than that measured in the experiments. Lopes et al. (2006) attributed the differences in the pressure coefficients measured experimentally and predicted in the simulations to the presence of the side walls in the experiment (Bandyopadhyay and Ahmed, 1993). The presence of the side walls resulted in the formation of strong corner vortices which thickened the boundary layer and decreased the adverse pressure gradient, resulting in flow acceleration.

The developing turbulent flow through a strongly curved *U*-duct was predicted using LES by Guleren and Turan (2007). The aim was to validate LES by making comparisons with available experimental data (Cheah et al., 1996) and the RANS computations (Suga, 2003). The WALE model was employed in conjunction with the WW wall function method. The 180^o *U*-bend was of square cross-section with a curvature ratio $R/D = 0.65$, where D is the cross-sectional width of the duct and R is the mean radius of curvature. The Reynolds number based on the width of the duct was 100,000. A bounded central-differencing scheme was used to

discretize the convection terms. The computational domain contained approximately 1.1 million cells. The node-to-wall distance satisfied $y^+ < 70$ throughout the whole domain. The inflow boundary condition for LES was defined using the predicted velocity profiles from the preliminary RANS simulations. A random two-dimensional vortex method proposed by Sergent (2002) was adopted, where perturbations were added to a specified mean velocity profile via a fluctuating vorticity field. Simulations were performed using a time step $\Delta t = 0.002U_o/D$. The computed profiles of mean velocity and Reynolds stresses in the large eddy simulations presented some discrepancies when compared with the experimental data. Generally, LES performed better than RANS in predicting quantitative features of the flow through the *U*-duct, where turbulence behaviour in particular was captured well. Flow separation with subsequent reattachment was computed on the convex wall of the *U*-duct past the 180^o bend. The secondary flow characteristics were identified indicating that the flow was directed from the inner wall (convex wall) to the outer wall (concave wall). Guleren and Turan (2007) related the discrepancies between LES and experiments, to grid resolution, the use of wall functions, and the inlet velocity profile.

2.5. Summary and conclusions

This chapter has detailed the previous research on curved wakes, separation over airfoils, and flow in curved ducts. Here, the key points from this review are outlined. The effect of curvature and pressure gradient, induce asymmetry on the profiles of mean and turbulence quantities in the wake. The studies concerning the evolution of wakes have shown that the near- and intermediate-wake is governed by two-dimensional spanwise vortices and streamwise vortices; which appear as counter-rotating pairs. Experimentally, the presence of peaks and troughs in the spanwise distributions of mean velocity and turbulence intensity, are an indication of these streamwise vortical structures. In most cases the investigators treated the study of airfoil boundary layers and of wakes, individually. For example, the large eddy simulations of airfoil boundary layers did not extend beyond the trailing edge, whereas in the investigation of wakes, the airfoil boundary layers were not studied. The present investigation considers both flow regimes since the wake is largely dependent on the boundary layers of the airfoil.

The literature search has highlighted that the present research is the first to consider a large eddy simulation of the turbulent wake in a curved duct. A review of the modelling parameters, namely, the numerical methods, inlet conditions, near-wall treatment, SGS model and grid

resolution were carried out. Based on the findings of previous investigators, the near-wall grid resolutions for a wall resolved LES should fall within Δx^+, Δy^+, Δz^+ = (50, 1, 30), respectively. However the restrictions of these limits tend to vary depending on the flow under study. In the LES of high Reynolds number airfoil boundary layer flows these limits are very stringent, and researchers often adopt finer near-wall grid resolutions by reducing the spanwise extent of the domain. On the other hand in the simulation of low Reynolds number flows these limits can be relaxed. The development of the secondary flow and the formation of the longitudinal vortices on the concave wall are the important features of flows in curved ducts. These features have a strong influence on the mean flow statistics, and, therefore, in the simulation of such flows they must be computed accurately. The modelling parameters most influential on the quality of the large eddy simulations, as reported by previous investigators, are the SGS model and the grid resolution, which are both investigated in the present work.

Chapter 3

3. EXPERIMENTAL INVESTIGATION: Facilities and Procedures

3.1. Introduction

The experimental investigation was carried out using the wind tunnel facility at Brunel University. In the present study, constant temperature hot-wire anemometry was used to investigate the turbulent near-wake of an airfoil subjected to the effects of curvature and pressure gradient. The boundary layer development on the upper surface of the airfoil was also investigated. As was reviewed in Chapter 2, this measurement technique has been employed by a number of investigators in the experimental study of curved wakes. These include, the works by Tulapurkara et al. (1994), Weygandt and Mehta (1995), Stark et al. (1999) and, more recently, Piradeepan and Mokhtarzadeh-Dehghan (2005). To determine the mean velocity and turbulence quantities a selection of DANTEC single-wire probes, a rake of single-wire probes (type 55P16), and a cross-wire probe (type 55P63), were used. The experiments in the near-wake were conducted for different angles of attack and three mainstream velocities. Measurements were also carried out in the spanwise direction to study the three-dimensional structure of the curved wake. In addition to this, the effect of angle of attack on the static pressure distributions on the airfoil was measured using a micromanometer. The present experimental data was used for direct comparisons to the results predicted by the present large eddy simulations.

The experimental study aims to provide quantitative data in the airfoil boundary layer and the curved near-wake, which can be used by other researchers to validate existing or new numerical models with the present flow configuration. In the proceeding section, details of the experimental rig, the test section, including the airfoil and the traversing systems are presented. This is followed by section 3.3 which describes the principals of hot-wire anemometry with particular reference to the present work. Details of the experimental measuring and recording, equipment and instrumentation are presented in section 3.4. The tunnel and probe calibration methods are described in section 3.5. The last section of this chapter details the uncertainty and error analysis in the experimental investigation.

3.2. The wind tunnel and test section

3.2.1. Tunnel operation

The experiments were conducted in the closed working section of a subsonic blower wind tunnel of open-return type. The tunnel draws air from the surrounding atmosphere which is then discharged through the downstream tangent into the laboratory. In Figure 3.1 a photograph of the wind tunnel test section and instrumentation is presented. A schematic of the tunnel is also shown in Appendix II.

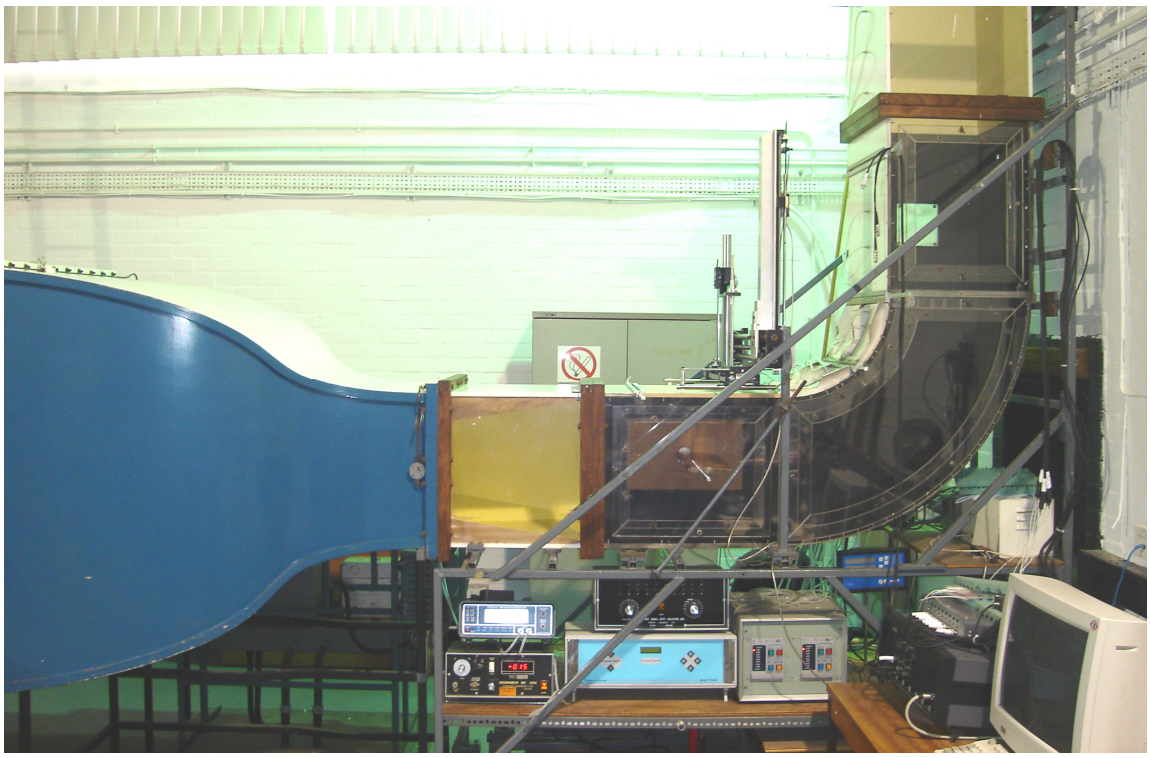

Figure 3.1: The wind tunnel test section and instrumentation.

The operation of the tunnel is described as follows. The centrifugal blower delivers air to the diffuser through a short honeycomb section which is designed to straighten the flow. The diffuser increases in cross-sectional area to 1.5 m^2, and is fitted with three wire meshed screens that further straighten the path of flow and reduce the turbulence by breaking up the larger eddies. The smooth stream of air then enters a contraction section that leads to a short straight section of 600 mm length. The centrifugal fan is driven by a 20 kW AC motor which is equipped with a variable speed pulley that allows the fan to operate between 470 to 1170 rpm. The tunnel is capable of delivering air to the test section with a maximum speed of 33

m/s. The static pressure drop across the contraction section was determined from the pressure tappings located at the entrance and exit of the contraction assembly. This pressure drop was used in the tunnel calibration process which will be outlined later.

3.2.2. The test section

In Figure 3.2 a schematic of the test section is presented. The honeycomb, diffuser and the contraction section, deliver a uniform low turbulence stream of air to the test section. The test section is a separate unit that consists of an upstream tangent, the bend and the downstream tangent. In the present investigation the wake was generated by placing an airfoil in the uniform stream of air within the test section, that is, the upstream tangent. The bend section subjects the flow to an abrupt 90^{o} curvature. The flow is then directed vertically upwards through the straight downstream tangent, which extends 5 m in the normal direction into the laboratory.

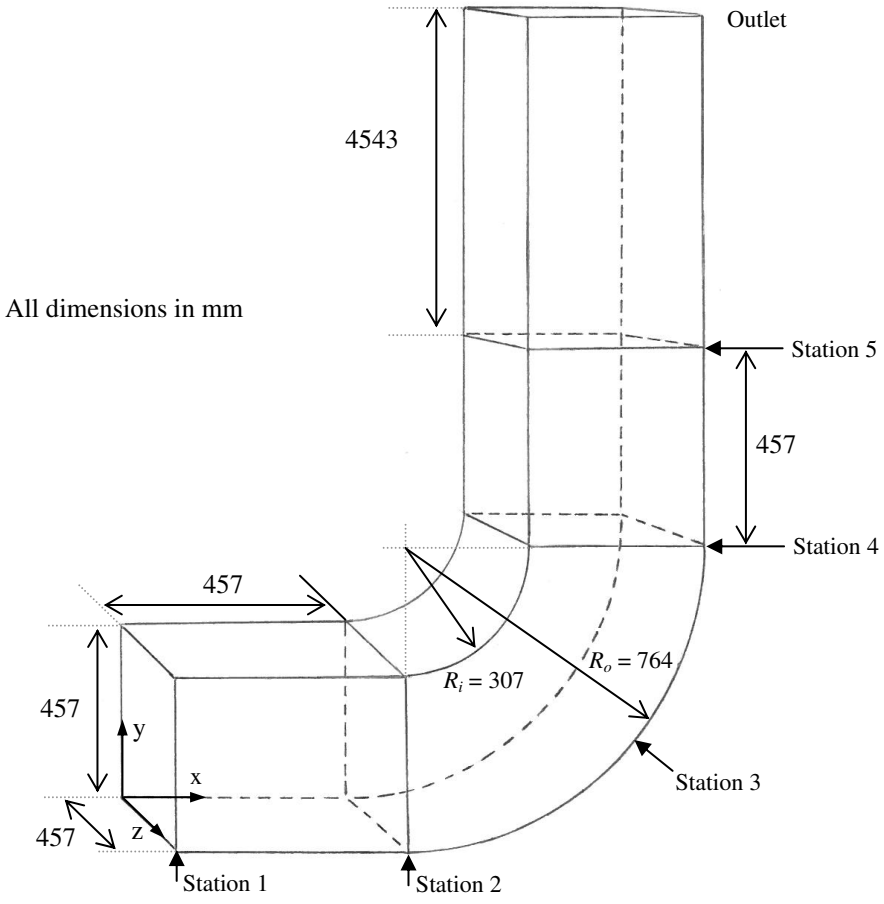

Figure 3.2: Schematic of the test section (not drawn to scale).

The duct cross-section measures 457 mm × 457 mm and the bend has a radius to height ratio of R/H = 1.17. The test section walls, are made from 12 mm thick plywood plates, except the front side of the tunnel, which is made from transparent Perspex sheets. Detachable panels are incorporated on the front side of the tunnel which can be used to access the interior of the test

section for maintenance, setting up the airfoil, probe insertion and alignment. The convex and concave walls of the bend are made from 3 mm thick plywood sheets. These are painted to ensure a smooth surface for the developing turbulent boundary layers on the duct walls.

There are five measuring stations, each incorporate a slot on the convex wall of the test section that extends across the full-span of the duct, and allow for the probe guide tubes to be traversed in the normal and spanwise planes. Station 1 is located 457 mm upstream of the bend entry. Station 2, 3 and 4 are located at the bend entry (0^o), middle (45^o) and the bend exit (90^o). Station 5 is part of the downstream tangent of the tunnel and is located 457 mm downstream of the bend exit. Experimental tests were conducted, in the airfoil boundary layer, and in the near-wake up to station 2. The RMS of the streamwise velocity fluctuations, measured in the central plane of the duct (without the airfoil), were less than 0.5 % of the mainstream velocity, which indicates a low level of turbulence in the test section.

3.2.2.1. Airfoil boundary layer measurements

To provide traverse access to the upper surface of the airfoil, and to accommodate a suitable traversing mechanism for this purpose, the upper wall (convex side) of the upstream tangent between stations 1 and 2 was redesigned (Figure 3.3).

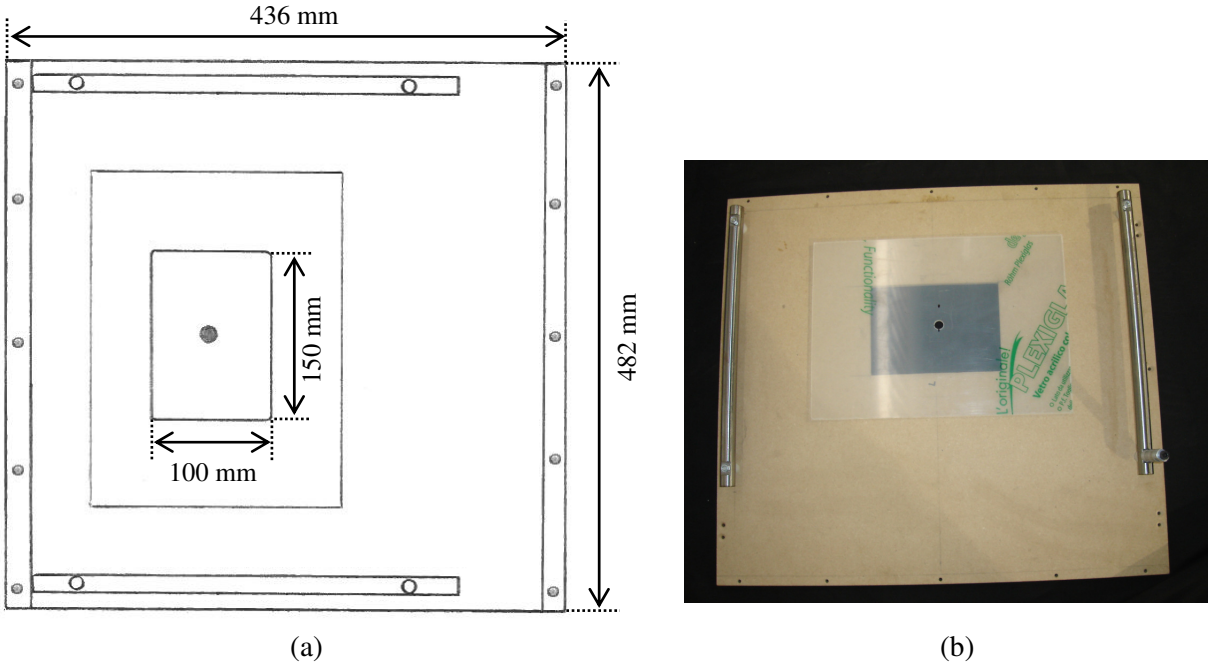

Figure 3.3: The modified upper wall section of the upstream tangent employed in airfoil boundary layer experiments: (a) plan schematic (not drawn to scale), (b) photograph.

This section of the convex wall consists of an open cavity of dimension 150 mm × 100 mm × 10 mm, as can be seen in Figure 3.3(a). A Perspex panel sheet of thickness 3 mm was placed on the outside to maintain an enclosed test section during the experiments. The probe guide tube was then inserted through a hole into the Perspex panel which was then traversed within the area of the cavity. The effect of the cavity on the mean and turbulence quantities in the surrounding regions was investigated, the results of which will be presented and discussed in Chapter 6. In general, the results indicated that the mean and turbulence quantities in the mainstream and in the vicinity of the airfoil were not affected as a result of the presence of the cavity in the wall.

3.2.3. Airfoil geometry

In the present investigation, the wake producing body was a NACA 0012 symmetrical airfoil with a chord length of 150 mm and spanwise extent of 457 mm. The airfoil was made from Plywood and varnished to maintain a smooth surface. A schematic of the airfoil is shown in Appendix III. To measure the static pressure distribution over the airfoil, a number of pressure tappings were incorporated along the mid-span plane, on the upper and lower surfaces. These pressure tappings were individually connected by stainless steel tubes inside the body, which were brought out of the airfoil mounting from the side wall of the test section and then connected to a digital manometer, through a pressure scanner that was used to monitor and record the pressure from all 23 tappings. The location of the airfoil in the upstream tangent is shown in Figure 3.4.

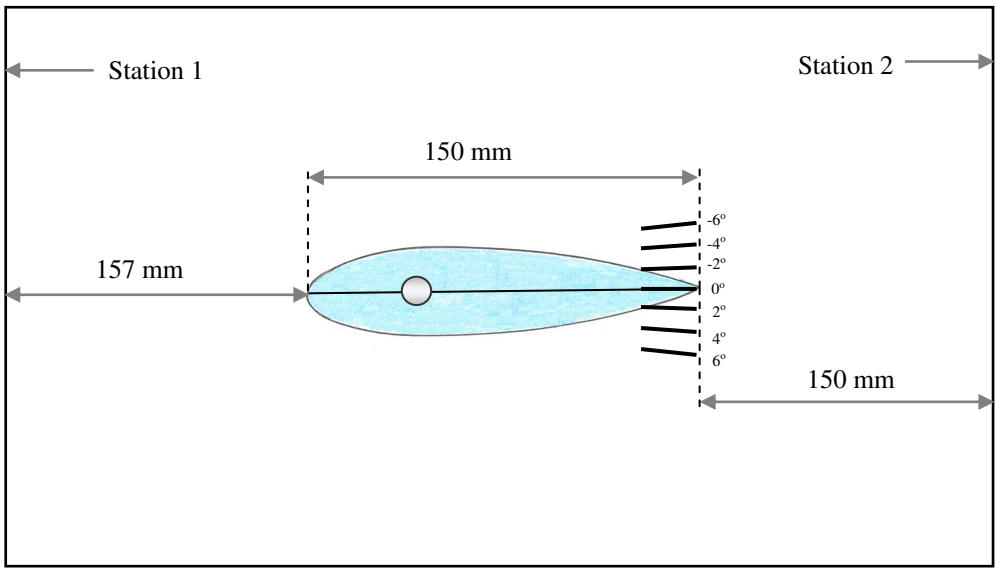

Figure 3.4: A diagrammatic of the airfoil mounted in the upstream tangent (not drawn to scale).

The airfoil was mounted horizontally at zero angle (α), relative to the concave and convex wall of the duct between stations 1 and 2. The angle α here after will be referred to as the angle of attack. In this configuration the trailing edge of the airfoil was one chord length from station 2 (bend entry) and the leading edge was 157 mm from station 1. The chord line of the airfoil was located at the mid-height of the test section.

One of the main objectives of the present experimental investigation was to provide new experimental data in the wake and to study the effect of angle of attack on the airfoil static pressure and the mean velocity and turbulence quantities. For the purpose of convention, anti-clockwise rotation (trailing edge up) is taken as negative, and the clockwise rotation (trailing edge down) as positive. As can be seen in Figure 3.4, the experiments in the near-wake were conducted at seven different airfoil angles of attack (α = 0^o, 2^o, 4^o, 6^o, -2^o, -4^o, -6^o). Prior to the experiment, the transparent Perspex access panel of the upstream tangent was detached from the test section and lines corresponding to the different angles of attack, relative to the horizontal, were marked on the panel. The chord line of the airfoil was then aligned with this line to set the desired angle of attack. The accuracy, by which the airfoil angle of attack was configured, was in part confirmed by assessing the repeatability of the experimental profiles in the wake, when the angle of attack was altered and then reset.

3.2.4. Traversing system

Two different traverse systems were used in the present study. A computer controlled traverse (Figure 3.5a) was employed for the most part of the experimental study that included the experiments in the near-wake, at station 1, and at station 2. For the airfoil boundary layer experiments, a separate manual traverse system was designed and fitted on the modified section of the upstream tangent, as shown in Figure 3.5(b).

3.2.4.1. Computer controlled traverse

The computer controlled traverse system was a completely separate system from the test section, which was mounted above the convex wall of the test section. The movement of the probe in the normal and spanwise directions was achieved by individual control of two stepping motors to drive a set of linear bearings. The linear bearings on both axes were powered by precision lead screws of 1 mm pitch. The lead screws were mechanically driven by the stepping motors with 200 steps per revolution. Two stepping motors were employed in

this setup, one to control probe movement in the normal direction (y) and the other to control the traverse in the spanwise (z) direction. The probe was traversed by inputting step displacements via an input control box that was connected to the stepping motors on the traverse system. The traverse position of the probe was indicated on a digital display. Using this traverse system, position increments of ±0.05 mm were achievable.

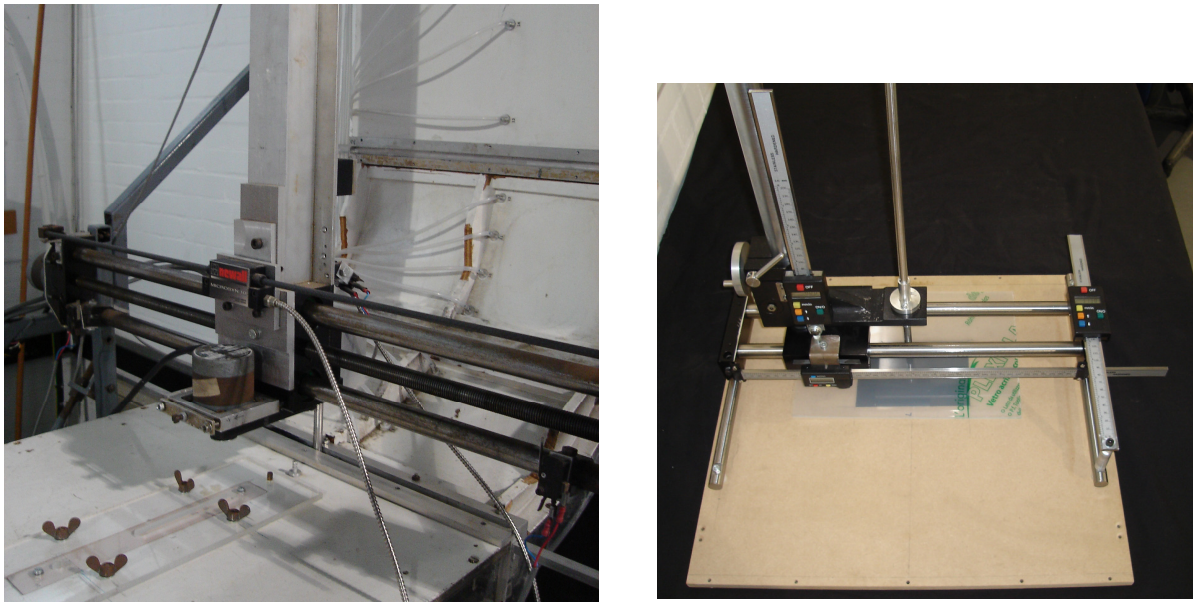

(a) (b)

Figure 3.5: Traversing systems used in the experimental investigation: (a) computer controlled traverse, (b) manual traverse.

3.2.4.2. Manual traverse

The manual system was used to traverse the probe in the normal and streamwise directions in the boundary layer along the upper surface of the airfoil. The vertical movement of the traverse was achieved by a rack and pinion system incorporated on a vertical column. The column had a toothed strip which engaged with the small pinion wheel that is connected to a hand wheel. When the hand wheel was turned the probe support moved in the normal direction. The direction of the movement was governed by the clockwise and anti-clockwise rotation of the hand wheel. A small clamp was then used to hold the support at the desired height. The horizontal movement in the streamwise direction along the chord of the airfoil had no mechanical assistance and was achieved solely by sliding the vertical column along the two guide rails and locking with a clamp.

The coordinates of the traversed position were read using the digital scales integrated in the traverse system. In the manual traverse position increments of ±0.01 mm were achievable.

3.2.4.3. Determining the probe reference coordinates

The reference coordinates (X_o, Y_o, Z_o) are used to define the location of the probe. The procedure for obtaining these coordinates is described below.

The reference height Y_o which is the normal distance between the centre of the probe sensor and the lower wall of the duct (concave wall) was obtained using the following procedure. A thin metal plate was placed onto a thicker plate, and the combined thickness of the plates was measured using a micrometer. The probe was then gradually traversed down until the prong(s) of the probe came into contact with the surface of the thin plate (Figure 3.6). For a single-wire probe the reference height was taken as the combined thickness of the plates.

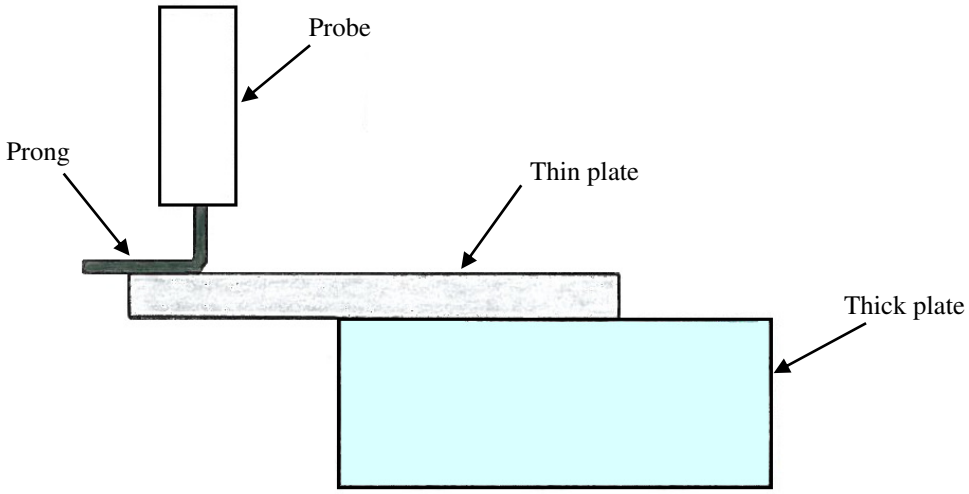

Figure 3.6: The method used to obtain the distance between the probe sensor and the wall of the duct

For the cross-wire probe the reference height from the lower wall was the sum of the combined thickness of the plates and one-half the distance between the probe prongs. The closest achievable distance to the wall for a cross-wire probe was 1.5 mm, and less than 1 mm for a single-wire probe. The streamwise (X_o) and spanwise (Z_o) reference coordinates were obtained using a similar technique. It should be noted that Z_o is the horizontal distance of the probe sensor(s) to the side wall of the tunnel, and X_o is the horizontal distance of sensor(s) from station 1.

3.3. The principles of the hot-wire measurement technique

3.3.1. Introduction

Hot-wire anemometry has been used extensively for many years as a research tool in fluid mechanics. It is based on the principle of convective heat transfer from a heated wire as a result of the flow passing over it. In hot-wire anemometers, very fine wires of about one micron, in diameter, are heated up to temperatures above ambient and the airflow past the wire has a cooling effect. There are two main modes of operation, namely, constant current (CC) and constant temperature (CT). In both these methods, the voltage output from the anemometer is from a circuit that tries to maintain a constant current or temperature. In constant current anemometry (CCA) the current through the wire is kept constant. Within this technique, the variation of the wire resistance due to the cooling effect of the cross flow, is measured from the voltage drop across the wire. In the present investigation constant temperature anemometry (CTA) was used to measure the mean velocity and turbulence quantities. Constant temperature anemometers are more widely used than constant current anemometers due to their reduced sensitivity to flow variations. For example, if the flow was to suddenly slow down in CCA, the wire could easily burn out. Conversely, if there was a sudden increase in flow velocity in CCA, then the wire may be cooled completely, and thus results in the anemometer not being able to read the data accurately.

3.3.2. Constant temperature anemometry (CTA)

In constant temperature anemometry the circuit tries to maintain a constant resistance and temperature in the wire, and the variation of current is measured. The advantage of CTA over other flow measuring principles is that, by using a very fine wire, it is possible to measure the velocity fluctuations of finer scales and higher frequencies. To maintain a constant wire temperature a feed back circuit is used as shown in Figure 3.7. The thin wire, located between A and B, is placed on one arm of a Wheatstone bridge and has a resistance of R_w. The resistance and temperature of the wire are maintained constant by the servo amplifier, which keeps the bridge in balance by controlling the current supply to the sensor wire. When the bridge is in balance the voltage difference across the wire is zero. As the flow velocity increases, the wire cools down; its resistance is decreases, and thus results in a bridge imbalance. This imbalance is represented by an error signal (voltage) across the Wheatstone bridge. To balance the bridge, the current in the circuit is increased, the sensor wire heats up

and the resistance is increased until the circuit is balanced. The voltage drop across the bridge can be used to represent the probe current. The servo amplifier gives a very fast response to the changes in the flow, and hence the sensor temperature and resistance can be maintained constant with changes in the flow velocity. The square of the voltage drop across the bridge (E^2) can be shown to directly represent the heat loss from the wire.

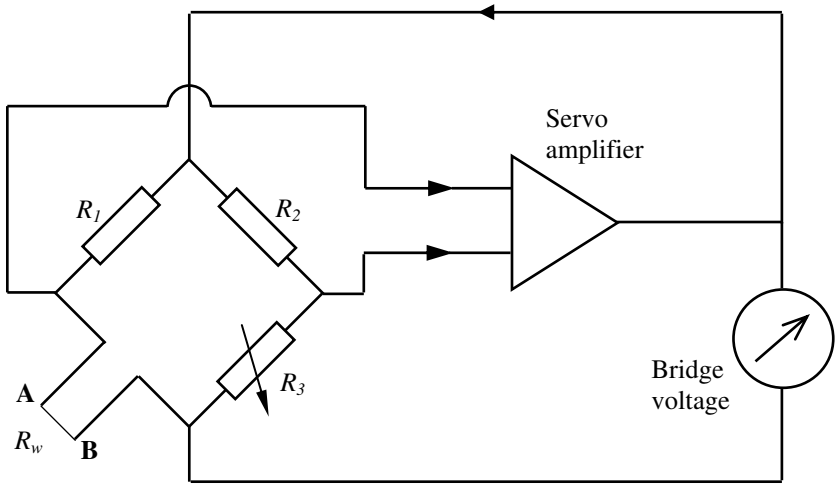

Figure 3.7: Schematic of a constant temperature anemometer, DANTEC Dynamics

The principles involved in hot-wire anemometry have been discussed by many researchers, including, Reynolds (1974), Hinze (1975), Perry (1982), Goldstein (1983), Lomas (1986) and Brunn (1995). The general hot-wire equation can be obtained by considering a small element of the wire, with diameter *d* exposed to a velocity U_N that is perpendicular to the wire (Figure 3.8).

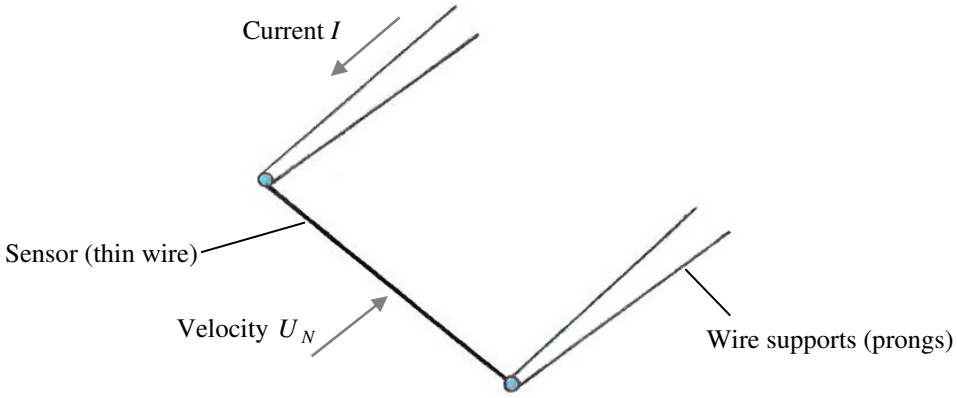

Figure 3.8: The basic principle of a hotwire.

When a current passes through the wire heat is generated. During the steady state equilibrium condition, the heat generated is balanced by the heat loss to the surroundings and the thermal energy stored in the wire. Neglecting conduction and radiation this yields the relationship,

$$I^2 R_w = \dot{Q} + \frac{dQ_i}{dt} \qquad (3.1)$$

where I is the current through the wire, R_w is the resistance of the wire, $\dot{Q}$ is the rate of heat transfer to the surroundings, and Q_i is the thermal energy stored in the wire, which is defined as,

$$Q_i = C_w T_w \tag{3.2}$$

The terms C_w and T_w in equation (3.2) represent the heat capacity and temperature of the wire, respectively. If the heat storage term in equation (3.1) is properly compensated, then the power $(I^2 R_w)$ generated by heating can also be expressed as,

$$I^2 R_w = \frac{\pi d^2}{4} h\left(T_w - T_a\right) \tag{3.3}$$

where T_a is the temperature of the surroundings and h is the heat transfer coefficient. The voltage difference E across the bridge in Figure 3.7 is related to the fluid velocity. It can be shown that, the relationship between the output bridge voltage E and the flow velocity U_N that is normal to an infinite length of wire, can be written in the form,

$$E^2 = A + B\left(U_N\right)^n \tag{3.4}$$

Equation (3.4) is also known as the King's Law, where E^2 represents the heat transfer from the wire and A, B, and n are the calibration constants. The heat transfer coefficient h in equation (3.3) can be eliminated using the correlation in equation (3.4). This yields the relationship,

$$A' + B'\left(U_N\right)^n = \frac{4 I^2 R_w}{\pi d^2 (T_w - T_a)} \tag{3.5}$$

As stated earlier, in a CTA, the current is adjusted to maintain a constant R_w and T_w. Provided that the surrounding air temperature T_a can be measured, the fluid velocity can be related to the input current (equation 3.5). It is also possible to represent the correlation between the bridge voltage and the fluid velocity using the nth order polynomial,

$$U = C_o + C_1 E + C_2 E^2 + C_3 E^3 ..... C_n E^n \tag{3.6}$$

where C_o, C_1 … C_n are the calibration constants, obtained from a least square fit.

3.3.3. Probe velocity decomposition

The complexity of the gathered data from a CTA anemometer is strongly dependent on the type of probe used. Probes may be selected on the basis of the expected velocity range, the number of velocity components to be measured, the spatial resolution and the available space for measurements (i.e. boundary layers, free shear layer). In the present investigation, experiments were conducted with both single-wire and cross-wire probes. In the probe velocity decomposition the velocity components of the wire coordinate system are converted into the laboratory coordinate system. Champagne et al. (1967a, b) found that for practical hot-wires with a finite length (Figure 3.9) the tangential velocity component also contributes to the heat loss from the wire.

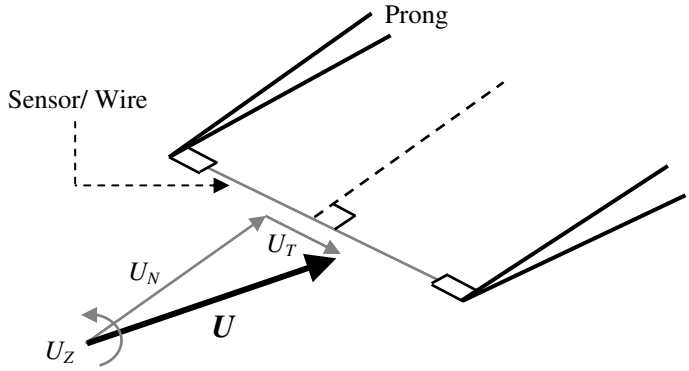

Figure 3.9: The resolved velocity components for a single-wire probe.

They defined an expression for the effective cooling velocity U_e in terms of the combined cooling effect of the normal velocity component U_N and the tangential velocity component U_T, written as,

$$(U_e)^2 = (U_N)^2 + k_1^2 (U_T)^2 \tag{3.7}$$

where k_1 is an empirical constant known as the yaw coefficient, found equal to 0.21 for a wire with length-to-diameter ratio of 200. Goldstein (1983) presents a formulation which also considers the spanwise velocity component U_Z that is also known to affect the heat transfer from the wire. The effective velocity that takes into account the effect of spanwise velocity was given as,

$$(U_e)^2 = (U_N)^2 + k_1^2 (U_T)^2 + k_h^2 (U_Z)^2 \tag{3.8}$$

The pitch factor coefficient k_h is a constant and can be taken as $k_h = 1.18$. To take into account the additional effect of the velocity component in the tangential and normal direction U_N in equation (3.4) can be replaced by the effective cooling velocity U_e. Figure 3.10 is a representation of a cross-wire probe with the sensors located in the *x*-*y* plane of the laboratory coordinate system.

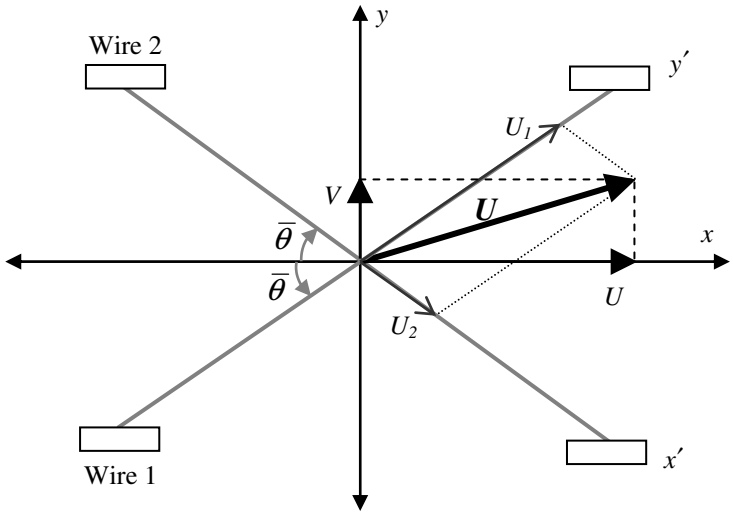

Figure 3.10: The resolved velocity components for a cross-wire probe.

The velocity components U_N, U_T and U_Z, for wire 1 (Figure 3.10) can be expressed as:

$$U_N = U_2 = U\cos\bar{\theta} - V\sin\bar{\theta}$$
$$U_T = U_1 = U\sin\bar{\theta} + V\cos\bar{\theta}$$
$$U_Z = W \qquad (3.9)$$

where U, V and W are the velocity components in the x, y and z directions, respectively. For wire 2, the velocity components are:

$$U_N = U_1 = U\sin\bar{\theta} + V\cos\bar{\theta}$$
$$U_T = U_2 = U\cos\bar{\theta} - V\sin\bar{\theta}$$
$$U_Z = W \qquad (3.10)$$

By substituting the terms of equation (3.9) into equation (3.8), the effective cooling velocity U_e for wire 1 can be defined,

$$U_{e1} = \left[\begin{array}{l} U^2\left(\cos^2\overline{\theta} + k_1{}^2\sin^2\overline{\theta}\right) + V^2\left(\sin^2\overline{\theta} + k_1\cos^2\overline{\theta}\right) \\ -UV\left(1-k_1{}^2\right)\sin 2\overline{\theta} + k_h{}^2W^2 \end{array} \right]^{\frac{1}{2}} \tag{3.11}$$

Similarly for wire 2, the expression for U_e yields,

$$U_{e2} = \left[\begin{array}{l} U^2\left(\sin^2\overline{\theta} + k_1{}^2\cos^2\overline{\theta}\right) + V^2\left(\cos^2\overline{\theta} + k_1\sin^2\overline{\theta}\right) \\ +UV\left(1-k_1{}^2\right)\sin 2\overline{\theta} + k_h{}^2W^2 \end{array} \right]^{\frac{1}{2}} \tag{3.12}$$

In the present implementation with the DANTEC StreamWare®/MiniCTA® software, the effective cooling velocity U_e is represented using the calibration velocity U_{cal}. The relationship between these two parameters is described by,

$$U_e = \frac{1}{\sqrt{2}} U_{cal}\left(1 + k_1{}^2\right)^{0.5} \tag{3.13}$$

The calibration velocity U_{cal} is obtained by substituting the digital output voltage across the anemometer bridge into the calibration transfer function, which in the present investigation is a fourth-order application of the polynomial correlation presented in equation (3.6). Substituting equation (3.13) into (3.7), gives

for wire 1,
$$\frac{1}{2}U_{1\,cal}{}^2\left(1 + k_1{}^2\right) = U_2{}^2 + k_1{}^2U_1{}^2 \tag{3.14}$$

and for wire 2,
$$\frac{1}{2}U_{2\,cal}{}^2\left(1 + k_1{}^2\right) = U_1{}^2 + k_1{}^2U_2{}^2 \tag{3.15}$$

Equations (3.14) and (3.15) can be solved simultaneously to obtain the normal and tangential velocities U_1 and U_2 in the wire coordinate system. Supposing that wires 1 and 2 (Figure 3.10) make angles $\overline{\theta}_1$ and $\overline{\theta}_2$ with the *x*-axis, respectively, the velocity components *U* and *V* in the laboratory coordinate system can be obtained from,

$$U = U_1\cos\overline{\theta}_1 + U_2\cos\overline{\theta}_2 \tag{3.16}$$

$$V = U_1\sin\overline{\theta}_1 - U_2\sin\overline{\theta}_2 \tag{3.17}$$

3.4. Experimental equipment

3.4.1. Data acquisition system

Data acquisition is the process by which information is gathered from analogue and digital measurement sources such as a hot-wire probe sensor. This often includes a combination of a measurement hardware and computer-based (PC) software. In the present study the data acquisition system comprised of an analogue to digital (A/D) converter board and software packages developed by DANTEC namely, the StreamWare® and MiniCTA® applications. The A/D converter was a National Instruments NI-AT-MIO-16E-10 type board consisting of 16 channels. The hardware was capable of sampling frequencies ranging from 0.015 kHz to 66.67 kHz and could produce 0 to 8.355×10^6 samples per channel. The analogue voltage signal of the probe wires were transferred through the CTA modules to the A/D converter for simultaneous sampling. The digital output signal in volts (between 0V to 10V) was then transferred to the StreamWare® software, which converts the voltage into mean velocity components using the probe velocity calibration algorithm. During data reduction the required turbulence quantities were also calculated.

There are two parameters of interest in the data acquisition, the sampling rate *SR* and the number of samples, *N*. The sampling time is therefore calculated using the ratio *N*/*SR*. For time-averaged analysis such as mean velocity and RMS quantities it is required that the time between samples is at least two times larger than the time scale of the velocity fluctuations (Jørgensen, 2005). In the present investigation a reference scale frequency f_o was used to determine an appropriate choice for the sampling frequency. The reference frequency scale is indicative of the outer layer motions and can be defined by (Yuan, 1991),

$$f_o = \frac{U_o}{\delta} \tag{3.18}$$

where δ is the boundary layer thickness. It is recommended that the selected sampling frequency be ten times the reference frequency scale. The sampling frequencies used in this work ranged between 8 kHz and 12 kHz, which was at least ten times the reference frequency scale. A number of preliminary tests were carried out at different mainstream velocities to determine the effect of the sampling frequency. Results indicated that beyond the optimum sampling frequency there was no significant changes in the parameters of interest namely,

mean velocity and RMS quantities. The experiments in the present study were conducted at sampling frequencies of 8 kHz, 10 kHz and 12 kHz for mainstream velocities 10, 15, 20 m/s, respectively. At each measuring location a sampling time of 15 seconds was employed. This corresponded to sample sizes in the range 120,000 to 180,000 samples per CTA channel for the three mainstream velocities.

3.4.2. Constant temperature anemometer

Constant temperature anemometry was employed to measure the mean velocity components, turbulence intensity and the Reynolds stresses. As stated earlier, in constant temperature anemometry the probe resistance and temperature are kept constant. Therefore, the output voltage across the bridge (see Figure 3.7) is a function of the effective cooling velocity acting on the probe sensor. In the present work, measurements that used stand alone single-wire or cross-wire probes were conducted with the DANTEC StreamLine® CTA system, whereas, experiments with the rake of single-wires were carried out using the DANTEC Multichannel® CTA system.

3.4.2.1. StreamLine® CTA system

The StreamLine® system consists of a frame (type 90N10) with room for six CTA modules and an input for a temperature probe. Temperature information is used to correct anemometer data when changes in the flow temperature occur. Each CTA module is served by a dedicated power supply. Additionally, the frame was fitted with a calibration module (type 90H10) which was connected to a flow unit that would permit automatic computer controlled calibration of the probes. The computer is directly connected to the frame (controller) via a serial port, and the output signals from the CTA modules are sent to the PC via the A/D converter. The StreamWare® application software was used in conjunction with the StreamLine® CTA system, during calibration, data acquisition and data reduction. Figure 3.11 presents a schematic of the experimental setup with two 90C10 CTA modules, a calibration module, a cross-wire probe, and a temperature probe connected to the frame.

The probe sensors were connected to the CTA modules using a coaxial cable through the BNC connectors on the front of each module. For the cross-wire probe, connections to two CTA modules were required (one for each wire sensor), whereas for a single-wire probe only one module was connected. The temperature module was built into the frame and temperature data

was communicated to the PC via the A/D board. The StreamLine® CTA system was automated in the sense that the frame automatically measured the sensor, leads, support and cables resistances prior to an experiment and configured the CTA bridge accordingly.

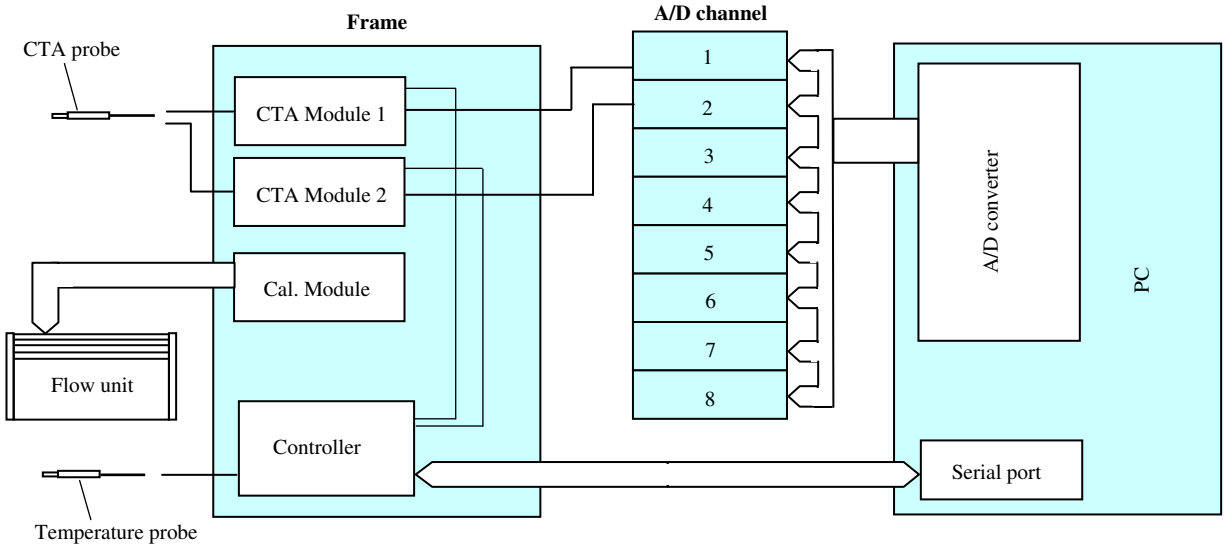

Figure 3.11: A diagrammatic of the experimental setup with the StreamLine® CTA system

3.4.2.2. Multichannel® CTA system

The DANTEC Multichannel® CTA (type 54N80) is a hot-wire anemometer system that can be used for the measurement of velocity and turbulence simultaneously in eight points in a flow field. The system allows for probe sensors in a rake to be monitored simultaneously, thus reducing the probe traverse cycle and cutting the experimental time. The frame consists of eight CTA channels, each with BNC connectors for probe input, and corresponding outputs for data acquisition via an A/D converter. The temperature was measured using a specially designed temperature system, which comprised of a probe connected to a box containing a thermister amplifier (type 54T40), operated by a separate 12 V DC power adaptor. The MiniCTA® application software was used in combination with the Multichannel® CTA system during the experiment, data acquisition, and data reduction.

A schematic of a typical experimental set-up with the Multichannel® system connected to four single-wire probes, the temperature box and the A/D board is shown in Figure 3.12. The temperature compensation is through the dedicated temperature box that is connected to one of the input channels of the CTA module through a BNC connector. In contrast to the automated system (Figure 3.11), in the Multichannel® system the probe sensor, cable, lead and support

resistances are input into the MiniCTA® software, and the dip switch settings for each CTA module are manually adjusted to reflect the properties of the probes used.

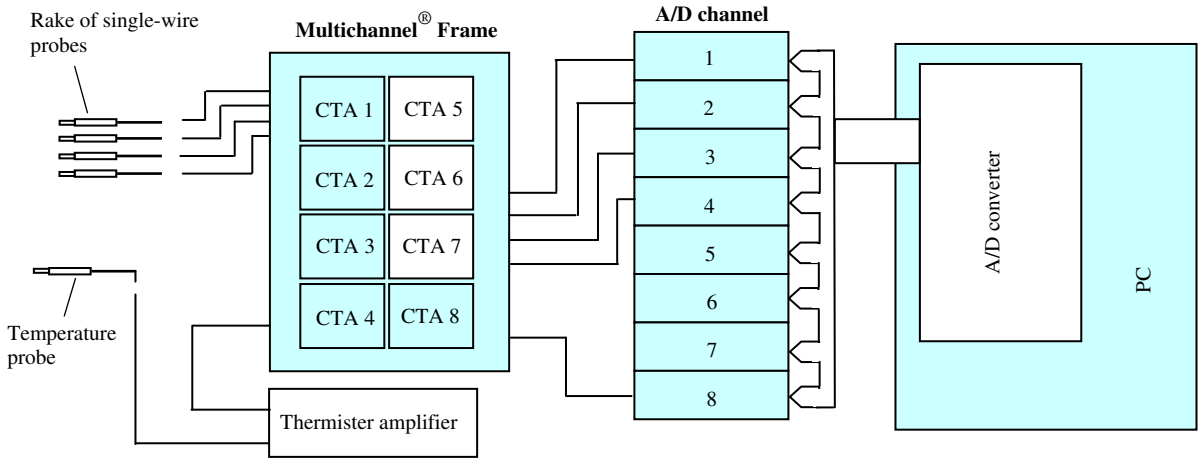

Figure 3.12: A diagrammatic of the experimental setup with the Multichannel® CTA system.

3.4.3. Hot-wire probes

The experimental investigation employed a selection of DANTEC hot-wire probes. These were of the single-wire and cross-wire type. The single-wire probes incorporated a single sensor and were used to measure the mean velocity and turbulence intensity. The cross-wire probes consisted of dual sensors, which were used to measure the mean velocity and turbulence quantities in two dimensions. These include the streamwise and normal components of velocity (*U* and *V*), the corresponding turbulence intensities (*Urms* and *Vrms*), and the turbulence shear stress ($-\overline{u'v'}$). Table 3.1 details the hot-wire probes used in the present study and the type of measurement conducted with each probe.

Probe type (DANTEC)	Sensor configuration	Measurement
55P14	Single-wire	Airfoil boundary layer
55P15	Single-wire	Airfoil boundary layer
(4×) 55P16	Single-wire	Near-wake
55P63	Cross-wire	Near-wake and station 2

Table 3.1: The hotwire probes used and the measurements carried out.

The probes presented in Table 3.1 are all miniature wire probes. The general properties of these probes are as follows. The sensors are made from platinum-plated tungsten wire, with length and diameter of 1.25 mm and 5 μm, respectively. The wires are welded directly onto the tip of the prongs and the entire wire length acts as a sensor. The sensor and supporting prongs are held by a probe stem made by a ceramic tube which is designed to provide a rigid aerodynamic mounting. Probes of this type can be used to measure air flow velocities in the range 0.2 to 500 m/s. The wire sensors have a typical resistance in the range 3.2 to 3.7 Ω with a maximum permissible sensor temperature of 300^{o}C, and are designed to operate at a maximum ambient temperature of 150^{o}C. Prior to each experiment the probe prongs were aligned with the *y*-axis (pitch) and the *x*-axis (yaw). The procedure for this is described in section 3.6.1.

3.4.3.1. Single-wire probes

Figure 3.13 illustrates the single-wire probes used in the present study. The type 55P14 and 55P15 (Figure 3.13a) were used to measure the airfoil boundary layer.

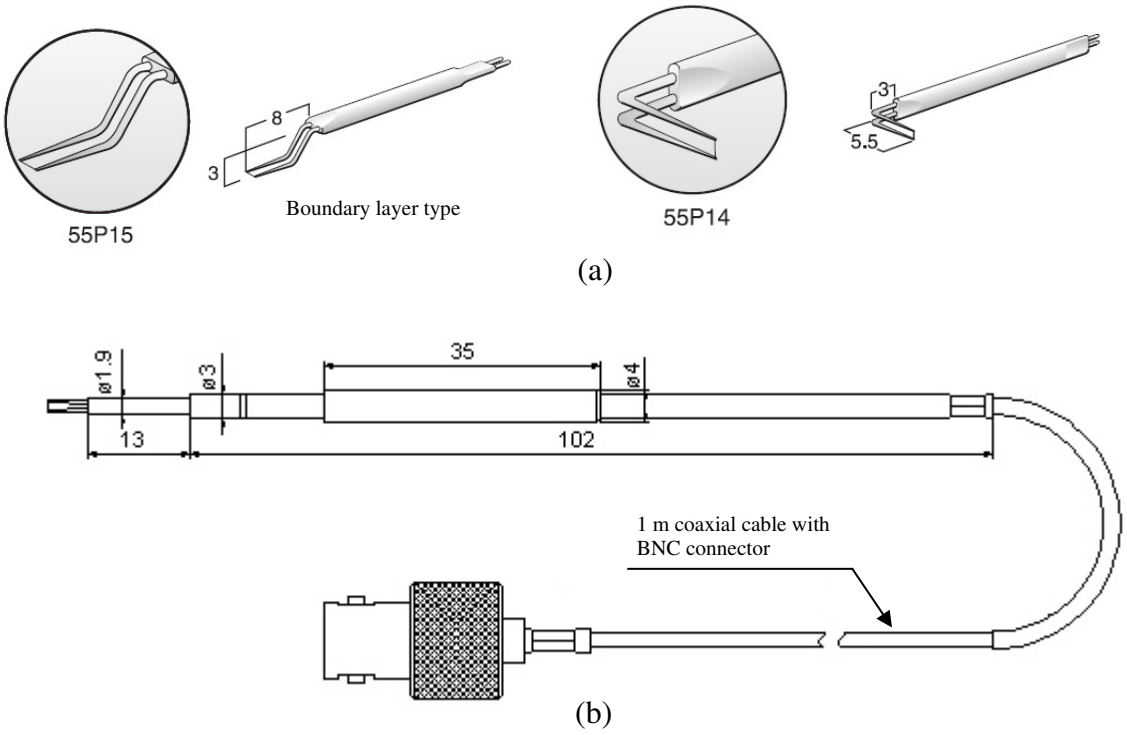

Figure 3.13: The single-wire probes used in the experimental investigation: (a) stand alone type 55P14 and 55P15, (b) cable equipped type 55P16, courtesy of DANTEC.

In the case of the 55P14 probe the prongs are at a right angle to the probe support and the sensor axis is perpendicular (90^{o}) to the probe axis, which makes the probe suitable for near-

wall measurements. The sensor and prongs of the 55P15 boundary layer type probe are offset to permit measurements closer to a solid wall, without disturbance from the prongs. During the airfoil boundary layer measurements the probes were traversed to within less than 1 mm of the wall. The probe stem for these two single-wire probes was a ceramic tube of length and diameter, 30 mm and 1.9 mm, respectively.

The 55P16 single-wire probe (Figure 3.13b) consists of a built-in straight support and a 1 m long cable with a BNC connector, which was connected to the Multichannel® CTA module using a coaxial cable. The 55P16 miniature wire is equipped with a protection sleeve that is used to protect the wire when not in use. The design of this probe made it suitable for implementation within a rake. The rake housing (described in section 3.4.6) was designed to accommodate eight type 55P16 probes, but for the final near-wake measurements only four of these probes were used.

3.4.3.2. Cross-wire probe

The DANTEC 55P63 cross-wire probe shown in Figure 3.14 is a dual sensor probe that consists of two sensors inclined at an angle of 90° with each other, and form an X-array configuration. As shown earlier (see Figure 3.10) if the two sensors are in the *x*-*y* plane then sensor 1 and sensor 2 form an angle of +45° and -45° with the *x*-axis, respectively.

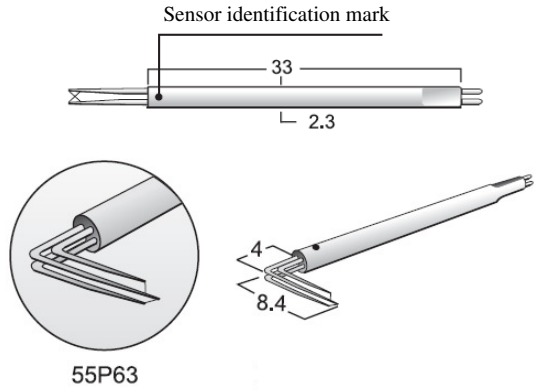

Figure 3.14: The cross-wire probe used in the experimental investigation, courtesy of DANTEC.

The wires of the 55P63 probe are parallel to the probe axis, thus enabling the measurement of the *U*- and *V*-components of mean velocity and turbulence quantities. The probe stem (2.3 mm diameter and 33 mm long) is marked with dots to indicate the sensor number. The right angled prongs make these probes practical for measuring flows in pipes or ducts where the traverse is

perpendicular to the flow direction. However, the interference of the supporting prongs makes this type of probe unsuitable for near-wall boundary layer measurements. The type 55P63 cross-wire probe was used for measurements in the near-wake and at station 2.

3.4.4. Temperature probe

The ambient temperature during the experiments varied by 1°C and was found to differ from the calibration temperature. It was therefore necessary to correct the output voltages prior to the velocity decomposition. For a typical hot-wire probe, the error in measured velocity is 2% per 1 °C of change in temperature (Jørgensen, 2005). The corrected voltage E_{corr} is therefore calculated from,

$$E_{corr} = \sqrt{\frac{T_w - T_{cal}}{T_w - T_a}} \cdot E \tag{3.19}$$

where T_{cal} is the ambient air temperature during probe calibration and T_a is the measured ambient air temperature during the acquisition of the bridge voltage E.

The DANTEC 90P10 temperature probe was used to measure the ambient fluid temperature and allow for temperature correction during the experiments. This probe is a thermister based thermometer with the sensing element embedded inside a 1.2 mm diameter stainless steel tube which is 50 mm long. A coaxial cable was used to connect the temperature probe to the CTA frame. The 90P10 probe can be used to measure temperatures in the range 0 to 150 °C with an accuracy of ± 0.5 °C. The temperature signal from the probe was sent to the computer via the A/D board. In the experiments with the Multichannel® system the temperature probe was connected to the CTA module through a separate temperature amplifier (type 54T40).

3.4.5. Probe support

Two different type of DANTEC probe supports were used in the experimental investigation, namely, the long-straight type and the long right-angled type. The 55P16 single-wire probe was a cable-equipped type probe with an integrated straight type probe support. The single-sensor 55P14 and dual-sensor 55P63 probes were supported using the long straight type 55H21 and 55H25 probe holders, respectively. To measure the airfoil boundary layer with the 55P15 probe, a right-angled probe support of type 55H22 was used, as shown in Figure 3.15.

The outside diameters of the single-wire and cross-wire probe supports were 4 mm and 6 mm, respectively. Furthermore, the cables on the dual sensor support were marked with one or two ring indicators that corresponded to the sensor number on the probe.

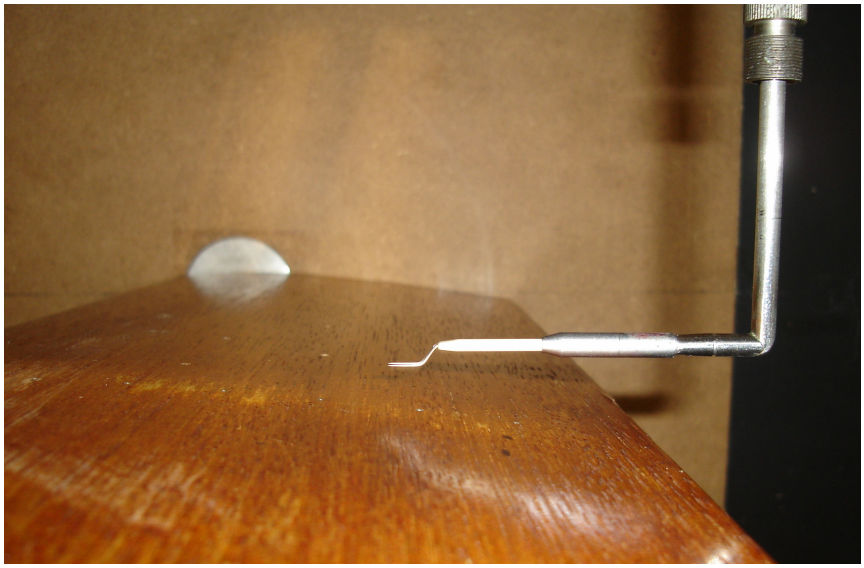

Figure 3.15: The airfoil boundary layer experiments with a 55P15 probe supported by a 55H22 right-angled probe holder.

3.4.6. The multi-probe housing

There were several reasons for adopting a rake of probes in the experiments. One of the main objectives of the experimental investigation was to measure the profiles of mean velocity and turbulence intensity at several streamwise locations in the near-wake, to study the effects of airfoil angle of attack on the wake. Using a rake reduced the experimental time and provided the added precision of simultaneously gathering data. The multi-probe housing was designed to accommodate a maximum of eight single-wire 55P16 probes. An orthographic projection drawing of the housing is presented in Appendix IV. As was stated previously, the cable equipped type probes were chosen due to the practicality of their integrated support. The housing was mounted on the probe guide tube of the traverse system at station 2 which was then used to traverse the entire rake.

The dimensions of the housing (in mm) are 50 × 62 × 22, in length, height and depth, respectively. The unit consists of a two-part aluminium casting, with a rubber strip at the interface between the two pieces. The larger aluminium piece is teethed with eight V-shaped rows, each sized to accommodate a 55P16 probe. The arrangement was designed to maintain a

normal centre to centre distance of 6 mm between successive probe sensors. The two piece housing was fixed together using the four tap screws located at the corners of the smaller aluminium casting. The traverse guide tube was inserted into the 10 mm diameter hole through the larger of the two aluminium castings. The grub lock screws located at the rear of the assembly were then used to firmly fix the housing to the traverse tube. A pictorial representation of the multi-probe housing and rake configuration is shown in Figure 3.16.

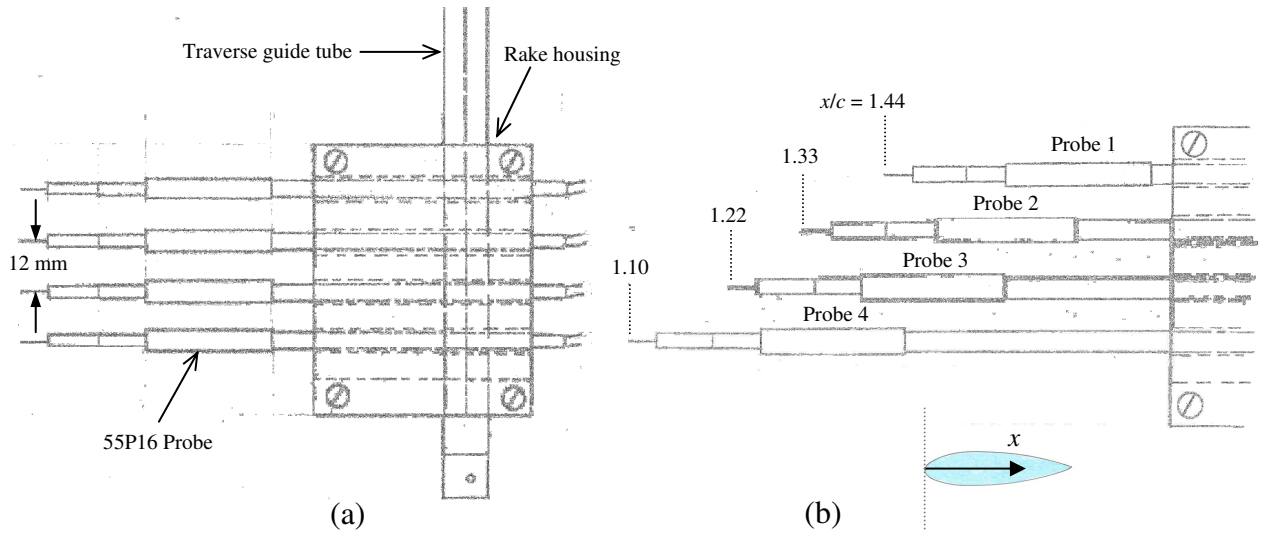

Figure 3.16: The multi-probe housing and typical probe configuration: (a) probe configuration during calibration, (b) probe configuration for near-wake measurements.

As can be seen in Figure 3.16(b), the rake was configured to allow simultaneous profile measurements at different streamwise locations, measured from the leading edge of the airfoil. The probes were protruded at a considerable streamwise distance from the housing. Prior to the experiment the probes were carefully aligned inside the fixture so that the sensor wires were horizontal with the z-axis. The final experiments were conducted with four 55P16 probes, and so the normal sensor to sensor distance was 12 mm. The procedure for the pitch and yaw angle alignment of the rake housing was similar to the steps described in section 3.6.1 for stand alone probes, but it was more involved due to the presence of four probes.

The shape of the unit was designed to be streamlined, similar to that of an airfoil, to minimise any interference with the upstream part of the flow. A preliminary investigation was therefore carried out to study the effect of the rake housing on the upstream part of the flow. In these tests a profile was measured in the near-wake, with the rake housing installed on the traverse tube at station 2. The results were then compared to a measurement taken at the same location in the near-wake, but in the absence of the housing. The findings suggested that aluminium

housing had a negligible effect on the mean and turbulence quantities measured upstream in the near-wake.

3.4.7. Probe calibration system

The rake of single-wire probes were calibrated inside the wind tunnel using the specially designed multi-probe housing. This was a manual calibration procedure at station 1, in that the tunnel air velocity was adjusted using the tunnel calibration equation. The bridge voltage was recorded simultaneously for all four probes using the MiniCTA® application software. The other stand alone cross-wire and single-wire probes used in the wake and boundary layer measurements were calibrated using the DANTEC StreamLine® calibrator.

The calibration system consists of a module of type 90H01 on the main frame and a separate flow unit connected to the calibration module via a cable. The air enters the flow unit via an external filter that filters away particles and oils. The calibrator is intended for probe calibration in air and other gases from 0.05 m/s to Mach 1. The calibration module directs the set parameters from StreamWare® application software to the flow unit. The module samples the signals from the pressure and temperature transducers in the flow unit and transmits them via the controller in the frame to the PC, where StreamWare® software uses these parameters to calculate the jet velocity at the exit of the nozzle. The calibration process was computer controlled and thus fully automated.

The flow unit operates from a pressurized air supply from an external compressor and creates a free jet through one of four outlet nozzles (diameter 42, 12, 8.7, 5 mm) to be selected based on the required velocity range of calibration. These nozzles have elliptical contours that are designed to minimise the boundary layer development at the tip, and thus ensure a flat jet profile. In the present study the 12 mm diameter nozzle was selected, applicable to velocities in the range 0.5 - 60 m/s. During the calibration process the probe to be calibrated was placed directly above the nozzle so that the probe sensor(s) were located at the centre of the free jet. The probe holder mounted on top of the flow unit was used to fix the probe into position to ensure that the prongs were parallel to the oncoming jet.

3.4.8. Manometers

An electronic precision micro-manometer of type FC0510 manufactured by Furness Controls Ltd was used to measure the static pressure on the upper and lower surfaces of the airfoil, in conjunction with a 20-channel pressure scanner box of type FCS421 (Furness Controls Ltd). The manometer could be used to measure pressures from 0.01 to 199.9 mm of water with an accuracy of 0.5 % as specified by the manufacturer.

3.4.9. Pitot-static tube

A Pitot-static tube was used to measure the static and stagnation pressures during the tunnel calibration. The end of the Pitot-static tube is turned through a 90^{o} angle, so that it could face the air stream and be aligned parallel with the flow. The nose (tip of the tube) had a single forward-facing hole, which measured the stagnation pressure. The static pressures were measured on a ring of side holes on the body of the tube.

For the tunnel calibration, the Pitot-static tube was placed at station 1. The difference between the stagnation pressure and the static pressure, which yields the dynamic pressure, was measured by connecting the static and stagnation pressure tapping to the digital micro-manometer. The velocity of air was then calculated using the recorded dynamic pressure in conjunction with the atmospheric pressure and temperature which were measured using a barometer.

3.5. Calibration procedure

The present investigation involved two types of calibration, namely, the wind tunnel calibration and the probe velocity calibration. For the stand alone probes (55P14, 55P15, 55P63) an automated calibration procedure was followed with the StreamLine® calibrator. For the rake of single-wires (55P16), a manual procedure was employed, whereby the rake housing was set up in the freestream region of the wind tunnel at station 1 and probes were calibrated simultaneously using the tunnel calibration data and the tunnel air velocity.

3.5.1. Tunnel calibration

The aim of the tunnel calibration was to obtain a relationship between the static pressure drop along the contraction section of the tunnel, and the Pitot-static pressure reading at station 1. The following part describes the procedures involved when conducting the tunnel calibration.

The Pitot-static tube was set up at the mid-height of the test section at station 1. The static pressure difference across the contraction section was obtained by connecting the pressure tappings at the entrance and exit of the contraction to the micro-manometer. The tunnel air velocity was progressively increased by increasing the speed of the centrifugal fan. At each incremental step the chamber pressure difference and the dynamic pressure from the Pitot-static tube were read. The atmospheric pressure and temperature were measured at the start and end of the tunnel calibration to monitor the changes in the ambient conditions. The density of air ρ_a was calculated from,

$$\rho_a = \frac{P_a}{R T_a} \tag{3.20}$$

where, R is the gas constant for air and P_a is the static atmospheric pressure. The results from the tunnel calibration are plotted in Figure 6.2, showing a linear relationship between the contraction section pressure and the dynamic pressure. During the experiments when the Pitot-static tube was removed, the mainstream velocity U_o at station 1 was obtained using,

$$\frac{1}{2}\rho_a U_o^{\,2} = \rho_w \, g \, \Delta h_w \tag{3.21}$$

which can be rearranged to yield,

$$U_o = \sqrt{\frac{2\rho_w \, g \, \Delta h_w}{\rho_a}} \tag{3.22}$$

In equation (3.22) ρ_w is the density of water and g = 9.81 m/s^2. The pressure difference across the Pitot-static tube Δh_w (in mm of water) represents the dynamic pressure, which can be obtained using of the linear relationship from tunnel calibration and the known chamber static pressure difference.

3.5.2. Probe velocity calibration with the StreamLine® calibrator

The automatic calibration of the probes was conducted using the DANTEC StreamLine® calibrator with the StreamWare® application software. The process of probe velocity calibration aims to establish a relationship between the CTA bridge output voltage and the flow velocity. In an automatic calibration the probe sensors are exposed to a set of known or predetermined flow velocities. The procedure was carried out in the following manner.

To set-up the hardware, the DANTEC calibration module of type 90H01 was installed into the slot of the StreamLine® anemometer frame (90N10). The calibration module was connected to the flow unit using the 90B01 system calibration cable. To achieve the desired air velocity range of 0 to 25 m/s, the 12 mm diameter nozzle was placed at the outlet of the flow unit. Finally, the probe was mounted on the flow unit so that the prongs were located in the core region of the jet and the sensor(s) in line with the exit plane of the nozzle. The jet from the nozzle of the flow unit, particularly in the core region, was classified as a straight, one-dimensional, and non-turbulent with $V = W = 0$. An external compressor was required to maintain a pressurised supply of 7 bar to the flow unit during the probe calibration. The StreamLine® system temperature probe was used to measure the ambient temperature changes during the calibration.

Upon initialization, StreamWare® automatically generated a set of equally spaced incremental velocity points that were based on the predefined velocity limits of the calibration and the number of specified calibration points. At each calibration point, the flow unit automatically adjusted the velocity of the jet to achieve the closest value of the corresponding point generated by the StreamWare® software. This was done by way of several iterations, until the difference between the calculated air velocity and the measured air velocity was small enough that it satisfied the user defined allowable error of the calibration. In the present investigation, a calibration error of ±0.6% was allowed. Once the flow unit had achieved the desired air jet velocity, the StreamLine® frame automatically measured the corresponding output bridge voltage from the probe sensor(s). The process was repeated for all the generated calibration points.

A fourth-order polynomial was then used to fit the calibration data for velocity U against output bridge voltage E, which was used by StreamWare® as a transfer function when converting the data from voltages into velocities. The probes were calibrated a number of

times during the experimental investigation to minimise the calibration drift error, which is associated with probe contamination, feedback in the circuitry, and changes in the properties of the probe sensor(s) over time.

3.5.3. Calibration of the rake in the wind tunnel

The rake of single-wire probes was calibrated in the wind tunnel at station 1. The procedure for this is described as follows.

Initially the computer controlled traverse system was moved to station 1. The single-wire probes were each connected to the CTA modules in the 54N80 Multichannel® system. The probes were then inserted into the rake housing and the sensors aligned with the *z*-axis. The housing was further aligned with respect to the pitch and yaw angles, when mounted on to the probe guide tube, as shown in Figure 3.16(a).

The air velocity of the tunnel was increased gradually by increasing the speed of the motor. The MiniCTA® software was then used to simultaneously record the bridge voltage across each sensor in the rake, at a given tunnel air velocity. A stand alone DANTEC temperature probe of type 90P10 connected to a dedicated thermister amplifier (type 54T40) was used to determine the changes in the flow temperature. The output bridge voltage was automatically corrected for the temperature variations, during calibration, using equation (3.19). This process was repeated for all the user defined velocity points of the calibration, in the range 0 to 25 m/s.

The data for flow velocity U and bridge voltage E gathered by each sensor was then fitted with a fourth-order polynomial. During a successful calibration, the error (% deviation of the points from the fitted curve) was less than 0.6%. In general, the power law curve based on the King's law was less accurate than the polynomial fits and hence was not used in the calibrations of the present investigation. The polynomial transfer function was incorporated into the experimental layout within the MiniCTA® software to determine the flow velocity for a given bridge voltage during the experiments. To minimise the calibration drift error, the rake was calibrated a number of times during the experimental work.

3.6. Uncertainty in the measurements and error analysis

3.6.1. Probe alignment

The misalignment of the probe can lead to significant error in the output signal from a hot-wire anemometer. Therefore, at the beginning and end of every experiment the sensor orientation with respect to the flow direction was checked. The procedure adopted in the present investigation considered alignment with respect to the pitch angle (*y*-axis) and the yaw angle (*x*-axis), as shown in Figure 3.17.

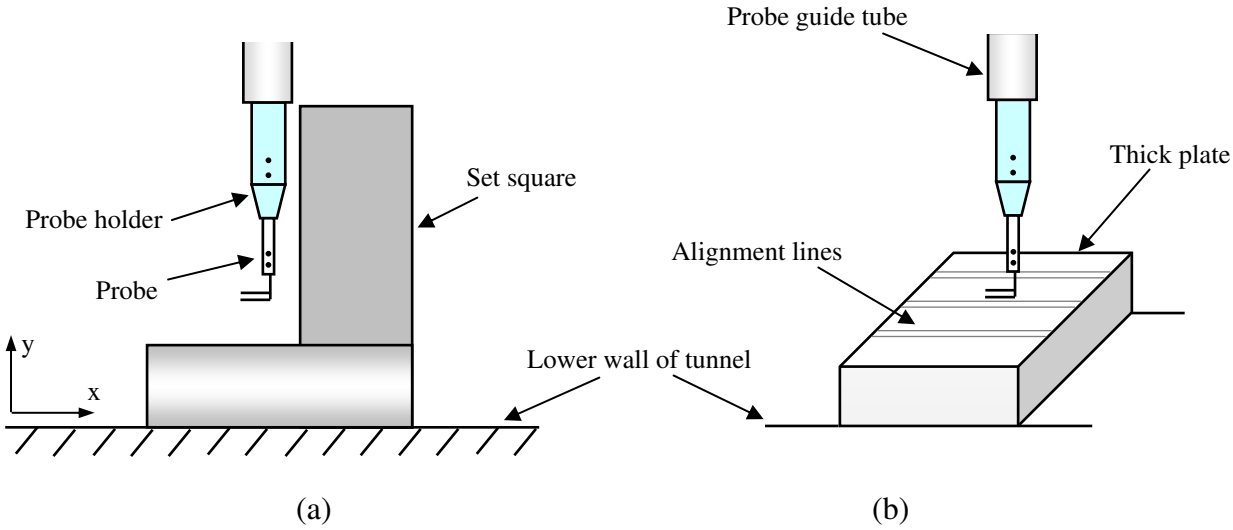

Figure 3.17: The alignment procedures employed in the present investigation: (a) pitch angle alignment, (b) yaw angle alignment.

For pitch angle alignment a set square was placed on the lower wall of the test section. The adjusting nuts either side of the traverse fixture were then turned accordingly to align the probe guide tube and probe support with the *y*-axis (Figure 3.17a). The set square was used to check the degree of alignment. During yaw angle alignment a thick plate marked with straight lines, parallel with the *x*-axis, was positioned on the lower surface of the test section. The probe was then lowered using the traverse so that the prongs were just above the parallel lines (Figure 3.17b). To fine tune the alignment of the probe prongs with the *x*-axis the probe guide tube was incrementally rotated (about the *y*-axis) until the prongs were parallel with the lines marked on the thick plate.

3.6.2. Uncertainty in the measurements

Experiments with hot-wire probes can be influenced by a number of factors which can have an effect on the output signal from the hot-wire anemometer. To estimate the overall accuracy of the measurements, all the different sources of error must be considered. These have been outlined by Perry (1982) and more recently by Jørgensen (2005), and include errors associated with calibration, such as the measurement of flow parameters and hot-wire voltages during calibration, the polynomial fitting of the calibration, calibration drift errors, sensor contamination and electronic noise. Other contributing factors to error are probe misalignment, temperature effects, pressure variations, sensor angle and the aerodynamics of the probe. The following part briefly discusses these factors with reference to the present investigation.

To reduce errors caused by variations in electronic noise and resistance, both the experiment and calibration processes comprised the complete chain of hardware, including the probe, probe support, cables, anemometer, and A/D board. The heat transfer from a sensor wire is directly proportional to the temperature difference between the sensor and the surrounding fluid. In CTA measurements temperature variations are the most common sources of error, where, under normal conditions, the error in the measured velocity is approximately 2% per 1 ^{o}C change in temperature. Changes in the ambient pressure can also influence the heat transfer from the wire. However, in CTA measurements the influence of pressure is usually neglected, since the pressure variation from calibration to experiment is normally small. Prior to the start of every experiment, the wind tunnel was run for at least two hours to maintain steady ambient conditions in the laboratory, and thus minimise the temperature variations. Furthermore, during every experiment a temperature probe was used to compensate for any temperature changes.

The contamination of the probe surface can reduce the heat transfer through the downward shift of the calibration curve. In the present setup the air entering the tunnel was subjected to a series of filters to reduce the risk of contaminants entering the test section and accumulating on the probe sensor. The sensor's angle can also contribute to changes in the expected results, and so the wires of the probes were checked regularly using a magnifier to assess the condition of the individual sensors. During the experimental work the probes were calibrated at regular intervals and several different probes were used. Therefore, the effect of calibration drift caused by changes in the properties of the wire, temperature variations, contamination of the sensors, sensor's angle, and electronic noise were significantly reduced.

The heat transfer from the wire can also be affected by the wake of the prongs (the wire support), especially when the oncoming flow is at an angle. However, in the present experiment the streamwise velocity component was much larger than the normal and spanwise components, thus the aerodynamic effects of the probe are taken as negligible.

The error associated with probe alignment and orientation can be minimised as long as the sensor is aligned identically with the flow during experiments and calibration. In the present investigation, the alignment of the probe was checked at the start and end of every experiment. Furthermore, during the calibration procedure, the probe(s) were aligned with the oncoming flow using the same principles as described in section 3.6.1, thus the effect of misalignment was significantly reduced.

3.6.3. Error analysis

In this section the procedure of Jørgensen (2005) is adopted to determine the percentage (%) uncertainty in the present experiments. The total relative uncertainty α_{tot} is determined by considering the individual contributions to error in the experiments. These are identified as the uncertainties due to calibration and data conversion, experimental conditions, and data acquisition. For each contributing factor the relative uncertainty α_i is calculated using the equations of Jørgensen (2005).

3.6.3.1. Uncertainty in calibration and data conversion

The calibration measurement errors are a combination of errors associated with the tunnel calibration, probe calibration equipment and linearization which is related to the curve fitting of the velocity calibration points.

The relative uncertainty from the tunnel calibration with the Pitot-static tube and micro-manometer is determined to be $\alpha_{Tcal} = 0.02$, and corresponds to a percentage uncertainty of ±2%. The percentage uncertainty from the velocity calibration using the calibrator is ±1% which results in a relative uncertainty of $\alpha_{Pcal} = 0.01$. On the other hand, for the probe velocity calibrations conducted in the wind tunnel, the uncertainty is taken as ±2% which corresponds to a relative uncertainty of $\alpha_{Rcal} = 0.02$. It should be noted that α_{Rcal} is associated

with the calibration of the rake of single hot-wire probes. The typical curve fitting error using the fourth-order polynomial is ±0.6% which yields a relative uncertainty of $\alpha_{lin} = 0.006$.

3.6.3.2. Uncertainty in experimental conditions

The uncertainties as a result of the experimental conditions are connected to probe alignment, airfoil alignment, the effect of temperature variation on the probe sensor(s), the changes in air density with temperature, and the variations of ambient pressure during the experiment.

The relative uncertainty due to probe misalignment can be calculated from,

$$\alpha_{pos} = \frac{1}{\sqrt{3}} \cdot (1 - \cos\theta) \tag{3.23}$$

where θ is the uncertainty angle. In the present study the uncertainty angle in the alignment of a stand alone probe after calibration was determined to be $\theta = 1^{o}$. Therefore, from equation (3.23), for a single probe, the relative uncertainty is $\alpha_{Spos} = 8.79 \times 10^{-5}$ which yields a percentage error of nearly 0.009%, that can be taken as negligible. For the rake of four single-wire probes the relative uncertainty is calculated using $\theta = 4^{o}$ and, therefore, $\alpha_{Rpos} = 0.0014$, which corresponds to a percentage uncertainty of 0.14%.

The alignment of the rake housing with respect to the yaw angle produced an uncertainty of 0.5^{o}, from which the relative and percentage uncertainties are obtained to be $\alpha_{Hpos} = 0.01$ and ±1%, respectively. The airfoil alignment procedure was carried out as described in section 3.2.3. The uncertainty in the airfoil alignment is 0.5^{o}, which results in a relative uncertainty of $\alpha_{A} = 0.01\,(\pm 1\%)$.

The temperature variations from calibration to experiment or during an experiment can introduce errors. The influence of temperature is considered in two parts; the first examines the effects on sensor temperature, and the second considers the change in the air density as a result of ambient temperature variation. In general, the difference between the ambient temperature at the start and the temperature at the end of an experiment was found to be $\Delta T = 1^{o}$C. The uncertainty in the sensor temperature due to changes in the ambient temperature is calculated from,

$$\alpha_{Stemp} = \frac{1}{\sqrt{3}} \cdot \frac{1}{U_o} \cdot \frac{\Delta T}{T_w - T_a} \cdot \left[\frac{A}{B} U_o^{-0.5} + 1 \right]^{0.5} \tag{3.24}$$

where A and B are the constants 1.396 and 0.895, respectively. As defined previously, (T_w – T_a) is the difference between the sensor temperature and the ambient temperature, which is taken as 200 ^{o}C (Jørgensen, 2005). Therefore, for the tests at a mainstream velocity of 10 m/s, the relative uncertainty in the effect of ambient temperature variation on the sensor temperature is calculated to be $\alpha_{Stemp} = 0.00035$ which corresponds to a percentage error of 0.035%. The effects of increased mainstream velocity on the relative uncertainty are very small in the present investigation and thus neglected.

The relative uncertainty related to the changes in air density with temperature is calculated using,

$$\alpha_{\rho temp} = \frac{1}{\sqrt{3}} \cdot \frac{\Delta T}{273} \tag{3.25}$$

where, for ΔT = 1 ^{o}C during a typical experiment, the relative uncertainty for changes in air density due to the ambient temperature variation is determined to be $\alpha_{\rho temp} = 0.002$ (0.2%). Changes in the ambient pressure can also influence the density and the calculated velocity. The ambient pressure at the start and end of every experiment was measured using a barometer. The relative change in pressure was determined to be ΔP = 300 Pa. The relative uncertainty that relates to the change in the ambient pressure can be deduced from,

$$\alpha_P = \frac{1}{\sqrt{3}} \cdot \left(1 - \frac{P_o}{P_o + \Delta P} \right) \tag{3.26}$$

where P_o is the ambient pressure at the start of the experiment. From equation (3.26) the relative uncertainty is $\alpha_P = 0.0017$ (0.17%).

3.6.3.3. Uncertainty in data acquisition

The uncertainty associated with the A/D board resolution is determined by,

$$\alpha_{A/D} = \frac{1}{\sqrt{3}} \cdot \frac{1}{U_o} \cdot \frac{E_{AD}}{2^n} \cdot \frac{\partial U}{\partial E} \tag{3.27}$$

where E_{AD} is the analogue to digital input range equal to 10 V, n is the resolution of the data acquisition board, which is 12 bit in the present setup with the NI-AT-MIO-16E-10 hardware. The inverse slope of the probe velocity calibration curve $\partial U/\partial E$ is on average determined to be 34 m/s/Volt, using the calibration data. The relative uncertainty as a result of A/D board resolution is calculated to be $\alpha_{A/D} = 0.005$, which yields a percentage uncertainty of 0.5%.

3.6.3.4. Total uncertainty in the measurements

The total uncertainty in the measurement of a single velocity sample under the above experimental conditions, including the calibration uncertainties, can be calculated using,

$$\alpha_{tot} = 2 \cdot \sqrt{\sum (\alpha_i)^2} \tag{3.28}$$

where α_i represents the relative uncertainties associated with the experimental setup, as obtained in sections 3.6.3.1, 3.6.3.2, and 3.6.3.3. Substituting the relative uncertainties for each variable into equation (3.28) yields a total uncertainty of $\alpha_{tot} = 0.033 = 3.3\%$ in the experiments with a stand alone single-wire probe and $\alpha_{tot} = 0.052 = 5.2\%$ for the experiments with the rake of single-wire probes. As expected the percentage uncertainty in a single velocity sample (U) obtained from the experiments with the rake, is higher than that obtained in the experiments with a stand alone probe. This is as a result of the additional contributions of probe and the rake-housing alignment error towards the overall uncertainty levels.

The estimated uncertainty in the measurement of static pressure, based on the accuracy of the micro-manometer, is ±2%. Using the error analysis above, the uncertainties in the measurement of parameters, namely, mean velocity (U), turbulence intensities (RMS) and turbulence shear stress ($\overline{u'v'}$), can be determined. These are displayed in Table 3.2 for the different probes used.

Probe type	% Uncertainty			
	U	***Urms***	***Vrms***	$\overline{u'v'}$
Single-wire	3.3%	3.3%	N/A	N/A
Rake	5.2%	5.2%	N/A	N/A
Cross-wire	3.3%	3.3%	3.3%	6.6%

Table 3.2: The estimated uncertainties in the measurement of mean and RMS parameters.

Chapter 4

4. NUMERICAL INVESTIGATION: Mathematical Model

4.1. Introduction

The bulk of the numerical investigation was based on the solution of the spatially filtered conservation equations of mass and momentum for three-dimensional, unsteady, turbulent, isothermal, and incompressible flow in a 90^o curved duct. LES presents an alternative to RANS modelling in that the governing equations are spatially filtered rather than time-averaged. While the RANS technique computes the mean flow field, LES presents a more accurate description of the physical mechanism of the flow by directly solving the filtered Navier-Stokes equations for the large and medium scales and thus improving the prediction of complex turbulent flows. In LES, the three-dimensional time-dependent length scales that are larger than the predefined filter width are resolved, whereas the effect of the unresolved parts of the flow are modelled using a SGS model.

This chapter first presents the conservation equations, then a brief overview of RANS turbulence modelling, followed by the formulation of LES and the discretization schemes. The numerical work adopted the use of FLUENT 6.3 CFD code. Therefore the general descriptions of the equations here follow the form given in the FLUENT User's Guide (2005), which also provides further details. Piradeepan (2002) presented a thorough description of the commonly used RANS turbulence models. Therefore, only the models of interest to the present numerical investigation, namely, the standard $k-\varepsilon$ model and RSM are described here. To assess the performance of SGS models in the large eddy simulations three different models were adopted, namely, the standard Smagorinsky model, its dynamic variant, and the dynamic kinetic energy by transport model, which are all discussed in this chapter. To study the effect of grid resolution on the results, the governing equations are discretized using the finite volume technique on three different block structured grids. In the present steady state RANS computations, the convection terms were discretized with a third-order QUICK scheme, while in LES the bounded central differencing scheme was adopted. In both cases, the pressure-velocity coupling was based on the SIMPLEC algorithm, which is an iterative procedure, in which the initially guessed values of pressure and velocity are step by step corrected until the

required accuracy is achieved. For the time integration an implicit second-order formulation was employed, details of which are also presented.

4.2. Governing equations

The fluid motion can be represented by mathematical models based on the conservation laws of mass, momentum and energy. The conservation laws can be expressed in the form of the continuity equation, the three components of the momentum equation and the energy equation. In the present computations the flow is considered as isothermal, and therefore, the energy equation is omitted. The evolution of an incompressible Newtonian fluid in the physical space with a constant viscosity, defined by a Cartesian coordinate system (x, y, z) with respective velocity components U, V and W, can be written in terms of instantaneous properties. The general form of the governing equations of continuity and momentum in tensor notation can be written as,

Continuity equation

$$\frac{\partial \rho}{\partial t} + \rho\left(\frac{\partial U_i}{\partial x_i}\right) = 0 \tag{4.1}$$

Momentum (Navier-Stokes) equation

$$\rho\frac{\partial U_i}{\partial t} + \rho\frac{\partial U_i U_j}{\partial x_j} + \frac{\partial P}{\partial x_i} - \mu\frac{\partial}{\partial x_j}\left(\frac{\partial U_i}{\partial x_j} + \frac{\partial U_j}{\partial x_i}\right) = 0 \tag{4.2}$$

The first two terms on the left-hand side of equation (4.2) represent the rate of change of momentum in the U_i component. The third and fourth terms on this side denote the pressure gradient and the viscosity effects on the fluid, respectively. It is assumed that there are no external fources acting on the fluid. The viscous stress component τ_{ij} for an incompressible and Newtonian fluid flow can be written as,

$$\tau_{ij} = \mu\left(\frac{\partial U_i}{\partial x_j} + \frac{\partial U_j}{\partial x_i}\right) \tag{4.3}$$

Therefore, the momentum equation in (4.2) can be rewritten as,

$$\rho \frac{\partial U_i}{\partial t} + \frac{\partial P}{\partial x_i} + \frac{\partial (\rho U_i U_j - \tau_{ij})}{\partial x_j} = 0 \tag{4.4}$$

4.3. RANS turbulence modelling

4.3.1. Time-averaged governing equations

The solution of the continuity and momentum equations for turbulent flows requires exceptional computer time and memory. Reynolds-averaged numerical simulations calculate the statistical average of the solution, across the whole computational domain. Supposing that the quantity ϕ varies instantaneously with time *t*, the process splits the exact solution of a variable ϕ into the sum of the mean $\overline{\phi}$ and fluctuating components ϕ',

$$\phi = \overline{\phi} + \phi' \tag{4.5}$$

Therefore, the time-averaged quantities can be obtained from,

$$\overline{\phi} = \lim_{T \to \infty} \frac{1}{T} \int_0^T \phi(t)\ dt \tag{4.6}$$

also the time average of the fluctuations ϕ' is by definition zero,

$$\overline{\phi'} = \lim_{T \to \infty} \frac{1}{T} \int_0^T \phi'(t)\ dt = 0 \tag{4.7}$$

In the above equations, *T* is the time interval over which the average is taken. The time-averaging process washes out the instantaneous length scales of the flow field. In the Reynolds-averaged approach the fluctuations are not resolved directly, but modelled using a turbulence model. The time-averaged form of the governing equations, namely, conservation of mass and momentum can be derived by substituting the mean and fluctuating components

of the flow variables (e.g. $U = \overline{U} + u'$, $P = \overline{P} + p'$) and applying the conventional ensemble rules of averaging, which state that the for two properties *a* and *b*,

$$\overline{ab} = \overline{a'b'} + \overline{a}\,\overline{b} \tag{4.8}$$

The continuity and momentum equations in (4.1) and (4.4) can be written in terms of the time-averaged terms. For a steady incompressible flow this yields,

Time-averaged continuity equation

$$\left(\frac{\partial \overline{U}_i}{\partial x_i}\right) = 0 \tag{4.9}$$

Time-averaged momentum equation

$$\frac{\partial \overline{P}}{\partial x_i} + \frac{\partial(\rho \overline{U}_i \overline{U}_j - \overline{\tau}_{ij})}{\partial x_j} = \rho \frac{\partial(-\overline{u_i' u_j'})}{\partial x_j} \tag{4.10}$$

The time-averaging of the governing equations results in the appearance of six independent unknown correlations known as Reynolds stresses. These correlations take the general form of $-\overline{u_i' u_j'}$ as shown in equation (4.10). The appearance of these unknowns means that the equations do not form a closed set, since we have more equations than the number of unknowns. Turbulence modelling is introduced to model the unknown correlations (Reynolds stresses) and close the set of governing equations, enabling solutions for the mean velocity and the pressure field. The models such as the Prandtl mixing length model and the $k-\varepsilon$ model use the eddy viscosity hypothesis.

4.3.2. Eddy-viscosity hypothesis

The concept of eddy-viscosity is based on an analogy between viscous stresses in laminar flow and the Reynolds stresses in turbulent flow. From Hooke's law in elastic solids, the shear stress is directly proportional to the strain. Therefore, in a viscous fluid the shear stress τ_{ij} is proportional to the rate of strain,

$$\tau_{ij} \propto e_{ij} \tag{4.11}$$

and hence for a Newtonian fluid,

$$\tau_{ij} = \mu e_{ij} \tag{4.12}$$

The rate of strain e_{ij} represents the velocity gradients in equation (4.3), and μ is the laminar viscosity. In turbulent flows the eddy viscosity μ_t is taken to be proportional to a length scale ℓ and a velocity scale υ, which characterise the turbulent motion. The relationship is defined as,

$$\frac{\mu_t}{\rho} \propto \upsilon \ell \tag{4.13}$$

and therefore,

$$\mu_t = \rho C \upsilon \ell \tag{4.14}$$

where *C* is a dimensionless constant. In contrast to the laminar viscosity in equation (4.12), μ_t in equation (4.14) is not a constant and depends on the state of turbulence, where it may vary with the flow from one point to another. In laminar flows, the shear stress is represented by the velocity gradients, but in turbulent flows, they are governed by eddy viscosity. Using the analogy expressed by equation (4.12) the turbulent stresses can be written as,

$$-\rho\overline{u_i' u_j'} = \mu_t\left(\frac{\partial \overline{U}_i}{\partial x_j} + \frac{\partial \overline{U}_j}{\partial x_i}\right) - \frac{2}{3}(\rho k \delta_{ij}) \tag{4.15}$$

where *k* is the turbulence kinetic energy and δ_{ij} is the Kronecker delta. Note that for $i = j$, $\delta_{ij} = 1$ and for $i \neq j$, $\delta_{ij} = 0$. Therefore, for the stress components such as $-\overline{u'v'}$, $-\overline{u'w'}$, and $-\overline{v'w'}$, the second term on the right hand side of equation (4.15) disappears. In the eddy-viscosity hypothesis, the assumption is taken that the turbulent viscosity μ_t is the same in all directions at any point (i.e. isotropic). The time-averaged momentum equation can therefore be written by considering both laminar and turbulent stress components,

$$\frac{\partial \overline{P}}{\partial x_i} + \rho\frac{\partial(\overline{U}_i \overline{U}_j)}{\partial x_j} = \rho\frac{\partial(-\overline{u_i' u_j'})}{\partial x_j} + \frac{\partial \overline{\tau}_{ij}}{\partial x_j} \tag{4.16}$$

By substituting the expressions in equations (4.3) and (4.15) for the viscous and turbulent stresses, respectively, into equation (4.16), and carrying out further simplifications, the time-averaged momentum equation that takes into account the laminar and turbulent viscosities can be written as,

$$\frac{\partial \overline{P}}{\partial x_i} + \rho \frac{\partial (\overline{U}_i \overline{U}_j)}{\partial x_j} = \frac{\partial}{\partial x_j}(\mu_{eff} \frac{\partial \overline{U}_i}{\partial x_j}) \tag{4.17}$$

where the effective dynamic viscosity $\mu_{eff} = \mu_t + \mu$. The turbulence models that are based on this method are known as eddy viscosity closure models. The $k-\varepsilon$ model adopts the eddy viscosity concept with the isotropic assumption for μ_t. The velocity scale previously defined in equation (4.14) can be obtained from the turbulence kinetic energy per unit mass, *k*, where,

$$\upsilon = \sqrt{k} \tag{4.18}$$

The term ε represents the rate of dissipation of turbulence kinetic energy and is given by,

$$\varepsilon = \frac{C_D k^{\frac{3}{2}}}{\ell} \tag{4.19}$$

where C_D is the model constant. The eddy-viscosity is obtained from k and ε, which are both computed from the solution of two differential equations, one for k and one for ε. Substituting the terms from equation (4.18) and (4.19) into equation (4.14) yields,

$$\mu_t = \rho C_\mu \frac{k^2}{\varepsilon} \tag{4.20}$$

where $C_\mu = C_D \cdot C = 0.09$ and is taken as a constant in the standard $k-\varepsilon$ model. The following section describes the main features of the RANS turbulence models, namely, the standard $k-\varepsilon$ and RSM models.

4.3.3. Standard $k-\varepsilon$ model

As was stated earlier, the standard $k-\varepsilon$ model (Launder and Spalding, 1974) is based on the solution of two transport equations, one equation for the turbulence kinetic energy k and one for the rate of dissipation of kinetic energy ε. These differential equations are solved simultaneously with the time-averaged governing equations of fluid motion. The eddy-viscosity is then calculated from equation (4.20) and the turbulence stresses from (4.15).

The modelled form of the turbulence kinetic energy equation can be written in tensor notation as,

k - equation

$$\rho\frac{Dk}{Dt}=\frac{\partial}{\partial x_i}\left[\mu\frac{\partial k}{\partial x_i}+\left(\frac{\mu_t}{\sigma_k}\frac{\partial k}{\partial x_i}\right)\right]+\mathbf{P}_k-\rho\varepsilon \qquad (4.21)$$

I II III IV

The term (I) on the left hand side of equation (4.21) represents the rate of change of turbulence kinetic energy plus the transport of k by convection. Term (II) models the transport of k by diffusion, where σ_k is an empirical constant. The production term $\mathbf{P}_k$ represents the generation of turbulence kinetic energy due to the interaction between the Reynolds stresses and the mean velocity gradients, and is defined as,

$$\mathbf{P}_k=-\rho\overline{u_i'u_j'}\frac{\partial U_i}{\partial x_j} \qquad (4.22)$$

Substituting equation (4.15) into (4.22) gives,

$$\mathbf{P}_k=\mu_t\frac{\partial U_i}{\partial x_j}\left(\frac{\partial U_i}{\partial x_j}+\frac{\partial U_j}{\partial x_i}\right) \qquad (4.23)$$

The term (IV) in equation (4.21) models the rate of destruction of turbulence kinetic energy. The modelled equation for ε can be written as,

ε - equation

$$\underbrace{\rho\frac{D\varepsilon}{Dt}}_{\text{I}} = \underbrace{\frac{\partial}{\partial x_i}\left[\mu\frac{\partial\varepsilon}{\partial x_i} + \left(\frac{\mu_t}{\sigma_\varepsilon}\frac{\partial\varepsilon}{\partial x_i}\right)\right]}_{\text{II}} + \underbrace{C_1\frac{\varepsilon}{k}\mathbf{P}_k}_{\text{III}} - \underbrace{C_2\rho\frac{\varepsilon^2}{k}}_{\text{IV}} \tag{4.24}$$

The term (I) on the left hand side of equation (4.24) represents the rate of change of ε plus the transport of ε by convection. The term denoted by (II) represents the diffusion of ε, whereas (III) and (IV) are the production and destruction of ε, respectively. C_1, C_2 and σ_ε are constants. The standard form of the $k-\varepsilon$ model as described above is applicable to high Reynolds number flows where the molecular viscosity is negligible. The values of the constants used in the model are given in Table 4.1,

C_μ	C_1	C_2	σ_k	σ_ε
0.09	1.44	1.92	1.0	1.217

Table 4.1: The constants of the standard $k-\varepsilon$ model.

The $k-\varepsilon$ model can provide good predictions for practical engineering purposes. Among its advantages, the model is relatively simple to implement and leads to stable calculations that converge easily. The weaknesses of the standard $k-\varepsilon$ model are in predicting swirling/rotating flows, flows with strong separation, and fully developed flows in non-circular ducts. Another disadvantage is that the model is only valid for fully turbulent flows.

Since the development of the $k-\varepsilon$ model in the 1970s, many attempts have been made to develop two equation models that improve on the standard $k-\varepsilon$ model. The equations of the RNG (Renormalization Group Method) $k-\varepsilon$ model (Yakhot et al., 1992) are similar to the standard $k-\varepsilon$ equations but include additional terms in the ε-equation for: interaction between turbulence dissipation and mean shear, the effect of swirl on turbulence, an additional formula for turbulent Prandtl number and a different formulation for the effective viscosity. The model improves on the predictions for high streamline curvature and strain rate, transitional flows, and those concerned with wall heat and mass transfer. The Realizable $k-\varepsilon$ model (Shih et al., 1995) shares the same turbulence kinetic energy equation as the standard $k-\varepsilon$ model, but for an improved equation for ε. Additionally, in this model, the

parameter C_μ is introduced as a variable, whereas in the standard model it is taken as a constant, as defined in Table 4.1. The Realizable $k-\varepsilon$ has provided improved predictions of flows involving planar and round jets, boundary layers undergoing strong adverse pressure gradient or separation, rotation, recirculation and strong streamline curvature. Further details of the RNG and Realizable variants of the $k-\varepsilon$ model are provided in the FLUENT User's guide (2005).

4.3.4. Reynolds Stress Model

The $k-\varepsilon$ based models take the assumption of isotropic eddy viscosity, where the unknown terms (Reynolds stresses) are related to one velocity scale, used to characterise the local state of turbulence. Therefore, in these models no information on the individual stresses can be obtained. The Reynolds Stress Model (RSM) closes the time-averaged Navier-Stokes equations by solving additional transport equations for the six independent Reynolds stresses in conjunction with the transport equation for the rate of dissipation of turbulence kinetic energy ε. RSM, therefore, does not use the eddy viscosity hypothesis, and is superior to two equation turbulence models with respect of capturing the anisotropic effects in complex turbulent flows, arising from streamline curvature, swirl, rotation, and flows involving separation.

The transport equations in RSM are derived by Reynolds averaging the product of the momentum equations with a fluctuating property. The closure assumptions used to model the additional terms in the Reynolds stress transport equations influence significantly the numerical predictions presented by RSM. The exact equation for the transport of the Reynolds stress R_{ij} can be written as,

$$\rho \frac{DR_{ij}}{Dt} = P_{ij} + D_{ij} - \varepsilon_{ij} + \phi_{ij} + \mathrm{O}_{ij} \qquad (4.25)$$

The term on the left hand side of equation (4.25) represents the rate of change of Reynolds stress R_{ij}, plus the transport of R_{ij} by convection. On the right-hand side of this equation, P_{ij} represents the rate of production of the Reynolds stresses, D_{ij} describes the transport by diffusion, ε_{ij} is the rate of dissipation, ϕ_{ij} expresses the transport due to pressure-strain interactions and O_{ij} represents the transport due to rotation.

Taking $R_{ij} = \overline{u_i' u_j'}$, the rate of change of momentum on the left-hand side of equation (4.25) can be expressed as,

$$\rho \frac{DR_{ij}}{Dt} = \frac{\rho \partial (\overline{u_i' u_j'})}{\partial t} + \frac{\rho \partial (U_k \overline{u_i' u_j'})}{\partial x_k} \tag{4.26}$$

To solve equation (4.25) the various terms on the right-hand side for diffusion, dissipation, and pressure-strain are modelled, except the stress production and rotation terms which are expressed in their exact form. The symbols, unless stated, have already been defined, and the values of the constants used in this model are shown in Table 4.2. The modelling of the terms as described below is for an incompressible flow.

The stress production term (P_{ij}) expressed in its exact form is written as,

$$P_{ij} = -\rho \left(R_{ik} \frac{\partial U_j}{\partial x_k} + R_{jk} \frac{\partial U_i}{\partial x_k} \right) \tag{4.27}$$

where $R_{ik} = \overline{u_i' u_k'}$ and $R_{jk} = \overline{u_j' u_k'}$.

The turbulent diffusion term (D_{ij}) is modelled by assuming that the rate of transport of Reynolds stress by diffusion is proportional to the gradients of Reynolds stresses. This can be written as,

$$D_{ij} = \frac{\partial}{\partial x_k} \left(\frac{\mu_t}{\sigma_k} \frac{\partial R_{ij}}{\partial x_k} \right) \tag{4.28}$$

The dissipation rate ε_{ij} is modelled by assuming isotropy of small dissipative eddies; the relationship reads,

$$\varepsilon_{ij} = \frac{2}{3} \rho \varepsilon \delta_{ij} \tag{4.29}$$

Because of the presence of the term δ_{ij}, the definition of ε_{ij} affects the normal stresses only.

In the implementation within FLUENT, the dissipation rate ε in equation (4.29) is computed from the transport equation for ε, as in the standard $k-\varepsilon$ model (equation 4.24).

The effects of the pressure-strain interactions (ϕ_{ij}) on the Reynolds stresses are described in two parts: pressure fluctuation as a result of two eddies interacting with each other, and the pressure fluctuations due to the interactions of an eddy with a region of the flow of different mean velocity. The pressure-strain term ϕ_{ij} can be expressed as,

$$\phi_{ij} = -C_3\rho\frac{\varepsilon}{k}\left(\overline{u_i'u_j'} - \frac{2}{3}k\delta_{ij}\right) - C_4\left((P_{ij} + \mathrm{O}_{ij} - C_{ij}) - \frac{2}{3}\delta_{ij}(P-C)\right) \tag{4.30}$$

where C_{ij} is the convection term defined by $C_{ij} = \rho\dfrac{\partial(U_k\overline{u_i'u_j'})}{\partial x_k}$ and $P = \dfrac{1}{2}P_{kk}$ and $C = \dfrac{1}{2}C_{kk}$.

The turbulence kinetic energy in equation (4.30) can be found by adding the three normal stresses, these yields,

$$k = \frac{1}{2}(\overline{u'^2} + \overline{v'^2} + \overline{w'^2}) \tag{4.31}$$

and in tensor notation can be written,

$$k = \frac{1}{2}(\overline{u_i'u_i'}) \tag{4.32}$$

The transport due to rotation O_{ij} is retained in its exact form, and is given by,

$$\mathrm{O}_{ij} = -2\rho\omega_k(R_{jm}e_{ijm} + R_{im}e_{jkm}) \tag{4.33}$$

where ω_k is the rotation vector, and the stresses are represented by $R_{jm} = \overline{u_j'u_m'}$ and $R_{im} = \overline{u_i'u_m'}$. The symbol $e_{ijk} = 1$ when *i*, *j* and *k* are different and in cyclic order, $e_{ijk} = -1$ when *i*, *j* and *k* are different and in anti-cyclic order, and $e_{ijk} = 0$, if any two indices are the same.

The values of the constants used in the Reynolds stress model are shown in Table 4.2.

C_1	C_2	C_3	C_4	σ_k	σ_ε
1.44	1.92	1.80	0.60	0.82	1.30

Table 4.2: Constants in the Reynolds Stress Model.

The Reynolds Stress Model is physically the most complete model in the RANS method, where the history, transport and anisotropy of turbulent stresses are all accounted for. Computations with RSM require increased in CPU effort which can be two or three times more than the $k-\varepsilon$ model.

4.4. Large eddy simulation

4.4.1. Introduction

Large eddy simulation is based on the theory that energy and information travel down the energy cascade to the smaller scales. The mass, momentum and energy are transported by the larger eddies. This follows the theory of self-similarity (Kolmogorov, 1941a, b) which stated that the large eddies of the flow are dependent on the domain geometry while the smaller scales are more universal. In LES, the flow field is separated into the resolved and sub-grid parts, through a filtering operation. The resolved part represents the large eddies, while the sub-grid part represents the small scales (Figure 4.1)

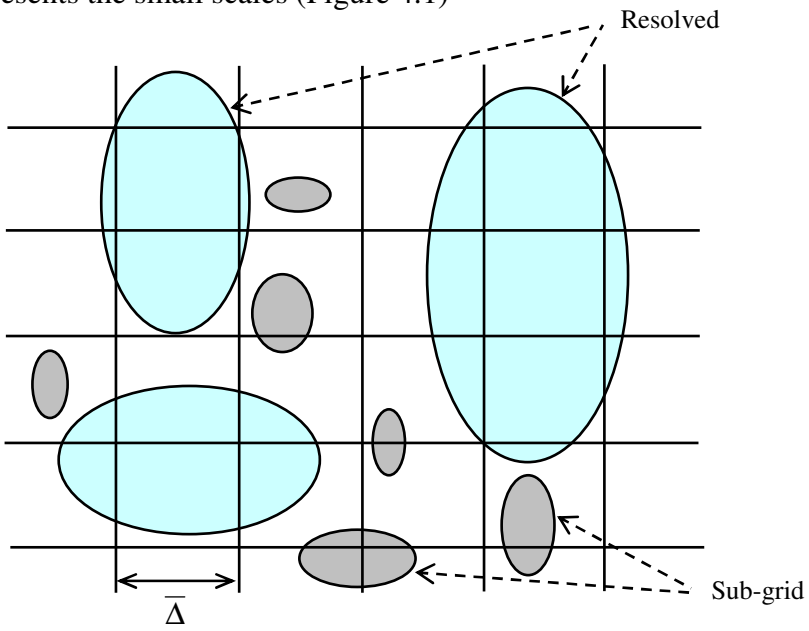

Figure 4.1: The resolved and sub-grid scales in large eddy simulation based on the grid filter width $\overline{\Delta}$, Sagaut (2006).

The Navier-Stokes equations are fully resolved for the larger scales defined by the filter width $\overline{\Delta}$, whereas the influence of the unresolved scales (smaller scales) are modelled using a sub-grid scale (SGS) model. In the present study, the size of the computational mesh is used to define the filter length. By resolving only the larger eddies, the method of LES allows for the use of coarser meshes (as compared with DNS), though these meshes are substantially finer than those used in RANS simulations. The most fundamental difference between the LES and RANS methods is that LES is an averaging process carried out spatially across the filter length, whereas RANS takes the time-average across the whole computational domain. Furthermore, LES is run for a substantial flow time to obtain stable mean flow statistics, and thus involves higher computational cost than RANS, in terms of storage and memory. Figure 4.2 describes the spatial filtering process of LES, where $U(x)$ is the sample velocity field and $\overline{U}(x)$ is the filtered velocity field for a filter width of $\overline{\Delta}$.

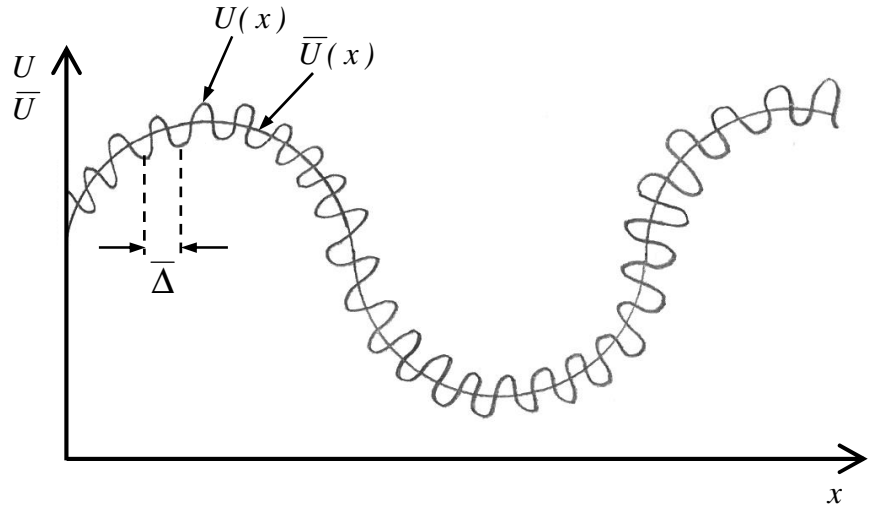

Figure 4.2: The filtering operation, Pope (2005).

The filtered profile agrees well with the profile of $U(x)$. In general, the filtered profile $\overline{U}(x)$ removes the residual part $u'(x)$, and the formulation is described by

$$U(x) = \overline{U}(x) + u'(x) \tag{4.34}$$

In RANS methodology the time-average of the fluctuations is taken as zero, whereas in LES the spatial average of the residual (sub-grid scales) across the filter length is not zero ($\overline{u'}(x) \neq 0$). To summarise, in LES the spatially filtered governing equations are resolved for the length scales that exceed the filter length, whereas in RANS the time-averaged conservation equations are modelled across all length scales in the computational domain. The

early publications that utilised LES (Smagorinsky, 1963; Lilly, 1967; Deardorff, 1973) were motivated by meteorological applications. The methodology was then developed for flows with isotropic turbulence (Chasnov, 1990; Kraichnan, 1976), and fully developed turbulent channel flows (Deardorff, 1970; Schumann, 1975; Moin and Kim, 1982; Piomelli, 1993). The main objective of these works was in the application of LES in complex geometries that are more relevant to the industry. The filter function, the filtering operation applied to the governing equations in physical space, and the modelling of the sub-grid scales are discussed in the following sections.

4.4.2. Definition of the filter

The idea of filtering, discussed briefly in the preceding section, is the most fundamental procedure in LES. The filtering process distinguishes between the larger and smaller scales. Figure 4.3(a) is a close-up of the sample velocity field shown in Figure 4.2, for one particular fluctuation.

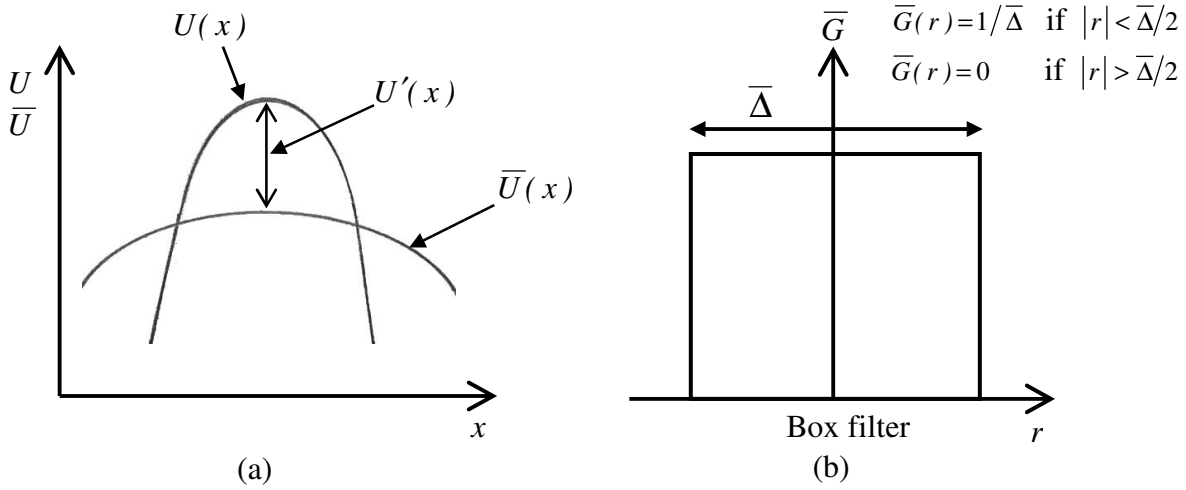

Figure 4.3: Concept of filtering a signal: (a) the breakdown of an instantaneous signal, (b) the box filter, Pope (2005).

As stated earlier $U(x)$, $\overline{U}(x)$ and $u'(x)$ represent the full scale velocity field, the filtered velocity field and the residual, respectively. Equation (4.34) can be used to describe the residual signal as the difference between the full scale flow and that of the filtered flow. Leonard (1974) introduced the general filtering operation, defined by,

$$\overline{U}(x) = \int_{-\infty}^{\infty} \overline{G}(r) U(x-r)\, dr \qquad (4.35)$$

In equation (4.35), $\overline{G}(r)$ is the homogenous filter function. The box filter and Gaussian filter are amongst commonly used filters in large eddy simulation. The present numerical investigation employs the box filter as shown in Figure 4.3(b). In circumstances when the length scale is less than half the filter length (i.e. $|r| < \overline{\Delta}/2$) the filter function becomes $\overline{G}(r) = 1/\overline{\Delta}$. The length scales falling in this range are not resolved, but their effects are modelled and they are referred to as the SGS scales. The filtering operation of equation (4.35) can then be rewritten,

$$\overline{U}(x) = \frac{1}{\overline{\Delta}} \int_{-\infty}^{\infty} U(x-r)\, dr \tag{4.36}$$

For length scales measuring above the filter length (i.e. $|r| > \overline{\Delta}/2$) the filter function becomes $\overline{G}(r) = 0$ and the filtering operation in equation (4.35) is described by,

$$\overline{U}(x) = 0 \tag{4.37}$$

where evidently no filtering is carried out. The Navier-Stokes equations are fully resolved for the larger scales that fall in this range. In the present work the filter length is defined locally by the size of a computational cell. Therefore, the grid spacing directly influences the filtering process, and hence, as the grid spacing is reduced the influence of the SGS model becomes smaller.

4.4.3. Filtering the governing equations in physical space

The equations governing the dynamics of the large eddies are obtained by applying the filtering operation discussed in section (4.4.2) to the governing equations. For incompressible flow the spatially filtered continuity and Navier-Stokes momentum equations can be written as,

Spatially filtered continuity equation

$$\left(\frac{\partial \overline{U}_i}{\partial x_i} \right) = 0 \tag{4.38}$$

Spatially filtered Navier-Stokes equation

$$\frac{\partial \overline{U}_i}{\partial t} + \frac{\partial (\overline{U_i U_j})}{\partial x_j} = -\frac{1}{\rho}\frac{\partial \overline{P}}{\partial x_i} + \frac{\mu}{\rho}\nabla^2 \overline{U}_i \qquad (4.39)$$

where $\nabla^2 = \frac{\partial^2}{\partial x_i^{\,2}} + \frac{\partial^2}{\partial x_j^{\,2}} + \frac{\partial^2}{\partial x_k^{\,2}}$.

The terms $\overline{P}$ and $\overline{U}_i$ in above equations are the spatially filtered pressure and velocity, respectively. The spatially filtered product $\overline{U_i U_j}$ is different to the product of the filtered velocities $\overline{U}_i \overline{U}_j$. The presence of the nonlinear term means that equation (4.39) is unusable unless $\overline{U_i U_j}$ is expressed as a function of the spatially filtered and the residual quantities. The procedure for the decomposition of the non-linear term is described below.

Leonard (1974) expresses the nonlinear term in the form,

$$\overline{U_i U_j} = \overline{(\overline{U}_i + u_i')(\overline{U}_j + u_j')} = \overline{\overline{U}_i \overline{U}_j} + \overline{\overline{U}_i u_j'} + \overline{\overline{U}_j u_i'} + \overline{u_i' u_j'} \qquad (4.40)$$

In equation (4.40) the nonlinear term is defined entirely as a function of the filtered quantity $\overline{U}_i$ and the residual quantity u_i'. By grouping together the terms that are not solely dependant on the large scales, the equation can be rewritten,

$$\overline{U_i U_j} - \overline{\overline{U}_i \overline{U}_j} = \underbrace{\overline{\overline{U}_i u_j'} + \overline{\overline{U}_j u_i'}}_{C_{ij}} + \underbrace{\overline{u_i' u_j'}}_{R_{ij}} \qquad (4.41)$$

where C_{ij} is the cross stress tensor representing the interaction between large and small scales, and R_{ij} is the SGS Reynolds stress that is representative of the interactions between the sub-grid scales. Therefore, using equation (4.41) the SGS stress tensor σ_{ij} can be defined as,

$$\sigma_{ij} = C_{ij} + R_{ij} = \overline{U_i U_j} - \overline{\overline{U}_i \overline{U}_j} \qquad (4.42)$$

rearranging equation (4.42) gives,

$$\overline{U_i U_j} = \sigma_{ij} + \overline{\overline{U}_i \overline{U}_j} \tag{4.43}$$

The term $\overline{\overline{U}_i \overline{U}_j}$ in equation (4.43) cannot be calculated directly due to the requirement of a second application of the filter. Therefore, Leonard proposes the triple decomposition,

$$\overline{\overline{U}_i \overline{U}_j} = \underbrace{\left(\overline{\overline{U}_i \overline{U}_j} - \overline{U}_i \overline{U}_j\right)}_{L_{ij}} + \overline{U}_i \overline{U}_j \tag{4.44}$$

where the term L_{ij} is the Leonard stress tensor representing the interactions between the large scales. Substituting equation (4.44) into (4.41) yields,

$$\overline{U_i U_j} - \overline{U}_i \overline{U}_j = C_{ij} + R_{ij} + L_{ij} \tag{4.45}$$

and hence the new definition of the SGS stress tensor takes the form,

$$\sigma_{ij} = \overline{U_i U_j} - \overline{U}_i \overline{U}_j \tag{4.46}$$

The spatially filtered momentum equation in (4.39) can therefore be rewritten by replacing equation (4.46) for the nonlinear term, this gives,

$$\frac{\partial \overline{U}_i}{\partial t} + \frac{\partial (\overline{U}_i \overline{U}_j)}{\partial x_j} = -\frac{1}{\rho}\frac{\partial \overline{P}}{\partial x_i} + \frac{\mu}{\rho}\nabla^2 \overline{U}_i - \frac{\partial \sigma_{ij}}{\partial x_j} \tag{4.47}$$

The filtering procedure introduces the residual (SGS) stresses σ_{ij}, and the closure of equation (4.47) is achieved by modelling the SGS stresses.

4.4.4. Modelling the SGS residual stresses

The SGS stresses σ_{ij} arising from the filtering operation are unknown. To close the set of the filtered Navier-Stokes equations a model for these SGS stresses is required. As with the RANS turbulence models, the SGS model in LES also adopts the Boussinesq hypothesis. The SGS turbulent stress for incompressible flows can be computed from,

$$\sigma_{ij} = \frac{-2\mu_t \bar{S}_{ij}}{\rho} \tag{4.48}$$

where μ_t is the SGS turbulent viscosity and $\bar{S}_{ij}$ represents the rate of strain which is defined as,

$$\bar{S}_{ij} = \frac{1}{2}\left(\frac{\partial \bar{U}_i}{\partial x_j} + \frac{\partial \bar{U}_j}{\partial x_i} \right) \tag{4.49}$$

The following sections describe the three SGS models used in the present numerical investigation, namely, the Smagorinsky-Lilly model, its dynamic variant, and the dynamic kinetic energy transport model. The emphasis is placed on the formulation and the procedure adopted to determine the SGS turbulent viscosity in each case. These models relate the eddy viscosity to the rates of strain through parameters C_s (Smagorinsky-Lilly), c_s (dynamic Smagorinsky), and C_k (dynamic kinetic energy transport). In the Smagorinsky model C_s is fixed at 0.1. On the other hand, the parameters c_s and C_k are dynamically determined, both spatially and temporally, thus providing better adaptation to local flow length scales. The dynamic kinetic energy transport model differs from the dynamic Smagorinsky model in that it additionally solves a turbulent kinetic energy transport equation to deduce k_{sgs} (SGS turbulence kinetic energy). Kim (2004) provides further details of these models.

4.4.4.1. Smagorinsky-Lilly model (SMG)

The first model for the SGS eddy viscosity was proposed by Smagorinsky in 1963. This model although simple formed the basis of the advanced models described later. From Prandtl's mixing length hypothesis the SGS turbulent viscosity can be defined as,

$$\mu_t = \rho \ell_s^{\,2} \left| \bar{S} \right| \tag{4.50}$$

where $\left| \bar{S} \right|$ is the characteristic magnitude of the spatially filtered local shear (rate of strain) defined by,

$$\left| \bar{S} \right| = \sqrt{2 \left| \bar{S}_{ij} \bar{S}_{ij} \right|} = \sqrt{2 \left| \bar{S}_{ij}^{\,2} \right|} \tag{4.51}$$

The Smagorinsky length scale ℓ_s is taken to be proportional to the filter width $\overline{\Delta}$,

$$\ell_s \propto \overline{\Delta} \tag{4.52}$$

In the implementation in FLUENT, ℓ_s is computed using,

$$\ell_s = \min\left(\kappa d, C_s \overline{\Delta}\right) \tag{4.53}$$

In equation (4.53) κ is the von Kàrmàn constant, *d* is the distance to the closest wall and C_s is the Smagorinsky constant. Since the grid itself is used as the filter, then the filter width will coincide with the width of a computational cell, where $\overline{\Delta} = V^{1/3}$ and V is the volume of a computational cell. The mixing length for the sub-grid scales in equation (4.53) can be rewritten in the form,

$$\ell_s = C_v \overline{\Delta} \tag{4.54}$$

where the constant $C_v = \min\left(\kappa d, C_s\right)$.

Lilly (1967) used the sharp spectral filter and the local equilibrium hypothesis to determine the following expression for the dimensionless constant C_s,

$$C_s \approx \frac{1}{\pi}\left(\frac{2}{3K_o}\right)^{\frac{3}{4}} \tag{4.55}$$

K_o is the Kolmogorov constant. Lilly derived the value of $C_s \approx 0.17$ for homogenous isotropic turbulence; however this was found to induce excessive damping of large scale fluctuations in transitional near-wall flows and had to be decreased in such regions. Therefore, C_s is not a universal constant, and has to be adjusted to yield improved results. Clark et al. (1979) uses $C_s = 0.2$ for isotropic homogenous turbulence, whereas, Deardorff (1970) takes $C_s = 0.1$ for plane channel flow. The experimental studies of Meneveau (1994) for the SGS stress modelled in a turbulent plane wake, and Uzun et al. (2003) for the sensitivity of

Smagorinsky's constant in turbulent jets, yield C_s in the range 0.1 to 0.12. In general, a value of 0.1 has been found to yield the best results for a wide range of flows.

Substituting equation (4.54) into (4.50) for the length scale, the SGS turbulent viscosity as described by the Smagorinsky-Lilly model can be expressed as,

$$\mu_t = \rho C_v^{\,2} \overline{\Delta}^2 \left|\overline{S}\right| \tag{4.56}$$

The SGS turbulent stress from equation (4.48) can therefore be written as,

$$\sigma_{ij} = -2C_v^{\,2} \overline{\Delta}^2 \left|\overline{S}\right| \overline{S}_{ij} \tag{4.57}$$

From equation (4.53), C_s governs the magnitude of the eddy length scale. For flows where a body is present (e.g. flow over an airfoil), it is recommended that the Smagorinsky constant be calculated locally. As mentioned earlier the length scale of eddies varies considerably in the freestream compared to the near wall. A lower value of C_s would then yield better computation of the eddy length scale, for the near wall region. In the present numerical simulations with the SMG model C_s is fixed at 0.1.

4.4.4.2. The dynamic Smagorinsky-Lilly model (DSMG)

The standard Smagorinsky model (SMG) provides reliable predictions when applied to homogeneous isotropic turbulent flows. However, in anisotropic flows the predictions are less acceptable. Although the SMG model is economical it has limitations. There exists no single value of the model constant C_s that satisfies, on a universal scale, the wide range of turbulent flows. Tests by McMillan et al. (1980) for SGS models confirmed that C_s decreases with increasing strain rate. Mason and Callen (1986) found that $C_s = 0.2$ gives good results for sufficiently fine resolutions, although it is required that C_s be less than 0.2 if the grid resolution is insufficient. Piomelli et al. (1988) found $C_s = 0.1$ to be an optimum value for simulations with the filter width equal to the cell grid size. The manner in which C_s is defined is dependent on the flow. The study of Mason and Callen (1986) was based on turbulence scales in the inertial range of the energy spectrum; where molecular viscosity is negligible,

whereas Piomelli et al. (1988) considered the additional effects of the viscous sublayer. Therefore unless the Smagorinsky constant is adjusted in the near wall region, the SMG model will yield incorrect values of length scale in this region.

Many methods have been proposed to calculate the parameters of SGS models dynamically. The procedure of Germano et al. (1991) and the modification proposed by Lilly (1992) formed one of the first dynamic SGS models. The methodology works by automatically adjusting the Smagorinsky constant spatially at each point and temporally at each time-step, thus providing better adaptation to the local flow length scales. The technique is based on the standard SMG model, where the parameter C_s, previously a constant, is now a function of space and time such that $C_s(x, y, z, t)$. The dynamic Smagorinsky model (DSMG) is based on flow variables at two filter widths, one at grid level denoted by $\overline{\Delta}$ (discussed earlier) and one at the test filter level denoted by $\tilde{\Delta}$. The test filter is taken to be larger than the grid filter (Germano et al., 1991) and associates itself with the larger length scales. Numerical test have shown $\tilde{\Delta} = 2\overline{\Delta}$ to be an optimum value for the test filter width. Similar to equation (4.35) for the grid filter operation, the test filtering operation can be defined as,

$$\tilde{U}(x) = \int_{-\infty}^{\infty} \tilde{G}(r) U(x - r)\, dr \tag{4.58}$$

where $\tilde{G}(r)$ is the test filter function corresponding to $\tilde{\Delta}$. The test filtered Navier-Stokes equation can be written as,

$$\frac{\partial \tilde{\overline{U}}_i}{\partial t} + \frac{\partial (\tilde{\overline{U}}_i \tilde{\overline{U}}_j)}{\partial x_j} = -\frac{1}{\rho}\frac{\partial \tilde{\overline{P}}}{\partial x_i} + \frac{\mu}{\rho}\nabla^2 \tilde{\overline{U}}_i - \frac{\partial T_{ij}}{\partial x_j} \tag{4.59}$$

The sub-test scale stress T_{ij} is associated with the larger scales resolved. The SGS stress σ_{ij} in equation (4.57) arising from the grid filtering operation can be rewritten in the form,

$$\sigma_{ij} = -2 c_s \overline{\Delta}^2 \left|\overline{S}\right| \overline{S}_{ij} \tag{4.60}$$

where the dynamic Smagorinsky parameter c_s replaces C_v^2 from the standard Smagorinsky model. As with the sub-grid scale stress tensor in equation (4.46), the sub-test scale stress tensor can be represented using,

$$T_{ij} = \widetilde{\overline{U_i U_j}} - \tilde{\overline{U}}_i \tilde{\overline{U}}_j \tag{4.61}$$

Therefore, similar to equation (4.60) the sub-test scale stress T_{ij} from the test filtering operation is defined as,

$$T_{ij} = -2 c_s \tilde{\Delta}^2 \left| \tilde{\overline{S}} \right| \tilde{\overline{S}}_{ij} \tag{4.62}$$

The resolved turbulent stress L_{ij} represents the contribution to Reynolds stresses by the smallest resolved scales, that is, the length scales that fall between the grid filter width $\overline{\Delta}$ and the test filter width $\tilde{\Delta}$. The resolved turbulent stress L_{ij} is defined by,

$$L_{ij} = T_{ij} - \tilde{\sigma}_{ij} \tag{4.63}$$

where, σ_{ij} is multiplied by Germano's identity (i.e. test filtered) in equation (4.63). Using the relationships in equations (4.46) and (4.61), the resolved turbulent stress yields,

$$L_{ij} = \left(\widetilde{\overline{U_i U_j}} - \tilde{\overline{U}}_i \tilde{\overline{U}}_j \right) - \left(\widetilde{\overline{U_i U_j}} - \widetilde{\overline{U}_i \overline{U}_j} \right) \tag{4.64}$$

and,

$$L_{ij} = \widetilde{\overline{U}_i \overline{U}_j} - \tilde{\overline{U}}_i \tilde{\overline{U}}_j \tag{4.65}$$

The sub-grid scale (σ_{ij}) and sub-test scale (T_{ij}) in equation (4.60) and (4.62) can be expressed in the form,

$$\sigma_{ij} = c_s \beta_{ij} \qquad \text{where } \beta_{ij} = -2\overline{\Delta}^2 \left| \overline{S} \right| \overline{S}_{ij} \tag{4.66}$$

$$T_{ij} = c_s \alpha_{ij} \qquad \text{where } \alpha_{ij} = -2\tilde{\Delta}^2 \left| \tilde{\overline{S}} \right| \tilde{\overline{S}}_{ij} \tag{4.67}$$

The resolved component of the stress tensor L_{ij}, from equation (4.63) that is associated with the scales between the test filter and the grid filter can be rewritten in the form,

$$L_{ij} = c_s \alpha_{ij} - \widetilde{c_s \beta_{ij}} \tag{4.68}$$

The assumption is made that c_s is constant along the defined test filter length, and,

$$L_{ij} = c_s (\alpha_{ij} - \tilde{\beta}_{ij}) \tag{4.69}$$

$$L_{ij} = c_s M_{ij} \tag{4.70}$$

Using the terms in equation (4.66) and (4.67) M_{ij} is written as,

$$M_{ij} = -2 (\tilde{\Delta}^2 \left|\tilde{\bar{S}}\right| \tilde{\bar{S}}_{ij} - \bar{\Delta}^2 \left|\bar{S}\right| \bar{S}_{ij}) \tag{4.71}$$

The dynamic Smagorinsky model works by obtaining the value of c_s such that it satisfies equation (4.70), and then applying this to equation (4.66) to deduce the SGS stress. Equation (4.70) is an overdetermined system of equation, with the single uknown c_s and the five independent components of L_{ij}. Following the procedure of Lilly (1992), c_s is obtained by minimizing the square of the error. Taking *E* to be the square of the error in equation (4.70), then,

$$E = (L_{ij} - c_s M_{ij})^2 \tag{4.72}$$

The logical root of equation (4.72) can be determined by evaluating the partial dervative $\partial E / \partial c_s$ and solving for $\partial E / \partial c_s = 0$. Multiplying out equation (4.72) gives,

$$E = L_{ij}{}^2 - 2 c_s M_{ij} L_{ij} + c_s{}^2 M_{ij}{}^2 \tag{4.73}$$

The partial derivative of *E* with respect of c_s yields,

$$\frac{\partial E}{\partial c_s} = -2 M_{ij} L_{ij} + 2 c_s M_{ij}{}^2 \tag{4.74}$$

Setting equation (4.74) to zero and solving for c_s gives,

$$c_s = \frac{M_{ij} L_{ij}}{M_{ij}^{\ 2}} \tag{4.75}$$

The sub-grid scale stress as defined in equation (4.66) can therefore be expressed as,

$$\sigma_{ij} = \frac{M_{ij} L_{ij}}{M_{ij}^{\ 2}} \beta_{ij} \tag{4.76}$$

The model parameter c_s is local and can vary temporally and spatially to result in both positive and negative values. A negative value of c_s is interpreted as backscatter, which describes the flow of energy from sub-grid scales to the resolved eddies. Although this is a desirable attribute of the dynamic model, a too large negative eddy viscosity can cause numerical instability that can lead to the divergence. In FLUENT c_s is clipped at zero and 0.23 to prevent the possibility of excess noise or numerical instability. In general LES of wall bounded turbulent flows with the dynamic SGS model indicate significant improvements over the computations that use the standard Smagorinsky model.

4.4.4.3. The dynamic kinetic energy transport model (DKET)

The dynamic SGS model developed by Germano et al. (1991) and the modification of Lilly (1992) base themselves on Smagorinsky's fundamental formulation, where the SGS stresses are calculated using the information from the resolved velocity scales. In these models assumptions are made for local equilibrium between energy transferred through the grid filter scales (large scales) and the dissipation of kinetic energy at the sub-grid scales (small scales). The SGS turbulence can be better represented by considering the transport of SGS turbulence kinetic energy (TKE). By utilising the TKE transport equation, the SGS model would benefit complex flows of non-equilibrium by accounting for the non-local effects. Several models have been proposed by numerous researchers. However, the present research considers the formulation of Kim and Menon (1997). In this model the total SGS stress σ_{ij} is related to the TKE that is computed via the solution of its transport equation. The dynamic kinetic energy transport (DKET) model has been successfully applied to vortex flows, rotating isotropic turbulence and turbulent mixing layers, as well as high Reynolds number flows.

As with the DSMG model the filtering in DKET is carried out across the grid level and the test level, where, k_{sgs} is defined as the SGS kinetic energy and K_{test} is the sub-test scale kinetic energy. Using the analogy in equation (4.46) the SGS turbulence kinetic energy can be expressed as,

$$k_{sgs} = \frac{1}{2}(\overline{U_k U_k} - \overline{U}_k \overline{U}_k) = \frac{1}{2}(\overline{U_k^{\,2}} - \overline{U}_k^{\,2}) \tag{4.77}$$

The SGS eddy viscosity, μ_t, is related to the sub-grid scale kinetic energy k_{sgs} by,

$$\mu_t = \rho C_k k_{sgs}^{\,1/2} \overline{\Delta} \tag{4.78}$$

where C_k is the adjustable model parameter. Assuming incompressible flow, the SGS stress is computed using,

$$\sigma_{ij} = -2C_k k_{sgs}^{\,1/2} \overline{\Delta}\, \overline{S}_{ij} \tag{4.79}$$

The turbulence energy k_{sgs} is obtained by solving the filtered turbulence kinetic energy transport equation,

$$\frac{\partial \overline{k}_{sgs}}{\partial t} + \frac{\partial \overline{U}_j \overline{k}_{sgs}}{\partial x_j} = \mathbf{P}_k - \varepsilon_{sgs} + \frac{1}{\rho}\frac{\partial}{\partial x_j}\left(\frac{\mu_t}{\sigma_k}\frac{\partial k_{sgs}}{\partial x_j}\right) \tag{4.80}$$

The Prandtl number σ_k is taken as a constant in the present formulation and is equal to 0.1. The three terms on the right hand side of equation (4.80) represent the production, dissipation and diffusion of k_{sgs}, respectively.

The production term is defined as,

$$\mathbf{P}_k = -\sigma_{ij}\frac{\partial \overline{U}_i}{\partial x_j} \tag{4.81}$$

The sub-grid scale dissipation is modelled as,

$$\varepsilon_{sgs} = C_{\varepsilon} \frac{k_{sgs}^{\frac{3}{2}}}{\overline{\Delta}} \tag{4.82}$$

where C_{ε} is an adjustable model parameter. Kim and Menon (1997) proposed a procedure to deduce the model parameters C_k and C_{ε} dynamically, similar to that used in the DSMG model to deduce c_s. The dynamic procedure of Kim and Menon is based on the hypothesis that there is a correlation between the sub-grid scale stress σ_{ij} and the resolved Leonard's stress L_{ij}. The experiments of Liu et al. (1994a, b) in the far field of a turbulent round jet at high Reynolds number indicated significant similarity between the stress tensors σ_{ij} and L_{ij}. Using the similarity argument, L_{ij} is written as,

$$L_{ij} = -2C_k K_{test}^{1/2} \tilde{\Delta} \tilde{\overline{S}}_{ij} \tag{4.83}$$

It should be noted that equation (4.83) does not involve any test filtering operation on C_k, whereas, in the formulation of the DSMG model, an assumption was necessary to remove c_s from the test filter operator in equation (4.68). The parameter K_{test} associates itself with the scales between the test filter level and grid level. Using an analogy with equation (4.65) K_{test} can be represented as,

$$K_{test} = \frac{1}{2}(\widetilde{\overline{U}_k \overline{U}_k} - \tilde{\overline{U}}_k \tilde{\overline{U}}_k) \tag{4.84}$$

The resolved turbulent stress in equation (4.83) can be rewritten in the form,

$$L_{ij} = C_k M_{ij} \quad \text{where } M_{ij} = -2\tilde{\Delta} K_{test}^{1/2} \tilde{\overline{S}}_{ij} \tag{4.85}$$

The model constant C_k, in equation (4.85), can be obtained by minimising the least square error, as in DSMG. From the similarity concept it is assumed that the dissipation of the sub-test scale kinetic energy (ε_{test}) can be modelled in a similar manner as the dissipation of the SGS kinetic energy (ε_{sgs}) defined in equation (4.82). Therefore,

$$\varepsilon_{test} = C_\varepsilon \frac{K_{test}^{\frac{3}{2}}}{\tilde{\Delta}} \tag{4.86}$$

The dissipation of sub-test kinetic energy can also be computed from,

$$\varepsilon_{test} = \frac{(\mu + \mu_t)}{\rho}\left(\frac{\partial \overline{U_i}}{\partial x_j}\frac{\partial \overline{U_i}}{\partial x_j} - \frac{\partial \tilde{\overline{U}}_i}{\partial x_j}\frac{\partial \tilde{\overline{U}}_i}{\partial x_j}\right) \tag{4.87}$$

Combining equation (4.86) and (4.87) yields an expression for the model parameter C_ε,

$$C_\varepsilon = \frac{\tilde{\Delta}(\mu + \mu_t)}{\rho K_{test}^{3/2}}\left(\frac{\partial \overline{U_i}}{\partial x_j}\frac{\partial \overline{U_i}}{\partial x_j} - \frac{\partial \tilde{\overline{U}}_i}{\partial x_j}\frac{\partial \tilde{\overline{U}}_i}{\partial x_j}\right) \tag{4.88}$$

The DKET model holds several advantages over the DSMG model. In DKET, the model coefficient remains unfiltered in the formulation of the resolved Leonard's stress L_{ij}. Furthermore, the definition of the denominator M_{ij} in the DSMG model (equation 4.71) can converge to small values across a large region of the domain, due to the similarity between the scales arising from the test filter and grid filter levels. This in turn would pose instability in the computed model coefficient c_s (equation 4.75) in the DSMG model. In DKET M_{ij} (equation 4.85) is presented by a more favourable definition. Therefore, computationally, less effort is required in DKET than DSMG since in the procedure for DKET the test filtering operation on the SGS stress tensor β_{ij} is not needed.

4.5. Discretization of the governing equations in space and time

The governing transport equations cannot be solved analytically, thus a numerical method is used. In the present numerical investigation a control volume technique is used to convert the governing equations into algebraic equations which are then solved using a suitable method. Adopting a numerical technique means that we restrict the solution to a finite number of discrete locations defined by the grid within the flow domain. The approach adopted for the discretization of the governing equations in physical space, follows the procedure described in Versteeg and Malalasekara (1995).

4.5.1. Discretization procedure

To introduce the principles of the discretization procedure a simple case of a steady, one-dimensional flow is considered, involving convection and diffusion through the boundaries of the control volume. The node identified by *P* in Figure 4.4 is surrounded by two neighbouring nodes; these are to the west and east of node *P* and are denoted by *W* and *E*, respectively. The west side face of the control volume is referred to by *w* and the east side control volume face by *e*. The distances between nodes *W* and *P*, and between nodes *P* and *E* are δ_{xWP} and δ_{xPE}, respectively.

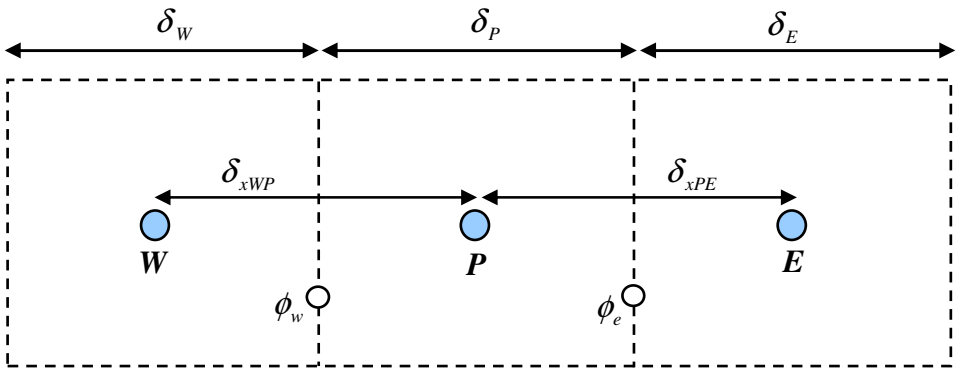

Figure 4.4: Control volume and neighbouring nodes for a one-dimensional cell.

In three dimensional flow (Figure 4.5) the cell containing node *P* has six neighbouring nodes. These are located on the west, east, north, south, top and bottom sides (*W*, *E*, *S*, *N*, *T*, *B*). The notations (*w*, *e*, *s*, *n*, *t*, *b*) in Figure 4.5 refer to the faces of the control volume located between node *P* and the six neighbouring nodes.

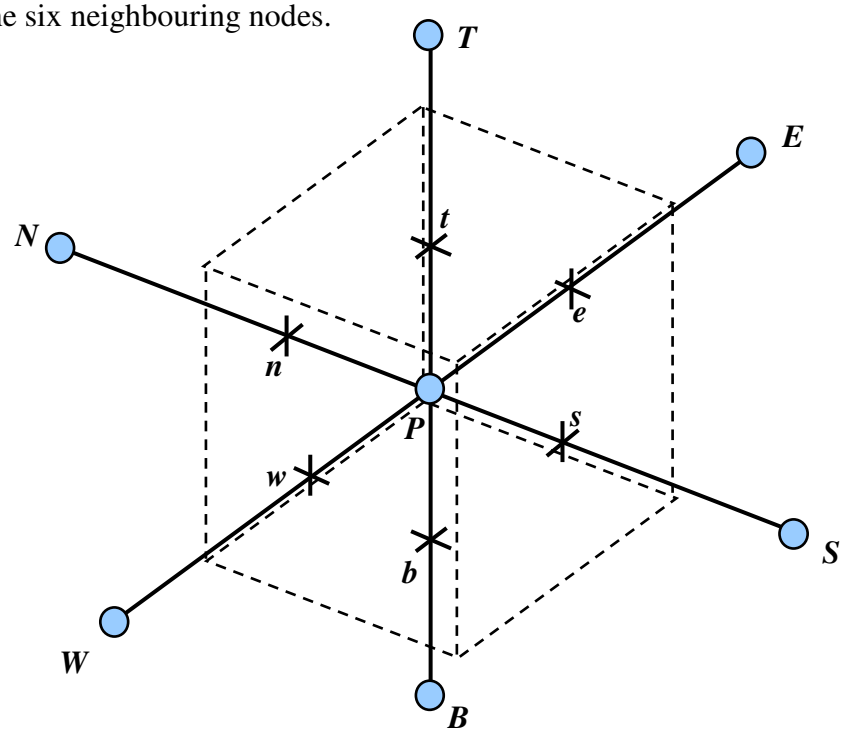

Figure 4.5: Control volume and neighbouring nodes for a three-dimensional cell.

In the proceeding section, a lower case subscript (*w*, *e*, *s*, *n*) is used to indicate the values at the face of the control volume, whereas the upper subscript (*W*, *E*, *S*, *N*) refers to the nodal values.

4.5.1.1. Steady one-dimensional diffusion

In this section, the finite volume numerical method is applied to the simplest transport process, that is, pure diffusion in the steady state. The steady state diffusion of a flow variable ϕ in a one-dimensional flow field is governed by,

$$\frac{d}{dx}\left(\Gamma\frac{d\phi}{dx}\right)=0 \tag{4.89}$$

where Γ is the diffusion coefficient. Integrating equation (4.89) over the control volume in Figure (4.4) gives,

$$\left(\Gamma A\frac{d\phi}{dx}\right)_e-\left(\Gamma A\frac{d\phi}{dx}\right)_w=0 \tag{4.90}$$

where A is the cross-sectional area of the control volume face. In order to derive the discretized form of the equations, the diffusion coefficient Γ and the gradient $d\phi/dx$, at the east (*e*) and west (*w*) faces are required. To calculate the gradients and the interface values at the control volume faces, a linear approximation can be used, where the truncated terms of the Taylor series are neglected. This gives,

$$\left(\Gamma A\frac{d\phi}{dx}\right)_e=\Gamma_e A_e\left(\frac{\phi_E-\phi_P}{\delta_{xPE}}\right) \tag{4.91a}$$

$$\left(\Gamma A\frac{d\phi}{dx}\right)_w=\Gamma_w A_w\left(\frac{\phi_P-\phi_W}{\delta_{xWP}}\right) \tag{4.91b}$$

The interpolated values of Γ_w and Γ_e are given by,

$$\Gamma_w=\frac{\Gamma_W+\Gamma_P}{2} \tag{4.92a}$$

$$\Gamma_e = \frac{\Gamma_P + \Gamma_E}{2} \tag{4.92b}$$

Substituting equation (4.91a) and (4.91b) into (4.90) yields,

$$\Gamma_e A_e \left(\frac{\phi_E - \phi_P}{\delta_{xPE}} \right) - \Gamma_w A_w \left(\frac{\phi_P - \phi_W}{\delta_{xWP}} \right) = 0 \tag{4.93}$$

Rearranging equation (4.93) gives,

$$\left(\frac{\Gamma_e}{\delta_{xPE}} A_e + \frac{\Gamma_w}{\delta_{xWP}} A_w \right) \phi_P = \left(\frac{\Gamma_w}{\delta_{xWP}} A_w \right) \phi_W + \left(\frac{\Gamma_e}{\delta_{xPE}} A_e \right) \phi_E \tag{4.94}$$

Introducing the coefficients a_W, a_E and a_P, equation (4.94) can be rewritten as,

$$a_P \phi_P = a_W \phi_W + a_E \phi_E \tag{4.95}$$

Equation (4.95) represents the discretized form of equation (4.89).

4.5.1.2. Steady one-dimensional diffusion and convection

For practical fluid flow problems the effects of convection must also be accounted for. This section examines the finite volume method for combined convection and diffusion problems. In the absence of sources the governing equation for a variable ϕ can be written in the form,

$$\rho \frac{\partial \phi}{\partial t} + \rho \frac{\partial (U_i \phi)}{\partial x_i} = \frac{\partial}{\partial x_i} (\Gamma \frac{\partial \phi}{\partial x_i}) \tag{4.96}$$

The second term on the left-hand side of equation (4.96) represents the convection and the term on the right-hand side represents the diffusion of variable ϕ. For a steady state flow, equation (4.96) is simplified to,

$$\rho \frac{\partial (U_i \phi)}{\partial x_i} = \frac{\partial}{\partial x_i} (\Gamma \frac{\partial \phi}{\partial x_i}) \tag{4.97}$$

Integrating equation (4.97) over the control volume for node *P* in Figure 4.4 gives,

$$\left(\rho U_i A \phi\right)_e - \left(\rho U_i A \phi\right)_w = \left(\Gamma A \frac{\partial \phi}{\partial x}\right)_e - \left(\Gamma A \frac{\partial \phi}{\partial x}\right)_w \tag{4.98}$$

Note that U_i is the velocity in the *x*- direction. Equation (4.98) can be solved by calculating the unknown value of the scalar variable ϕ at the faces *w* and *e* of the control volume. There are several discretization schemes for this purpose, and those considered in the present investigation are described in the proceeding sections. Using equation (4.95), the general form of the discretized equation for a control volume can be written as,

$$a_P \phi_P = \sum_{nn} a_{nn} \phi_{nn} + S \tag{4.99}$$

where *S* is the source term. The subscript *nn* refers to the neighbour cells and a_{nn} are the coefficients a_W, a_E, a_S, a_N, a_B, a_T describing the combined convection and diffusion at the cell boundaries. The symbol defined by ϕ_{nn} is the value of ϕ at each neighbouring node.

4.5.2. Discretization of the diffusion term

The discretization of the diffusion term was described in section (4.5.1.1.). If one considers the west face of the control volume, then, from equation (4.91b), the diffusion flux at the west face can be written,

$$\Gamma_w A_w \left(\frac{\phi_P - \phi_W}{\delta_{xWP}} \right) = \frac{\Gamma_w A_w}{\delta_{xWP}} \left(\phi_P - \phi_W\right) = D_w (\phi_P - \phi_W) \tag{4.100}$$

In equation (4.100) A_w is the area of the cell on the west face and D_w is the west face diffusion coefficient. In the formulation of the discretized equation, a suitable method is used to obtain the value of the properties at the required face of the control volume.

4.5.3. Discretization of the convection terms

In the discretization of the convection terms the value of the variable ϕ at the control volume faces and the convective flux across these boundaries are calculated. Various discretization schemes can be chosen ranging from first-order schemes to higher-order accurate schemes. The method adopted determines the accuracy of the solution. In the present investigation, two schemes are considered for the discretization of the convection terms. The QUICK scheme was adopted for the RSM and $k-\varepsilon$ computations, and the bounded central differencing scheme was applied in the large eddy simulations.

4.5.3.1. The central-differencing scheme

In section (4.5.1.1.) the central-differencing scheme was used to represent the diffusion coefficients Γ_e and Γ_w which appear in equation (4.94). For the uniform grid shown in Figure 4.4, we can deduce the cell face values of the property ϕ at faces *e* and *w* using,

$$\phi_e = \frac{\phi_P + \phi_E}{2} \tag{4.101a}$$

$$\phi_w = \frac{\phi_W + \phi_P}{2} \tag{4.101b}$$

Substituting the above equations into equation (4.98), and using equation (4.91a, b) yields,

$$\rho U_e A_e \frac{(\phi_P + \phi_E)}{2} - \rho U_w A_w \frac{(\phi_W + \phi_P)}{2} = \frac{\Gamma_e A_e}{\delta_{xPE}}(\phi_E - \phi_P) - \frac{\Gamma_w A_w}{\delta_{xWP}}(\phi_P - \phi_W) \tag{4.102}$$

Simplifying equation (4.102) for the diffusion coefficients on the right-hand side and the convective mass flux on the left-hand side, and assuming $A_w = A_e = A$, the equation can be rewritten in the form,

$$\frac{F_e}{2}(\phi_P + \phi_E) - \frac{F_w}{2}(\phi_W + \phi_P) = D_e(\phi_E - \phi_P) - D_w(\phi_P - \phi_W) \tag{4.103}$$

where D_i and F_i represent the diffusion coefficient and the convective mass flux, respectively. The expression in equation (4.103) can be rearranged to identify the coefficients of ϕ_W and ϕ_E, namely a_W and a_E, as defined in equation (4.99). These are given by,

a_W	a_E
$D_w + \frac{F_w}{2}$	$D_e - \frac{F_e}{2}$

Table 4.3: Neighbouring coefficients of the central-differencing scheme, (Versteeg and Malalasekara, 1995).

To solve a convection-diffusion problem, discretization equations of this form are written for all grid nodes. This results in a set of algebraic equations that are solved to obtain the distribution of the property ϕ.

In FLUENT, a second order accurate central-differencing discretization scheme is available for the momentum equations. It is commonly known that central-differencing schemes can produce non-physical wiggles, which can lead to stability problems. These stability problems can be avoided if a deferred (upwind) approach is used for the central-differencing scheme. The FLUENT implementation calculates the face value of a variable using:

$$\phi_i = \phi_{i,\mathrm{UP}} + \left(\phi_{i,CD} - \phi_{i,UP}\right) \qquad (4.104)$$

In this method ϕ_i is calculated using the upwind part (UP) which is treated implicitly, and the difference between the central-difference (CD) and upwind values which is treated explicitly.

4.5.3.2. The first-order upwind scheme

In strongly convective flow, from west to east, the central-differencing scheme is unsuitable because of the stronger effects on the west face cell, from node *W* than node *P*. The upwind differencing scheme takes into account the flow direction when determining the value at a cell face. In this scheme the values of the variable ϕ at the faces of the control volume are taken to be equal to the values at the upstream nodes.

When the flow is in the positive direction $(U_w, U_e > 0)$, i.e. from west to east in Figure 4.4, then the variable takes the value on the cell boundary as,

$$\phi_w = \phi_W \quad \text{and} \quad \phi_e = \phi_P \tag{4.105}$$

On the other hand if the flow is in the negative direction $(U_w, U_e < 0)$, from east to west, then,

$$\phi_w = \phi_P \quad \text{and} \quad \phi_e = \phi_E \tag{4.106}$$

The coefficients of ϕ_W and ϕ_E are obtained by substituting equations (4.105) and (4.106) into equation (4.98); these are presented in Table 4.4.

a_W	a_E
$D_w + \max(F_w, 0)$	$D_e + \max(0 - F_e)$

Table 4.4: Neighbouring coefficients of the upwind differencing scheme, (Versteeg and Malalasekara, 1995).

In Table 4.4, $F_w = (\rho U)_w$ and $F_e = (\rho U)_e$ are the convective mass flux per unit area at the west face and the east face, respectively.

4.5.3.3. The second-order upwind scheme

In the second-order accurate upwind scheme, the quantities at the cell faces are computed using the multidimensional linear construction approach of Barths and Jespersen (1989). Using this method, higher-order accuracy is achieved at cell faces through a Taylor series expansion of the cell-centred solution about the cell centroid.

4.5.3.4. Quadratic Upwind Differencing Scheme (QUICK)

The Quadratic Upwind Interpolation for Convective Kinetics (QUICK) scheme (Leonard, 1979) is a third-order accurate differencing scheme for the convection terms. This scheme uses a three point upstream weighted quadratic interpolation (two upstream nodes and one downstream node) to determine the value of the variable at a cell face. If the flow is from west

to east, the value of ϕ on the east cell face (e) in Figure 4.4 between the two nodes P and E can be written as,

$$\phi_e = \theta\left[\frac{\delta_E}{\delta_P + \delta_E}\phi_P + \frac{\delta_P}{\delta_P + \delta_E}\phi_E\right] + (1-\theta)\left[\frac{\delta_W + 2\delta_P}{\delta_W + \delta_P}\phi_P - \frac{\delta_P}{\delta_W + \delta_P}\phi_W\right] \qquad (4.107)$$

The traditional QUICK scheme can be obtained by setting $\theta = 1/8$. However, in FLUENT a solution dependant value of θ is implemented. The QUICK scheme is typically more accurate on structured grids which are aligned with the flow direction.

4.5.3.5. Bounded central-differencing scheme

The central-differencing scheme can lead to unphysical oscillations in the solution field, especially on coarse grids and at high Reynolds numbers. In large eddy simulation the effects can worsen by very low SGS turbulent diffusivity. The implementation of the bounded central-differencing scheme in FLUENT is based on the approach of Leonard (1991), with a convection boundedness criterion. The method is a composite scheme that consists of a central-differencing scheme and second-order upwind scheme, a pure central-differencing scheme and the first-order upwind scheme.

In theory the numerical results obtained may be indistinguishable from the exact solution irrespective of the differencing method used, if the number of computational cells is infinitely large. In practice, however, one can only use a finite number of cells and, therefore, the numerical results can only be realistic if an appropriate discretization scheme is used.

4.5.4. Temporal discretization

To seek a numerical solution for the partial differential equations, in unsteady simulations, the governing equations must be discretized in both space and time. The discretization of the transient term is referred to as temporal discretization, which involves the integration of every term in the differential equation over a time-step Δt. The following part describes the integration of the transient terms.

The time evolution of a variable ϕ is given by,

$$\frac{\partial \phi}{\partial t} = F(\phi) \tag{4.108}$$

where the function $F(\phi)$ incorporates any spatial discretization. If the time derivative is discretized using a forward difference scheme, the first-order accurate temporal discretization is given by,

$$\frac{\phi^{n+1} - \phi^{n}}{\Delta t} = F(\phi) \tag{4.109}$$

and the second-order accurate discretization is given by,

$$\frac{3\phi^{n+1} - 4\phi^{n} + \phi^{n-1}}{2\Delta t} = F(\phi) \tag{4.110}$$

In equations (4.109) and (4.110), ϕ is a scalar quantity, $(n+1)$ denotes the value at the next time-step $t + \Delta t$, n is the value at the current time level t, and $(n-1)$ represents the value at the previous time-step.

With the time derivative discretized, the function $F(\phi)$ needs to be evaluated. One must consider the value of ϕ that should be used in evaluating $F(\phi)$. In the implicit time integration scheme, the function $F(\phi)$ is evaluated at the future time level,

$$\frac{\phi^{n+1} - \phi^{n}}{\Delta t} = F(\phi^{n+1}) \tag{4.111}$$

In this scheme, ϕ^{n+1} in a generic cell is related to ϕ^{n+1} in the neighbouring cells through $F(\phi^{n+1})$. From a re-arrangement of equation (4.111), for the first-order implicit formulation, the value of ϕ at the next time level can be computed from,

$$\phi^{n+1} = \phi^{n} + \Delta t\, F(\phi^{n+1}) \tag{4.112}$$

Similarly, for the second-order implicit formulation, the value of ϕ at the next time level can be calculated using the rearrangement of equation (4.110), which gives,

$$\phi^{n+1} = \frac{4}{3}\phi^{n} - \frac{1}{3}\phi^{n-1} + \frac{2}{3}\Delta t\, F(\phi^{n+1}) \tag{4.113}$$

The implicit equations presented above can be solved by replacing ϕ^{n} by ϕ^{i} and iterating the equation. For the first-order and second-order implicit formulation, this yields,

$$\phi^{i} = \phi^{n} + \Delta t\, F(\phi^{i}) \tag{4.114}$$

and,

$$\phi^{i} = \frac{4}{3}\phi^{n} - \frac{1}{3}\phi^{n-1} + \frac{2}{3}\Delta t\, F(\phi^{i}) \tag{4.115}$$

respectively.

The iteration is carried out until ϕ^{i} stops changing and the equation converges. The fully implicit scheme has its advantages in that it is unconditionally stable with respect to the specified time-step size Δt.

The time discretization error depends on the temporal discretization method. In the FLUENT solver, both the first-order and second-order implicit schemes, described here, are available. The corresponding truncation errors for the first and second-order scheme formulations are $O(\Delta t)$ and $O\left[(\Delta t)^{2}\right]$, respectively. In the present study the second-order implicit time-discretization scheme is employed.

4.6. The derivation of pressure

The velocity components appear in the momentum and the continuity equations. However, there is no equation for the pressure. The solution strategies such as the SIMPLE (Semi-Implicit Method for Pressure Linked Equations) algorithm of Patankar and Spalding (1972) were developed to derive the pressure by an iterative method. The main features of the SIMPLE and SIMPLE-Consistent (SIMPLEC) algorithms are described in the following.

The discretized *U*-momentum equation for the west face of the control volume in Figure 4.4 can be written in terms of the guessed pressure P^* and guessed velocity U^*,

$$a_p U_w{}^* = \sum_{nn} a_{nn} U_{nn}{}^* + A_w (P_W{}^* - P_P{}^*) \tag{4.116}$$

If the correct pressure field is applied to equation (4.116), then the velocity field should satisfy the continuity equation. If the continuity equation is not satisfied, the required correction P' is defined as the difference between the correct pressure field P^{**} and the guessed pressure field P^*, therefore,

$$P^{**} = P^* + P' \tag{4.117}$$

In a similar way for the velocity correction U', it can be written,

$$U^{**} = U^* + U' \tag{4.118}$$

By substituting the correct pressure field P^{**} into equation (4.116) one can obtain the correct velocity field U^{**}, this gives,

$$a_P U_w{}^{**} = \sum_{nn} a_{nn} U_{nn}{}^{**} + A_w (P_W{}^{**} - P_P{}^{**}) \tag{4.119}$$

Subtracting equation (4.119) from (4.116) yields,

$$a_P U'_w = \sum_{nn} a_{nn} U'_{nn} + A_w (P'_W - P'_P) \tag{4.120}$$

At this point the SIMPLE algorithm applies a simplification by omitting $\sum a_{nn} U'_{nn}$ from equation (4.120). The SIMPLEC algorithm does not share this approximation in that $\sum a_{nn} U'_{nn}$ is not omitted. The velocity correction from equation (4.120) required for the SIMPLE algorithm can therefore be written as,

$$U'_w = \frac{A_w(P'_W - P'_P)}{a_P} \tag{4.121}$$

The equation for pressure correction P' in the SIMPLE algorithm is obtained by substituting equations (4.118) and (4.121) into the continuity equation, this gives the pressure-correction equation as,

$$a_P P' = \sum_{nn} a_{nn} P'_{nn} + b \tag{4.122}$$

The term b in equation (4.122) is the mass flow rate into the cell and can be written as,

$$b = \sum_{nn} \rho A_{nn} U_{nn}^{*} \tag{4.123}$$

Once the pressure correction is obtained from the solution of the pressure correction equation in (4.122), the corrected pressure field can be deduced from equation (4.117). The corresponding corrected velocity field is then obtained from equations (4.121) and (4.118). The procedure outlined here requires several iterations, because of the use of approximate equations to obtain P'. In general, the use of the modified SIMPLEC correction equation has been shown to accelerate convergence in problems where the pressure-velocity coupling can deter a stable solution.

Because of the non-linearity of the equations, it is necessary to control the change of the variable ϕ. This is achieved by under-relaxation which reduces the change of ϕ during each iteration. To bring stability to the solution during the iterative process, the pressure is under-relaxed as,

$$P^{**} = P^{*} + f P' \tag{4.124}$$

where the term f is the under-relaxation factor and is specified between 0 and 1.

Chapter 5

5. NUMERICAL INVESTIGATION: Computational Details

5.1. Introduction

In this chapter the computational details of the numerical investigation such as the grid distribution, boundary conditions and solution procedures are presented. The first part of this chapter describes the three-dimensional flow domain within which the numerical equations are solved. A description of the grids used and the grid distribution adopted in the simulations are also presented. The second part of this chapter presents the boundary conditions employed at the inlet, outlet, and the walls. The procedure adopted in selecting an appropriate time-step is also described. In the final part of this chapter the solution procedures incorporated in the FLUENT code, for the unsteady segregated solver, are detailed.

5.2. Computational flow domain

5.2.1. Geometry

In the present investigation simulations were conducted on three different grids. The geometry of the computational domain was constructed using GAMBIT 2.3 mesh generator. In all cases a multi-block approach was followed, where the full-scale domain is broken down into smaller blocks. The blocks were created in the physical space by defining a set of coordinates, and were connected together through the shared common faces with the neighbouring blocks. The multi-block approach allows for local control of grid refinement in the flow domain. Finer grids can be used in high velocity gradient regions, such as the near the wall and the wake, whereas a coarser grid distribution can be implemented elsewhere. The method can result in a reduction in CPU time and memory requirement.

As mentioned previously, to assess the contribution of the grid resolution on the quality of the results, a selection of grids was investigated. For the discussion that follows, the geometry was divided into three sections, namely, the upstream tangent, the bend and the downstream tangent, as in the experimental duct. In all simulations, the NACA 0012 (chord length c = 150 mm) airfoil was placed so that it was parallel to the upper and lower walls of the duct, so as to

represent an angle of attack $\alpha = 0^o$ with respect to the horizontal. The grid used in the RANS computations of Piradeepan (2002) was also considered in the present numerical investigations. Our initial aim was to assess the degree of improvement, if any, which may be achieved by using LES on this grid. Therefore this grid was first used to study the performance of the three SGS models considered in the present large eddy simulations. A second grid was set up, which as in the grid of Piradeepan, was also representative of a full-scale duct. This grid incorporated refined resolutions in the streamwise, normal and spanwise direction. Both these grids utilised the full spanwise extent of the duct which is equivalent to $3c$. For this reason, the near wall spanwise resolution on these grids may have been compromised, unless a large number of grid points were placed in the spanwise direction. In the present case, it was not practical to distribute a large number of grid nodes in the spanwise direction due to the large streamwise extent of the domain, which was necessary to study the wake. Therefore, to assess the effect of a considerably increased spanwise resolution, a third grid was designed, but with a reduced spanwise extent. The extent of this grid in the spanwise direction was $0.5c$, which is smaller than in the case of the previous two grids, but enabled simulations which are more representative of classical LES cases. For this grid, periodic conditions were defined in the spanwise direction. This was in line with the majority of LES investigations conducted by previous researchers.

The flow domain and grid distribution in the streamwise and spanwise planes for each of the three grids considered is presented in Figure 5.1-5.3, at the end of section 5.2. The entire flow domain of the 3D structured grid used by Piradeepan (2002), shown in Figure 5.1, consists of 25 blocks. The upstream tangent is constructed of 15 blocks, most of which are located in the central part of the section, around the airfoil. The distance of the trailing edge of the airfoil to the bend entry plane is equal to one chord length. A C-type mesh was employed around the airfoil. The intermediate section (the bend), located between the upstream tangent and the downstream tangent, is constructed with 5 blocks and has a turning angle of 90^o. The downstream tangent is an extended section of the bend outlet constructed of 5 rectangular blocks. The cross-section of each block in the y-z plane is identical to the adjacent block of the bend section.

On the finer grids it was necessary to increase the number of blocks to enable a finer resolution near the duct walls. The domain of refinedPiradeepan (Figure 5.2) comprised 38 blocks. A total of 17 blocks were located in the upstream tangent, whilst the bend section consisted of 7 blocks. The downstream tangent was divided into two separate parts, the

smallest of which was equal to the extent upstream tangent, and extended a distance H in the normal direction from the bend outlet. This allowed for a better control of the streamwise resolution in the downstream bend section. A total of 14 blocks were constructed in the downstream tangent. The grid topology of the classical LES case in Figure 5.3 is similar to that employed in refinedPiradeepan, however, the extent of the blocks in the z-direction is shorter due to the reduced spanwise extent of this grid. The block structured topology for the three grids considered is presented in Table 5.1.

Grid	**Number of blocks**		
	Upstream tangent	**Bend**	**Downstream tangent**
Piradeepan (2002)	15	5	5
refinedPiradeepan	17	7	14
classical LES	17	7	14

Table 5.1: Details of the block structure employed on the three grids.

5.2.2. Grid distribution

The blocks of the flow domain are designed to allow for a large number of grid cells in regions where steep variations are likely to occur, namely, near the walls and in the wake. In the bend and the downstream tangent an H-type mesh was employed, whereas in the upstream tangent a C-type grid distribution was used near the airfoil. Structured quadrilateral cells are used to mesh the domain. For this type of geometry, where the domain is continuous, these types of cells can be easily compressed or expanded, to allow for different gradients.

The grid of Piradeepan (2002) consisted of 676,000 cells and the full spanwise extent of the duct is represented by 40 cells spread evenly in the spanwise direction (Figure 5.1). A fine resolution was adopted close to the airfoil and in the near-wake region. On the airfoil, grid nodes were placed within the viscous sublayer so that the condition $y^+ < 2$ for the nodes adjacent to the wall was satisfied. The near-wall grid distribution was stretched with increasing normal distance from the surface of the airfoil. In contrast to this, the distribution in the normal direction on the bend walls is coarse, where the nearest grid point was at $y^+ < 100$. Furthermore, there is a jump in streamwise grid spacing near the bend entry. In the wake, steep changes were expected, therefore, a uniformly distributed fine grid was used.

In the refinedPiradeepan grid the full spanwise extent of the duct is represented by 80 uniformly distributed grid points. As can be seen in Figure 5.2, the additional blocks defined in the domain near the bend walls have allowed for a finer wall-normal resolution on the concave and convex walls. There is generally an improved streamwise, wall normal and spanwise resolution throughout the domain, which consists of approximately 4.6 million cells.

To resolve the boundary layers accurately, a finer grid resolution is required throughout the domain, especially, in the spanwise direction. However, due to the immense number of grid nodes that this would entail, and the limits of the present computational capabilities, this was not practical. For both grids described above, the spanwise resolution throughout the domain, relative to the normal resolution, is very coarse. This is known to substantially affect the boundary layer growth and, therefore, the wake development. For the cases where the flow domain comprises the full-scale geometry of the duct, the use of an appropriate near-wall treatment method is necessary, due to the coarse grid spacing in the normal and spanwise directions on the bend walls. The grid for the classical LES case shown in Figure 5.3 has a spanwise extent that is six times smaller than the other two grids, but consists of approximately 6 million grid cells. A total of 70 grid nodes are distributed evenly in the spanwise direction within this extent. The effect of the side walls is replaced by the definition of a periodic boundary condition on the spanwise extents of the flow domain. The reduced spanwise extent, with this number of grid nodes, significantly improves the grid resolution in the spanwise direction. There is a further improvement in the streamwise and wall normal resolution throughout the domain especially on the concave and convex walls of the duct.

The grid resolutions on the upper surface of the airfoil, the concave and convex walls of the duct are compared in Chapter 7, where RANS computations are used to obtain the streamwise, wall normal and spanwise resolutions in terms of the non-dimensional wall units. The results of the simulations on the coarsest grid (Piradeepan, 2002) are referred to as coarseSMG, coarseDSMG, and coarseDKET, for the three different SGS models considered. The simulations on the two finer grids were conducted with the DSMG model. The results from the refinedPiradeepan grid are referred to as refinedPiradeepanDSMG, and those from the classical LES case with a reduced spanwise extent are termed refinedDSMG. It should be noted that, in the assessment of the SGS models and grid resolution, all other modelling parameters such as boundary conditions and discretization scheme were fixed so that a fair comparison could be achieved.

The number of grid cells used in the various regions of the flow domain for the different grids used is shown in Tables 5.2, 5.3 and 5.4.

H-type grid distribution				
Section	**N_x (streamwise)**	**N_y (normal)**	**N_z (spanwise)**	**Total nodes**
Upstream tangent	40	40	40	64,000
Bend	35	80	40	112,000
Downstream tangent	60	80	40	192,000
C-type grid distribution				
Section	**N_x (tangential)**	**N_y (radial)**	**N_z (spanwise)**	**Total nodes**
Upstream tangent	140	55	40	308,000

Table 5.2: The H- and C-type mesh distribution used in the geometry of the flow domain for the grid of Piradeepan (2002), spanwise extent equivalent to 3*c* (676,000 grid cells in total).

H-type grid distribution				
Section	**N_x (streamwise)**	**N_y (normal)**	**N_z (spanwise)**	**Total nodes**
Upstream tangent	80	80	80	512,000
Bend	80	150	80	960,000
Downstream tangent	140	150	80	1,680,000
C-type grid distribution				
Section	**N_x (tangential)**	**N_y (radial)**	**N_z (spanwise)**	**Total nodes**
Upstream tangent	215	85	80	1,462,000

Table 5.3: The H- and C-type mesh distribution used in the geometry of the flow domain for refinedPiradeepan, spanwise extent equivalent to 3*c* (4,614,000 grid cells in total).

H-type grid distribution				
Section	**N_x (streamwise)**	**N_y (normal)**	**N_z (spanwise)**	**Total nodes**
Upstream tangent	100	100	70	700,000
Bend	80	190	70	1,064,000
Downstream tangent	150	190	70	1,995,000
C-type grid distribution				
Section	**N_x (tangential)**	**N_y (radial)**	**N_z (spanwise)**	**Total nodes**
Upstream tangent	265	110	70	2,040,500

Table 5.4: The H- and C-type mesh distribution used in the geometry of the flow domain for the classical LES case, spanwise extent equivalent to 0.5*c* (5,799,500 grid cells in total).

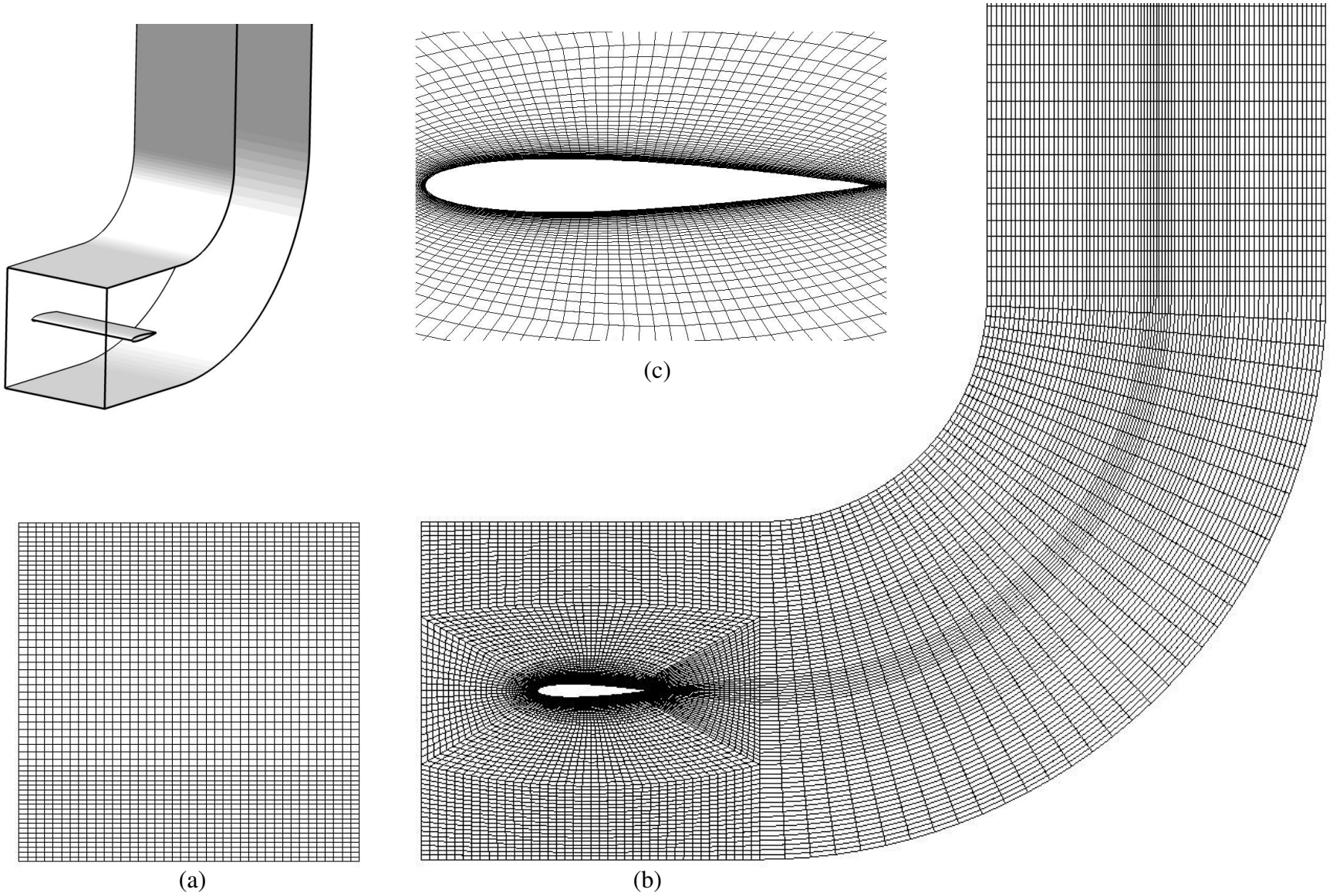

Figure 5.1: Grid distribution of the computational flow domain for coarseDSMG simulations: (a) *y-z* plane, (b) *x-y* plane, (c) airfoil close-up in the *x-y* plane, (676,000 grid cells in total).

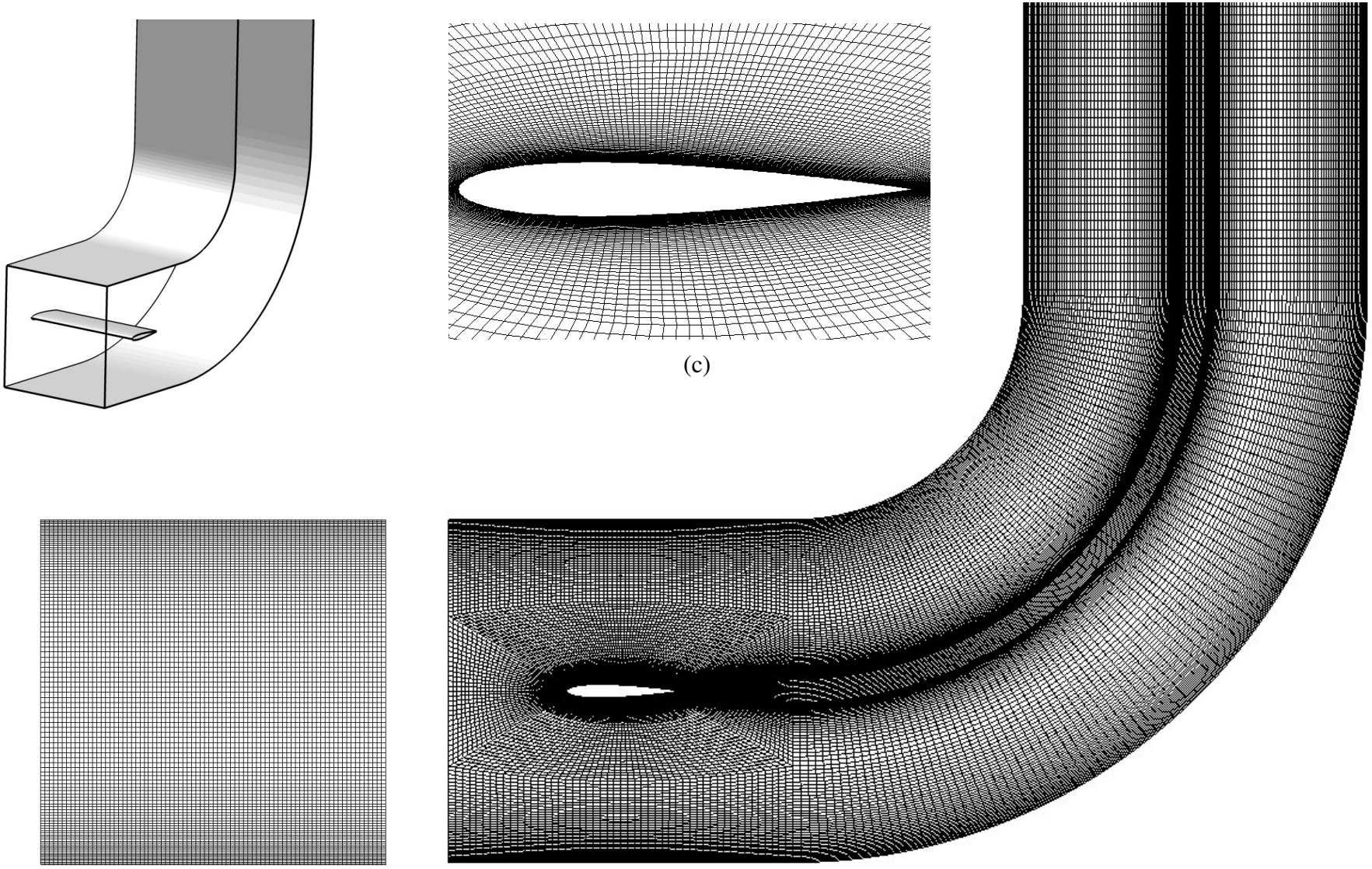

Figure 5.2: Grid distribution of the computational flow domain for refinedPiradeepanDSMG simulations: (a) *y*-*z* plane, (b) *x*-*y* plane, (c) airfoil close-up in the *x*-*y* plane, (4,614,000 grid cells in total).

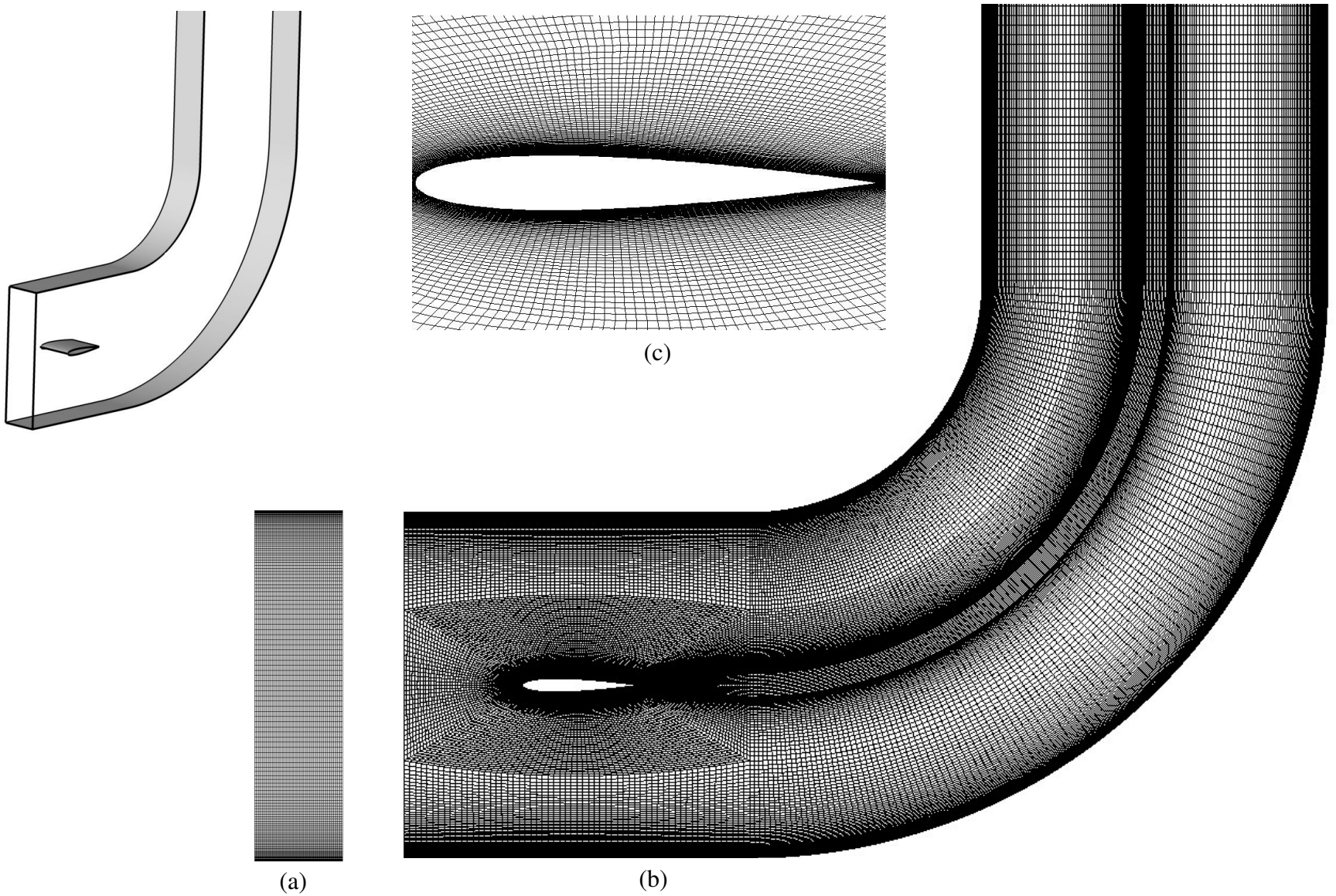

Figure 5.3: Grid distribution of the computational flow domain for refinedDSMG simulations: (a) *y-z* plane, (b) *x-y* plane, (c) airfoil close-up in the *x- y* plane, (5,799,500 grid cells in total).

5.3. Implementation of the boundary conditions

In this section the details regarding the incorporation of the boundary conditions on the boundary surfaces, such as the inlet, outlet and walls of the flow domain are presented. This is followed by the procedure adopted for the time-step selection. The inlet, outlet boundary, the wall and periodic surfaces are all defined during the mesh generation process in GAMBIT. The grid is then imported into the FLUENT solver for the solution process.

5.3.1. Inlet boundary condition

The values of all flow variables need to be specified at the inlet boundary. In the present numerical investigation profiles of mean velocity and turbulence quantities measured upstream of the airfoil, at station 1, by Piradeepan (2002) are used to define the inlet boundary condition. The measured turbulence quantities were used to calculate the turbulence kinetic energy k and its dissipation rate ε at the inlet. A point profile method was used to define the boundary profiles at the inlet to the flow domain. The solver used an interpolation method to obtain the values at the cell boundary faces. The turbulence kinetic energy and its rate of dissipation were calculated using equations (5.1) and (5.2),

$$k = \frac{1}{2}(\overline{u'^2} + \overline{v'^2} + \overline{w'^2}) \tag{5.1}$$

$$\varepsilon = \frac{k^{\frac{3}{2}}}{\ell} \tag{5.2}$$

where ℓ is the length scale which needs to be determined. Near the walls, based on the Prandtl mixing length model, the length scale can be taken as κy, where κ is the Von Kármán constant equal to 0.41, and y is the normal distance from the wall. For the region outside the boundary layer, ℓ is approximated by $0.5cH$ where c is a constant and H is the duct height. The constant c was obtained by testing different values of length scale at the inlet boundary, and then comparing the predicted profile of k at station 2 with the measured experimental profile. The constant c was taken to be 0.25 for a mainstream velocity of 10 m/s through this procedure, which gives a length scale of $0.125H$.

Modelling the fluctuating velocity

In large eddy simulation a substantial computational time is required to reach a state of developed turbulence. The definition of the initial flow field and the implementation of the turbulent inflow conditions are important in the accuracy of the simulations. The random flow generation (RFG) technique proposed by Smirnov et al. (2001) is employed within the implementation of the inlet boundary conditions. The RFG procedure was developed on the basis of the work of Kraichnan (1970), and is based on samples of Fourier harmonics that are used to generate the non-homogeneous anisotropic flow field, representing turbulent inflow conditions. The inputs for this procedure, are obtained from available experimental data at station 1 (Piradeepan, 2002); these include the mean streamwise velocity U, mean normal velocity V, the turbulence kinetic energy k and its dissipation rate ε. The advantages of the RFG procedure are that it provides the desired statistical characteristics of turbulence at the boundaries and is relatively inexpensive with regards to the computational cost. Smirnov et al. (2001) validated the RFG technique for the flat plate wake flow of Ramaprian et al. (1981). In their simulation, the inflow boundary was generated with the aid of experimental data taken from the work of Ramaprian. Comparisons in the wake between numerical and experimental data for mean velocity and turbulence intensities indicated very good agreement using the RFG procedure.

In the implementation of this technique in FLUENT the number of harmonic functions N representing the turbulence spectrum is fixed at $N = 100$. By increasing the spectral sample size N, it is possible to increase the accuracy of reproducing the turbulence spectrum although this is at a cost of longer computational time and higher memory requirement.

5.3.2. Outlet boundary

The outlet boundary should generally be located far away from the geometrical disturbances so that the flow reaches a fully developed state. Convergence may be affected if there is recirculation through the outflow boundary. Therefore, the location of the outflow boundary is chosen such that there are no anticipated changes in the flow direction. In the present investigation, the outflow boundary was placed $5H$ downstream of the bend exit (station 4). In the grid of Piradeepan (2002), the outflow plane consisted of five individual block faces which were combined together to form one individual face. For the two finer grids, the outflow boundary is represented by seven individual faces that are combined to create a single face.

The Neumann boundary conditions are applied at the outflow boundary. In this condition the gradient of all flow variables, except pressure, is set to zero. The normal and spanwise component of velocity are set to zero, and the value of streamwise velocity is obtained using the upstream value such the global mass conservation for the whole domain is satisfied. The pressure is obtained by extrapolation of the upstream value.

5.3.3. Wall boundary conditions and near-wall treatment

Wall boundaries are the most common boundaries encountered in fluid flow problems. Turbulent flows are significantly affected by the presence of walls. The successful prediction of wall bounded turbulent flows relies on the accuracy with which the flow in the near wall region is represented. Experiments have shown that the near-wall region can be subdivided into several layers; these include, the viscous sublayer for $y^+ < 5$, where the laminar property is dominant, the fully-turbulent region which consists of the turbulent logarithmic layer for $30 < y^+ < 500$, and the outer layer. The no-slip condition at stationary walls forces the mean velocity components to a zero magnitude, and can also significantly affect the turbulence quantities. If the grid distribution is fine enough so as to satisfy the no-slip condition, near-wall treatment is not necessary. However, as mentioned previously, the grid of Piradeepan (2002) has a coarse normal mesh distribution near the duct walls, and that of refinedPiradeepan, also representative of the full extent of the duct, attains a poor spanwise resolution throughout the computational domain.

In the present study the $k-\varepsilon$, RSM and LES models are all considered, thus care needs to be taken in the near-wall approach for each of these methods. Two different methods were employed to model the near-wall regions. In the steady state RANS simulations, a two-layer zonal model was applied, whereas, in the large eddy simulations, the Werner and Wengle wall law was adopted. For consistency, in the comparison of the modelling parameters in LES, the same wall approach is applied to the three grids of the present numerical investigation. The near-wall models used in the present investigation are described in more detail in the following sections.

Two-layer zonal model

In the two-layer zonal model the flow is divided into a viscosity-affected region and a fully-turbulent region, otherwise known as the near-wall and the outer regions, respectively. The

near-wall region includes the viscous sublayer, buffer layer (interim region between viscous sublayer and fully-turbulent layer) and part of the turbulent layer. The outer region includes the rest of the flow. The boundary between these two regions is determined by the wall-distance-based turbulent Reynolds number, defined as,

$$\mathrm{Re}_y = \frac{\rho y \sqrt{k}}{\mu} \tag{5.3}$$

where y is the normal distance from the wall. For grid nodes that satisfied $\mathrm{Re}_y > 200$, the adopted turbulence model, $k-\varepsilon$ or RSM is employed. In the viscosity-affected region ($\mathrm{Re}_y < 200$) the one-equation turbulence model of Wolfstein (1969) is employed. The eddy viscosity is then computed from,

$$\mu_t = \rho C_\mu \ell_t \sqrt{k} \tag{5.4}$$

where ℓ_t is a length scale and k is obtained from the solution of the turbulence kinetic energy equation. The length scale (ℓ_t) is calculated using (Chen and Patel, 1988)

$$\ell_t = C_l y \left(1 - e^{-\mathrm{Re}_y / A_t}\right) \tag{5.5}$$

The dissipation of turbulence kinetic energy is obtained from,

$$\varepsilon = \frac{k^{\frac{3}{2}}}{\ell_\varepsilon} \tag{5.6}$$

where the length scale ℓ_ε is given by,

$$\ell_\varepsilon = C_l y \left(1 - e^{-\mathrm{Re}_y / A_\varepsilon}\right) \tag{5.7}$$

In equation (5.5) and (5.7) the variation of ℓ_t and ℓ_ε approach a linear relationship as the distance from the wall is increased. The constants C_l, A_t, A_ε are given by,

$$C_l = \kappa C_\mu^{-3/4}, \quad A_t = 70, \quad A_\varepsilon = 2C_l, \quad C_\mu = 0.09, \quad \kappa = 0.418 \tag{5.8}$$

In the implementation of the two layer zonal model the value of y^+ at the cell adjacent to the wall should be ideally about 1. However, grid points within the upper limit of the viscous sublayer ($y^+ < 5$) are generally acceptable.

LES near-wall treatment

The law of the wall is used in the implementation of the wall boundary condition within FLUENT. Therefore, for the best results with LES; in the absence of any near-wall treatment, it is required that a very fine mesh is used near the wall ($y^+ \approx 1$). For such a fine mesh the wall shear stress is calculated from the relationship,

$$u^+ = y^+ \tag{5.9}$$

The non-dimensional parameters in equation (5.9) can be written as,

$$u^+ = \frac{U}{(\tau_w / \rho)^{1/2}} \tag{5.10}$$

and,

$$y^+ = \frac{\rho (\tau_w / \rho)^{1/2} y}{\mu} \tag{5.11}$$

where τ_w is the wall shear stress. If the mesh is too coarse to resolve the viscous sublayer, it is assumed that the first grid point is in the logarithmic region of the flow and thus the law of the wall approximation is employed,

$$u^+ = \frac{1}{\kappa} \ln (\mathrm{E}\, y^+) \tag{5.12}$$

where κ is the von Kármán constant and E = 9.793.

However, for the reasons discussed earlier, the near-wall approach of Werner and Wengle (1991) was adopted in the simulations. The Werner and Wengle wall law consists of a two layer approximation based on the viscous sublayer and the assumption of a one-seventh power law outside the viscous sublayer. The tangential velocity next to the wall is calculated from,

$$u_1^+ = \begin{cases} y_1^+ & if \quad y_1^+ \le 11.8 \\ 8.3(y^+)^{1/7} & if \quad y_1^+ > 11.8 \end{cases} \qquad (5.13)$$

where $u_1^+ = \mathrm{U}_1/u_\tau$ and $y_1^+ = \rho\, y_1\, u_\tau/\mu$. Here, U_1 is the resolved tangential velocity at the centroid of the first cell from the wall, y_1 is the corresponding normal distance from the wall and u_τ is the friction velocity. The wall shear stress is obtained by integrating the velocity profile in (5.13) over the distance separating the first cell from the wall, this yields,

$$\tau_w = \begin{cases} \dfrac{2\mu\,\mathrm{U}_1}{y_1} & for \quad |\mathrm{U}_1| \le \dfrac{\mu}{2\rho\, y_1}\mathrm{A}^{\frac{2}{1-\mathrm{B}}} \\ \rho\left[\dfrac{1-\mathrm{B}}{2}\mathrm{A}^{\frac{1+\mathrm{B}}{1-\mathrm{B}}}\left(\dfrac{\mu}{\rho\, y_1}\right)^{1+\mathrm{B}} + \dfrac{1+\mathrm{B}}{\mathrm{A}}\left(\dfrac{\mu}{\rho\, y_1}\right)^{\mathrm{B}}|\mathrm{U}_1|\right]^{\frac{2}{1+\mathrm{B}}} & for \quad |\mathrm{U}_1| \ge \dfrac{\mu}{2\rho\, y_1}\mathrm{A}^{\frac{2}{1-B}} \end{cases} \qquad (5.14)$$

The constants A and B in equation (5.14) are equal to 8.3 and 1/7, respectively. The employed wall method presents advantages over the standard wall function models based on the logarithmic laws, by providing a more accurate representation of the near-wall layers.

5.3.4. Periodic boundary conditions

In periodic flows the expected flow pattern within the computational domain has a periodically repeating nature, i.e. the flow entering the computational domain through one periodic plane has the same velocity to the flow exiting the domain through the opposite plane. In the present numerical investigation, periodic boundary conditions were defined in the case with reduced spanwise extent. As mentioned previously, the classical LES case was designed to incorporate a central spanwise segment of the tunnel equivalent to 0.5*c*. The focus of this simulation was in the prediction of the airfoil boundary layer and the near field wake. The purpose of the periodic boundary was to represent the spanwise flow in the central span of the tunnel away from the side walls. The assumption made here is that the effect of the tunnel side walls on the developing airfoil boundary layer and near-wake is small. Furthermore, the suitability of the shortened extent, in representing a periodic flow condition in the spanwise direction, was confirmed experimentally. The results from the experiments in the wake indicated that at least

two wavelengths of the characteristic peak-trough variation, in the mean velocity and turbulence intensity were evident over the 0.5*c* extent.

During the process of setting up the grid and mesh generation in GAMBIT, the sides of the domain were created so as to satisfy translational periodicity. The constructed faces of a translationally periodic boundary must be parallel to each other and equal in size. This type of boundary condition is applicable to fully-developed flows. In FLUENT, when calculating the flow through the cells on one side of the periodic boundary, the flow conditions at the fluid cells on the opposite periodic plane are used. Figure 5.4 can be used to define the periodic flow condition.

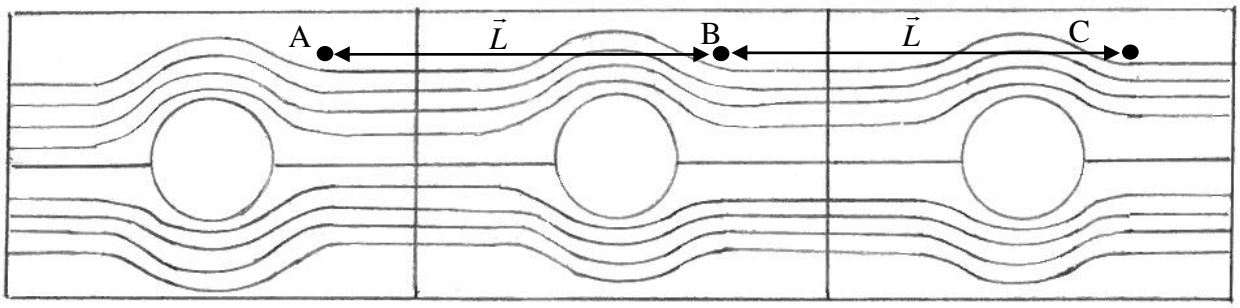

Figure 5.4: Definition of the periodic boundary, FLUENT 6.3 User's Guide (2005)

Taking $\vec{r}$ as the position vector and $\vec{L}$ as the periodic length vector of the domain, it can be written,

$$u(\vec{r}) = u(\vec{r} + \vec{L}) = u(\vec{r} + 2\vec{L}) \tag{5.15}$$

and from Figure 5.4,

$$u_A = u_B = u_C \tag{5.16}$$

where u_A is the streamwise velocity at location *A*, u_B and u_C are the corresponding velocities at locations *B* and *C*, respectively. A similar analogy can be used to describe the normal and spanwise velocity components. With regards to the pressure calculation, for viscous flows, it is the pressure drop across the length $\vec{L}$ that is periodic (not the pressure itself), this gives,

$$\Delta p = p(\vec{r}) - p(\vec{r} + \vec{L}) \tag{5.17}$$

and from Figure 5.4,

$$p_A - p_B = p_C - p_B \tag{5.18}$$

The segregated solver in FLUENT divides the local pressure gradient into two parts, these comprise the gradient of a periodic component $\nabla\tilde{p}(\vec{r})$ and the gradient of a linearly-varying component $\beta\frac{\vec{L}}{|\vec{L}|}$. It can be written that,

$$\nabla p(\vec{r}) = \nabla\tilde{p}(\vec{r}) + \beta\frac{\vec{L}}{|\vec{L}|} \tag{5.19}$$

The linearly varying component of pressure results in a force acting on the fluid, where, β is the specified pressure gradient in the periodic direction. The periodic pressure $\tilde{p}(\vec{r})$ is obtained by a simple re-arrangement of the above equation. Within the implementation of the spanwise periodic conditions in FLUENT, an initial value of zero is specified for the pressure gradient (β in equation 5.19), i.e. there is no external force acting on the fluid in the momentum equations. The correction of β occurs in the pressure correction step of the SIMPLEC algorithm (described in Chapter 4) where the value of β is updated based on the difference between the desired mass flow rate and the calculated mass flow rate.

5.3.5. Time-step selection

As was mentioned earlier in chapter 4, in the present large eddy simulations, the time integration is based on a second-order implicit formulation. To properly simulate the time-dependent scales of the flow, the selected time-step should be at least one order of magnitude smaller than the smallest time scale being modelled. Kolmogorov (1941a, b) introduced the idea that the smallest scales of turbulence are universal, i.e. they are similar for every turbulent flow. The Kolmogorov length scales are the smallest scales in turbulent flow, and are dependent on the average rate of energy dissipation per unit mass (ε) and the kinematic viscosity of the fluid (ν). Choi and Moin (1994) investigated the effect of the time-step on

turbulent statistics using DNS. They found that the turbulent statistics in a channel flow can only be accurately simulated if the computational time-step is less than the Kolmogorov time scale.

A common way of assessing the choice of Δt is to consider the Courant-Friedrichs-Lewy (CFL) number, which is defined as,

$$CFL = \Delta t / \left(\Delta x / U \right) \tag{5.20}$$

where Δx is the length interval and U is the velocity. The term $(\Delta x/U)$ represents the cell residence time. Within the FLUENT solver it is recommended that the CFL number not exceed the value of 20-40 in the most turbulent region of the flow. The choice of Δt may also be determined by monitoring the number of iterations the solver requires to converge at each time-step. Generally, if FLUENT requires 5-10 iterations per time-step then the size of the selected time-step can be regarded as appropriate, however, if a larger number of iterations are required then the time-step size needs to be reduced.

In the unsteady simulations presented here, a fixed time-step (in seconds) of,

$$\Delta t = 8.33 \times 10^{-3} \frac{c}{U_o} \tag{5.21}$$

was chosen based on the mainstream velocity U_o and airfoil chord length c. With this time-step, the CFL condition was satisfied throughout the flow domain which indicated levels of CFL < 1 near the airfoil trailing edge (for all three grids). This confirmed that the time-step size was capable of capturing the characteristic time scales of the flow. The selected time-step was also consistent with the experimental sample rate of 8 kHz, which corresponded to a time interval of 0.000125 seconds between consecutive samples. In the collection of turbulence statistics for the numerical investigation a sample was taken every 10 time-steps and the equivalent numerical sample rate was 0.8 kHz which is one order lower than in the experiments, and corresponds to a time interval of 0.00125 between consecutive samples in the simulations.

The majority of previous large eddy simulations for airfoil flows with high chord Reynolds numbers of the order 1×10^6 and finer grids (as reviewed in Chapter 2), used smaller time-steps

of the order $10^{-6}(c/U_o)$. In the present numerical investigation a comparatively larger time-step is used; this is in response to lower chord Reynolds number in the present flow configuration (1.03×10^5) and the mesh density employed.

5.4. Solution of the discretized algebraic equations

5.4.1. Introduction

There are two numerical solution methods available in FLUENT, namely, the coupled solver and the segregated solver. The coupled method, also known as the direct method, solves the governing equations of continuity, momentum and energy simultaneously. This method can result in a considerable amount of computational effort. The segregated solution method (also referred to as the indirect or iterative method) is based on a simple algorithm in which the governing equations are solved in sequence (i.e. segregated from one another). Convergence is then achieved after a number of iterations. In the present study, the segregated solver was used. The processes within segregated solution algorithm and the iterative method for time-dependent calculations are described in the following section.

5.4.2. The segregated solver

In the segregated solver the governing equations are solved sequentially. The stages in the segregated solution method for time dependent flows are outlined in Figure 5.5. The equations are solved iteratively at a given time-step, until the convergence criterion is satisfied. Because of the non-linearity of the governing equations, a number of outer iterations are required before the solution is advanced by one time-step. The *U*-, *V*- and *W*- components of the momentum equation are solved in sequence using a guessed or current values of variables, such as the pressure field throughout the domain. The velocity field is then updated. However, the velocities obtained in the above procedure may not satisfy the continuity equation, thus the pressure-correction equation in the SIMPLEC algorithm is solved to deduce improved values of the pressure and velocity field. Subsequently, the equations for scalars such as turbulence kinetic energy and dissipation rate, if required by the simulation, are solved using the updated values of the flow variables. The solution steps outlined above are repeated a number of times, and when convergence is met, the solution is progressed by one time-step. The same procedure is then carried out for the next time-step.

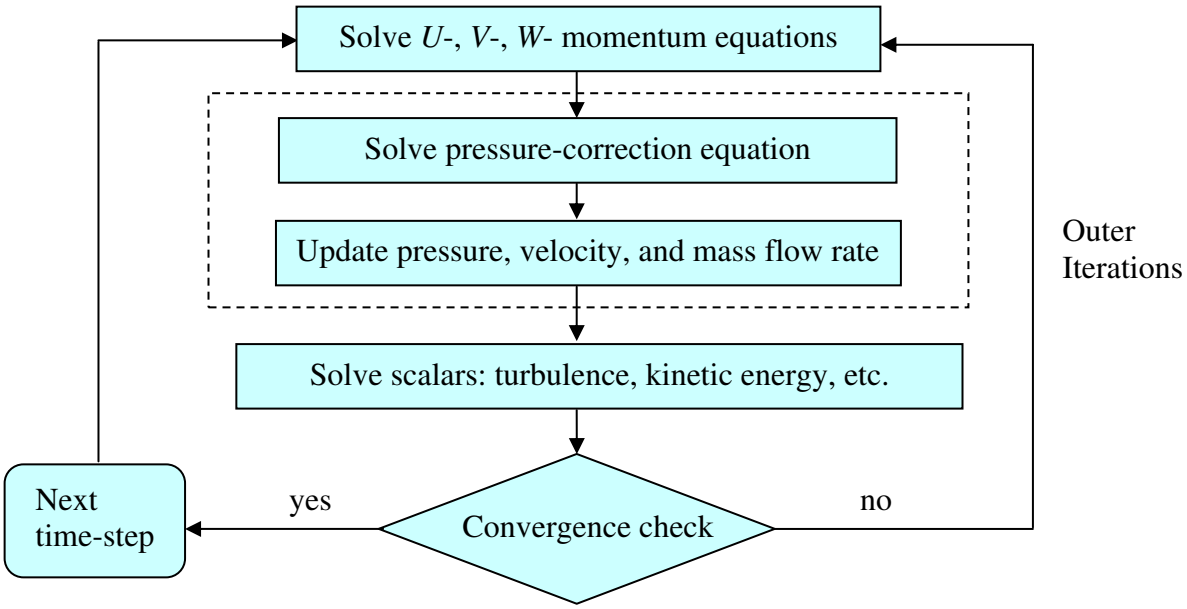

Figure 5.5: The stages of the segregated solution method for time-dependent flows, FLUENT 6.3 User's Guide (2005)

5.4.3. Under-relaxation

To stabilise the solution process, the segregated solver uses under-relaxation to control the change of a variable ϕ at each iteration. For unstable or divergent behaviour, it is required to reduce the under-relaxation factor for pressure, momentum, *k*, and ε. The process of under-relaxation is described as follows. Taking ϕ_C and ϕ_O as the current and old values of a variable, the new value of the variable ϕ_N obtained through the under-relaxation process can be express as,

$$\phi_N = \phi_O + URF(\phi_C - \phi_O) \tag{5.22}$$

where the under-relaxation factor URF takes a value between 0 and 1. In the FLUENT segregated solver every equation has an associated under-relaxation factor. Generally, the smaller the value of URF, the more under-relaxation is implemented, which in turn results in a slower solution process. The solver default and adjusted under-relaxation values for each variable are shown in Table 5.5.

VARIABLE (ϕ)	URF (default)	URF (used)
U, *V*, *W*	0.7	0.2
P	0.3	0.2
k, ε	0.5	0.4

Table 5.5: The under-relaxation factors used in the present investigation.

5.4.4. Convergence criterion

The computed variable ϕ will only satisfy equation (4.99) when the solution is converged. The residual R_ϕ computed by the segregated solver is the imbalance in equation (4.99). For a single computational cell the residual can be written as,

$$R_{\phi\,cell} = \sum_{nn} a_{nn}\phi_{nn} + S - a_P\phi_P \tag{5.23}$$

By summing the residuals over all of the computational cells the global residual can be obtained. The sum of the residuals will decrease as the solution progresses, and decay to zero as the solution converges. To determine the level of convergence based on the global residual value, FLUENT adopts a scaling factor which is representative of the flow rate of the variable ϕ through the domain. The scaled residual can be defined as,

$$R_\phi = \frac{\sum_{cells}\left|\sum_{nn} a_{nn}\phi_{nn} + S - a_P\phi_P\right|}{\sum_{cells}\left|a_P\phi_P\right|} \tag{5.24}$$

For the continuity equation the unscaled residual is defined as,

$$R_C = \sum_{cells}\left|\,Rate\ of\ \ mass\ creation\ in\ a\ cell\,\right| \tag{5.25}$$

The scaled residual for the continuity equation is obtained by dividing the unscaled residual in equation (5.25) with the largest absolute value of the continuity residual in the first five iterations. The scaled residual provides a useful way of determining the convergence of a solution. In a converged solution the scaled residuals reduce to appreciably small values. For the present numerical investigation the convergence criterion was satisfied when the scaled residual for all the variables became smaller than 0.001.

5.5. Other computational details

5.5.1. Computer power, effort and memory required

Several factors can influence the processing time, these include the numerical method employed (i.e. RANS, LES), the solution technique, the under-relaxation, and most importantly the central processing unit (CPU) power and available random access memory (RAM). Due to the employed mesh density of the grids and the computational demand placed by large eddy simulation in the present study, it was not possible to compute the flow on a stand alone computer. The FLUENT parallel solver allows for the computations to be done on a network of computers. The process involves interaction between the solver, a host and a set of computer-nodes. The grid is split into multiple partitions which are then assigned to the different computer nodes. In general, the solution time will decrease as the number of computer-nodes is increased. However, the efficiency of parallel computing can reduce if the problem is not large enough for the parallel processing machine. This is mainly due to the increase in the computer-node communication time. The host process uses a single computer-node (node-0) to execute commands, communicate with the other computer-nodes and perform operations on the data.

As was previously stated, the FLUENT parallel solver partitions the grid into groups of cells that can be solved on separate processors. In the present numerical investigation, the simulations were conducted on a COMPUSYS parallel processing cluster in the Linux 64-bit environment. In each computational case, the grid was partitioned on 8 Intel Xeon dual processor nodes, running at 3.3GHz each. The partitioning algorithm was based on the Cartesian axes method, which bisects the parent domain into child subdomains that are perpendicular to the coordinate direction.

The starting flow was allowed to develop for a substantial computational time so that the statistically steady state (SSS) condition for turbulence was achieved. A total of 140,000 time-steps (50 flow-through times) were computed to reach SSS. On the coarsest grid (Piradeepan, 2002) this required an average of 3 s per time-step resulting in 117 CPU hours to reach SSS. The simulations on the finest grid, otherwise known as the classical LES case (refinedDSMG) took 12 s per time-step with a considerably larger running time of 470 CPU hours to reach SSS. Generally, the simulations with the standard SMG model required the least computational effort, whereas those with the dynamic SGS models (DSMG and DKET) took

longer to compute. This was due to the additional steps required to calculate the SGS turbulent viscosity, at each time-step throughout the flow domain.

5.5.2. The pre-processor, solver, and the post-processor

The numerical part of the present study was carried out using FLUENT 6.3. The FLUENT program consists of a pre-processor, solver, and post-processor. The Geometry of the flow domain and the mesh were created within the GAMBIT pre-processor. As mentioned before due to the size of the grids and the complexity of LES, a parallel processing method was employed. The grids were imported into the parallel version of FLUENT and partitioned across the computer-nodes of the COMPUSYS parallel processing cluster. A text command script was used to communicate with the host node on the cluster. The solver residuals and time were printed online to check for convergence and stability. The simulations were run for a substantial computational time. Once the SSS condition for turbulence was achieved, numerical results in the form of distribution profiles were obtained via the command line script from the FLUENT post-processor. The vector and contour plots were obtained by outputting a General Notation System (CGNS) data file from the solution and post-processing on a stand alone computer with TECPLOT 360 software package.

During the mesh generation in GAMBIT and post-processing with TECPLOT a stand alone computer-node running an Intel Xeon processor with 4GB of RAM was used. The structure of the flow of work between the pre-processor, solver and the post-processor is shown in Figure 5.6.

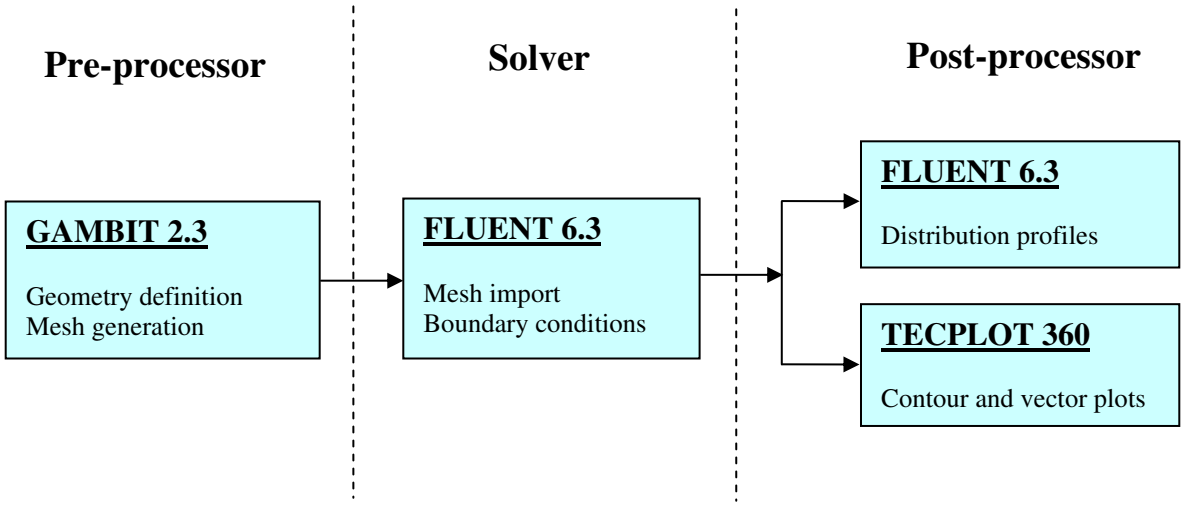

Figure 5.6: Basic structure of the work flow between the pre-processor, solver and the post-processors

Chapter 6

6. EXPERIMENTAL RESULTS AND DISCUSSION

6.1. Introduction

In this chapter the measurements of static pressure, mean velocity and turbulence quantities from the experimental investigations are presented. The structure of the presented results is displayed in Figure 6.1. The main results are divided into static pressure distribution, the near-wake region, and the airfoil boundary layer. Experimental data obtained at the nominal condition of freestream velocity 10 m/s and zero angle of attack in the near-wake and at station 2 are the only set presented in tabular form in Appendix V.

Hot-wire measurements were conducted using stand alone single-wire probes, a rake of single-wire probes and cross-wire probes. The near-wake measurements were taken at six streamwise locations at the trailing edge of the airfoil, x/c = 1.05, 1.10, 1.22, 1.33, 1.44, 2, where x is the distance measured from the leading edge of the airfoil. In the airfoil boundary layer, the mean velocity and streamwise intensity were measured at x/c = 0.44, 0.64, 0.74, 0.83, 0.93, 0.98. The normal component of turbulence intensity and turbulence shear stress are only presented in locations where tests were conducted using a cross-wire probe. Spanwise turbulence intensities were not measured. The hot-wire measurements in the near-wake are divided into two sets. The first set of data is taken at mid-span and measurements are obtained in the normal direction. For a fixed spanwise distance (z/H), quantities were measured with increasing normal distance (y/H) from the lower wall. In the second set of measurements, for fixed values of normal distance, measurements were obtained with increasing spanwise distance (z/H) from the side wall. The y/H locations tested in the spanwise measurements corresponded to the inner and outer sides of the wake.

The effect of mainstream velocity and angle of attack in the near-wake on the mean and turbulence quantities were investigated by conducting experiments at three mainstream velocities U_o = 10, 15, 20 m/s and seven different angles of attack α = -6°, -4°, -2°, 0°, 2°, 4°, 6°. Data in the region of the near-wake with the absence of the airfoil at the three mainstream velocities is also presented.

6.2. Normalized form of the experimental results

The mean velocity and turbulence quantities were normalized with respect to the freestream velocity at station 1. The pressure coefficient was calculated using the static pressure P_o and freestream velocity U_o at station 1, from the relationship,

$$C_p = \frac{P - P_o}{\frac{1}{2}\rho U_o^2} \tag{6.1}$$

The wall shear stress was estimated using the value of skin friction coefficient C_f, measured using the Clauser chart method, where C_f is defined as

$$C_f = \frac{\tau_w}{\frac{1}{2}\rho U_o^2} \tag{6.2}$$

6.2.1. Tunnel calibration

The tunnel calibration is presented in Figure 6.2. There is a linear relationship between the dynamic pressure measured using a Pitot-static tube and the static pressure measured using pressure tappings on the contraction section. The repeatability of tunnel calibration was checked regularly.

6.2.2. Hot-wire calibration

The velocity calibration data for the DANTEC single-wire probes 55P14, 55P15, 55P16 and cross-wire 55P63 probes are presented in Figure 6.3. The variation of anemometer voltage against the jet velocity from the calibrator nozzle, for the range of 0 to 25 m/s, for typical single-wire and cross-wire probe sensors are shown in Figure 6.3(a,b). A fourth-order polynomial was used to fit the data. The fitted curves for the rake of single-wire probes and the cross-wire probes showed identical trends with closely agreed values. This indicates that the probes were experiencing similar effective cooling velocities. During calibration, the error between the measured jet velocity and calculated air velocity, based on the curved fits, was less than ±0.6%. The deviations of measured velocities from the values obtained from the fitted curve are presented in Figure 6.3(c) and 6.3(d).

6.2.3. Pressure distributions on the airfoil

The wake characteristics depend strongly on the boundary layer development on the airfoil, which in turn is influenced by the orientation of the airfoil with respect to the oncoming flow. For this reason, a series of experiments were conducted at different angles of attack. Note that the angle of attack referred to here represents the angle between the chord of the airfoil and the horizontal axis. The static pressure distribution over the upper and lower surfaces of the airfoil at different angles of attack α = -6°, -4°, -2°, 0°, 2°, 4°, 6° are presented in Figure 6.4(a-g). The clockwise rotation of the airfoil (leading edge up) is taken as positive, and the anti-clockwise rotation (leading edge down) is taken as negative.

At α = 0° (Figure 6.4a), the pressure variation over the upper and lower surfaces of the airfoil shows an asymmetric distribution, being smaller on the upper surface which is caused by the downstream bend. The existence of an adverse pressure gradient on most part of the upper surface is evident. The profile shows a sudden change in gradient around *x/c* = 0.65 which, although not occurring at this configuration, could relate to favourable conditions for flow separation to occur. In comparison, on the lower surface, the profile of pressure coefficient displays a favourable pressure gradient up to *x/c* = 0.13 followed by a wide region of slowly increasing adverse pressure gradient towards the leading edge. There is no indication of flow separation on the lower surface.

By increasing the angle of attack to α = 2° (Figure 6.4b), the variations of the pressure on the upper surface enhance and the sudden change in pressure gradient moves upstream. For α = 4° and α = 6° (Figure 6.4c,d), the profiles show very similar patterns and the position of the sudden change is now more abrupt, and moved further upstream located between *x/c* = 0.1 and *x/c* = 0.15. Just preceding to this abrupt change in the profile, a region of nearly constant pressure is also noticeable. The profiles seen here indicate the presence of a separation bubble near the leading edge at the larger angles of attack. On the lower surface, the overall features remain the same and the changes in the profiles are less significant.

For negative angles of attack, both upper and lower side pressure profiles approach the same distribution, where at α = -4° they nearly collapse (Figure 6.4f) and attain profiles which would be expected for an airfoil parallel to the oncoming flow. At α = -6° (Figure 6.4g), the pressure distribution is similar to the case for α = 0°, but reversed. Interestingly, the sudden change in the profile occurs on the lower surface between *x/c* = 0.7 and *x/c* = 0.8. The results

suggest that for the configuration shown in Figure 1.4 the flow approaching the airfoil is not parallel to the airfoil, but has an angle of about -4°. In order to investigate the angle of the oncoming stream further, the flow angle was calculated at station 1 using the measured values of streamwise and normal velocity components and neglecting the spanwise component. Figure 6.5 shows a plot of the mean flow angle (relative to the horizontal *x*-axis) at the mid-span of the duct. The maximum flow angle in the freestream region is approximately -2°.

6.2.4. Experimental consistency

Before the full results are presented, the consistency with the previous work of Piradeepan is first demonstrated, followed by showing the effect of probe calibration, and the consistency of the readings by the rake of single-wire probes. As was stated in Chapter 3, the traversing mechanisms used for the measurements of boundary layers on the upper surface of the airfoil involved a modification to the upper wall which created a recession in the wall. Therefore, the effect of this cavity on the mean and turbulence quantities is also presented.

6.2.4.1. Consistency with previous work

The profiles of mean velocity and turbulence quantities measured at the mid-span, one chord length downstream of the trailing edge of the airfoil at station 2 are presented in Figure 6.6. Also shown, are the results of Piradeepan (2002). The distributions shown in Figure 6.6(a,b) are in good agreement with the previous measurements, in the wake and in the boundary layers on the convex and concave walls of the duct. There are, however, small quantitative differences in the profiles of normal turbulence intensity and turbulence shear stress (Figure 6.6c,d). The peak value of *Vrms* measured in the wake at this station is slightly lower than previous experiments. These differences may be attributed to differences in the experimental conditions.

6.2.4.2. Consistency of rake measurements

The rake consisted of four single-wire probes with a centre to centre normal distance of 12 mm between each probe (see Figure 3.16). To assess the level of consistency of the reading from each single-wire in the rake, a series of experiments were carried out at station 1 (without the airfoil) and in the near-wake of the airfoil at $x/c = 1.33$.

First, the rake was setup as shown in Figure 3.16(a), such that the distance of each probe wire from the lower wall was fixed at y = 223 mm, 235, 247 and 259 mm. The fixture was then traversed in the spanwise (z) direction and measurements taken to determine the variation of mean velocity and turbulence intensity in this plane (Figure 6.7). The results indicated little or no variation of mean velocity and turbulence in the spanwise direction at station 1. The boundary layers on the tunnel side walls were not measured due to the difficulties associated with the placement of the traverse mechanism near the wall. The flow can be taken as uniform and two-dimensional in the spanwise direction for the central region at station 1. This is in agreement with the results of Piradeepan (2002), who further found very small values of normal and spanwise velocity components.

In the second test, the fixture was set up so that the sensors were located in the trailing edge of the airfoil at x/c = 1.33. Measurements were then conducted at the mid-span (z/H = 0.5) location. The rake was then traversed in the normal (y) direction so that each probe recorded a complete profile of the wake at this streamwise location. The mean velocity and turbulence intensity profiles are presented in Figure 6.8(a,b). Results show that the profiles collapse in the freestream as well as in the wake region, indicating a low level of relative error in the probe calibrations, even at the lower velocities. The turbulence intensity profile in Figure 6.8(b) shows a double-peak variation in the wake. The peak with the larger magnitude of turbulence intensity is located on the inner side of the wake defect. These results confirm the reliability of the rake measurements and the repeatability of readings within the wake.

6.2.4.3. Probe calibration error

The sensitivity of present probe calibration on the mean and turbulence quantities is assessed for the cross-wire probe and the rake of single-wire probes. Two calibration data of a DANTEC 55P63 cross-wire probe were chosen to reduce a set of raw data in the near-wake of the airfoil at x/c = 1.05. The results presented in Figure 6.9 show virtually no differences in the profile of turbulence intensities and turbulence shear stress. However, the mean streamwise velocity component shows some sensitivity to the calibration, indicating differences of about 2%. A second set of calibration data for the single-wire 55P16 probes was used to reduce the raw data from the rake measurements presented in Figure 6.8(a,b). These results are shown in Figure 6.8(c,d). It is evident that the effect of calibration is more significant on the mean velocity than the turbulence intensity, where the results of one calibration show slightly higher values than the other.

Figure 6.10 presents the variation of temperature versus time during a typical experiment. The test case was conducted on a day with steady atmospheric conditions. It is evident that even on a steady day the temperature from the start to the end of an experiment could vary by nearly 1 ^{o}C. It was therefore important to implement temperature compensation during the hot-wire experiments and probe velocity calibration.

6.2.4.4. The effect of the upper wall cavity on the mean flow

To conduct airfoil boundary layer measurements, the upper wall of the straight test section between station 1 and 2 was replaced with one designed to cater for a dedicated traverse system (Figure 3.3). This modified section contained a cavity of area 150 mm × 100 mm and depth 10 mm. In Figure 6.11(a,b), the profiles of mean velocity and turbulence intensity, measured in the normal direction at the mid-span in the vicinity of the cavity are presented at several streamwise locations $0.51 < X/H < 0.71$, where X is the streamwise distance from station 1. In Figure 6.11, the line denoted by $y/H = 1$ shows the location of the upper wall of the tunnel. The depth of the cavity extends to $y/H = 1.02$. The measurement taken at $X/H = 0.51$ is at the upstream of the cavity where the approaching boundary layer on the convex wall is measured. At all other locations the measurements extend to the inside of the cavity. As expected, the flow in the cavity has resulted in some changes to the velocity profile near the upper wall boundary. The streamwise intensity exhibits a peak of approximately 17% of the bulk freestream velocity near $y/H = 1$, followed by a steady decrease inside the cavity. Below $y/H = 0.9$, the effects of the cavity on the mean velocity and streamwise turbulence intensity are negligible. Therefore, measurements conducted in the airfoil boundary layer are unaffected.

6.2.5. Profiles of mean and turbulence quantities in the near-wake

In this section the distribution of quantities in the normal and spanwise directions, in the near-wake, are presented. Initially, the profiles measured in the normal direction are presented on individual figures along with data obtained in the absence of the airfoil. The profiles are also aligned with respect to the wake centre line. The wake parameters, namely, the wake half-width (b') and the maximum velocity defect (w_o) are also presented. The velocity defect is defined as the difference between the velocities at that point without the wake (in the absence of the wake producing body) and with the wake. The maximum velocity defect occurs at the

wake centre line. The half-width of the wake is defined as the normal distance between the maximum velocity defect and the point where the wake defect equals half its maximum value. It is observed that b' is not the same on the inner and outer sides of the wake.

6.2.5.1. Results measured in the normal direction

The normal profiles presented below are measured at the midspan location $z/H = 0.5$.

Mean velocity profiles

The variation of mean velocity in the normal direction at $x/c = 1.05$ to $x/c = 2$ (station 2) are presented for each angle of attack in Figure 6.12(a-g). The profiles are also aligned with respect to the wake centre and shown on separate graphs in this figure. In general, as the distance from the airfoil is increased, the thicknesses of the inner and outer side wake increase while the differences between the velocities in the wake and the mainstream decrease.

Previous investigations have shown that for a wake developing under the present conditions, the inner side of the wake grows more rapidly than the outer side, and also the shifting of the wake centreline with respect to the duct centre line. These overall features are confirmed in the profile presented in Figure 6.12(a), for $\alpha = 0^o$. The shift of the wake is first noticed at $x/c = 1.33$, where the wake is shifted by a small amount of $0.005H$. This appears to be the location where the effect of the curvature of the duct starts to become noticeable. Before this location, the differences in the profile are mainly due to the differences in the boundary layer development on the upper and lower surfaces. At station 2, the wake is shifted by a large amount of about $0.02H$. The lateral shift of the wake is attributed to the normal pressure distribution in the flow. As will be evident from the results which will be presented later, and also shown earlier (Piradeepan and Mokhtarzadeh-Dehghan, 2005), the inner and outer side of the wake develop under varying streamwise and normal pressure gradients which result in the different growth rates noted here.

When the angle of attack is changed from zero, the velocity and pressure distributions about the airfoil are modified, causing changes in the main characteristics of the wake as were described above. For $\alpha = 2^o, 4^o, 6^o$, the centre of the wake in the vicinity of the trailing edge (Figure 6.12b-d) is first shifted downwards in the normal direction, up to $x/c = 1.33$, and then moved upwards again due to the bend. The distance by which the wake centre is shifted

downwards increases progressively with angle of attack ($+\alpha$) and the maximum shift occurs at x/c = 1.05, which is observed to be of the order 0.025H for $\alpha = 6^o$. For $\alpha = 2^o$ and 4^o, the wake is above the centre line of the duct at station 2, whereas for $\alpha = 6^o$ it is just below the centre line at this location. As angle of attack is increased the difference between velocities in the wake and the freestream is also increased. It is also observed that the widths of the wake on the inner and outer sides are also significantly affected by increased angle of attack. In general, as the trailing edge is deflected downwards the wake thickens in profile. Another qualitative observation is that, as the angle of attack ($+\alpha$) is increased, the asymmetry in the profile of the wake is enhanced near the trailing edge of the airfoil (x/c = 1.05, 1.10). The increase in the thickness of the wake on the inner side, in the vicinity of the trailing edge, can be related to a thicker boundary layer on the upper surface of the airfoil and changes in the pressure distribution as α is increased.

The results for $\alpha = -2^o, -4^o, -6^o$ in Figure 6.12(e-g) are consistent with the changes in the pressure distribution on the airfoil and, therefore, can also be explained similarly. It is seen that the wake centre remains above the centre line of the duct and move progressively towards the convex wall as streamwise distance is increased. The maximum shift of the wake above the centre line of the duct at station 2 is measured to be 0.062H at $\alpha = -6^o$. The symmetry in the profiles increases as the airfoil trailing edge is deflected upwards. At $\alpha = -4^o$ the profiles measured near the trailing edge (x/c = 1.05-1.44) are almost symmetrical about the wake centre line. The effect of the bend has become apparent at station 2, where the profiles for $\alpha = -2^o$ and $\alpha = -4^o$ display an asymmetric distribution.

The changes described above can be more clearly seen in Figure 6.13 where the profiles are plotted together. As can be seen the changes in the profiles are greater for positive angles of attack (Figure 6.13a) than the profiles for the negative angles of attack (Figure 6.13b); the latter figure displays the progressive alignment of the oncoming flow with the airfoil.

Wake parameters

The results indicate two contributory effects on the flow, one induced as a result of the airfoil angle of attack and the other from the curvature and pressure gradient imposed by the duct. Qualitatively, it is observed that near the trailing edge the dominating factor is the airfoil angle of attack, which induces changes in the airfoil boundary layer. Closer to station 2, the pressure gradient and curvature from the duct play a more dominant role. To quantitatively examine the

properties of the wake, the variation of wake parameters such as the wake half-width and maximum velocity defect are presented in Figures 6.14(a-h). Generally, the results show that the wake half-width increases on both sides with streamwise distance from the airfoil. For $\alpha = 0^o$, the value on the inner side is always greater than the outer side. The results are in good agreement with the results of Piradeepan (2002). For $\alpha = 2^o$ and 4^o, close to the trailing edge (x/c = 1.05, 1.10) the half-width of the wake on the inner side is increased, whereas further downstream the half-width on the inner side becomes closer to that measured at $\alpha = 0^o$. For $\alpha = 6^o$, a considerably larger half-width is measured on the inner side, which remains constant in the near-wake up to x/c = 1.44. The results show that the total wake half-width increases with angle of attack. The maximum velocity defect and its rate of decay decrease as distance from the airfoil is increased (Figure 6.14d). A positive increase in the angle of attack results in an increase in maximum velocity defect, although the rate of decay is not significantly affected.

The results for negative angles of attack (Figure 6.14e-h), show similar variations to those of the positive angle of attack for the total wake half-width. Note that, due to the alignment of the flow with the airfoil, at $\alpha = -4^o$, the wake half-widths on the inner and outer sides are almost equal near the trailing edge. The results for the maximum velocity defect (Figure 6.14h) show a decrease with negative angle of attack.

Effect of mainstream velocity on mean velocity

The effect of mainstream velocity on the near-wake profiles is shown in Figure 6.15, for $\alpha = 0^o$ and $\alpha = 4^o$. The results show that the maximum velocity defect increases with mainstream velocity, but normalization of the profile with respect to the mainstream velocity leads to collapse of the data as shown in Figures 6.15(a) and 6.15(b). Furthermore, the wake half-width, on both sides, decays with mainstream velocity, but the effect is more apparent at station 2.

Streamwise turbulence intensity

The streamwise turbulence intensities measured at different angles of attack are presented in Figure 6.16(a-g). The profiles of streamwise turbulence intensity show a characteristic double peak profile. The location of the minimum in the profile, between the two peaks, corresponds to the position of the maximum velocity defect in the streamwise velocity profile (Figure

6.12). Near the trailing edge (x/c = 1.05, 1.10) the lateral shift in the turbulence intensity profiles can be attributed to the airfoil angle of attack, whereas further downstream it is mainly the effect of duct curvature which causes the profiles to move in the normal direction towards the convex wall.

The effect of angle of attack can be more clearly seen in Figure 6.17(a,b), where the profiles are aligned with the wake centre. In general, as the angle of attack is increased (positively or negatively) the double peak moves away from the centre line of the wake resulting in a wider profile. In Figure 6.17(a), at the first location past the trailing edge (x/c = 1.05), the region engulfed in turbulence is much greater on the inner side than that on the outer side. As the angle of attack is increased positively, the profile on the inner side is further enhanced but little change is observed in the outer side. This is attributed to the changes in the boundary layer development on the upper surface of the airfoil. At x/c = 1.22 and 1.44, with an increase in angle of attack the peaks in the profile become more distinguishable and the turbulence increases, especially on the outer side. It is observed that the turbulence intensity increases by about 60% at the wake centre when angle of attack is increased from $\alpha = 0^o$ to $\alpha = 6^o$. At station 2 (x/c = 2), the peak on the inner side is more pronounced than that on the outer side. This effect is enhanced as the trailing edge of the airfoil is deflected downwards. The level of turbulence intensity in the wake decreases with distance downstream of the trailing edge. The effects of curvature and pressure gradient in enhancing turbulence on the inner side and suppressing it on the outer side (Tulapurkara et al., 1994) is evident at station 2.

The effect of negative angles of attack on the streamwise turbulence intensity is shown in Figure 6.17(b). The changes in the profiles are less pronounced, which is in line with the results for the mean velocity profile stated earlier. The double peak becomes less distinguishable with streamwise distance. For $\alpha = -4^o$ the variation of turbulence intensity is almost symmetrical about the wake centre up to x/c = 1.44, beyond which the curvature and pressure gradient due to the bend start to affect the flow.

As was stated in Chapter 3, there was no tripping of the boundary layer on the airfoil. The results of Ramjee and Neelakandan (1990), Tulapurkara et al. (1994) and Weygandt and Mehta (1995) showed a distinguishable double peak in the wake for tripped boundary layers on the airfoil. In the untripped case of Weygandt and Mehta (1995), the less distinguishable double peak was attributed to the presence of spanwise variations in the wake. In tripping the airfoil boundary layer, the aim of previous investigators was to promote earlier transition to

turbulence and enhance the development of the shear layer. The present results indicate that, there appears to be a similar effect produced by a positive increase in the angle of attack. The effect of increasing the angle of attack (positively) promotes the boundary layer development on the upper surface of the airfoil resulting in more distinguishable double peaks in the profiles of streamwise intensity.

The effect of increasing mainstream velocity is to enhance streamwise turbulence intensity, although this is not seen in Figure 6.18(a,b), due to the normalization.

Normal turbulence intensity

The distributions of normal turbulence intensity near the trailing edge and at station 2 are presented in Figure 6.19(a-g) and Figure 6.20(a,b). In contrast to streamwise turbulence intensity, the profiles of normal turbulence intensity display a single peak. At the trailing edge, the general trends in relation to the effects of angle of attack and airfoil boundary layer are in line with the findings of the streamwise intensity. Further downstream, at station 2, the effect of curvature is different from that seen on the streamwise intensity. While in streamwise intensity, the larger peak moves towards the convex wall for both positive and negative angles of attack, in normal intensity the opposite occurs for the positive angles. To give a quantitative measure of the changes in the magnitude, the values of the peaks in *Vrms* can be compared. Close to the trailing edge, at x/c = 1.05, the peak value has increased by about 76% when the trailing edge is deflected upwards by 4^o, whereas at station 2 this increase is just less than 40%. The effect of mainstream velocity on the profile of normal turbulence intensity in the wake in Figure 6.21 is consistent with those described for streamwise fluctuations.

Turbulence shear stress

Figure 6.22(a-g) shows the profiles of turbulence shear stress $-\overline{u'v'}$ in the normal direction. The turbulence shear stress becomes zero and changes sign at the wake centre, which coincides with the location of minimum velocity. The profiles generally show a positive peak on the inner side and a negative peak on the outer side, which correspond to the point of maximum mean shear $(\partial U/\partial y)$ either side of the wake centre line in Figure 6.12. To assess the effects of angle of attack, the turbulence shear stress profiles aligned with the wake centre are shown in Figure 6.23(a) and 6.23(b). For α = 0^o at the trailing edge, the magnitude of the positive peak is larger than its corresponding negative peak. For positive angles of attack, the

width of the profile becomes considerably enhanced on the inner side, whereas little or no change is observed on the outer side. At station 2, the profiles become more symmetrical, where the effect of the bend is more influential. For negative angles of attack, at the trailing edge (Figure 6.23b), the magnitude of the peak values are increased. The profiles here are consistent with the alignment of the airfoil with the flow. As with mean streamwise velocity, the effect of negative angle of attack on the profile is smaller at station 2 (Figure 6.23b). The profile of turbulence shear stress is asymmetric for all negative angles tested at this location; the magnitude of the positive peak is larger than the negative peak. The changes in the profiles at station 2 as a result of negative angle of attack are less significant than those seen for positive angle of attack.

The effect of mainstream velocity on the turbulence shear stress is indicated in Figure 6.24(a,b). The findings are similar to those for turbulence intensities, where the profiles collapse when normalized with mainstream velocity.

The changes observed in the Reynolds stresses at station 2 due to the effects of curvature, that is, the enhancement of turbulence on the inner side of the wake and its suppression on the outer side, can be explained theoretically by inspecting the production terms in the transport equations of these quantities. Weygandt and Mehta (1995) presented the transport equations for the Reynolds stresses based on approximations by Bradshaw (1973). The production terms for the effect of curvature on the normal stresses $\overline{u'^2}$ includes

$$-\overline{u'v'}\left[\left(1+\frac{n}{R}\right)\frac{\partial U}{\partial n}-\frac{U}{R}\right] \tag{6.3}$$

where n denotes the normal direction, R is the local radius of curvature and U is the streamwise velocity component. The term $1+n/R$ is always positive, and $U/R < 0$ on both sides of the wake (Weygandt and Mehta, 1995). From the profiles presented in Figures 6.12(a) and 6.22(a), on the inner side of the wake, $\partial U/\partial n > 0$ and $\overline{u'v'} < 0$ $(-\overline{u'v'} > 0)$, and on the outer side $\partial U/\partial n < 0$ and $\overline{u'v'} > 0$ $(-\overline{u'v'} < 0)$. Therefore, it follows that the increase in streamwise intensity on the inner side of the wake is due to a positive contribution of the production terms in equation 6.3, and a decrease on the outer side is due to the negative contribution of these terms.

The turbulence shear stress also appears in the production term for $\overline{v'^2}$. The change in sign of $-\overline{u'v'}$ at the wake centre results in asymmetry in the profile of the normal turbulence intensity in Figure 6.19(a). For the turbulence shear stress $-\overline{u'v'}$ the production term for the effect of curvature is

$$\overline{u'^2}\left[\frac{\partial V}{\partial s}-\frac{U}{R}\right]+\overline{v'^2}\left[1+\frac{n}{R}\right]\frac{\partial U}{\partial n} \qquad (6.4)$$

where s defines the streamwise coordinate and V is the normal component of velocity. The term $\partial V/\partial s$ is approximated by $-U/R$ (Weygandt and Mehta, 1995). Therefore, the first term in equation 6.4 makes a positive contribution to the production of $-\overline{u'v'}$ on the inner and outer sides, increasing the magnitude of positive shear stress on the inner side and decreasing the negative level on the outer side. Owing to the change in sign of mean shear $\partial U/\partial n$ either side of the wake centre, the second term of equation 6.4 makes a positive contribution to the production levels on the inner side and a negative contribution to the production levels on the outer side.

6.2.5.2. Results measured in the spanwise direction

The spanwise distributions of mean velocity and turbulence intensity in the wake are presented in Figures 6.25 and 6.26, respectively, for the nominal mainstream velocity of 10 m/s and angle of attack α = 0°. These measurements were conducted within a span of approximately 1/3 of the central region of the duct, which covered approximately 12 wake half-widths at station 2 and 40 wake half-widths at x/c = 1.05. In the distribution of mean velocity shown in Figure 6.25(a), little or no spanwise variations are measured in the freestream regions at all streamwise locations, indicating the two dimensionality of the flow in the mean. In the near-wake at x/c = 1.10, spanwise variations are measured on the inner side of the wake, corresponding to the normal locations y = 231 mm and y = 234 mm, and to standard deviations of about 9-10%. On the outer side of the wake (y = 227 mm), the spanwise variations are less. The variations persist in the streamwise direction on the inner side of the wake at x/c = 1.22 and 1.33, but the magnitude of variations decay with increase in streamwise distance. At x/c = 2, the standard deviations on the inner side of the wake defect are approximately 4-5%. In general, in the freestream and outer wake regions the standard deviations are than 2%. The profiles on the inner side show an approximately wavy pattern with variable amplitudes and wavelengths. It is observed that the wavelength of the spanwise variations increases with

streamwise distance (Figure 6.25d), whereas the amplitude decreases. On the outer side of the wake there is little evidence of a wavy pattern; on this side the spanwise variations are considerably smaller in magnitude.

The spanwise variations are observed more clearly in the profiles of turbulence intensity in Figure 6.26, characterised by strong peak and valley wavy structure. As with the mean velocity, the magnitude is seen to decrease with increased streamwise distance away from the trailing edge. By station 2, the variations have decayed considerably on the inner side of the wake. Again, on the outer sides, there is little variation of turbulence intensity in the spanwise direction, and the distributions become flatter and more two-dimensional in the regions outside of the wake.

A distinct relationship is observed between the near-wake turbulence profiles in Figure 6.26 and the mean velocity profiles in Figure 6.25. It is observed that a decrease in turbulence intensity coincides with an increase in streamwise velocity, and vice versa. This correlation is apparent at all locations. In general, the results indicate the presence of three-dimensional structures in the flow demonstrated by the variations in the profiles of mean velocity and turbulence intensity on the inner side of the wake. Mokhtarzadeh-Dehghan and Yuan (2002) reported similar characteristics in the concave wall boundary layers of the present duct (Figure 1.4), where they attributed the wavy patterns in the mean velocity and turbulence intensity profiles to the formation of streamwise vortices. Weygandt and Mehta (1995) reported large spanwise variations in their untripped curved wake. Their results also showed evidence of the formation of streamwise vortices, where the rate of decay of vorticity on the unstable side of the wake (inner side) was significantly reduced compared to the outer side.

The present results can be interpreted in a similar manner as described above. The peak valley patterns seen in Figures 6.25 and 6.26 point towards the formation of streamwise vortices in the wake. These vortical motions are strong enough to cause significant spanwise variations in the mean velocity and turbulence intensity profiles. A peak in the profile of streamwise velocity corresponds to a trough in the profile of turbulence intensity, indicating down flow of fluid with a lower turbulence level, and vice versa. The results indicate that the formation of streamwise vortices is more significant on the inner side than the outer side. It should be noted that the variations in the profile referred to here relate mainly to the inner side of the wake. On the wake centre line, consistent with the results of Piradeepan (2002), the flow is nearly uniform in the spanwise direction. The occurrence of the spanwise patterns was confirmed by

repeated measurements. Weygandt and Mehta (1995) report that the mean streamwise vorticity had a considerable effect on the wake width and velocity defect. The presence of streamwise vortices in untripped wakes is known to produce additional entrainment and thus result in a faster decay of mean velocity defect. In curved untripped wakes, the effects of streamwise vorticity in the near field are stronger resulting in even faster decay of velocity defect.

The effect of angle of attack

The effects of increasing angle of attack and mainstream velocity on the spanwise variations at x/c = 2 (station 2) are presented in Figure 6.27 and 6.28. When the angle of attack is increased to $\alpha = 4^o$ the structure of spanwise variations in the velocity defect changes considerably. In both the mean streamwise velocity and streamwise turbulence intensity in Figure 6.27(a,b) large spanwise variations occur on the inner side of the wake defect, characterised by wavy patterns. The wavelength and magnitude of these variations is increased significantly from that measured at $\alpha = 0^o$. In order to investigate further, the spanwise measurements at $\alpha = 4^o$ were conducted over a larger spanwise extent. Generally, the three-dimensionality in the wake has increased with increasing angle of attack, demonstrated by larger differences of the peaks and troughs in the profiles of mean streamwise velocity and streamwise turbulence intensity. The standard deviation of the spanwise variations of velocity on the inner side of the wake (y = 235 mm) is nearly 25%, this is an increase from the deviation of nearly 5% at $\alpha = 0^o$ seen in Figure 6.25(d). As before, the organised wavy structures in Figure 6.27 show good correlation between peaks and troughs in the profiles of U and $Urms$. The wavy patterns in the distribution of streamwise turbulence intensity on the inner side of the wake show pronounced peaks near z/H = 0.3 and z/H = 0.5, where a minimum is observed at z/H = 0.4. These structures are consistent with the troughs in the spanwise distributions of mean velocity. On the outer side of the wake, some spanwise variations are observed, however these are smaller in magnitude compared to the inner side.

The effect of mainstream velocity

Figure 6.28(a-d) shows the effect of increasing the mainstream velocity from 10 m/s to 20 m/s on the spanwise distribution of the wake velocity defect and streamwise turbulence intensity. The spanwise distribution of the wake velocity defect is less sensitive to increasing the mainstream velocity than the angle of attack. The wavy pattern in the mean velocity profiles at

U_o = 20 m/s are more distinct than those at U_o = 10 m/s, especially for $z/H > 0.5$ (Figure 6.28b). The results indicate enhanced spanwise variations at station 2 when the mainstream velocity is increased to 20 m/s. The standard deviations of the velocity defect at U_o = 20 m/s are approximately 11-12% for the profiles measured on the inner side of the wake. A smaller spanwise component is measured on the outer side of the wake compared to the inner side. The effect on the streamwise turbulence intensity is shown in Figure 6.28(c). Similarly, it is observed that the spanwise variations in *Urms* increase with mainstream velocity.

6.2.6. Profiles of mean and turbulence quantities in the airfoil boundary layer

Hot-wire measurements were carried out on the airfoil to study the boundary layer development on the upper surface. Tests were conducted at the mid-span (z/H = 0.5) for a configuration of zero angle of attack and mainstream velocity 10 m/s. Figure 6.29(a-d) shows profiles of mean velocity and turbulence intensity through the boundary layer. The measuring locations were x/c = 0.44, 0.64, 0.74, 0.83, 0.93, 0.98. The normal distance from the upper surface of the airfoil Y_a is normalized with the duct height H. To confirm the repeatability of measurements a second set of data is presented in Figure 6.29(a) and 6.29(c) at each location. The repeat measurements show good consistency with the first set of data.

Significant changes in the boundary layer takes place (Figure 6.29a,b). Initially, the boundary layer is very thin, and the velocity increases linearly. The profiles take a shape more closely associated with transitional or turbulent boundary layers when the position of the measurement is close to the trailing edge, at x/c = 0.93. The boundary layer thickness, δ, increases from $0.0038H$ at x/c = 0.44 to $0.012H$ at x/c = 0.98. It is noted that δ has nearly doubled from x/c = 0.83 to x/c = 0.93. As will be discussed later when the numerical results are presented (Chapter 7), the flow appears to be close to separation, although there is no direct evidence of separation. This deduction is also consistent with the pressure distribution on the airfoil (Figure 6.4a).

The turbulence intensity profiles in Figure 6.29(c,d) show an increase in the maximum value of *Urms* (as a percentage of freestream velocity) from 3% to 7% between x/c = 0.44 to x/c = 0.64. At x/c = 0.74, the turbulence intensity peaks at 15% of the freestream. The peak value in turbulence intensity is nearly constant beyond this streamwise location. At the two upstream locations (x/c = 0.44, 0.64) the turbulence activity is confined to a thin region next to the wall. Further downstream, greater width of the flow is involved and the profiles become thicker, and

the location of the peak moves away from the wall. Between x/c = 0.83 and x/c = 0.93, there is a significant increase in the thickness of the profile, which is consistent with the change in the velocity profile seen at this location in Figure 6.29(a).

In order to assess the conformity with the standard law of the wall, the velocity profiles are plotted on a Clauser chart in Figure 6.30(a). An estimation of the friction coefficient can also be made from these graphs. In Figure 6.30(a), Re_y is defined as

$$\mathrm{Re}_y = \rho Y_a U_o / \mu \tag{6.5}$$

It can be seen that the profiles at x/c = 0.93, 0.98 show reasonable correlation with the log-law. The skin friction coefficient is observed to increase closer to the trailing edge where estimated values are C_f = 0.006 and C_f = 0.0064 at x/c = 0.93 and x/c = 0.98, respectively. The velocity profiles measured between x/c = 0.44 and 0.83 do not correlate with the log-law, as expected from the profile of a boundary layer in the early stages of development. Further presentation of the results in the form of u^+ vs. y^+ indicate a small deviation from the log-law for a flat plate boundary layer with the constants A = 2.44 and B = 5.0, which supports the suggestion put forward above with regard to the boundary layer status close to the trailing edge.

The results can be compared with recent experimental, direct numerical simulation (DNS) and LES results of other investigators. Kerho and Bragg (1997) measured boundary layers on a NACA 0012 airfoil at $\alpha = 0^o$ and at different Reynolds numbers. Their results showed that the start and end of boundary layer transition is within x/c = 0.65-0.775 for Re = 7.5×10^5, x/c = 0.57-0.675 for Re = 1.25×10^6 and x/c = 0.431-0.5 for Re = 2.25×10^6. These results show that transition occurs earlier and over a shorter distance as the Reynolds number is increased. The movement of the transition point upstream contradicts the finding of Yarusevych et al. (2004) who used a NACA 0025 airfoil at 5^o. They found that the transition point moved towards the trailing edge from x/c = 0.62 to x/c = 0.72, as Reynolds number is increased from 1×10^5 to 1.5×10^5. The differences between these results could be attributed to several factors such as the flow configuration, angle of attack and the airfoil type. The location of transition on NACA 0012 airfoils has been determined numerically by several researchers using LES and DNS. Shan et al. (2005) found that transition took place near x/c = 0.63 for airfoil angle of attack $\alpha = 4^o$ and chord Reynolds number 1×10^5. Marsden et al. (2006) reported the point of transition on the upper surface of a NACA 0012 airfoil at $\alpha = 0^o$ and Reynolds number Re =

5×10^5 to be between x/c = 0.54 and 0.72. For the same conditions as Marsden, the experiments of Lee and Kang (1998) for a higher Reynolds number of 6×10^5 put the transition location between x/c = 0.62 and 0.78. The present results for zero angle of attack are consistent with these findings as, for a lower chord Reynolds number of Re = 1×10^5 (U_o = 10 m/s), the location of transition is closer to the trailing edge, between x/c = 0.83-0.93.

The present investigation also involved measurements at different freestream speeds and angles of attack in the wake. These tests, conducted at U_o = 15 m/s and U_o = 20 m/s, correspond to chord Reynolds numbers of 1.53×10^5 and 2.04×10^5, respectively. The inspection of the velocity and turbulence fields in the wake showed increase turbulence activity and three-dimensionality in the wake, which tends to support the movement of the transition point upstream, in agreement with the findings of the Kerho and Bragg (1997).

The increase in angle of attack positively also causes the movement of the transition point upstream, as may be deduced from the increased turbulence in the wake, and also the pressure distribution on the upper surface of the airfoil. The pressure distributions (Figure 6.4) indicated an abrupt change in the gradient of C_p the location of which was seen to move upstream as the angle of attack was increased (positively). At $\alpha = 4^o$ and 6^o results indicated the presence of a short separation bubble near the leading edge (x/c = 0.1) characterised by a sudden decrease in C_p on the upper surface of the airfoil.

Experimental results

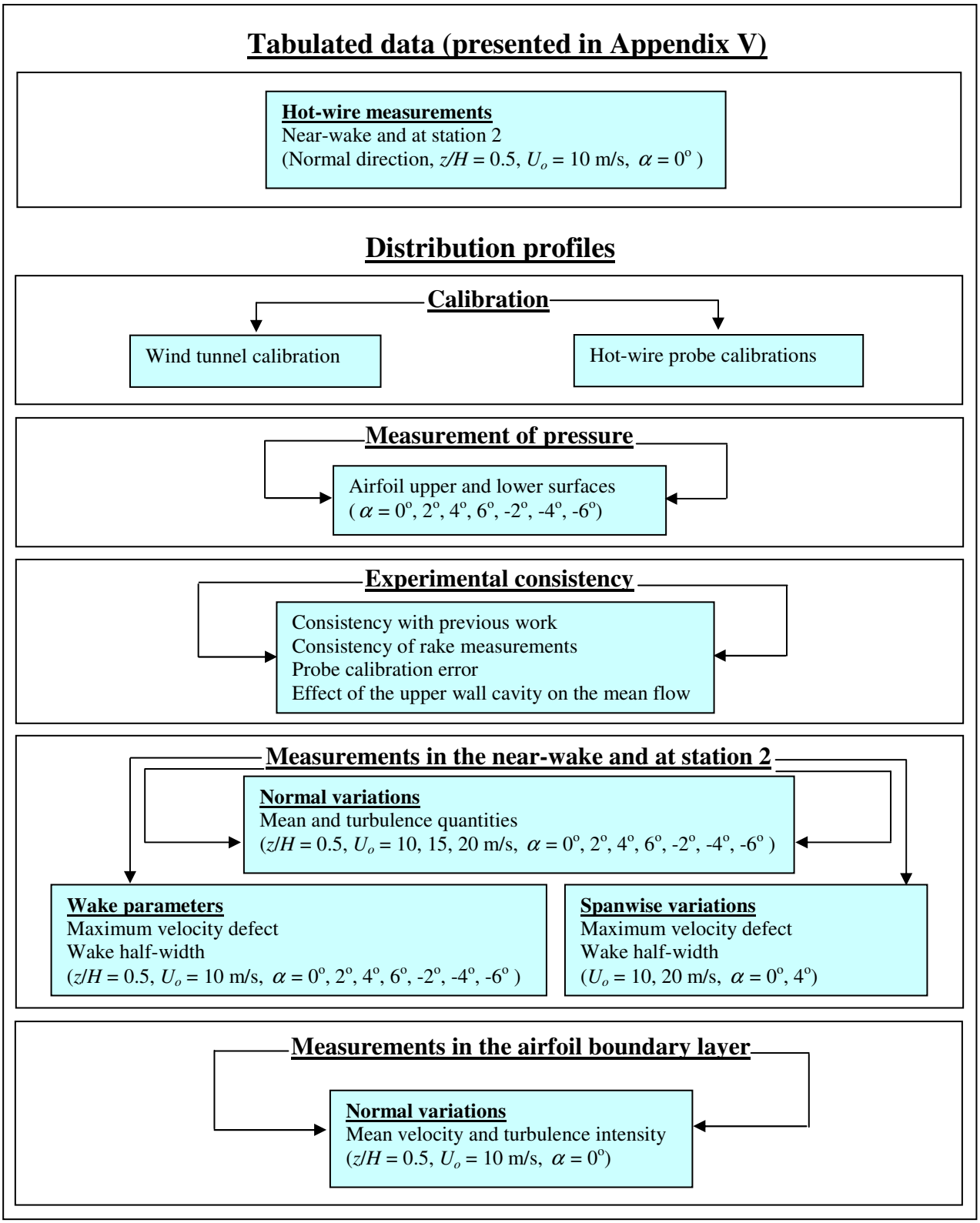

Figure 6.1: The structure of the presented experimental results.

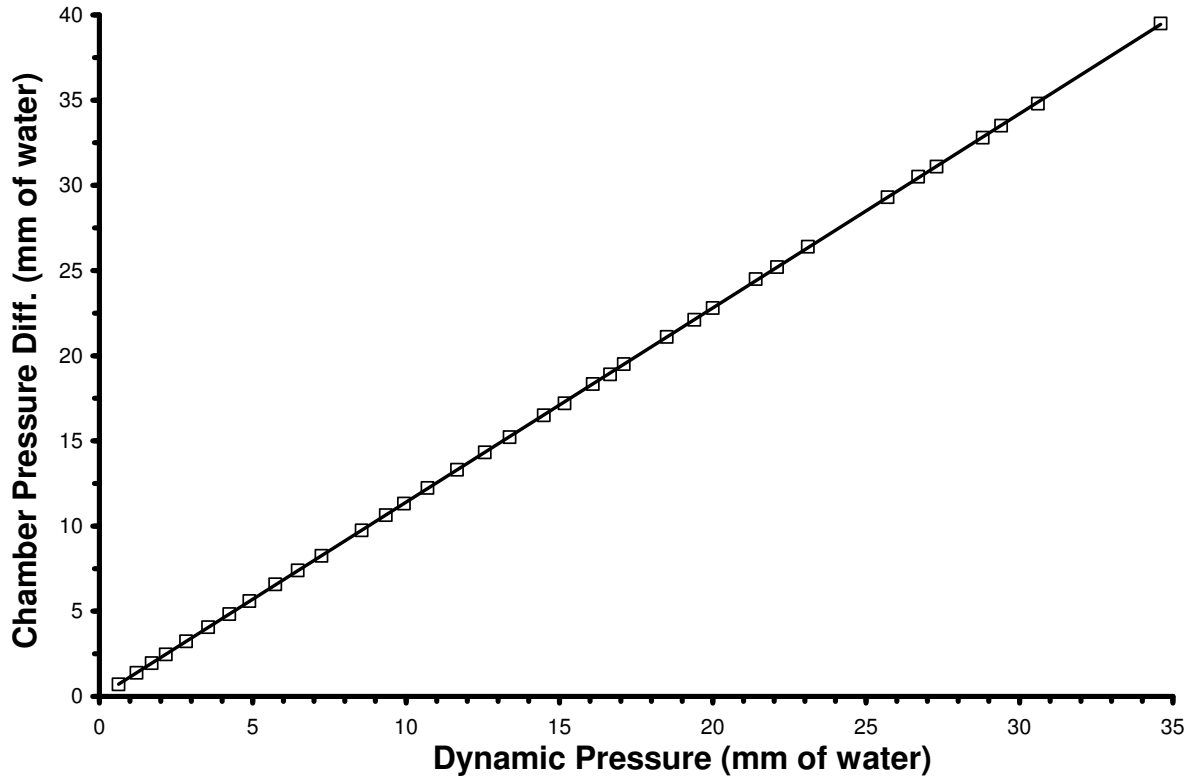

Figure 6.2: Tunnel calibration

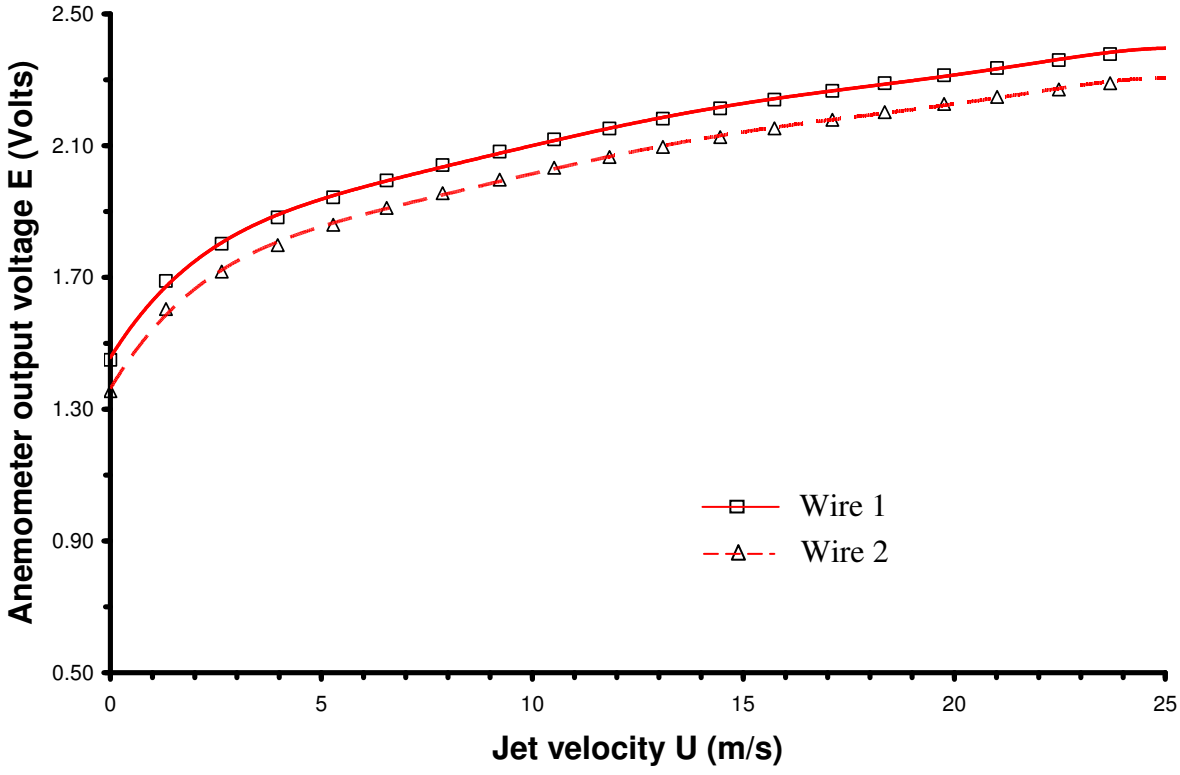

(a)

Figure 6.3: For caption see head of figure.

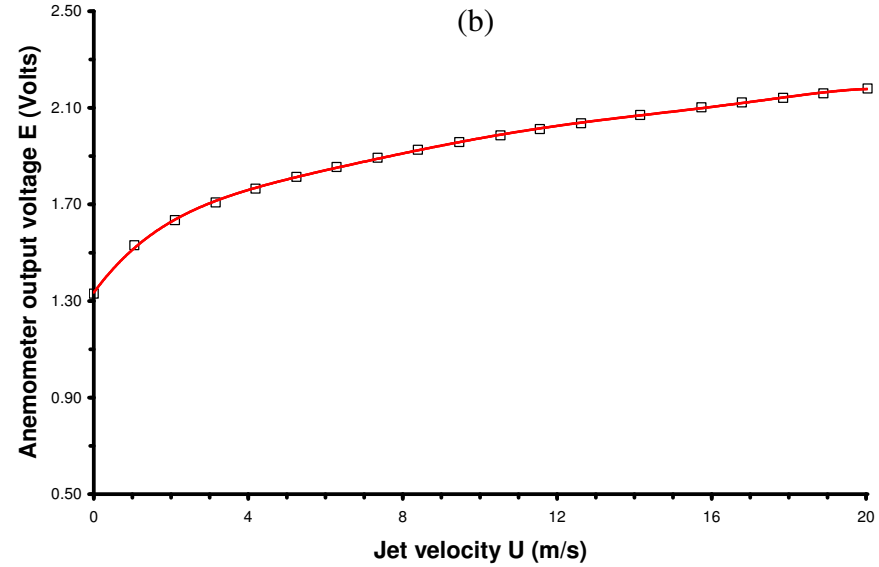

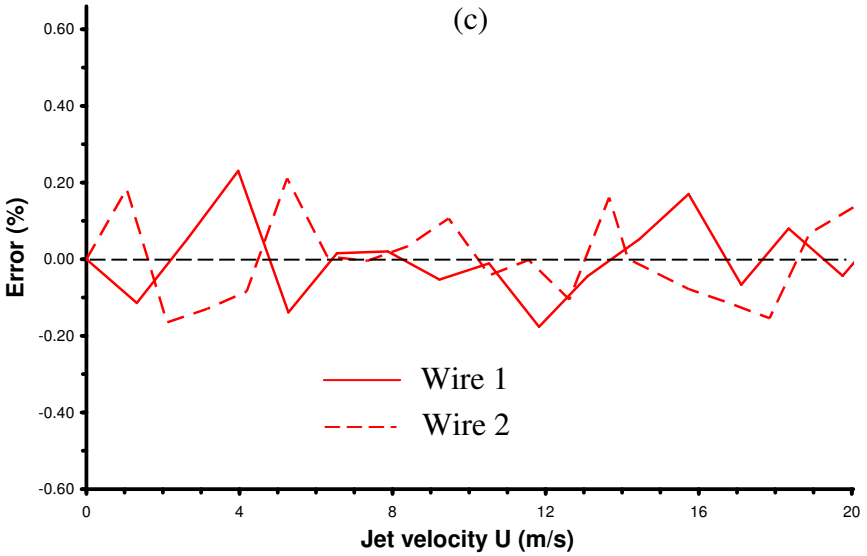

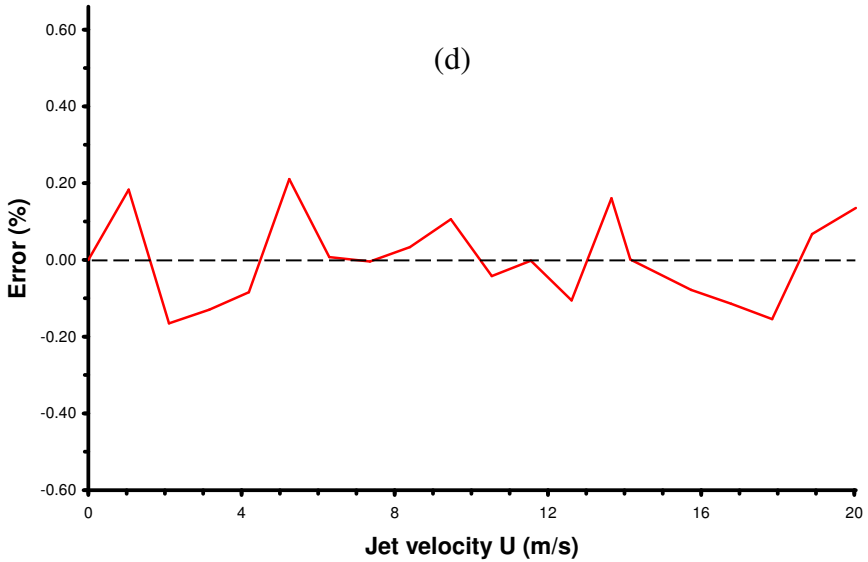

Figure 6.3: Probe velocity calibration data: (a) cross-wire probe voltage output, (b) single-wire probe voltage output, (c) cross-wire probe calibration error, (d) single-wire probe calibration error.

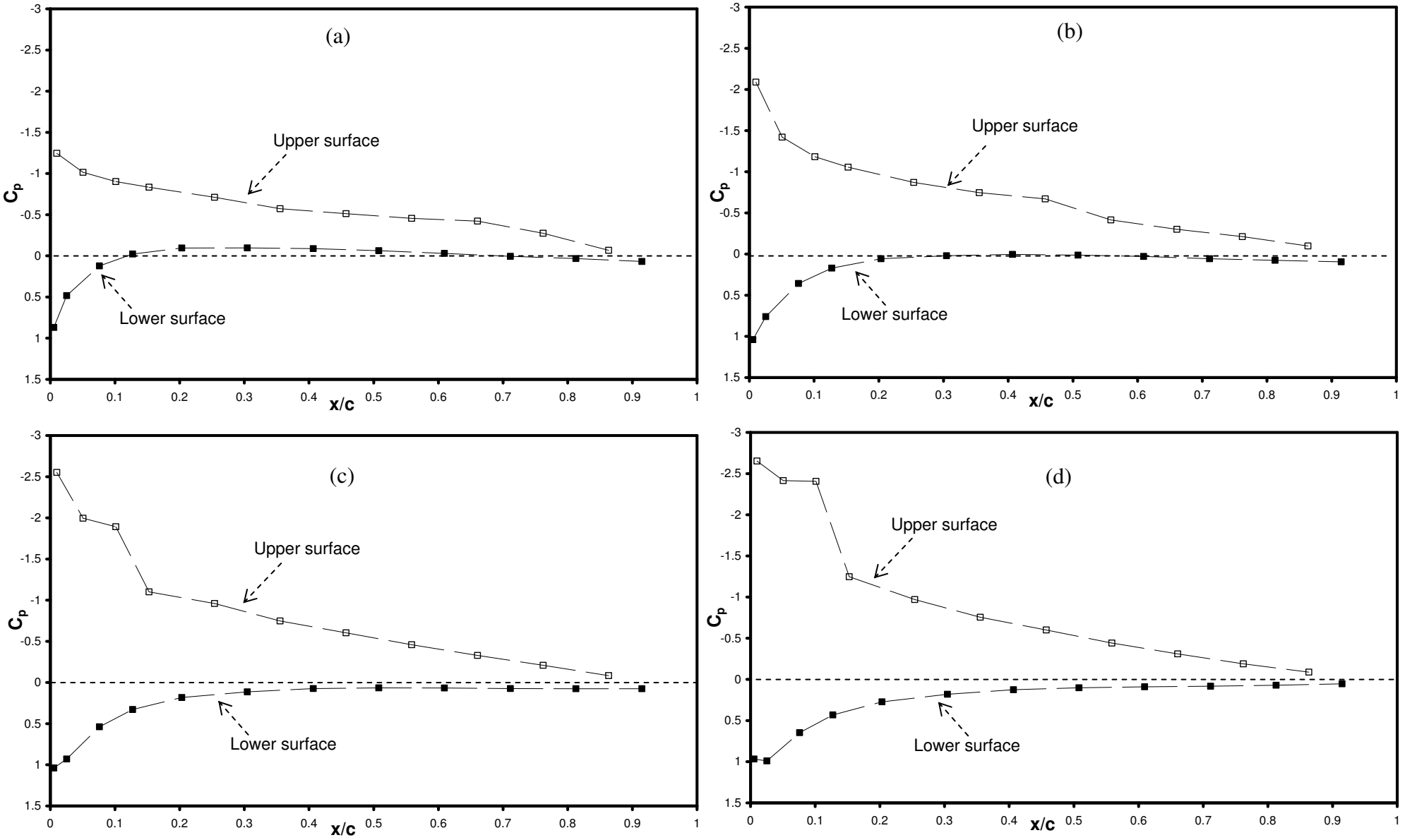

Figure 6.4: For caption see head of figure.

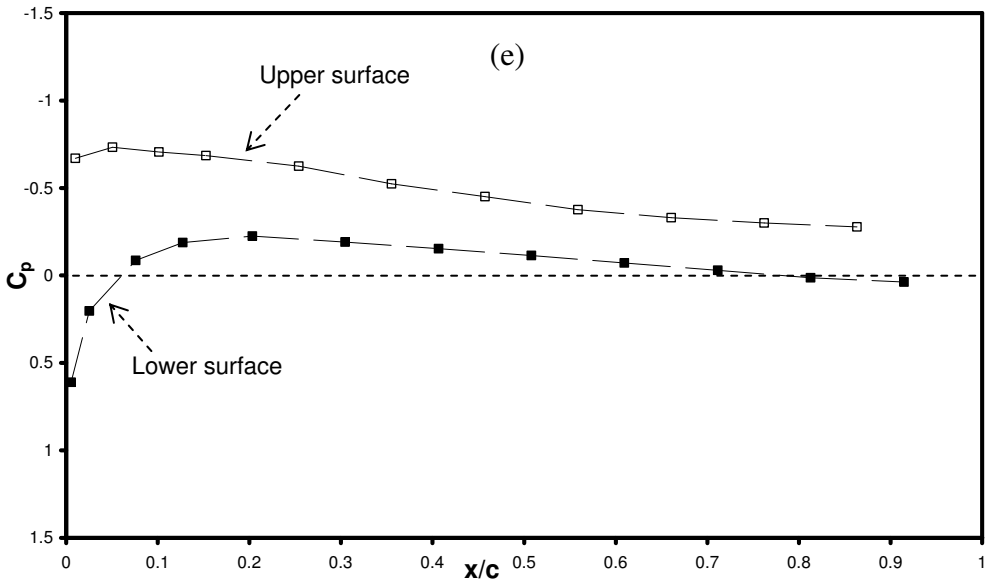

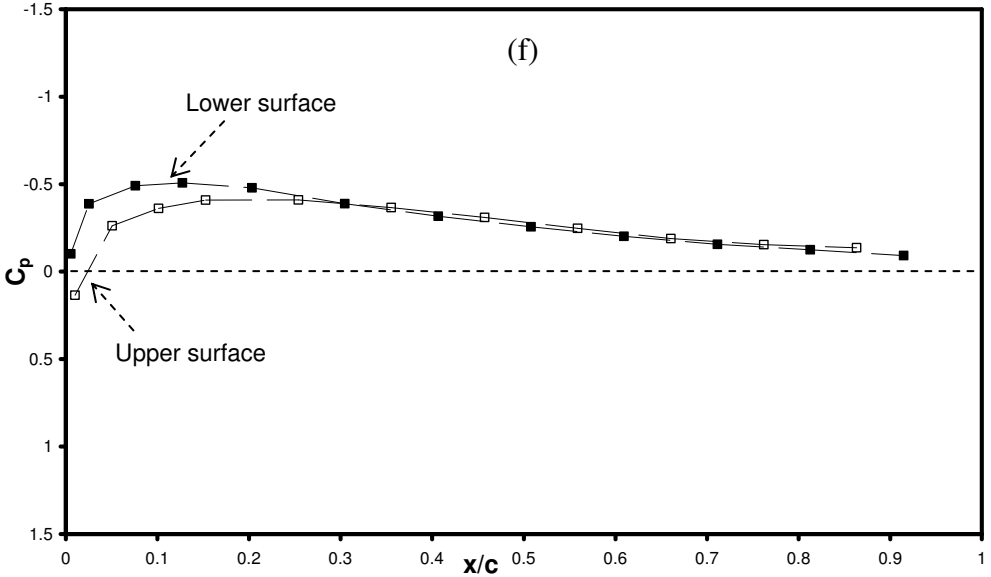

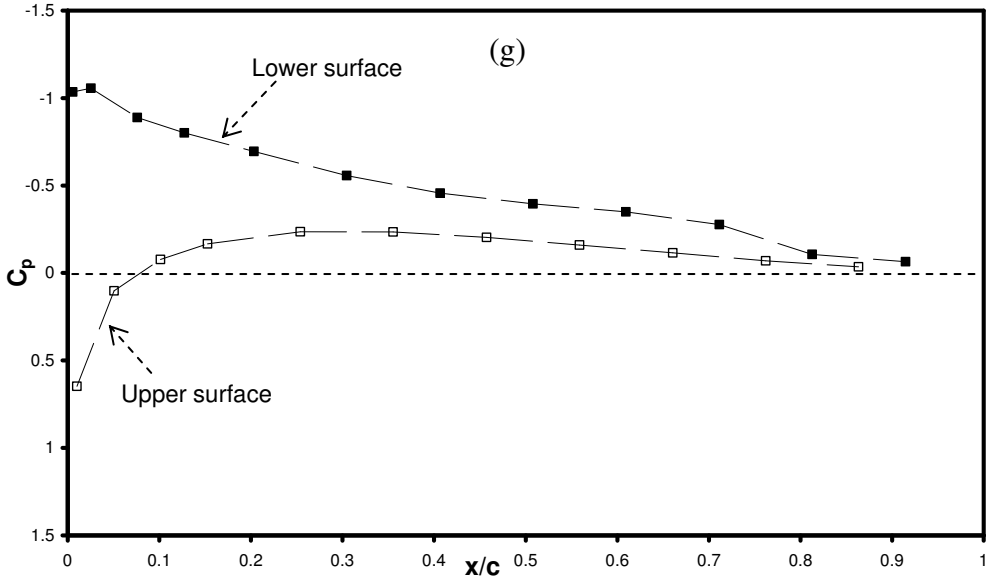

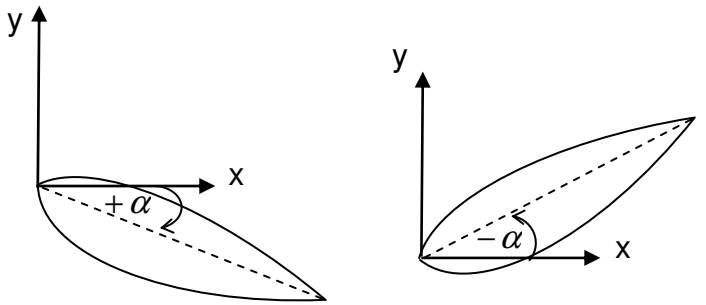

Figure 6.4: Pressure coefficient on the airfoil ($z/H = 0.5$) at various angles of attack: (a) $\alpha = 0^o$, (b) $\alpha = +2^o$, (c) $\alpha = +4^o$, (d) $\alpha = +6^o$, (e) $\alpha = -2^o$, (f) $\alpha = -4^o$, (g) $\alpha = -6^o$

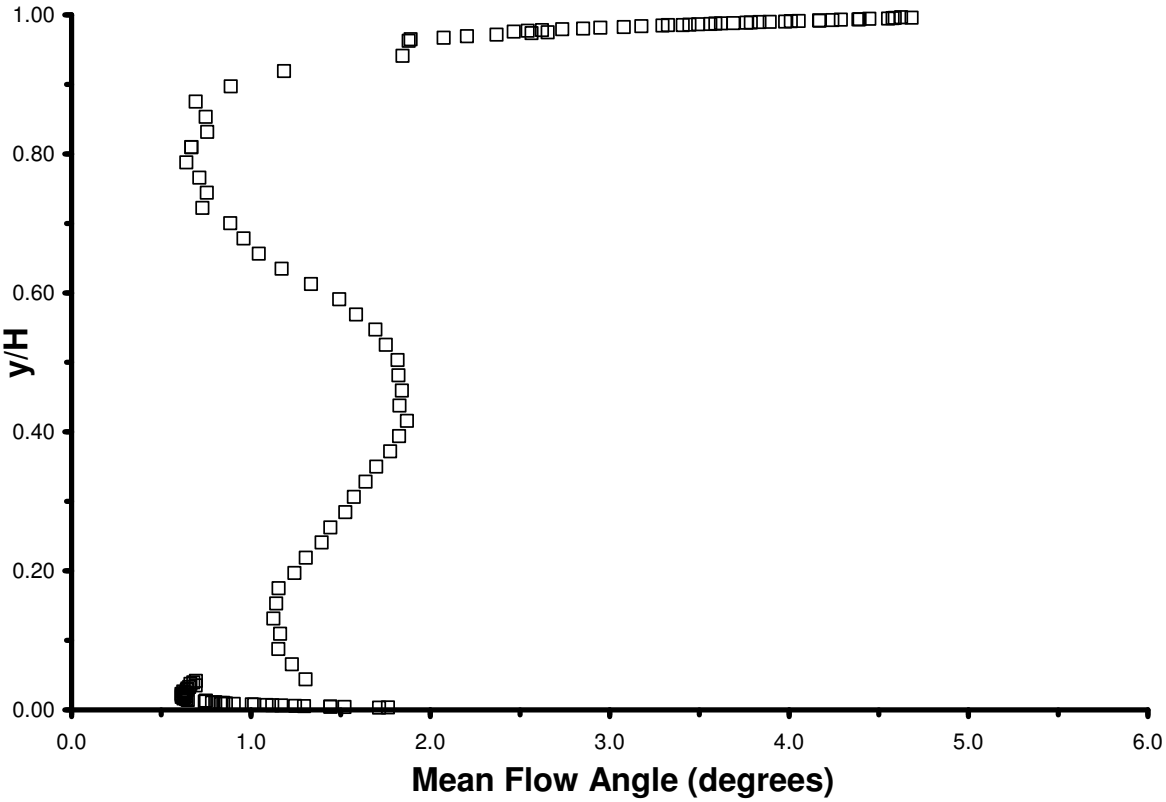

Figure 6.5: Mean flow angle at station 1 (z/H = 0.5), Piradeepan (2002)

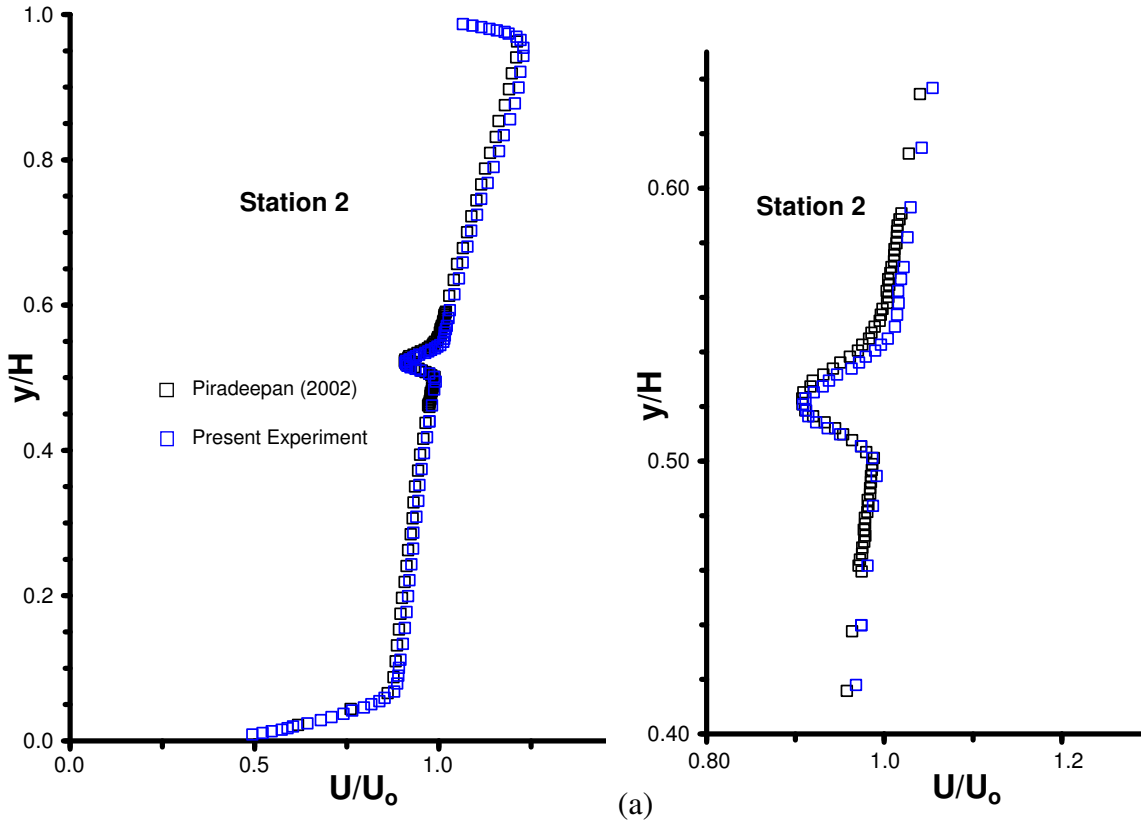

(a)

Figure 6.6: For caption see head of figure

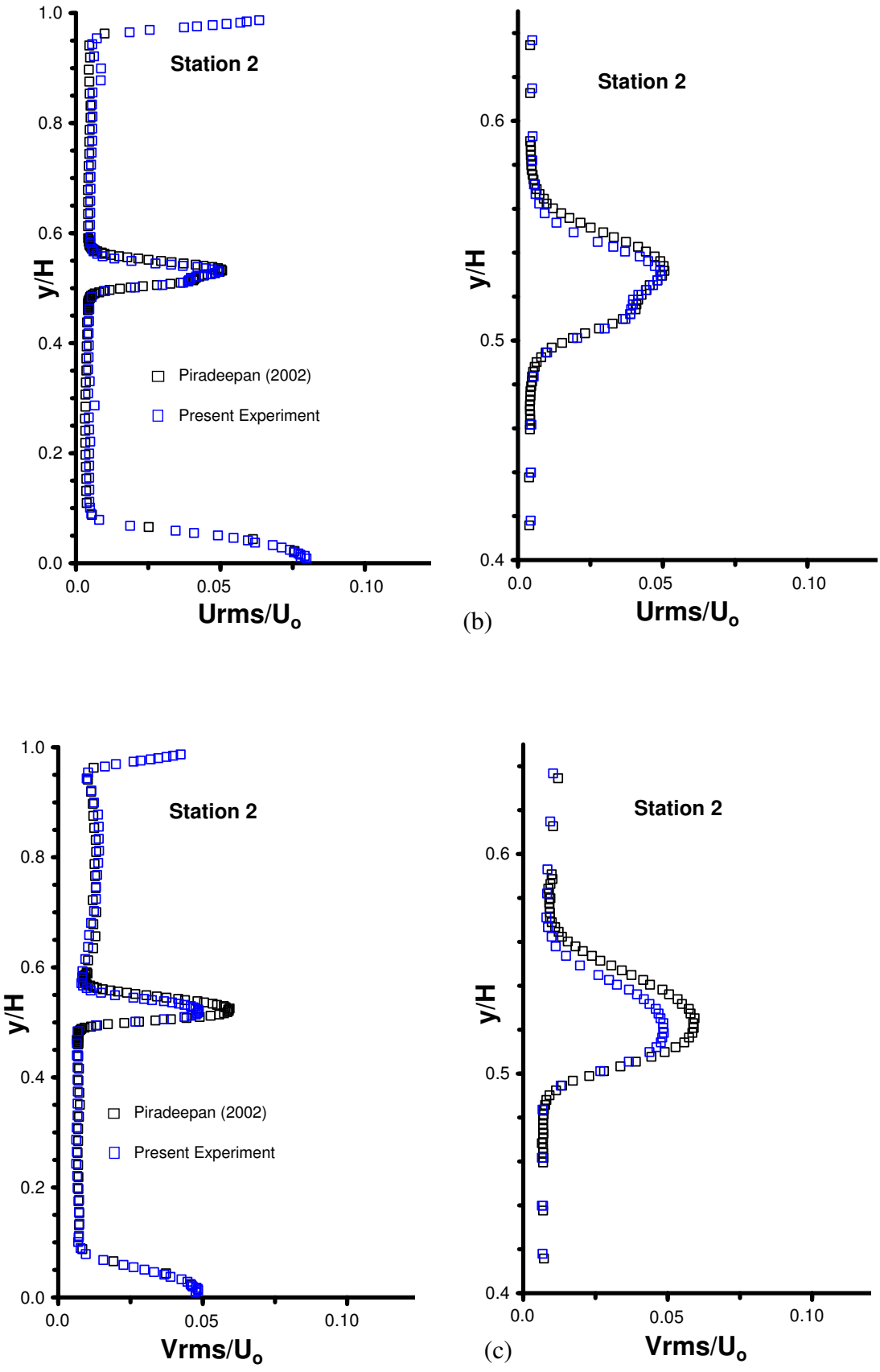

Figure 6.6: For caption see head of figure

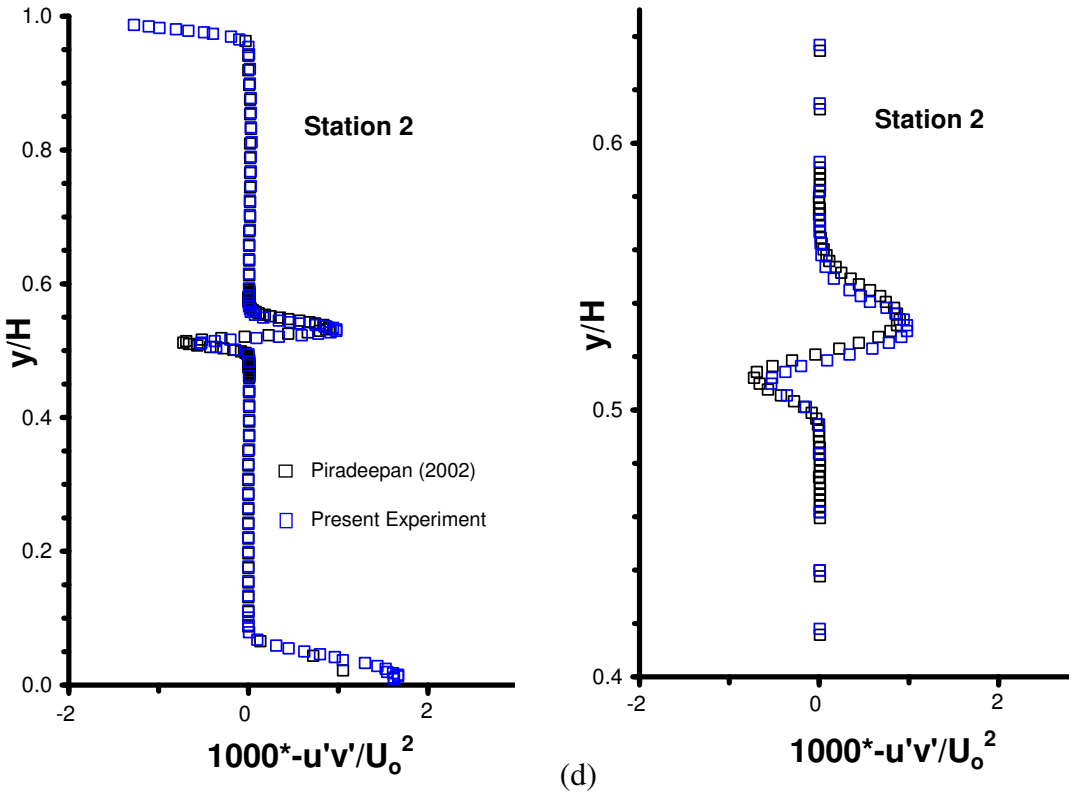

Figure 6.6: Profiles of mean velocity and turbulence quantities (z/H = 0.5) measured one chord length downstream of the airfoil trailing edge (station 2), displayed across the whole cross-section of the duct and in the wake: (a) mean streamwise velocity, (b) streamwise turbulence intensity, (c) normal turbulence intensity, (d) turbulence shear stress

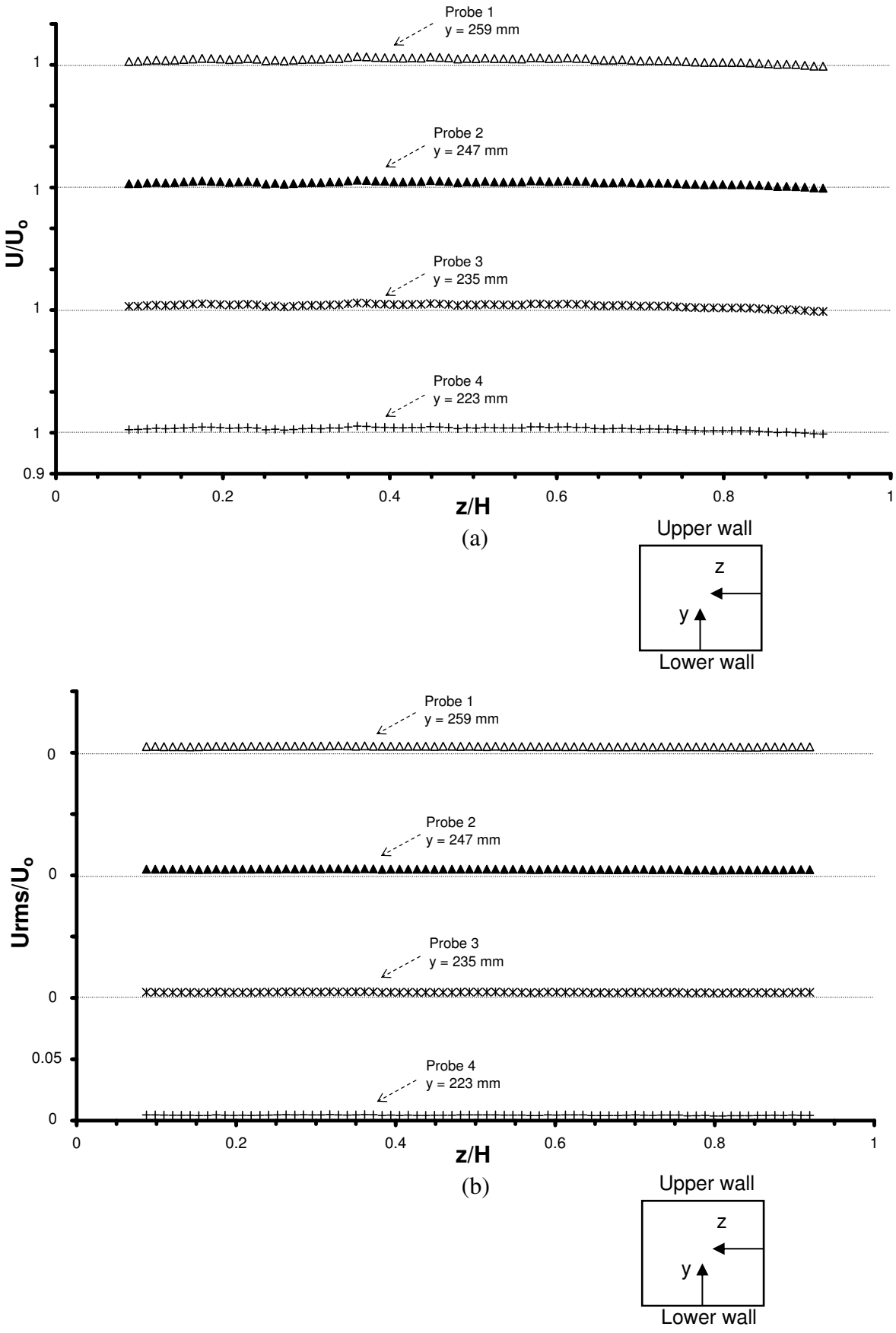

Figure 6.7: Rake measurement of mean streamwise velocity and turbulence intensity in the spanwise direction at station 1 (without the airfoil), for fixed normal distances: (a) mean velocity, (b) turbulence intensity.

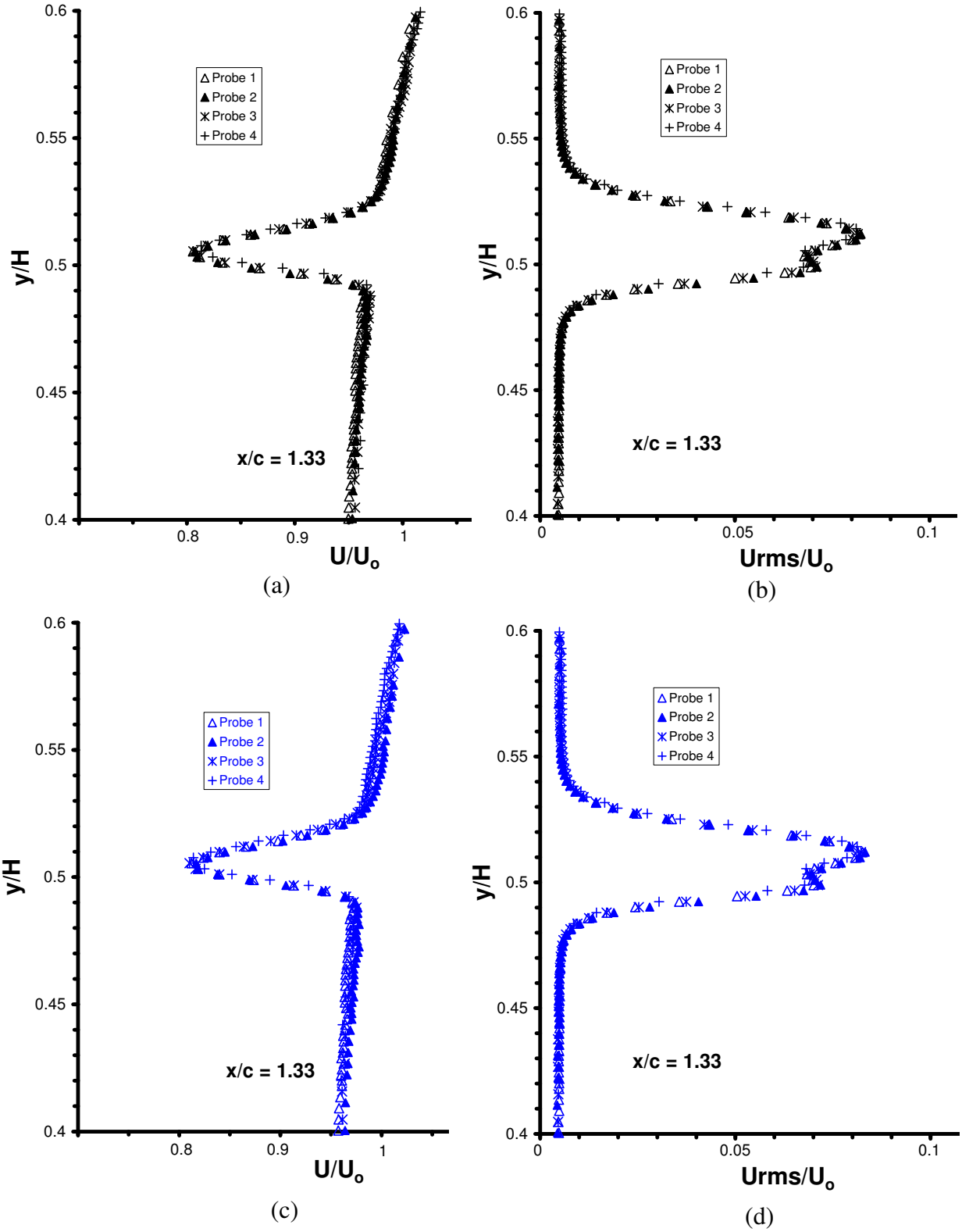

Figure 6.8: Rake measurements of mean velocity and turbulence in the wake at x/c = 1.33, taken at midspan (z/H = 0.5): (a) mean velocity, (b) turbulence intensity, (c) the effect of calibration on mean velocity, (d) the effect of calibration on turbulence intensity. Symbols in black are for calibration 1, and those in blue are for calibration 2.

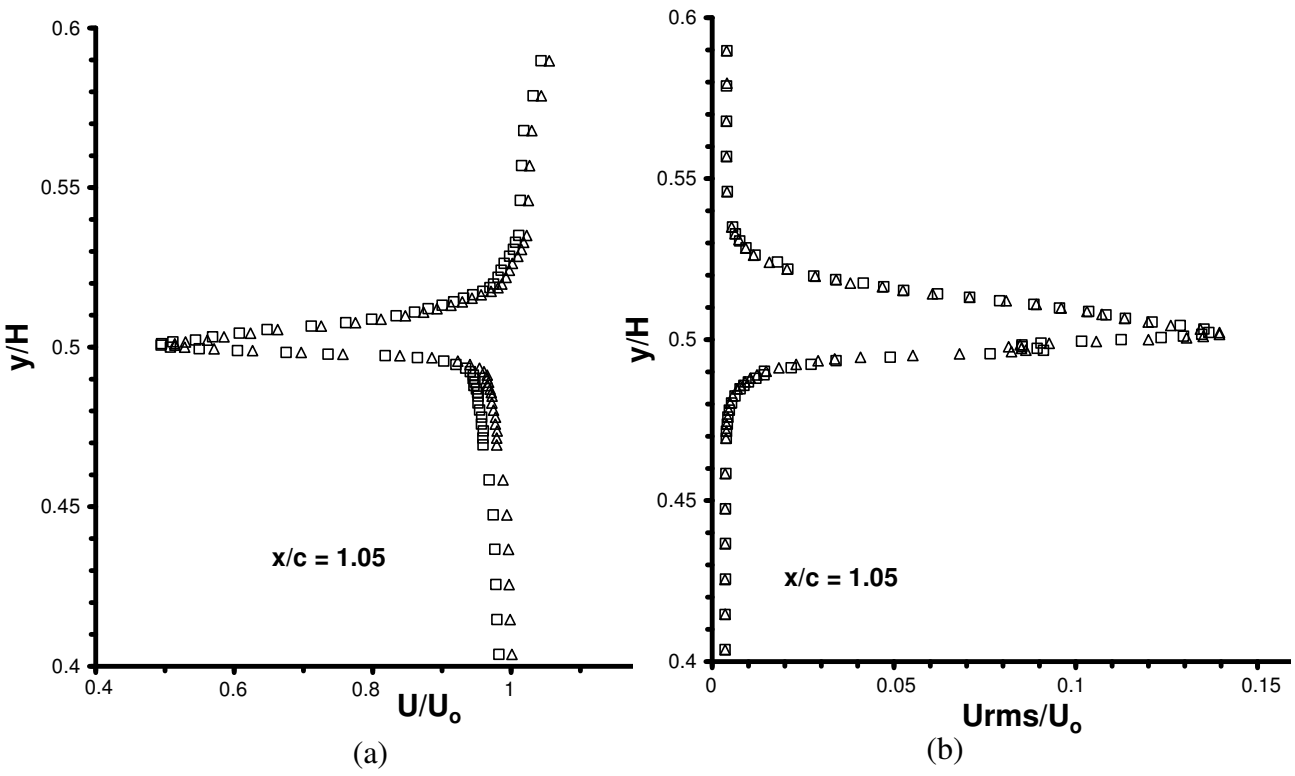

(a) (b)

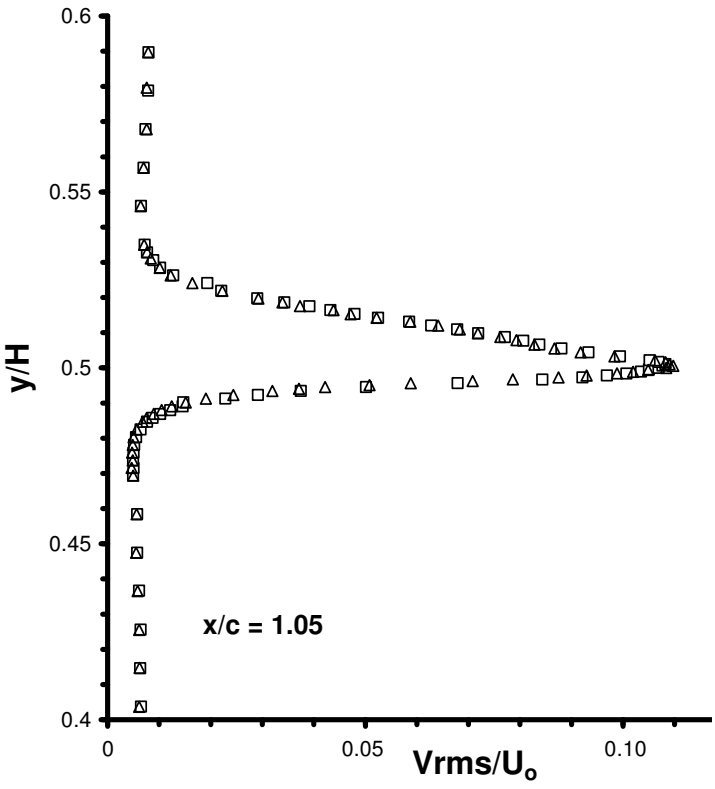

(c)

Figure 6.9: For caption see head of figure.

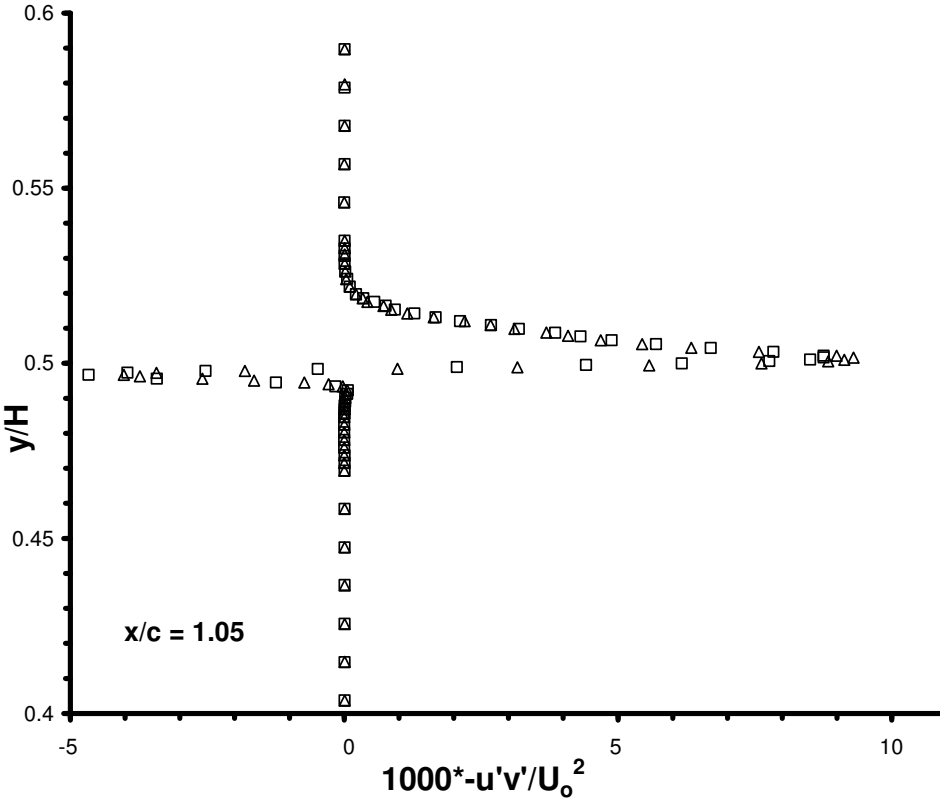

(d)

Figure 6.9: The effect of cross-wire probe calibration on the mean and turbulence quantities in the wake at x/c = 1.05: (a) mean streamwise velocity component, (b) streamwise turbulence intensity, (c) normal turbulence intensity, (d) turbulence shear stress.

Δ, calibration 1; □, calibration 2.

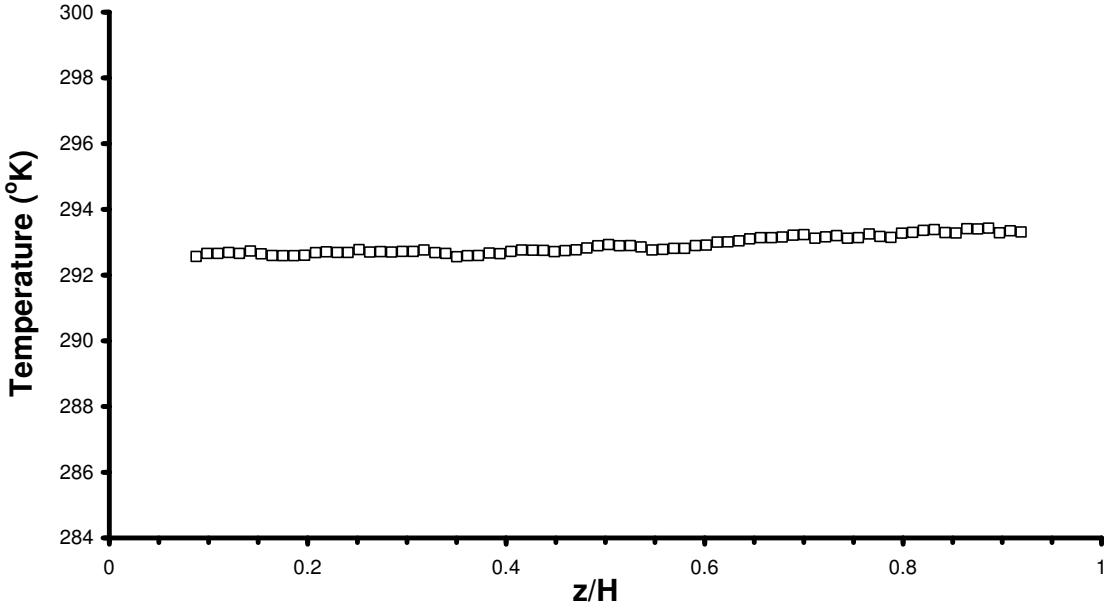

Figure 6.10: Variation of temperature with time during a typical experiment in the tunnel.

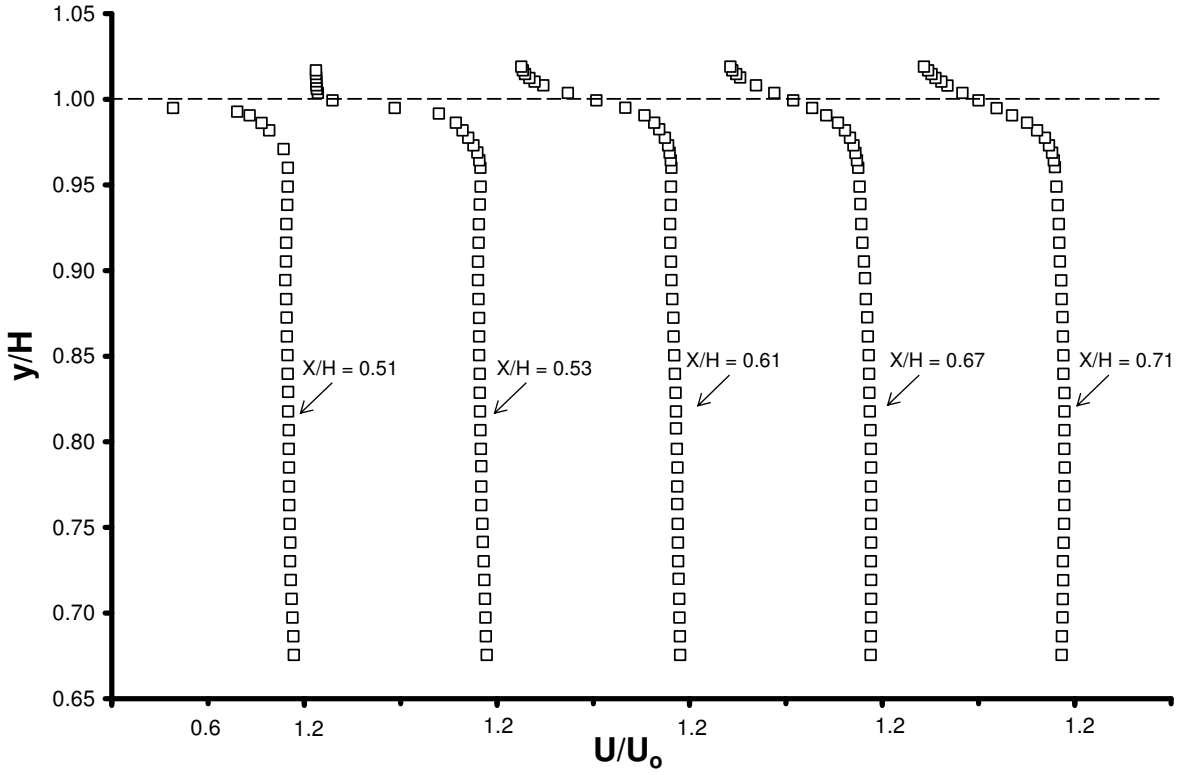

(a)

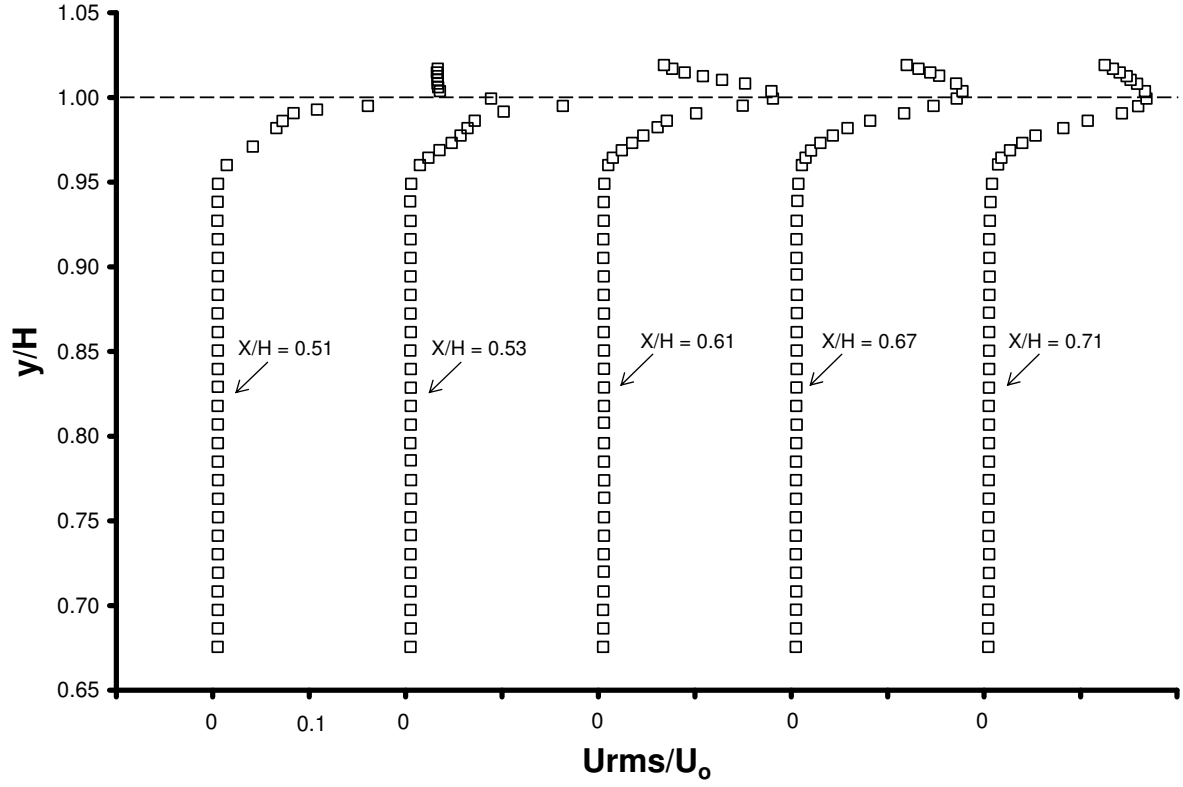

(b)

Figure 6.11: The effect of the upper wall tunnel cavity on the measured mean velocity and turbulence intensity at several streamwise locations in the cavity as measured by a single-wire probe: (a) mean velocity, (b) turbulence intensity.

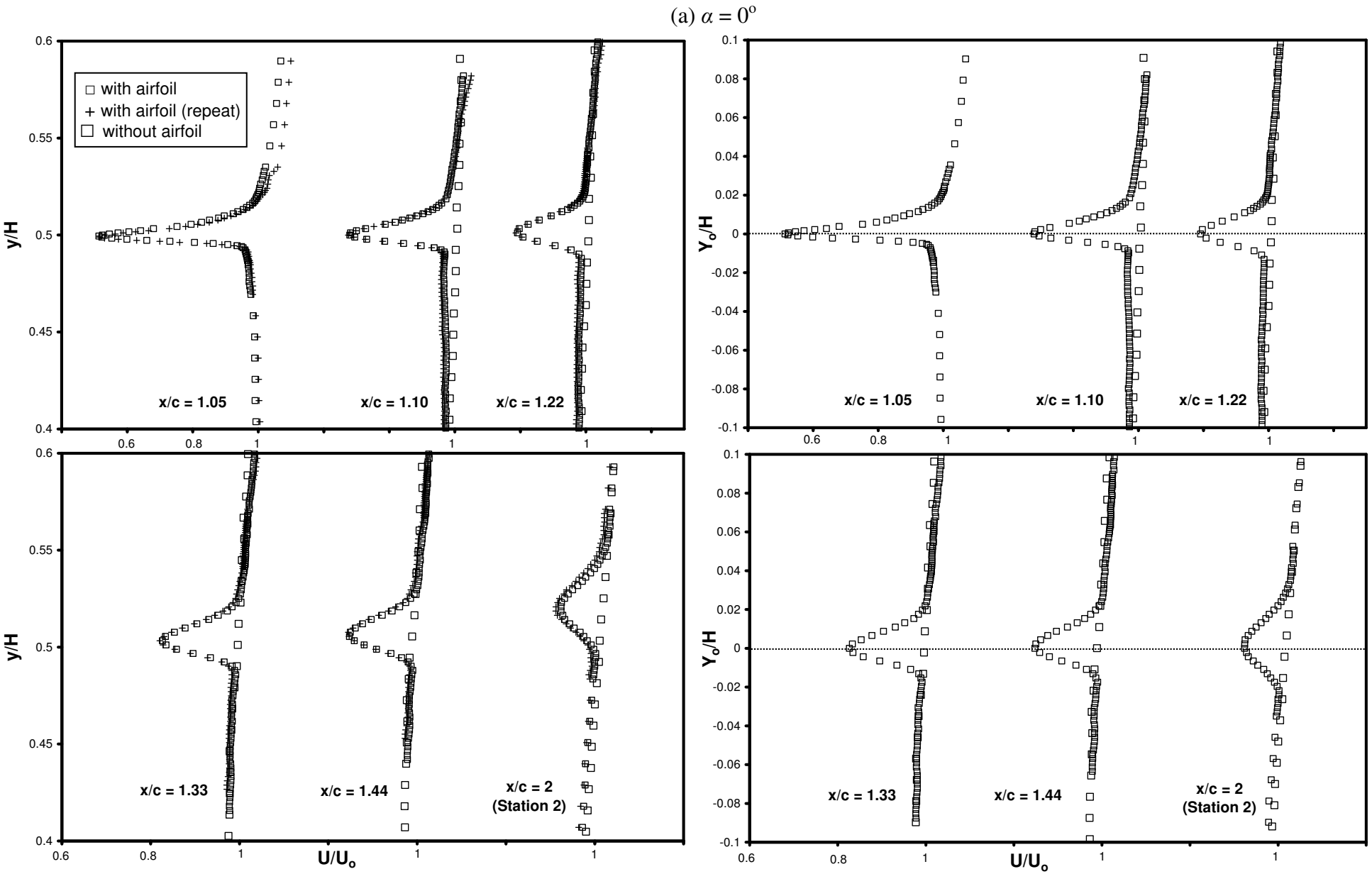

Figure 6.12: For caption see head of figure.

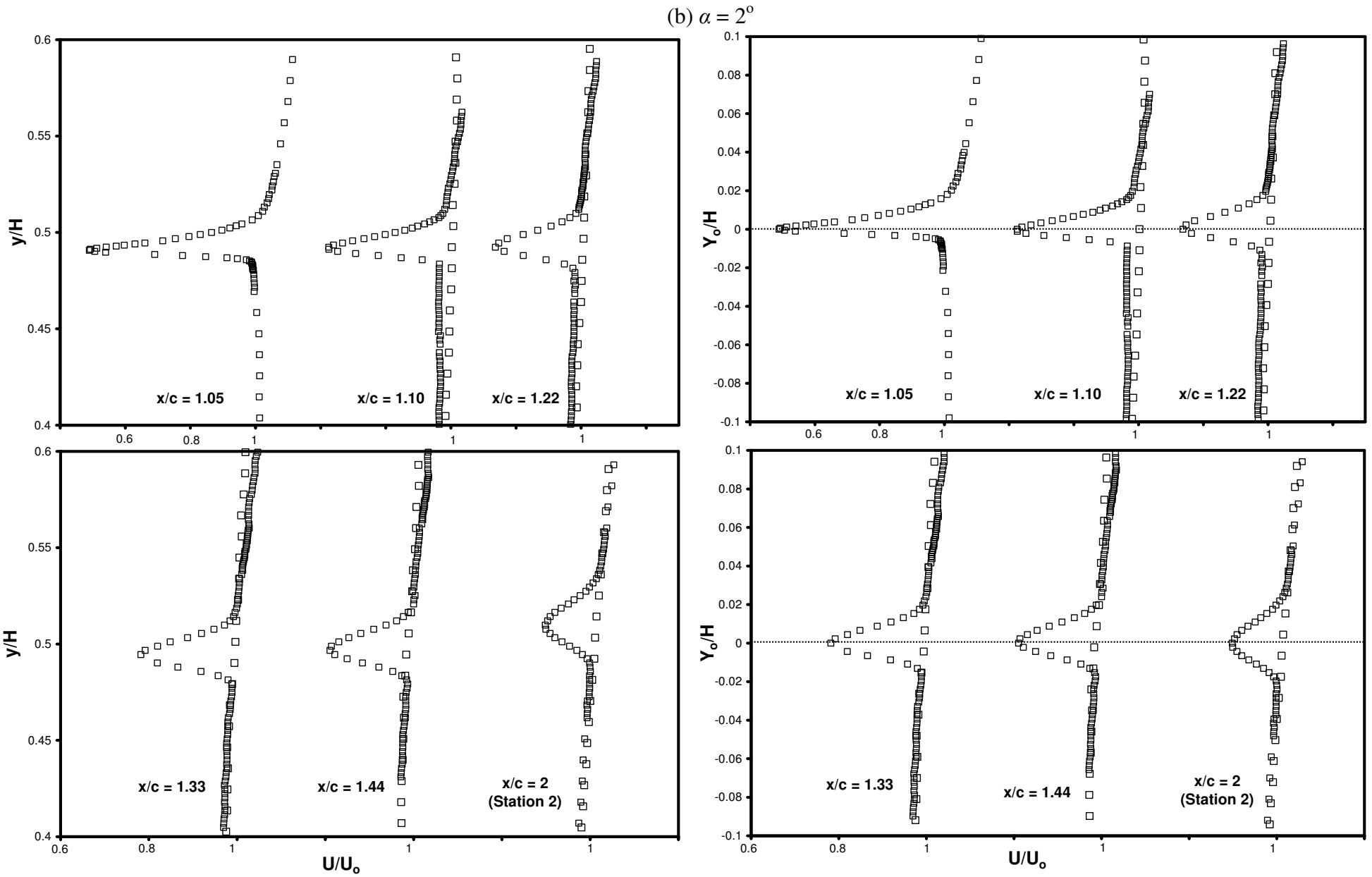

Figure 6.12: For caption see head of figure.

(c) $\alpha = 4^{o}$

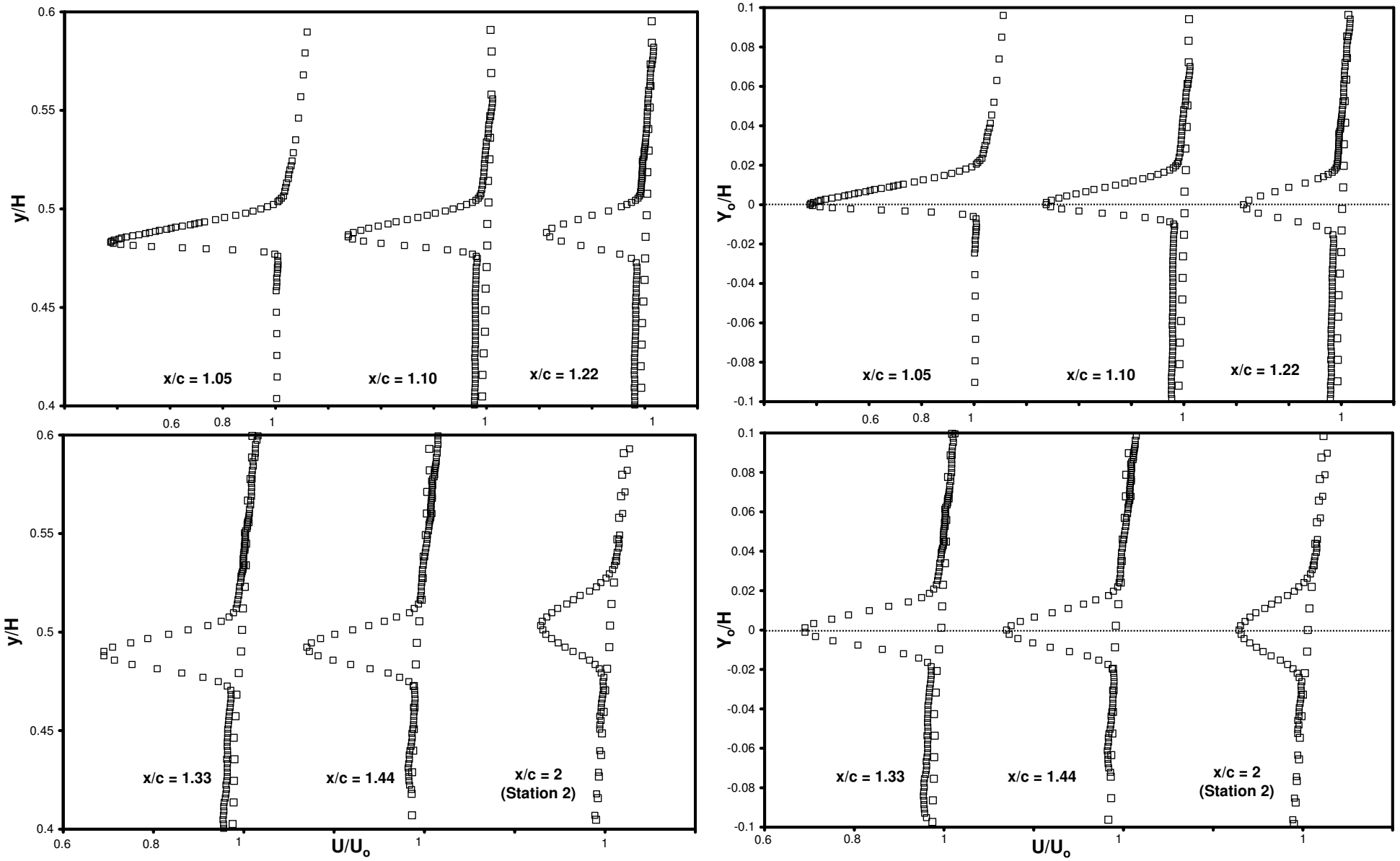

Figure 6.12: For caption see head of figure.

(d) $\alpha = 6^o$

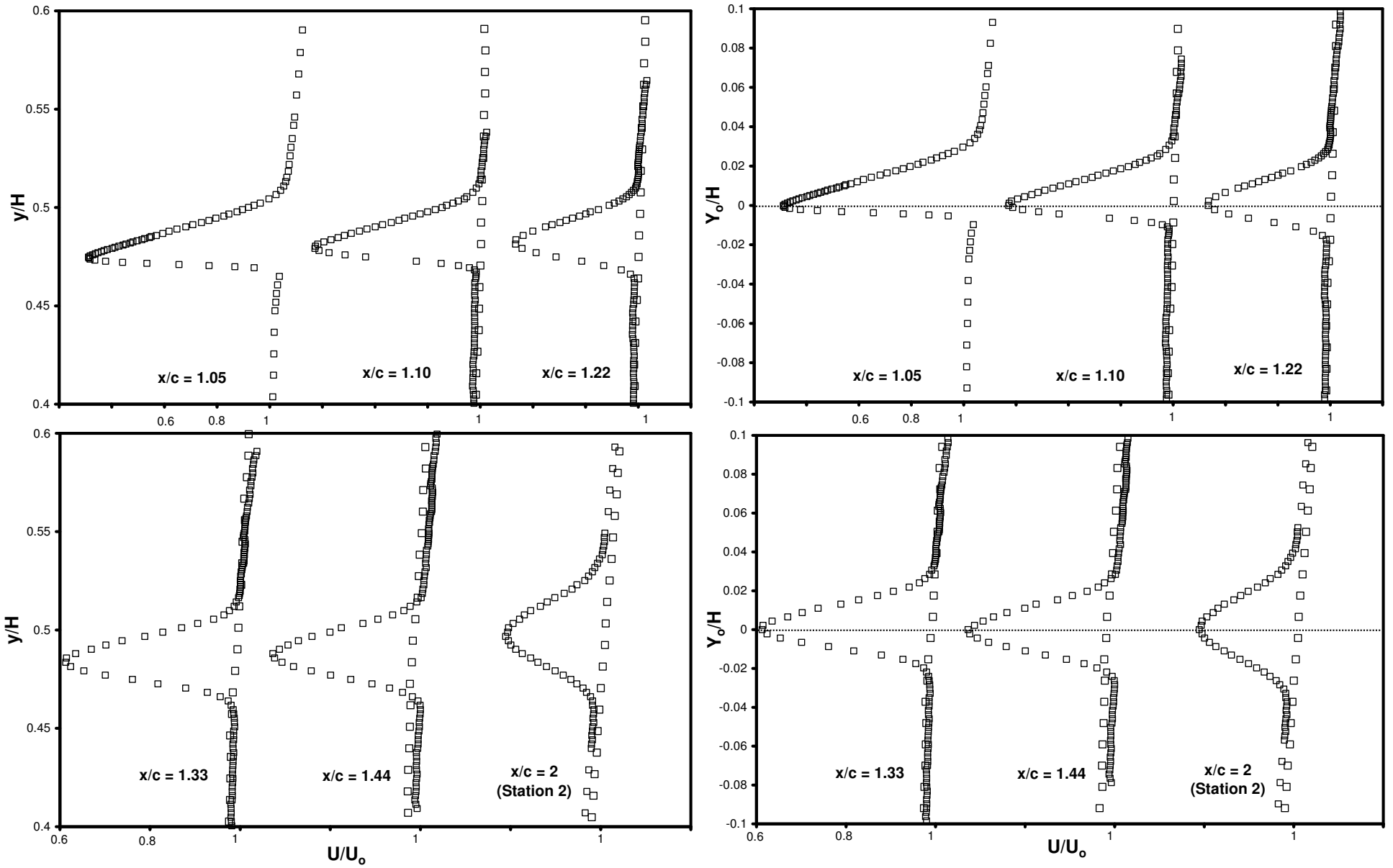

Figure 6.12: For caption see head of figure.

(e) $\alpha = -2^{o}$

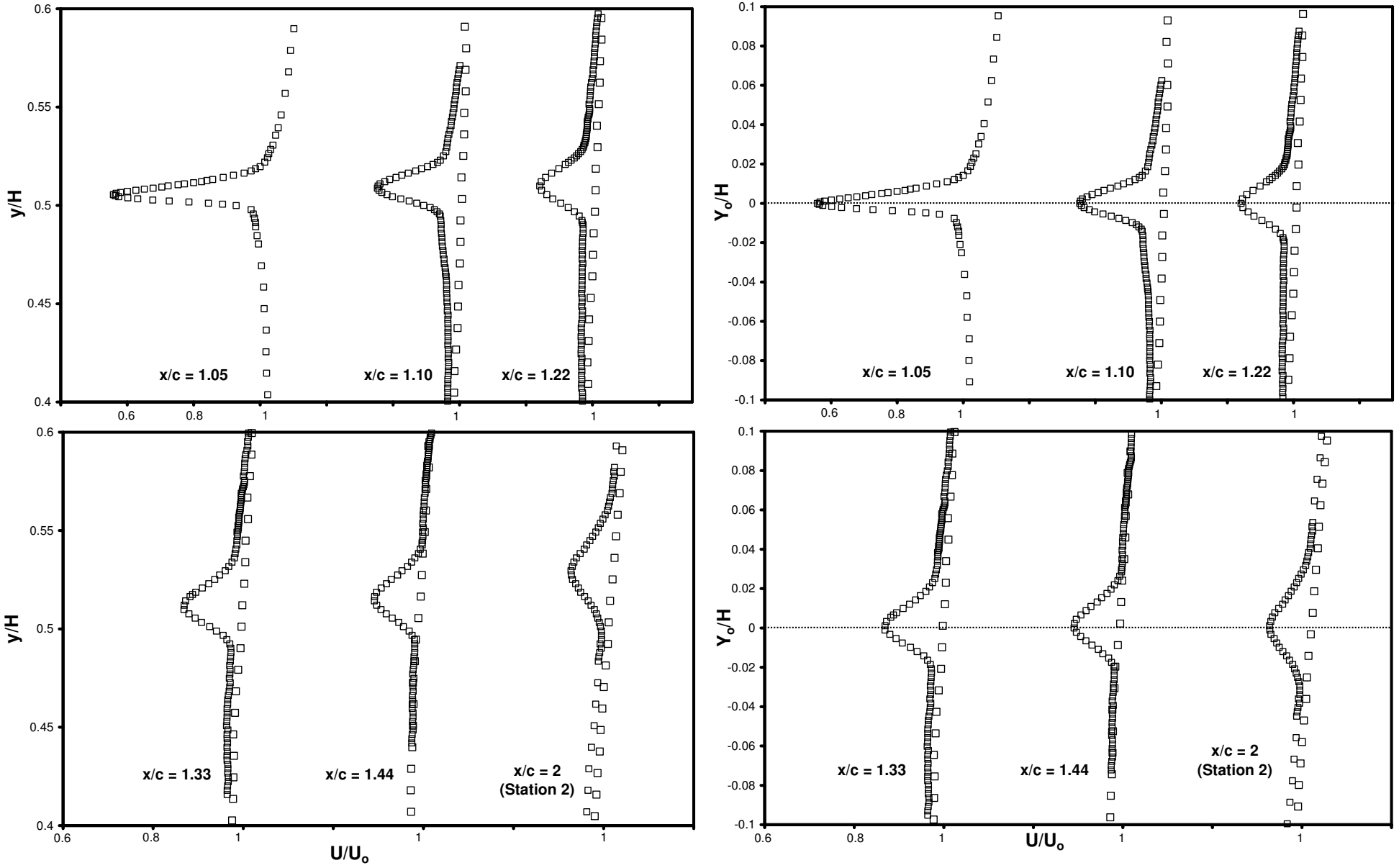

Figure 6.12: For caption see head of figure.

(f) $\alpha = -4^{o}$

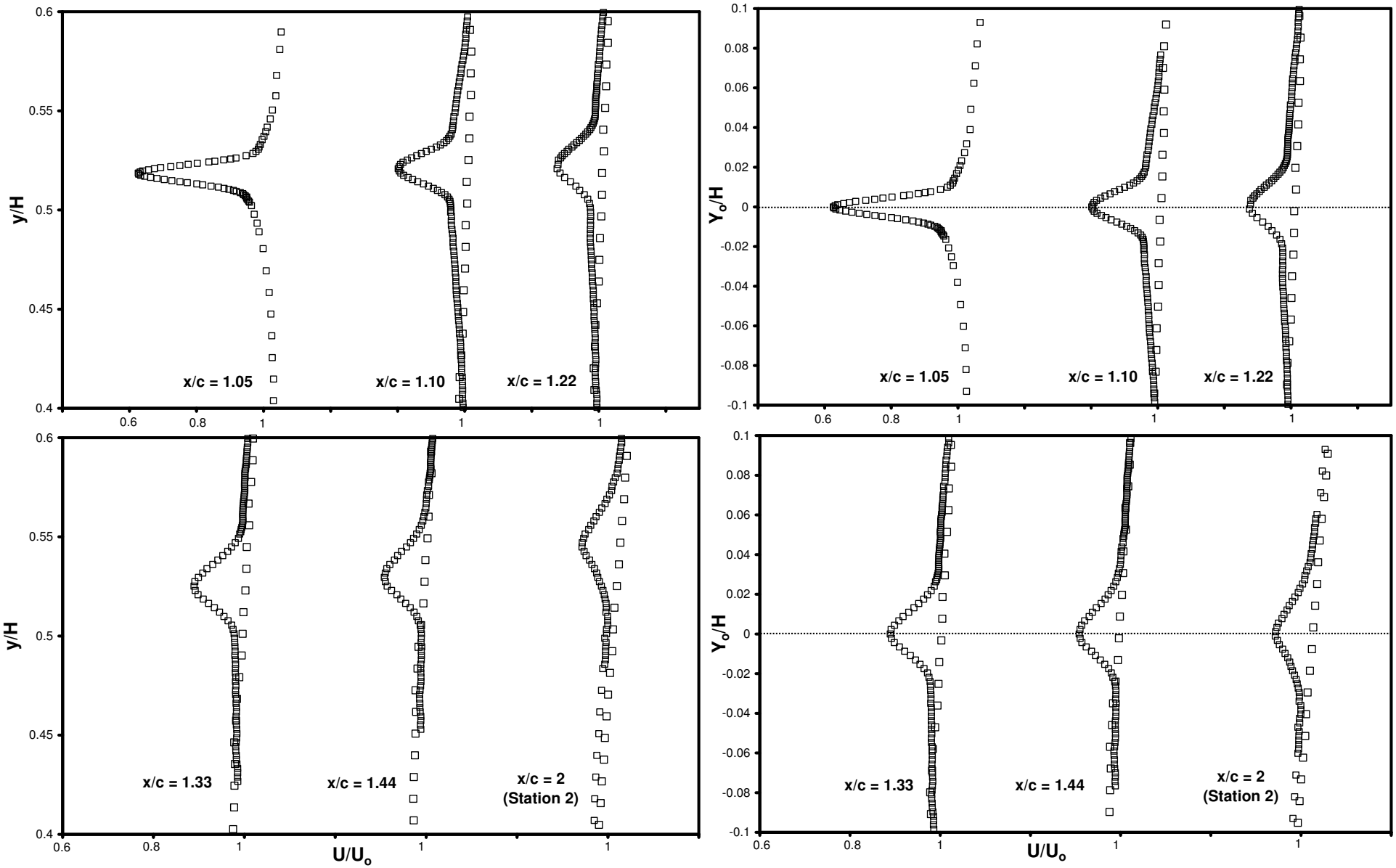

Figure 6.12: For caption see head of figure.

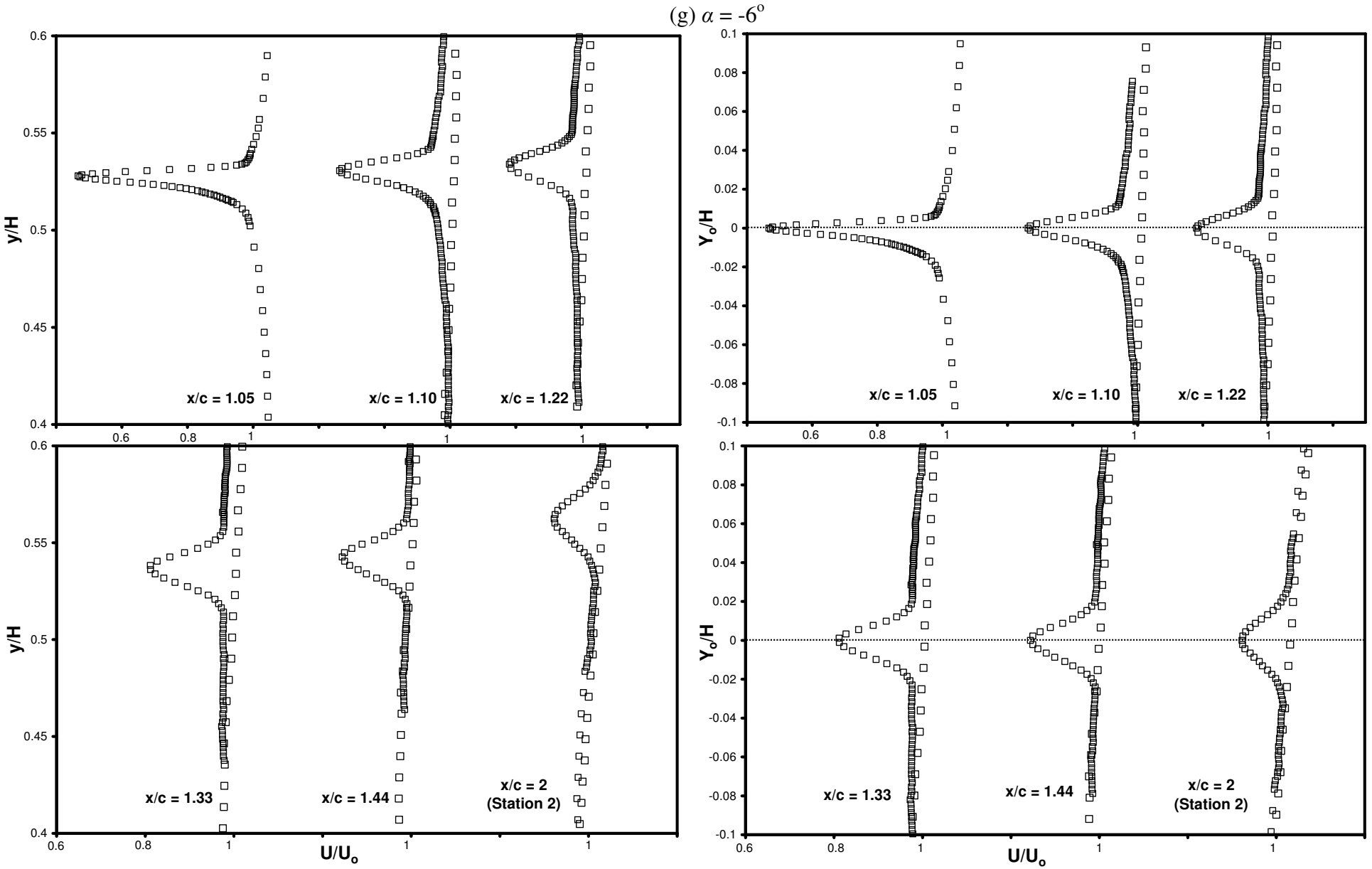

Figure 6.12: Profiles of mean streamwise velocity in the near-wake in the normal direction ($z/H = 0.5$) as measured by a cross-wire at $x/c = 1.05$, 2; the other locations were measured using a single-wire: (a) $\alpha = 0^o$, (b) $\alpha = 2^o$, (c) $\alpha = 4^o$, (d) $\alpha = 6^o$, (e) $\alpha = -2^o$, (f) $\alpha = -4^o$, (g) $\alpha = -6^o$. For each angle the profiles on the right are aligned with respect to the wake centre line.

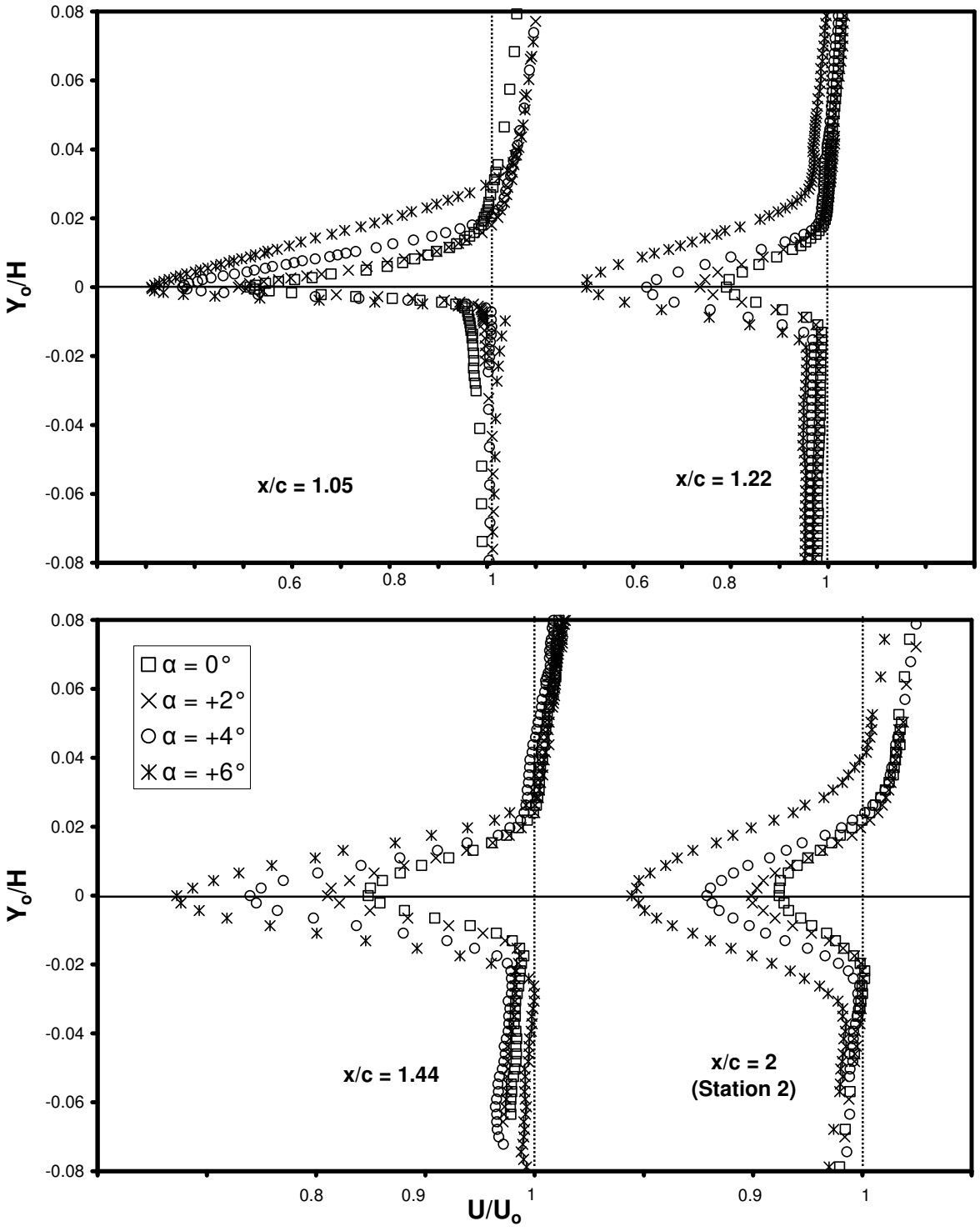

(a)

Figure 6.13: For caption see head of figure.

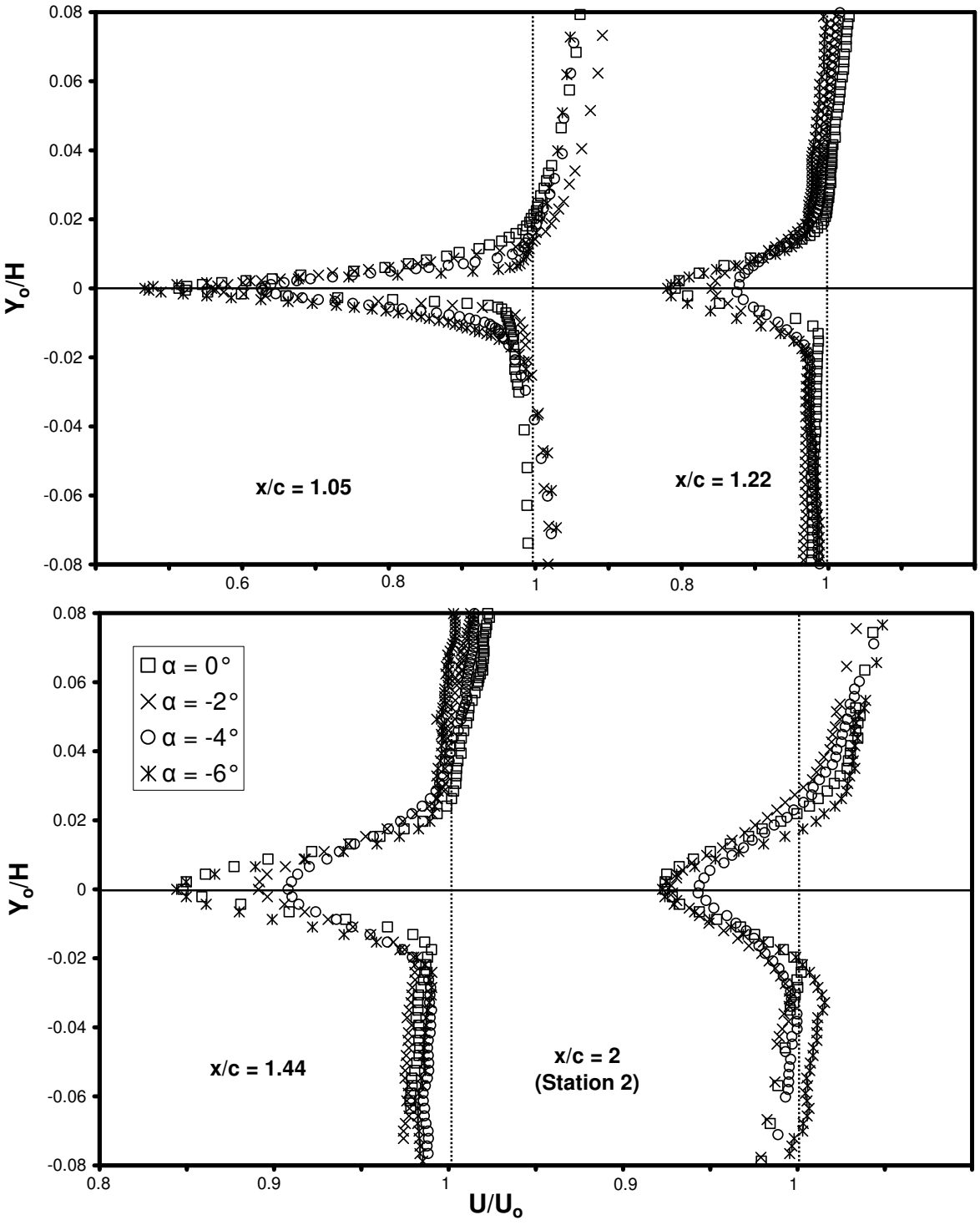

(b)

Figure 6.13: Profiles of mean streamwise velocity in the near-wake measured in the normal direction (z/H = 0.5), aligned with the wake centre line for different angles of attack, as measured by a cross-wire at x/c = 1.05, 2; the other locations were measured using a single-wire: (a) $\alpha = 0^o$, $+2^o$, $+4^o$, $+6^o$, (b) $\alpha = 0^0$, -2^o, -4^o, -6^o.

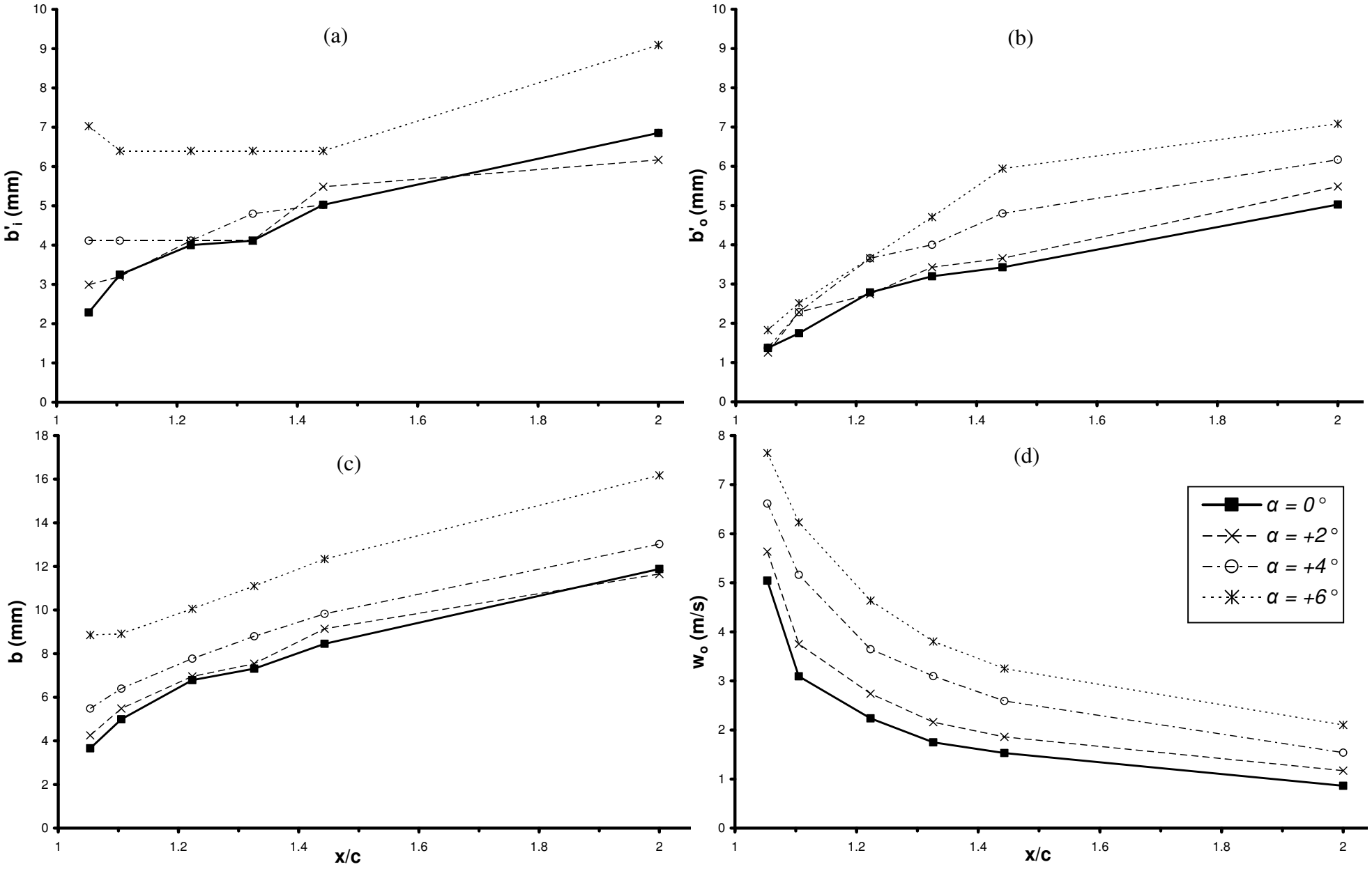

Figure 6.14: For caption see head of figure.

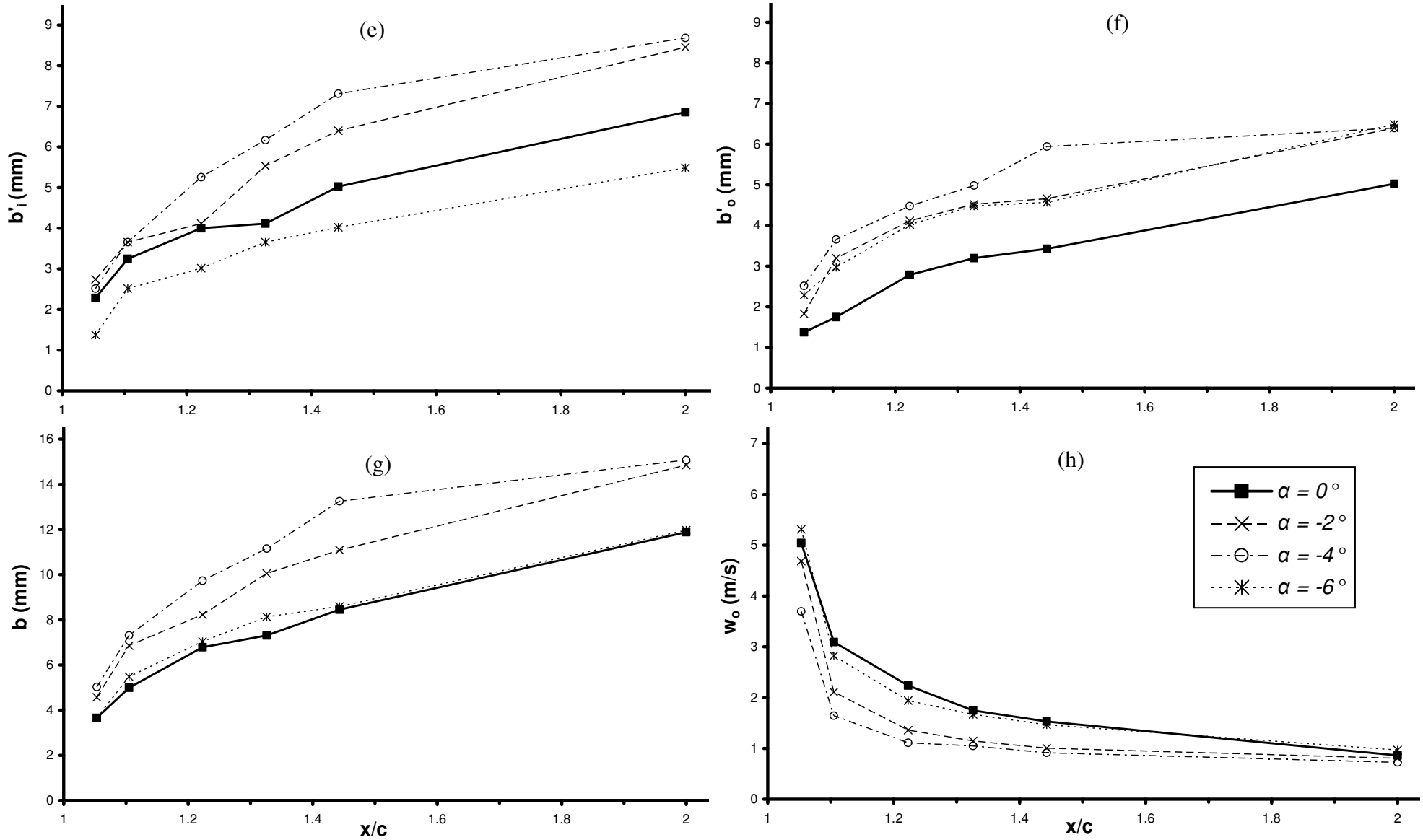

Figure 6.14: Profiles of wake parameters at station 2: for positive angle of attack $\alpha = 0^o$, $+2^o$, $+4^o$, $+6^o$ (a) wake half-width on the inner side, (b) wake half-width on the outer side, (c) total wake half-width, (d) maximum velocity defect; for negative angle of attack $\alpha = 0^o$, -2^o,-4^o, -6^o (e) wake half-width on the inner side, (f) wake half-width on the outer side, (g) total wake half-width, (h) maximum velocity defect.

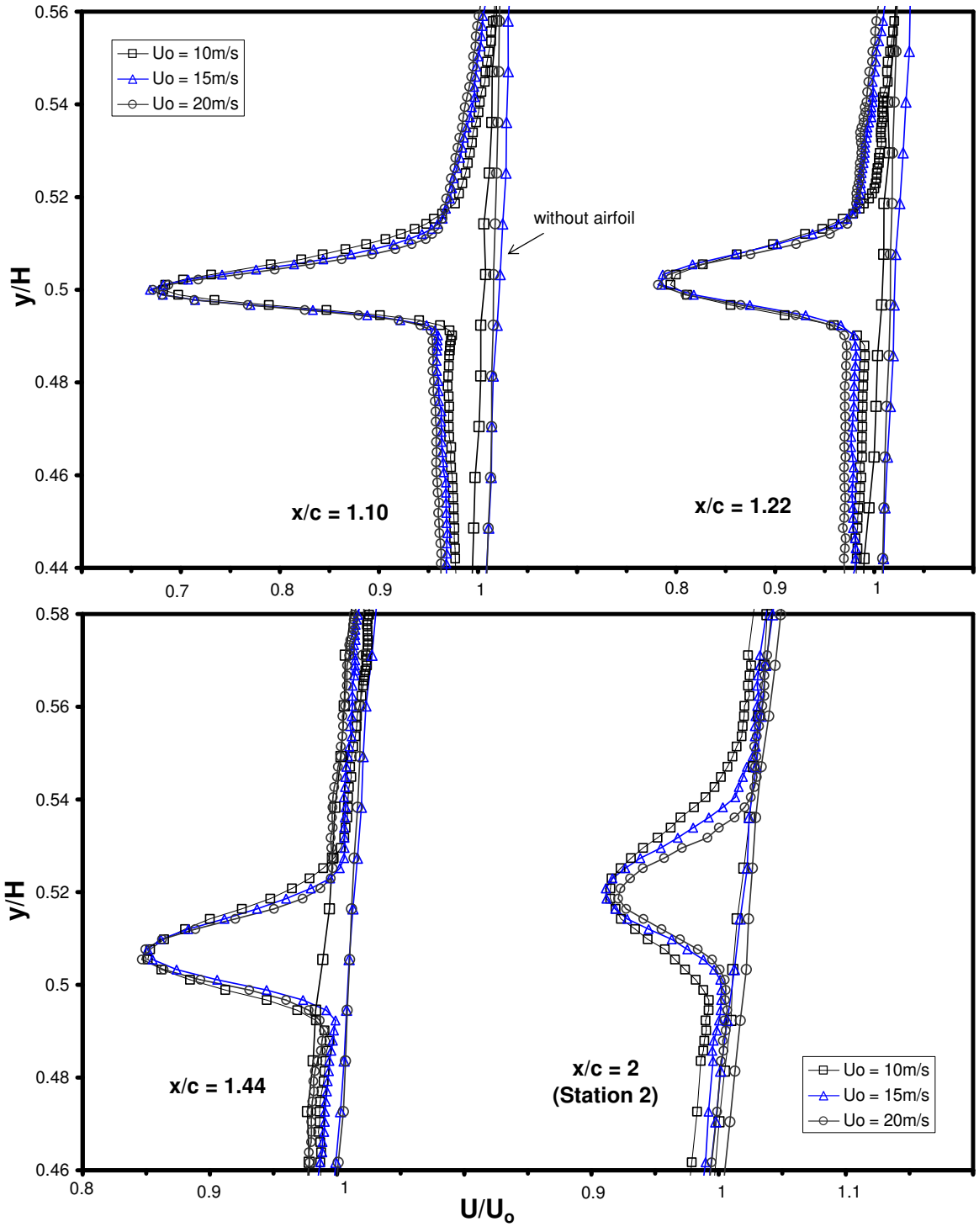

(a)

Figure 6.15: For caption see head of figure.

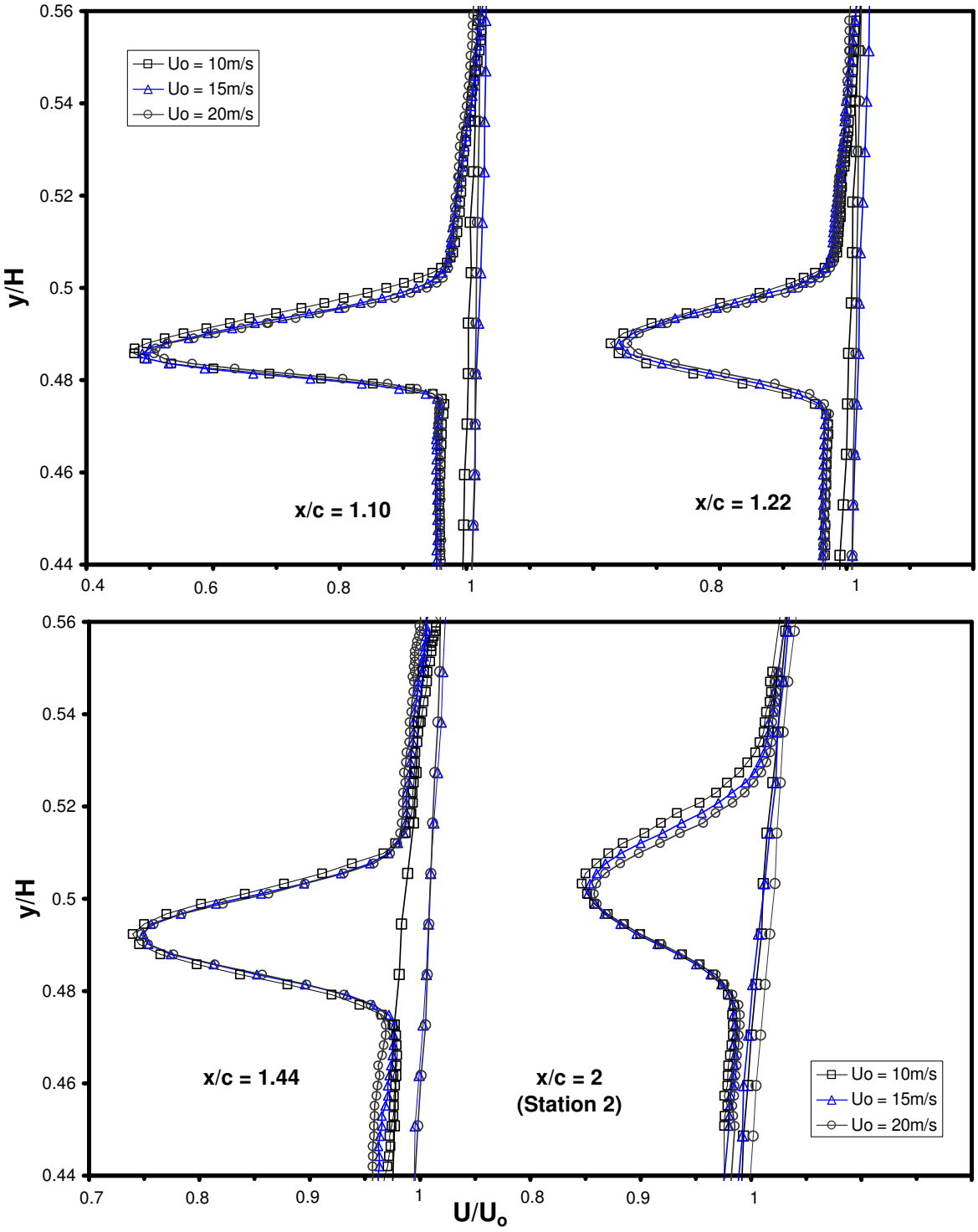

(b)

Figure 6.15: The effect of mainstream velocity on the mean streamwise velocity measured in the near-wake region ($z/H = 0.5$) as measured by a cross-wire at $x/c = 1.05, 2$; the other locations were measured using a single-wire: (a) $\alpha = 0^o$, (b) $\alpha = +4^o$.

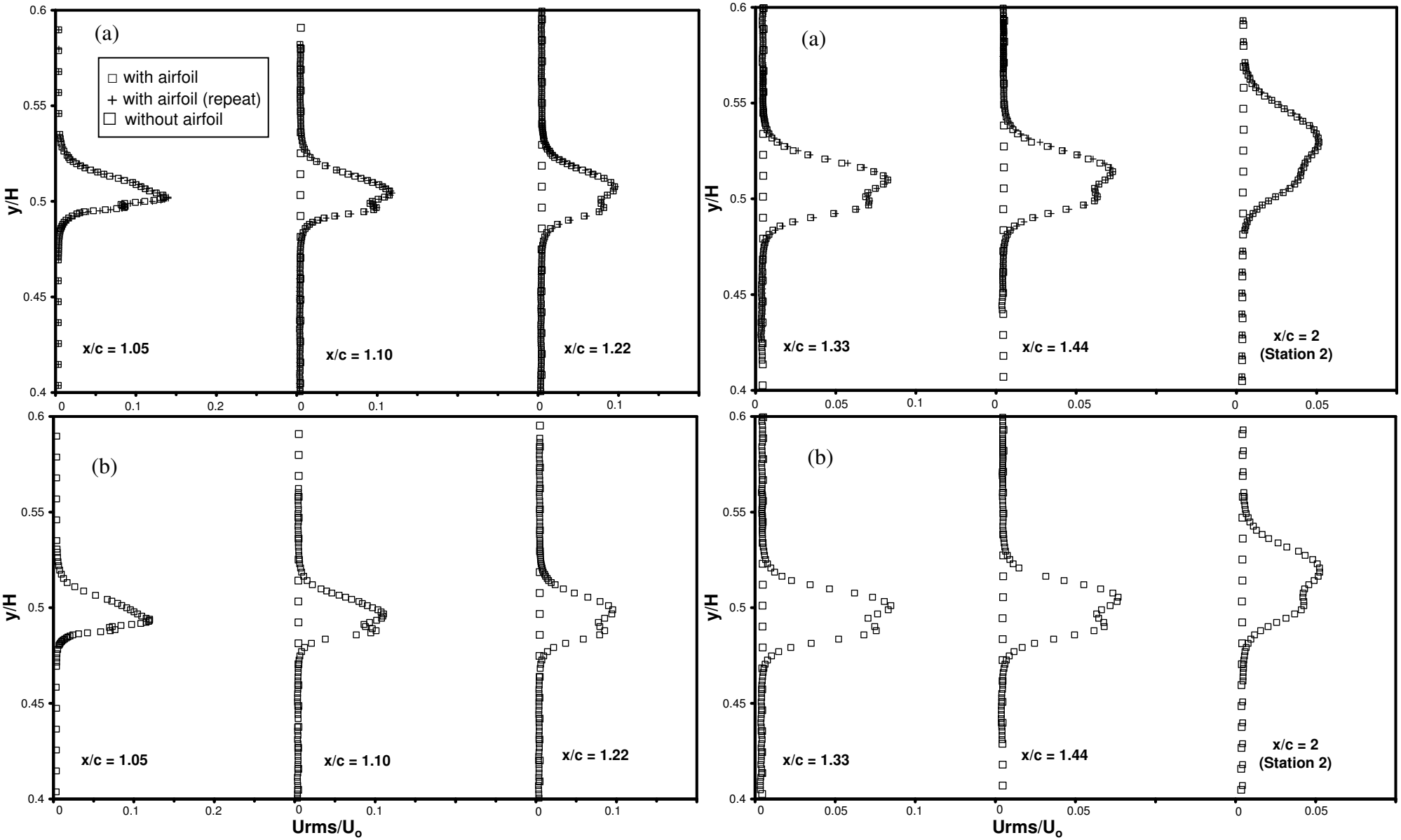

Figure 6.16: For caption see head of figure.

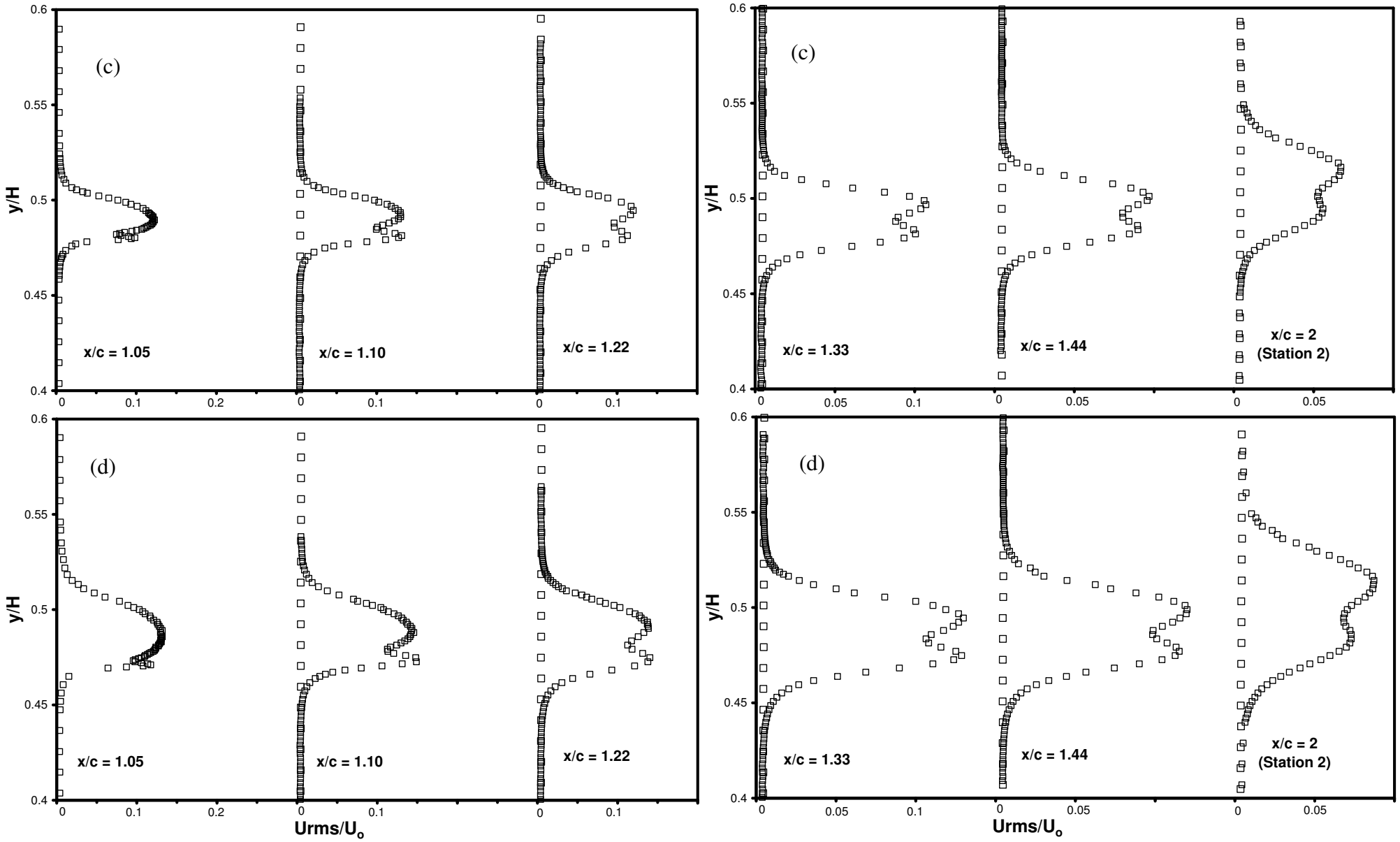

Figure 6.16: For caption see head of figure.

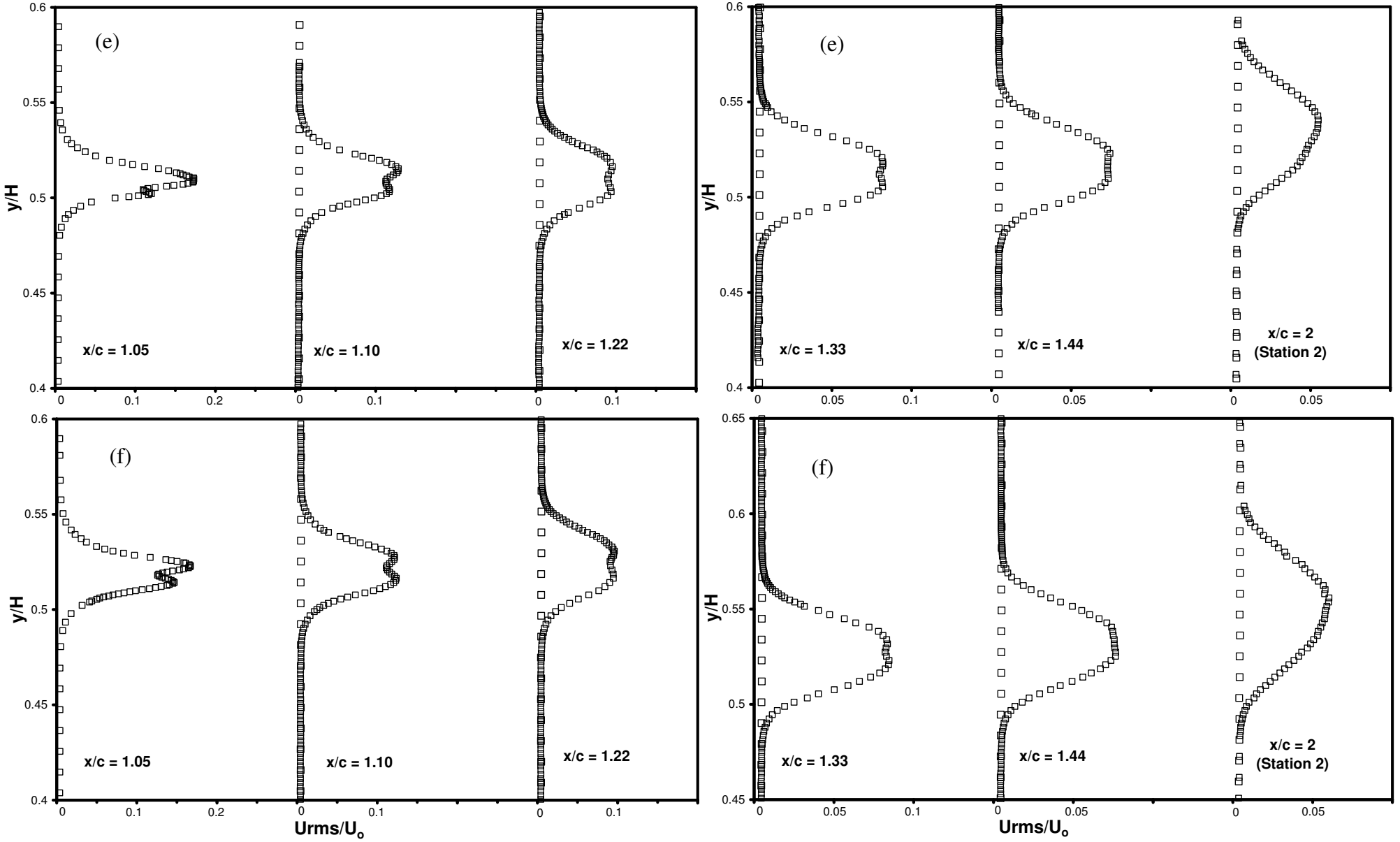

Figure 6.16: For caption see head of figure.

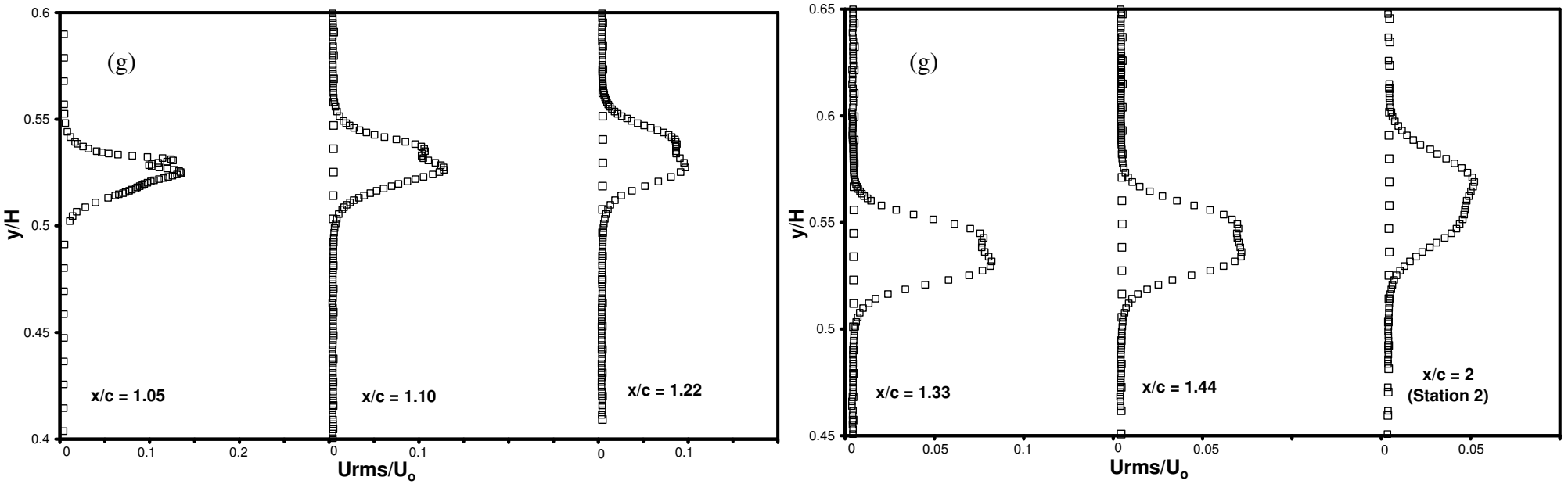

Figure 6.16: Profiles of streamwise turbulence intensity in the near-wake measured in the normal direction ($z/H = 0.5$) as measured by a cross-wire at $x/c = 1.05, 2$; the other locations were measured using a single-wire: (a) $\alpha = 0^o$, (b) $\alpha = 2^o$, (c) $\alpha = 4^o$, (d) $\alpha = 6^o$, (e) $\alpha = -2^o$, (f) $\alpha = -4^o$, (g) $\alpha = -6^o$.

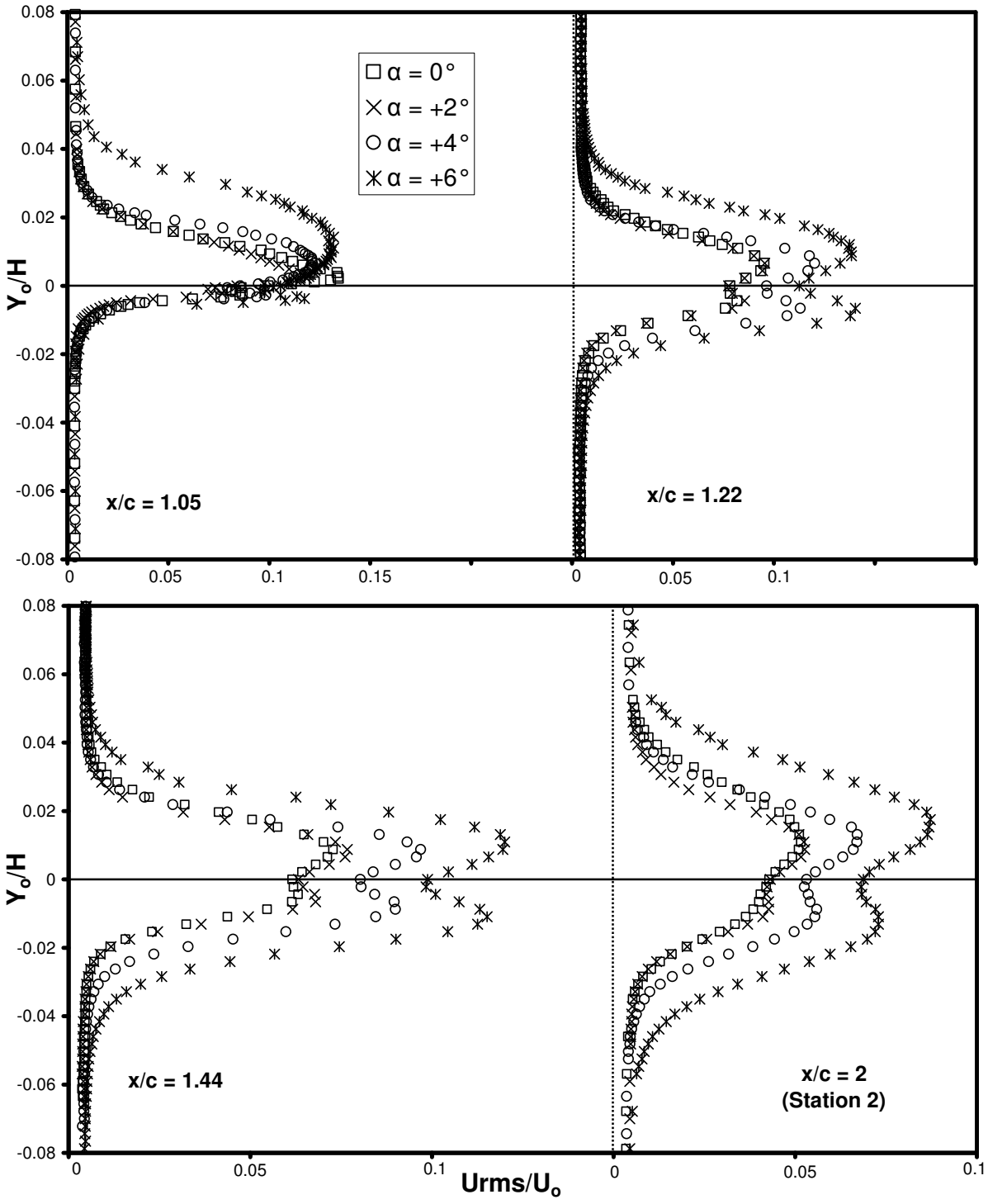

(a)

Figure 6.17: For caption see head of figure.

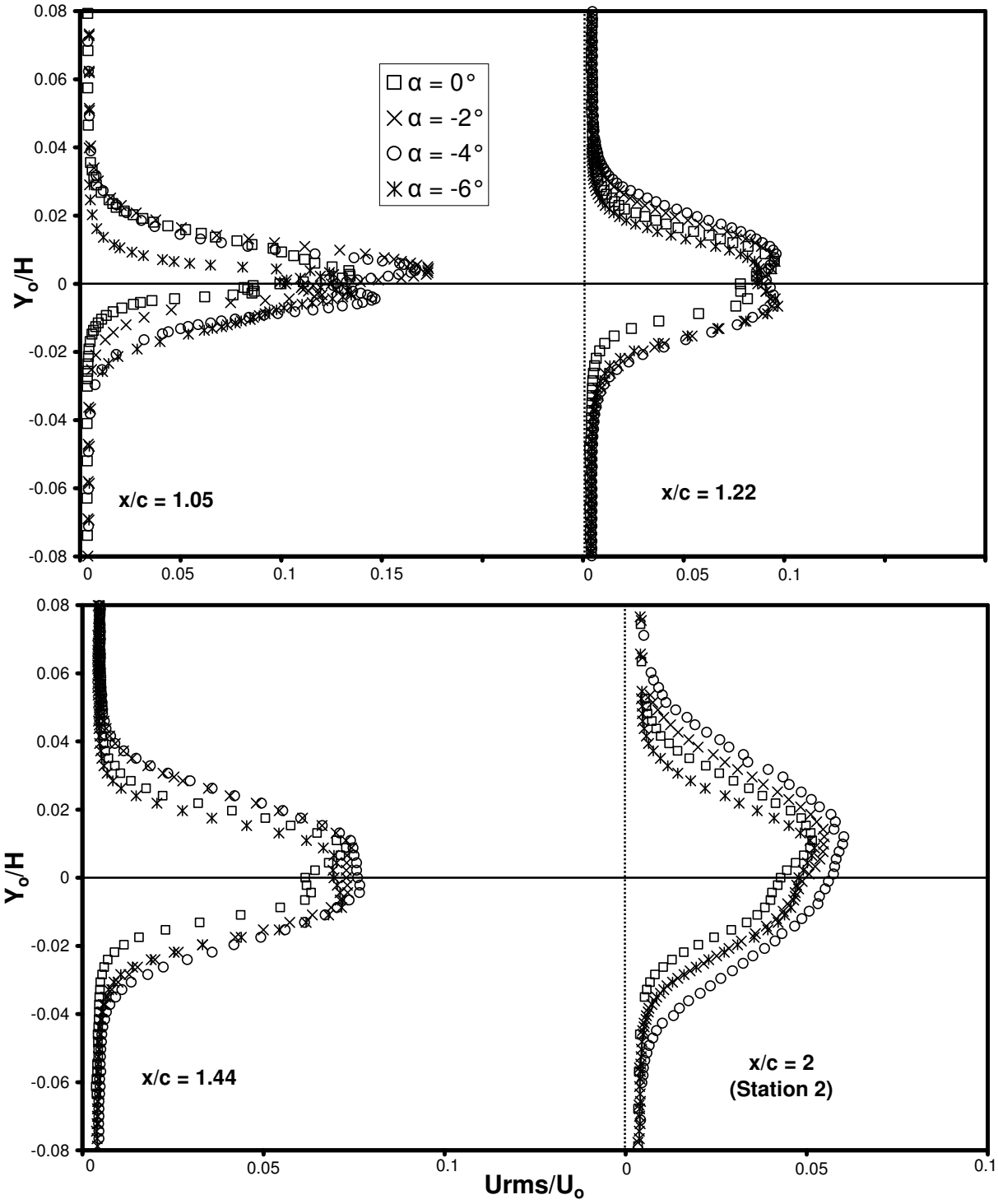

(b)

Figure 6.17: Profiles of streamwise turbulence intensity in the near-wake measured in the normal direction ($z/H = 0.5$), aligned with the wake centre line, as measured by a cross-wire at $x/c = 1.05, 2$; the other locations were measured using a single-wire: (a) $\alpha = 0^o, +2^o, +4^o, +6^o$, (b) $\alpha = 0^0, -2^o, -4^o, -6^o$.

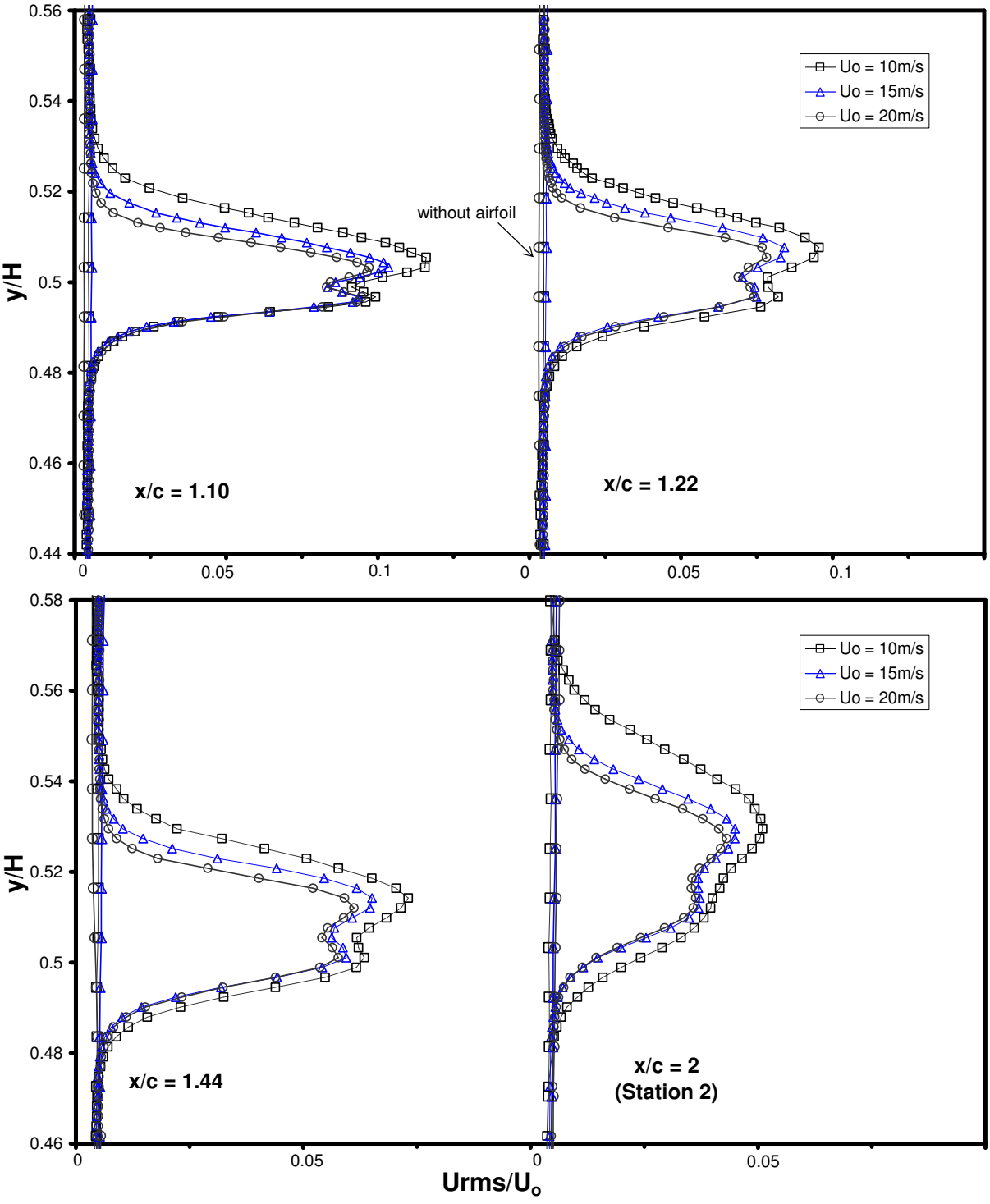

(a)

Figure 6.18: For caption see head of figure.

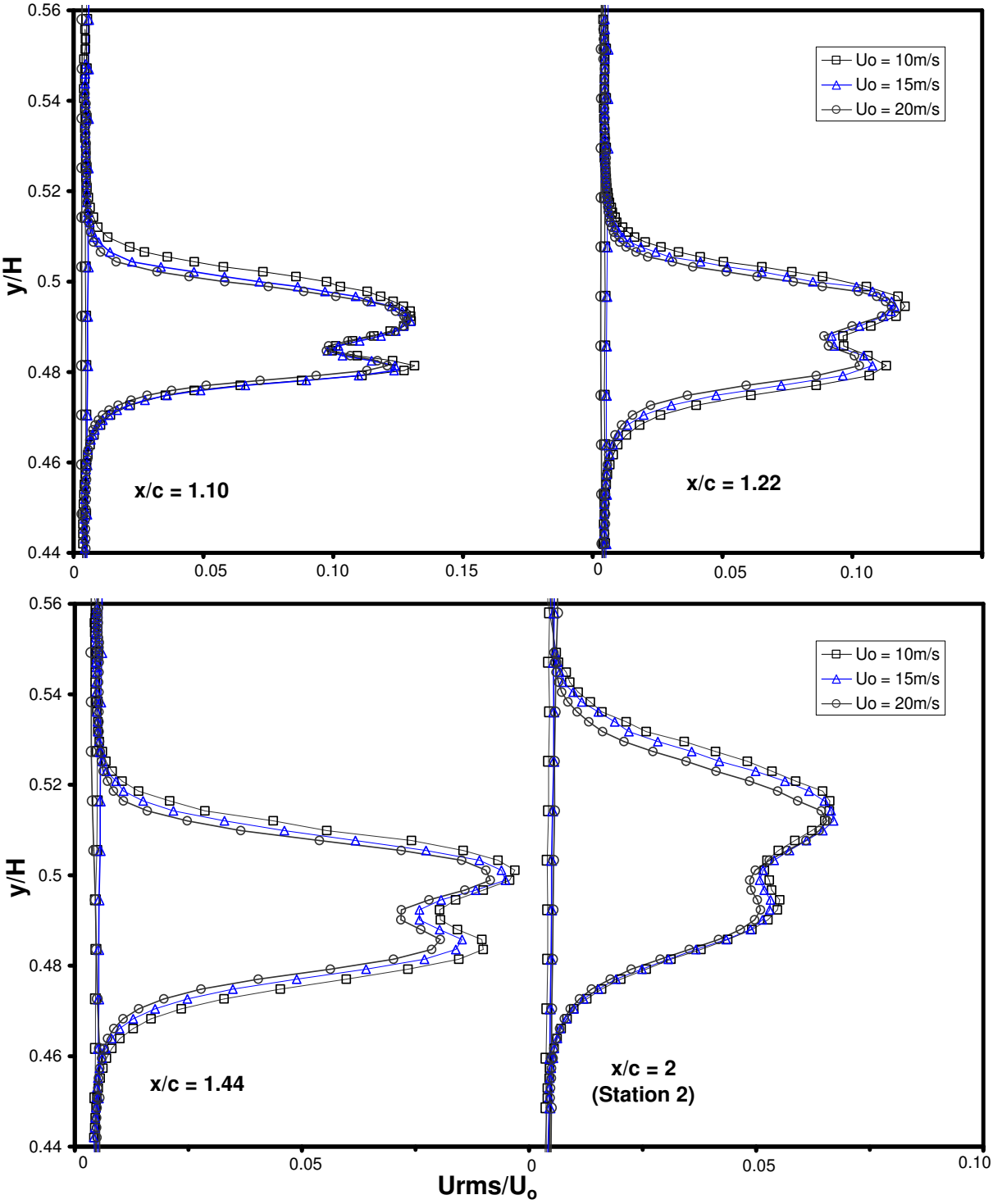

(b)

Figure 6.18: The effect of mainstream velocity on turbulence intensity in the near-wake region ($z/H = 0.5$) as measured by a cross-wire at $x/c = 1.05, 2$; the other locations were measured using a single-wire: (a) $\alpha = 0^o$, (b) $\alpha = +4^o$.

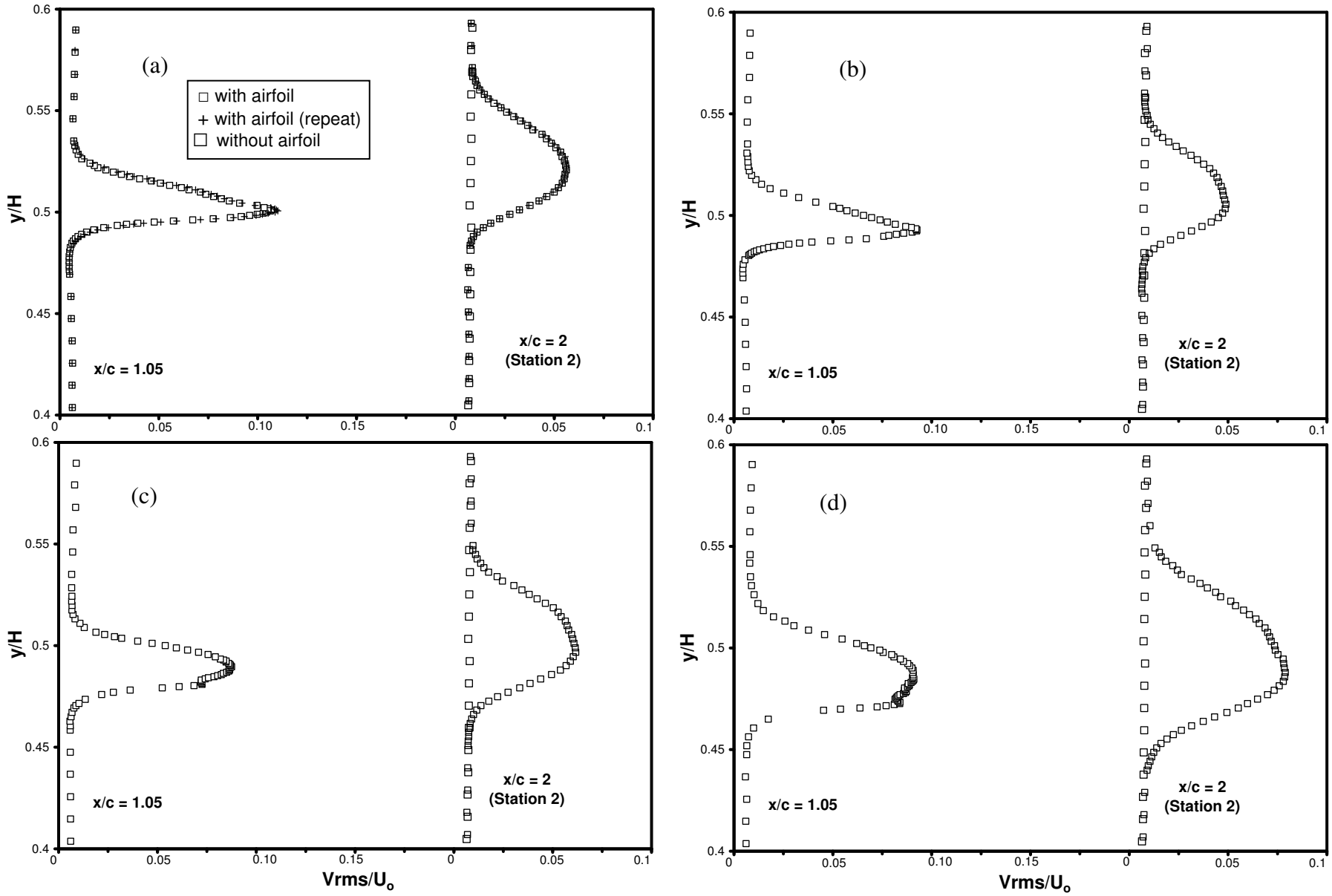

Figure 6.19: For caption see head of figure.

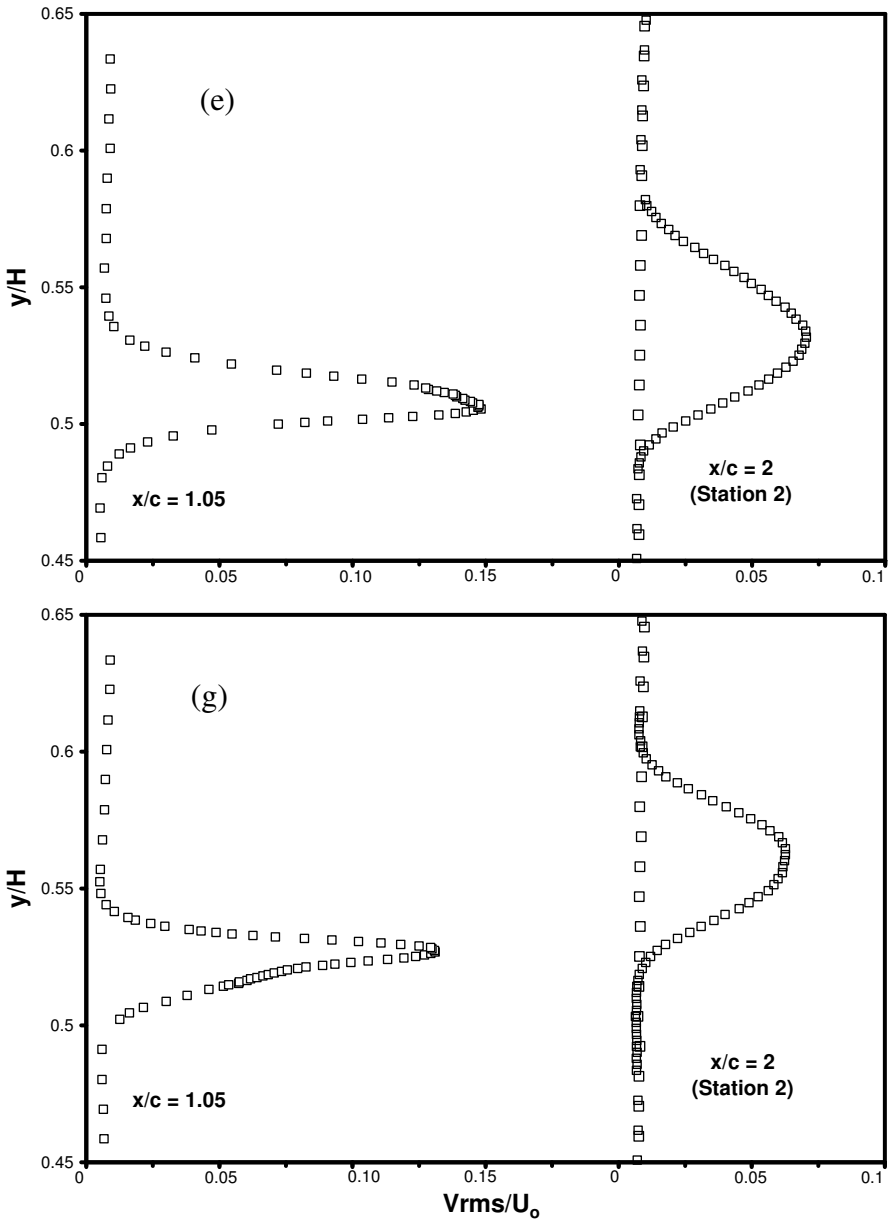

Figure 6.19: Profiles of normal turbulence intensity in the near-wake measured in the normal direction ($z/H = 0.5$): (a) $\alpha = 0^o$, (b) $\alpha = 2^o$, (c) $\alpha = 4^o$, (d) $\alpha = 6^o$, (e) $\alpha = -2^o$, (f) $\alpha = -4^o$, (g) $\alpha = -6^o$.

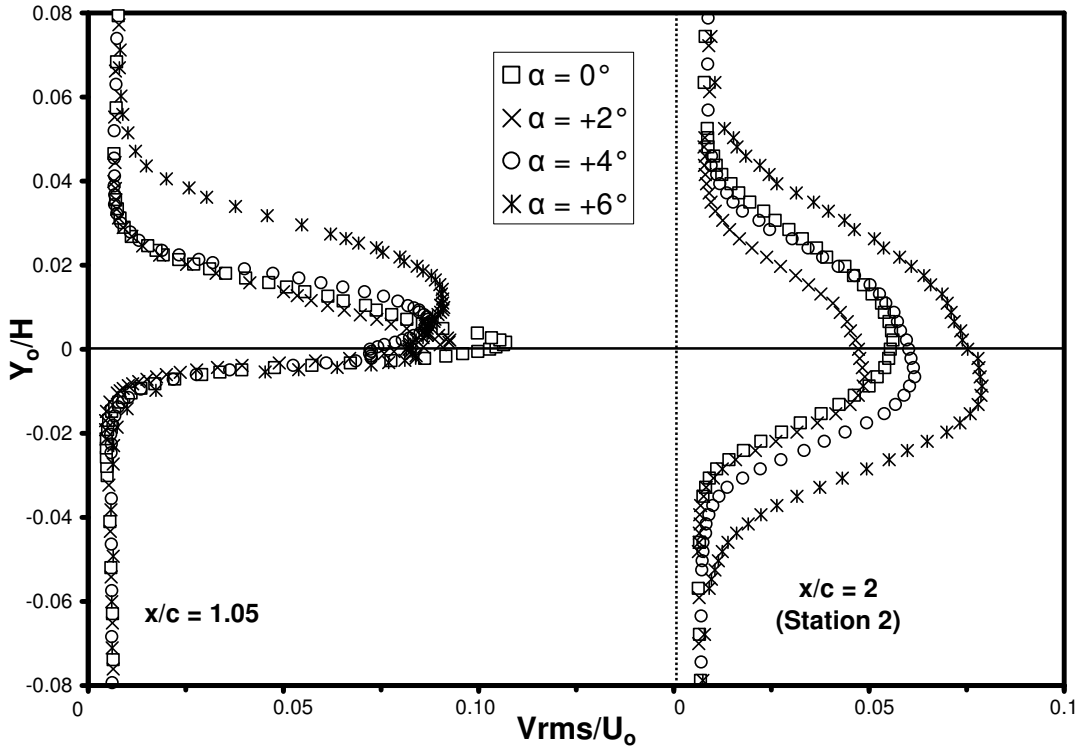

(a)

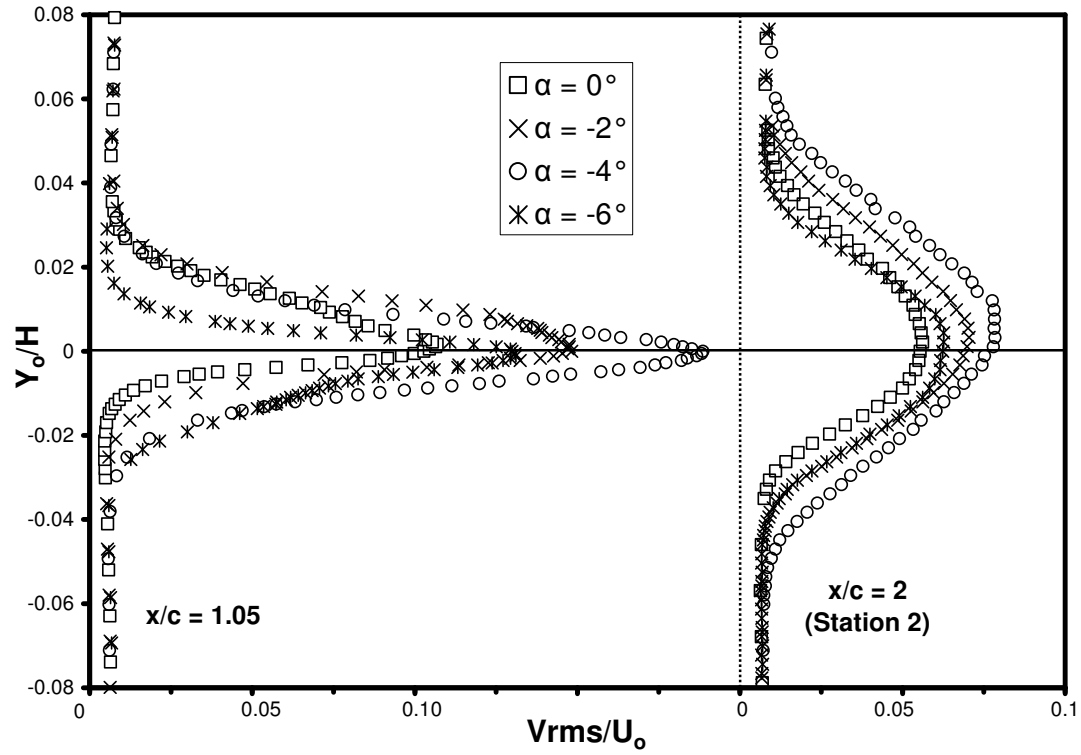

(b)

Figure 6.20: Profiles of normal turbulence intensity in the near-wake measured in the normal direction (z/H = 0.5), aligned with the wake centre line: (a) positive angles of attack $\alpha = 0^o$, $+2^o$, $+4^o$, $+6^o$, (b) negative angles of attack $\alpha = 0^0$, -2^o, -4^o, -6^o.

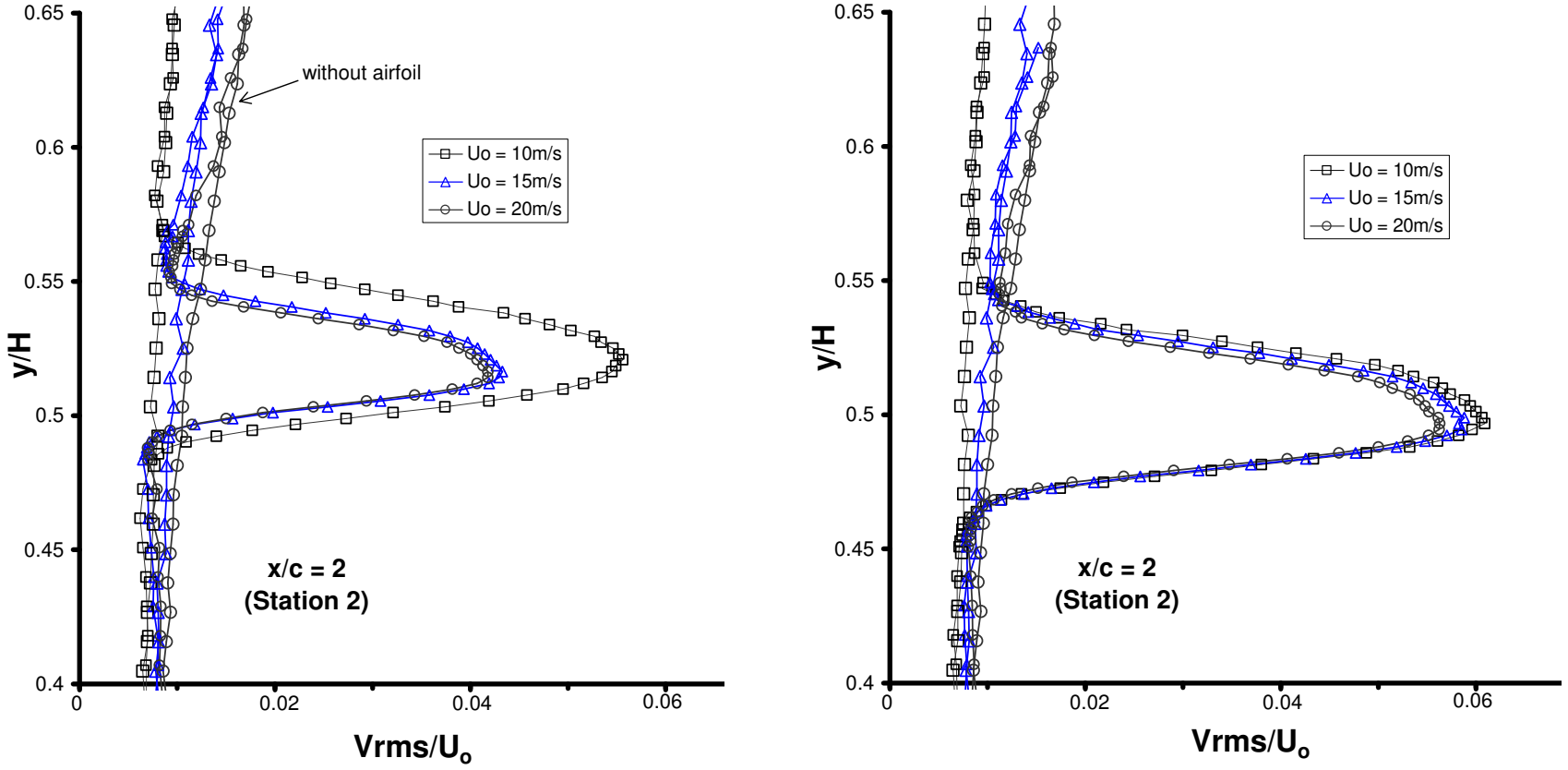

Figure 6.21: The effect of mainstream velocity on the normal turbulence intensity measured at station 2 ($z/H = 0.5$): (a) $\alpha = 0^{o}$, (b) $\alpha = +4^{o}$.

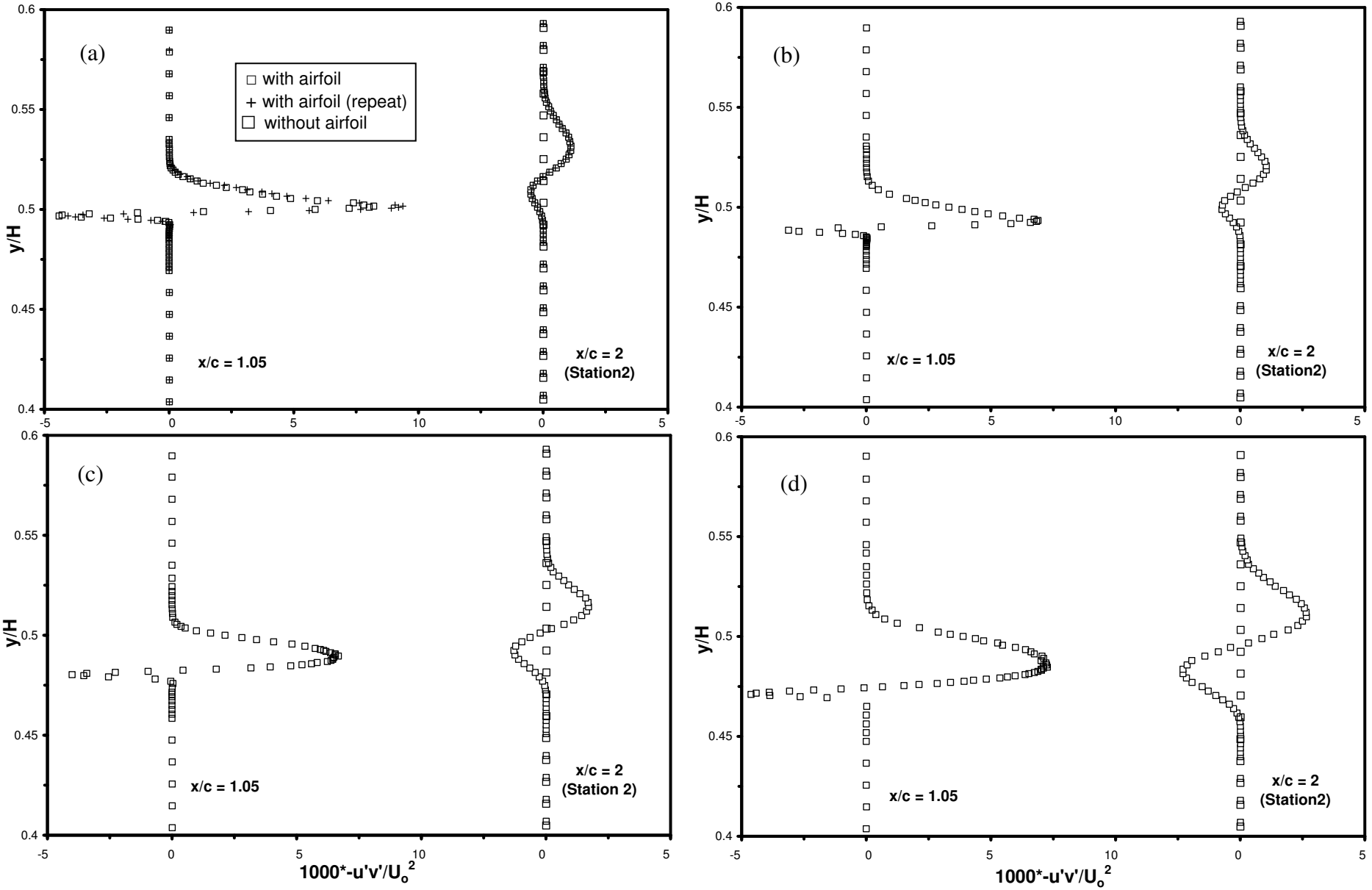

Figure 6.22: For caption see head of figure.

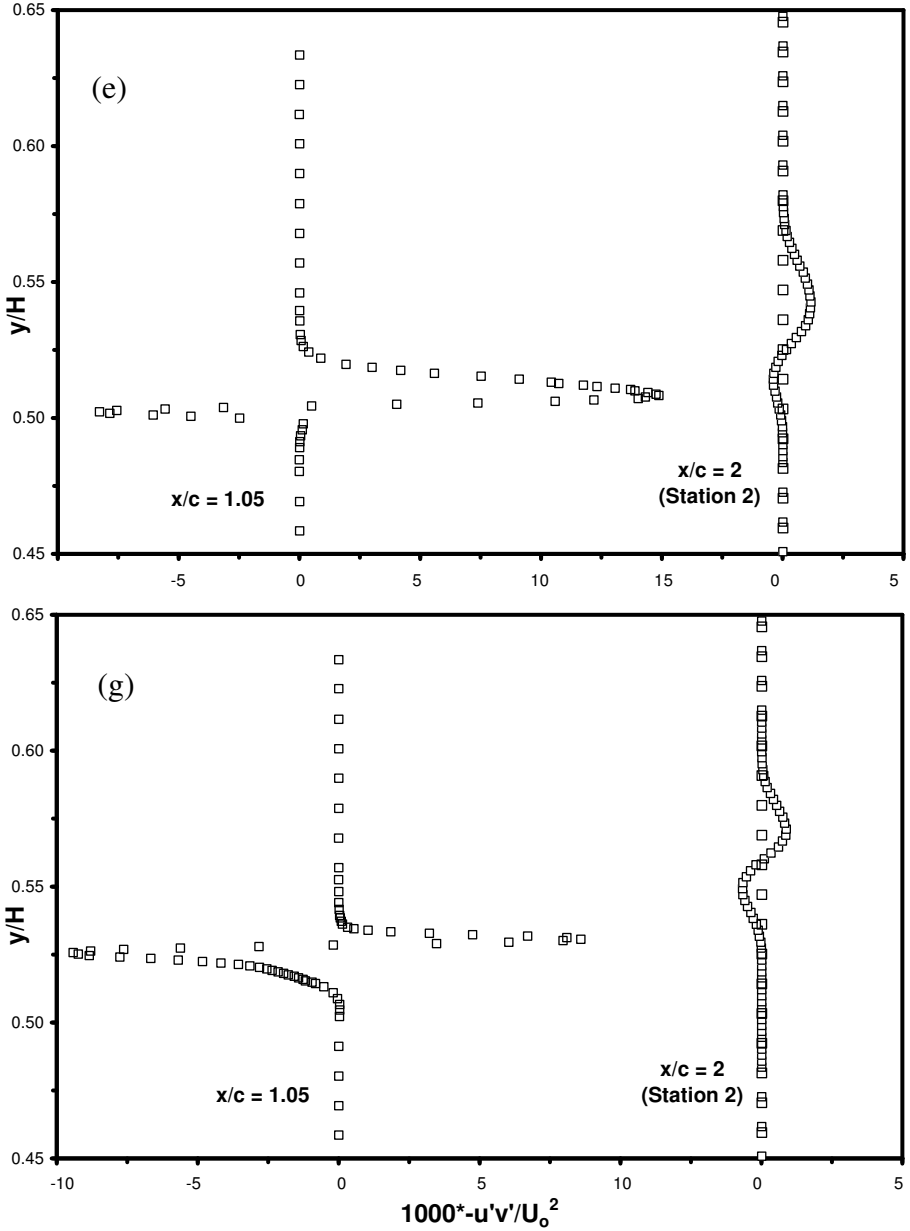

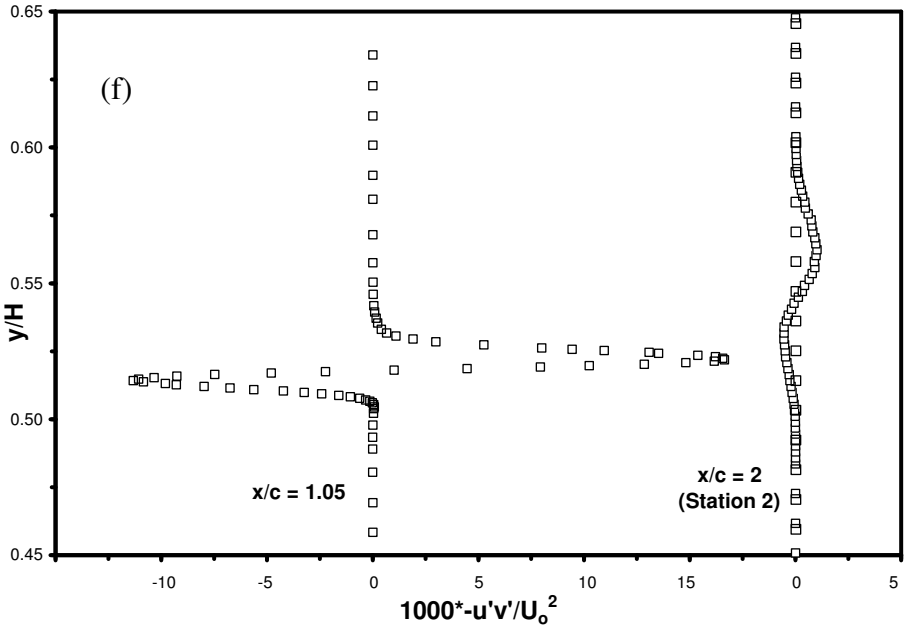

Figure 6.22: Profiles of turbulence shear stress in the near-wake measured in the normal direction ($z/H = 0.5$): (a) $\alpha = 0^o$, (b) $\alpha = 2^o$, (c) $\alpha = 4^o$, (d) $\alpha = 6^o$, (e) $\alpha = -2^o$, (f) $\alpha = -4^o$, (g) $\alpha = -6^o$.

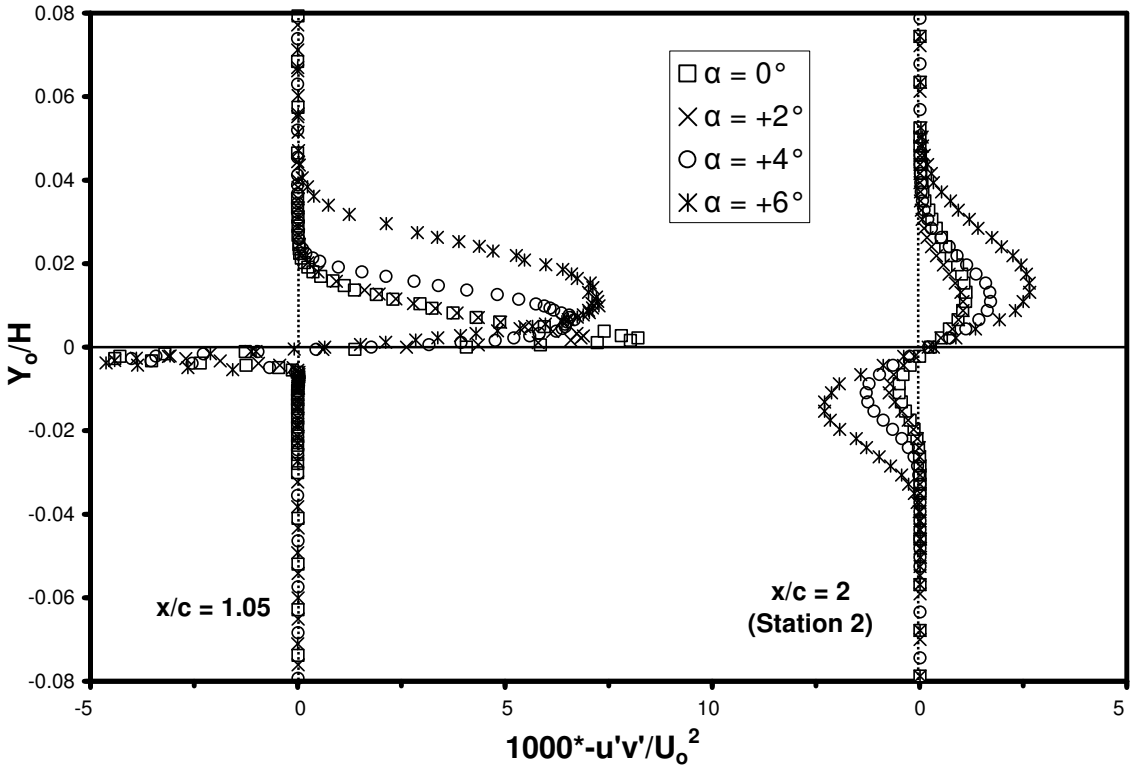

(a)

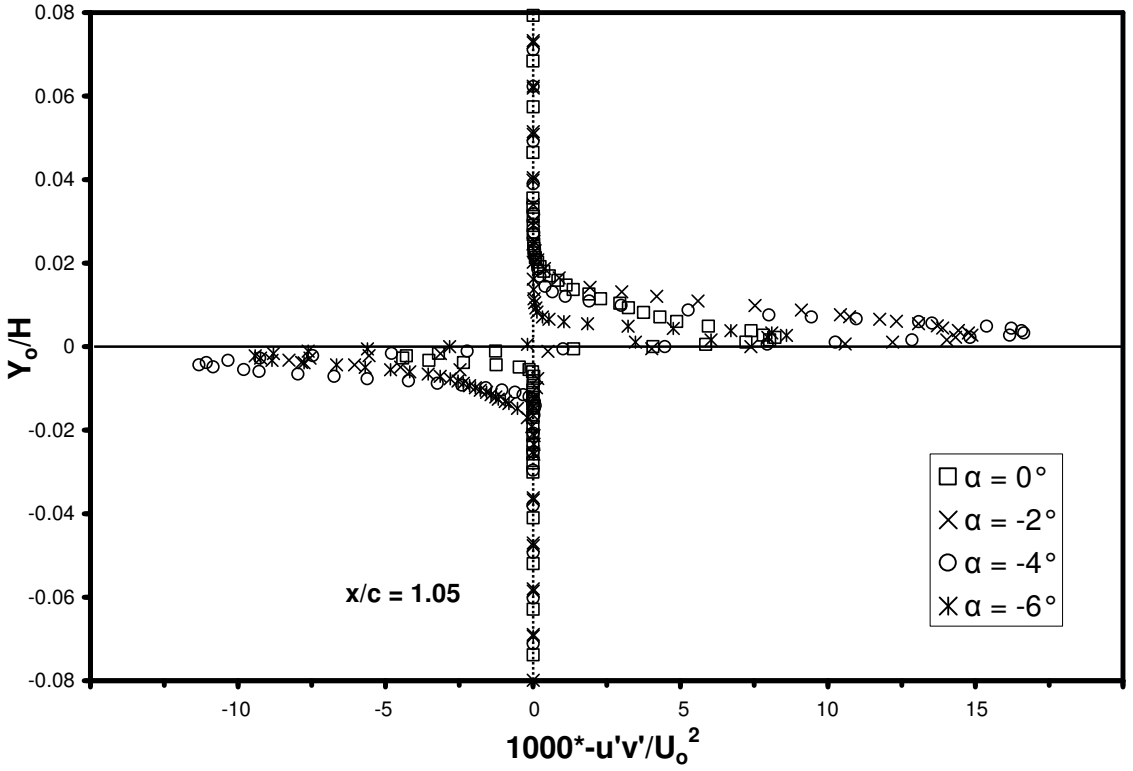

(b)

Figure 6.23: For caption see head of figure.

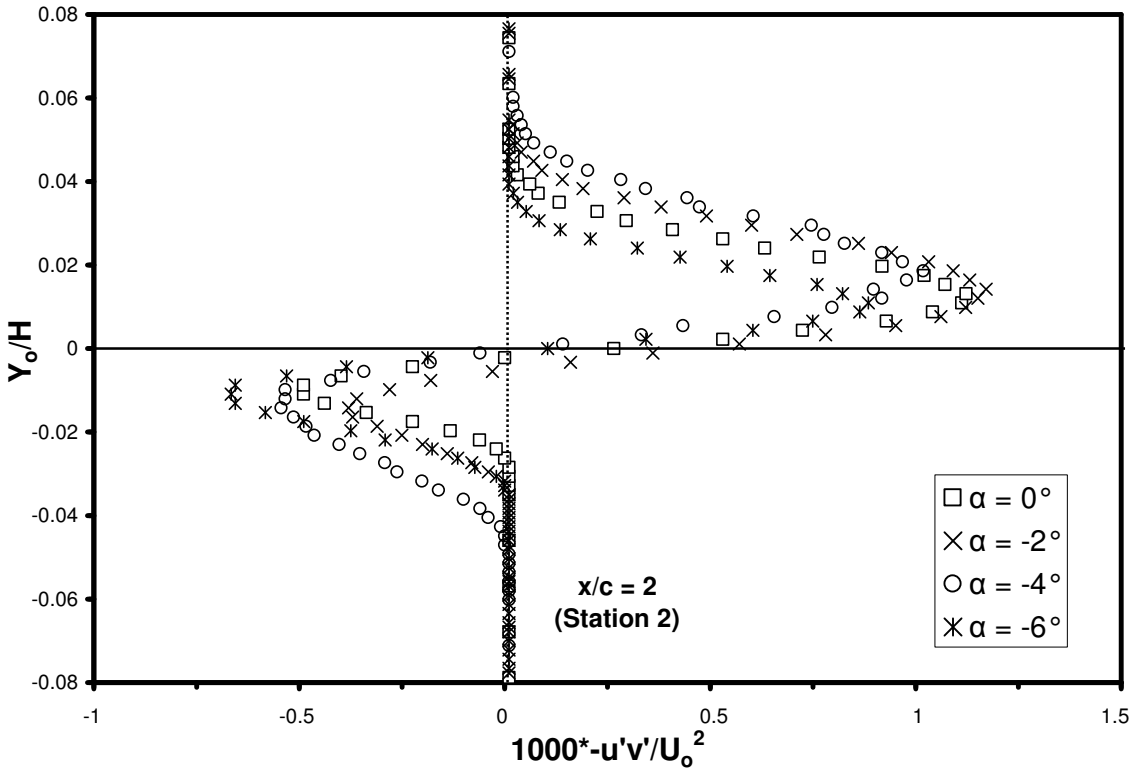

(b)

Figure 6.23: Profiles of turbulence shear stress in the near-wake measured in the normal direction (z/H = 0.5), aligned with the wake centre line: (a) positive angles of attack $\alpha = 0^o$, $+2^o$, $+4^o$, $+6^o$, (b) negative angles of attack $\alpha = 0^0$, -2^o, -4^o, -6^o.

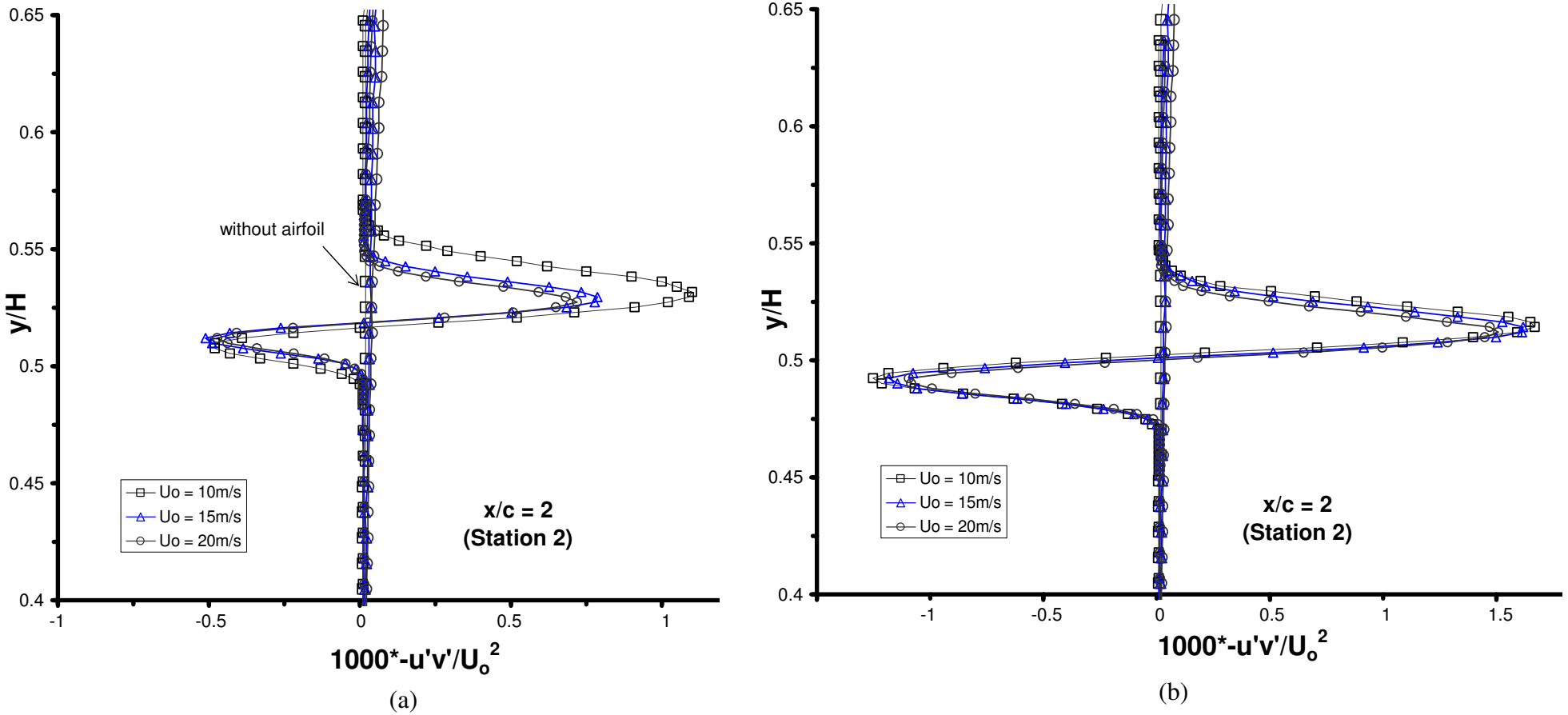

Figure 6.24: The effect of mainstream velocity on the turbulence shear stress measured at station 2 (z/H = 0.5): (a) $\alpha = 0^{o}$, (b) $\alpha = +4^{o}$.

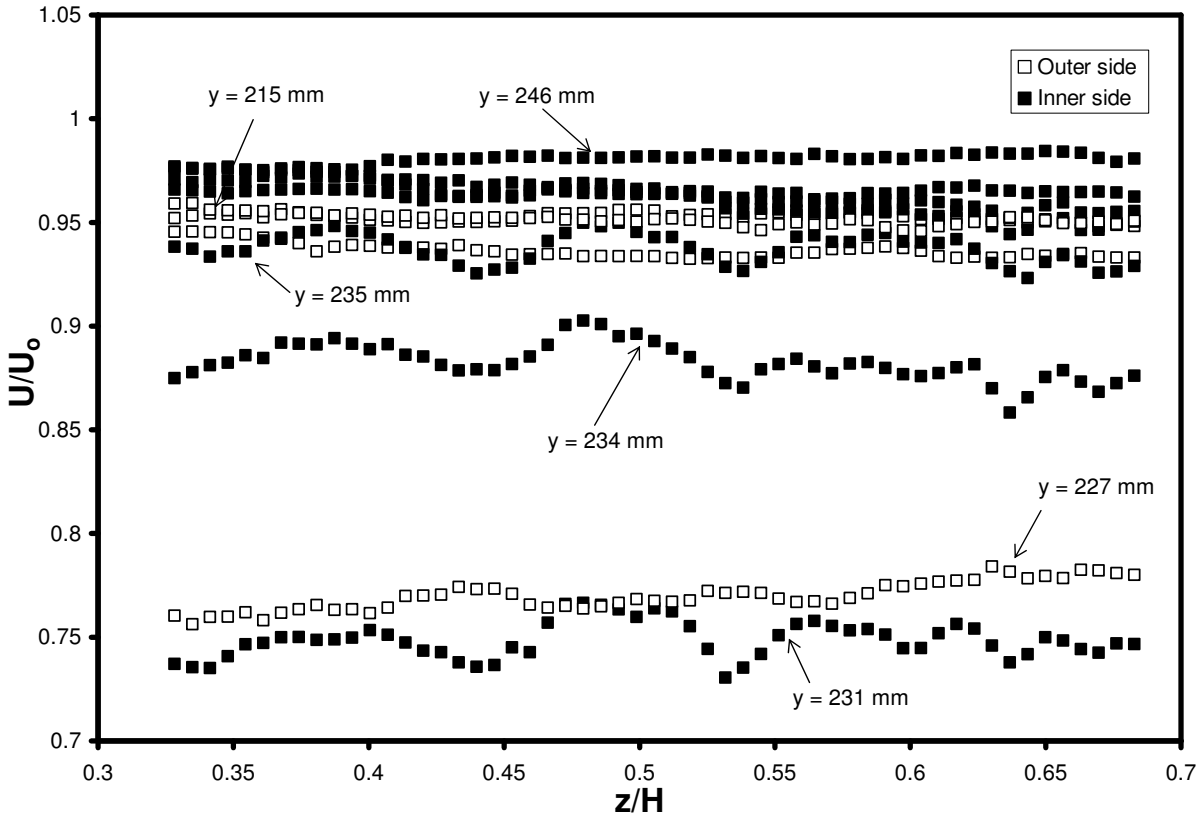

(a)

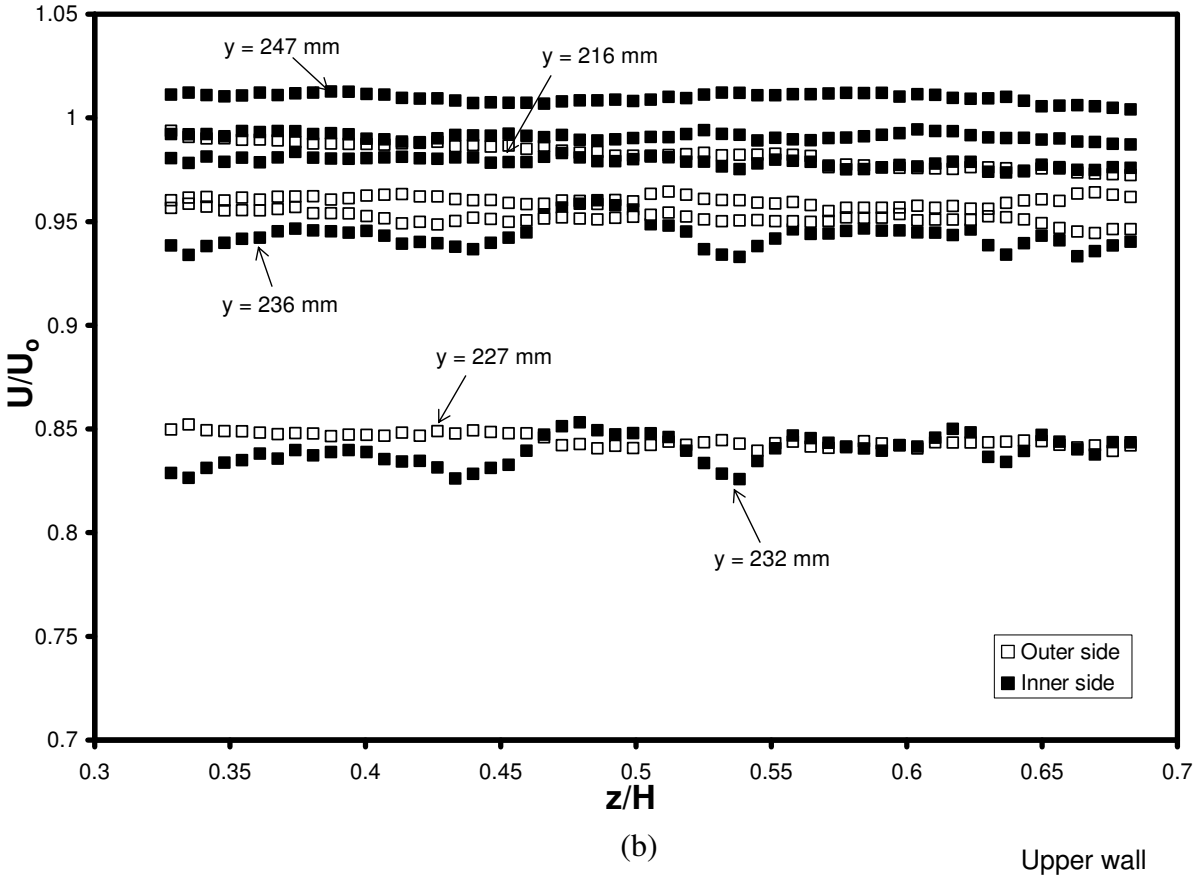

(b)

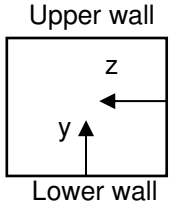

Figure 6.25: For caption see head of figure.

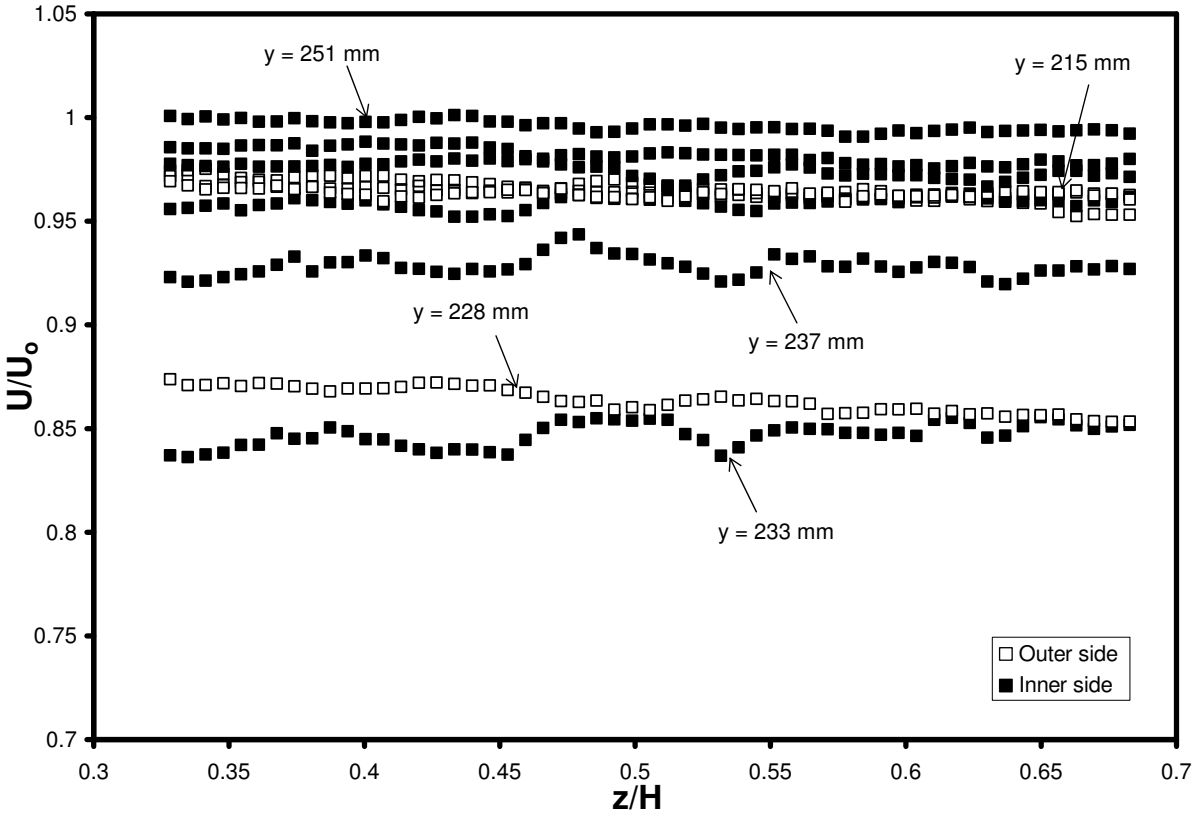

(c)

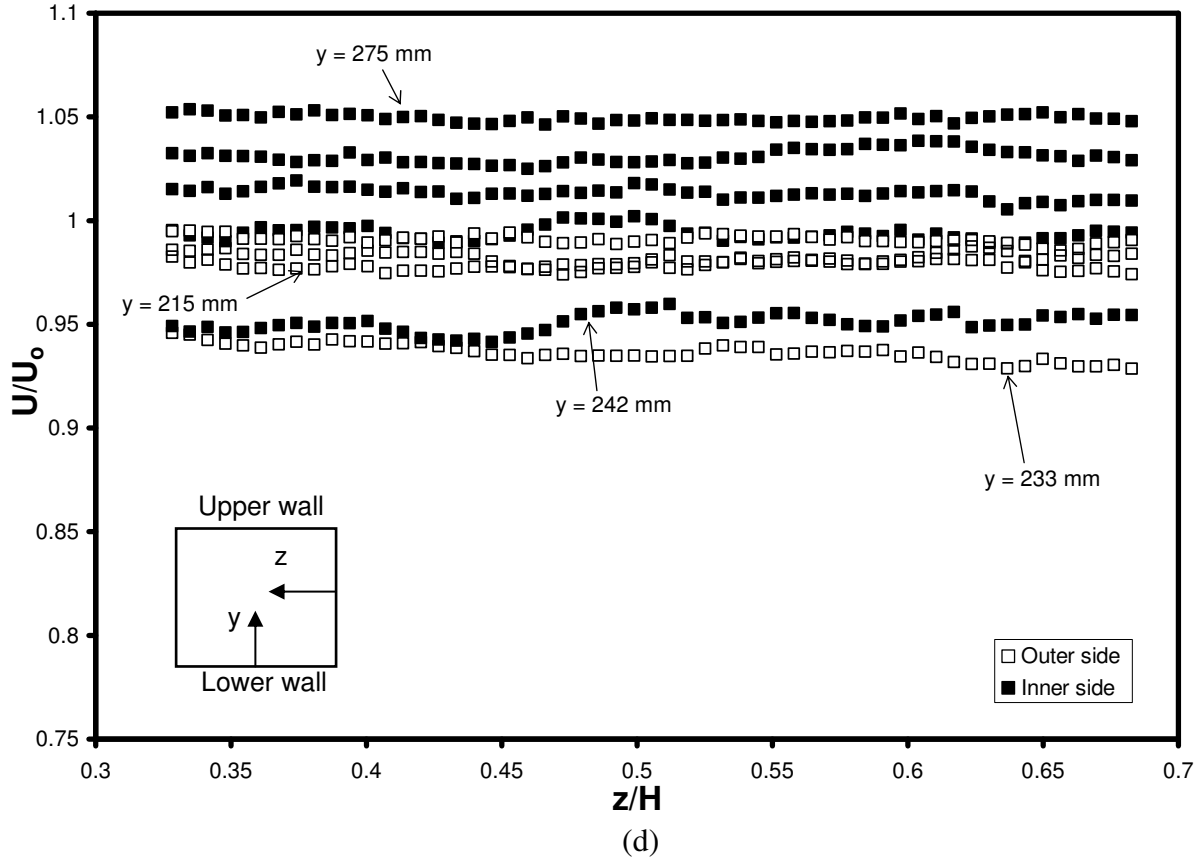

(d)

Figure 6.25: Spanwise profiles of mean velocity at the nominal mainstream velocity of 10 m/s and $\alpha = 0^o$: (a) $x/c = 1.10$, (b) $x/c = 1.22$, (c) $x/c = 1.33$, (d) $x/c = 2$ (station 2). (a-c) using a rake of single-wires, (d) cross-wire.

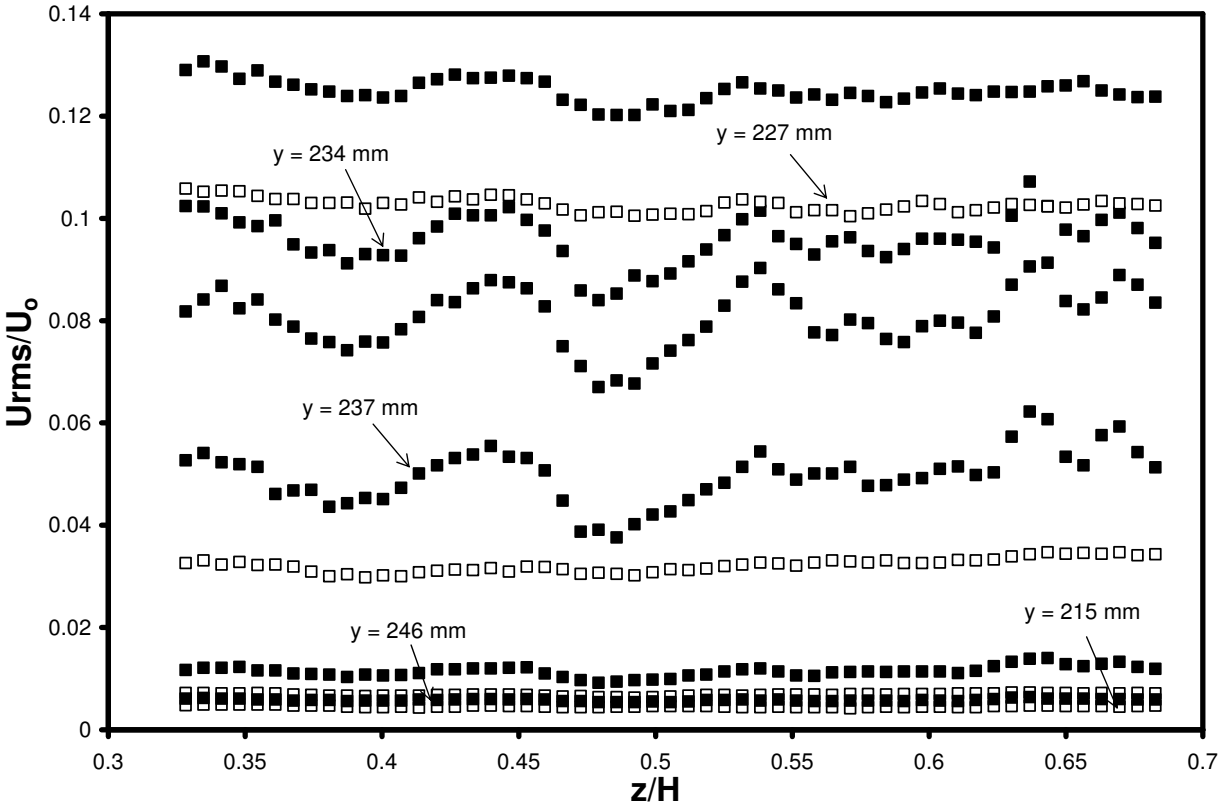

(a)

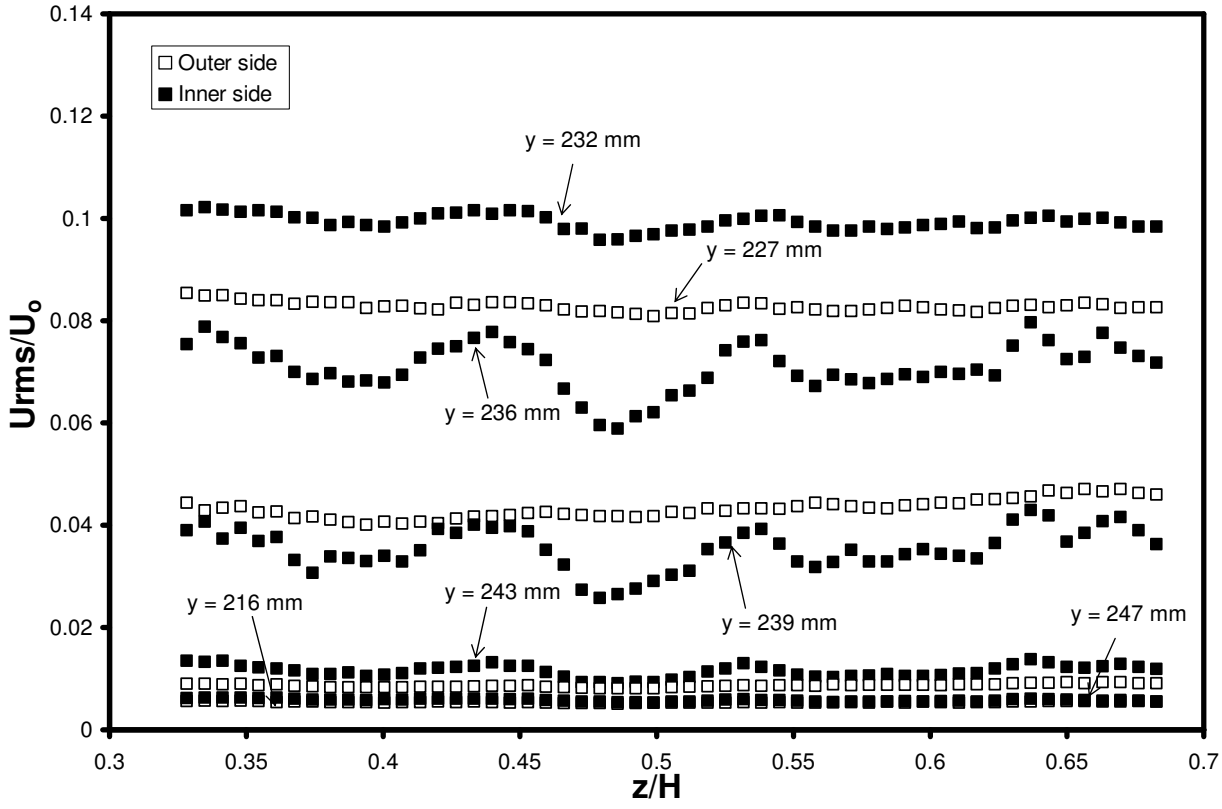

(b)

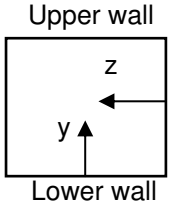

Figure 6.26: For caption see head of figure.

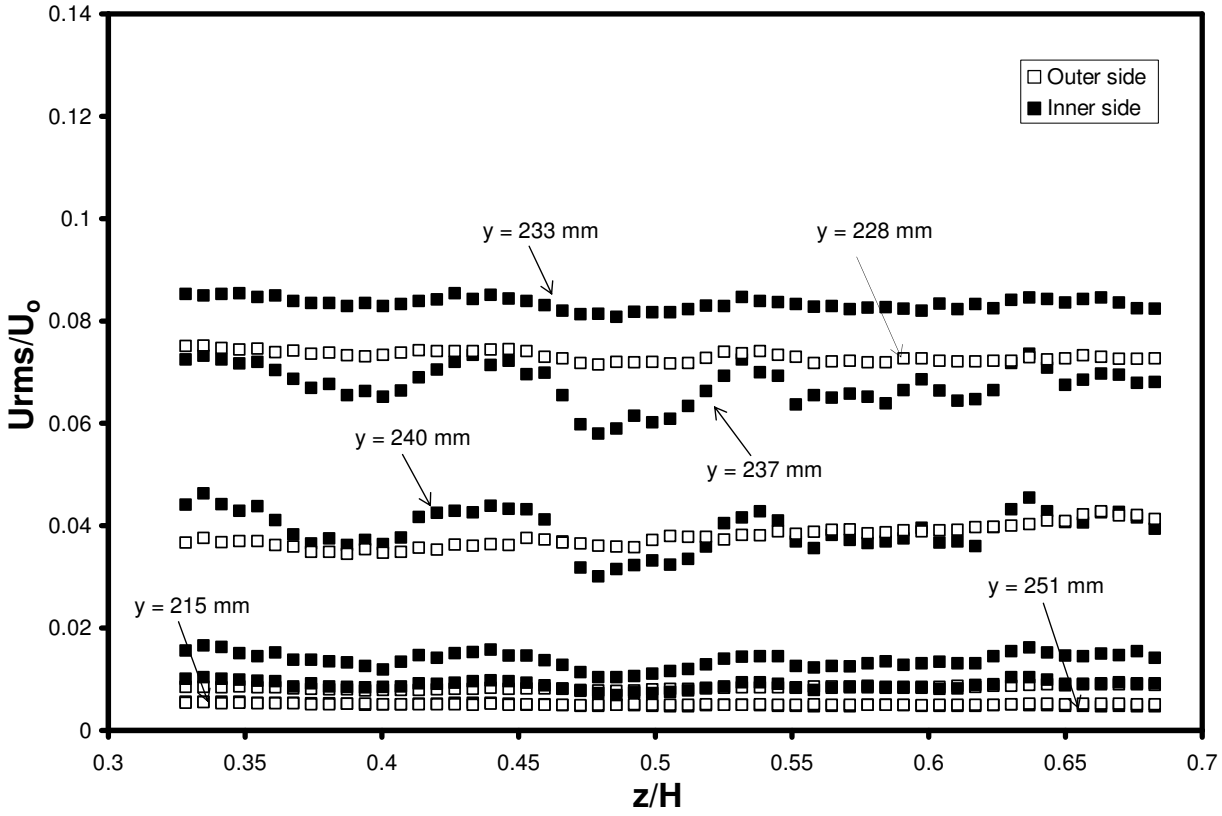

(c)

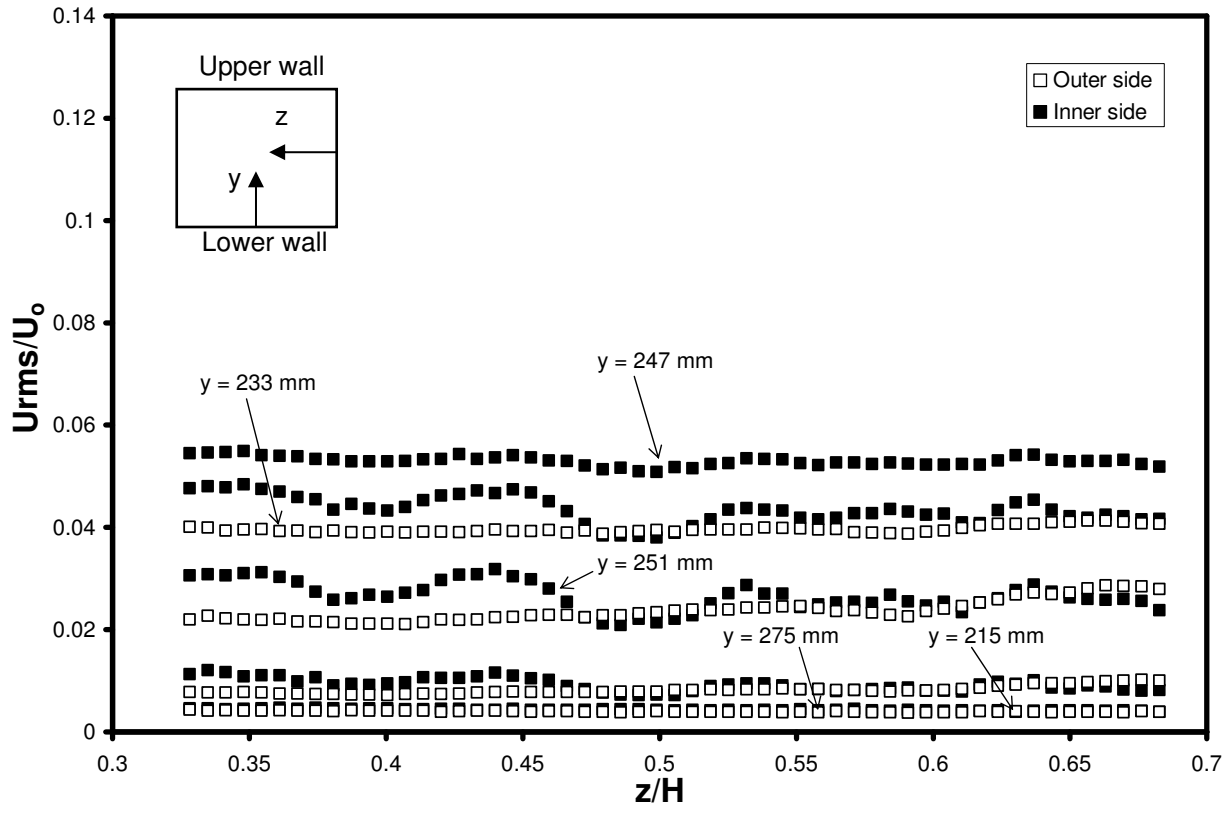

(d)

Figure 6.26: Spanwise profiles of turbulence intensity obtained at the nominal mainstream velocity of 10 m/s and $\alpha = 0^{o}$, at several near wake locations: (a) x/c = 1.10, (b) x/c = 1.22, (c) x/c =1.33, (d) x/c = 2 (station 2). (a-c) using a rake of single-wires and (d) cross-wire.

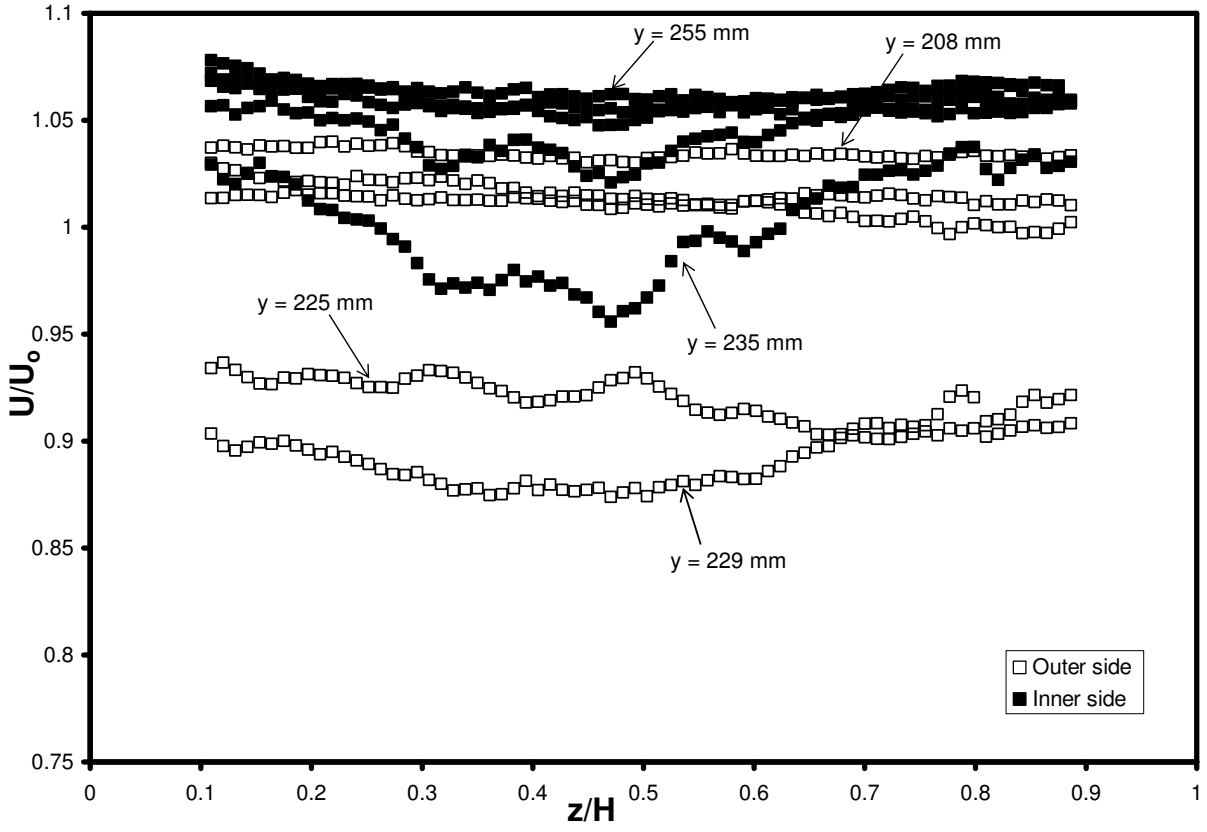

(a)

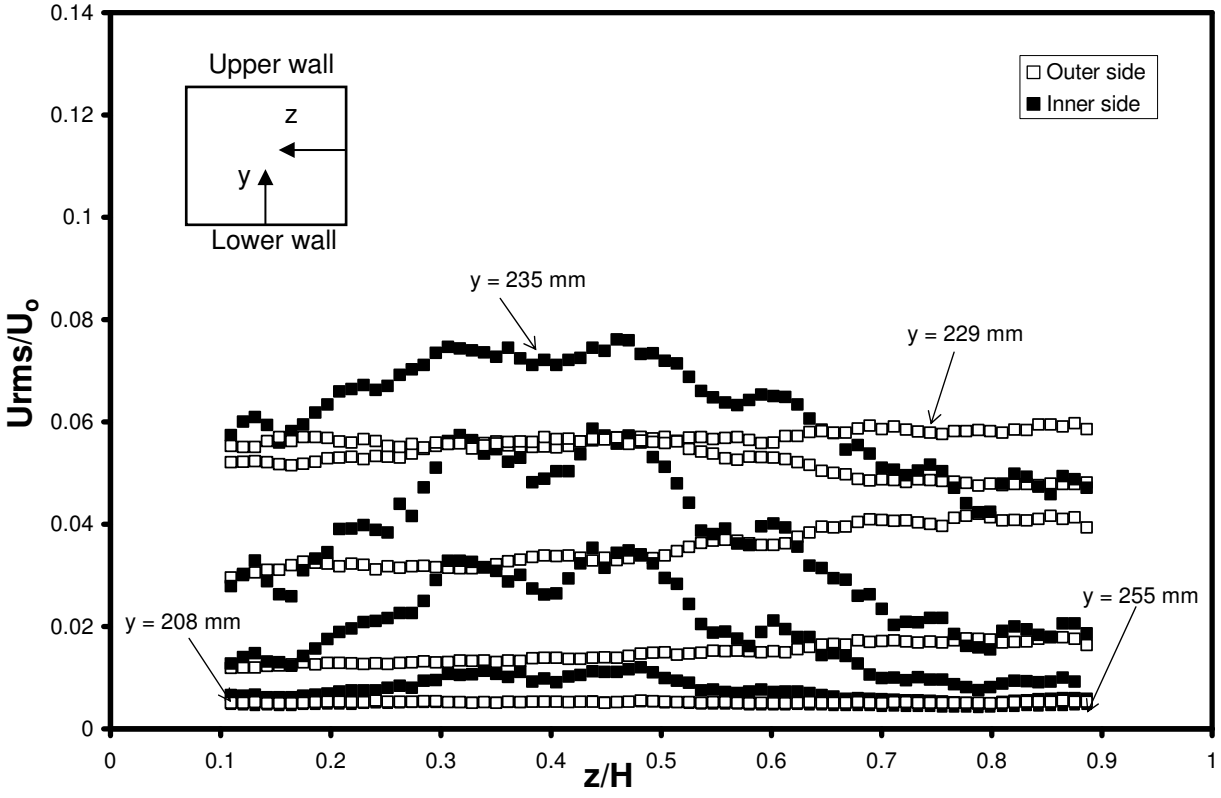

(b)

Figure 6.27: Spanwise profiles of mean streamwise velocity and turbulence intensity at angle of attack α of 4^o and mainstream velocity 10 m/s, at station 2: (a) mean streamwise velocity, (b) streamwise turbulence intensity.

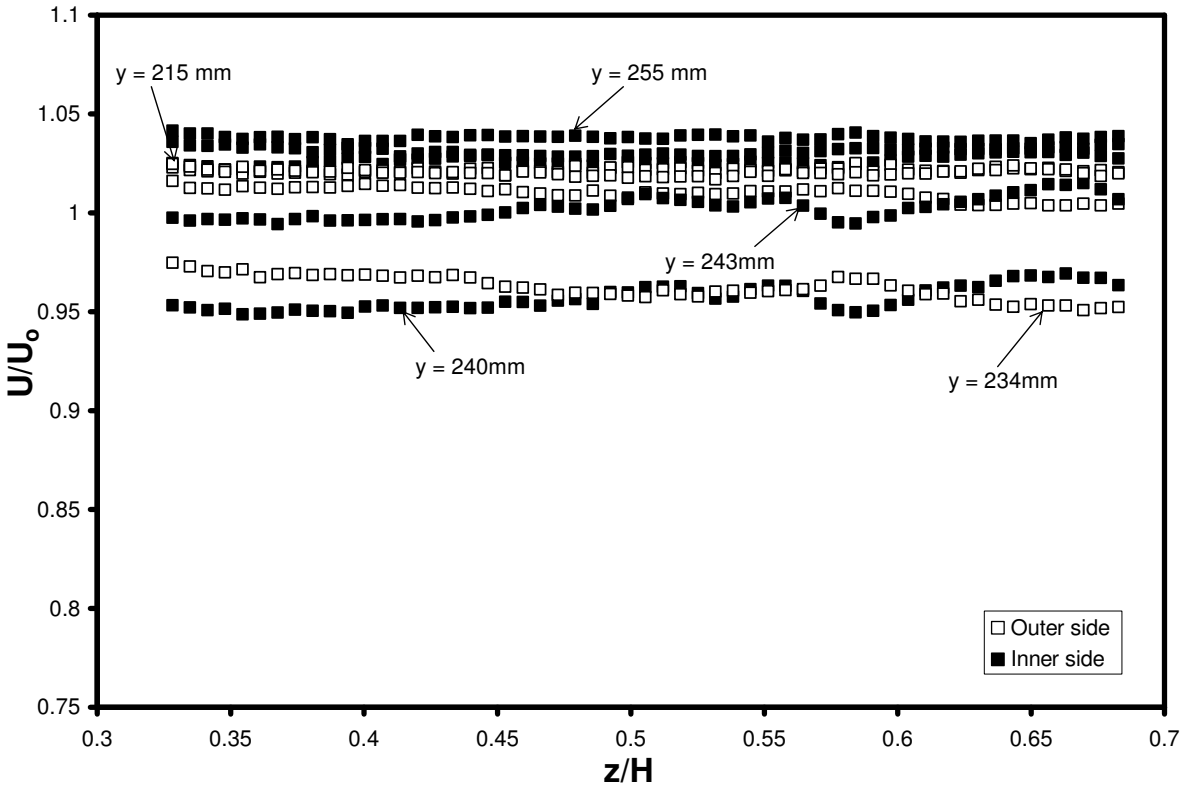

(a)

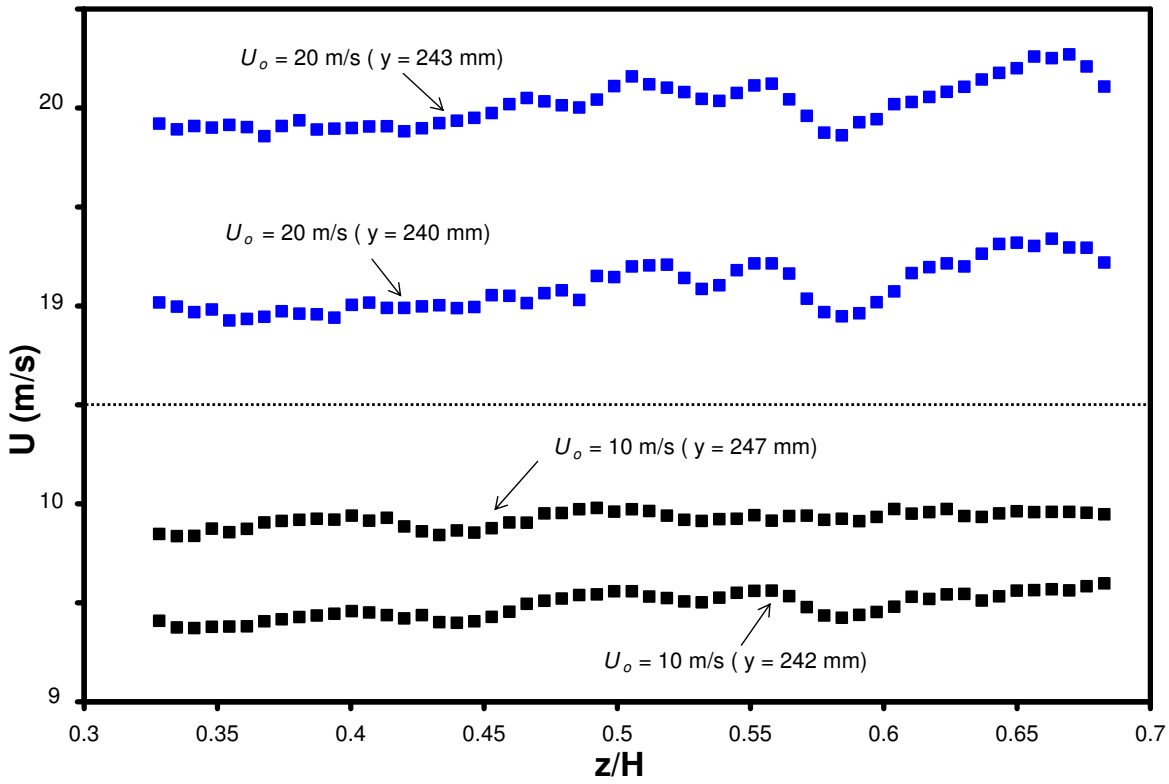

(b)

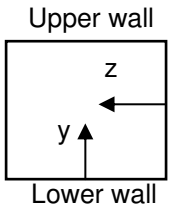

Figure 6.28: For caption see head of figure.

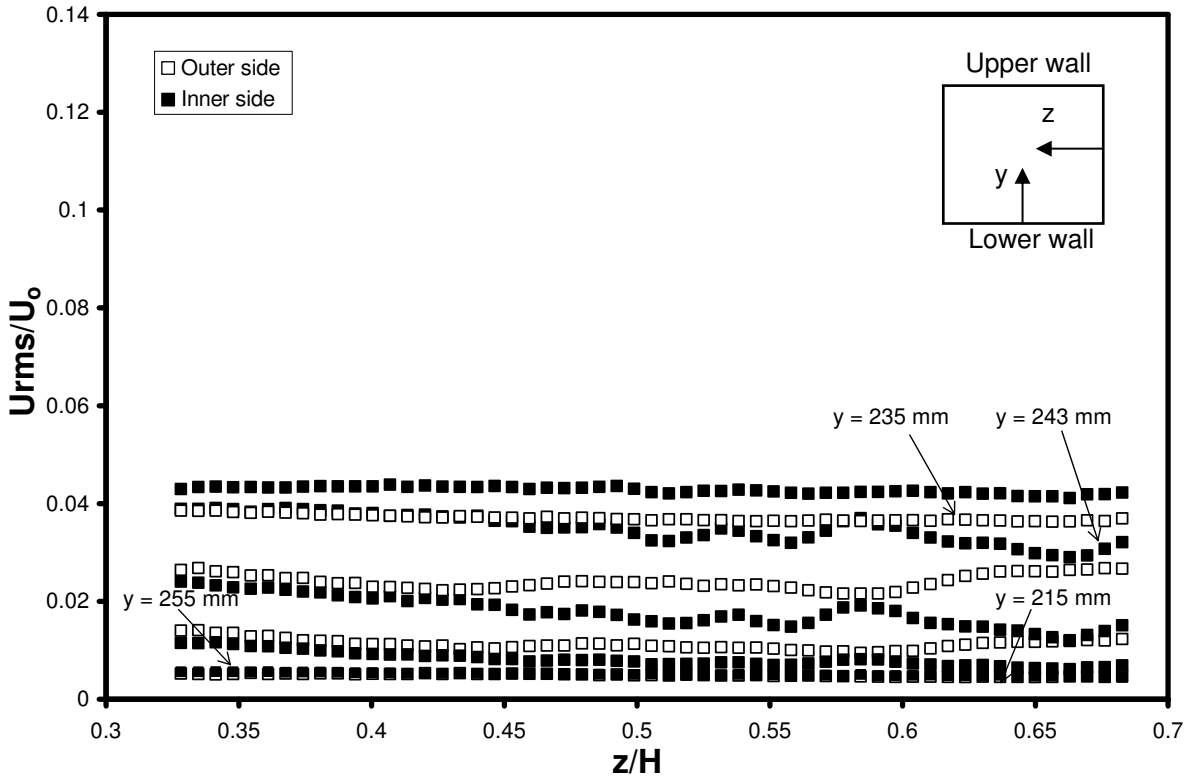

(c)

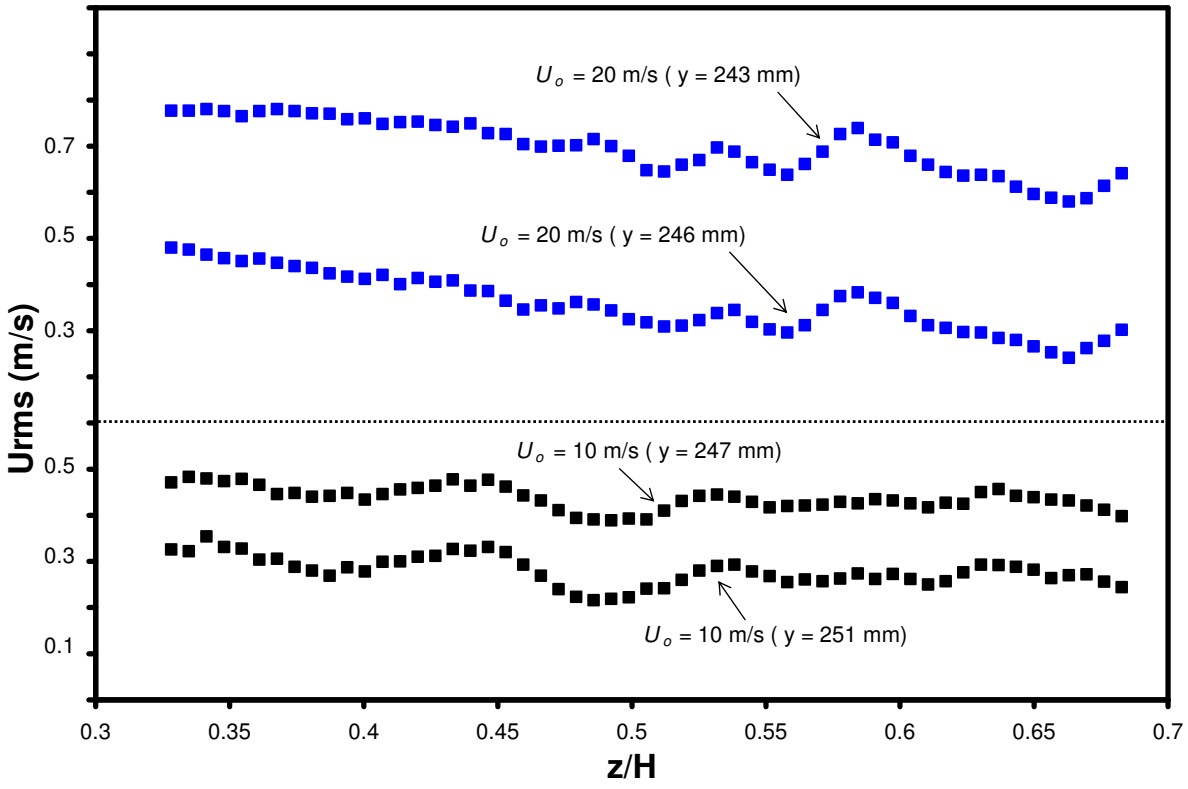

(d)

Figure 6.28: Spanwise distributions of mean streamwise velocity and turbulence intensity obtained at a mainstream velocity of 20 m/s and zero angle of attack, at station 2: (a) mean streamwise velocity, (b) comparison with velocity profiles at 10 m/s, (c) streamwise turbulence intensity, (d) comparison with turbulence intensity profiles 10 m/s.

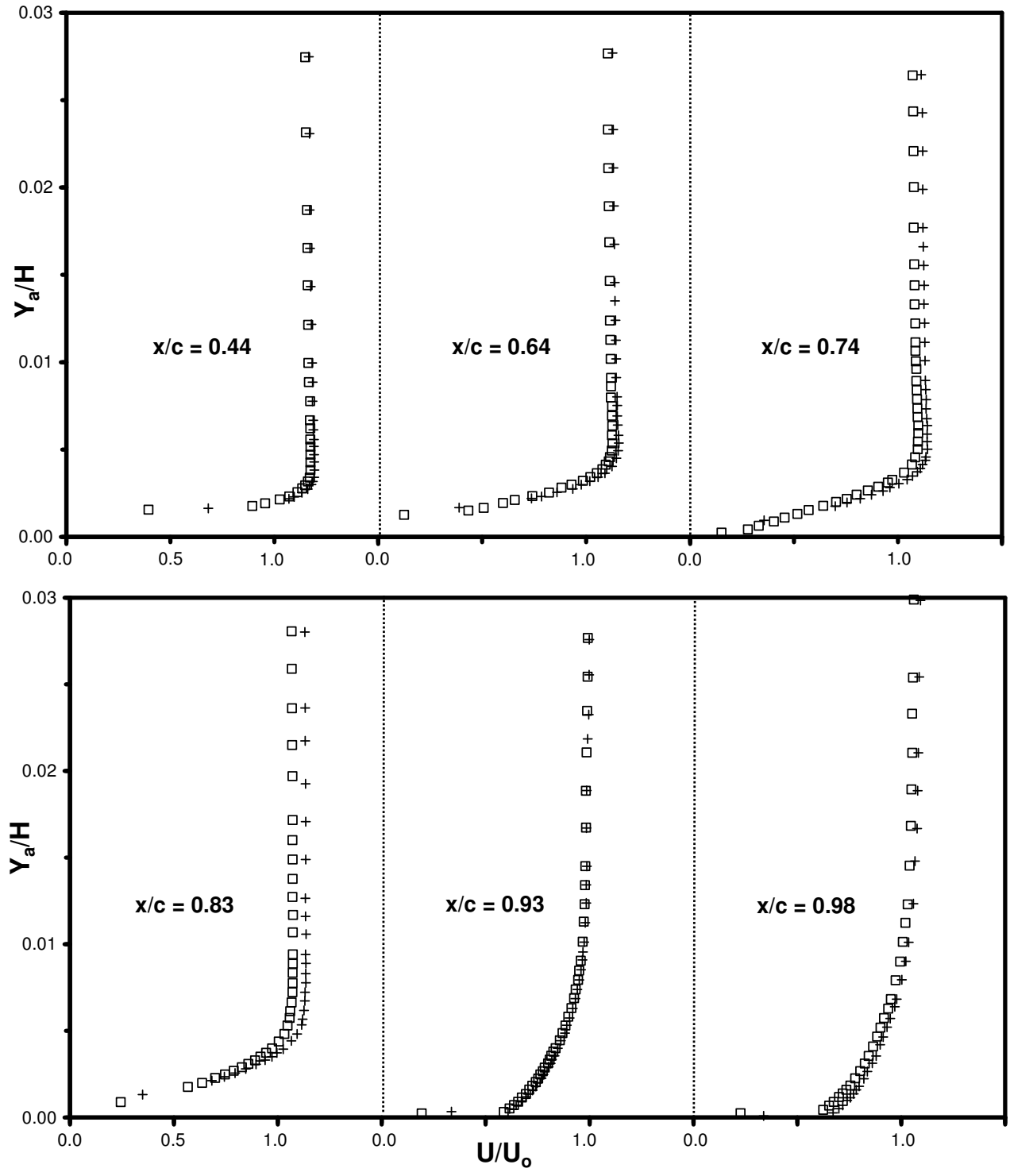

(a)

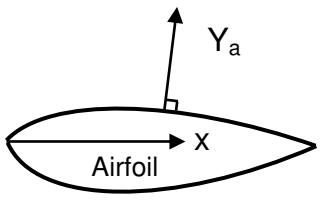

Figure 6.29: For caption see head of figure.

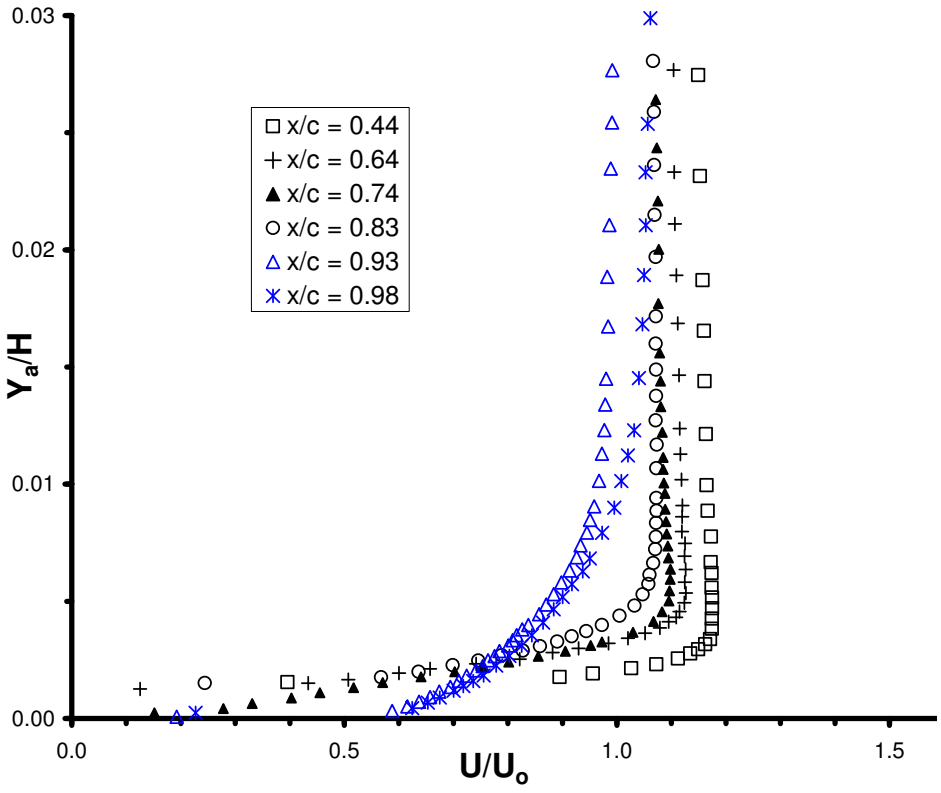

(b)

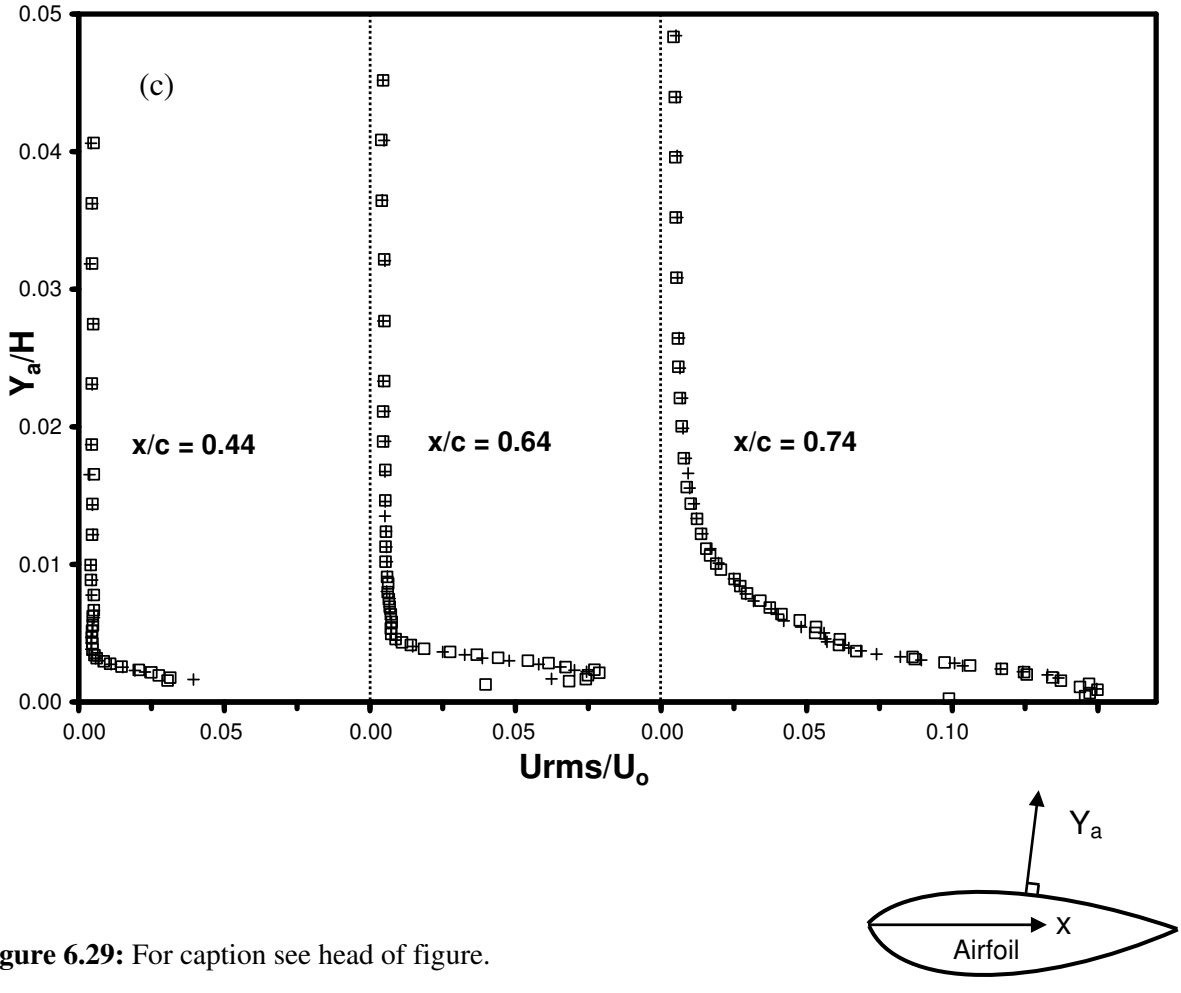

Figure 6.29: For caption see head of figure.

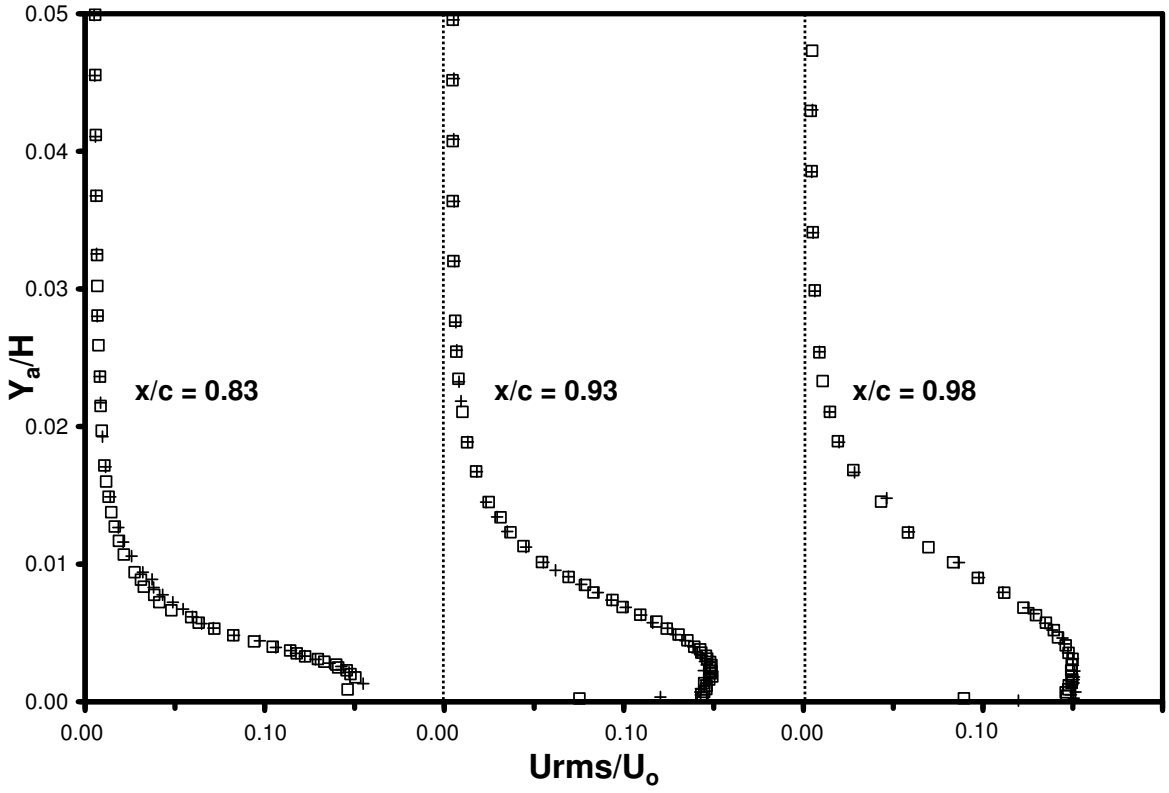

(c)

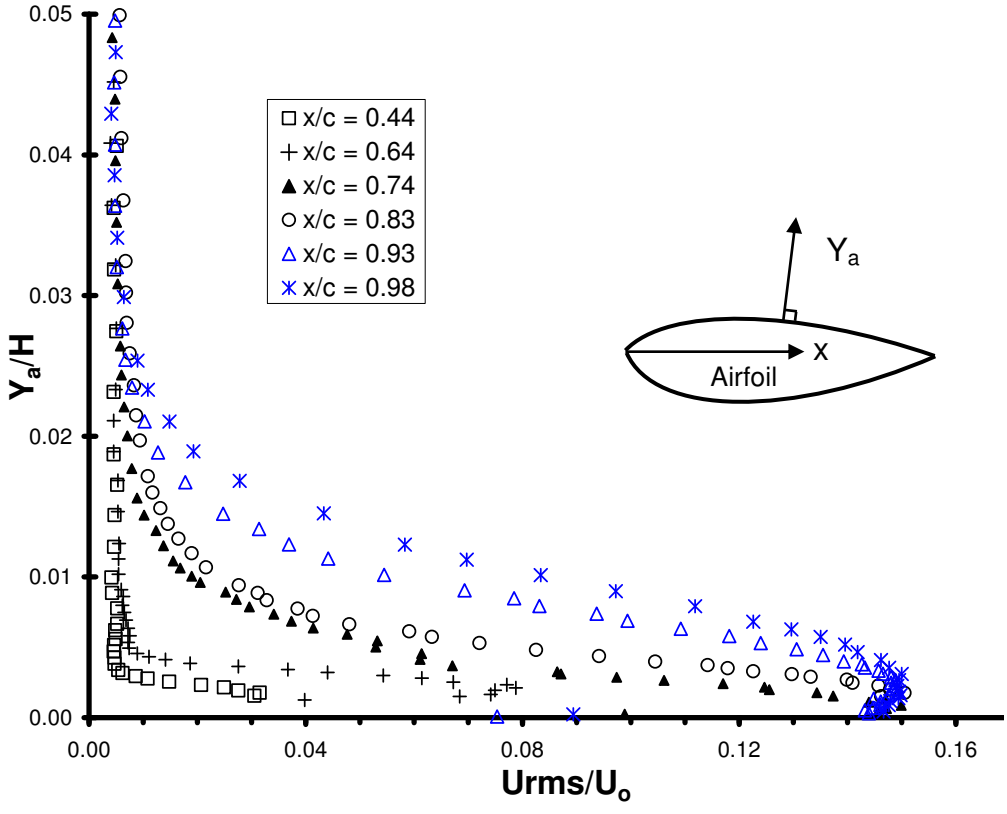

(d)

Figure 6.29: Profiles of mean velocity and turbulence intensity through the upper surface airfoil boundary layer ($z/H = 0.5$), at the nominal mainstream velocity of 10 m/s and zero angle of attack as measured using a single-wire: (a) mean velocity profiles, (b) grouped velocity profiles, (c) turbulence intensity, (d) grouped turbulence intensity profiles.

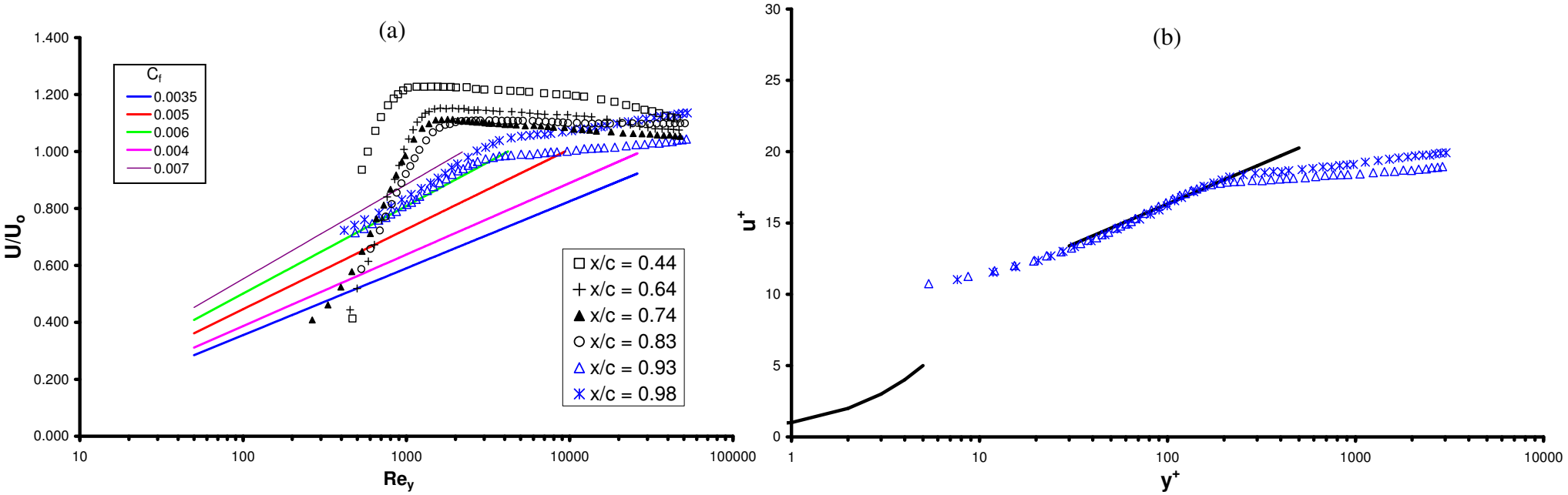

Figure 6.30: Non-dimensionalized velocity distributions in the boundary layer on the upper surface of the airfoil for nominal mainstream velocity of 10 m/s and zero angle of attack (z/H = 0.5): (a) Clauser chart representations, (b) u^+ vs. y^+ distribution for the profiles at x/c = 0.93, 0.98, The solid lines represent the viscous sub layer and the logarithmic law of the wall with constants A = 2.44, B = 5.0.

Chapter 7

7. NUMERICAL RESULTS AND COMPARISON WITH EXPERIMENT

7.1. Introduction

In this chapter the results of the numerical investigation of the wake of an airfoil in a duct with 90^o curvature are discussed. There are three main objectives in this part of the investigation. Firstly, to compare the present large eddy simulations with the experimental results, which would indicate the suitability of this numerical method in predicting the experimental trends, and secondly, to assess the contribution of LES modelling parameters, such as grid resolution and SGS modelling to the quality of the simulations. Finally, to deduce quantitative and qualitative information from the flow field, especially in the wake, in order to obtain a better understanding of the flows studied.

The present simulations were performed using FLUENT 6.3. Three SGS models were considered in the simulations, namely, the Smagorinsky model (SMG), its dynamic variant (DSMG) and the dynamic kinetic energy transport model (DKET). The simulations were conducted using three different grids. The coarsest grid was identical to that used by Piradeepan (2002) and simulations were conducted with all three SGS models on this grid. The results of these computations are referred to as coarseSMG, coarseDSMG, and coarseDKET. For the second grid, the computational domain of Piradeepan (2002) was refined especially near the walls to increase the grid resolution in the streamwise, normal and spanwise directions. The computational domain for the above two grids spanned the full width of the experimental tunnel. In the finest grid the spanwise extent of the computational domain was reduced to $0.5c$, with periodic boundary conditions set in the spanwise direction. On both the finer grids, simulations were conducted with DSMG; these computations are referred to as refinedPiradeepanDSMG and refinedDSMG.

The code was executed on a COMPUSYS parallel processing cluster with the Linux 64-bit operating system, and the grids were partitioned on Intel Xeon dual processor nodes running at 3.2GHz each.

7.2. Presentation of numerical results

The presentation of numerical results is in three forms, numerical distribution profiles, vector plots and contour plots. The distribution profiles (Figure 7.4-7.24) are obtained at mid-span (z/H = 0.5), and include static pressure, skin friction coefficient, mean velocity, turbulence intensity and turbulence shear stress. The computed spanwise distributions of mean velocity and streamwise turbulence intensity in the wake are presented in Figure 7.25 to 7.28. The spanwise variations are presented downstream of the trailing edge of the airfoil and correspond to the same near-wake locations tested experimentally. The results of the present experimental investigations in the airfoil boundary layer and the near-wake, and those of Piradeepan (2002), are extensively used to validate the large eddy simulations. The performance of LES in depicting the experimental flows is compared with the results predicted by RSM in Piradeepan (2002), where available.

To compare directly with the experimental results, the numerical distributions of mean velocity and turbulence intensities are normalised with respect to mean velocity U_o at the inlet (station 1). The turbulence shear stress is normalised using U_o^2. These comparisons revealed that the computed shift of the wake region with respect to the centre line of the duct was not consistent with the experimental shift. This finding was also reported by Piradeepan (2002), and caused additional difficulties in the direct comparisons of the wake profiles. Therefore, to compare the computed mean and turbulence quantities with the experimental results in the near-wake, the profiles were aligned using the wake centre (the point of minimum velocity in the wake). The profiles obtained from all computations, including those on the coarsest grid, and the results for the finer grids are displayed together where possible, and compared with the experimental data. The numerical profiles of the present investigation and the corresponding experimental results for the whole cross-section of the duct at station 2 to 5 (Piradeepan, 2002) are included to show the flow characteristics and the performance of LES, especially in the wake, airfoil boundary layer and on the convex and concave walls of the duct, where local variations are assessed. The FLUENT post processor uses a fixed coordinate system, therefore the streamwise velocity component at station 4 and 5 become the normal components, and vice versa. At station 3 the coordinate transform technique (Appendix VI) was used to resolve the correct streamwise and normal components.

The procedure for the collection of mean and turbulence statistics in the large eddy simulations is different from the steady state RANS computations. From a starting flow at the

inlet, as defined by boundary conditions, flow was allowed to develop for a substantial computational time so that a statistically steady state (SSS) condition for turbulence was achieved at station 5 (Appendix VII). The SSS condition was reached after approximately 50 flow-through times. A further 40,000 time steps were computed with a sample taken every 10 time steps to obtain turbulence statistics. A sample of instantaneous data for the velocity in the wake of the airfoil can be found in Appendix VIII.

The contour and vector plots presented here are obtained from data files post processed using TECPLOT 360. While the distribution profiles provide direct comparison of the performance of LES to experiments, the contour plots reveal the overall flow features within the flow domain, which can be used to describe the patterns seen in distribution profiles. The variations of static pressure and mean velocity magnitude in the *x*-*y* and *y*-*z* planes of the duct are presented in Figure 7.29 to 7.34. The vector plots obtained in the *x*-*y* and *y*-*z* planes are presented in Figure 7.35 to 7.37. The vorticity components are shown in Figures 7.38, 7.39, and 7.40. The streamwise component of vorticity (ω_x) is plotted in the *y*-*z* plane and the spanwise component (ω_z) is plotted in the *x*-*y* plane.

7.2.1. Assessment of grid resolution

At present there is no definitive griding criterion available that can be used in LES in conjunction with SGS models to achieve the best results in an efficient manner. It has been recommended by several authors, such as Mellen et al. (2003) for high Reynolds number flows over airfoils, and Lopes et al. (2006) for flow through ducts, that near-wall grid spacings in non-dimensional wall units should be within $\Delta x^+ < 50$, $\Delta y^+ < 1$ and $\Delta z^+ < 30$, such as to resolve approximately 80% of the energy producing structures. Using LES with wall functions, as opposed to the no-slip condition, the near wall resolution may be coarser (Fröhlich and Mellen, 2001). Furthermore, for lower Reynolds numbers (1×10^5) as opposed to high Reynolds number (1×10^6) these resolutions are not as stringent (Jovičić and Breuer, 2004). To compare near wall grid spacings on the three grids used here, steady state RANS simulations with the standard $k-\varepsilon$ model were performed. The computed friction velocity was then used for the normalisation of the grid spacings. The streamwise, normal and spanwise spacings in non-dimensional wall units are Δx^+, Δy^+ and Δz^+, and can be obtained from,

$$\Delta x^+ = \frac{\rho \Delta x u_\tau}{\mu} \tag{7.1}$$

$$\Delta y^+ = \frac{\rho y_1 u_\tau}{\mu} \tag{7.2}$$

$$\Delta z^+ = \frac{\rho \Delta z u_\tau}{\mu} \tag{7.3}$$

where the friction velocity u_τ is obtained from the local mean wall shear stress, and y_1 is the normal distance from the wall to the first grid point. The resolutions on the upper surface of the airfoil, convex wall and concave wall in terms of wall units are presented in Figure 7.1, 7.2 and 7.3 for the three grids, respectively.

In Figure 7.1(a) for the coarsest grid, the near-wall grid spacings after $x/c = 0.2$ on the upper surface of the airfoil are within $40 < \Delta x^+ < 140$, $200 < \Delta z^+ < 600$, $\Delta y^+ < 2$. Beyond $x/c = 0.85$ the streamwise spacing rapidly decreases to $\Delta x^+ \approx 40$. On the concave wall for the coarse grid (Figure 7.1b), $\Delta y^+ \approx 100$, and $200 < \Delta z^+ < 400$, over most of the domain. In the region $0 < X/H < 1$, the streamwise spacing is approximately $\Delta x^+ \approx 200$-400. After $X/H = 1$ (past station 2) the streamwise spacing abruptly increases to about 600, and the resolution in this direction becomes even coarser further downstream on this wall. The resolutions on the convex wall are similar to that on the concave wall.

The grid spacings in Figure 7.2(a-c) for refinedPiradeepan show considerable increase in the resolution throughout the flow domain. The most noticeable improvements on the upper surface of the airfoil are in the streamwise and spanwise spacings, where after $x/c = 0.2$, $\Delta x^+ < 80$ and $100 < \Delta z^+ < 300$. On the concave wall, the wall normal resolution is of the order of $\Delta y^+ \approx 20$ throughout the domain, and Δz^+ is between 100 and 200. The streamwise spacing before $X/H = 1$ (station 2) is about 200 and starts to become coarser steadily beyond this point. At $X/H = 1$ the distributions exhibits a minimum, this is because $u_\tau \rightarrow 0$ in this region. A similar trend of improved resolution is observed on the convex wall, although the minimum values in Δx^+, Δy^+ and Δz^+ are just after $X/H = 2$. The coarse spanwise spacings of both grids in Figure 7.1 and Figure 7.2 are due to the large spanwise extent of the flow domain ($H = 3c$) and the limited number of grid points distributed in this direction.

On the finest grid in Figure 7.3(a-c) the near-wall resolutions are closer to those of a traditional LES. The wall normal resolution on the upper surface of the airfoil is $\Delta y^+ < 0.5$ for more than 90% of the chord. The streamwise and spanwise cell sizes are $\Delta x^+ < 80$ and $20 < \Delta z^+ < 50$ for 80% of the chord, respectively. The improvement in spanwise resolution on the

finest grid is due to the substantially reduced extent of the flow domain in the z-direction (from $3c$ to $0.5c$). On the duct walls, the spacings in the wall normal and spanwise directions are significantly reduced and fall in the range of $5 < \Delta y^+ < 10$ and $20 < \Delta z^+ < 40$, respectively.

In the LES of Marsden et al. (2006) grid spacings of $\Delta x^+ \approx 20$, $\Delta y^+ \approx 2.5$, and $\Delta z^+ \approx 20$ were used near the surface of the NACA 0012 airfoil for a Reynolds number of 5×10^5. The reason for not adopting a higher streamwise and spanwise resolution on the upper surface of the airfoil (Figure 7.3a) is due to the lower Reynolds number (1×10^5), and also the large streamwise extent of the flow domain which was necessary to study the wake.

7.2.2. Distribution profiles

The static pressure distribution on the upper surface of the airfoil is shown in Figure 7.4. The computed flow angle of the fluid stream approaching the leading edge of the airfoil is presented in Figure 7.5. The distributions of static pressure on the concave and convex walls of the duct are shown in Figures 7.6. Figures 7.7 and 7.8 present the skin friction coefficient distribution on the upper surface of the airfoil, the concave wall and the convex wall. The boundary layer predictions for the upper surface of the airfoil are presented and compared with the experiment, where possible, in Figure 7.9 to Figure 7.15. The variations of streamwise velocity component in the near-wake and at station 2-5 are shown in Figure 7.16, while the wake parameters such as the variations of wake half-width and wake velocity defect are shown in Figure 7.17. The turbulence intensities in the near-wake region up to station 2 are shown in Figures 7.19(a,b), 7.20(a,b), and 7.21(a,b), while those across the full height of the duct at stations 2-5 are shown in Figures 7.19(c-e), 7.20(c-e), and 7.21(c-e). The distributions of turbulence shear stress are shown in Figure 7.22. In Figure 7.23, the profiles of mean velocity and turbulence intensity on the concave wall, approaching station 2, are shown. The spanwise variation of velocity and turbulence intensity in the near-wake locations are presented in Figure 7.25 to 7.28.

7.2.2.1. Static pressure

Airfoil upper and lower surfaces

Figure 7.4(a) presents the experimentally measured and numerically predicted variations of pressure coefficient on the upper and lower surface of the airfoil. Results from coarseSMG and

coarseDKET are not shown, since they produced similar profiles to coarseDSMG. Comparisons are made between the RSM computations on the coarser grid and LES on the refined grids. There is general agreement between computations and experiment for the overall profiles on the upper and lower surfaces. The pressure on the upper surface is lower than on the lower surface, resulting in an asymmetric pressure distribution. The pressure gradient is adverse for the most part on the upper surface of the airfoil. As discussed before, close to the mid-chord, the experimental profile is observed to flatten, and further downstream, near x/c = 0.65, the experiments indicate that the adverse pressure gradient forms again, characterised by a steep change in the gradient of C_p. The DSMG computations are consistent with each other and compare well with the results from RSM on the upper surface up to approximately the mid- chord x/c = 0.5.

The results for mean pressure coefficient distribution in the region near the trailing edge of the airfoil are shown more closely in Figure 7.4(b). In coarseDSMG and refinedPiradeepanDSMG the profiles on the upper side of the airfoil flatten beyond the mid-chord. This feature can be attributed to separation and reversed flow on this surface, as was also stated by Shan et al., (2005). In refinedDSMG the profile of C_p is similar to RSM up to about x/c = 0.7, beyond which it deviates from RSM with a steeper gradient. The flow near the trailing edge computed by refinedDSMG is close to separation. In all computations, it is observed that an adverse pressure gradient forms again near the trailing edge on the upper surface past x/c = 0.9. However, the effect is greater for refinedDSMG where, very close to the trailing edge, the pressure on this side becomes positive. In general, the results from refinedDSMG are the closest to the experiments near the trailing edge of the airfoil.

The flow angle (θ) relative to the x-axis is calculated near the inlet of the flow domain and is shown in Figure 7.5 for RSM, coarseDSMG, refinedPiradeepanDSMG and refinedDSMG. Comparisons are also made with the experiments of Piradeepan (2002) at station 1, in which a maximum flow angle close to -2^o was measured near the duct centre line (y/H = 0.5). It is observed that the magnitude of the flow angles in the bulk region of the duct ($0.4 < y/H < 0.8$) increase with increasing streamwise distance (X) from station 1, but the location of the peaks relative to the duct centre line is not significantly affected, as indicated in the simulations. In general, at X = 50 mm, LES computes a peak flow angle of approximately -2.5^o, whereas for RSM the peak angle is closer to -1.5^o at this location. The location of the maximum flow angle in the bulk region is consistent across all computations, and occurs near y/H = 0.6, which is closer to the convex wall than measured in the experiments. The asymmetric pressure

distribution observed between the upper and lower surfaces of the airfoil is attributed to the computed flow angle of the approaching fluid stream. However, there appears to be some disagreement between experiment and computations with regard to the magnitude of the mean flow angle of the approaching flow, and the location of the maximum value relative to the duct centre line. This can contribute to differences in the computations over the airfoil.

Concave and convex walls

The distribution of static pressure on the walls of the duct is shown in Figure 7.6 and compared with the experimental results of Piradeepan (2002). The experiments indicate the widely varying nature of the pressure on the walls. On the concave wall, the pressure coefficient (C_p) increases from station 1 to 2, remains constant up to about station 4 and then decreases towards station 5. The developing boundary layer is, therefore, subjected to an adverse and then favourable pressure gradient. The opposite trend occurs on the convex wall. Piradeepan and Mokhtarzadeh-Dehghan (2006) reported intermittent flow separation on the convex wall at station 4, observed by flow visualization. The flattening of the profile on the convex wall close to $X/H = 2$ near the bend exit (Figure 7.6) can be attributed to this separation phenomena. In the downstream tangent the static pressure on the concave wall gradually drops towards the exit of the bend and approaches a constant value similar to that measured on the convex wall in this region.

There is general agreement between the experiment and the computation for the overall profile (Figure 7.6). The differences are mainly in the way that the flattening of the profile due to flow separation is represented. On the convex wall, this feature is not computed by RSM, which may be attributed to the general difficulties in predicting unsteady separation from continuous surfaces by RANS methods. The simulations of refinedDSMG also do not compute this plateau and produce similar results to RSM towards the downstream tangent. This is believed to be due to the shortened spanwise extent of the flow domain, and the imposition of spanwise periodic conditions in place of the side walls. In general, the large eddy simulations that incorporate the full spanwise extent and the side walls of the tunnel compute this feature. Among these, the SMG model exaggerates this plateau, whereas DSMG and DKET present better comparison to experiments. As was stated before in Chapter 4, the latter model uses an additional transport equation, which describes the physics of turbulence better and provides improved results compared with DSMG. With regard to the pressure recovery downstream of station 4 and for the overall pressure loss, the results of coarse LES show closer agreement

with experiment. The results from refinedPiradeepanDSMG on the convex wall (not shown here) were similar to those of coarseSMG, DSMG and DKET.

On the concave wall between stations 1 and 2, coarse LES predicts a small plateau in the pressure profile, a feature not computed in RSM, refinedPiradeepanDSMG, refinedDSMG or the experiments. This can be attributed to the occurrence of a small flow separation region upstream of station 2 on the coarse grid, and is believed to be due to the jump in streamwise grid spacing in this region. The result highlights the sensitivities of LES to streamwise grid resolution on the concave wall. Simulations with the two refined grids present better comparisons with the experiments on the concave wall. Of these two finer grids, the results for refinedPiradeepanDSMG provide a more accurate prediction of the downstream pressure recovery on this wall.

7.2.2.2. Skin friction

Airfoil upper surface

The distribution of mean skin friction coefficient on the upper surface of the airfoil is shown in Figure 7.7(a). The values of C_f are based on the local mean wall shear stress. For comparison, the figure also shows the calculated values of C_f with the Clauser chart from the present experiments conducted in the airfoil boundary layer. The large eddy simulations with the DSMG model are shown for the coarse grid and are compared to the simulations on the finer grids. The high values of friction coefficient computed near the leading edge in all simulations correspond to the strong favourable pressure gradient and acceleration of the flow in this region. The RANS computation yields a nearly constant value of skin friction coefficient of approximately 0.01 after $x/c = 0.1$. The results from LES are generally consistent with each other for the distribution of skin friction. Compared with RSM, however, the local values of C_f in the large eddy simulations are generally much smaller in magnitude after $x/c = 0.1$. The differences noted here are believed to be due to the different ways that wall shear stress is calculated, for example RSM uses the standard wall functions whereas, refinedDSMG uses the Werner and Wengle wall function approach.

The distribution of C_f and mean x-wall shear stress are shown more clearly for the LES cases in Figure 7.7(b) and 7.7(c), respectively. In general a sudden decrease in C_f to a minimum is indicative of flow separation and transition phenomena (Shan et al. 2005). An abrupt recovery

of C_f corresponds to reattachment of the separated flow. In refinedDSMG, the profile of skin friction coefficient shows two minimums between x/c = 0.5 and x/c = 0.65 where $C_f \rightarrow 0$. In this region, the flow is reversed by a small amount, as can be seen in Figure 7.7(c), where the mean x-wall shear stress exhibits very small negative values. Beyond this region there is a short period of recovery (increase in C_f) and flow reattachment takes places. The friction coefficient reaches a peak at x/c = 0.8 and then starts to decrease again further downstream. This is consistent with the existence of a small adverse pressure gradient in this vicinity. In refinedPiradeepanDSMG the skin friction reaches its minimum near x/c = 0.7 and takes negative values of mean x-wall shear stress, indicating flow reversal past this point. For about 30% of the chord flow is reversed in both refinedPiradeepanDSMG and coarseDSMG, which suggests the formation of small separation bubbles near the trailing edge of the airfoil.

The magnitude of mean skin friction coefficient computed by LES on the upper surface of the airfoil in Figure 7.7 ($1 < C_f \times 10^{-3} < 2$) is very close to that computed in the DNS of Shan et al. (2005) for a NACA 0012 airfoil at an angle of attack of 4^o to the flow. The experimentally obtained values of skin friction with the Clauser chart method at the two locations near the trailing edge fall in between the predictions by RSM and LES. As was shown in Figure 6.30 the experimental velocity profiles had developed to that of a turbulent boundary layer in this vicinity, where the log-law had been re-established.

Concave and convex walls

The variations of mean skin friction coefficient on the concave wall and convex wall are shown in Figure 7.8(a) and 7.8(c), respectively. The corresponding distribution of mean x-wall shear stress on the concave wall is shown in Figure 7.8(b). The results are presented for all simulations conducted with DSMG model, and the RANS computations with RSM. The experimental data shown was obtained from the investigations of the developing turbulent boundary layers on the concave and convex walls of the duct by Mokhtarzadeh and Yuan (2002).

On the concave wall, the wall friction is expected to drop in the straight section between stations 1 and 2 (X/H = 0 and X/H = 1). This effect is enhanced due to the presence of an adverse pressure gradient. Between stations 2 and 3 an overall rise in C_f is attributed to the effect of concave curvature which overcomes the opposite effects of pressure gradient here. Between stations 3 and 4, the effect of curvature is still dominant, causing an increase in wall

friction. The general trend described above for the experiments on the concave wall is computed correctly across all computations. In coarseDSMG the skin friction rapidly decreases to a minimum value of about zero before $X/H = 1$ (station 2). The results from LES on the coarse grid suggest that the flow has separated in this region and is reversed, just before the start of concave curvature. The computed velocity field (shown later) indicates that the reattachment takes place shortly after station 2. As was stated earlier, the prediction of this separation is attributed to the sudden change in streamwise grid spacing in this region. The refinedPiradeepanDSMG simulations also show similar features but the location and extent of separation are different (Figure 7.8b). The results from refinedDSMG also indicate that the skin friction decreases to a minimum value near $X/H = 0.5$. But, although the flow is retarded upstream of the concave curvature, the positive values of x-wall shear stress suggest that flow does not reverse in this case. The local variations seen in the profile of C_f beyond station 2 for refinedDSMG and refinedPiradeepanDSMG indicate that a turbulent boundary layer is developing on this surface. In general, there are quantitative differences between the computed skin friction and those obtained in the experiments by the Clauser chart approach. It has been reported that while the Clauser chart method is accurate for equilibrium boundary layers, it can result in significant error when applied to non-equilibrium situations (Lund and Moin, 1996). The boundary layers predicted by the present simulations are close to separation, or have separated, and, therefore, lack of conformity with the law of the wall may be attributed to this.

On the convex wall (Figure 7.8c), a favourable pressure gradient exists between stations 1 and 3, that results in an increase in friction coefficient in this region. At station 4 the wall friction falls to nearly zero, attributed to flow separation from this wall. The effects of this separation are also observed in the pressure profile on the convex wall between stations 3 and 4 in Figure 7.6. The wall friction increases at station 5 after reattachment. In general, the predicted profiles of mean skin friction coefficient are consistent across all computations, including RANS. The values are also comparable with the experimental data, but notable differences exist. In the RSM predictions, the distribution of C_f indicates that flow does not separate from the convex wall. In coarseDSMG a similar profile is observed up to about station 3. However, there is a minimum in the profile of C_f just before station 4, followed by a small peak and a second minimum just after station 4. This is consistent with the plateau observed in the static pressure distribution in this region. These results suggest that on the convex wall flow separates before station 4 and reattaches before station 5. The small peak between the two minimums is indicative of a recirculation zone. In refinedPiradeepanDSMG the distribution of C_f indicates that the flow separates earlier, past station 3, from the convex wall. The results

from refinedDSMG are similar to RSM, in that there is no indication of separation from the convex wall in the profile of C_f.

7.2.2.3. Airfoil boundary layer predictions

Mean velocity profiles

Figure 7.9(a-f) presents the predicted mean streamwise velocity at different locations on the upper surface of the airfoil. Comparisons are made with the present experimental results. With the RSM, the predicted boundary layer thickness is very thin near x/c = 0.44, but starts to increase with streamwise distance and reaches a maximum thickness of about 10 mm near the trailing edge. The boundary layer thicknesses resolved in coarseSMG are considerably higher than those predicted in the other computations; they provide poor comparisons with the experiments. This is evident from x/c = 0.44 through to x/c = 0.98, and is attributed to a combination of the effect of using a coarse grid and the standard Smagorinsky SGS model, which does not account for the local length scales when modelling the missing interactions between the resolved and unresolved parts of the flow. The effect of the model may be deduced by comparison of these results with those of coarseDSMG and coarseDKET, where the boundary layer thicknesses are considerably smaller than coarseSMG. The effect of the grid resolution is also apparent, that is, the boundary layers computed by refinedPiradeepanDSMG and refinedDSMG are thinner than those on the coarser grid, especially beyond x/c = 0.74.

At x/c = 0.44 and x/c = 0.64, the velocity profiles predicted with the dynamic SGS models are in good comparison with the experimental profiles. Beyond x/c = 0.64, the differences between the simulations and also with experiments increase. The differences in the profiles originate from the degree by which the separation and reversed flow are predicted. The boundary layer thicknesses resolved in refinedDSMG, with a considerably finer near-wall grid resolution in the spanwise direction are the closest to the experiments, especially near the trailing edge of the airfoil. In this simulation, however, the flow reversal is not computed near the trailing edge, as apparent in the velocity profile close to the wall and the distribution of mean x-wall shear stress in Figure 7.7(c). Despite the improvements shown by LES on the finest grid, differences still exist in the overall shape of the computed profiles especially close to the trailing edge at x/c = 0.93 and 0.98. It is observed that, after the recovery in C_f near x/c = 0.65 (see Figure 7.7b), the mean velocity profile predicted by refinedDSMG starts to

resemble the velocity profile of a turbulent boundary layer, but does not become as fully established as in the experiments. The development of the boundary layer predicted by refinedDSMG can be seen more clearly in figure 7.10. The numerical simulations of Alam and Sandham (2000) and the experiments of Castro and Epik (1998) have shown that the log-law may re-establish after a considerable distance after flow reattachment. In the present computations the Clauser chart representations of the computed velocity profiles (Figure 7.11) for RSM and refinedDSMG, indicate that the flow leaves the airfoil into the wake before the log-law is established in the reattached boundary layer.

Streamwise turbulence intensity

The profiles of streamwise turbulence intensity on the upper surface of the airfoil are shown in Figure 7.12(a-f). Experimentally, it is observed that the location of the peak fluctuations moves towards the wall as distance from the leading edge increases. In LES this is effect is only observed in refinedDSMG, which also shows a distinct double peak after $x/c = 0.83$ with the larger peak located nearer to the wall. In general, for $x/c = 0.44$ the results from the finest grid (refinedDSMG) are in good agreement with the experiments and display a peak value of *Urms* of about 3% of the mainstream velocity. The profiles from coarse LES and RANS predict a larger turbulence region near the wall with higher magnitudes of the peak. At $x/c = 0.64$ differences appear between the turbulence intensity profiles predicted by refinedDSMG and the experiment. These coincide with the region where a minimum wall friction and nearly zero x-wall shear stress were computed as shown in Figure 7.7(c). The differences persist at $x/c = 0.74$ and 0.83, but become smaller at $x/c = 0.93$ where the profile from refinedDSMG matches more closely to that of the experiment. In general, the peak turbulence intensities computed on the finest grid were about 15% larger than the experiment at $x/c = 0.93$ and nearly 40% larger compared to the experiment at $x/c = 0.98$. In RSM the predicted magnitudes of peak turbulence intensity are closer to the experiment although the extent of the turbulent region is considerably greater. The discrepancies in the results of coarse LES as compared to refinedDSMG and the experiment are attributed to the increase in turbulent fluctuations in the region of separation and reversed flow that has been computed on the upper surface of the airfoil in these cases. In Figure 7.12(g) the predicted profiles of streamwise turbulence intensity by refinedDSMG are grouped together at the corresponding locations on the upper surface of the airfoil. The profile thicknesses increase with increasing streamwise distance along the chord of the airfoil. There is a significant change in the peak of the profile of

streamwise turbulence intensity between x/c = 0.44 and x/c = 0.64 which is similar to that seen in the experiments.

Experimental data was not available on the upper surface of the airfoil for normal and spanwise turbulence intensities, and turbulence shear stress. Therefore, in the discussion that follows, the results of the computations on the finest grid (refinedDSMG) are used as reference when discussing these parameters.

Normal, spanwise intensities and turbulence shear stress

A comparison of the profiles of normal turbulence intensity on the upper surface of the airfoil is presented in Figure 7.13. The corresponding comparisons of the profiles of spanwise turbulence intensity are shown in Figure 7.14. As with the streamwise turbulence intensity, the profiles of normal and spanwise turbulence intensities in refinedDSMG have a small peak near x/c = 0.44, which then increases considerably in magnitude by x/c = 0.83. The profiles generally become thicker and turbulence intensity increases with distance. These variations are consistent with the increase in thickness of the boundary layer on the upper surface of the airfoil. The results of the computations with refinedDSMG suggest that the increase in turbulent fluctuations near the wall (especially near the trailing edge) is more evident in the streamwise component of turbulence intensity. It can also be noted that the magnitudes of streamwise turbulence intensity are higher than the normal and spanwise components, at the corresponding locations. The computed profiles of turbulence shear stress $-\overline{u'v'}$ are compared at the same locations on the airfoil in Figure 7.15. The findings here with regards to the performance of the different computations are consistent with those discussed for the turbulence intensity profiles.

Further comments

The influence of grid resolution on the resolved profiles of streamwise, normal and spanwise turbulence intensity on the upper surface of the airfoil is apparent across the LES cases in Figure 7.12, 7.13 and 7.14. The simulations on the finest grid (refinedDSMG) generally compute a thinner profile of turbulence intensity and a lower magnitude in its peak. LES on the coarser grids predicts thicker profiles of spanwise, normal and streamwise turbulence intensity with higher magnitudes of the peak value. The effect is more pronounced towards the trailing edge and was attributed to the differences in the thickness of the resolved boundary

layer on the surface of the airfoil. In coarse LES the presence of a large separation region that occupies a considerable portion of the upper surface of the airfoil is computed, which is the main reason for the high levels of turbulence in these simulations near the trailing edge. In general, the results from RSM indicate high levels of turbulence intensity, for example, the predicted magnitude of streamwise fluctuations exceeded the experimental values by more than 50% at $x/c = 0.44$ as can be seen in Figure 7.12(a). The prediction by RSM, however, is improved further downstream, but the thickness of the profile is still greater in comparison to those of the experiment and refinedDSMG. The results from coarseSMG were poorer than the simulations that adopted dynamic SGS models, in comparison to the experiment. The predicted boundary layer velocity and turbulence profiles with refinedPiradeepanDSMG, in which the grid was refined with double the number of nodes in the spanwise direction ($100 < \Delta z^+ < 300$ near the wall for about 80% of the airfoil), showed little improvements when compared to coarseDSMG. However, the predictions were substantially improved in refinedDSMG, where $\Delta z^+ < 50$ over most of the airfoil.

7.2.2.4. The near-wake and stations 2 to 5: mean velocity and wake parameters

The profiles of computed streamwise velocity in the wake and at stations 2 to 5 are presented in Figure 7.16(a-c). The variations of mean streamwise velocity across the whole cross-section of the duct are shown in Figure 7.16(d). Comparisons are made with the experimental results from the present investigation and also those of Piradeepan (2002). It should be noted that the calculations of the present wake start with the differences between the prediction and experiment at the trailing edge, which is believed, at least partly, to be responsible for the differences in the wake that will be evident in the following discussion. As was already mentioned in the review of the previous work, in contrast to this approach, Narasimhan et al. (1991) and Tulapurkara et al. (1996) placed the inlet boundary conditions at the trailing edge, excluding the upstream boundary layers.

Mean streamwise velocity component in the wake

The previous studies showed that relative to the duct centre line the wake is shifted towards the convex wall at stations 2 and 3, and then towards the concave wall at stations 4 and 5. This was confirmed by the present simulations, but only qualitatively. In general the computed shift of the wake centre above the centre line of the duct in the near-wake region (Figure 7.16a,b) is always higher than the experimental one. In coarse LES with the SMG model, the wake centre

is shifted towards the convex side by approximately 20 mm at station 2, whereas in the experiments this is measured to be 10 mm. Close to the trailing edge of the airfoil at x/c = 1.05, coarseSMG, DSMG, DKET predict a small shift of the wake centre towards the convex wall, a feature not seen in the experiments nor significantly in refinedDSMG (Figure 7.16a). The prediction of the wake centre is improved in refinedDSMG, but differences remain at x/c = 2 and further downstream. In comparison to RSM, LES on the coarser grid resolves an increased wake width between x/c = 1.05 and x/c = 2 (Figure 7.16a,b), a feature that is consistent throughout the downstream stations (Figure 7.16c). In the near-wake coarseSMG predicts a considerably enhanced profile, especially on the inner side of the wake with a larger velocity defect. Furthermore, it is noted that the dynamic models on the coarse grid compute a smaller velocity defect in the near-wake which remains the case in the downstream stations. The peak in the wake as predicted by coarse LES has reduced considerably in magnitude by station 5, with less distinguishable features.

As already seen, there were some differences between experiments and numerical predictions on the airfoil especially near the trailing edge, where the prediction in the case of coarse LES had worsened and thus led to larger differences in the wake. In general, the predictions with coarse LES close to the trailing edge of the airfoil are consistent with the poor boundary layer predictions observed in these cases. In coarse DSMG and coarse DKET, it appears that there is greater mixing and interactions with the outer inviscid fluid, thus resulting in a more uniform velocity in the wake at all locations. The profiles predicted by RSM are less susceptible to change as distance is increased from the trailing edge.

The wake features are generally depicted better by LES on the finer grids. Closer comparisons of the near-wake profiles are also shown in Figure 7.16(a,b), where they are aligned with respect to the wake centre. Note that this has not been done for coarseSMG, DSMG and DKET due to the poorer predictions and larger differences in these cases. In refinedDSMG and refinedPiradeepanDSMG, the maximum velocity defect is over predicted at x/c = 1.05 and 1.10, but is computed better after x/c = 1.22. The results from refinedDSMG indicate a vast improvement in the prediction of the wake, where the profiles between x/c = 1.33 and 2 collapse well on the experimental ones. In refinedPiradeepanDSMG, the thickness of the wake on both the outer and the inner sides (especially on the inner) is over predicted. Also, the maximum of the wake velocity defect is observed to decay faster with increased streamwise distance in comparison to refinedDSMG. At station 2 to 5 the differences between different

computations, and also between computations and experiment, become larger and larger due to the effects of curvature and varying pressure gradient on the wake development.

Wake parameters

The experimental and numerical values of the wake half-width and maximum velocity defect are presented in Figure 7.17(a-d). In the near-wake (Figure 7.17a), the computed half-width in refinedDSMG shows similar values to the experimental values, but the values predicted by RSM and refinedPiradeepanDSMG are always higher. As the streamwise distance from the airfoil increases the half-width also increases due to the wake spreading. However, the rate of increase is greater in refinedPiradeepanDSMG compared to RSM, refinedDSMG and experiments. The over-prediction of the wake half-width in refinedPiradeepanDSMG persists at all downstream stations (Figure 7.17b). In RSM the growth of the wake half-width is less steep between stations 3 and 4. In general, the computed wake half-width in refinedDSMG at stations 2, 3, 4 are the closest to the values obtained experimentally. A comparison of the half-widths on the inner side and outer side (not presented here) indicated that the inner half-width is always larger than the corresponding outer half-width at all locations in the near-wake and the downstream stations.

The maximum velocity defect in the near-wake at x/c = 1.05 (Figure 7.17c) as computed by RSM exactly matches the experiment. Beyond x/c = 1.05, the computed rate of decay of velocity defect in RSM is less in comparison to the experiments; this is consistent through to stations 2, 3 and 4 (Figure 7.17d), where the RANS computation generally over predicts the maximum velocity defect. In refined LES the maximum velocity defect is overpredicted close to the trailing edge of the airfoil, but the differences disappear due to a higher rate of decay further downstream. The predictions of velocity defect with refinedPiradeepanDSMG are closer to the experiments than in refinedDSMG, especially at stations 2, 3 and 4. This is due to the increased mixing with the inviscid region in a duct with a larger spanwise extent. The performance of SGS models in the wake suggest that the dynamic models perform better than the standard SMG model on the coarse grid, but compute an increased rate of decay of velocity defect compared to the experiments. The effect of increased spanwise resolution results in a considerably smaller wake width in the near-wake, which provides better comparison to the experiments.

Mean streamwise velocity profiles across the whole duct

The profiles of mean streamwise velocity obtained across the whole duct cross-section (Figure 7.16d) show good agreement with the experimental results of Piradeepan (2002). At station 5, coarseDSMG and refinedPiradeepanDSMG have resolved the correct velocity field near the convex wall and provide good comparisons with experiment, which indicate the presence of a separation region here. Despite the improvements in the wake, the results from refinedDSMG show some deterioration near the convex wall, by predicting a similar profile to RSM at station 5, which points to a lack of prediction of separation in this region. This is believed to be due to the shortened spanwise extent of the flow domain, the absence of side walls and the imposition of periodic conditions.

Figure 7.16(e) shows the profiles on the concave wall. The boundary layer velocity profiles are better predicted at stations 3, 4 and 5 by the refined grids than those on the coarser grid, which indicate the response to increased wall normal and spanwise resolution. At station 2 there is good agreement between the profiles of RSM, refinedDSMG and refinedPiradeepanDSMG. The profiles computed in coarseDSMG are indicative of a boundary layer close to separation and are consistent with the plateau in the pressure profile computed here in Figure 7.6. At station 3, the near-wall profile computed by refinedDSMG is in good agreement with the experimental results. Further downstream at stations 4 and 5 the profiles predicted by refinedDSMG and RSM diverge away from the experiments, whereas those computed by refinedPiradeepanDSMG present a closer comparison. This better comparison can in part be attributed to the better prediction of the secondary flow in the duct by this method, a feature that will be discussed later.

Mean normal velocity component in the near-wake

The computed profiles of mean normal velocity component in the near-wake are presented in Figure 7.18. The distributions are generally similar among the computations. Comparisons with available experimental data in the near-wake at x/c = 1.05 and at station 2 indicate general agreement in the shape of the profile, but the simulations compute a higher magnitude of normal velocity compared to the experimental value at these locations. These results suggest that the velocity vector approaching the inner side of the wake from the trailing edge is facing down, whereas on the outer side the resulting vectors are facing up. These results are typical for the adjoining boundary layers from the upper and lower surfaces of a symmetrical

airfoil. Further downstream the profile of normal velocity develops a nearly symmetrical distribution about the centre line of the wake. It is also noted that the normal velocity is entirely positive from $x/c = 1.33$, due to the effect of the bend.

7.2.2.5. The near-wake and stations 2 to 5: streamwise turbulence intensity

Figure 7.19 presents the profiles of numerical streamwise intensity in the near-wake and at stations 2 to 5, including comparisons with the experimental data.

Streamwise turbulence intensity in the wake

The profiles of streamwise intensity in the near-wake show a characteristic double-peak, where the larger peak occurs on the inner side (Figure 7.19a,b). The quality of the results for the turbulence field can, in part, be related to the quality of the predicted velocity field. Up to station 2, in comparison to RSM, the existence of a double peak in the profile of streamwise intensity is more pronounced in the large eddy simulations. Turbulence intensity is over-predicted considerably on the inner side by the dynamic SGS models in coarse LES. The SMG model predicts an exaggerated double peak on the inner and outer sides of the near-wake, which then leads to further deterioration in the downstream stations of the duct; thus omitted from Figure 7.19(c).

The results for coarseSMG correlate well with the results for turbulence intensity in the airfoil boundary layer predicted by this simulation, and are a further display of the limitations of the standard SMG model in predicting wake flows, when used in conjunction with coarse grids. Further downstream of station 2, the streamwise turbulence intensity profiles computed by coarseDSMG are washed out considerably and are not noticeable at stations 4 and 5. Despite the increase in grid resolution in refinedPiradeepanDSMG, the computed distribution of turbulence intensities does not vary significantly from coarseDSMG in the near-wake, but owing to these improved resolutions, the turbulence profiles are better resolved compared to coarseDSMG downstream of station 2. The results suggest that a reduction in the spanwise grid spacing on the upper surface of the airfoil, from $200 < \Delta z^+ < 600$ on the coarsest grid to $100 < \Delta z^+ < 300$ in refinedPiradeepan, does not significantly improve the prediction of streamwise turbulence in the near-wake.

The refinedDSMG computations indicate vast improvements in the predictions of streamwise turbulence intensity in the near-wake, where the peaks on the inner and the outer sides are well resolved and are in close agreement with the double peak structure of the experimental profile. The effects of increased spanwise resolution on the surface of the airfoil, from $100 < \Delta z^+ < 300$ in refinedPiradeepanDSMG to $30 < \Delta z^+ < 50$ in refinedDSMG, have resulted in considerably better predictions of turbulence in the wake, which stem from the improved results on the upper surface of the airfoil in Figure 7.12. At stations 3 and 4 (Figure 7.19c), it is observed that the double peak still persists, with the larger peak located on the inner side of the wake. The predicted results by refinedDSMG indicate that the streamwise intensity at the wake centre reduces in the streamwise direction, by 78% between $x/c = 1.05$ and $x/c = 2$, by 47% between stations 2 and 3, and by 32% between stations 3 and 4. There is further reduction in turbulence intensity at station 5 in the wake region compared to station 4. The predicted and experimentally measured profiles in the wake region at station 5 show completely different patterns. The results from refinedDSMG and RSM tend to agree with each other, but deviate significantly from the experiments above the centreline of the duct, whereas refinedPiradeepanDSMG follows a better trend.

Streamwise turbulence intensity profiles across the whole duct

The computed streamwise intensity profiles across the whole cross-section of the duct are shown in Figure 7.19(d). There is general agreement between RSM and experiment in the inviscid region at stations 2-4. At station 5, the experimental and RSM profiles show greater differences particularly above $y/H = 0.5$ towards the convex wall, where the experimental values are well above the computed values.

On the convex wall at station 5, the computed turbulence field by coarseDSMG and refinedPiradeepanDSMG is in very good agreement with experiment. The enhancement of turbulence is attributed to the presence of flow separation and recirculation, which is resolved by LES. Lack of prediction of flow separation on the convex wall by RSM and refinedDSMG is evident by very low levels of turbulence demonstrated in Figure 7.19(d). These results suggest that in a large eddy simulation the application of the correct spanwise extent and presence of side walls are important factors in resolving the correct flow field. Just before this location at station 4, the results of LES predict higher levels of turbulence near the convex wall compared to RANS and those measured in the experiment. On the coarser grids the thickness of the profile in this vicinity is substantially increased. The discrepancies between

LES and experiment in this region is attributed to the earlier separation from the convex wall which is observed to take place before station 4 (closer to station 3), and also can be verified from the variation of skin friction coefficient in Figure 7.8(c). Experimentally, the flow separates slightly after the location computed by LES, and thus results in a less enhanced profile of streamwise turbulence intensity at station 4.

The effect of concave curvature on enhancing turbulence is evident in Figure 7.19(e). However, in coarse LES (coarseDSMG) the enhancement of streamwise turbulence intensity is over-predicted, especially at station 2 to 4, in comparison to the experiment. Simulations on the finer grids show considerable improvement in the prediction of streamwise turbulence intensity at these locations. At station 2, the high turbulence levels computed in coarseDSMG is attributed to the presence of separation and recirculation in this vicinity. This feature is consistent with the plateau in the profile of the pressure distribution on the concave wall as shown in Figure 7.6. With a finer grid in the region near the concave wall at station 2 the turbulence levels are significantly reduced but are still higher than in the experiment. Experimentally, it is shown that a greater width of the flow in the duct is affected by the boundary layer on the concave wall between stations 2 to 4 (Mokhtarzadeh-Dehghan and Piradeepan, 2006); this is confirmed in the simulations although the effect is somewhat over-predicted by LES on the coarse grid. The increased level of turbulence as a result of the formation of streamwise vortices on the concave wall, which are predicted by present simulations, will be discussed later in section 7.2.4.

7.2.2.6. The near-wake and stations 2 to 5: normal and spanwise intensities

The profiles of normal and spanwise intensities are shown in Figure 7.20(a-e) and Figure 7.21(a-e), respectively. The experimental data for comparison of normal turbulence intensity, in the near-wake, was only available at x/c = 1.05 and x/c = 2. Spanwise intensities were not measured in the near-wake. As before, the experimental data of Piradeepan (2002) is used for comparisons at stations 2-5.

Normal and spanwise turbulence intensity in the wake

Experimentally, the profiles of normal and spanwise turbulence intensities in the wake exhibit a single peak distribution. At x/c = 1.05, refinedPiradeepanDSMG and coarse LES predict a greater peak in normal turbulence intensity at the wake centre, whereas refinedDSMG predicts

a lower magnitude, in comparison to the experiment. The results of LES on the coarser grids consistently predict thicker profiles of normal and spanwise turbulence intensities on the inner and outer sides of the wake (Figure 7.20a,b and 7.21a,b). The computed peaks in spanwise intensity near the trailing edge of the airfoil at x/c = 1.05 are of similar magnitudes in all computations, but as with the normal turbulence intensity, the predicted profiles in refinedDSMG are thinner on the inner and outer sides of the wake. The distributions of spanwise intensity show a characteristic double peak in the near-wake (Figure 7.21a,b), with the larger peak being located on the inner side. In general, the predictions of both intensities in the near-wake are consistent with the levels seen in the boundary layer at the trailing edge of the airfoil. In refinedDSMG the maximum peak in normal turbulence intensity decreases by approximately 44% between x/c = 1.05 and x/c = 2, whereas the corresponding decrease in the experiments is 45%. The peak in spanwise intensity at x/c = 1.05 decreases by about 70% at station 2, in the refinedDSMG simulations.

It can be seen that the peak levels for both intensities are somewhat under predicted by LES at station 2, in comparison to the experiments and RSM (Figure 7.20c and 7.21c). At stations 3 and 4, the computed profiles of spanwise and normal intensity from the coarse grids engulf a greater region of increased turbulence activity in the wake. It is observed that the distributions of the normal and spanwise intensities computed by coarseDSMG are washed out in the wake at station 4 and are nearly unnoticeable at station 5. Furthermore, at stations 3 and 4, the patterns of both intensities, in refinedDSMG are in general agreement to RSM and corresponding experimental profiles. However, at station 5 the results of RSM and refinedDSMG diverge away from the experimental profile. LES on the coarser grids with full spanwise extent provides better comparisons with the higher turbulence intensity levels measured above the centre line of the duct.

Normal and spanwise turbulence profiles across the whole duct

The computed normal and spanwise turbulence intensity profiles obtained across the whole cross-section of the duct are presented in Figure 7.20(d) and 7.21(d), respectively. The corresponding comparisons near the concave wall are shown more clearly in Figure 7.20(e) and 7.21(e) for both intensities. The general agreement between the main characteristics of the predicted and experimental profiles is similar to those seen in the distributions of streamwise turbulence intensity. At station 5 near the convex wall, the turbulence intensity values computed by LES on the coarser grids are similar to the experimental values, which is as a

result of flow separation on this wall. However, at station 4, for both normal and spanwise components, the profiles predicted by coarseDSMG and refinedPiradeepanDSMG, display significant discrepancies near the convex wall with over-predicted turbulence intensity levels. As was stated earlier, this is attributed to the effect of flow separation in the upstream.

On the concave wall there are significant differences between experiments and the profiles of normal and spanwise intensity computed by coarseDSMG (SMG and DKET not shown). In general, LES on the refined grids shows better agreement with the experimental results between stations 2 to 4 on this wall.

7.2.2.7. The near-wake at stations 2 to 5: turbulence shear stress

The computed profiles of normalized turbulence shear stress $-\overline{u'v'}$ are presented in Figure 7.22(a-e).

Turbulence shear stress in the wake

The enhancement of shear stress on the inner side of the wake and its suppression on the outer side are predicted qualitatively by all the simulations. Quantitatively, however, the results of coarseSMG, DSMG and DKET and refinedPiradeepanDSMG indicate large discrepancies in the near-wake where the positive and negative peaks are overpredicted. On the coarser grids, close to the trailing edge of the airfoil, the computed value of the peak on the outer side is greater than on the inner side. The results from refinedDSMG are in good agreement with the experimental data between $x/c = 1.05$ and $x/c = 2$, where the peak and the shape of the profiles are accurately computed. Comparisons between the experiments and refinedDSMG at station 2 (Figure 7.22b) indicate good correlation in relation to the positions of the predicted and measured negative and positive peaks.

The large eddy simulations have difficulties dealing with the destabilizing effect of curvature in the wake where at station 3 this is over-predicted in all cases (Figure 7.22c). On the other hand, the stabilizing effect of curvature is better predicted by refinedDSMG even at stations 4 and 5. The results, therefore, indicate the greater effects of streamwise curvature and pressure gradient on the inner side of the wake, while the effect on the outer side is more sensibly predicted. In RSM it was observed that the suppression of shear stress on the outer side is over-predicted to such a degree that the negative peak is indistinguishable. Therefore, at

station 3, 4 and 5 the profiles predicted by RSM show a single peak on the inner side of the wake. The shift of the profile of turbulence shear stress is predicted consistently with the shift of the wake centre in the streamwise velocity profiles. The large discrepancies noted here are attributed to the difference in the predicted velocity profiles (Figure 7.16). As was discussed in Chapter 6 the gradient of the velocity profile appears in the production term of the transport equation for $-\overline{u'v'}$.

Turbulence shear stress profiles across the whole duct

The profiles of $-\overline{u'v'}$ obtained across the whole cross section are shown in Figure 7.22(d). The increase in turbulence shear stress near the convex wall at station 5, in coarseDSMG and refinedPiradeepanDSMG, is consistent with the enhancement of turbulence quantities in this region, which is as a result of flow separation from this wall. The results of refinedDSMG are similar to RSM in that a smaller peak is computed near the convex wall. At station 4, similar to the profiles of turbulence quantities, refinedPiradeepanDSMG over-predicts the magnitude of turbulence shear stress. This can be attributed to discrepancies in the location of the point of flow separation. The double peak of differing signs in the profile of the coarseDSMG is due to the prediction of reversed flow by this model.

The results for the concave wall are shown more clearly in Figure 7.22(e). LES on the coarse grid over-predicts the enhancement of turbulence shear stress. The computed values of turbulence shear stress with the finer grids are in better agreement with the experiment between stations 3 and 5. The results of refinedPiradeepanDSMG at station 4 and 5, in particular, collapse very well on the experimental profiles and surpass prediction by all other computations. The results at station 2 on this wall are consistent with computed flow retardation and separation in this region.

7.2.2.8. The boundary layer upstream of the concave curvature

To assess the development of the boundary layer approaching the concave curvature the computed profiles of mean velocity and streamwise turbulence intensity are presented at X/H = 0.49, 0.65, 0.82 and 1, in Figure 7.23(a) and 7.23(b). Comparisons are made with the present experimental data taken at X/H = 1 (station 2). The streamwise velocity profiles of refinedDSMG, refinedPiradeepanDSMG and RSM are in close agreement with each other. However, the experiments at X/H = 1 deviate from the large eddy simulations. The differences

noted here can be attributed to the way that the boundary layer development in this region is predicted. LES tends to predict a boundary layer which is closer to separation. The different nature of the boundary layer development can also be seen in the Clauser chart representation shown in Figure 7.24(a), which shows the establishment of the log-law at X/H = 1 (station 2) only experimentally. With regards to turbulence intensity, the magnitudes predicted by LES at X/H = 0.49 are very small, but increase significantly when approaching the concave curvature, surpassing the experimentally measured levels even on the finest grid. In contrast, the profiles of streamwise intensity predicted by RSM show, initially, much higher values for the turbulence intensity and slower changes with distance.

7.2.2.9. Spanwise variations in the near-wake

The computed spanwise variations of mean streamwise velocity and streamwise turbulence intensity in the wake at x/c = 1.10, 1.33, and 2 are presented in Figure 7.25(a-c) and 7.26(a-c) for refinedPiradeepanDSMG. The solid and dashed lines represent the profiles on the inner and outer sides of the wake, respectively. At x/c = 1.10, the distribution of mean velocity (Figure 7.25a) indicates the presence of large spanwise variations on the inner and outer sides of the wake. These display a well organised peak valley wavy structure as measured in the experiments in Figure 6.25. Experimentally, it was found that the spanwise variations decay with increased streamwise distance from the trailing edge of the airfoil, where the decay on the inner side was at a slower rate than the corresponding outer side.

The distributions of streamwise turbulence intensity in Figure 7.26 indicate distinctly higher magnitudes in the peak and troughs on the inner side of the wake, compared to the outer side. This is especially evident at station 2 (Figure 7.26c) where the variations on the outer side of the wake have decayed considerably compared to those on the inner side. The wavelength of the spanwise variations varies by about 20-40 mm in the near-wake. These findings are in agreement with the present experiments. The peak valley wavy structure is attributed to the presence of streamwise vortices in the wake. The decay of the amplitude of spanwise variations with streamwise distance, as measured experimentally, is consistent in the computations. However, in the experiments, smaller spanwise variations were measured in the outer side of the wake, than computed in the large eddy simulations.

The corresponding spanwise profiles for refinedDSMG in the near-wake are shown in Figures 7.27(a-c) and 7.28(a-c). In these simulations a reduced spanwise extent of 0.5c was adopted.

The findings are similar to those of refinedPiradeepanDSMG, however the predicted amplitude of spanwise variations on the inner side of the wake are lower. Furthermore, the results predicted by refinedDSMG suggest that the rates of decay of variations on the inner and outer sides of the wake are more comparable.

7.2.3. Contour plots

In the following sections the contour plots of mean static pressure and mean velocity magnitude obtained in the *x*-*y* and *y*-*z* planes are presented and discussed.

7.2.3.1. Static pressure

Figure 7.29, 7.30 and 7.31 show the static pressure distribution in the *x*-*y* and *y*-*z* planes of the flow domain for coarseDSMG, refinedPiradeepanDSMG and refinedDSMG, respectively. The airfoil wake develops in a curved flow of non-uniform pressure, especially in the radial direction. The experimental and numerical investigations suggest that the effect of the airfoil on the static pressure distribution in the duct is small. However, the effect of the bend on the static pressure distribution on the airfoil is evident in these figures. The existence of lower pressures on the upper surface, higher pressures on the lower surface and the shifting of the stagnation point to the lower surface of the leading edge, due to the effects of the bend, are also evident.

The static pressure contours in the *y*-*z* plane are generally in agreement with each other in the three cases of simulations shown. The results at stations 2 to 5 indicate, generally, insignificant variations in the spanwise direction, although in the case of coarseDSMG (Figure 7.29) and refinedPiradeepanDSMG (Figure 7.30) some variations are noticeable near the convex wall at station 4 and near the concave wall at station 3. In contrast, a high degree of uniformity is observed in the spanwise distributions of static pressure for refinedDSMG (Figure 7.31), which is attributed to the absence of side walls in this simulation. In general, the contours plots indicate that the region of positive static pressure (concave side) is significantly greater than the region of negative static pressure (convex side). Furthermore, the changes in the static pressure distribution in the radial direction near the convex curvature and between stations 2 to 4 are more significant than the corresponding concave side.

7.2.3.2. Velocity magnitude

The contours of mean velocity magnitude in the *x-y* plane and *y-z* planes of the flow domain are presented in Figure 7.32, 7.33 and 7.34.

Upstream of the curvature, the velocity magnitude on the convex side of the bend is significantly higher than the corresponding concave side. On the convex side, the flow accelerates between stations 1 and 3 and decelerates between stations 3 and 4, which reflects the presence of a favourable and then an adverse pressure gradient here. Upstream of the bend, the boundary layer growth on the concave wall is greater than the corresponding one on the convex wall. In the downstream tangent, the boundary layer on the convex wall grows more rapidly than the corresponding one that develops on the concave wall.

In coarseDSMG (Figure 7.32), the contour lines near station 2 on the concave wall indicate the formation of a separation bubble. The velocity magnitudes here suggest that flow separates before station 2 and reattaches before station 3 on this wall. This feature is not apparent in refinedDSMG (Figure 7.34) and refinedPiradeepanDSMG (Figure 7.33) computations, where the flow is retarded only by a small amount in the region close to station 2.

The response of the grids to the developing boundary layer on the convex wall downstream of the curvature is also different. In coarseDSMG and refinedPiradeepanDSMG a thicker boundary layer is computed on the convex wall than in refinedDSMG. On the full extent grids the contour levels indicate the formation of a separation bubble close to the convex wall. The bubble is more distinct in coarseDSMG than refinedPiradeepanDSMG, but not computed in refinedDSMG. As stated earlier, in refinedDSMG the discrepancies with the experiments in this region is related to the reduced spanwise extent of the domain and the absence of side walls. For coarseDSMG and refinedPiradeepanDSMG, downstream of station 5 the boundary layer thickness on the convex wall grows to about 40-50% of the duct height, whereas in refinedDSMG the maximum thickness is about 20% of the duct height. The results suggest the inclusion of the side walls have greater influence than the grid resolution in predicting the downstream effects of separation.

The contour plots for the duct cross-section (in the *y-z* plane) show that the central region of the duct is free from spanwise variations and that the effect of the side walls are limited to a narrow region of the flow next to the wall. Better resolution of the velocity field for the

refinedPiradeepanDSMG is evident. In refinedDSMG, there are no spanwise variations and absence of flow separation on the convex wall is also apparent.

7.2.4. Vector plots

The velocity vector plots in the *x*-*y* (in the mid-plane) and *y*-*z* planes are presented in Figure 7.35(a-g), 7.36(a-g) and 7.37(a-g). The vector field is shown at an instant in time, where a statistically steady state condition for turbulence has been achieved in the simulations.

7.2.4.1. Velocity vectors near the airfoil in the *x*-*y* plane

These results show more clearly the features already indicated through the discussions of the velocity and pressure contours, as well as the line plots. Flow separation and reversal is observed on the airfoil in coarseDSMG (Figure 7.35a). Close to the trailing edge of the airfoil the separation bubble extends a considerable distance along the chord. The streamwise length and vertical thickness of the computed separation bubble is about $0.1c$ and $0.026c$, respectively. In refinedPiradeepanDSMG (Figure 7.36a), a smaller separation bubble is computed further upstream from the trailing edge, with a length and thickness of approximately $0.026c$ and $0.007c$, respectively. Again the results in this region are consistent with the distributions of mean skin friction coefficient, and mean streamwise velocity observed in this simulation. In contrast to the two coarser grids, the velocity vectors in refinedDSMG do not indicate any reversed flow near the trailing edge of the airfoil (Figure 7.37a). Although the flow is retarded and is close to separation, the instantaneous vectors do not show any evidence of a sizeable separation. This absence of separation is a direct consequence of reduced spanwise grid spacing on the upper surface of the airfoil. The airfoil boundary layers are, however, resolved better in refinedDSMG leading to substantially improved profiles in the near-wake. The over-predicted airfoil boundary layer thicknesses, enhanced turbulence profiles and poor comparisons with the experiments in the near-wake on the two coarser grids can in part be attributed to the flow phenomena observed on the upper surface of the airfoil in these cases (Figure 7.35a, 7.36a).

7.2.4.2. Velocity vectors near the convex and concave walls in the *x*-*y* plane

The velocity vector plots of coarseDSMG indicate flow separation from the convex wall just before station 4 in Figure 7.35(b). The flow reattachment is observed to take place at a short

distance before station 5. A similar pattern is seen near the convex wall for refinedPiradeepanDSMG in Figure 7.36(b), but flow separates earlier from the convex wall and reattaches shortly downstream. These provide support for the discussions provided earlier for the existence of a plateau in the distribution profile of static pressure on this wall, changes to the mean streamwise velocity and also the enhancement of turbulence quantities in the region near stations 4 and 5. The results suggest that the location of the separation from the convex wall is sensitive to the grid resolution in the vicinity. In Figure 7.37(b), for simulations on the grid with reduced spanwise extent (refinedDSMG), some degree of flow retardation is observed before station 4, but the velocity vectors do not indicate separation from the convex wall and flow remains attached.

On the concave wall between stations 1 and 2, coarseDSMG predicted a small plateau in the profiles static pressure (Figure 7.6), a feature not measured in the experiments. This is attributed to the occurrence of small flow separation upstream of station 2 as indicated by the velocity vectors in Figure 7.35(c). In the velocity vectors of refinedPiradeepanDSMG and refinedDSMG (Figure 7.36c and 7.37c) this feature is not computed, although in both cases some flow retardation is observed upstream of station 2.

7.2.4.3. Velocity vectors at stations 2 to 5 in the *y*-*z* plane

The velocity vector plots in the *y*-*z* planes at stations 2-5 are presented for coarseDSMG in Figure 7.35(d-g). The corresponding vector plots for refinedPiradeepanDSMG and refinedDSMG are displayed in Figures 7.36(d-g) and 7.37(d-g), respectively. The development of secondary flow is best described in coarseDSMG and refinedPiradeepanDSMG where the flow domain includes the full spanwise extent of the duct. At station 2, the fluid is pushed from the concave wall towards the convex wall, due to the effect of higher pressure on the concave side and lower pressure on the convex side. The radial pressure gradient at station 3 results in an upwards current near the side walls, however the centrifugal effects induce flow towards the concave wall at the mid-plane. This contributes to the increase in wall friction past station 3 on the concave wall in Figure 7.8(a). A pair of counter-rotating vortices is observed at station 5, on the convex wall, as shown in Figure 7.35(g) and 7.36(g). These vortices are formed in conjunction with the secondary flow motions in a curved duct and have been reported in the large eddy simulations of Hébrard et al. (2004) and Lopes et al. (2006). In refinedDSMG there is no large secondary motion,

although small vortices are formed which are thought to develop from the thickening of the boundary layer pasts the abrupt convex curvature.

The formation of counter-rotating vortices near the concave wall is also noted. In refinedPiradeepanDSMG, small streamwise vortices are observed near the concave wall at station 2. Further downstream on the concave wall streamwise rotations become more significant and grow in size. At station 5 a well defined system of counter-rotating streamwise vortices is observed near the concave wall (Figure 7.36g). The formation of streamwise Taylor-Görtler vortices have been reported in the large eddy simulations of Lopes et al. (2006) in an *S*-shaped duct, and were found to contribute significantly to turbulence production on the concave wall. These vortices are also observed in the refinedDSMG simulations and are more distinguishable in the instantaneous velocity vector plots at stations 4 and 5 (Figure 7.37f and 7.37g). The reduced spanwise extent and periodic conditions in refinedDSMG are similar to the conditions adopted by Lopes et al. (2006). It is known that these vortices can contribute to the production of turbulence kinetic energy on the concave wall, and so, the accurate prediction of Taylor Görtler vortices on the concave surface is important in resolving the correct near-wall turbulence field. It appears that the over-prediction of turbulence is due to two main factors, one is the state of the flow in relation to separation and the other is the formation of longitudinal vortices. The results presented earlier for turbulence intensities showed over-prediction at station 2 on the concave wall. This was particularly the case for coarseDSMG which predicted a small flow recirculation zone. For the finer grids in refinedDSMG and refinedPiradeepanDSMG, in which this separation zone was not predicted, the over-prediction of turbulence was still evident to some extent.

7.2.5. Vorticity field

7.2.5.1. Spanwise vorticity (ω_z) on the duct walls

The instantaneous contours of spanwise vorticity are presented in Figure 7.38(a-d). As for the previous vector plots, the vorticity field is shown at an instant in time where a statistically steady state condition for turbulence has been achieved. The positive and negative magnitudes refer to anti-clockwise and clockwise rotations about the *z*-axis, respectively. Large spanwise vortices are observed to develop near station 4 on the convex wall, in coarse LES and refinedPiradeepanDSMG. The high magnitude of spanwise vorticity observed near station 5 is consistent with the enhancement of turbulence quantities measured in this region. Further

downstream these vortices decay in magnitude, but spread across the boundary layer occupying approximately 50% of the characteristic duct height. In Figures 7.38(a) and 7.38(b), a similar pattern is observed on the convex wall with the SMG model and the DSMG model on the coarse grid. This suggests the effect of SGS model on a coarse grid is small near the convex curvature, and that the relative size of the length scales are on average larger than the filter width (grid cell sizes) in the vicinity. The effect of grid resolution is evident in refinedPiradeepanDSMG (Figure 7.38c), where it is apparent that the smaller length scales have been resolved, especially in the downstream straight section of the duct on the convex wall. The extent and spread of spanwise vorticity on this wall is similar to that seen on the coarser grid in Figure 7.38(a,b). The formation and development of spanwise vortical structures can also be seen on the concave wall. These are more apparent in refinedDSMG compared to refinedPiradeepanDSMG and coarse LES, especially past station 5, due to the finer grid resolutions. The lack of prediction of separation from the convex wall in refinedDSMG results in a thinner region of computed spanwise vortices on this wall, in comparison to the development on the concave wall (Figure 7.38d).

7.2.5.2. Spanwise vorticity (ω_z) in the wake

The contours of spanwise vorticity in the near-wake are shown in the close-ups presented in Figure 7.38 (a-d). In general, the merging shear layers on the upper and lower surfaces of the airfoil have resulted in the formation of counter rotating spanwise vortices in the wake. The effects of curvature on the inner side of the wake compared with the outer side are evident in these figures. As with the velocity and turbulence profiles, the near-wake vorticity is also shifted above the duct centre line. The results from coarseSMG present a somewhat different pattern compared with the pattern of coarseDSMG, where the latter provides a more plausible representation of the development of dynamic vortical structures on the coarse grid. This is considered to be in response to the limitations of the standard SMG model in representing the local length scales. The effect of increased grid resolution is apparent on the finer grids. Results from the classical LES case described by refinedDSMG indicate a highly resolved vorticity field near the trailing edge, which is in direct response to the increased spanwise, wall-normal and streamwise grid resolution in the region of the airfoil. In refinedDSMG (Figure 7.38d) the spanwise vortices are still evident past station 5, whereas on the coarser grids in Figures 7.38(a-c) the effect of spanwise vorticity in the wake is nearly washed out in this region.

7.2.5.3. Streamwise vorticity at stations 2-5 in the *y-z* plane

Figures 7.39(a-c) present the contours of streamwise vorticity in the *y-z* plane at each station, for the three grids tested with the DSMG model. Consistent with the velocity vector plots shown earlier, in coarseDSMG and refinedPiradeepanDSMG, large vortical structures are formed on the convex wall at stations 4 and 5. These vortices affect a considerable region of the duct at station 5, as can be seen in Figures 7.39(a) and 7.39(b). On the concave wall, the formation of Taylor-Görtler vortices is clearly seen in these results. These structures are observed to grow in the streamwise direction, and are better resolved in the cases with the finer grids.

The streamwise vortical structures in the wake are smaller in size at station 2 and are observed to stretch in the normal direction with increased streamwise distance towards station 5. The magnitude of streamwise vorticity in the wake decays with increased streamwise distance. These findings are consistent in all the simulations. The normal shift of the wake can also be seen in these results. In general, the vorticity field is better depicted in refinedPiradeepanDSMG than coarseDSMG. In coarseDSMG the streamwise vortices in the wake are observed to wash out past station 2 (Figure 7.39a), but are still resolved on the finer grid (Figure 7.39b). In refinedDSMG the missing effect of a developed secondary flow is noted, however, the effect of increased spanwise resolution is apparent on the relative sizes of the resolved streamwise vortices in the wake (Figure 7.39c) compared to the other two grids.

7.2.5.4. Streamwise vorticity in the near-wake (*y-z* plane)

The contours of streamwise vorticity in the near-wake are presented in Figure 7.40(a,b) in the *y-z* plane for the simulations conducted on the finer grids. Close to the trailing edge of the airfoil there exists a thin band of counter-rotating streamwise vortices. The magnitude of vorticity decays with streamwise distance from the trailing edge; this is more so in refinedPiradeepanDSMG than in refinedDSMG. The vortices are stretched in the normal direction and are consistent with the location of the wake relative to the duct centre line. These results correlate well with the wavy spanwise patterns in the distributions of mean velocity and turbulence intensity, measured experimentally (Figures 6.25-6.26) and numerically (Figures 7.25-7.28).

(a)

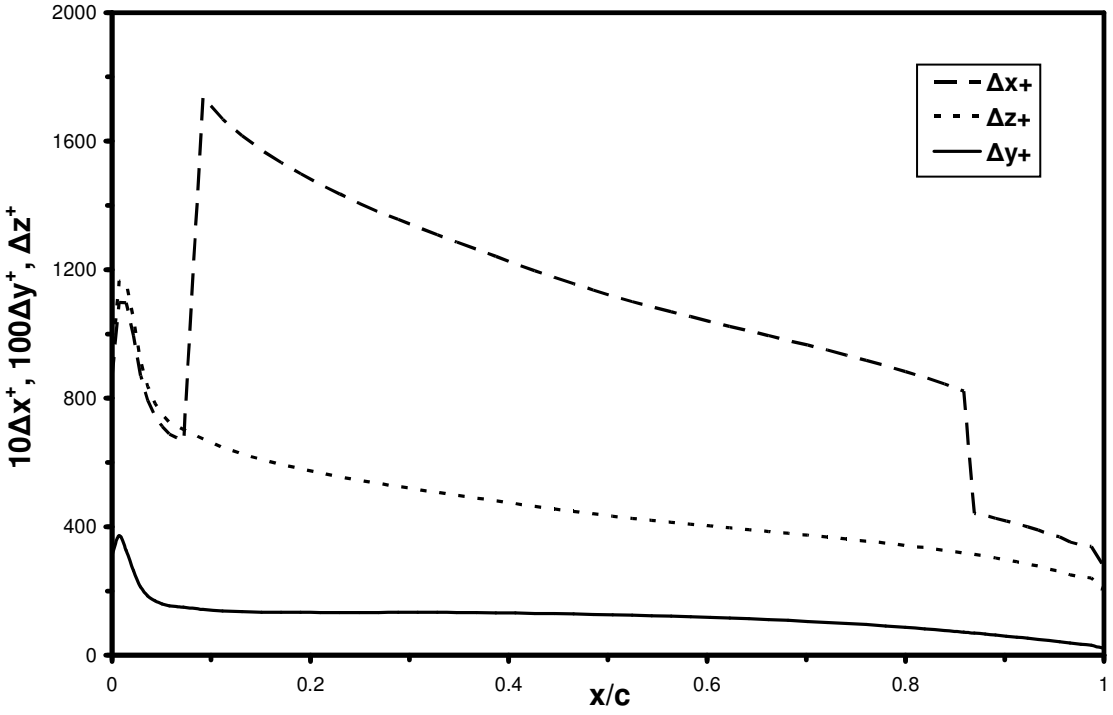

(b)

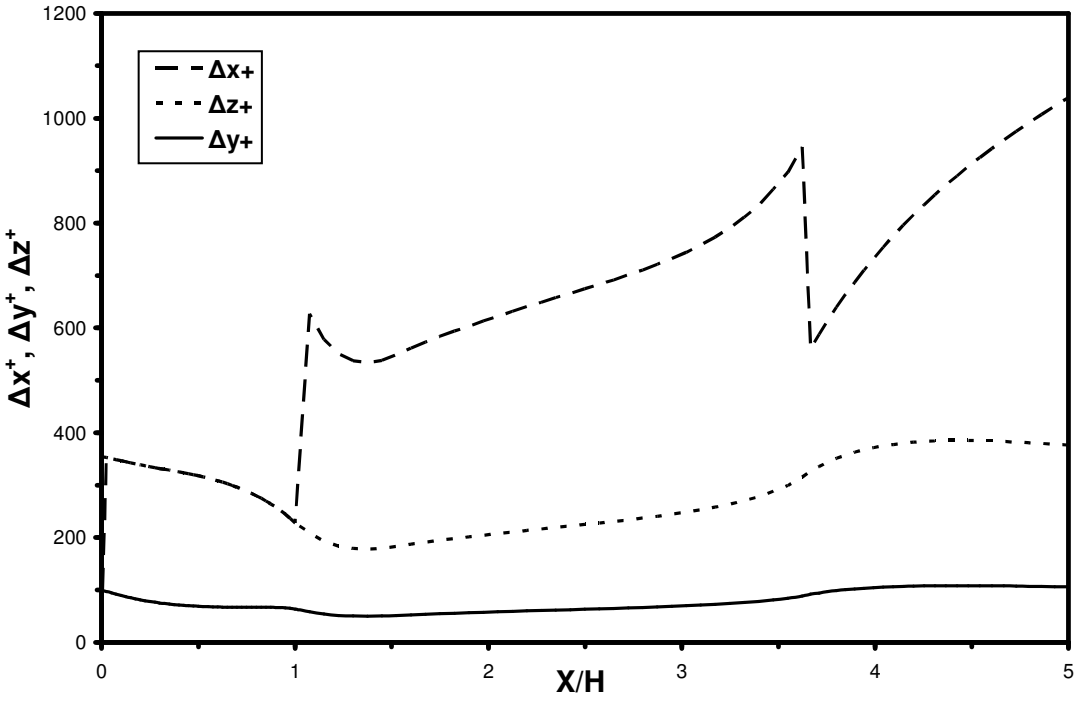

Figure 7.1: For caption see head of figure.

(c)

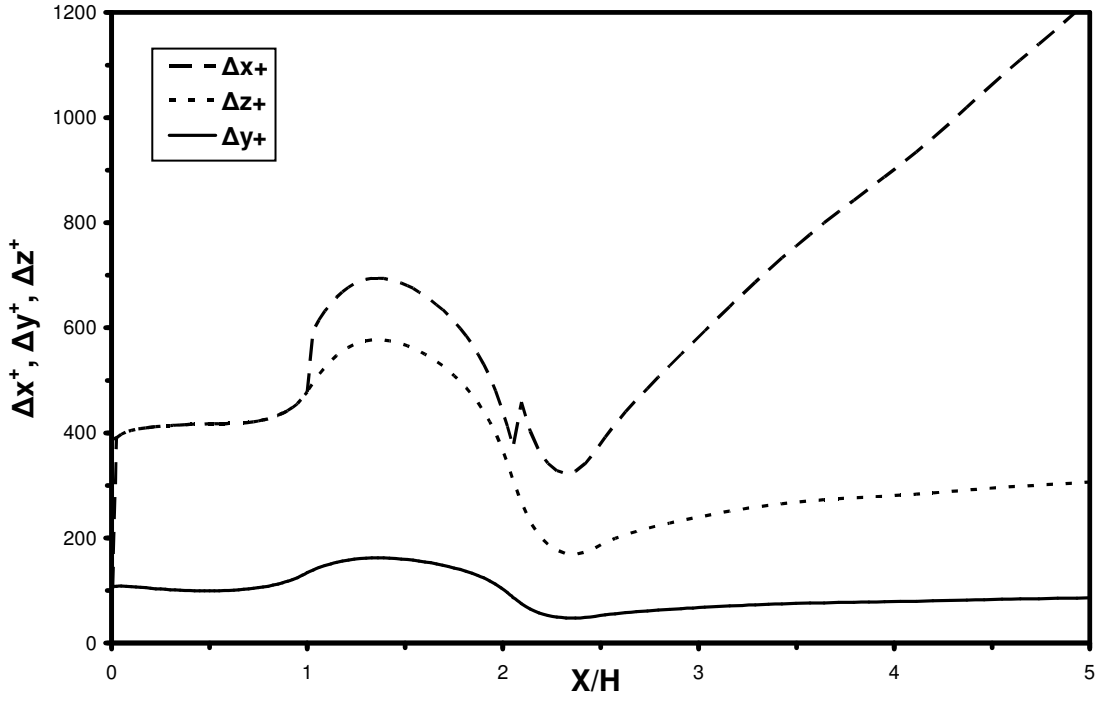

Figure 7.1: Δx^+, Δy^+, and Δz^+ distribution for coarseSMG, DSMG, and DKET: (a) upper surface of the airfoil, (b) concave wall, (c) convex wall.

(a)

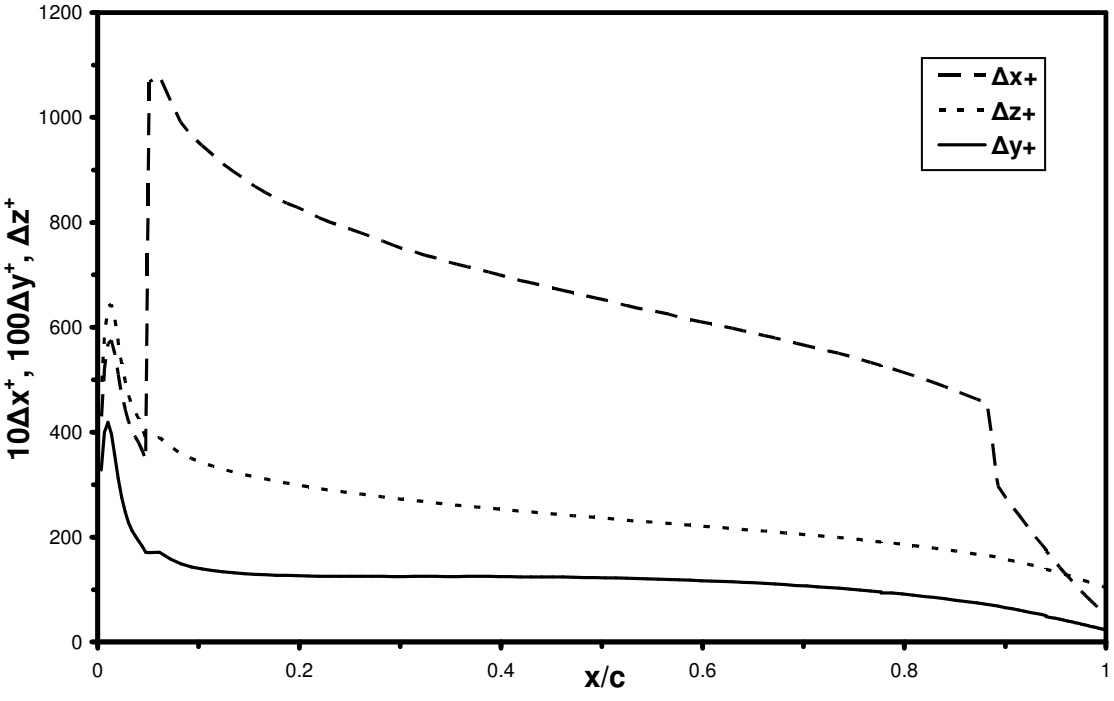

Figure 7.2: For caption see head of figure.

(b)

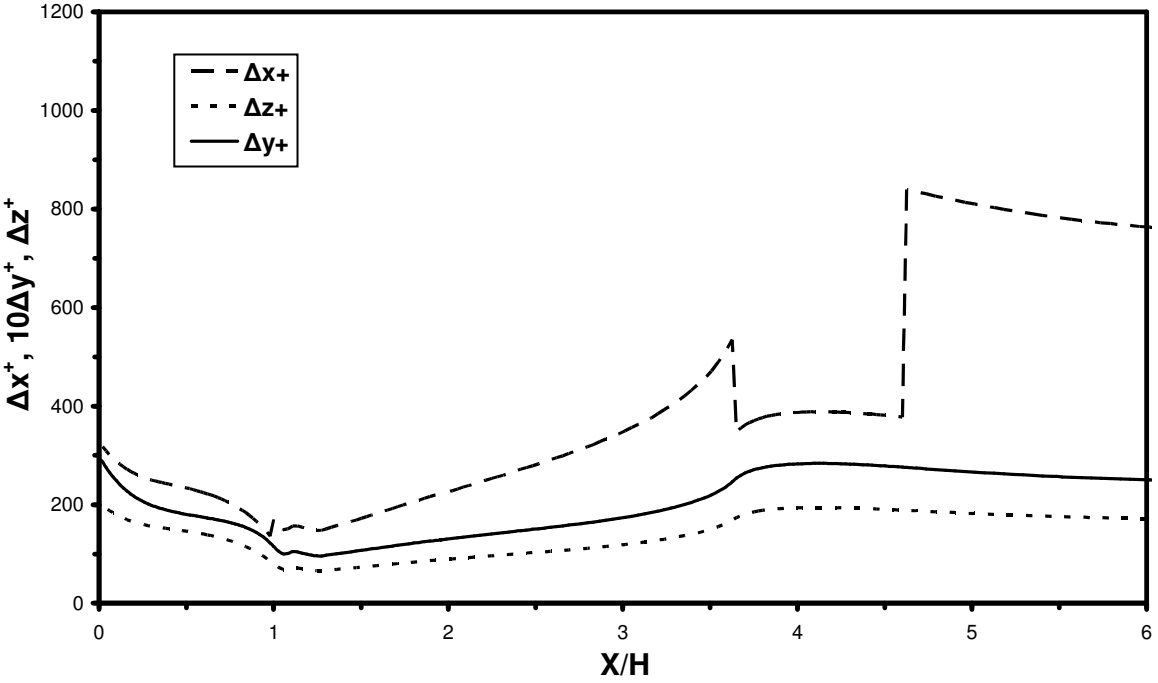

(c)

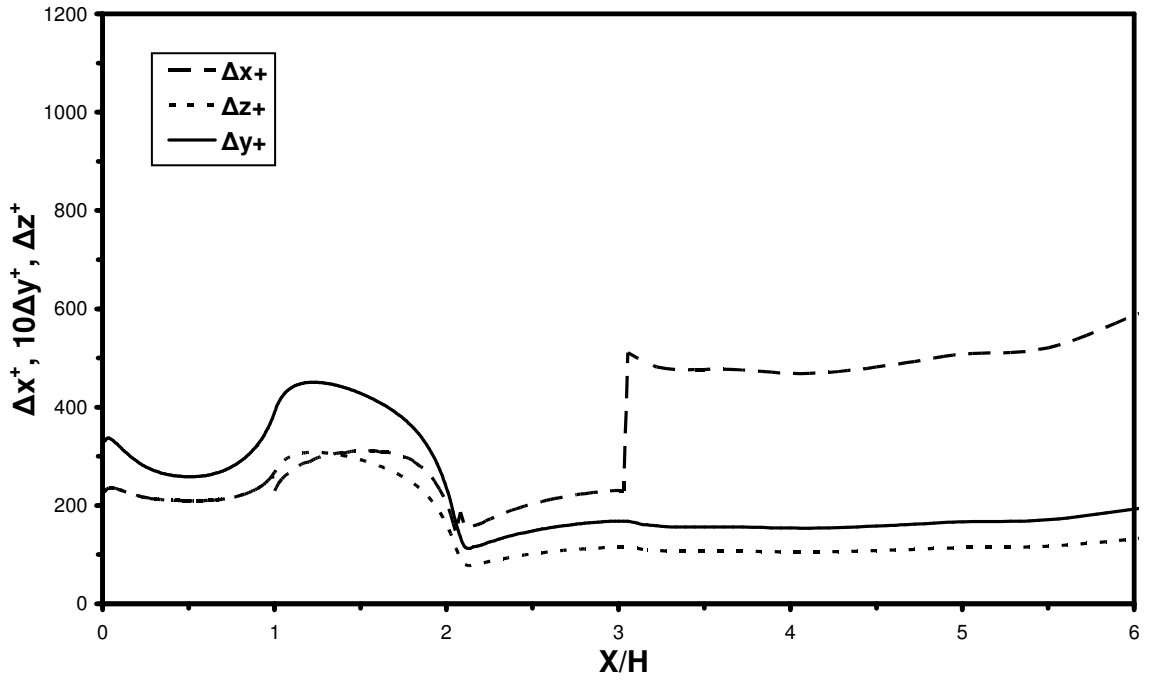

Figure 7.2: Δx^+, Δy^+, and Δz^+ distribution for refinedPiradeepanDSMG: (a) upper surface of the airfoil, (b) concave wall, (c) convex wall.

(a)

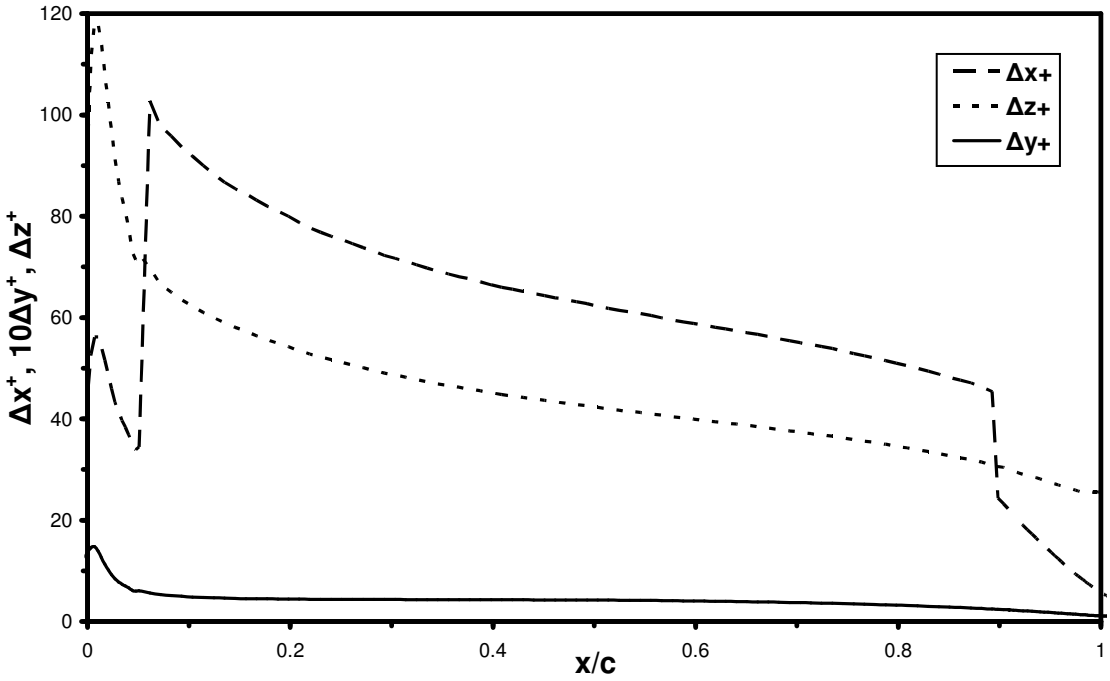

(b)

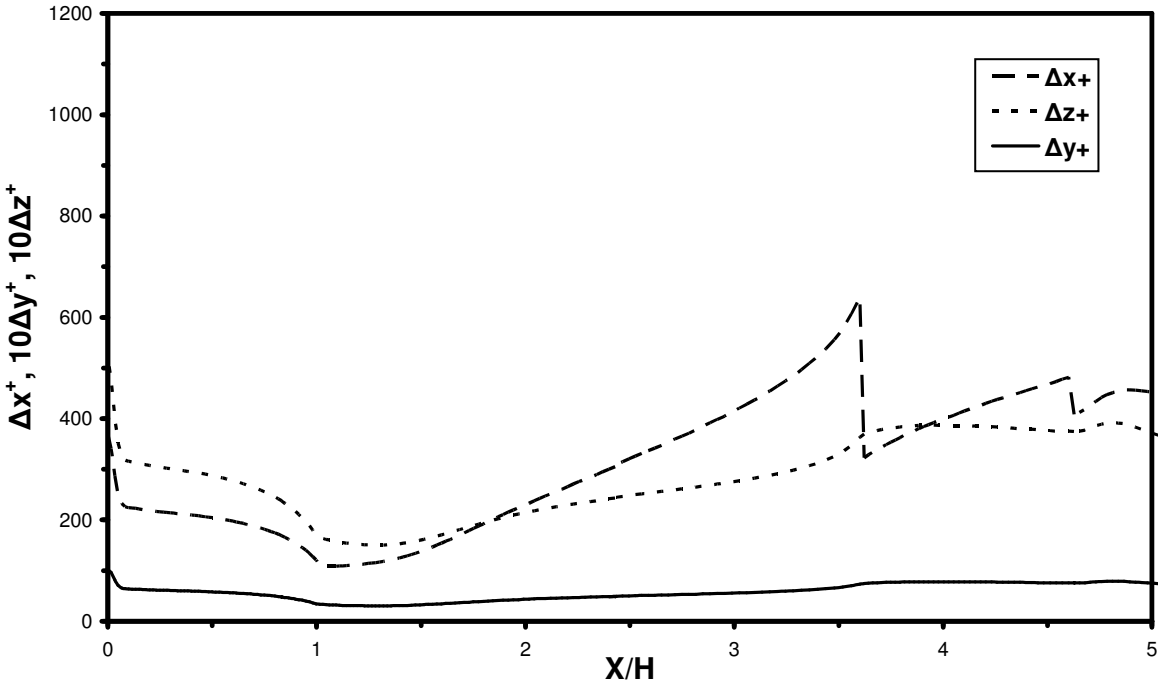

Figure 7.3: For caption see head of figure.

(c)

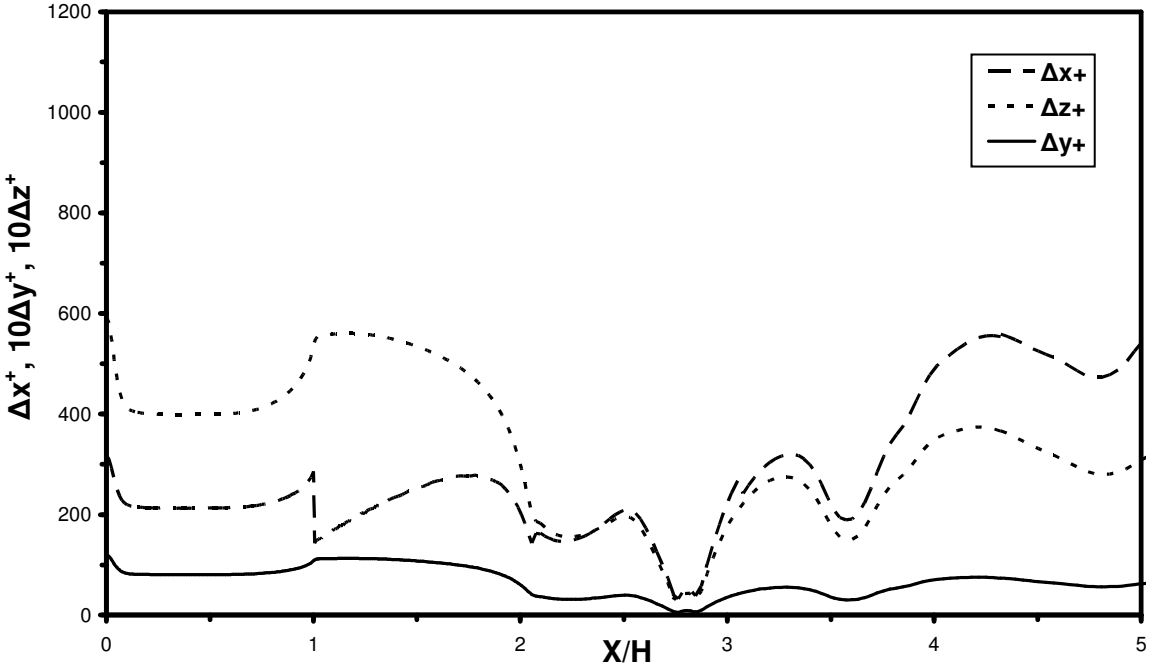

Figure 7.3: Δx^+, Δy^+, and Δz^+ distribution for refinedDSMG: (a) upper surface of the airfoil, (b) concave wall, (c) convex wall.

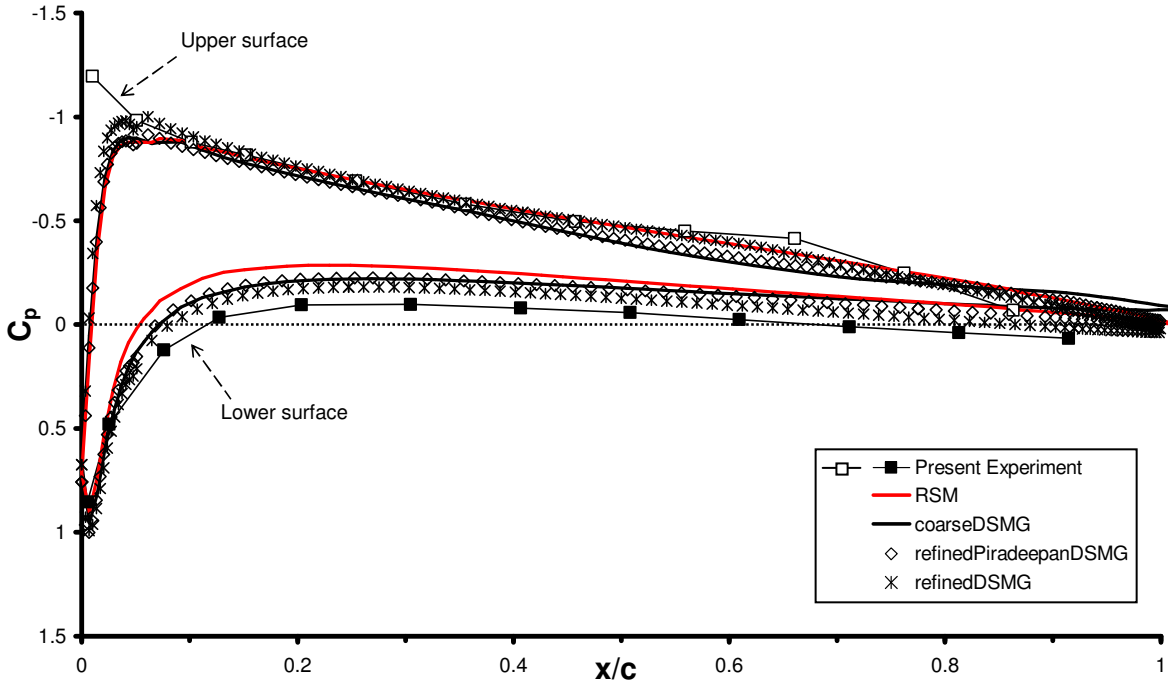

(a)

Figure 7.4: For caption see head of figure.

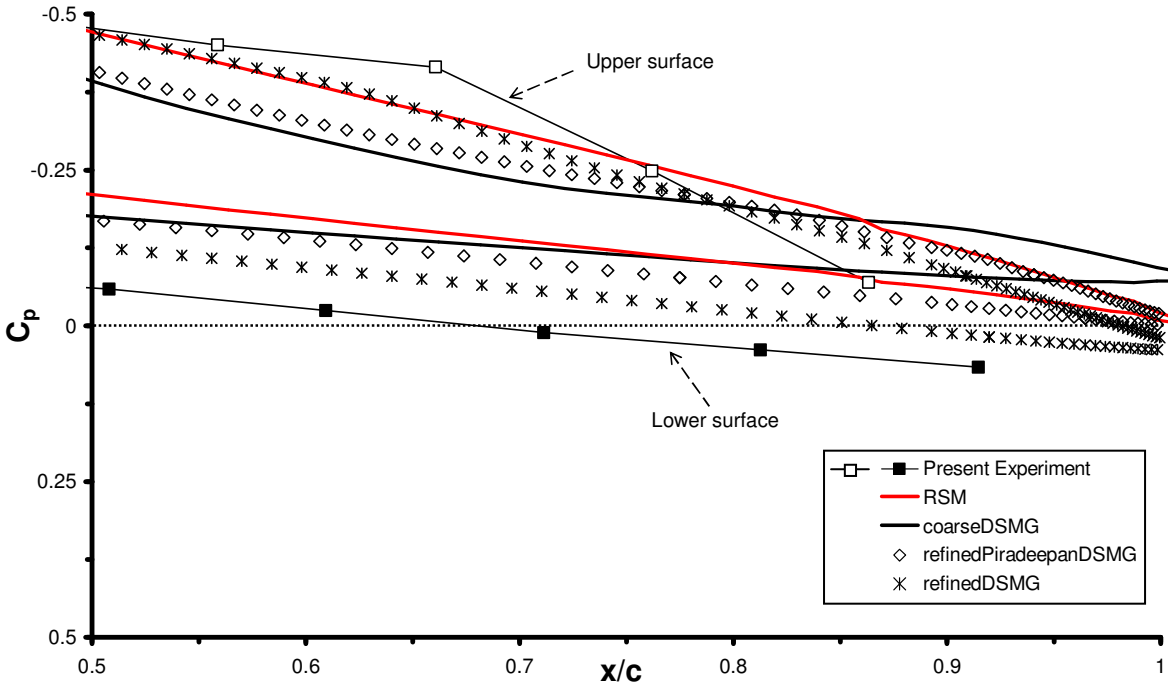

(b)

Figure 7.4: Comparison of numerical pressure coefficient on the upper and lower surfaces of the airfoil at $z/H = 0.5$ with the experimental values: (a) along the chord length, (b) near the trailing edge.

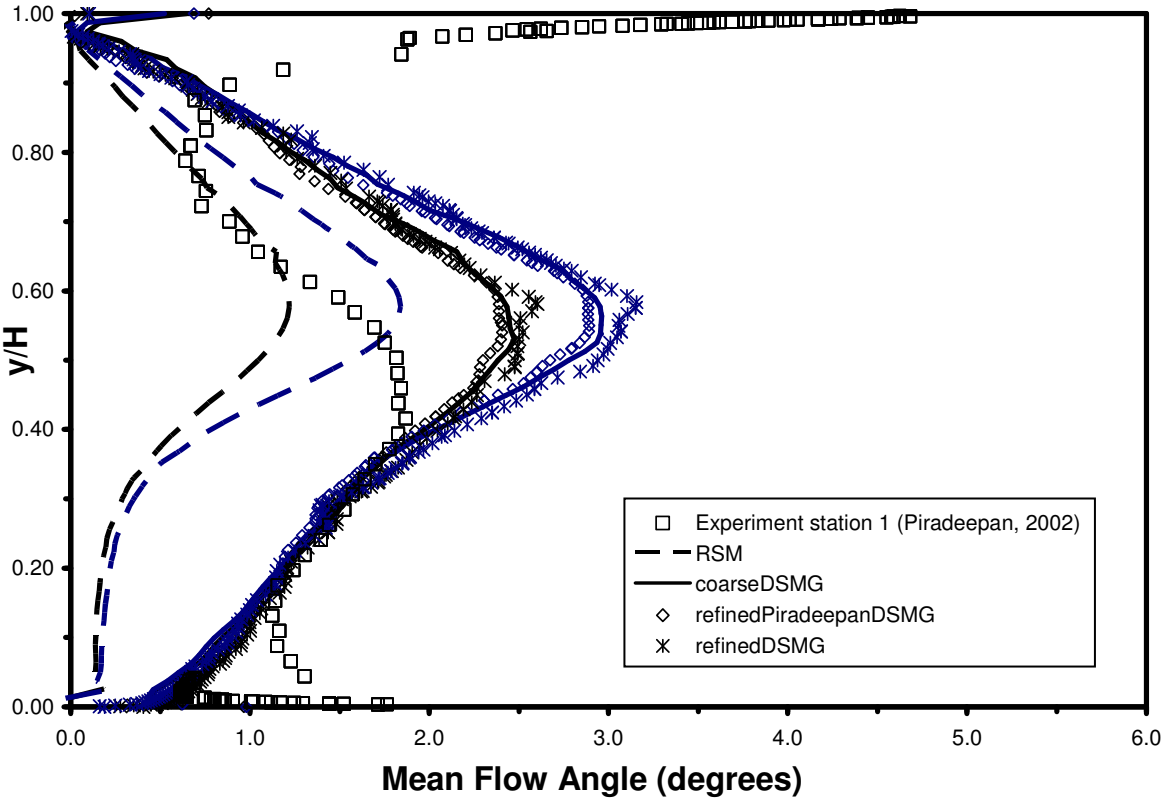

Figure 7.5: Mean flow angle relative to the x-axis ($z/H = 0.5$). With the exception of the experiments of Piradeepan (2002) at station 1, the black symbols represent the distributions at $X = 50$ mm, and the blue symbols represent the distributions at $X = 70$ mm, where X is the streamwise distance from station 1.

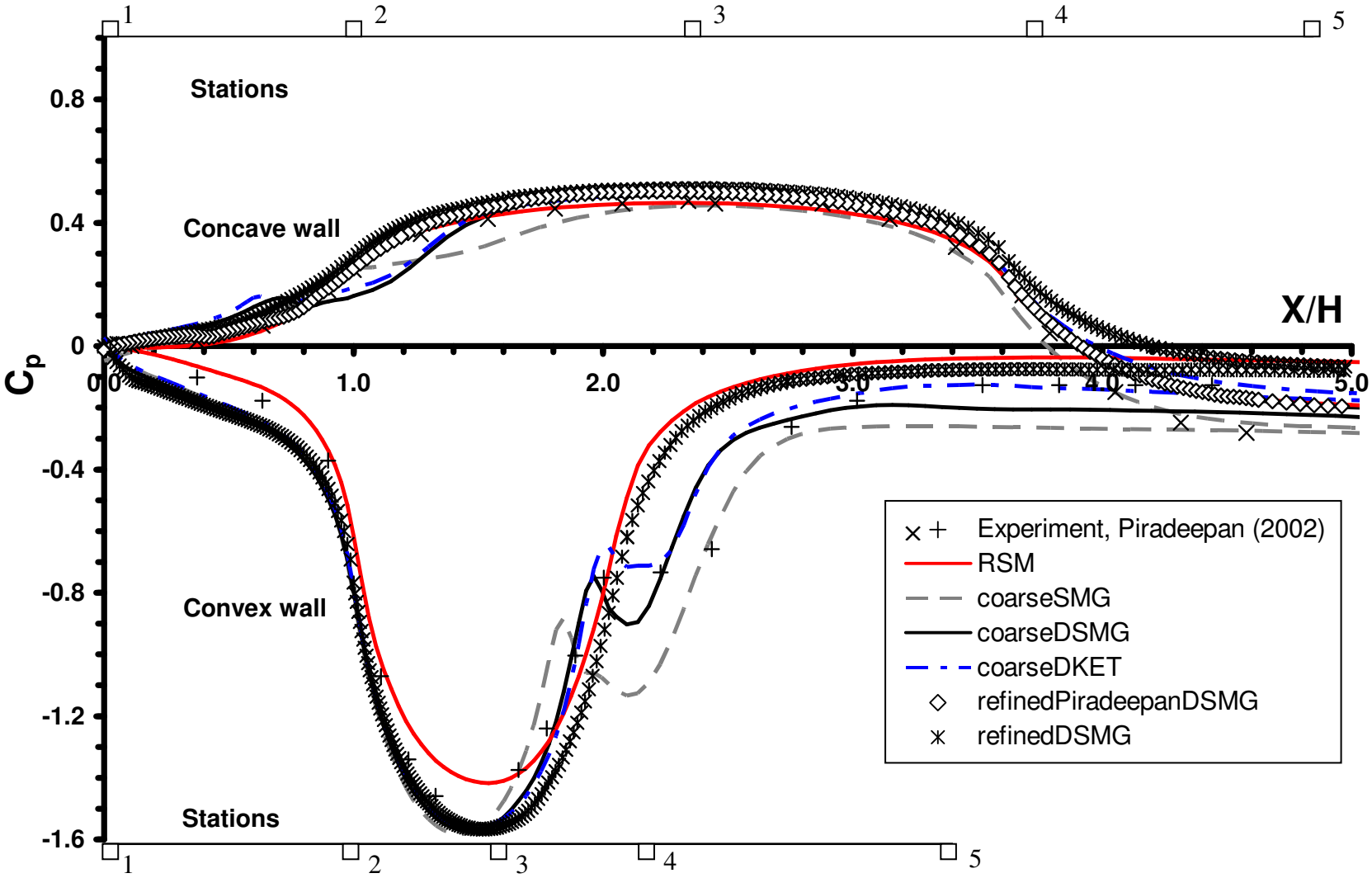

Figure 7.6: Comparison of numerical pressure coefficient along the concave and convex walls of the duct ($z/H = 0.5$) with the experimental values.

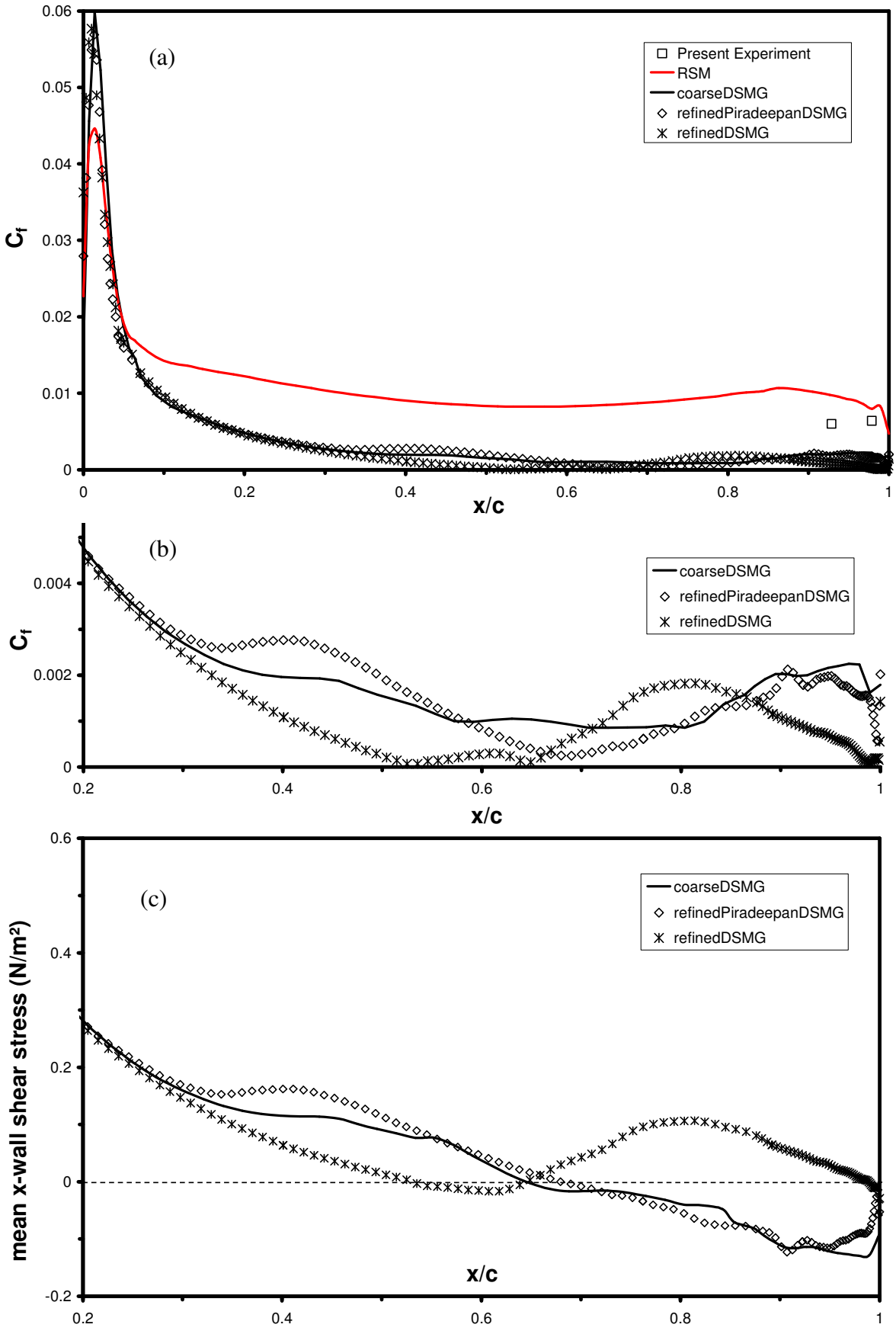

Figure 7.7: Comparison of numerical skin friction coefficient and mean *x*-wall shear stress on the upper surface of the airfoil ($z/H = 0.5$): (a) skin friction coefficient along the chord length, (b) close-up of skin friction coefficient, (c) close-up of mean *x*-wall shear stress.

(a)

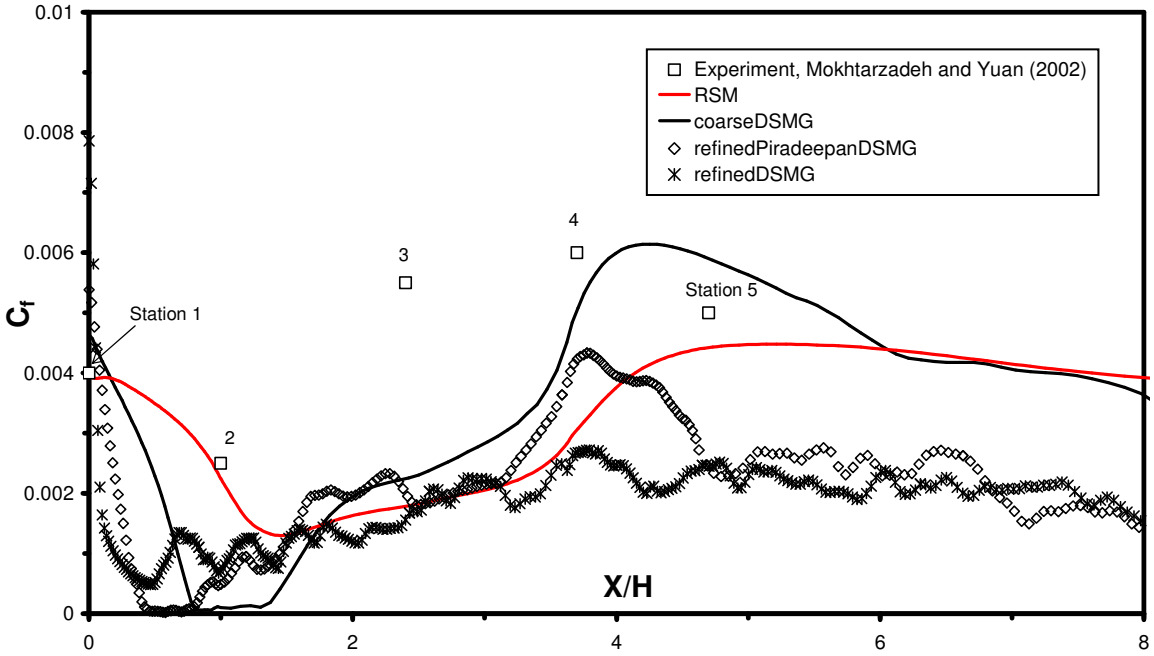

(b)

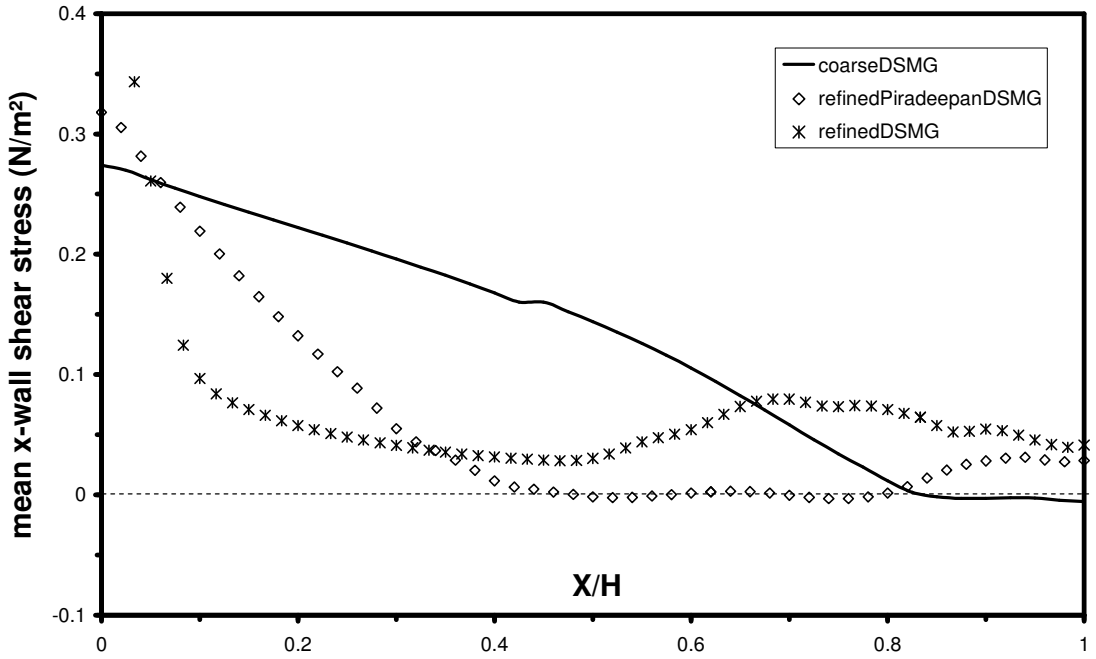

Figure 7.8: For caption see head of figure.

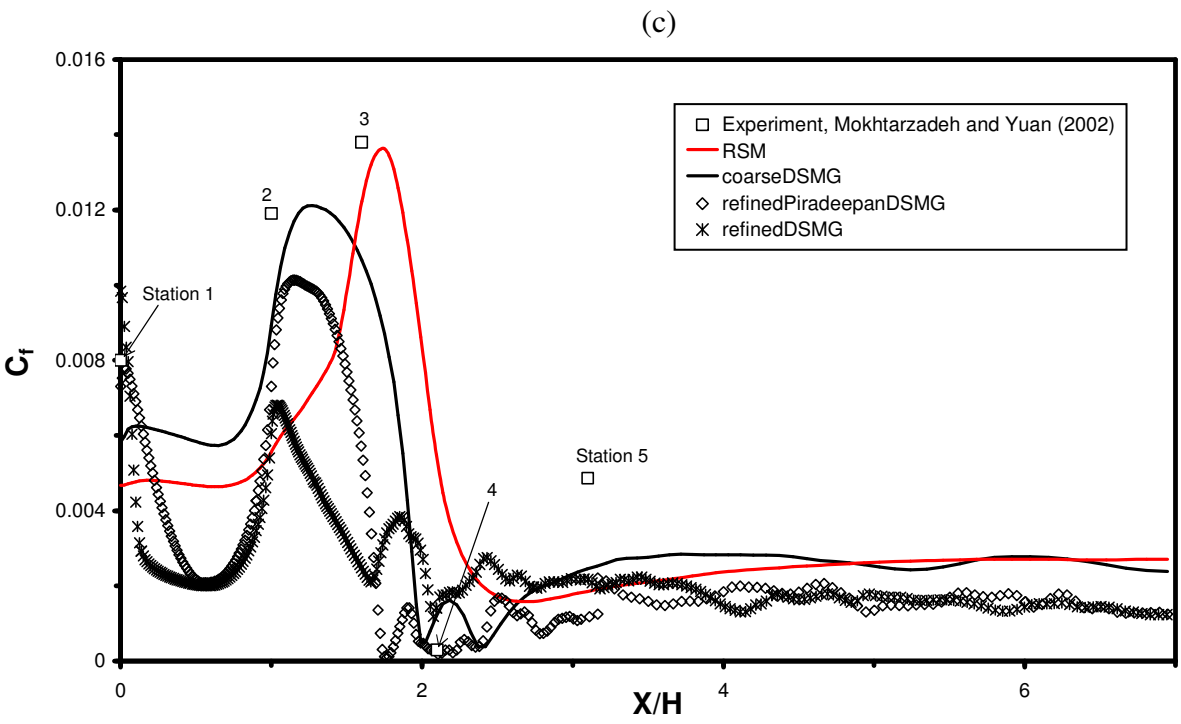

Figure 7.8: Comparison of numerical skin friction coefficient and mean *x*-wall shear stress across the concave and convex walls ($z/H = 0.5$): (a) skin friction coefficient along the concave wall, (b) mean *x*-wall shear stress along the concave wall up to $X/H = 1$, (c) skin friction coefficient along the convex wall.

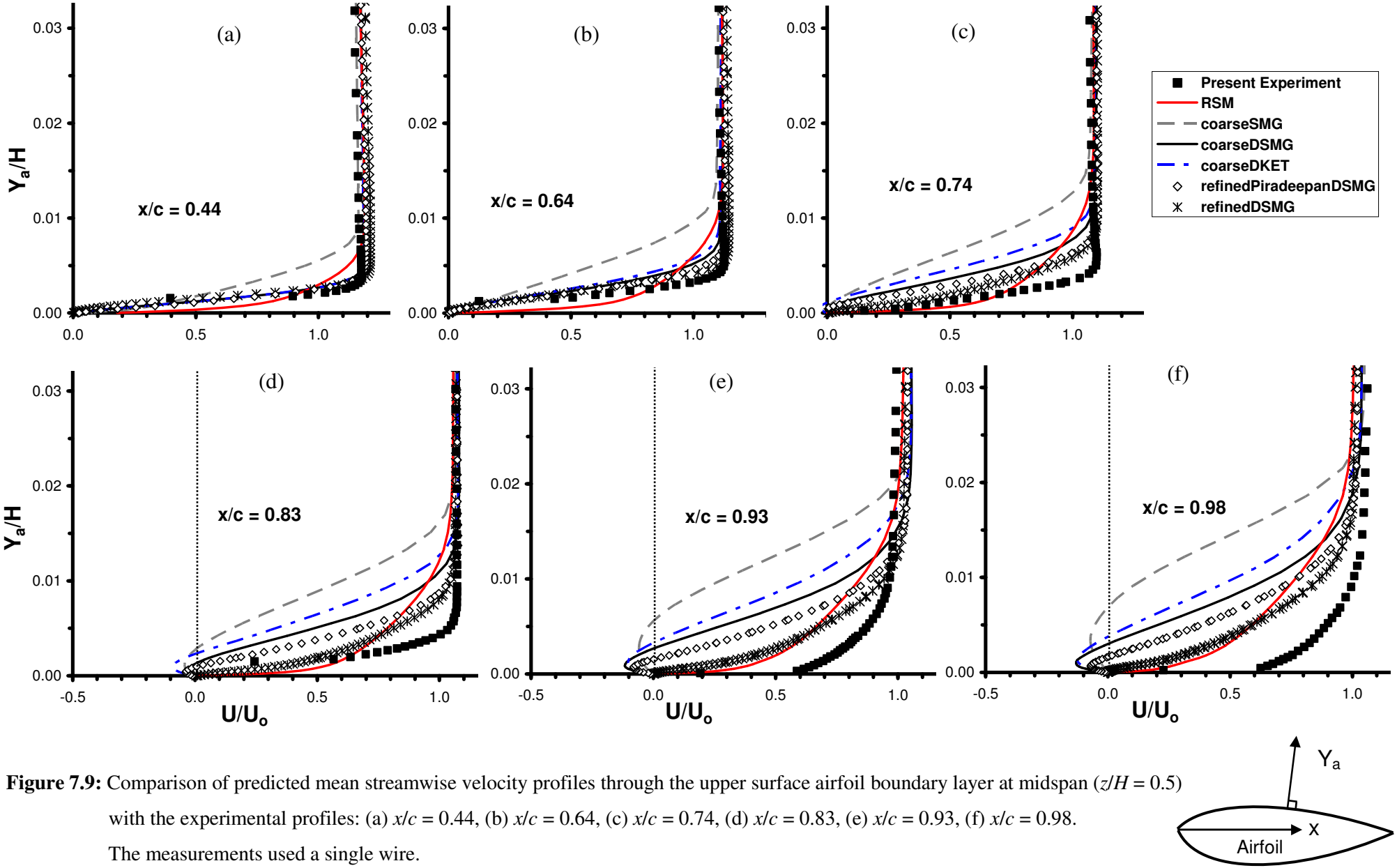

Figure 7.9: Comparison of predicted mean streamwise velocity profiles through the upper surface airfoil boundary layer at midspan ($z/H = 0.5$) with the experimental profiles: (a) $x/c = 0.44$, (b) $x/c = 0.64$, (c) $x/c = 0.74$, (d) $x/c = 0.83$, (e) $x/c = 0.93$, (f) $x/c = 0.98$. The measurements used a single wire.

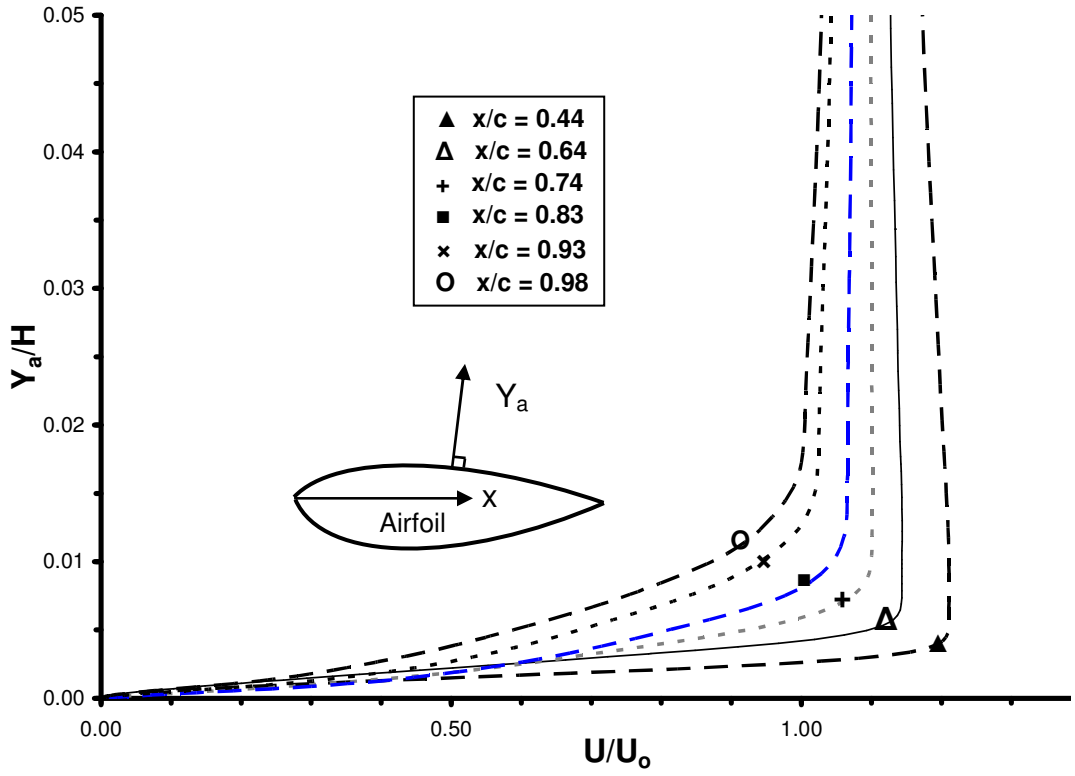

Figure 7.10: Comparison of the predicted mean streamwise velocity profiles for refinedDSMG grouped together at the corresponding locations on the upper surface of the airfoil.

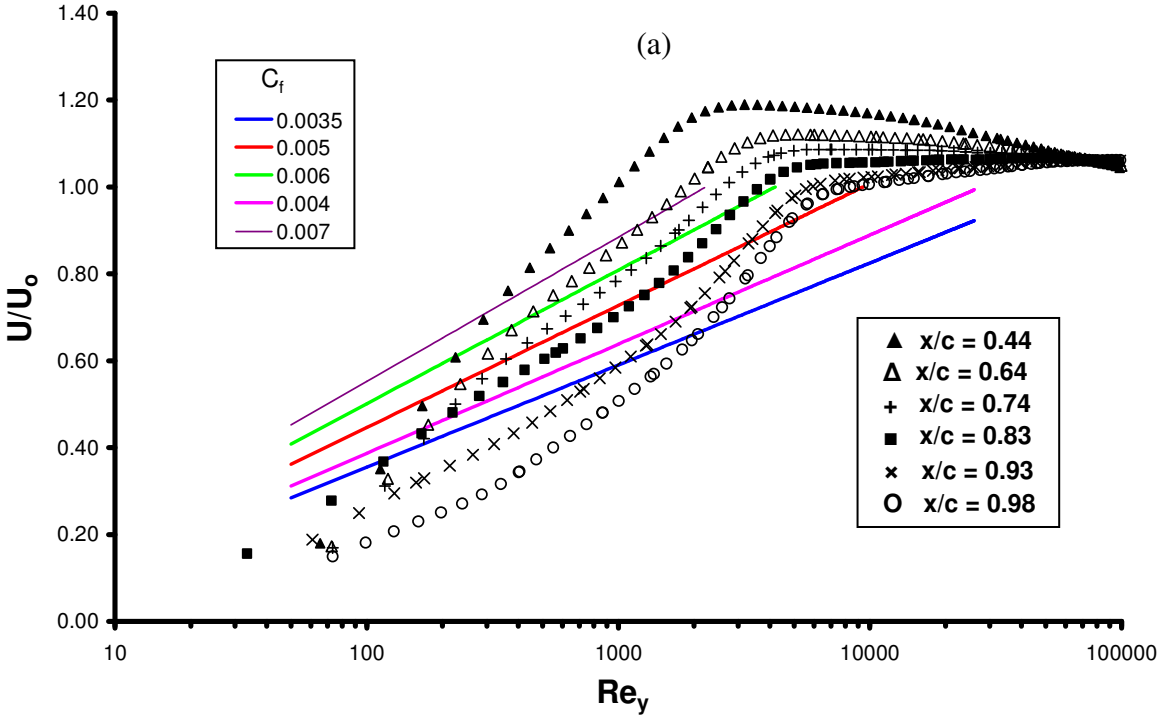

Figure 7.11: For caption see head of figure.

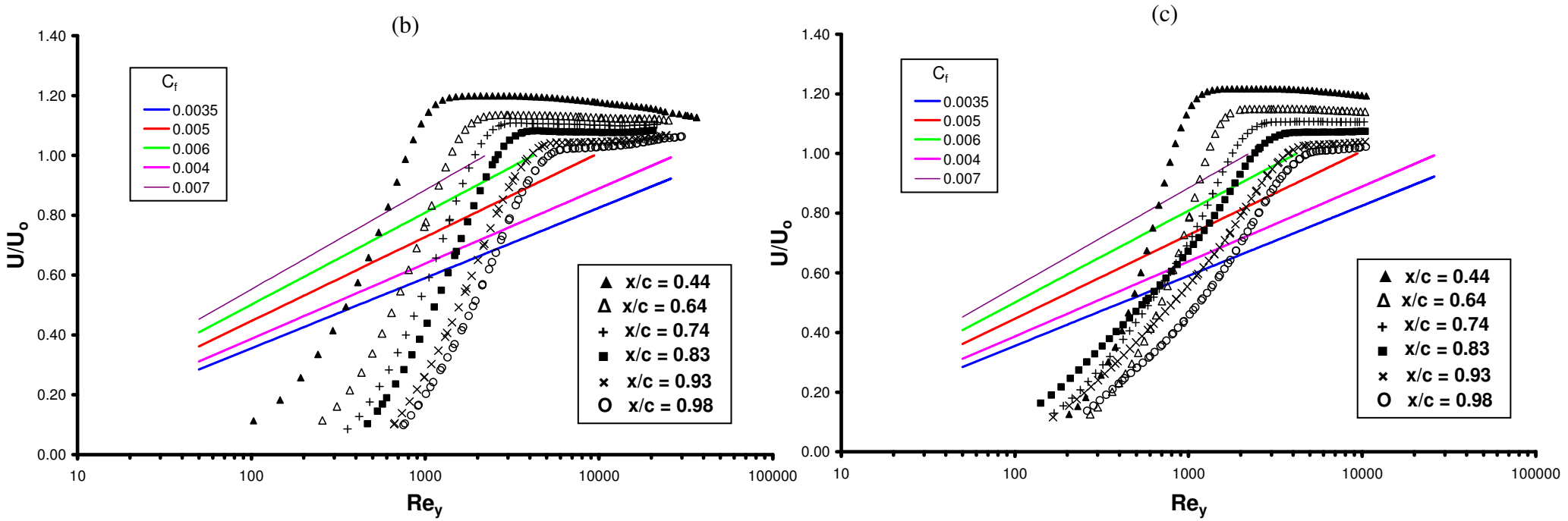

Figure 7.11: Clauser chart representations of the velocity profiles in the boundary layer on the upper surface of the airfoil ($z/H = 0.5$): (a) RSM, (b) refinedPiradeepanDSMG, (c) refinedDSMG

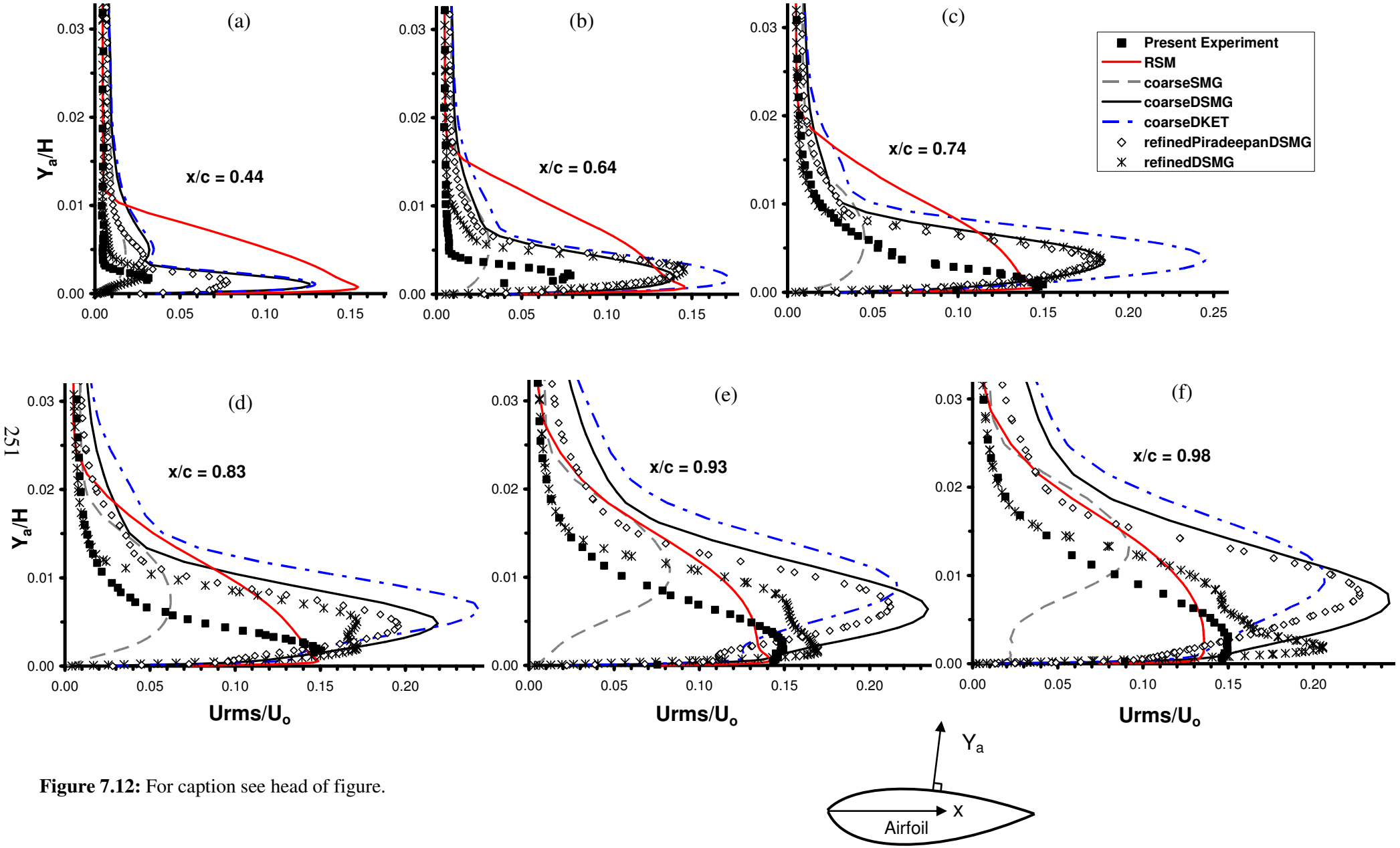

Figure 7.12: For caption see head of figure.

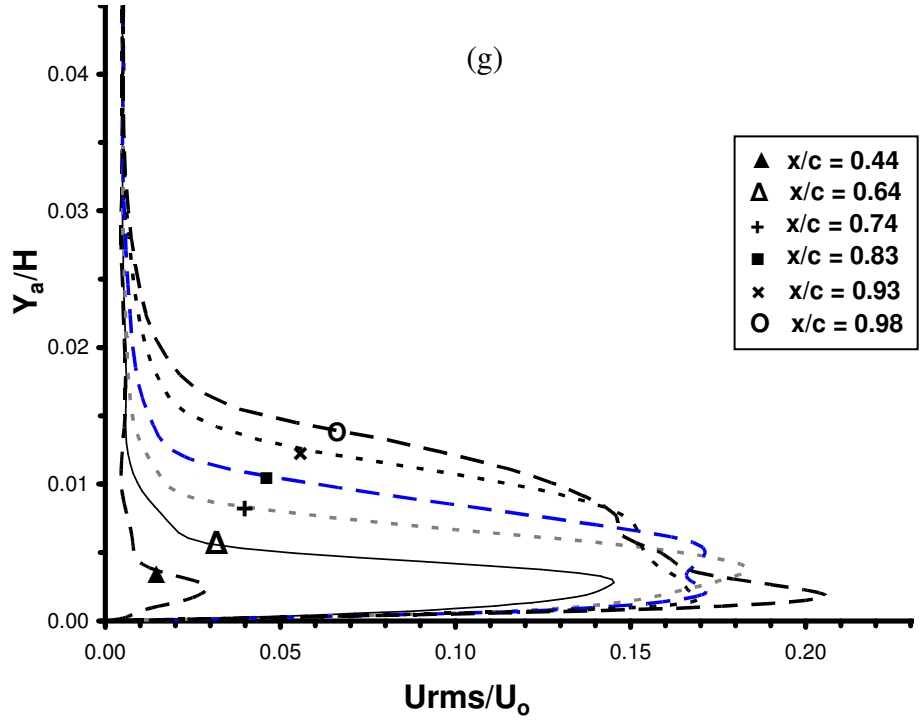

Figure 7.12: Comparison of predicted streamwise turbulence intensity profiles through the upper surface airfoil boundary layer at midspan ($z/H = 0.5$) with the experimental profiles: (a) $x/c = 0.44$, (b) $x/c = 0.64$, (c) $x/c = 0.74$, (d) $x/c = 0.83$, (e) $x/c = 0.93$, (f) $x/c = 0.98$, (g) refinedDSMG grouped profiles.

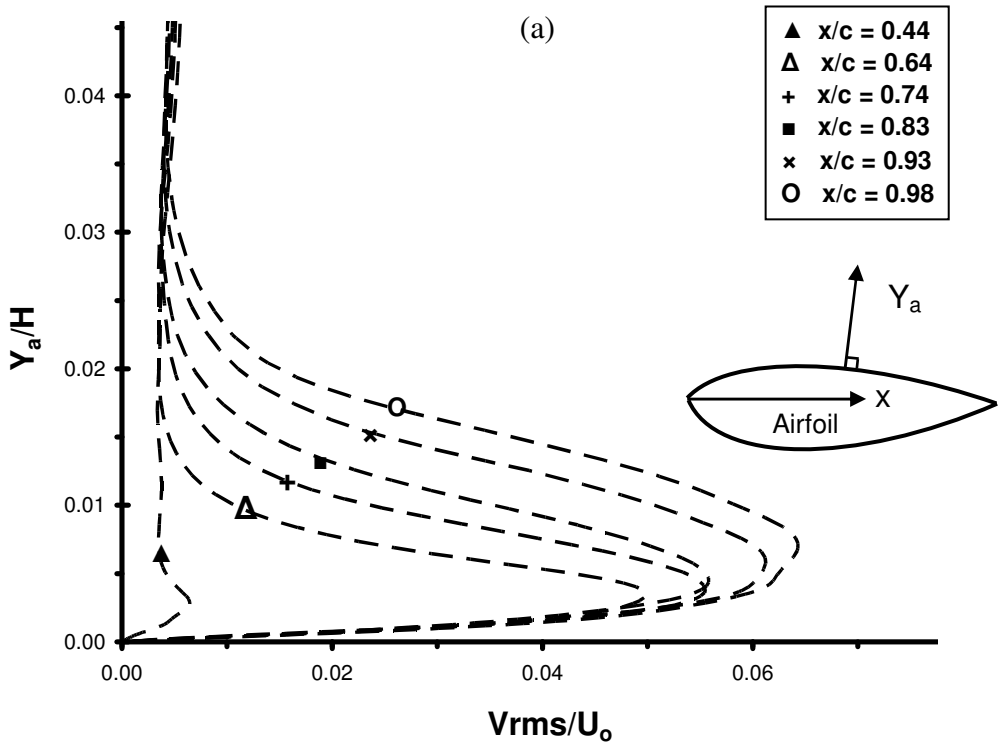

Figure 7.13: For caption see head of figure.

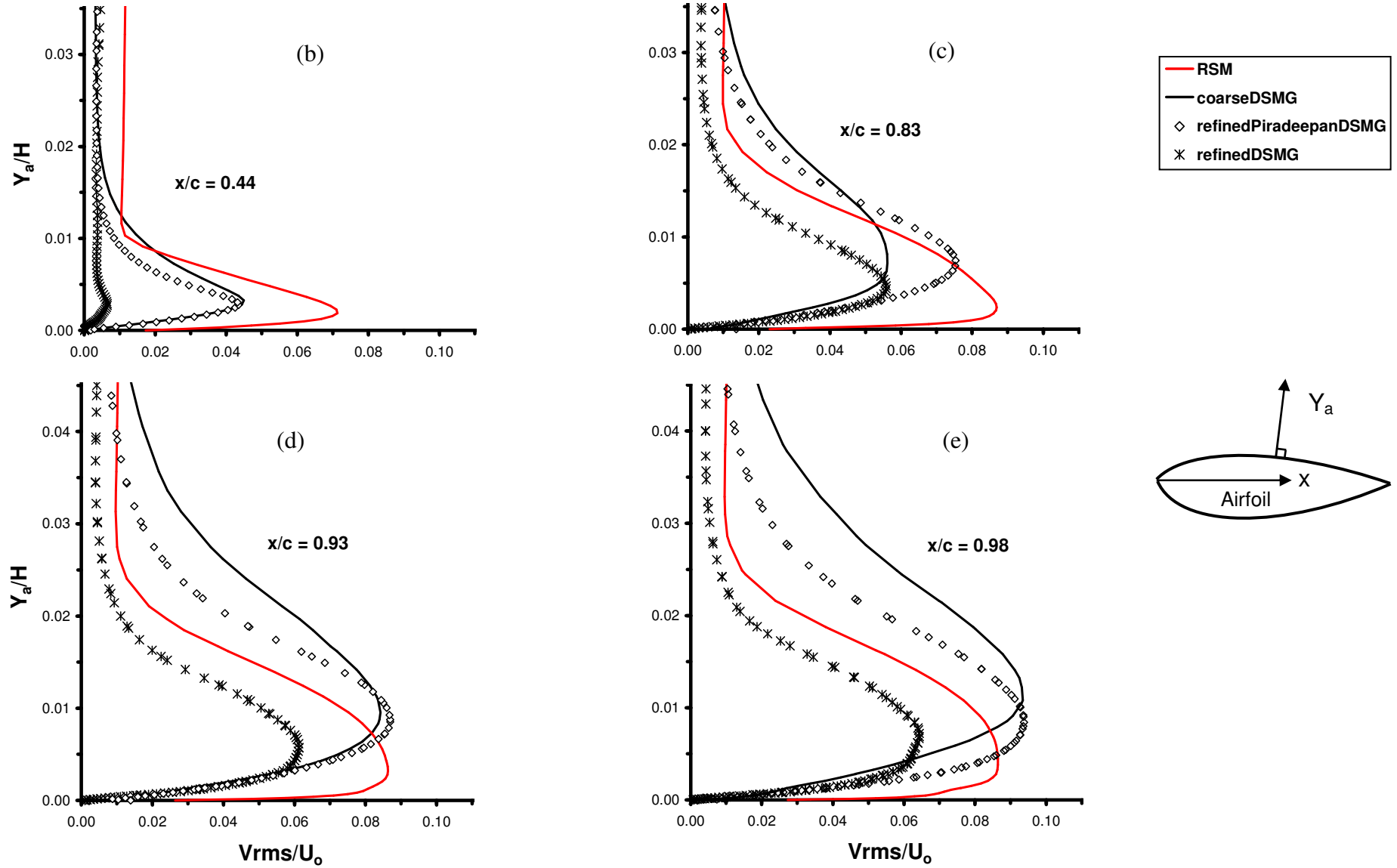

Figure 7.13: Comparison of predicted normal turbulence intensity profiles on the upper surface airfoil boundary layer at mid-span ($z/H = 0.5$): (a) refinedDSMG grouped profiles, (b) $x/c = 0.44$, (c) $x/c = 0.83$, (d) $x/c = 0.93$, (e) $x/c = 0.98$.

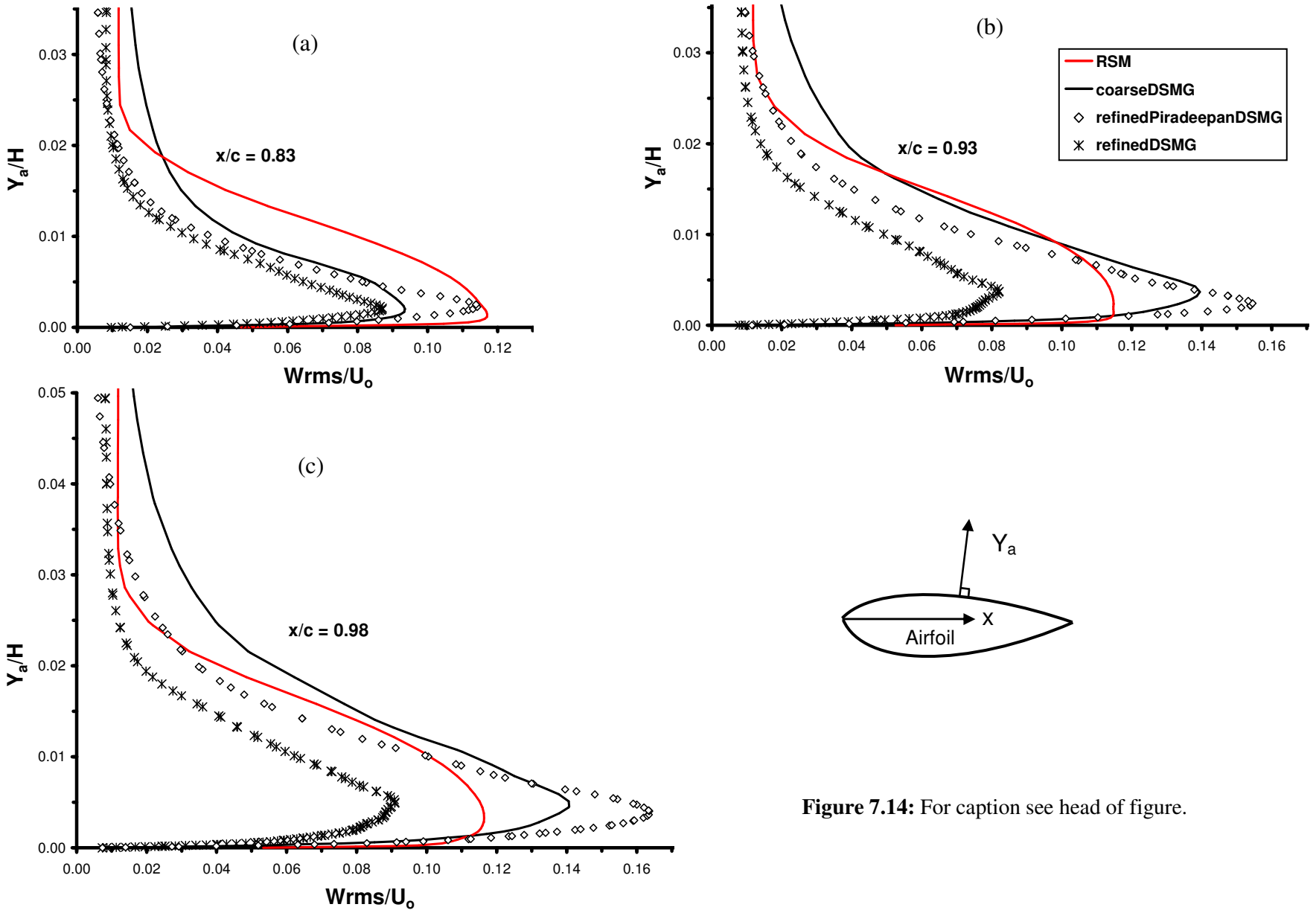

Figure 7.14: For caption see head of figure.

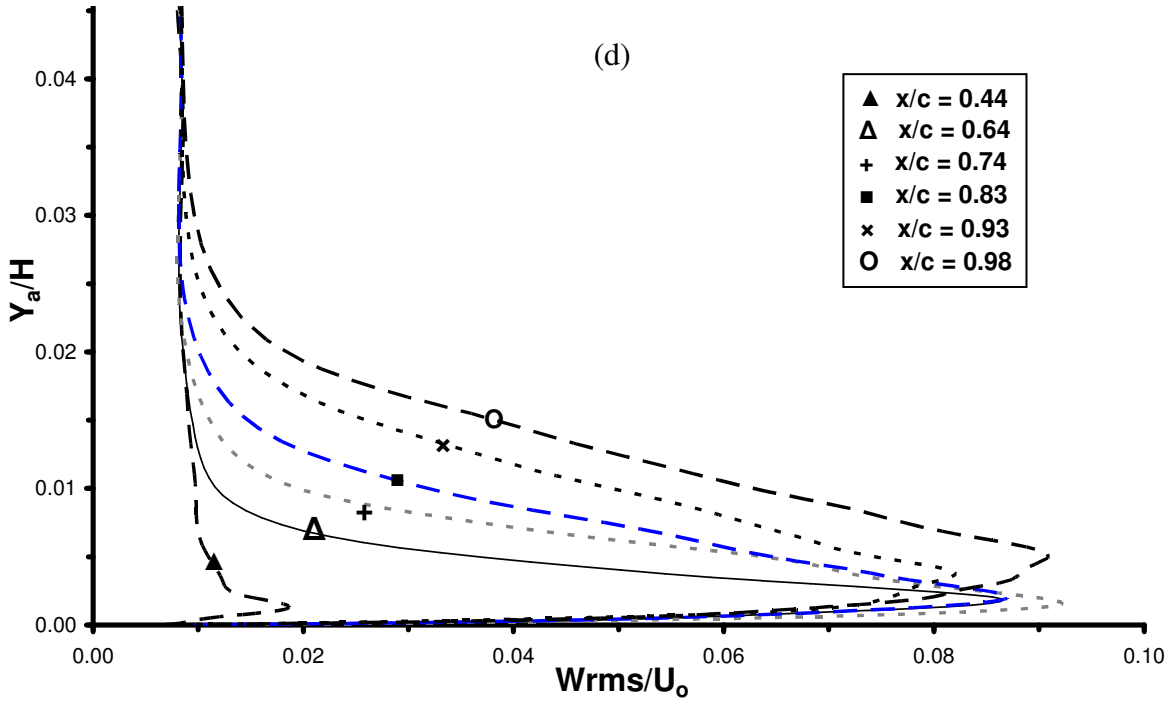

Figure 7.14: Comparison of predicted spanwise turbulence intensity profiles on the upper surface airfoil boundary layer at mid-span ($z/H = 0.5$): (a) $x/c = 0.83$, (b) $x/c = 0.93$, (c) $x/c = 0.98$, (d) refinedDSMG grouped profiles.

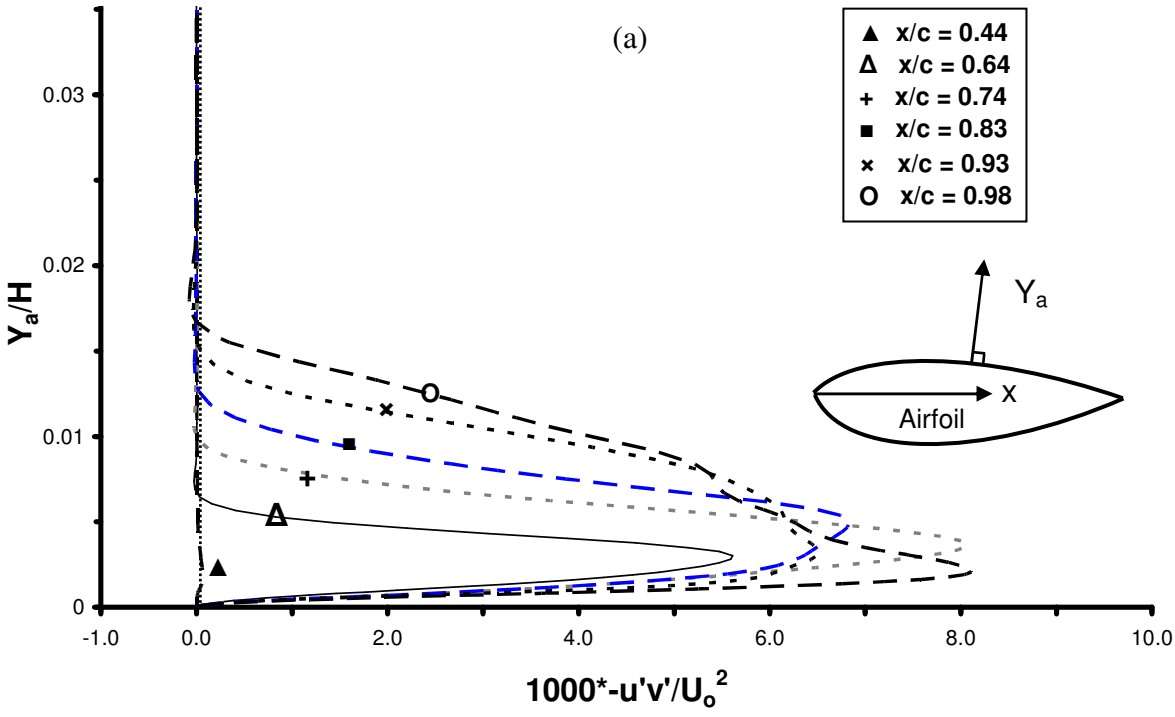

Figure 7.15: For caption see head of figure.

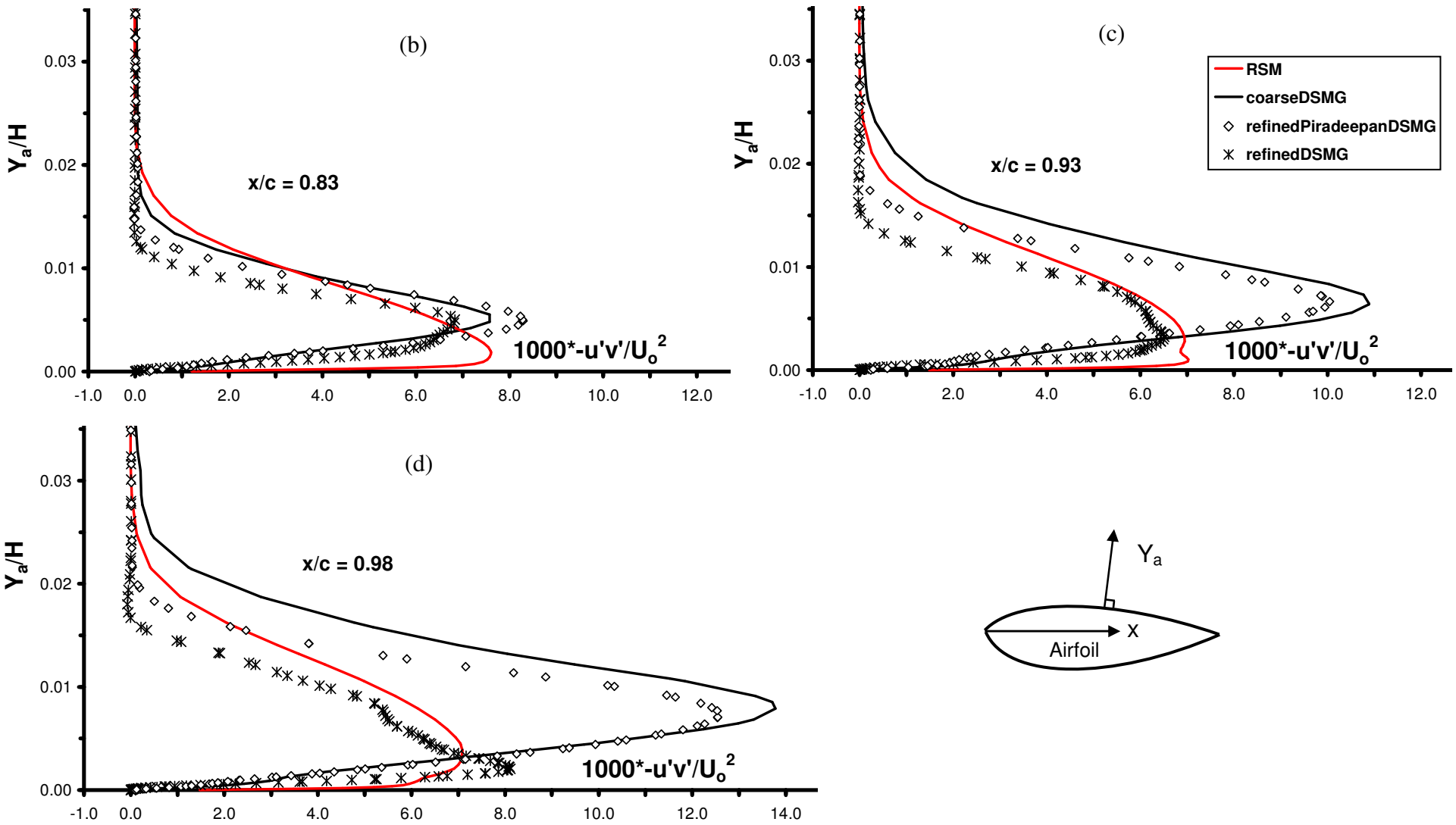

Figure 7.15: Comparison of the predicted turbulence shear stress profiles on the upper surface airfoil boundary layer at mid-span ($z/H = 0.5$): (a) refinedDSMG grouped profiles (b) $x/c = 0.83$, (c) $x/c = 0.93$, (d) $x/c = 0.98$.

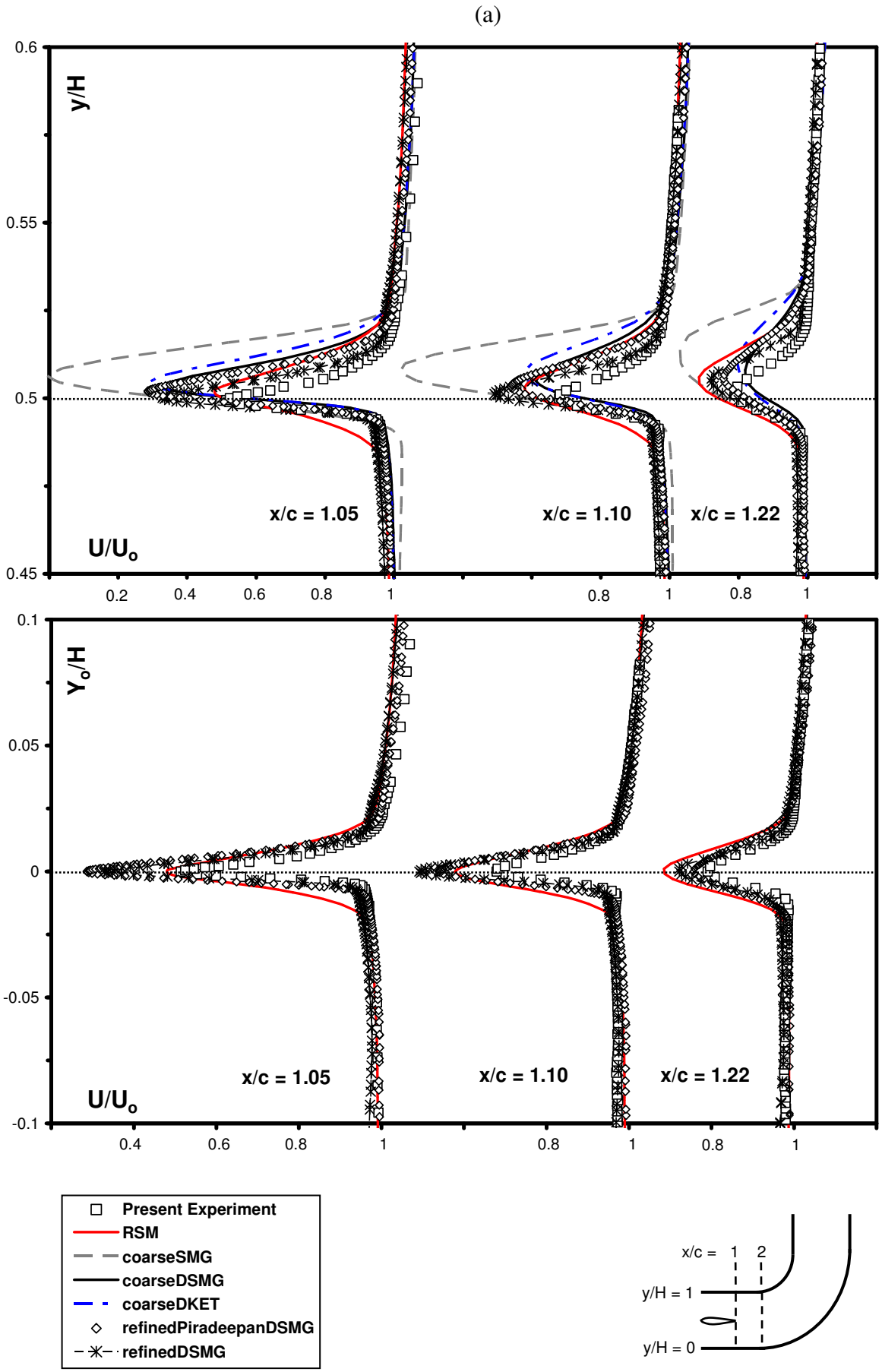

Figure 7.16: For caption see head of figure.

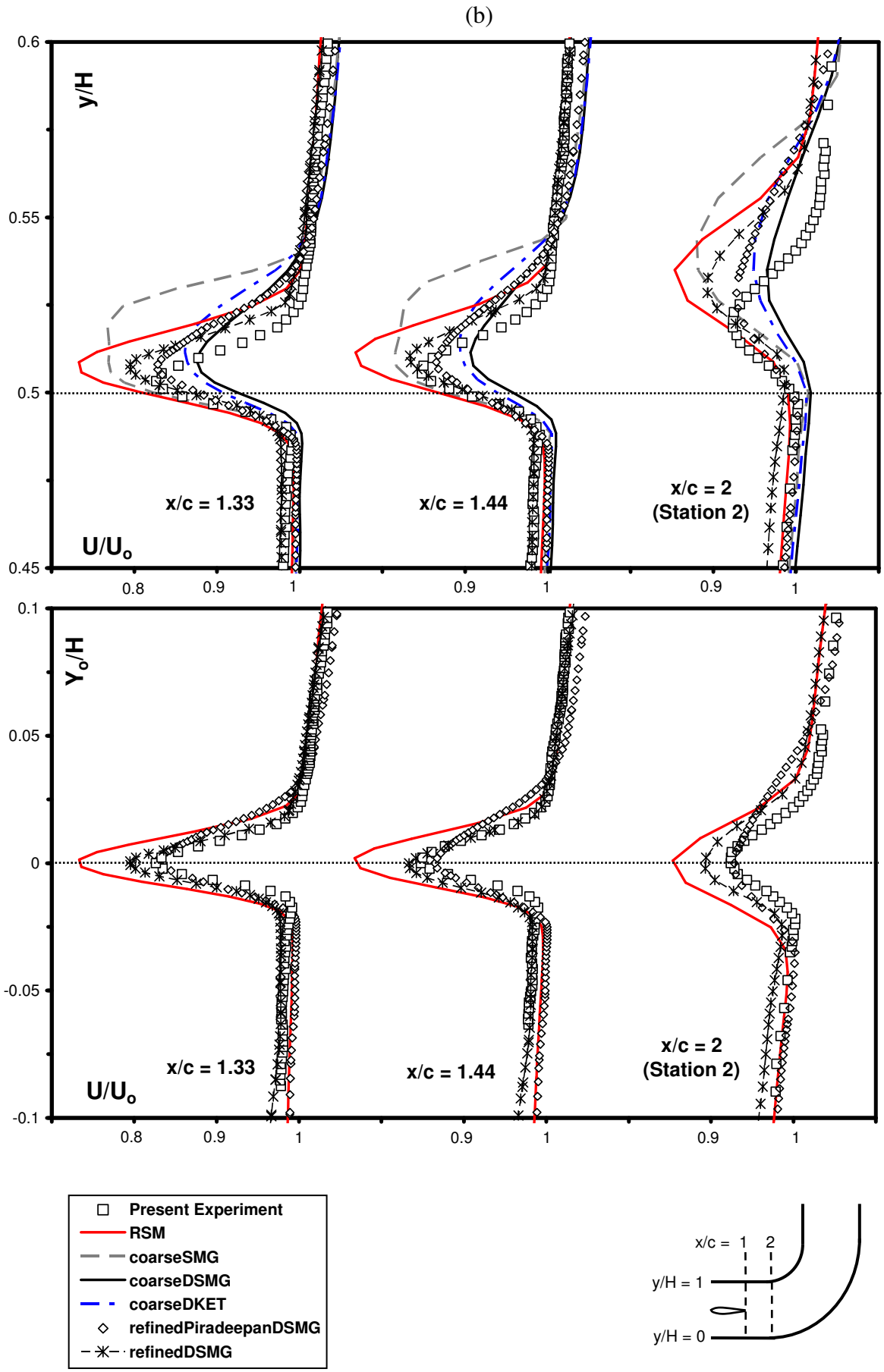

Figure 7.16: For caption see head of figure.

(c)

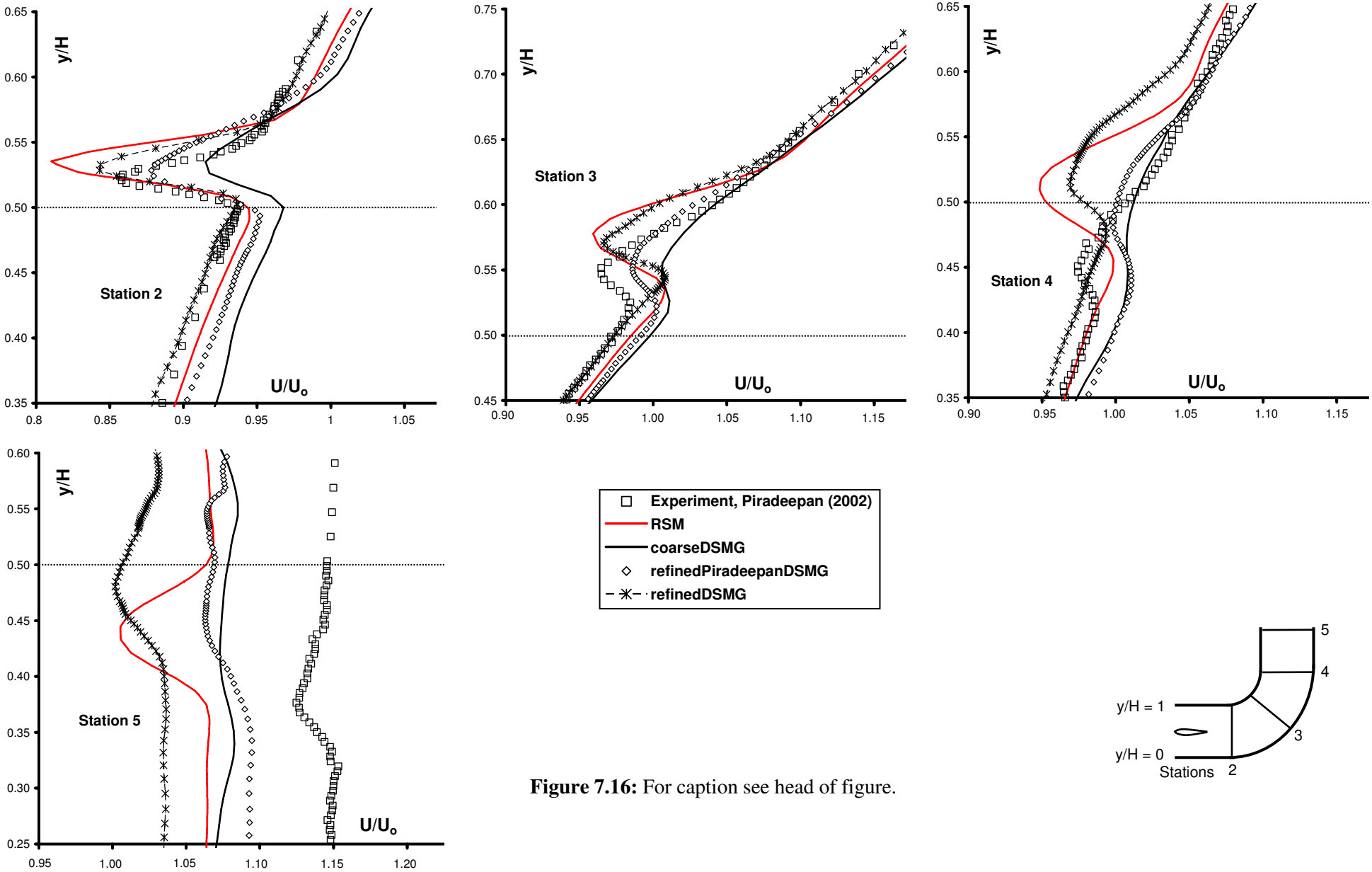

Figure 7.16: For caption see head of figure.

(d)

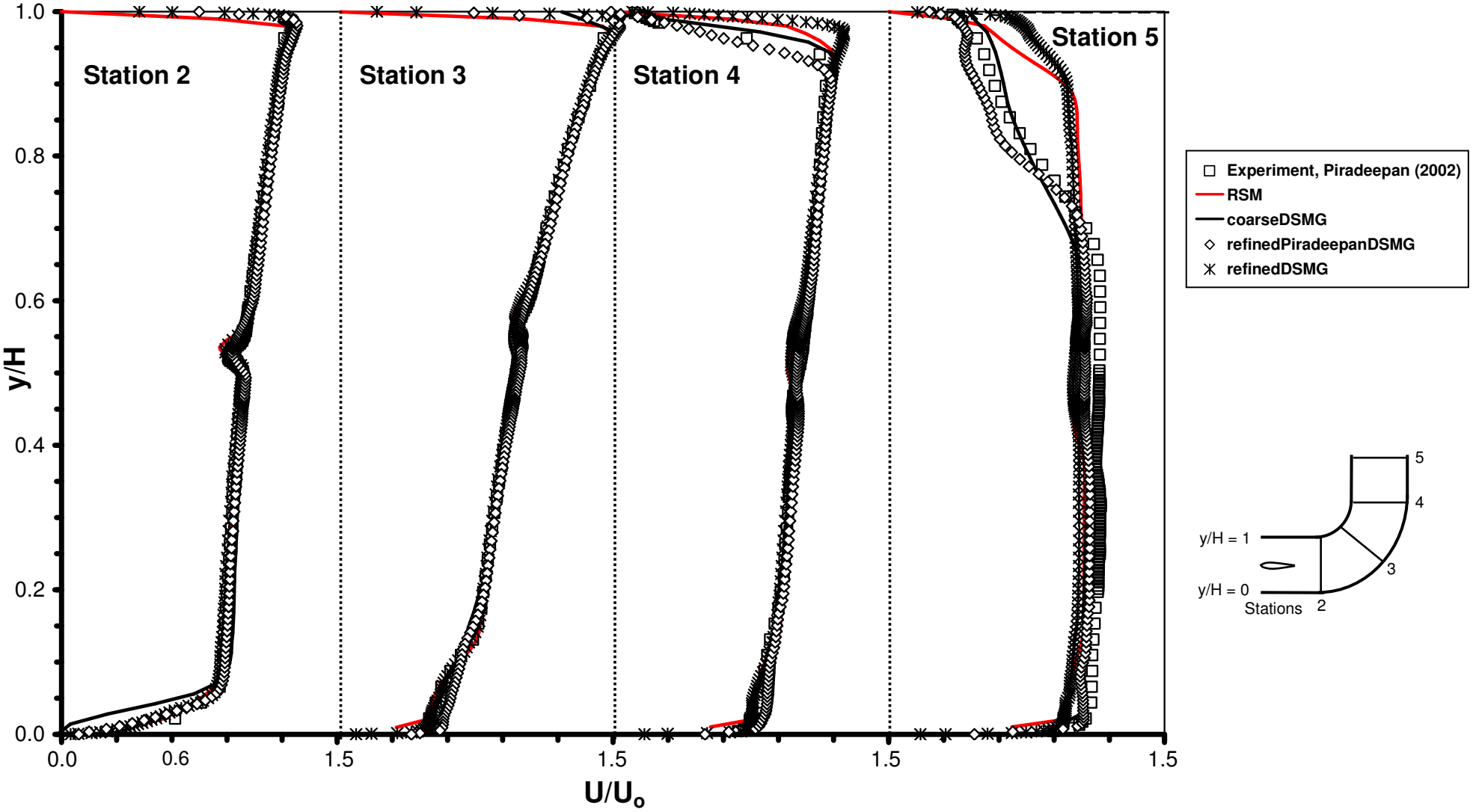

Figure 7.16: For caption see head of figure.

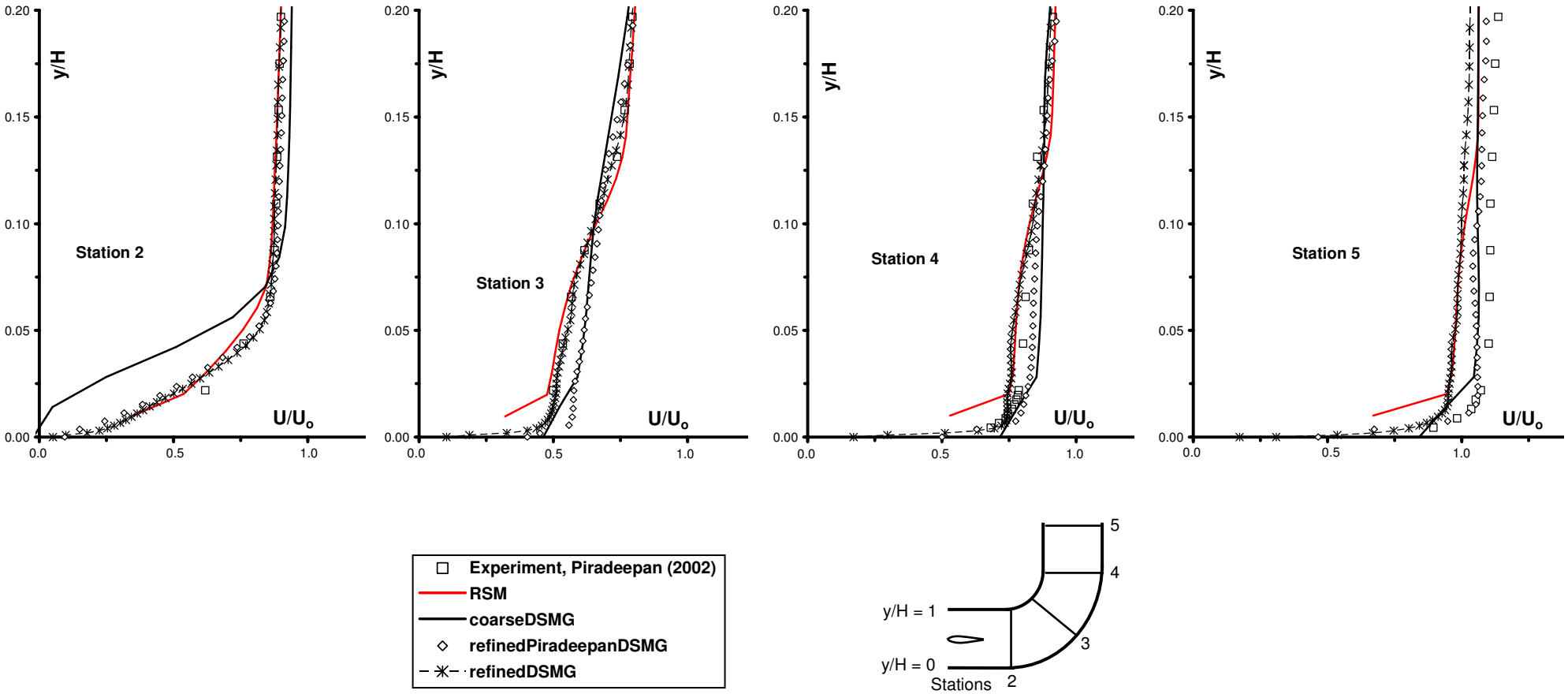

Figure 7.16: Comparison of numerical streamwise velocity in the near-wake and at stations 2 to 5 ($z/H = 0.5$) with experimental data: (a) near-wake $x/c = 1.05$ to 1.22, (b) near-wake $x/c = 1.33$ to 2, (c) in the wake region at stations 2 to 5, (d) across the whole duct cross-section at stations 2 to 5, (e) profiles near the concave wall at stations 2 to 5. The near-wake profiles are plotted for normal distance y, and also aligned with respect to the wake centre line and plotted on a separate graph for Y_o.

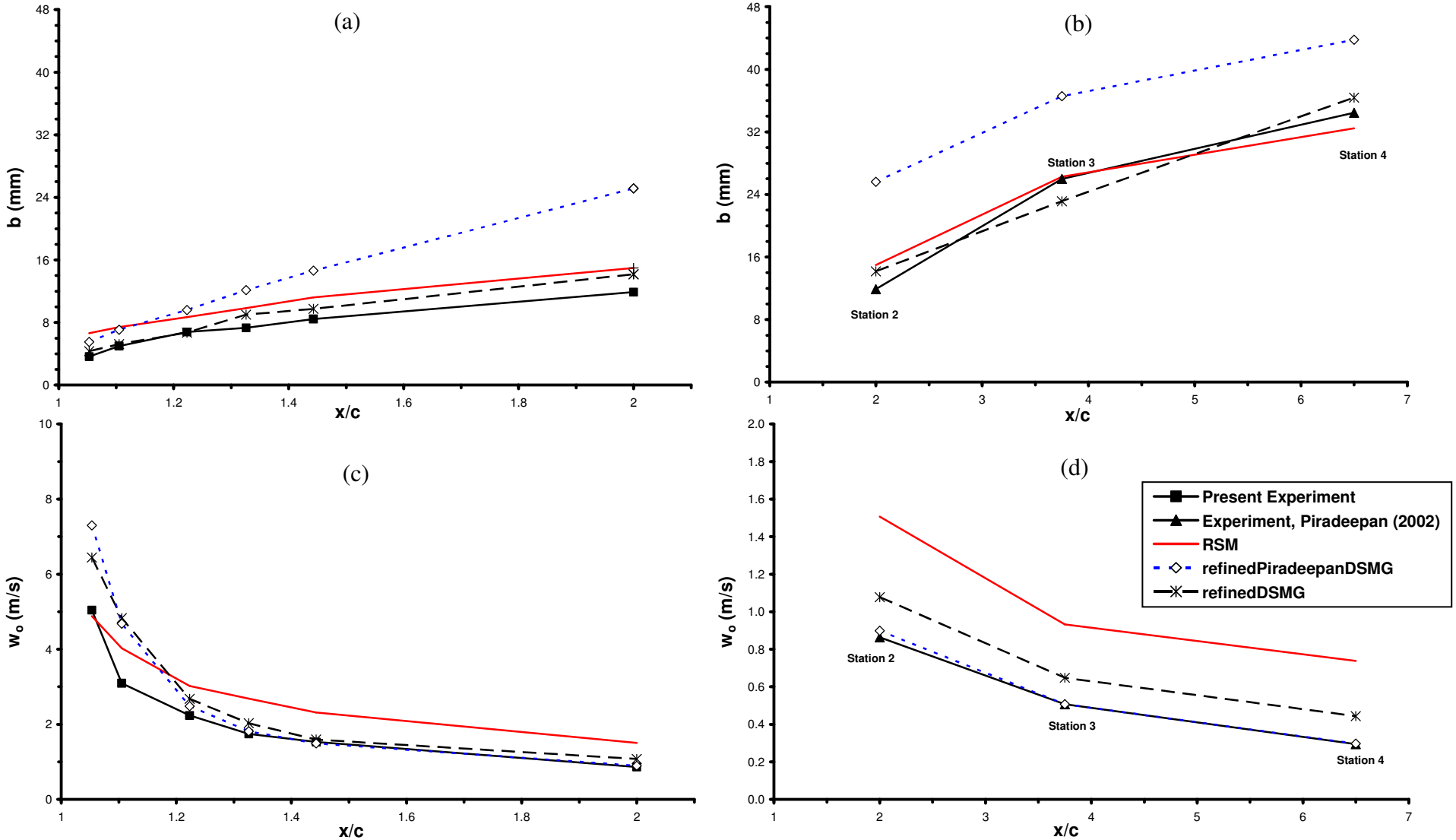

Figure 7.17: Comparison of the wake parameters in the near-wake and at stations 2 to 4: (a) total wake half-width (inner side and outer side) in the near-wake, (b) total wake half-width at stations 2 to 4, (c) maximum velocity defect in the near-wake, (d) maximum velocity defect at stations 2 to 4.

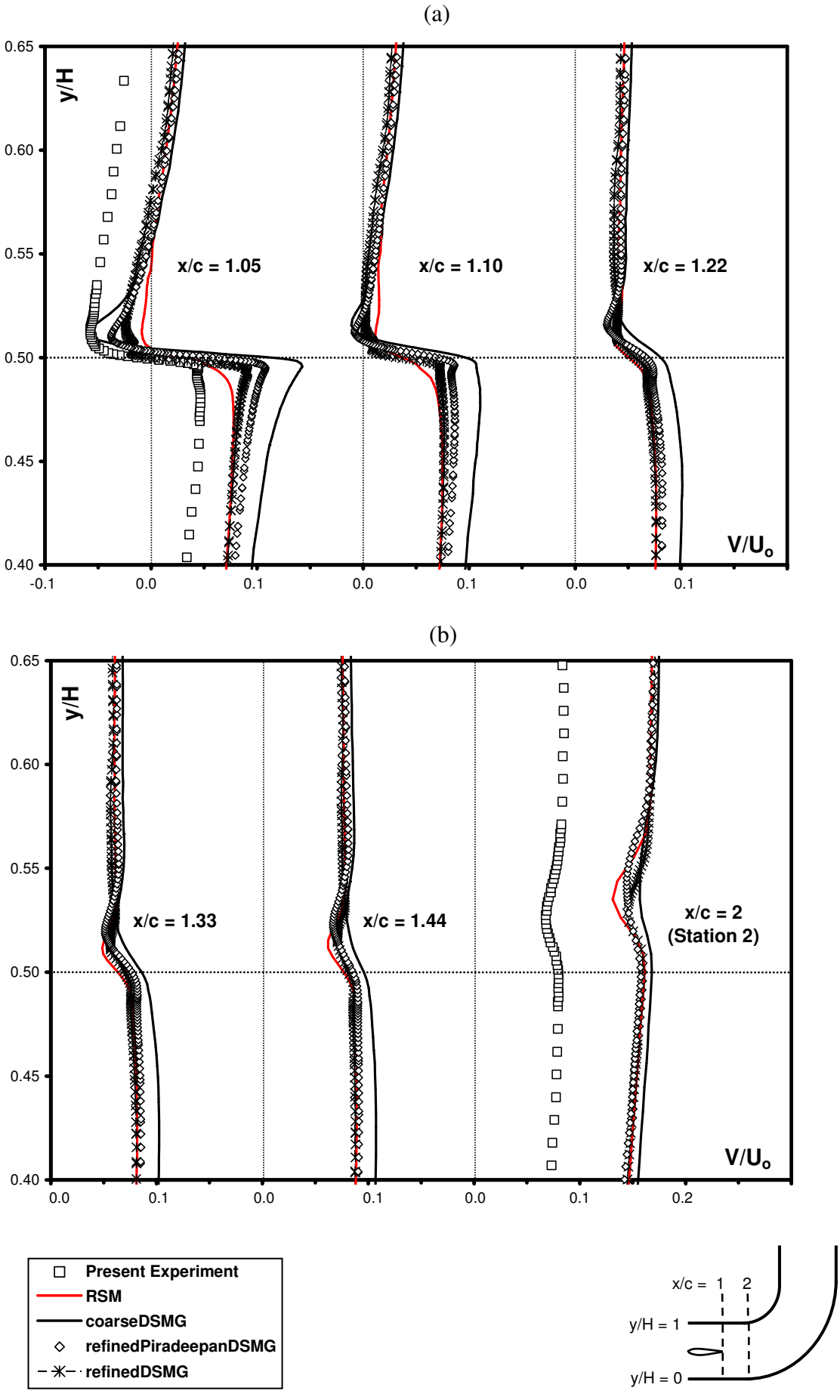

Figure 7.18: Comparison of the predicted profiles mean normal velocity in the near wake (z/H = 0.5) with experimental data: (a) x/c = 1.05 to 1.22, (b) 1.33 to 2.

(a)

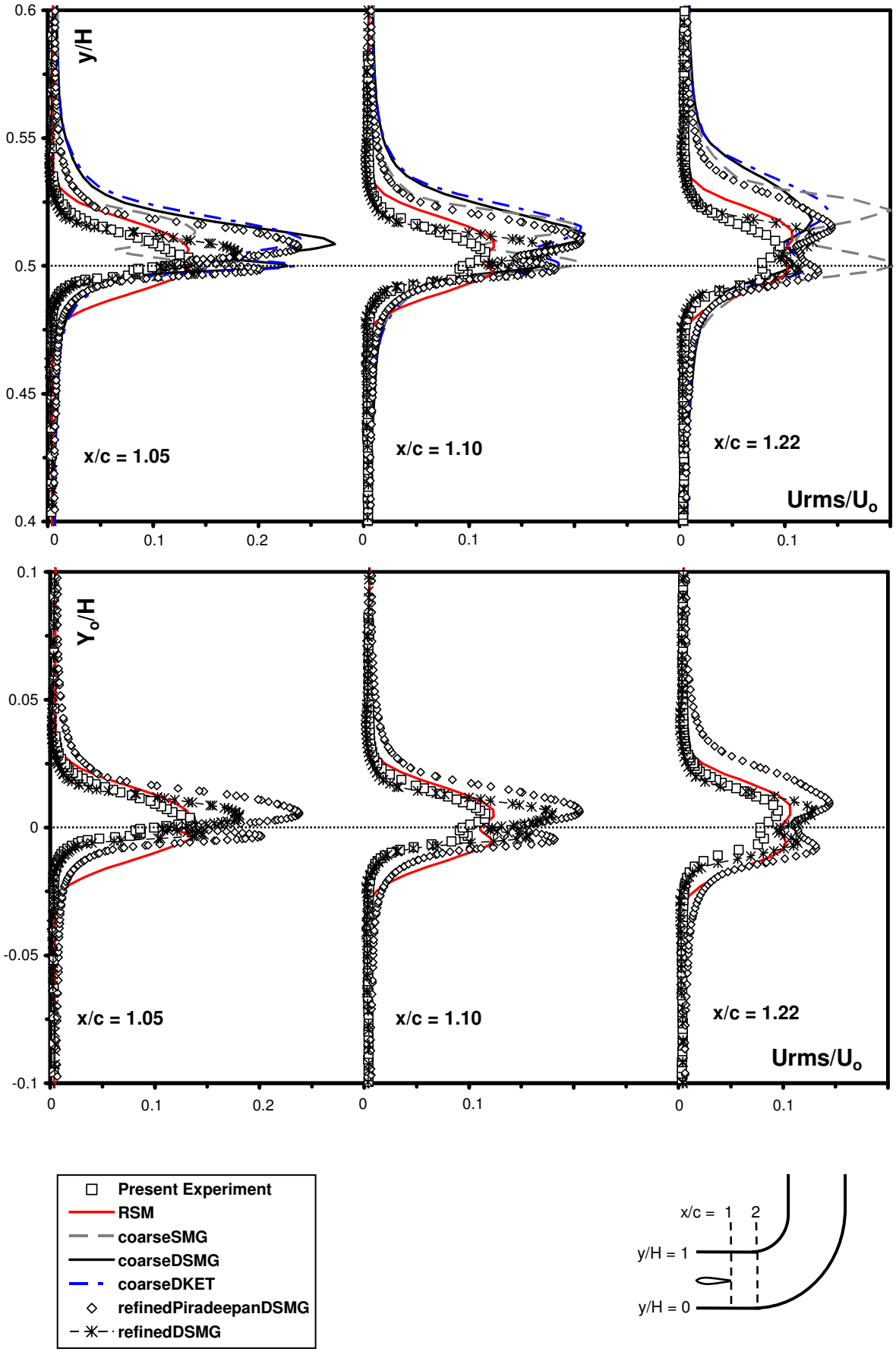

Figure 7.19: For caption see head of figure.

(b)

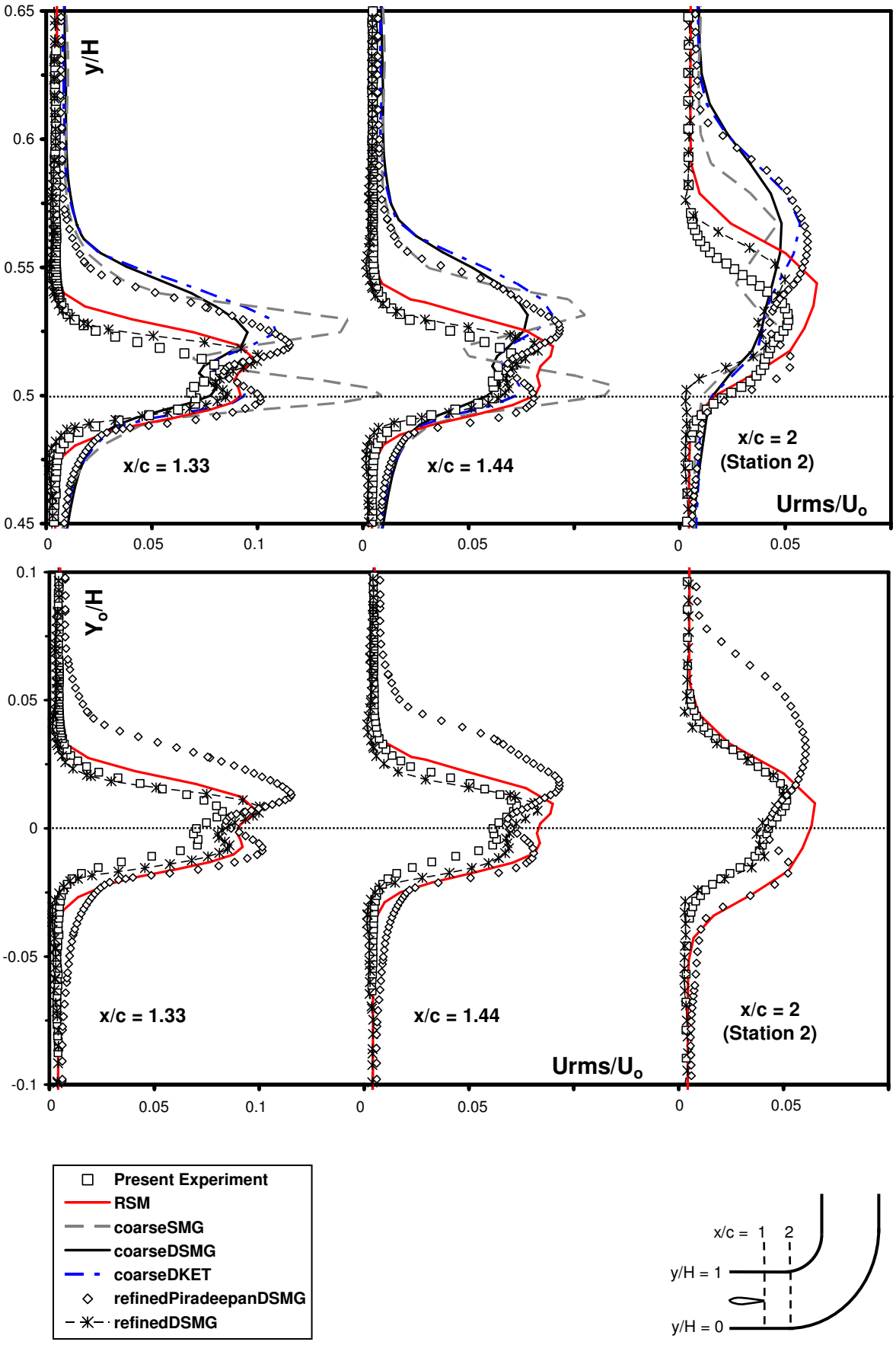

Figure 7.19: For caption see head of figure.

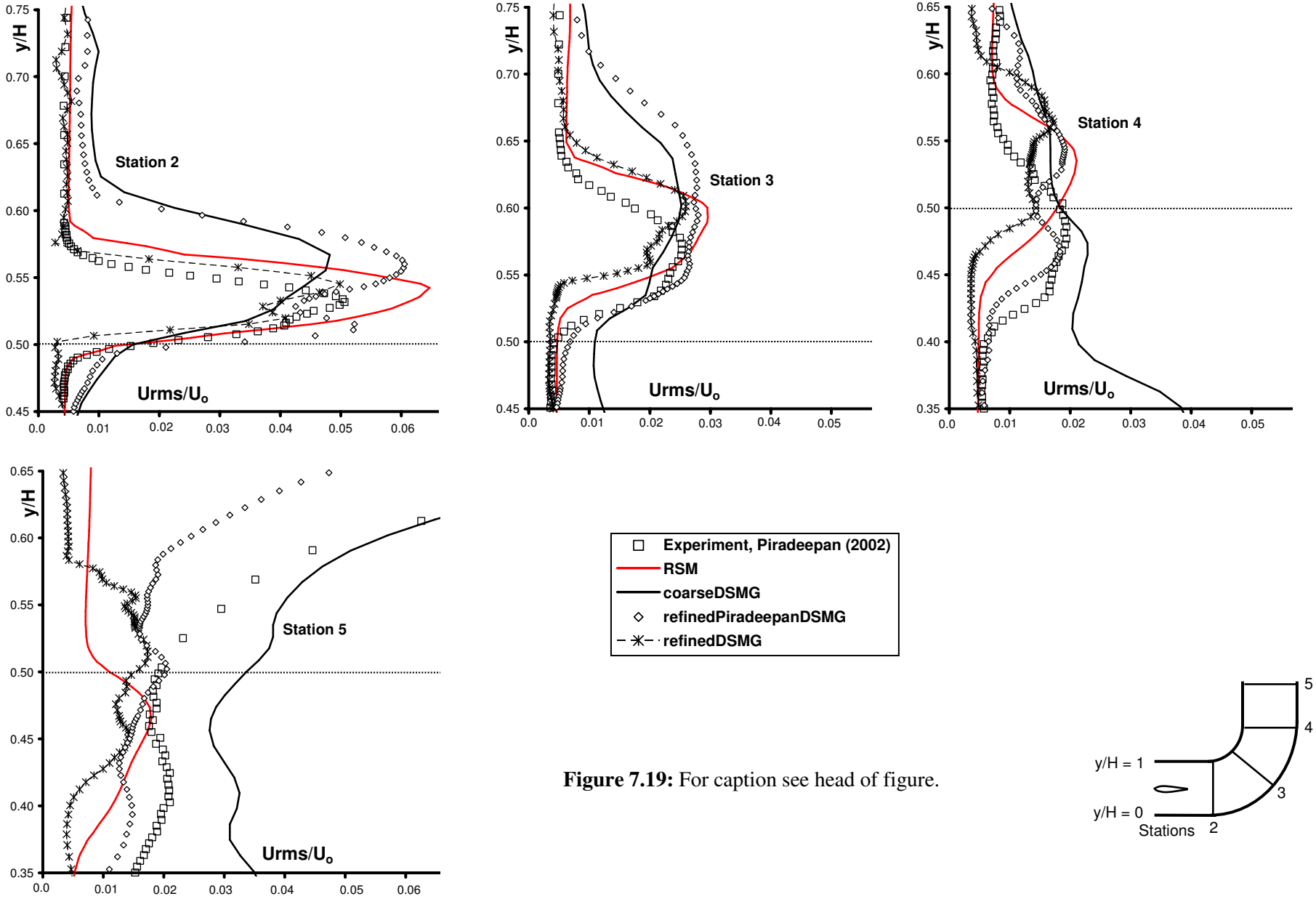

Figure 7.19: For caption see head of figure.

(d)

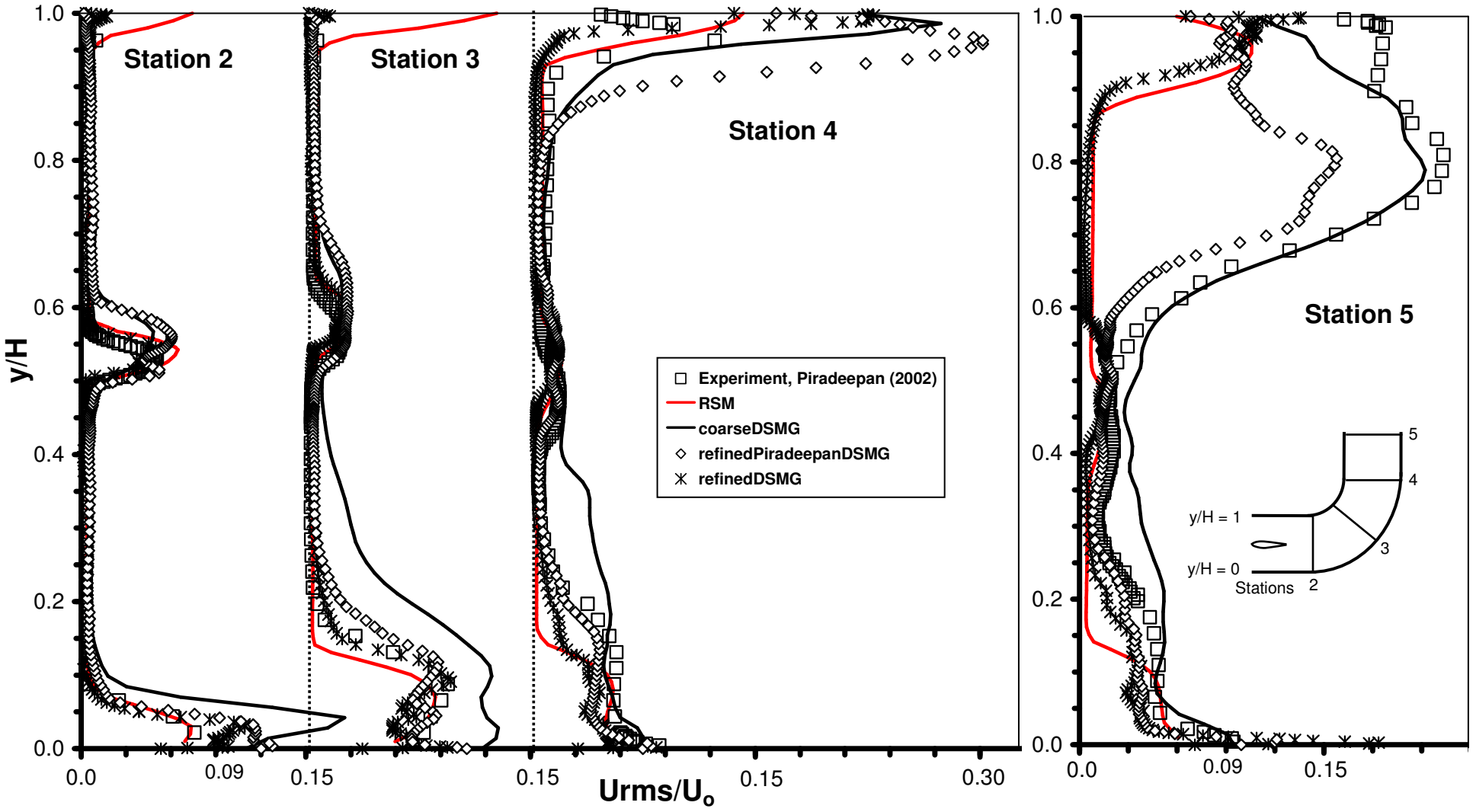

Figure 7.19: For caption see head of figure.

(e)

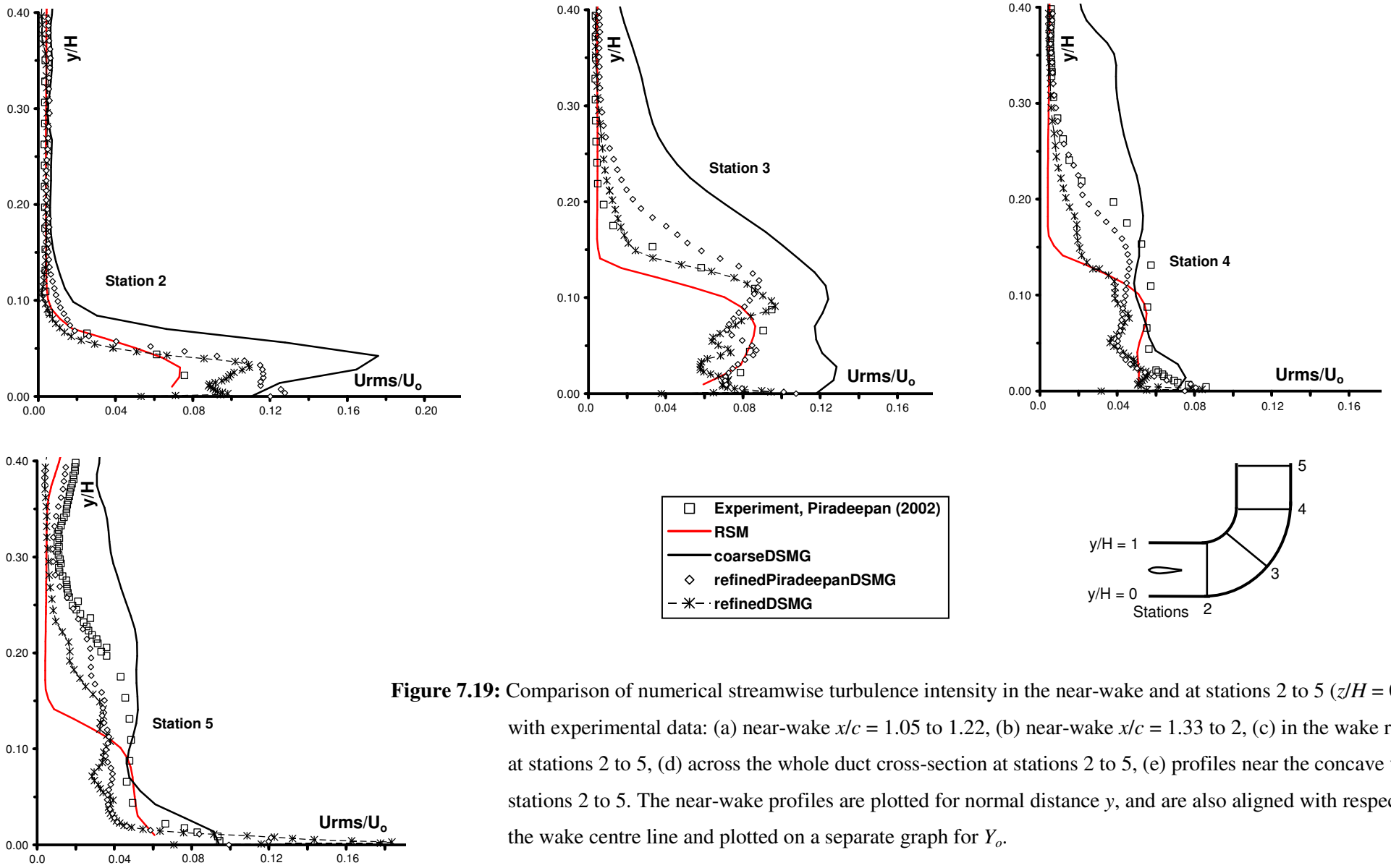

Figure 7.19: Comparison of numerical streamwise turbulence intensity in the near-wake and at stations 2 to 5 ($z/H = 0.5$) with experimental data: (a) near-wake $x/c = 1.05$ to 1.22, (b) near-wake $x/c = 1.33$ to 2, (c) in the wake region at stations 2 to 5, (d) across the whole duct cross-section at stations 2 to 5, (e) profiles near the concave wall at stations 2 to 5. The near-wake profiles are plotted for normal distance y, and are also aligned with respect to the wake centre line and plotted on a separate graph for Y_o.

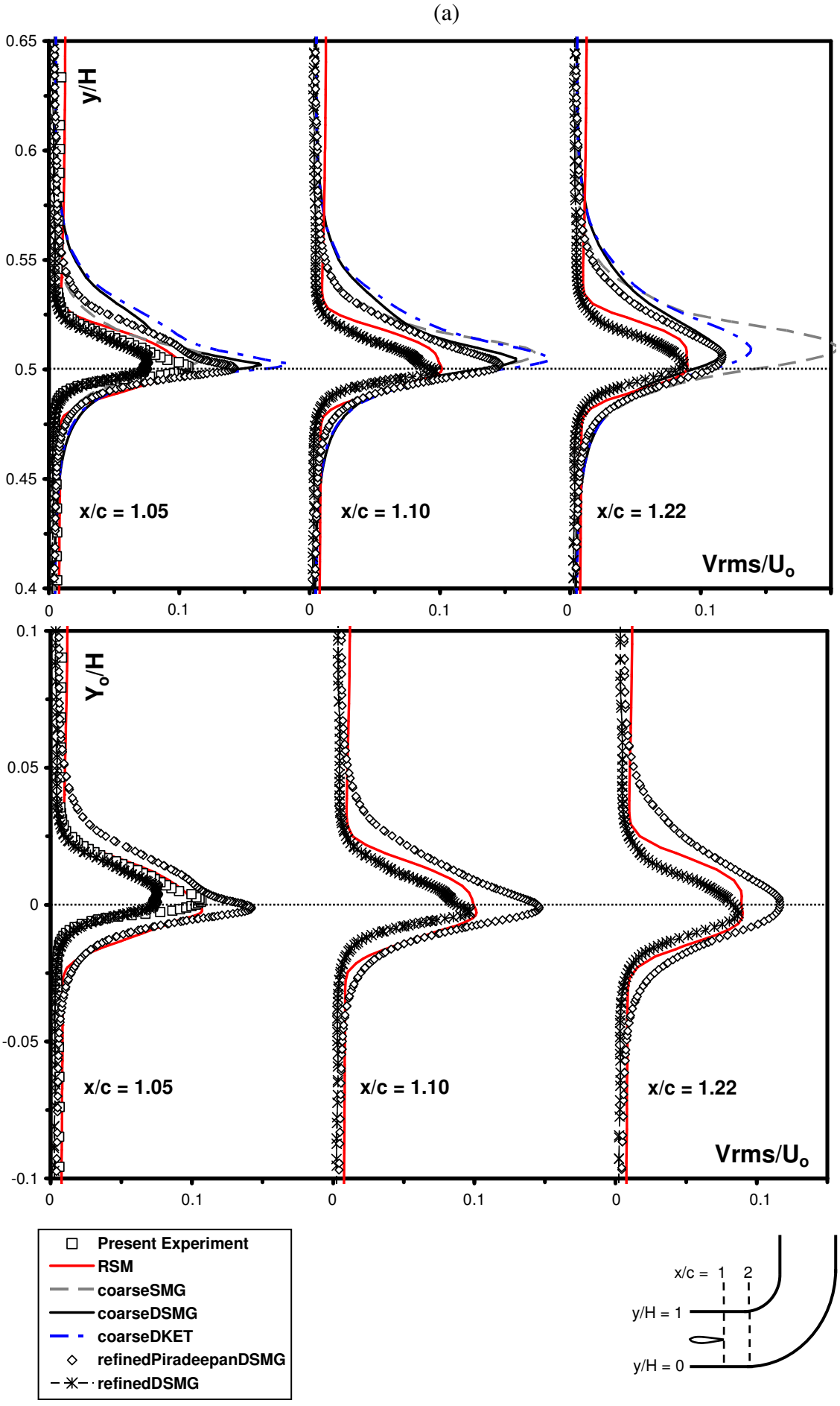

Figure 7.20: For caption see head of figure.

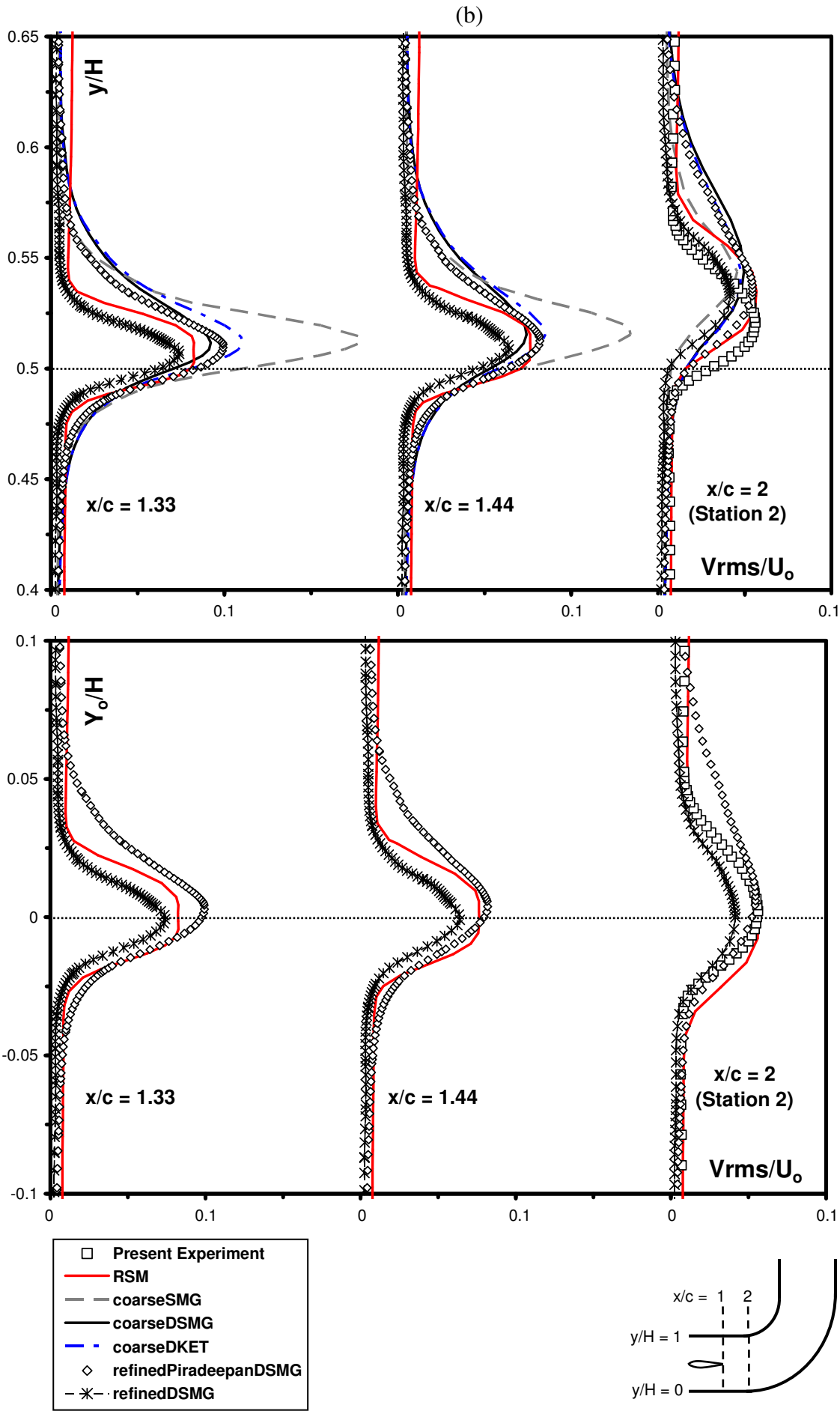

Figure 7.20: For caption see head of figure.

(c)

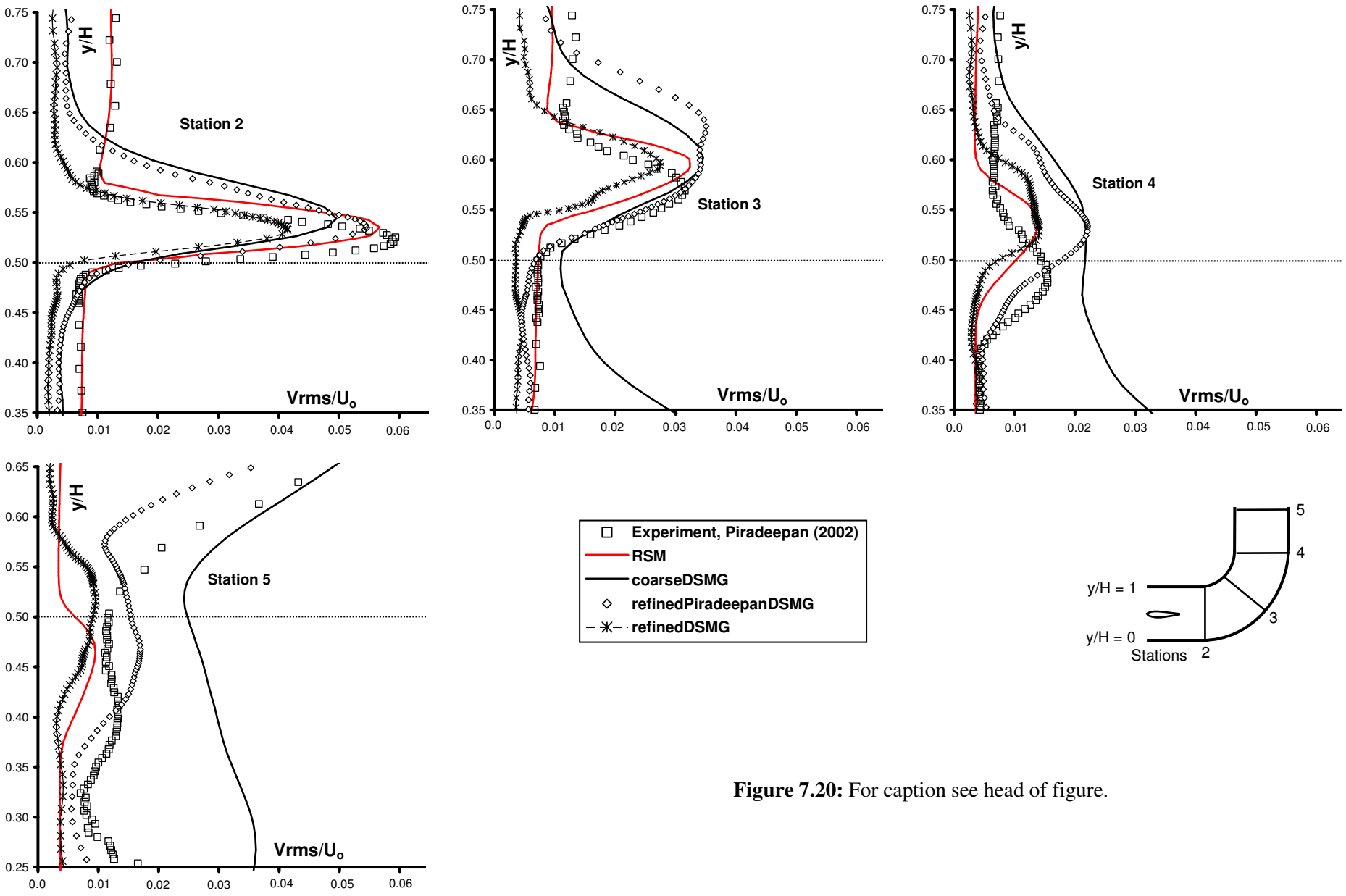

Figure 7.20: For caption see head of figure.

(d)

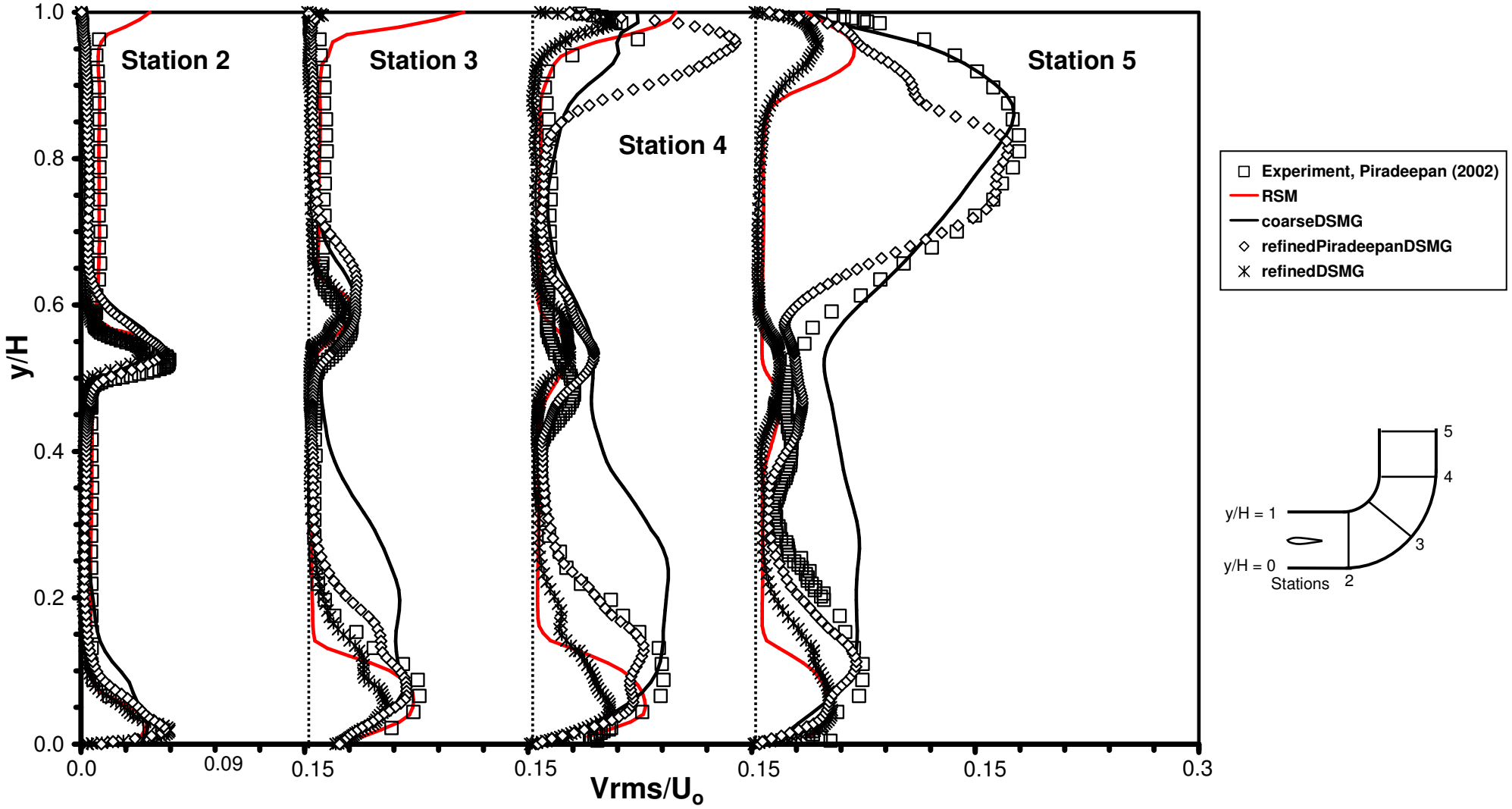

Figure 7.20: For caption see head of figure.

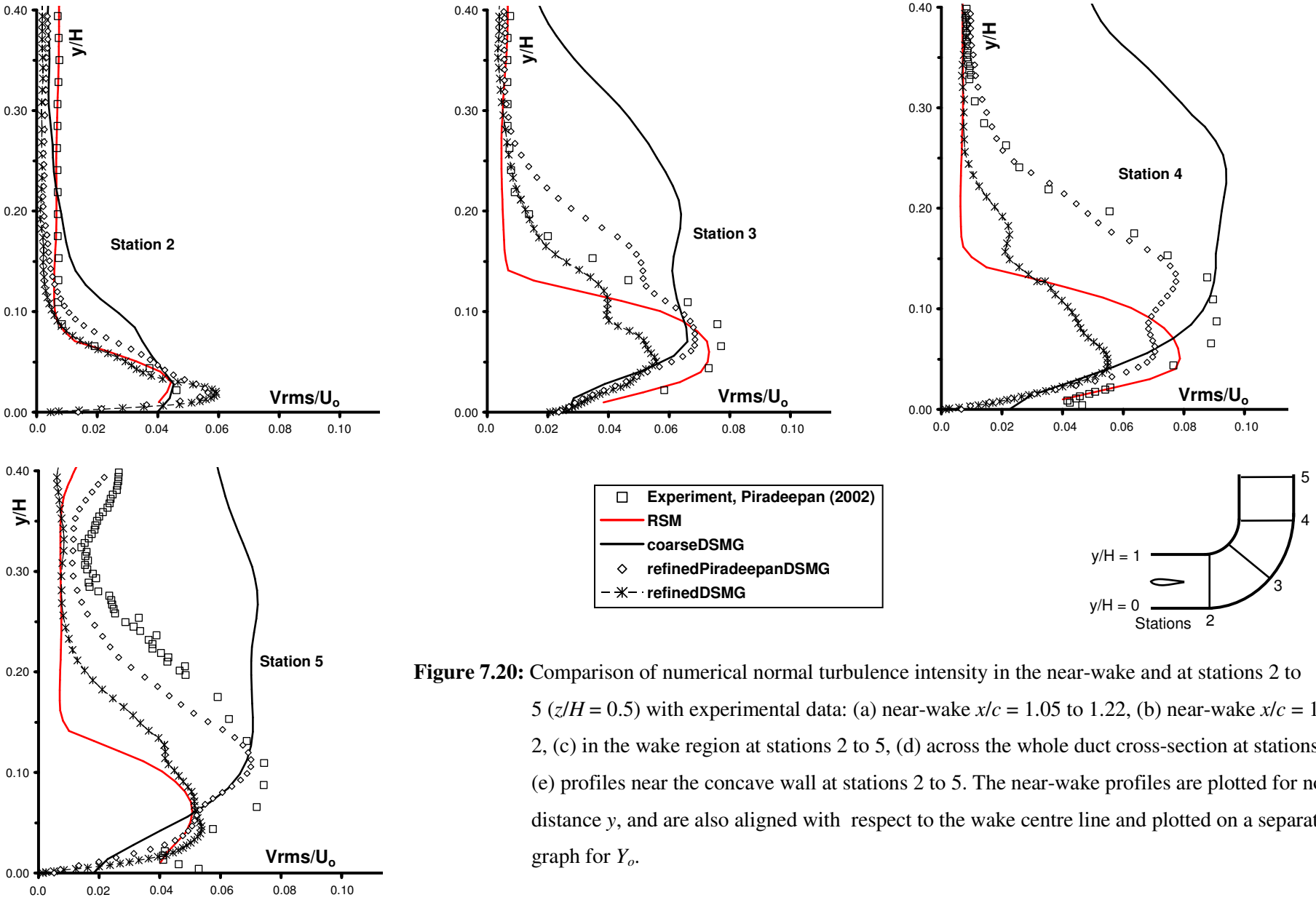

Figure 7.20: Comparison of numerical normal turbulence intensity in the near-wake and at stations 2 to 5 ($z/H = 0.5$) with experimental data: (a) near-wake x/c = 1.05 to 1.22, (b) near-wake x/c = 1.33 to 2, (c) in the wake region at stations 2 to 5, (d) across the whole duct cross-section at stations 2 to 5, (e) profiles near the concave wall at stations 2 to 5. The near-wake profiles are plotted for normal distance y, and are also aligned with respect to the wake centre line and plotted on a separate graph for Y_o.

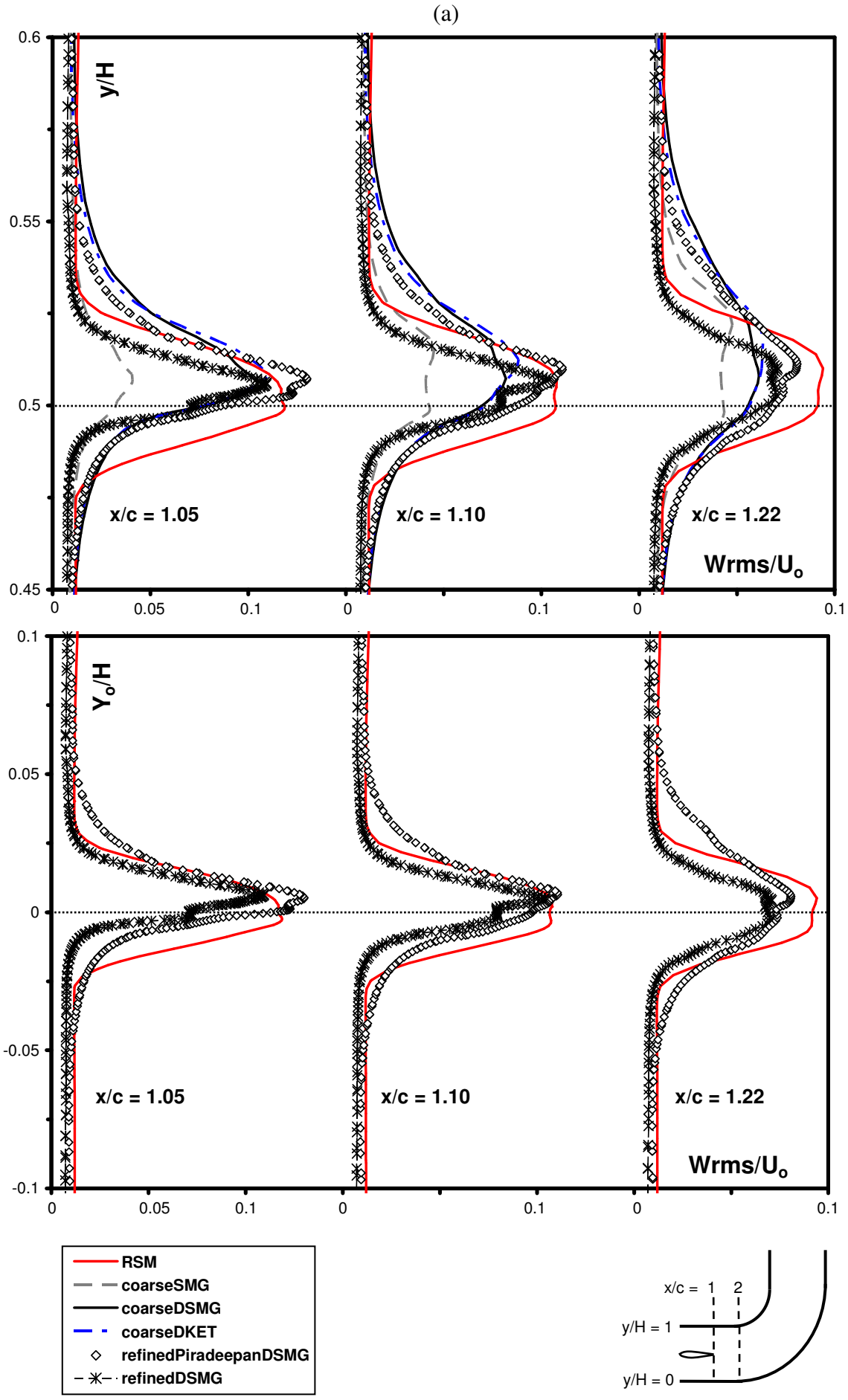

Figure 7.21: For caption see head of figure.

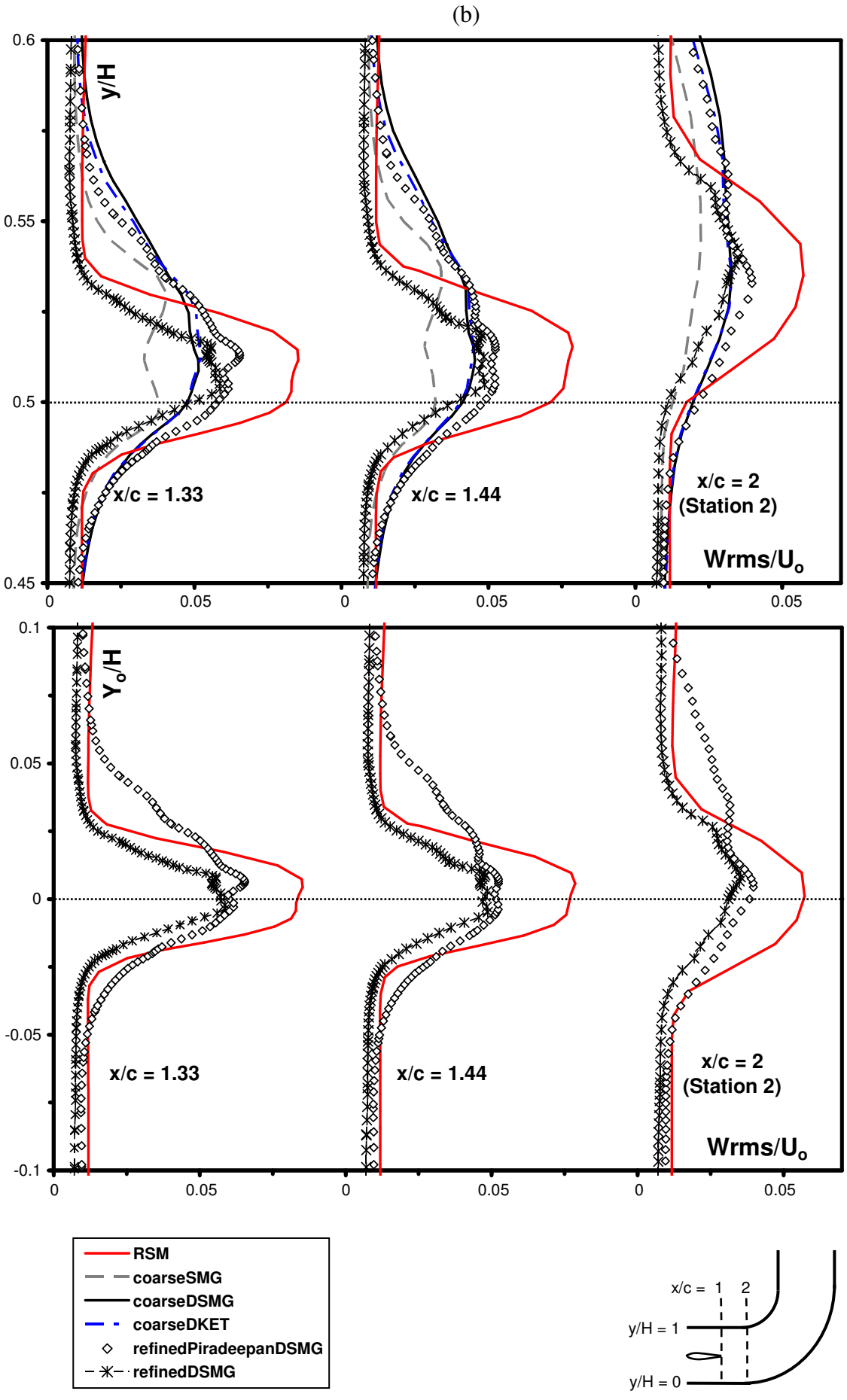

Figure 7.21: For caption see head of figure.

(c)

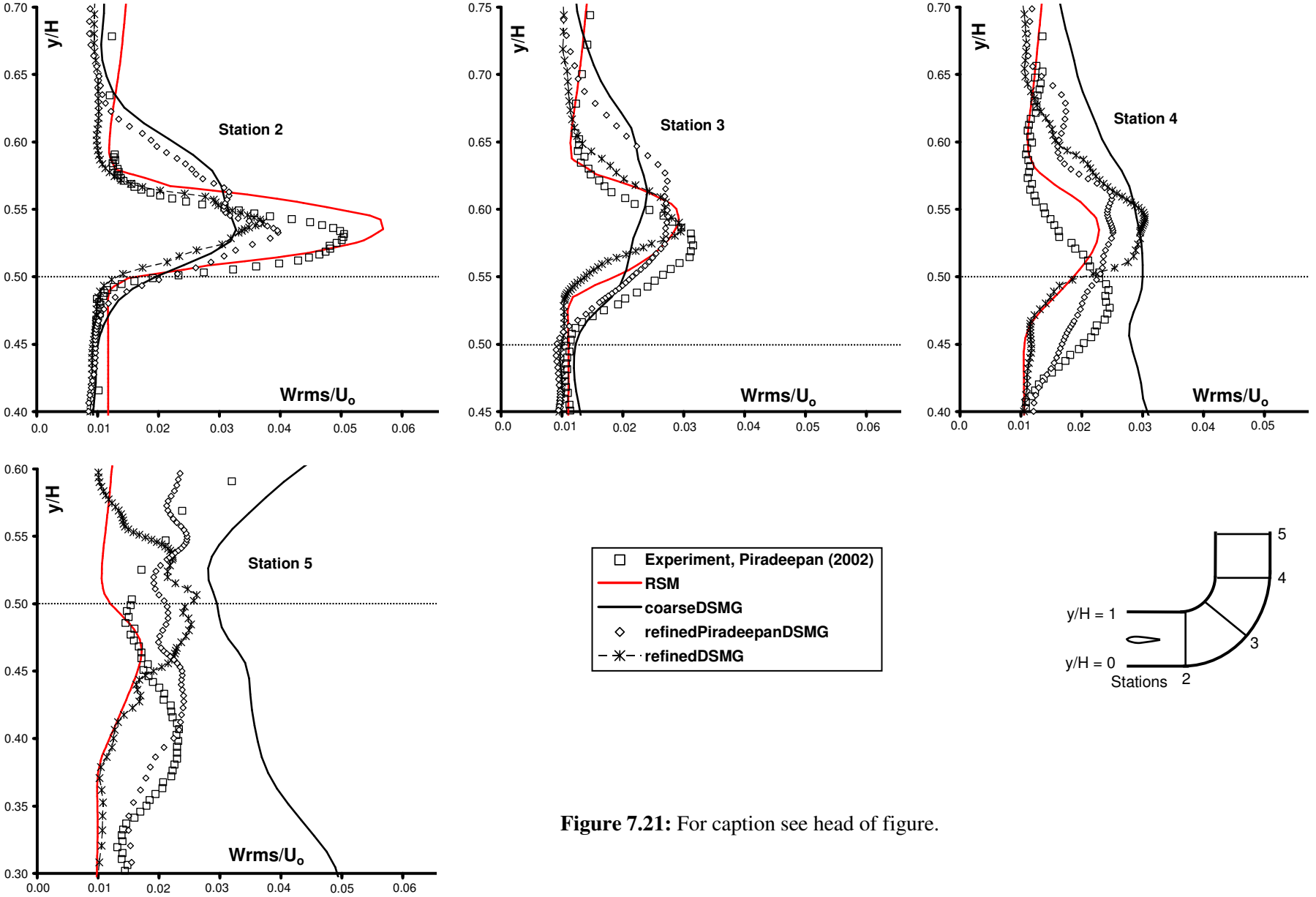

Figure 7.21: For caption see head of figure.

(d)

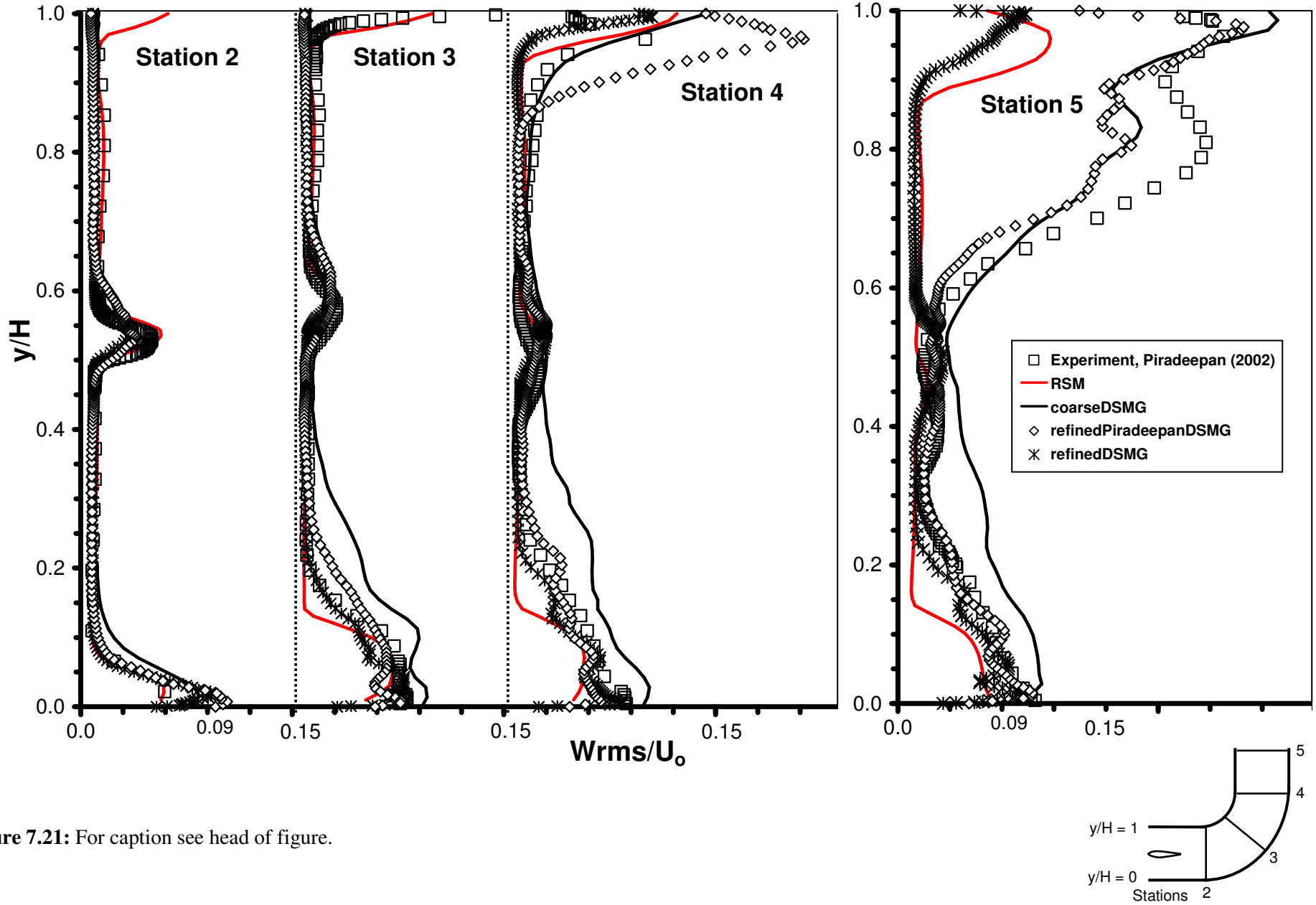

Figure 7.21: For caption see head of figure.

(e)

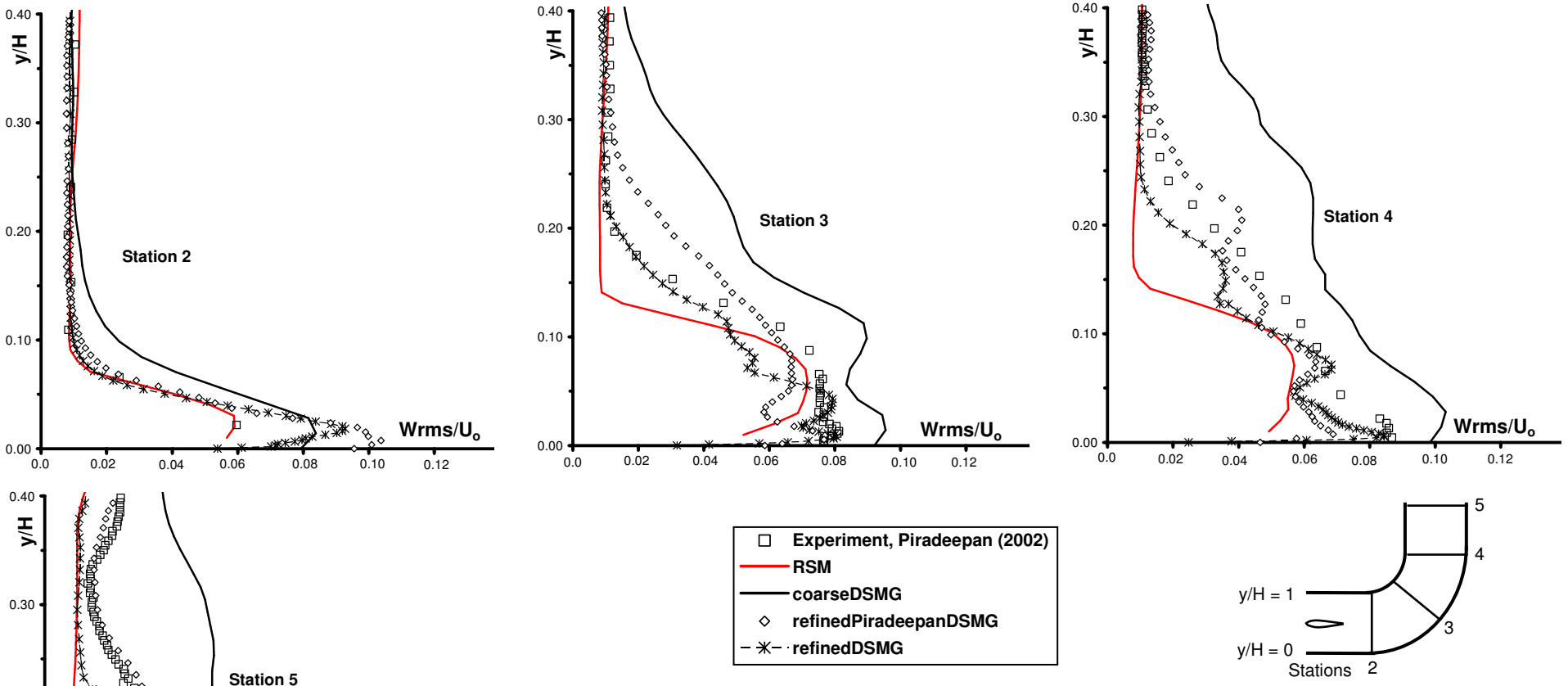

Figure 7.21: Comparison of spanwise turbulence intensity in the near-wake and at stations 2 to 5 ($z/H = 0.5$) with experimental data: (a) near-wake x/c = 1.05 to 1.22, (b) near-wake x/c = 1.33 to 2, (c) in the wake region at stations 2 to 5, (d) across the whole duct cross-section at stations 2 to 5, (e) profiles near the concave wall at stations 2 to 5. The near-wake profiles are plotted for normal distance y, and are also aligned with respect to the wake centre line and plotted on a separate graph for Y_o.

(a)

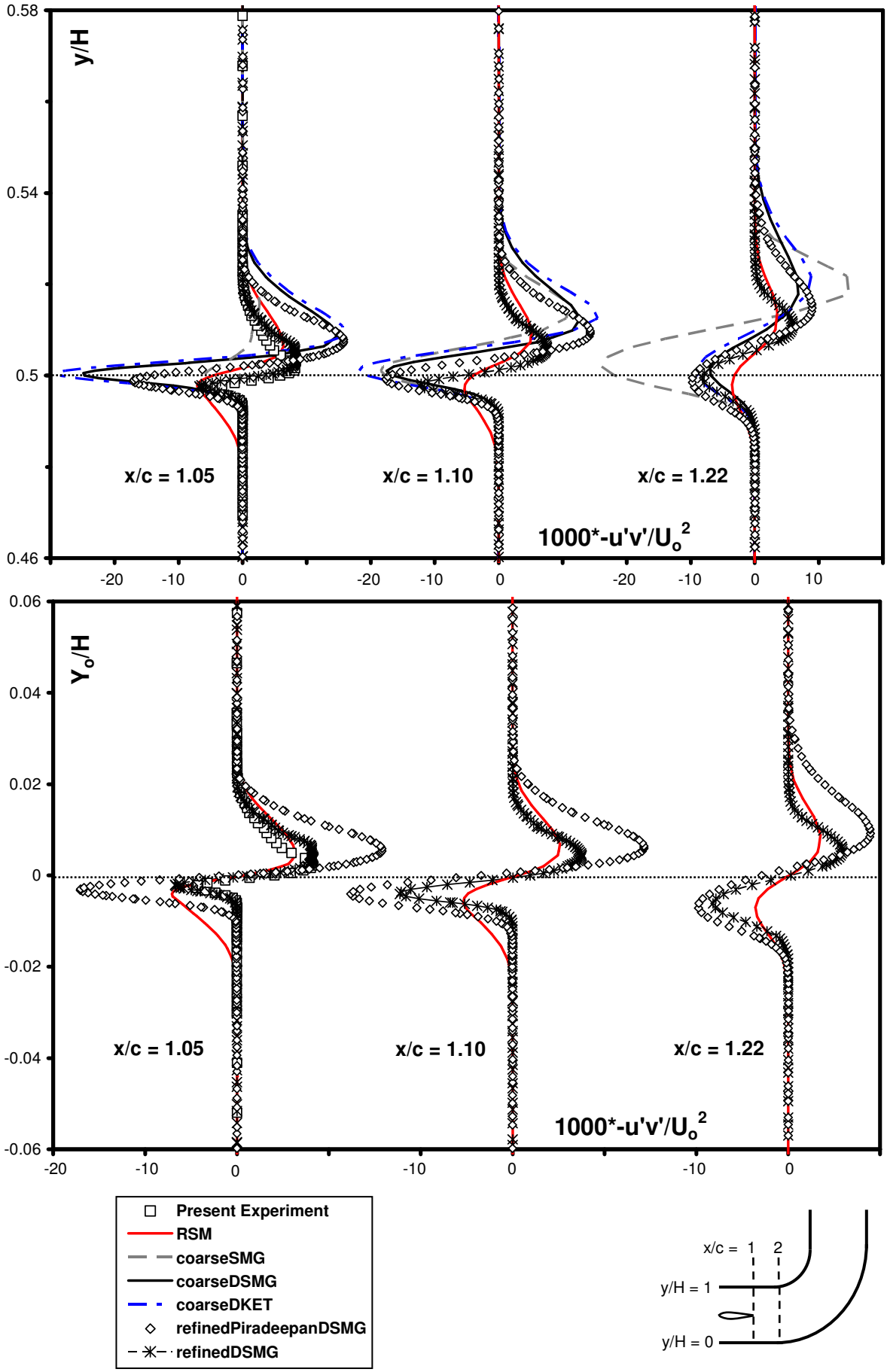

Figure 7.22: For caption see head of figure.

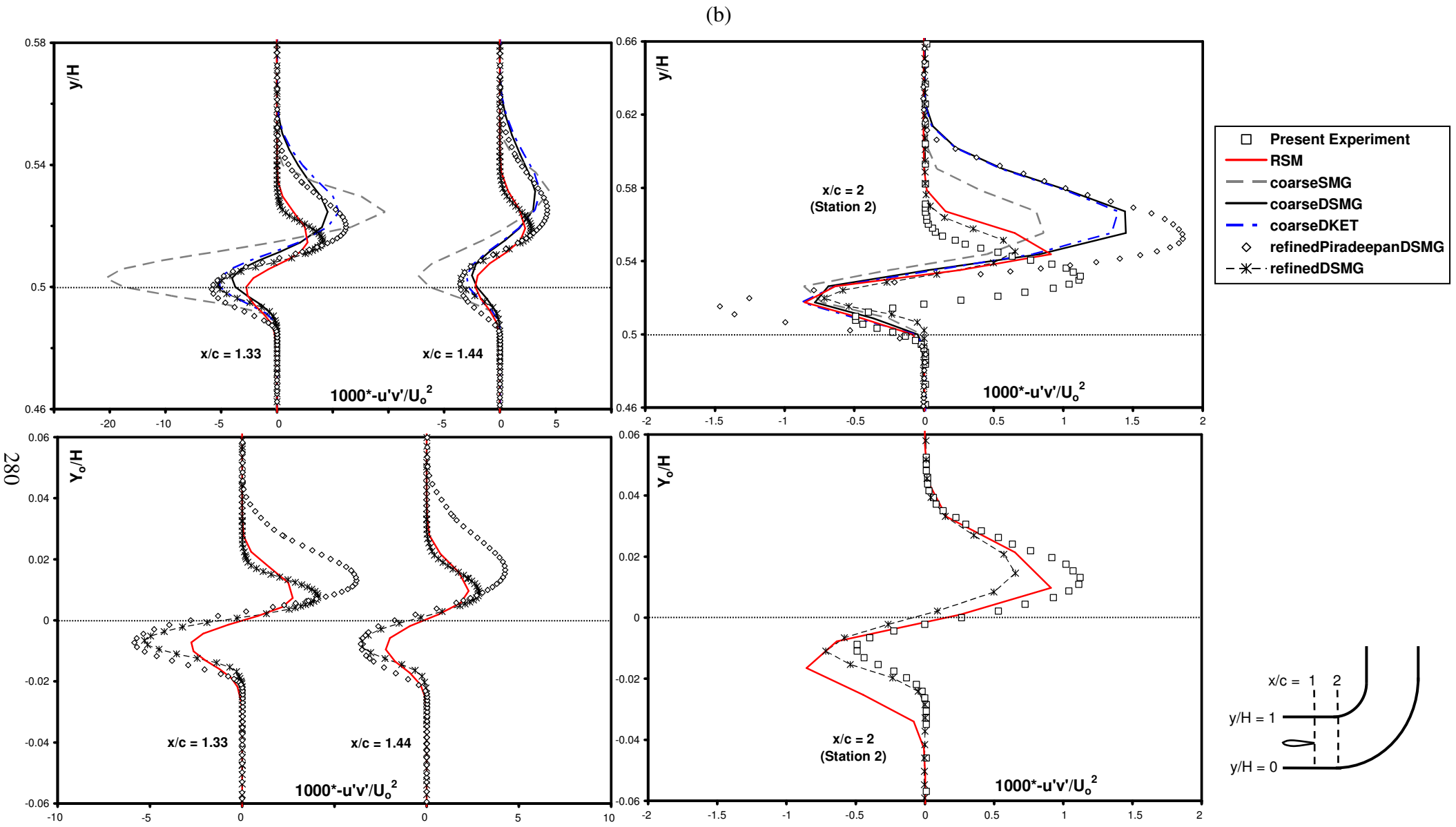

Figure 7.22: For caption see head of figure.

(c)

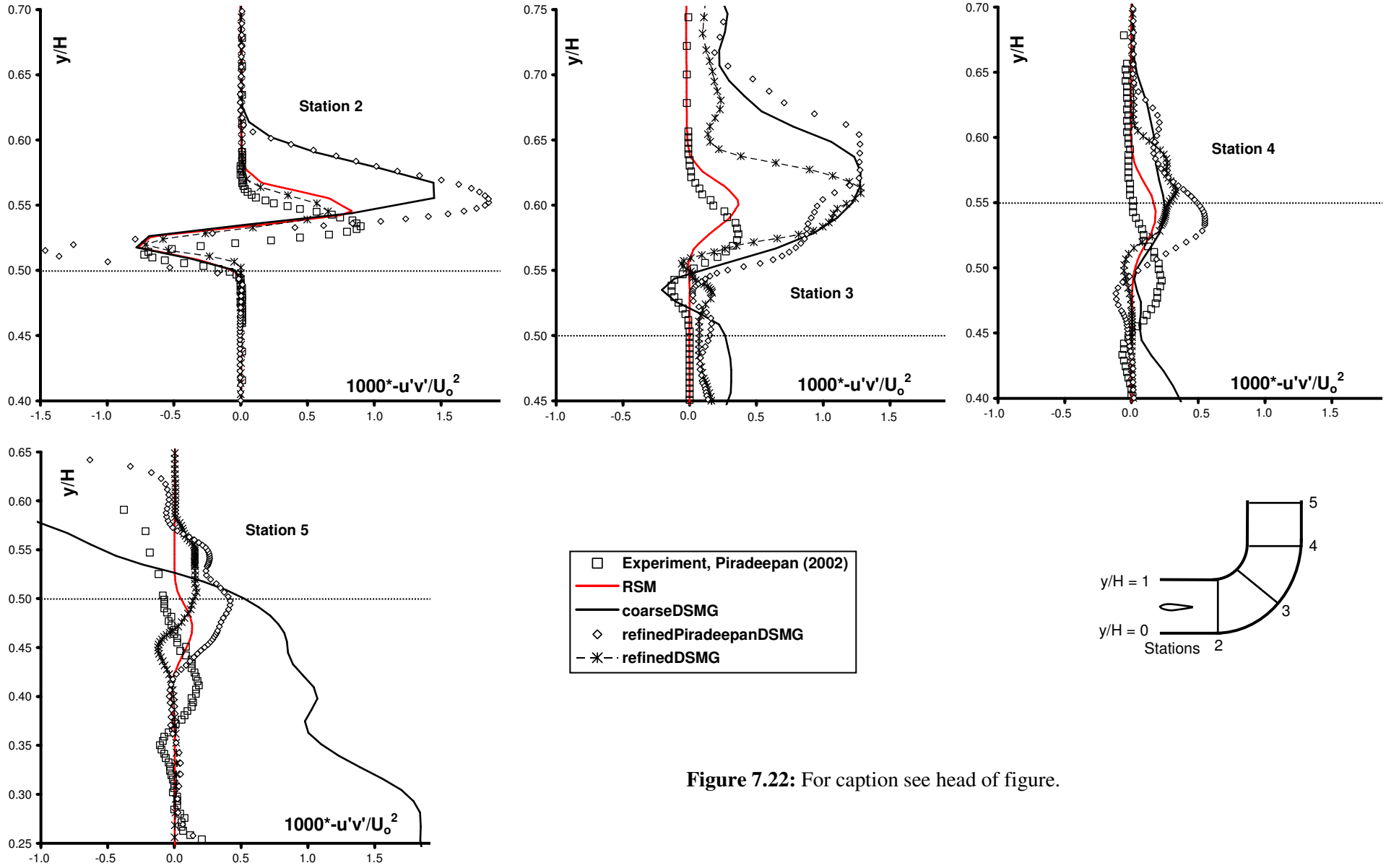

Figure 7.22: For caption see head of figure.

(d)

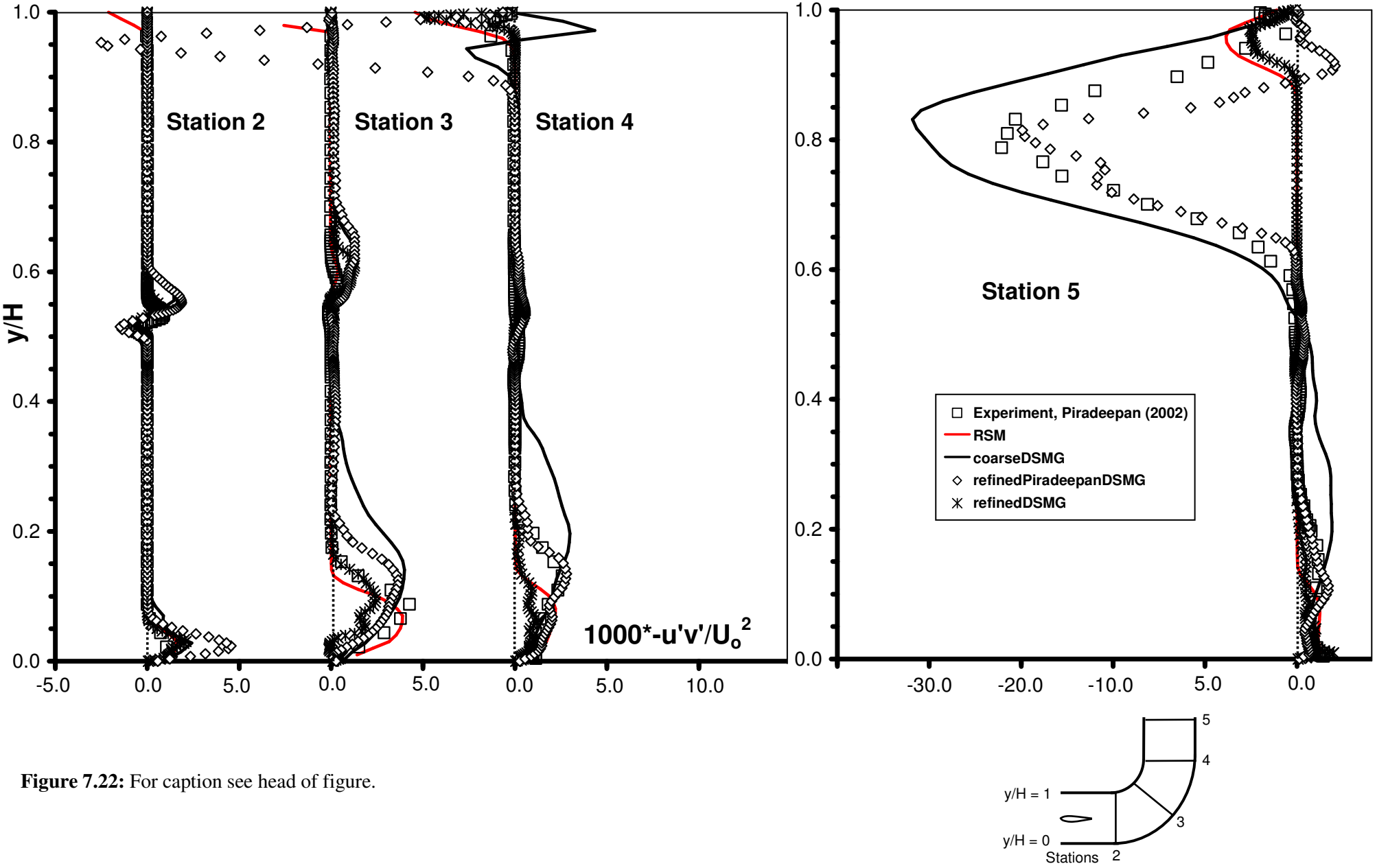

Figure 7.22: For caption see head of figure.

(e)

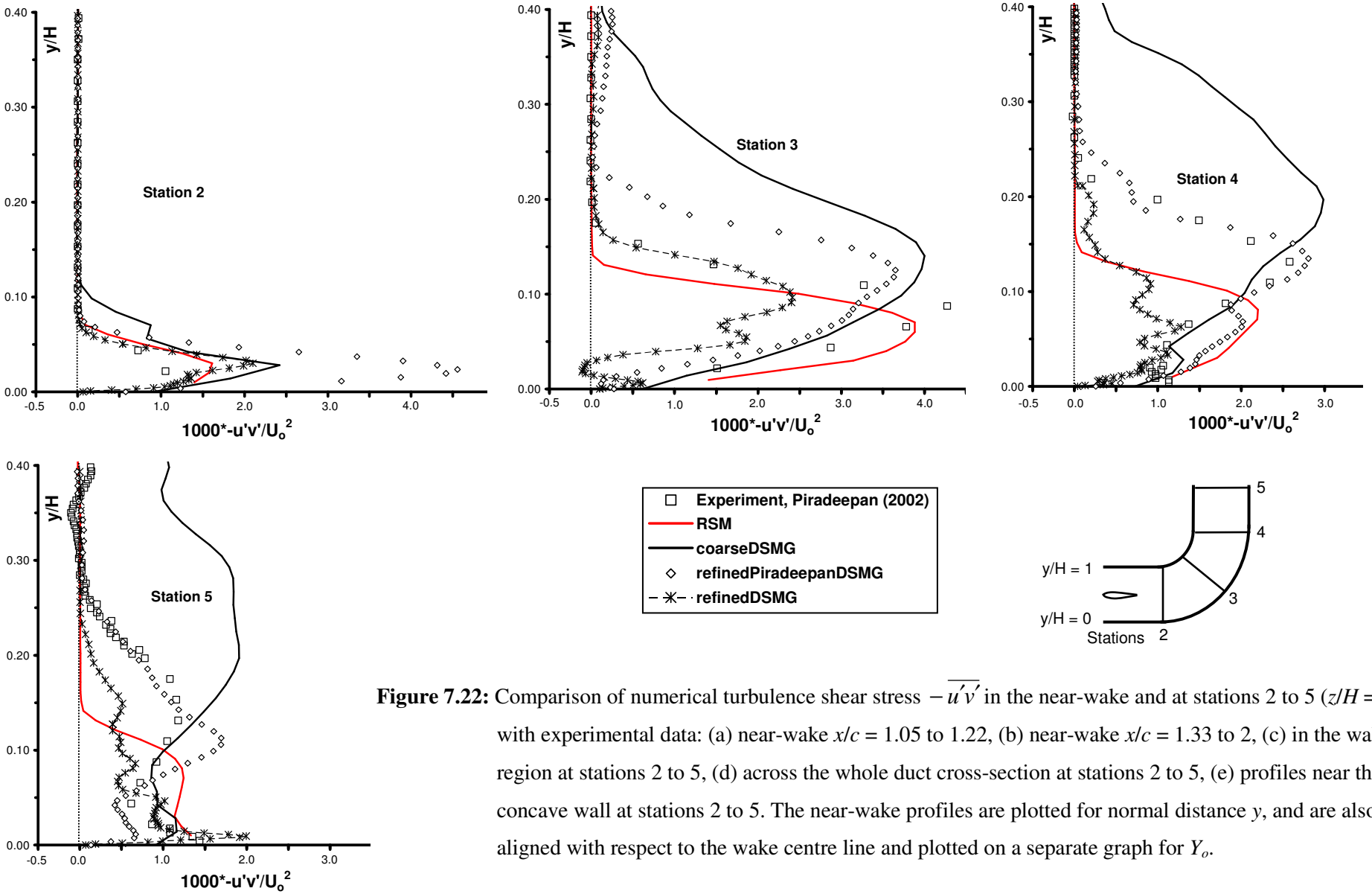

Figure 7.22: Comparison of numerical turbulence shear stress $-\overline{u'v'}$ in the near-wake and at stations 2 to 5 ($z/H = 0.5$) with experimental data: (a) near-wake $x/c = 1.05$ to 1.22, (b) near-wake $x/c = 1.33$ to 2, (c) in the wake region at stations 2 to 5, (d) across the whole duct cross-section at stations 2 to 5, (e) profiles near the concave wall at stations 2 to 5. The near-wake profiles are plotted for normal distance y, and are also aligned with respect to the wake centre line and plotted on a separate graph for Y_o.

(a)

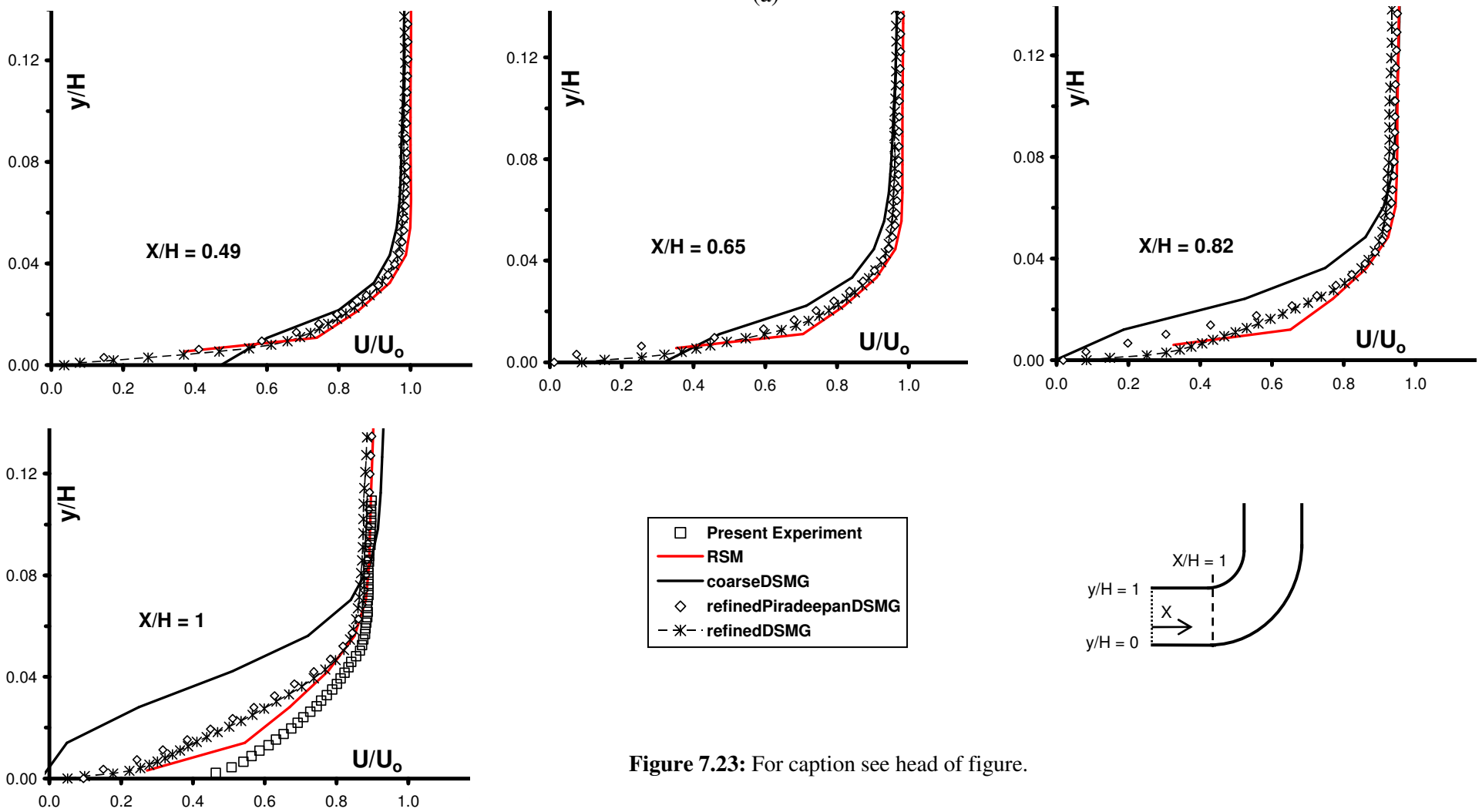

Figure 7.23: For caption see head of figure.

(b)

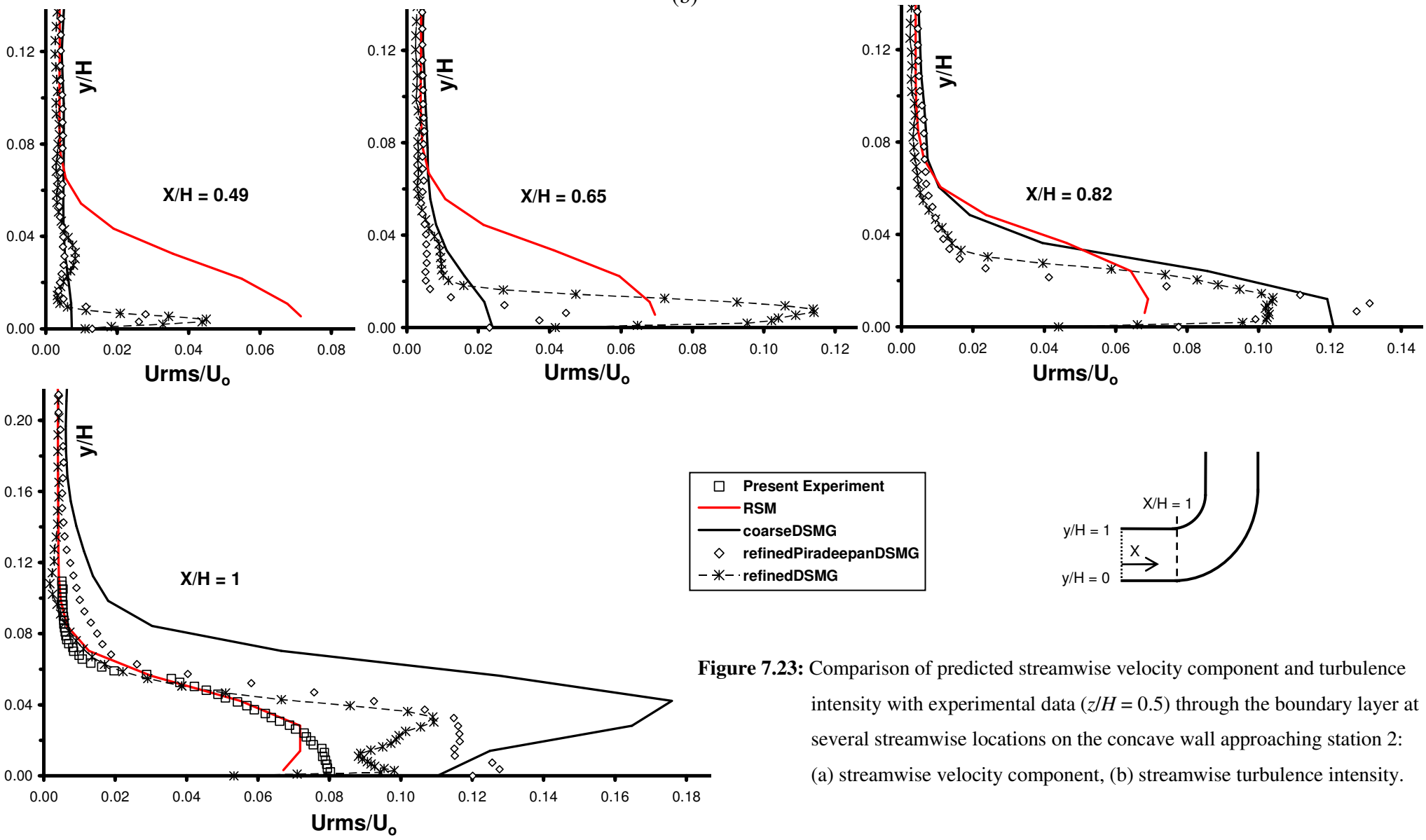

Figure 7.23: Comparison of predicted streamwise velocity component and turbulence intensity with experimental data ($z/H = 0.5$) through the boundary layer at several streamwise locations on the concave wall approaching station 2: (a) streamwise velocity component, (b) streamwise turbulence intensity.

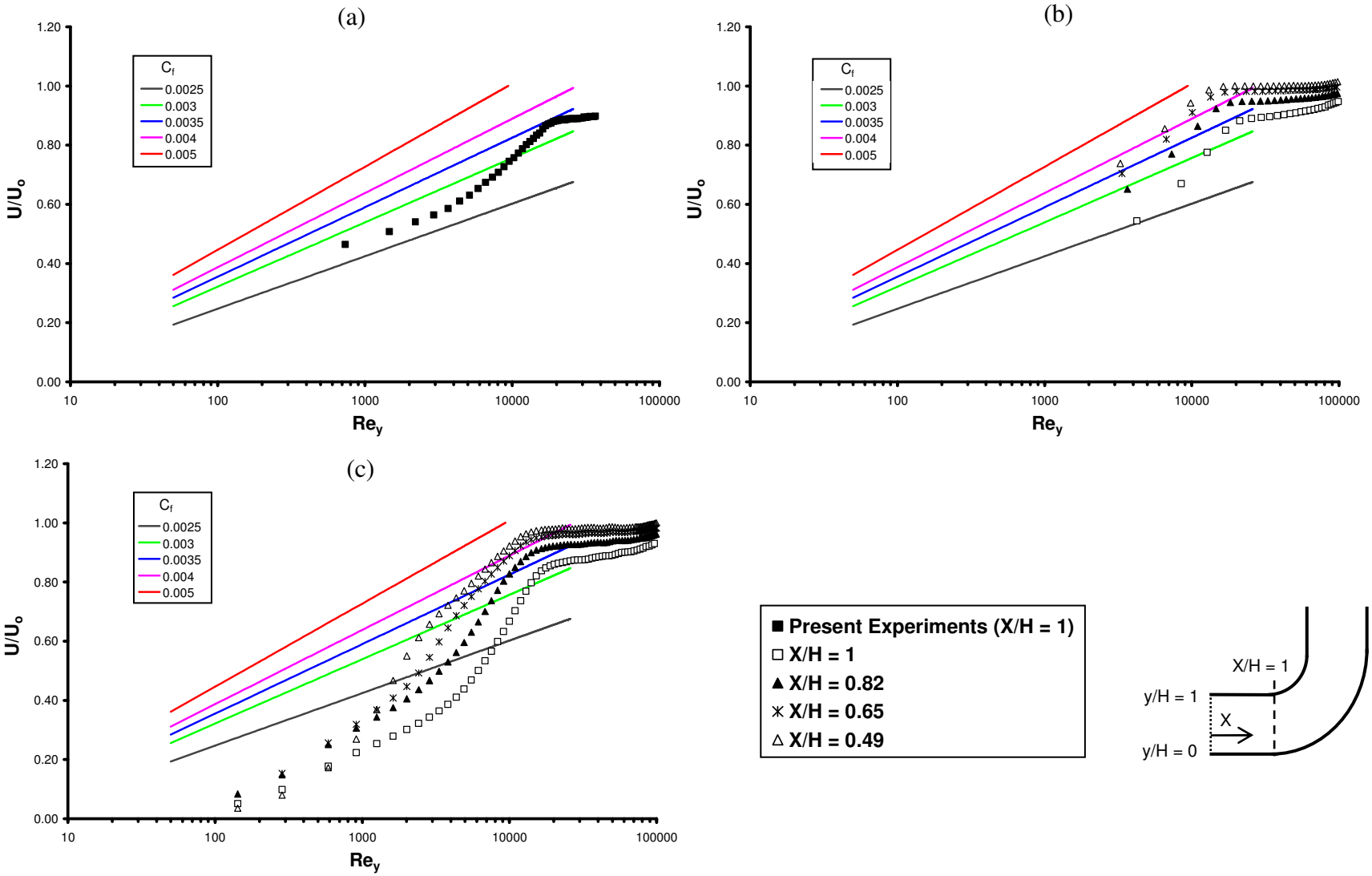

Figure 7.24: Clauser chart representations of the velocity profiles in the concave wall boundary layer ($z/H = 0.5$): (a) Present Experiments, (b) RSM, (c) refinedDSMG.

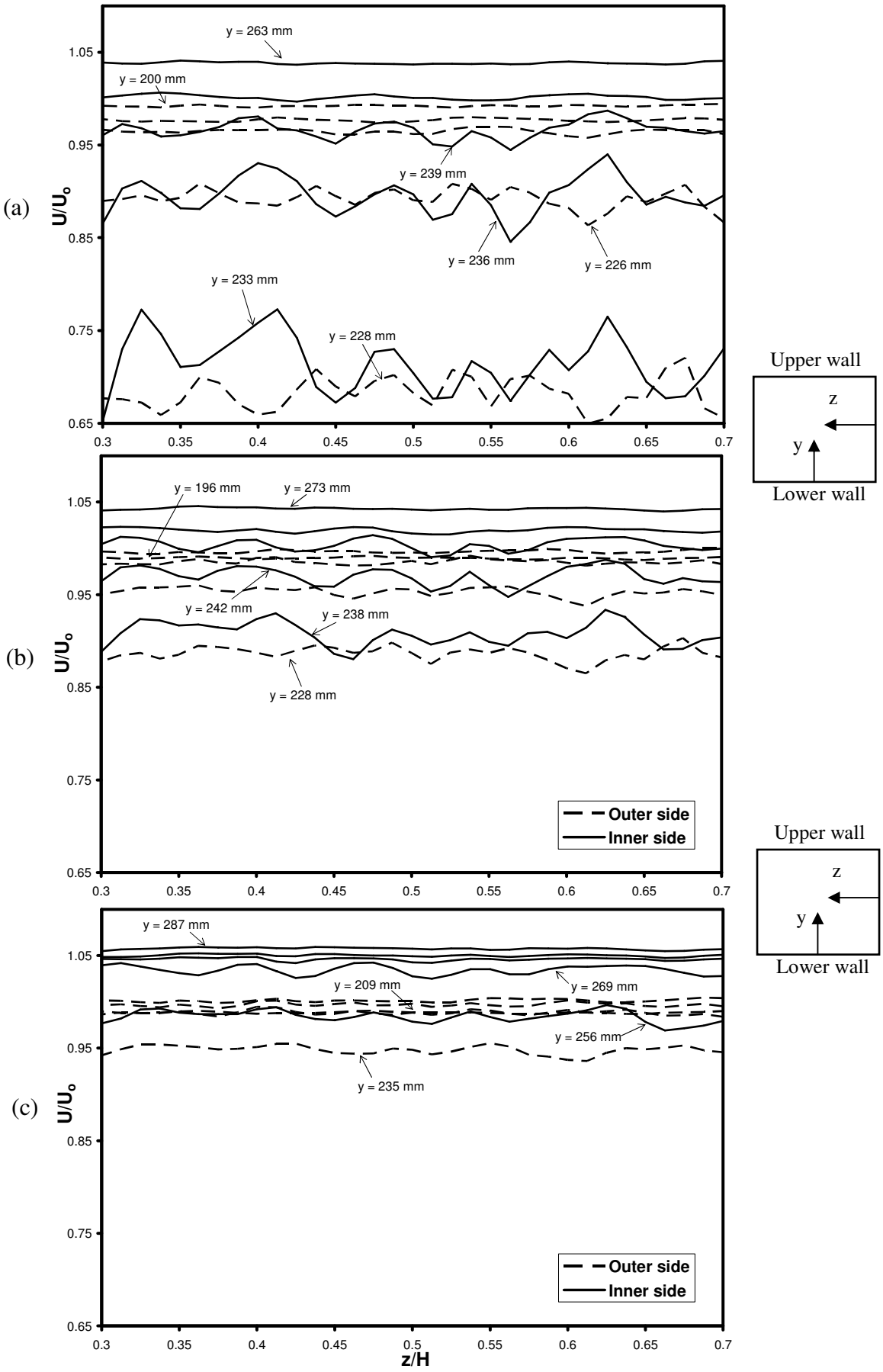

Figure 7.25: Computed spanwise distributions of mean streamwise velocity in the near-wake, for refinedPiradeepanDSMG, at several streamwise locations past the trailing edge of the airfoil: (a) x/c = 1.10, (b) x/c = 1.33, (c) x/c = 2. The distance x is measured from the leading edge of the airfoil.

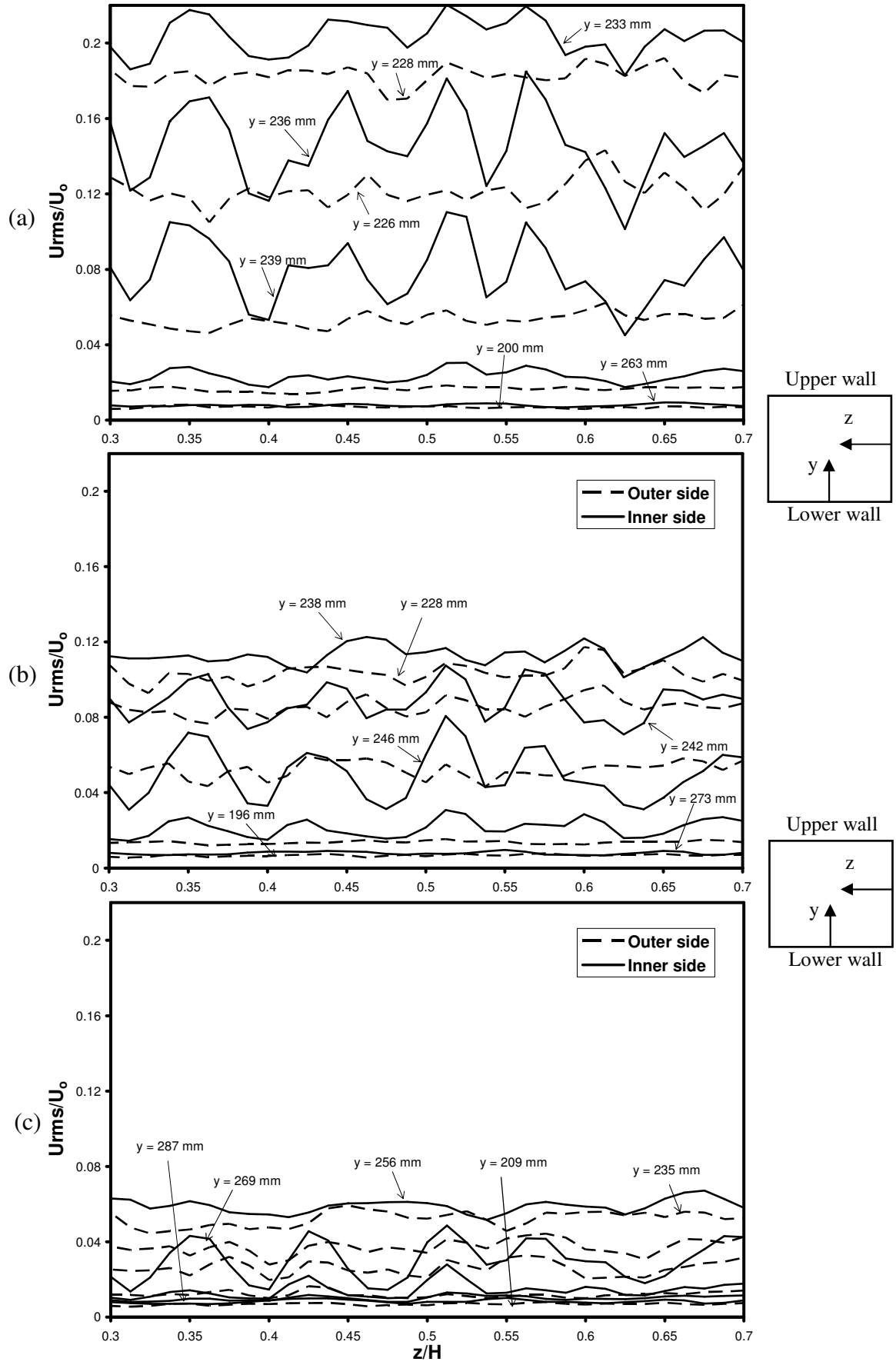

Figure 7.26: Computed spanwise distributions of streamwise intensity in the near-wake, for refinedPiradeepanDSMG, at several streamwise locations past the trailing edge of the airfoil: (a) x/c = 1.10, (b) x/c = 1.33, (c) x/c = 2. The distance x is measured from the leading edge of the airfoil.

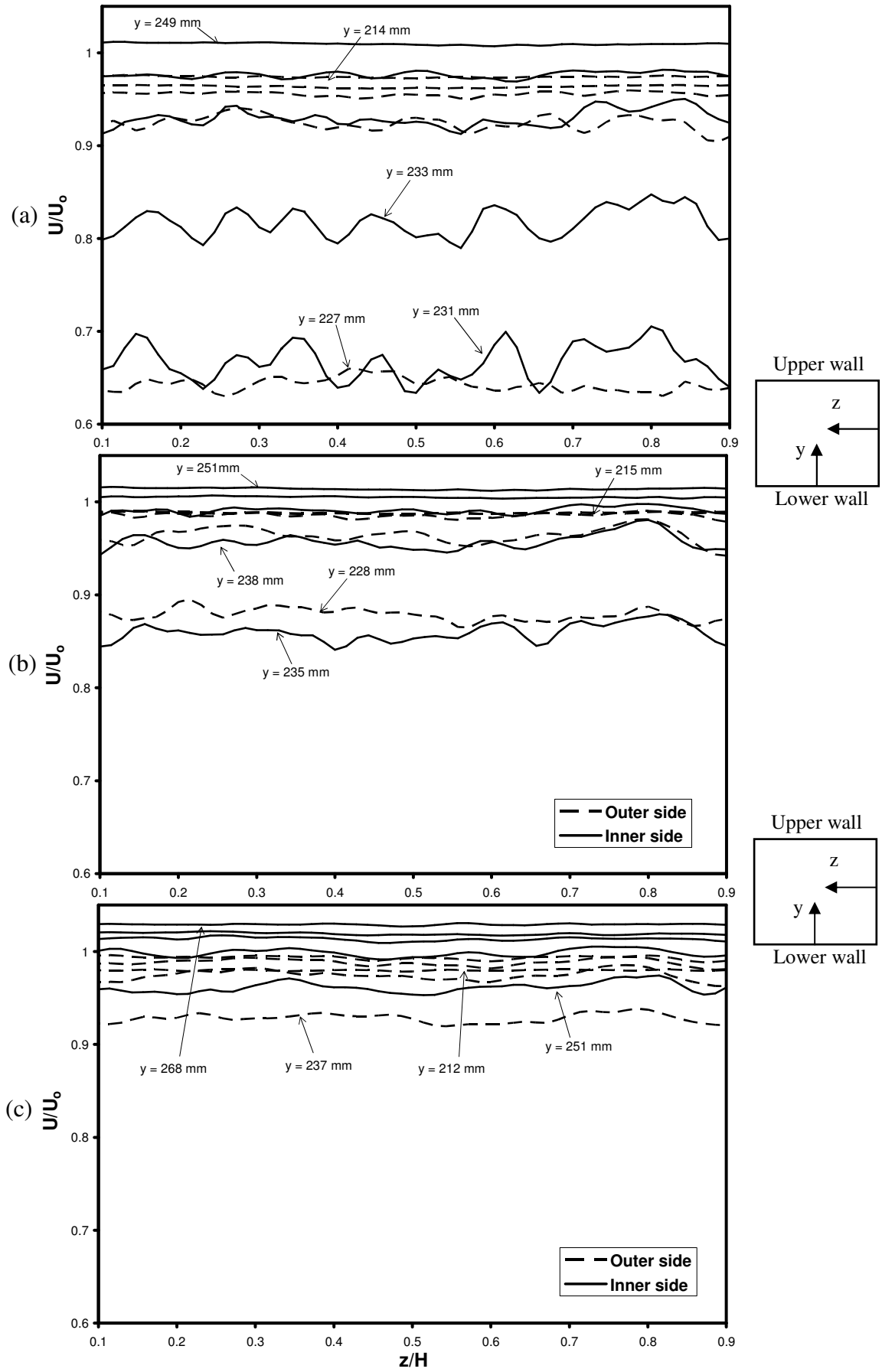

Figure 7.27: Computed spanwise distributions of mean streamwise velocity in the near-wake, for refinedDSMG, at several streamwise locations past the trailing edge of the airfoil: (a) x/c = 1.10, (b) x/c = 1.33, (c) x/c = 2. The distance x is measured from the leading edge of the airfoil.

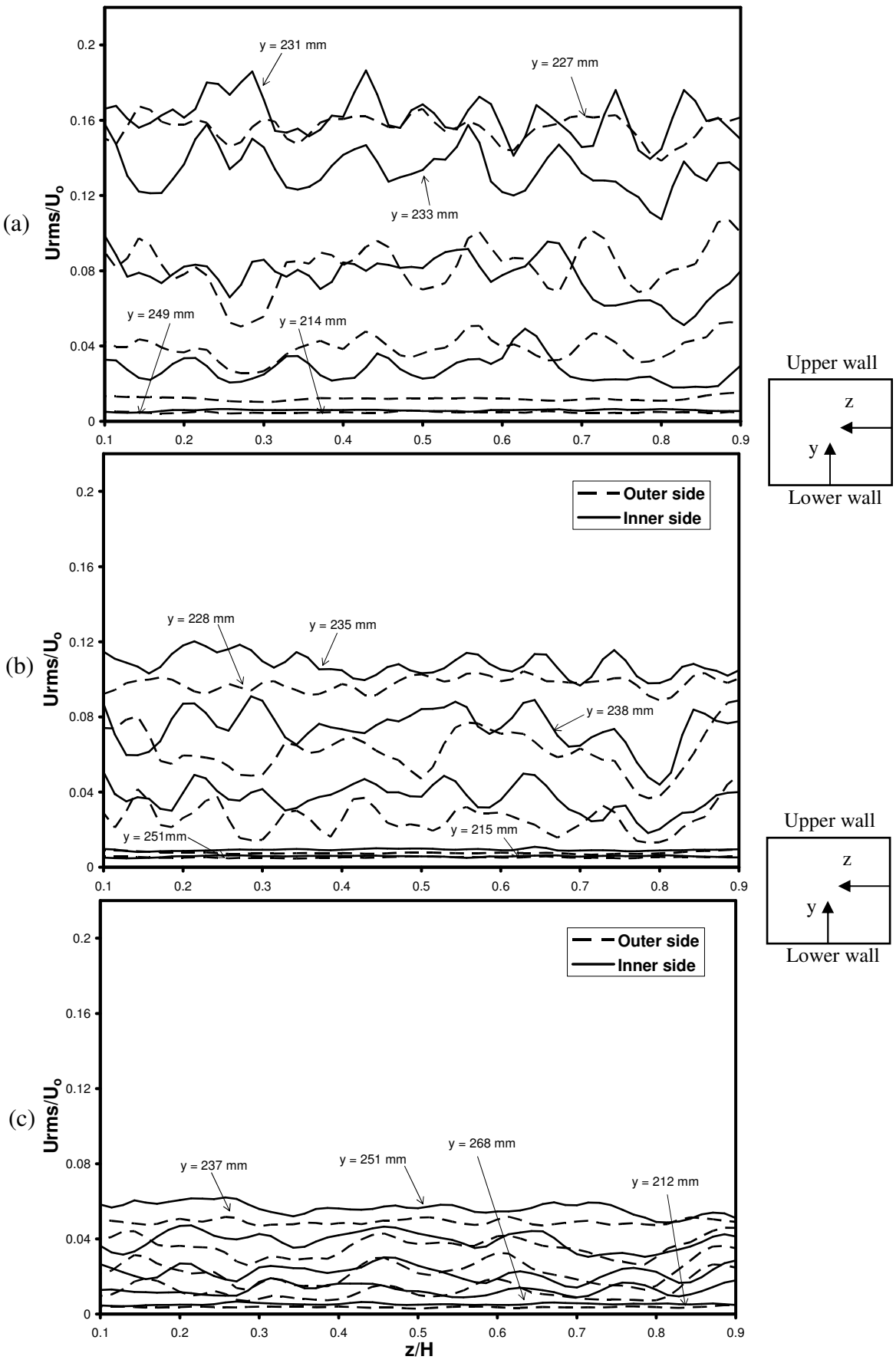

Figure 7.28: Computed spanwise distributions of streamwise intensity in the near-wake, for refinedDSMG, at several streamwise locations past the trailing edge of the airfoil: (a) x/c = 1.10, (b) x/c = 1.33, (c) x/c = 2. The distance x is measured from the leading edge of the airfoil.

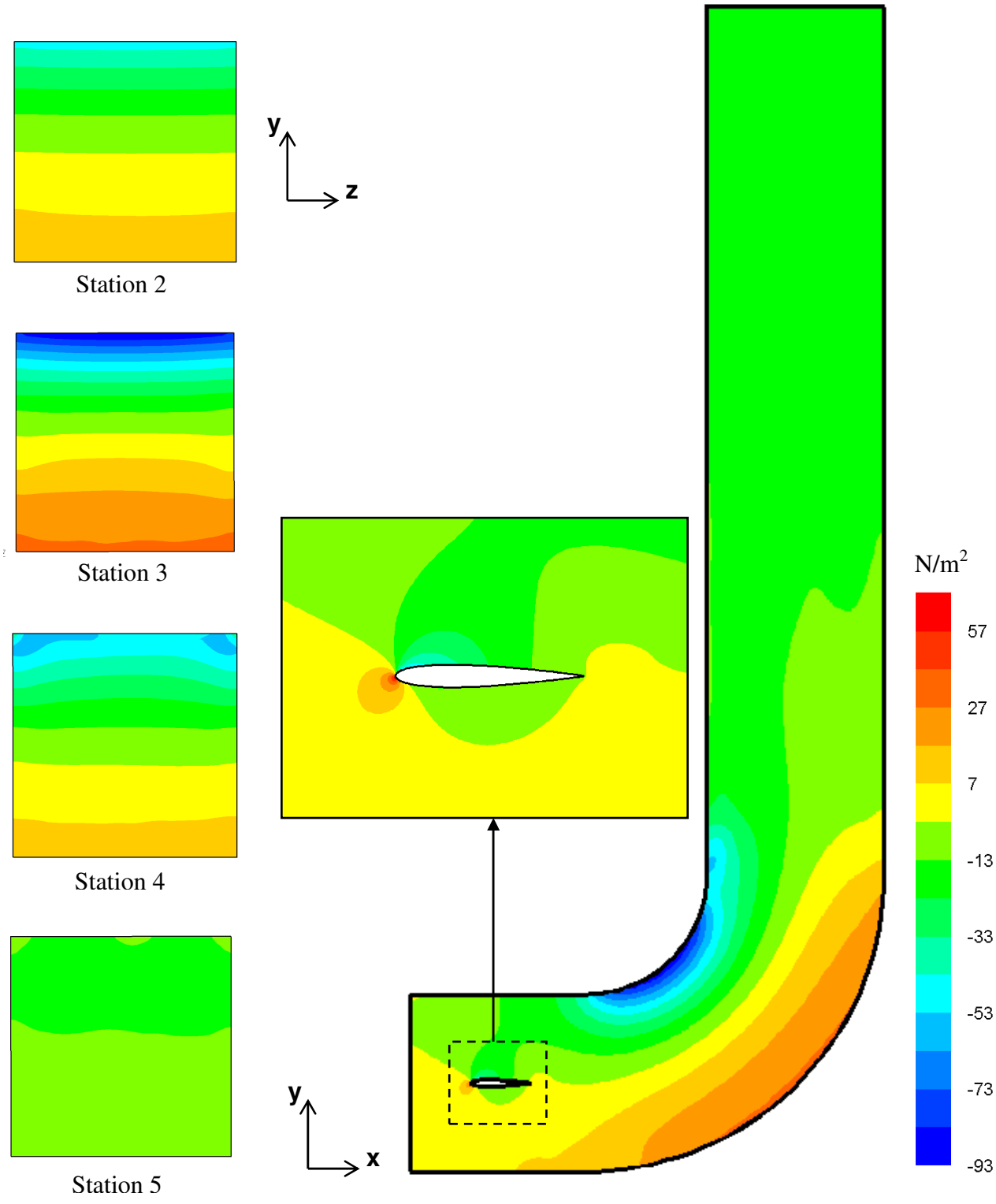

Figure 7.29: Mean static pressure (N/m^2) distribution (obtained with coarseDSMG) of the flow domain at $z/H = 0.5$ in the x-y plane , and at stations 2 to 5 on the y-z plane. The pressure reference point is set at the lower corner of the inlet (Original in colour).

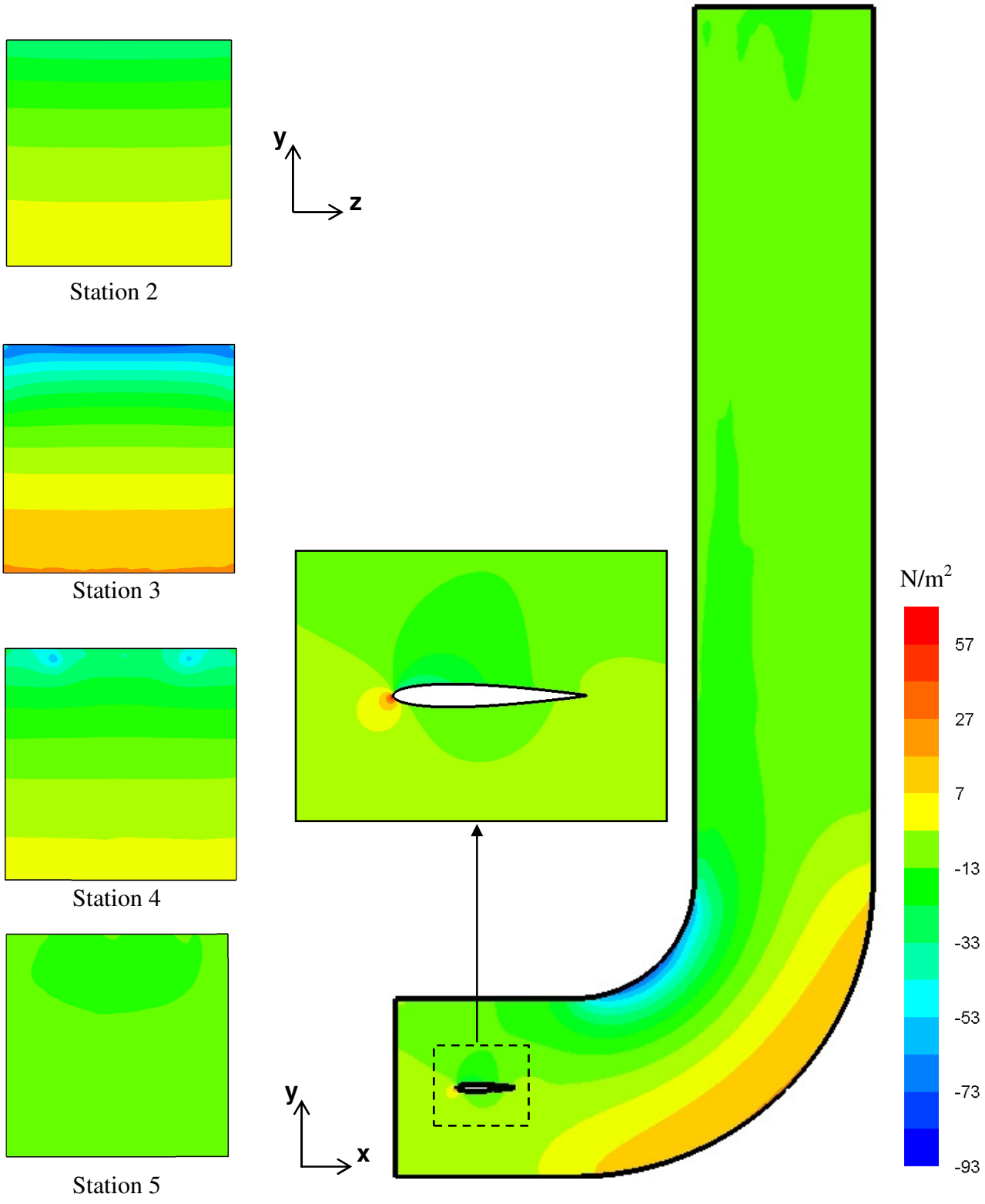

Figure 7.30: Mean static pressure (N/m^2) distribution (obtained with refinedPiradeepanDSMG) of the flow domain at $z/H = 0.5$ in the x-y plane , and at stations 2 to 5 on the y-z plane. The pressure reference point is set at the lower corner of the inlet (Original in colour).

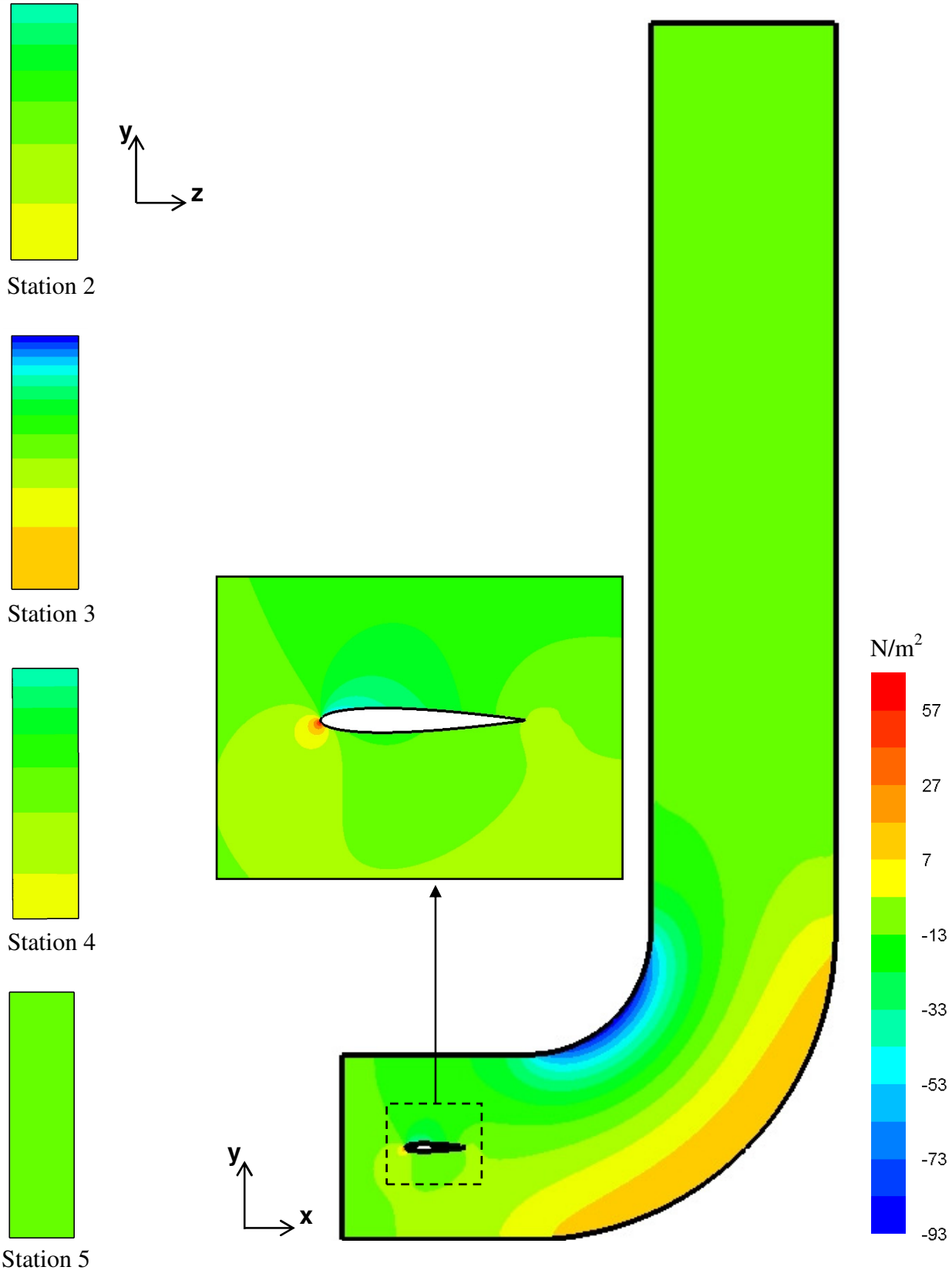

Figure 7.31: Mean static pressure (N/m^2) distribution (obtained with refinedDSMG) of the flow domain at $z/H = 0.5$ in the x-y plane , and at stations 2 to 5 on the y-z plane. The pressure reference point is set at the lower corner of the inlet (Original in colour).

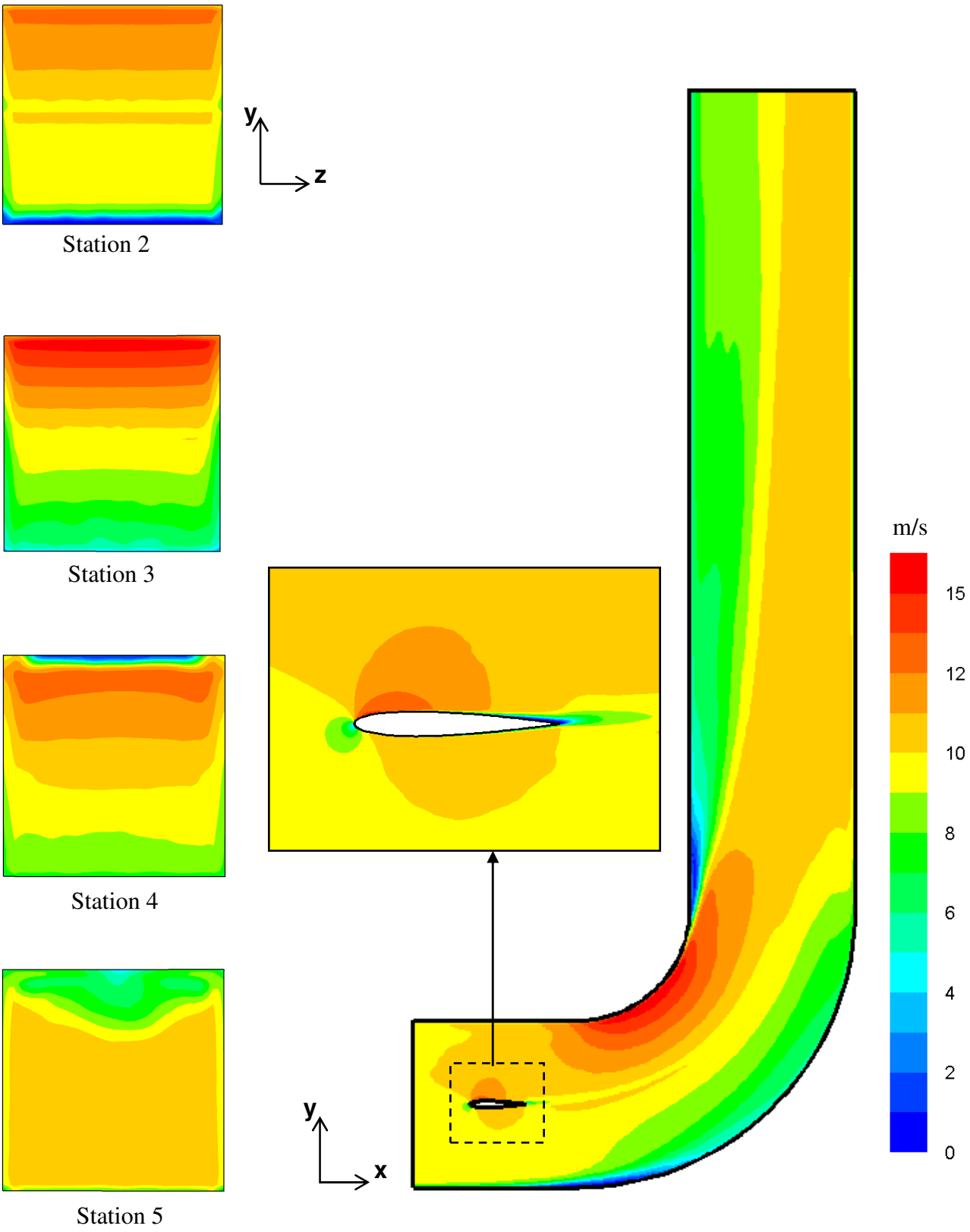

Figure 7.32: Mean velocity magnitude (m/s) obtained with coarseDSMG at $z/H = 0.5$ in the x-y plane, and at stations 2 to 5 on the y-z plane (Original in colour).

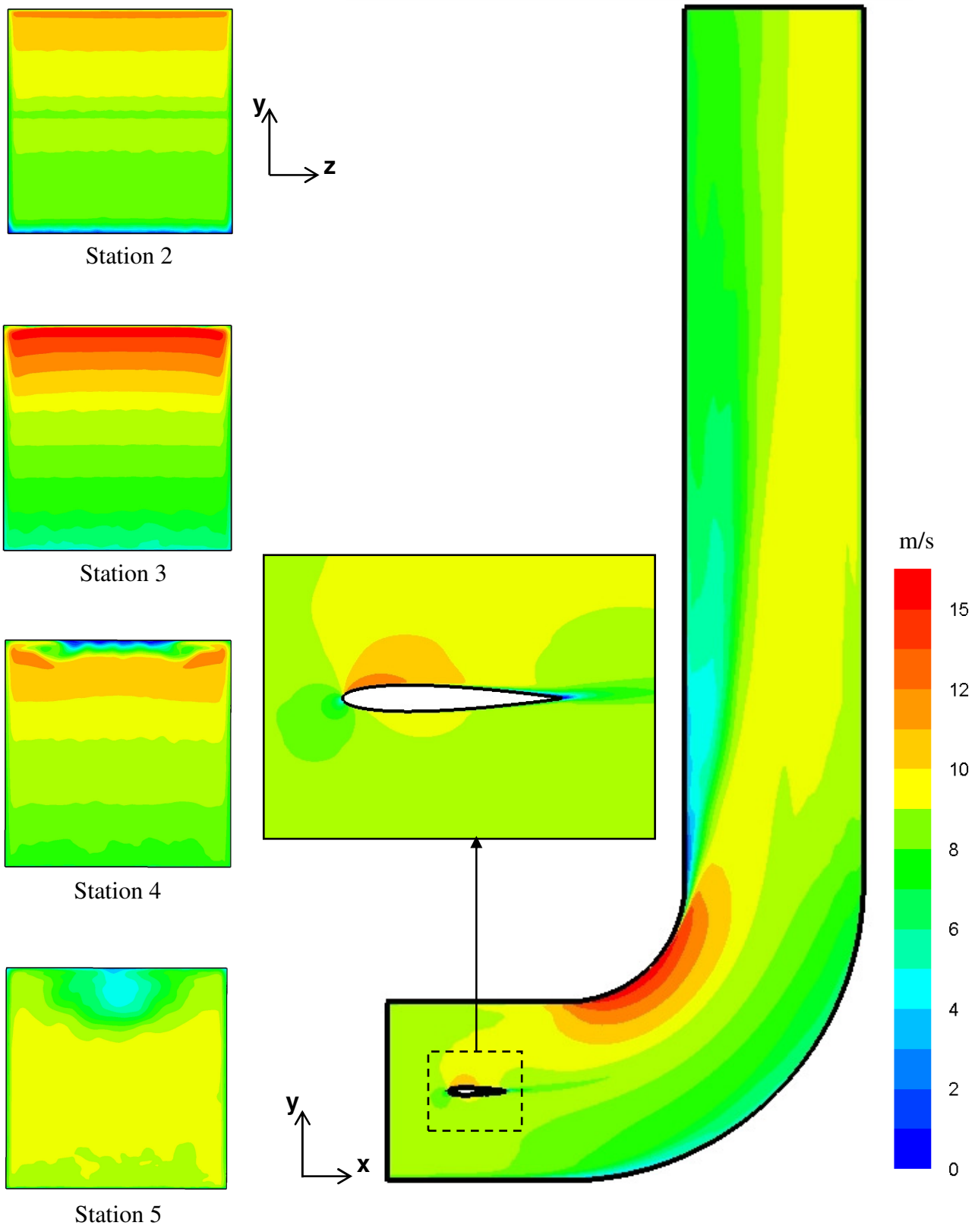

Figure 7.33: Mean velocity magnitude (m/s) obtained with refinedPiradeepanDSMG at $z/H = 0.5$ in the x-y plane, and at stations 2 to 5 on the y-z plane (Original in colour).

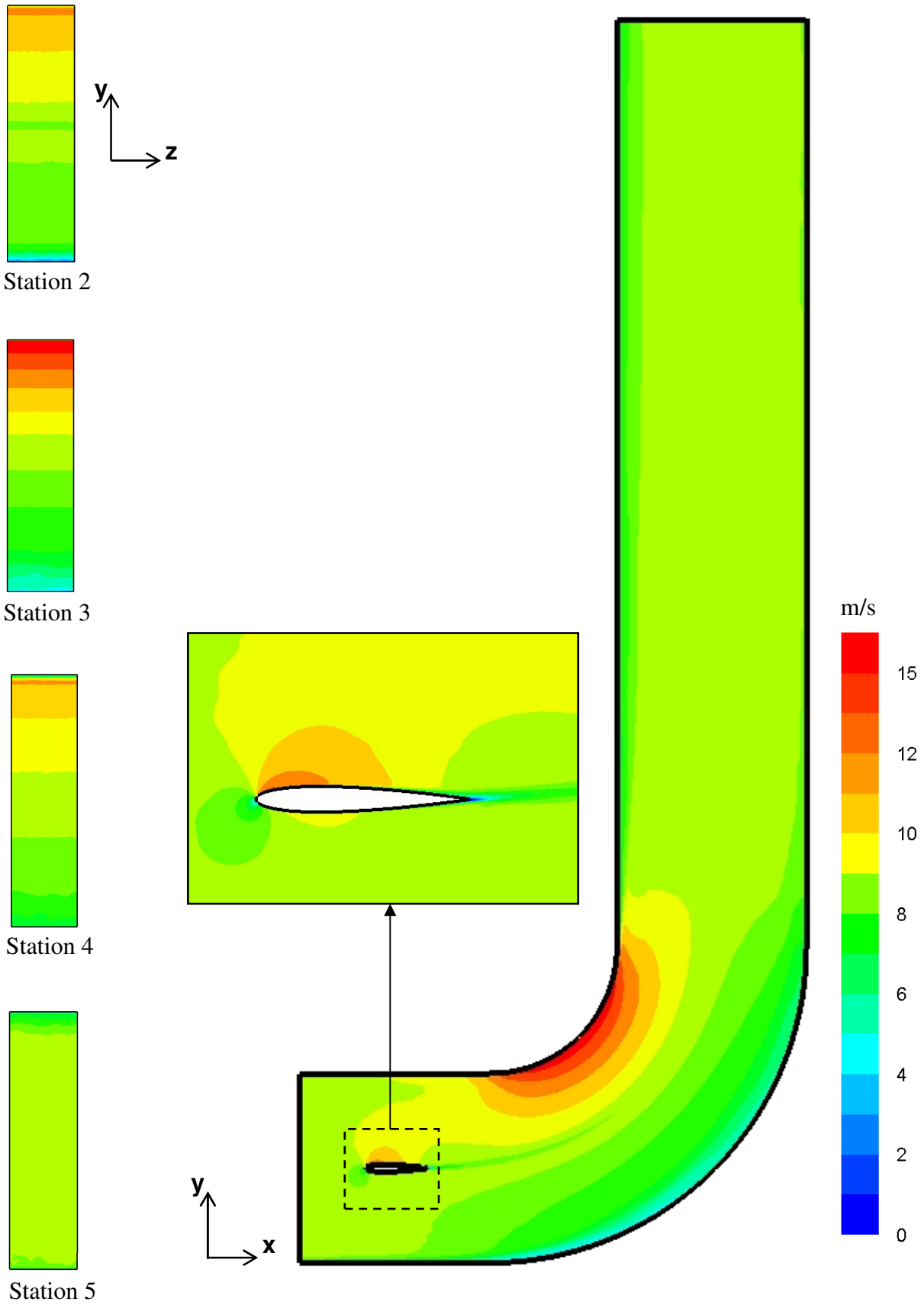

Figure 7.34: Mean velocity magnitude (m/s) obtained with refinedDSMG at $z/H = 0.5$ in the x-y plane, and at stations 2 to 5 on the y-z plane (Original in colour).

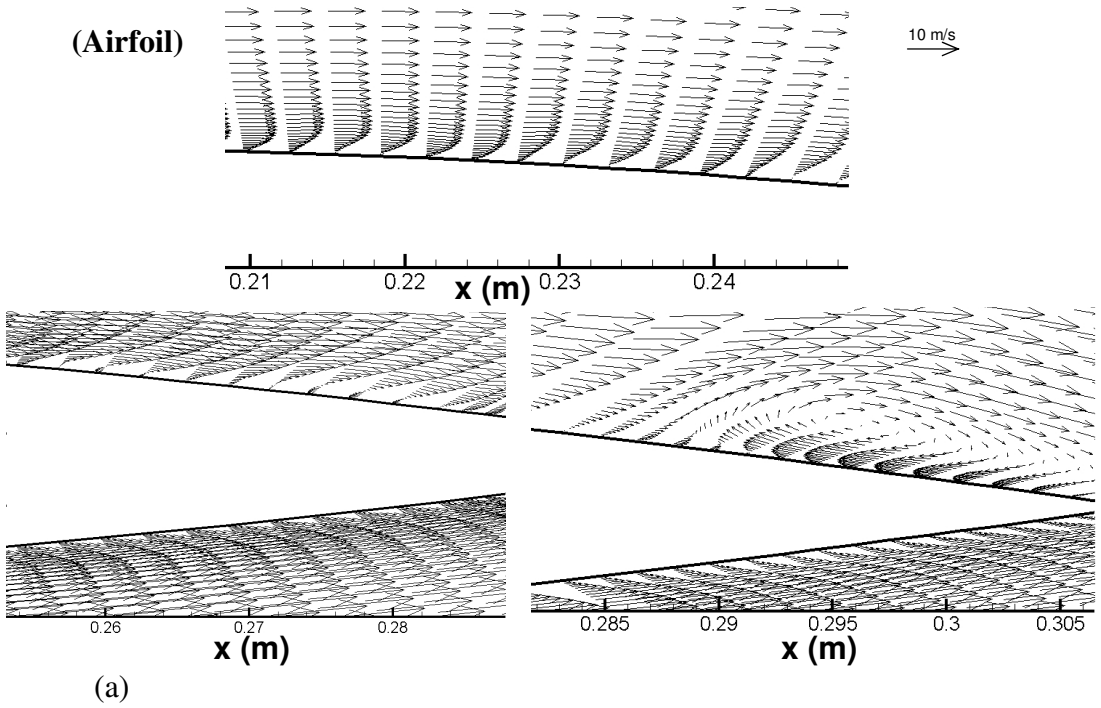

(a)

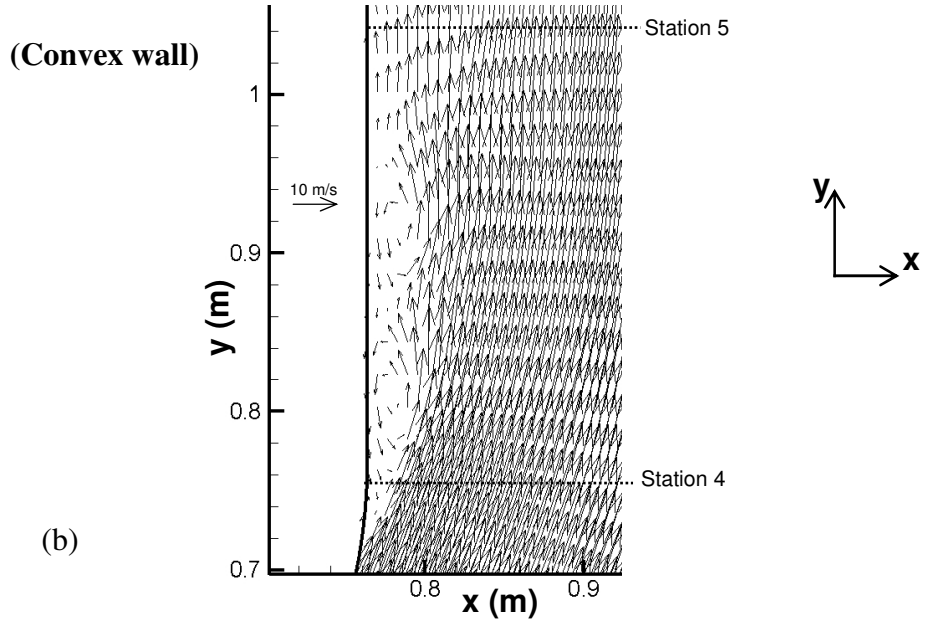

(b)

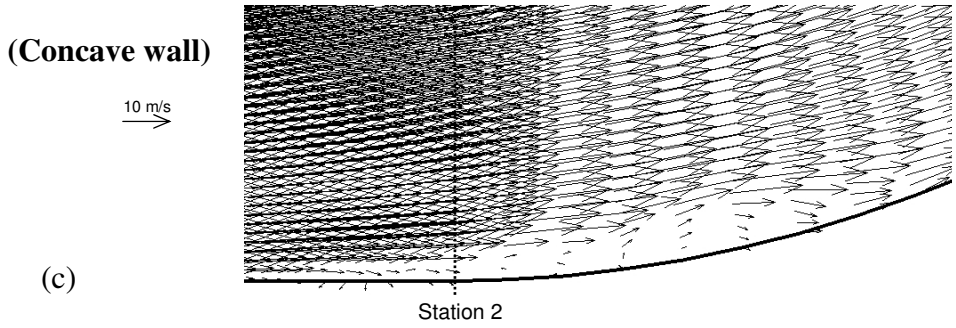

(c)

Figure 7.35: For caption see head of figure.

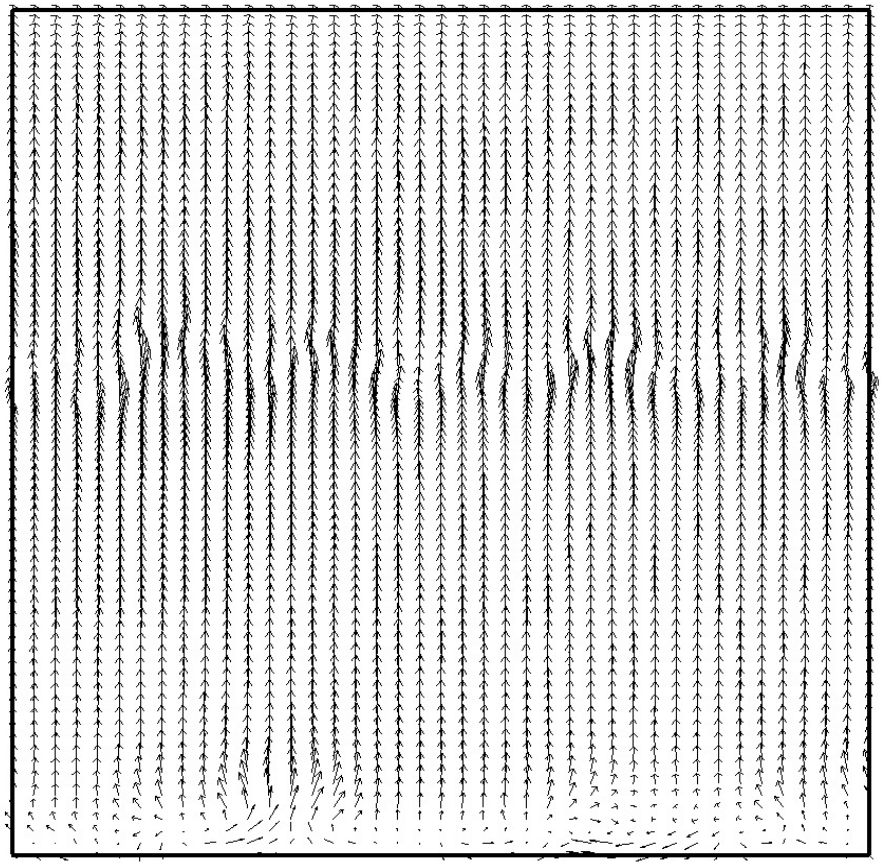

(d) **Station 2**

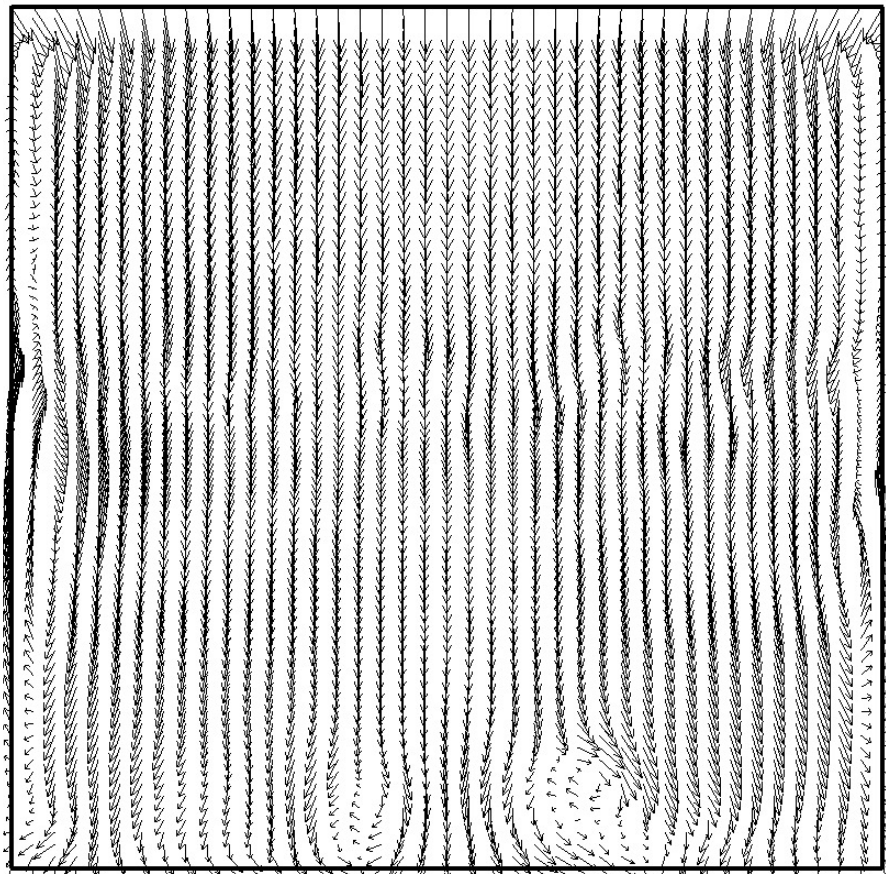

(e) **Station 3**

Figure 7.35: For caption see head of figure.

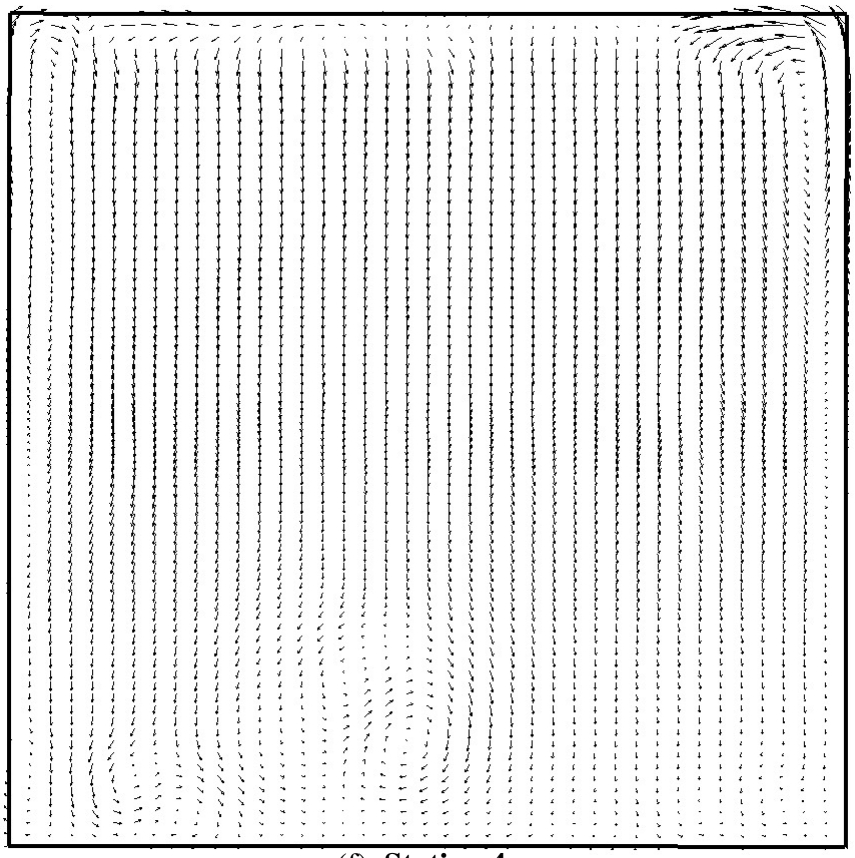

(f) **Station 4**

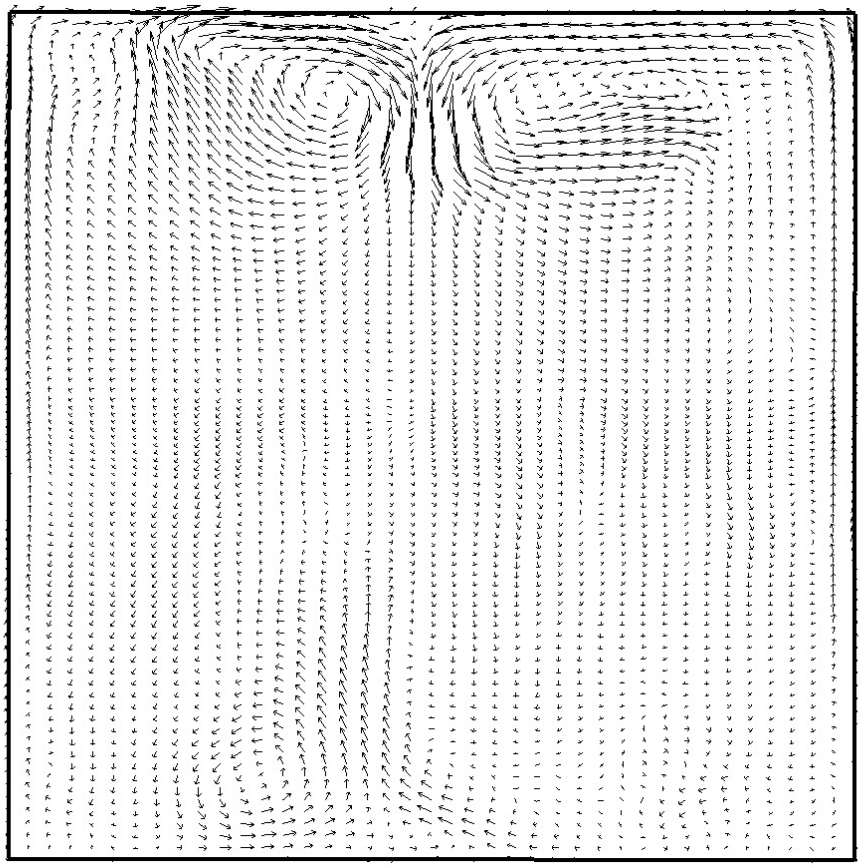

(g) **Station 5**

Figure 7.35: Velocity vector plot (obtained with coarseDSMG) in the *x*-*y* and *y*-*z* planes of : (a) airfoil *x*-*y* plane, (b) convex wall *x*-*y* plane, (c) concave wall *x*-*y* plane, (d) station 2 *y*-*z* plane, (e) station 3 *y*-*z* plane, (f) station 4 *y*-*z* plane, (g) station 5 *y*-*z* plane.

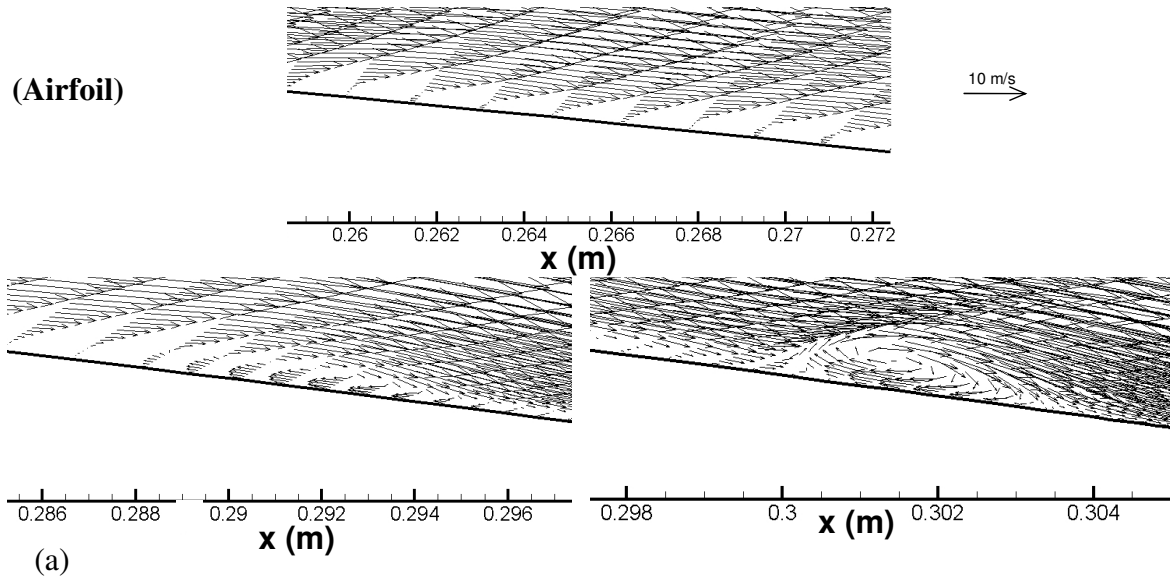

(a)

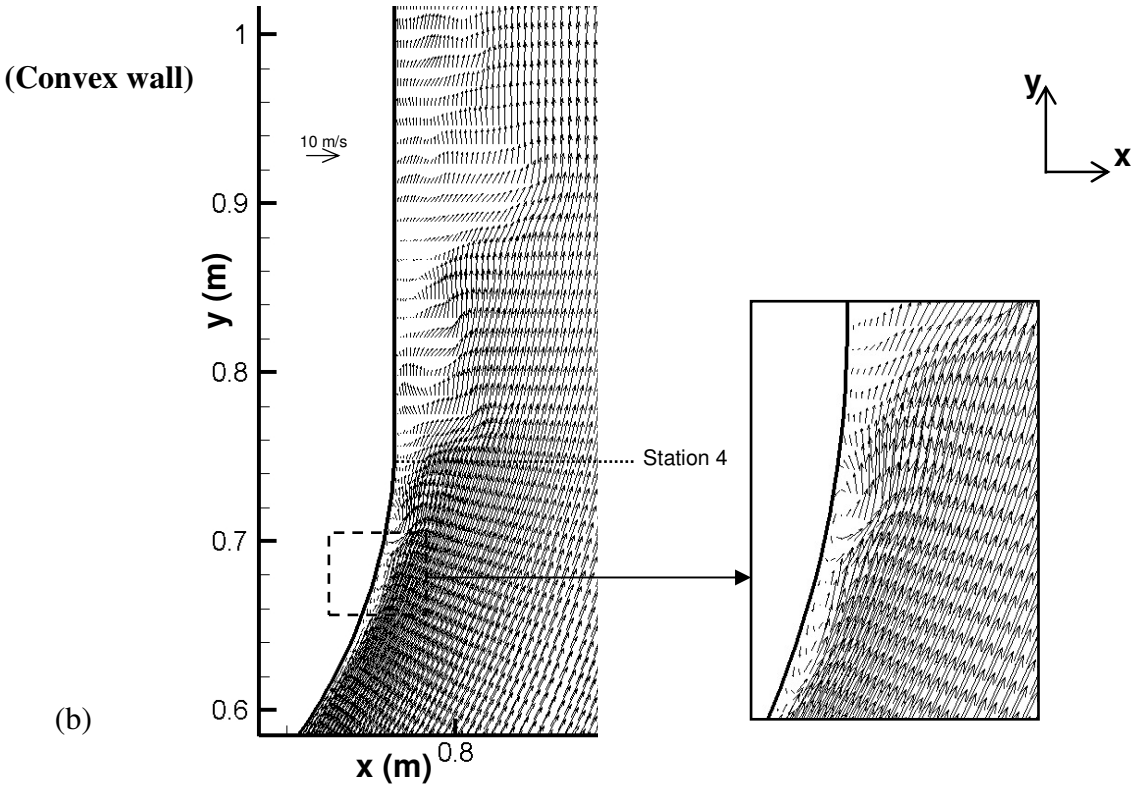

(b)

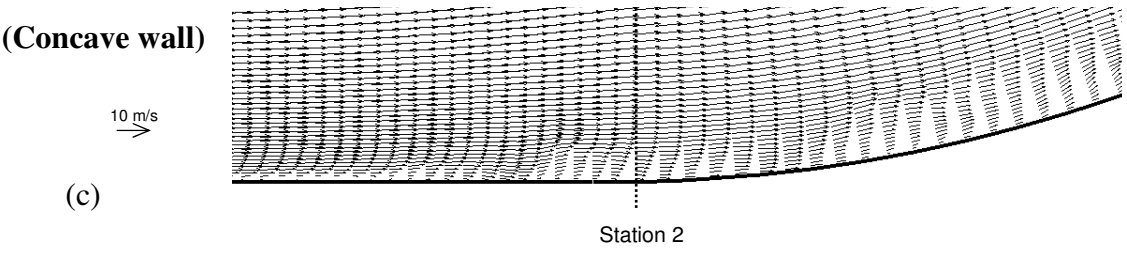

(c)

Figure 7.36: For caption see head of figure.

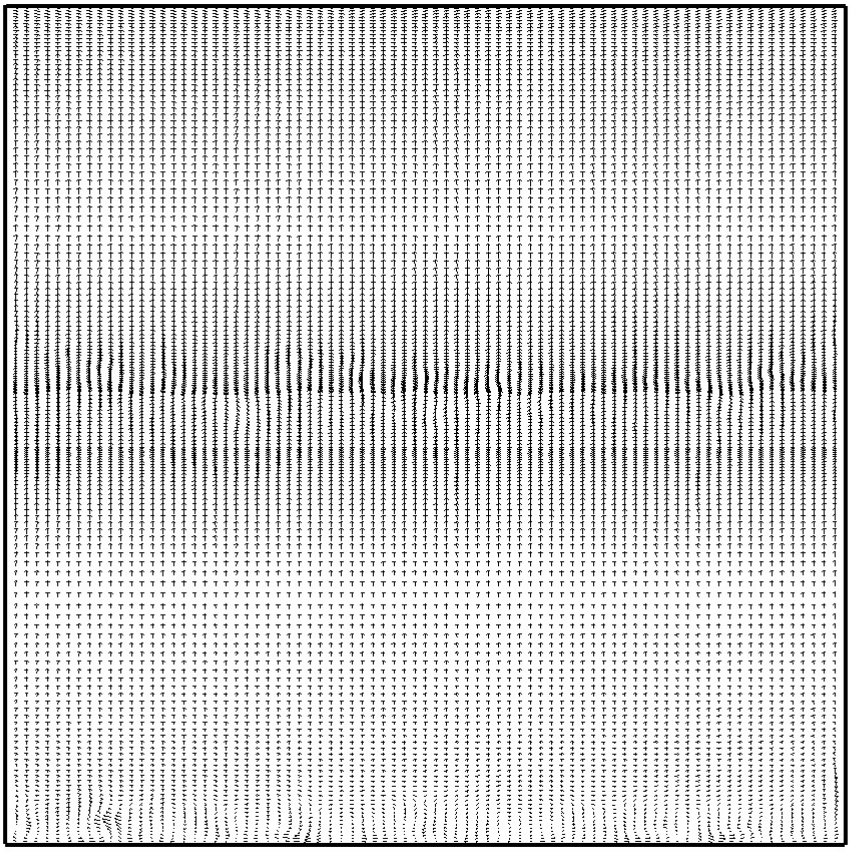

(d) **Station 2**

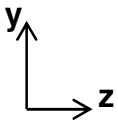

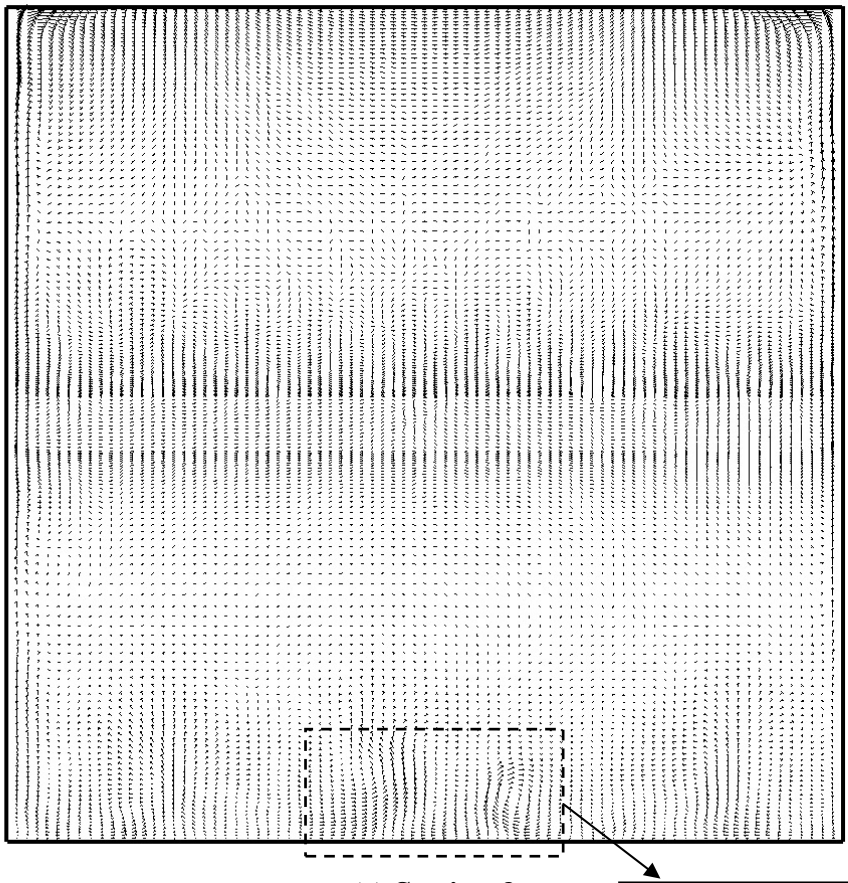

(e) **Station 3**

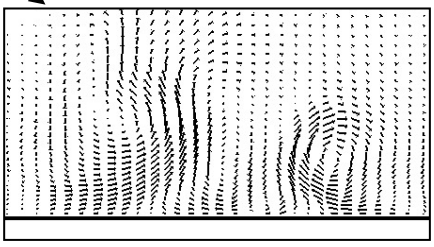

Figure 7.36: For caption see head of figure.

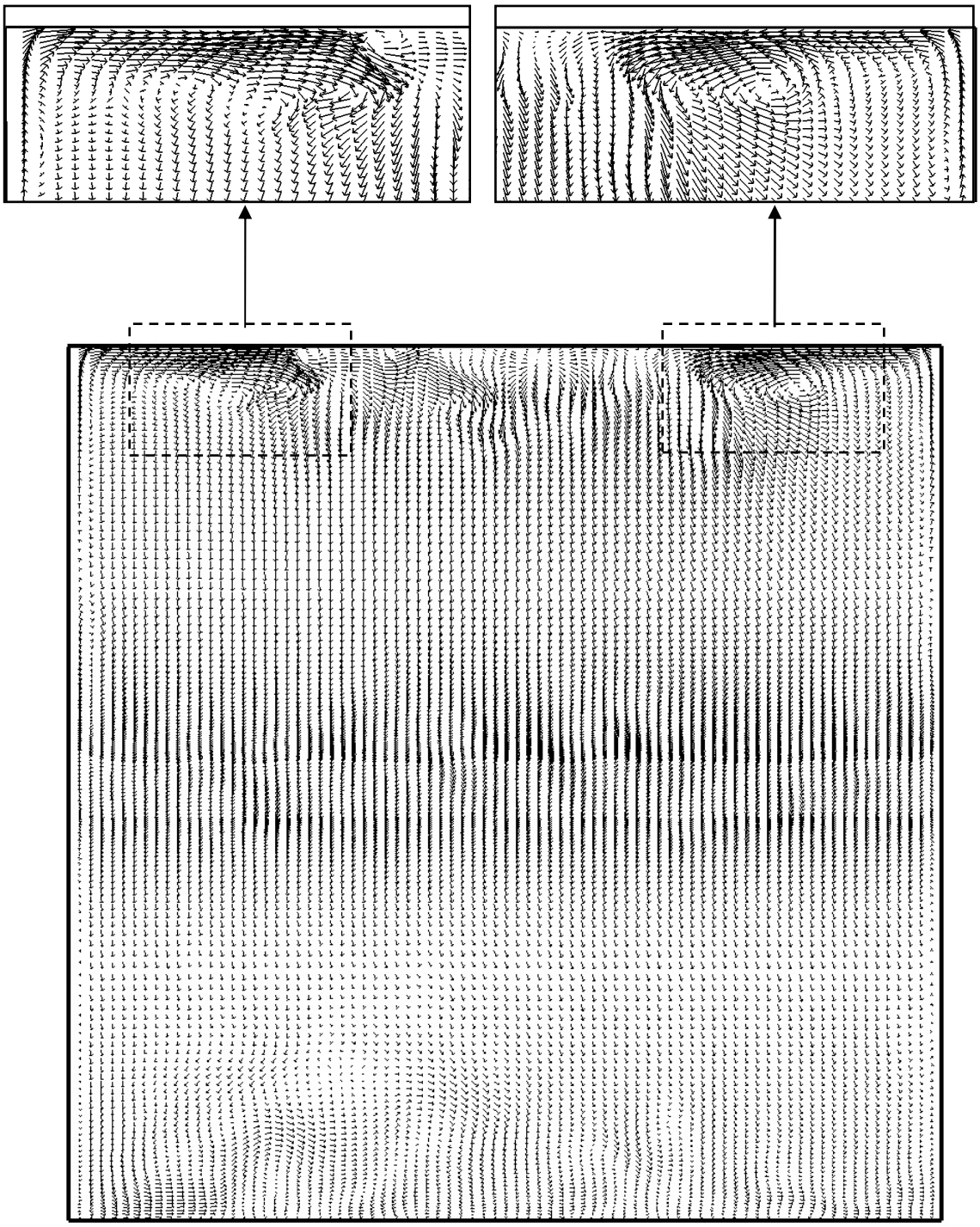

(f) **Station 4**

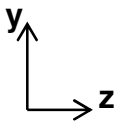

Figure 7.36: For caption see head of figure.

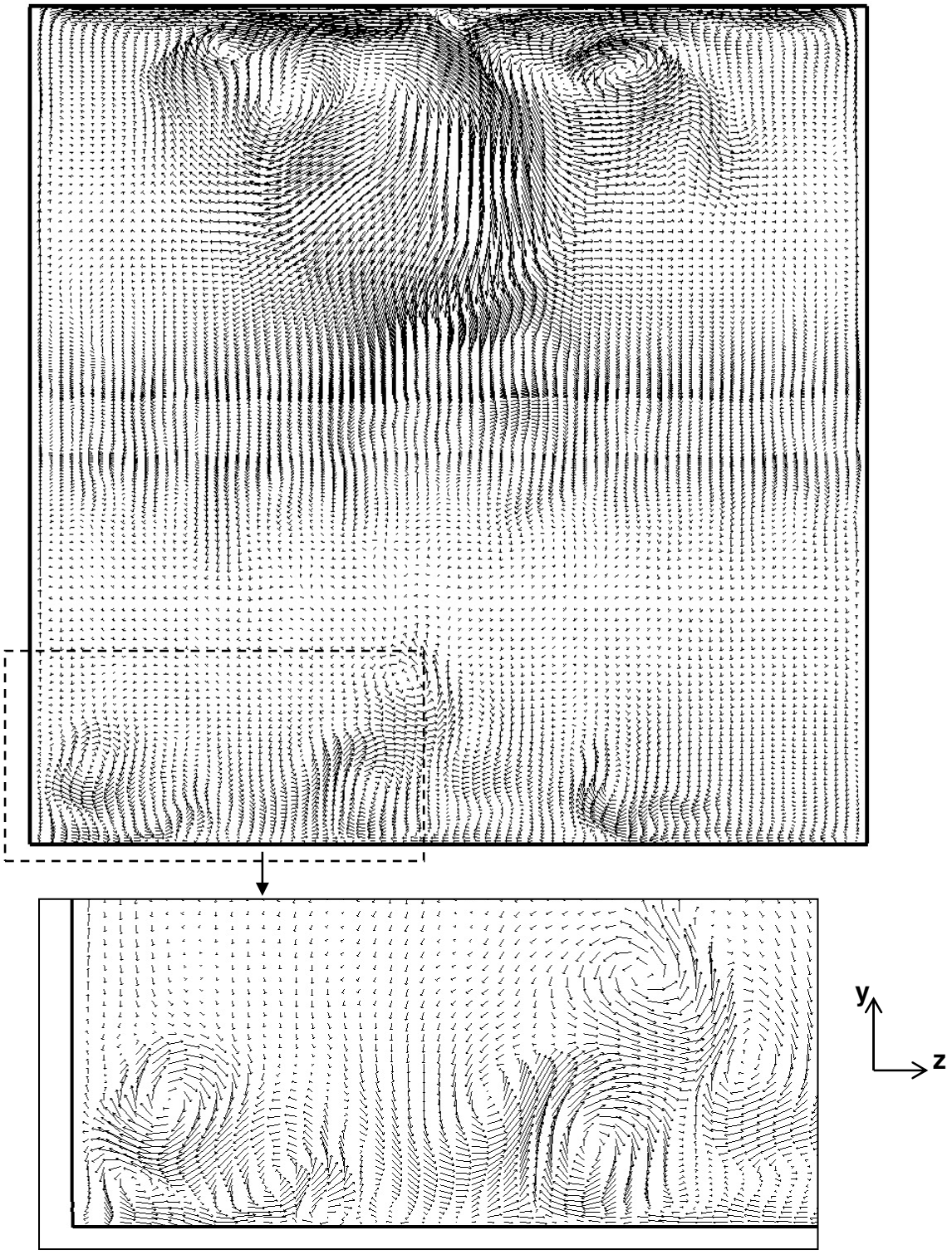

(g) **Station 5**

Figure 7.36: Velocity vector plot (obtained with refinedPiradeepanDSMG) in the *x*-*y* and *y*-*z* planes of the flow domain: (a) airfoil *x*-*y* plane, (b) convex wall *x*-*y* plane, (c) concave wall *x*-*y* plane, (d) station 2 *y*-*z* plane, (e) station 3 *y*-*z* plane, (f) station 4 *y*-*z* plane, (g) station 5 *y*-*z* plane.

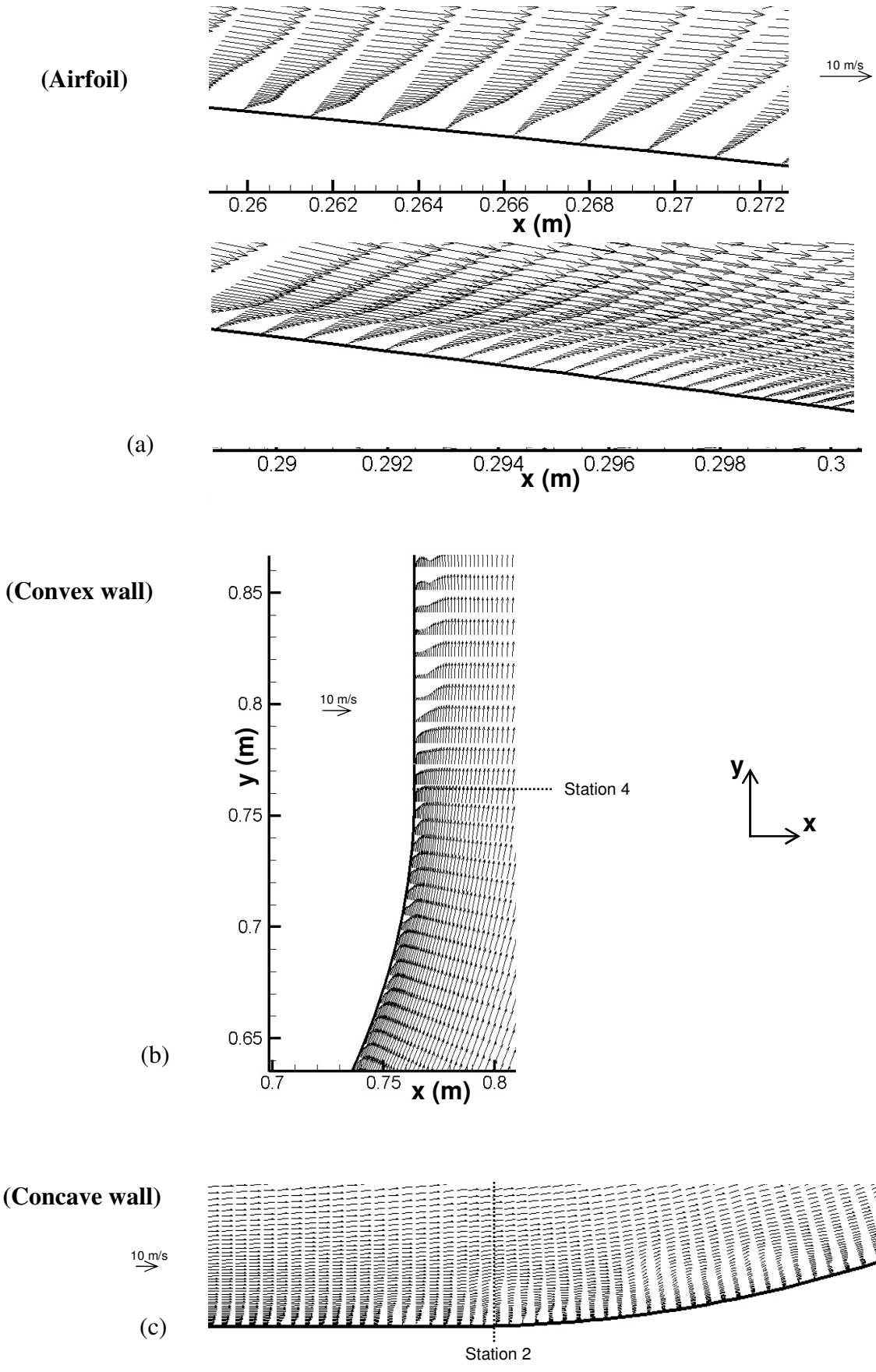

Figure 7.37: For caption see head of figure.

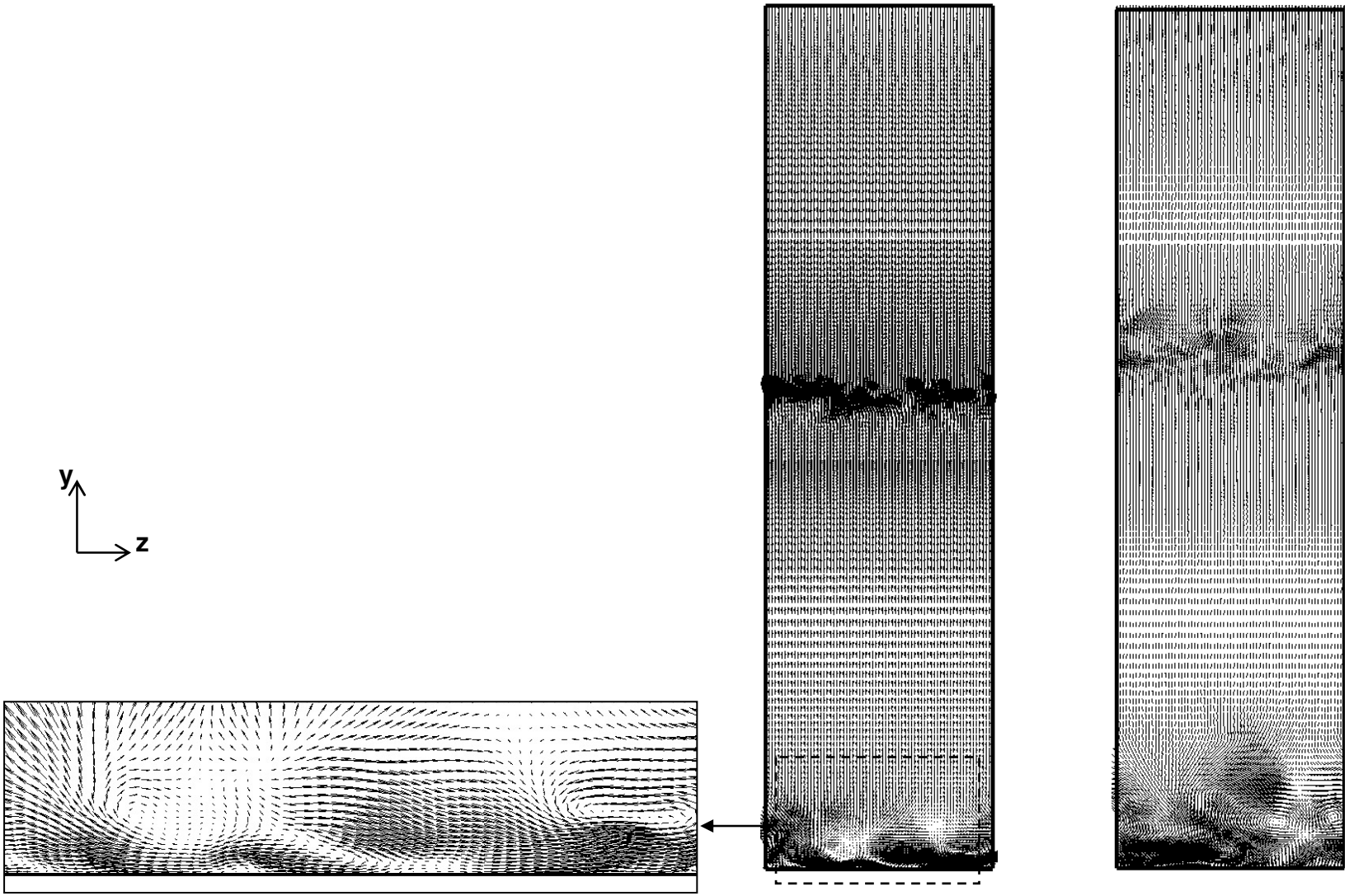

(d) **Station 2**

(e) **Station 3**

Figure 7.37: For caption see head of figure.

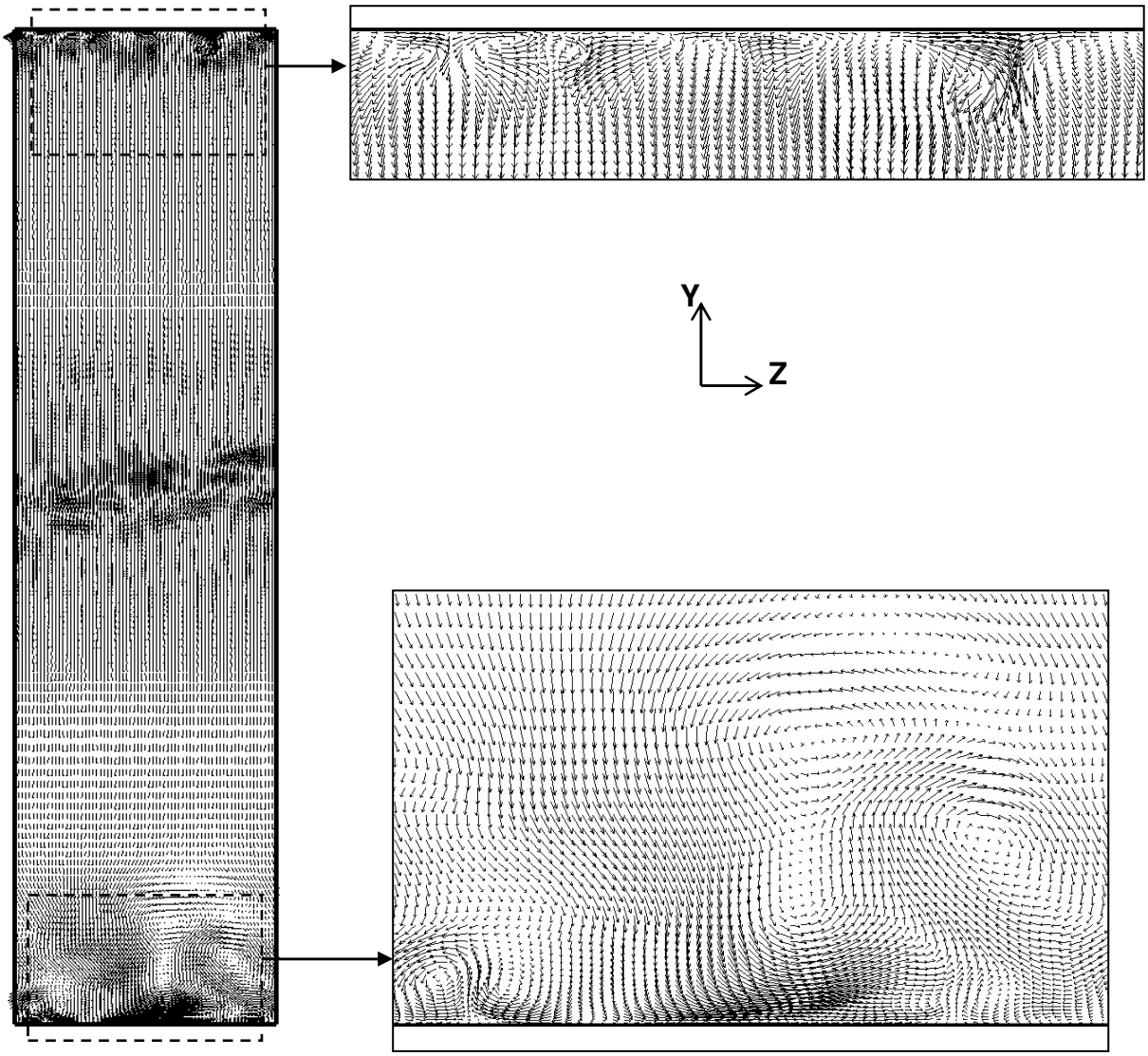

(f) **Station 4**

Figure 7.37: For caption see head of figure.

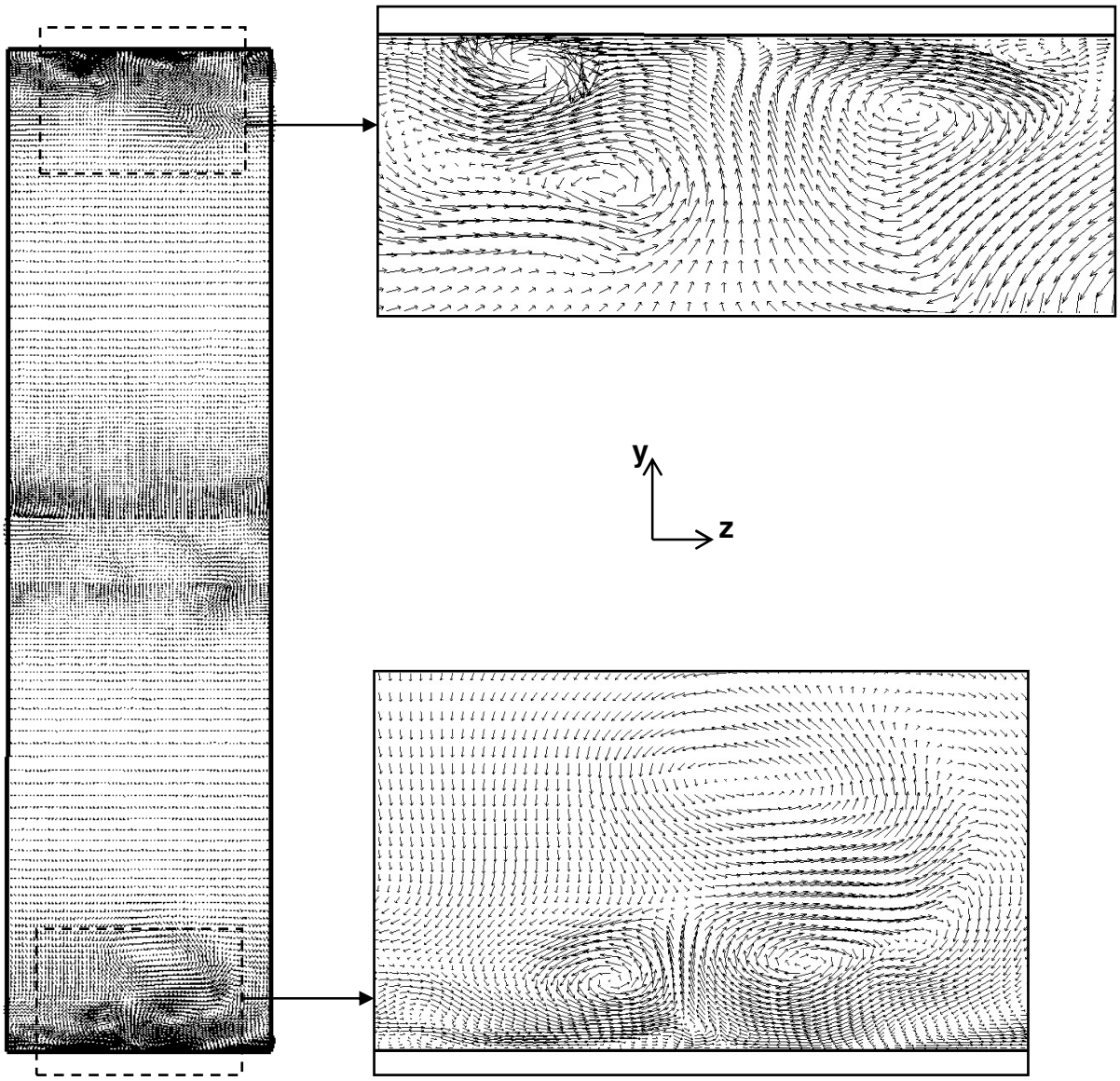

(g) **Station 5**

Figure 7.37: Velocity vector plot (obtained with refinedDSMG) in the *x*-*y* and *y*-*z* planes of the flow domain: (a) airfoil *x*-*y* plane, (b) convex wall *x*-*y* plane, (c) concave wall *x*-*y* plane, (d) station 2 *y*-*z* plane, (e) station 3 *y*-*z* plane, (f) station 4 *y*-*z* plane, (g) station 5 *y*-*z* plane.

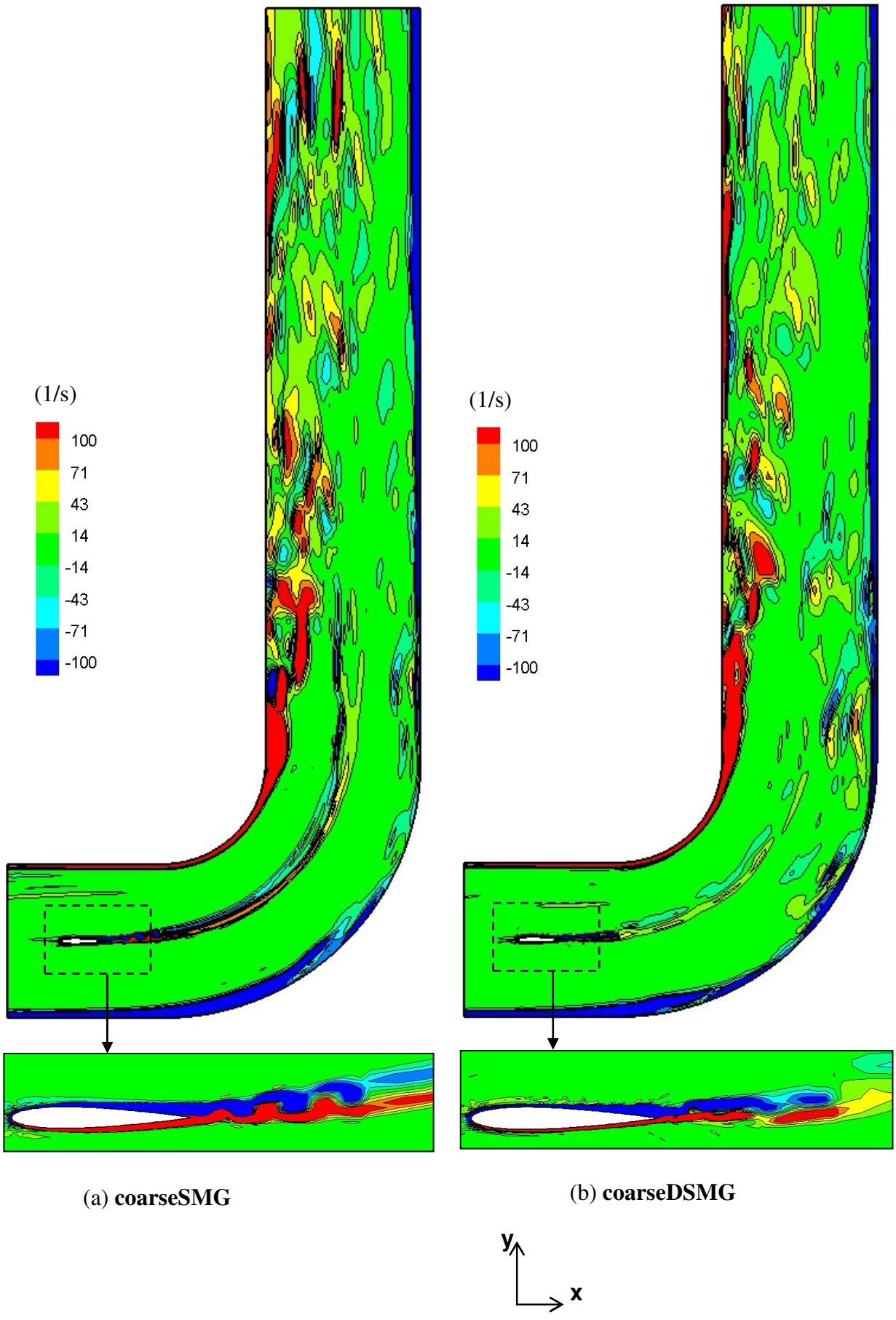

(a) **coarseSMG**

(b) **coarseDSMG**

Figure 7.38: For caption see head of figure.

(c) **refinedPiradeepanDSMG**

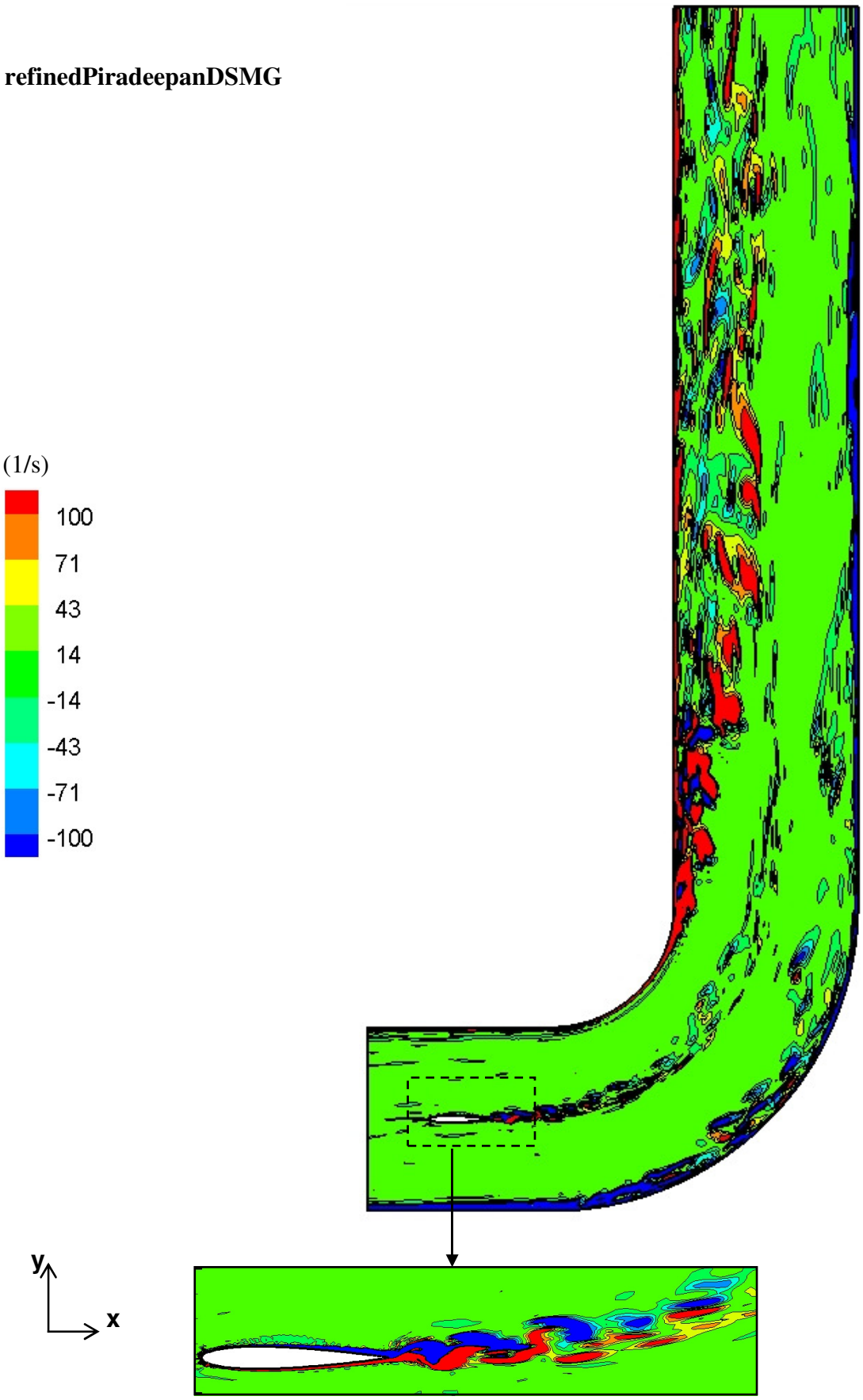

Figure 7.38: For caption see head of figure.

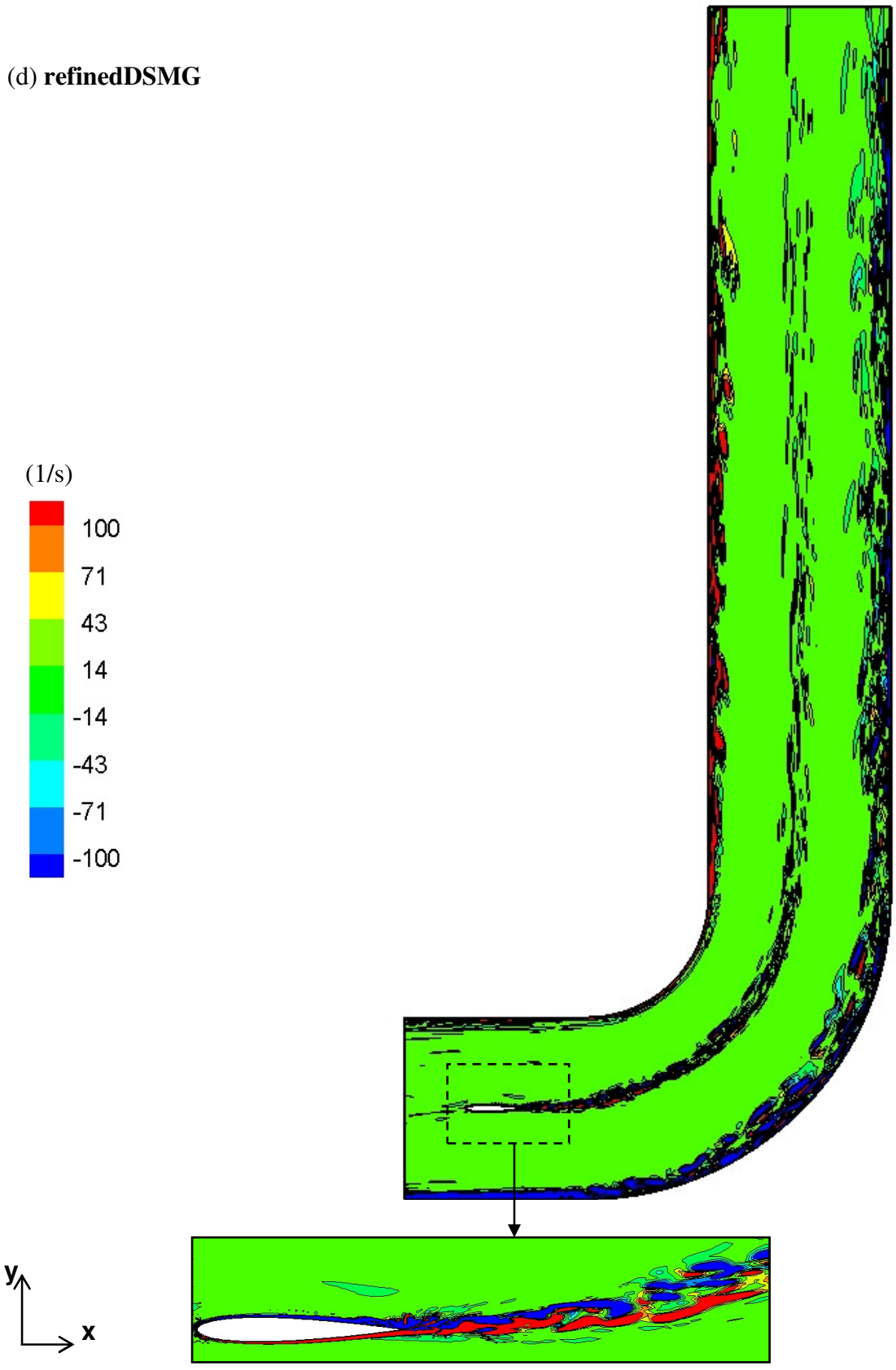

Figure 7.38: Contours of spanwise vorticity (ω_z) in the *x*-*y* plane at mid-span (*z*/*H* = 0.5): (a) coarseDSMG, (b) coarseDSMG, (c) refinedPiradeepanDSMG, (d) refinedDSMG.

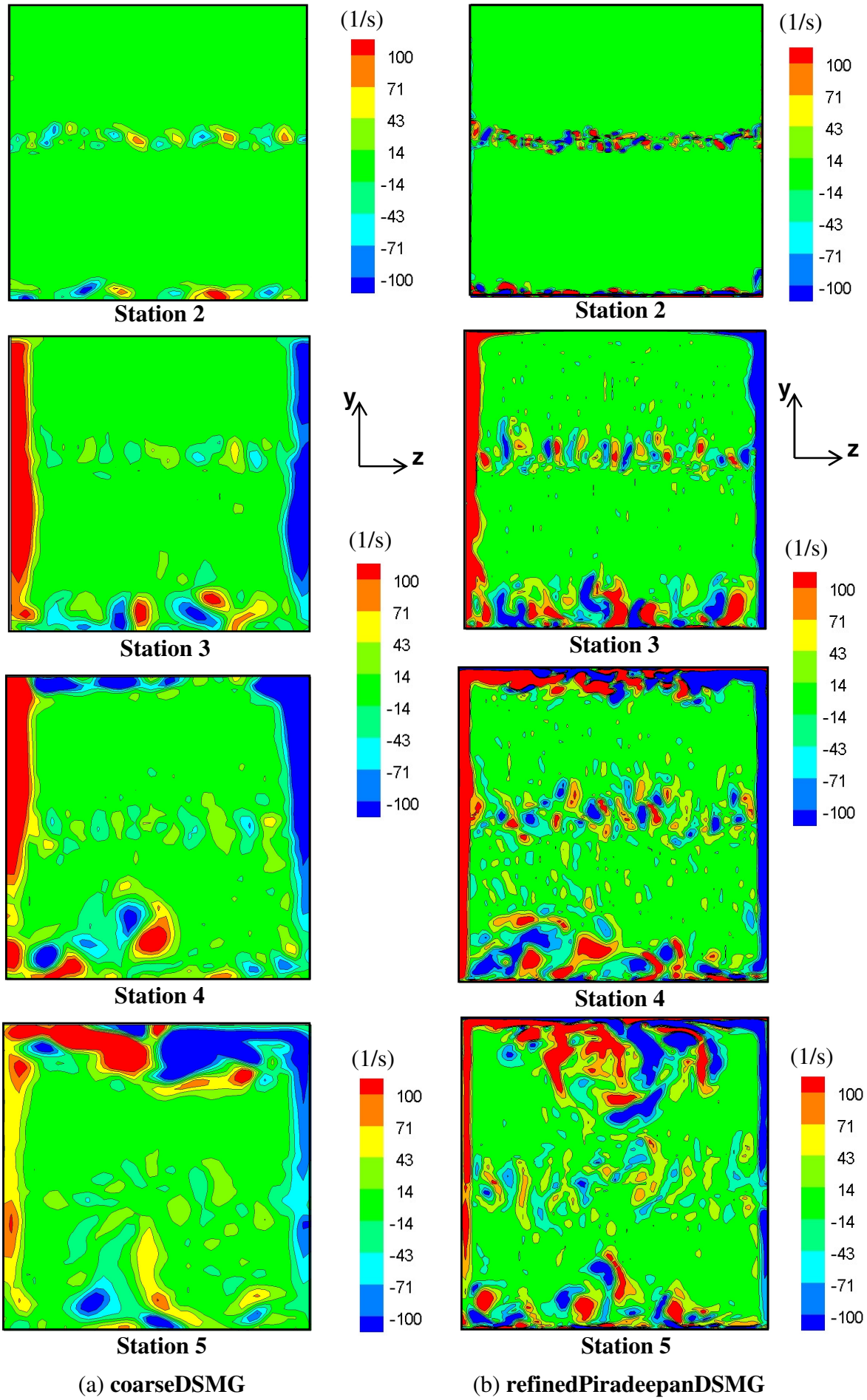

(a) **coarseDSMG** (b) **refinedPiradeepanDSMG**

Figure 7.39: for caption see head of figure.

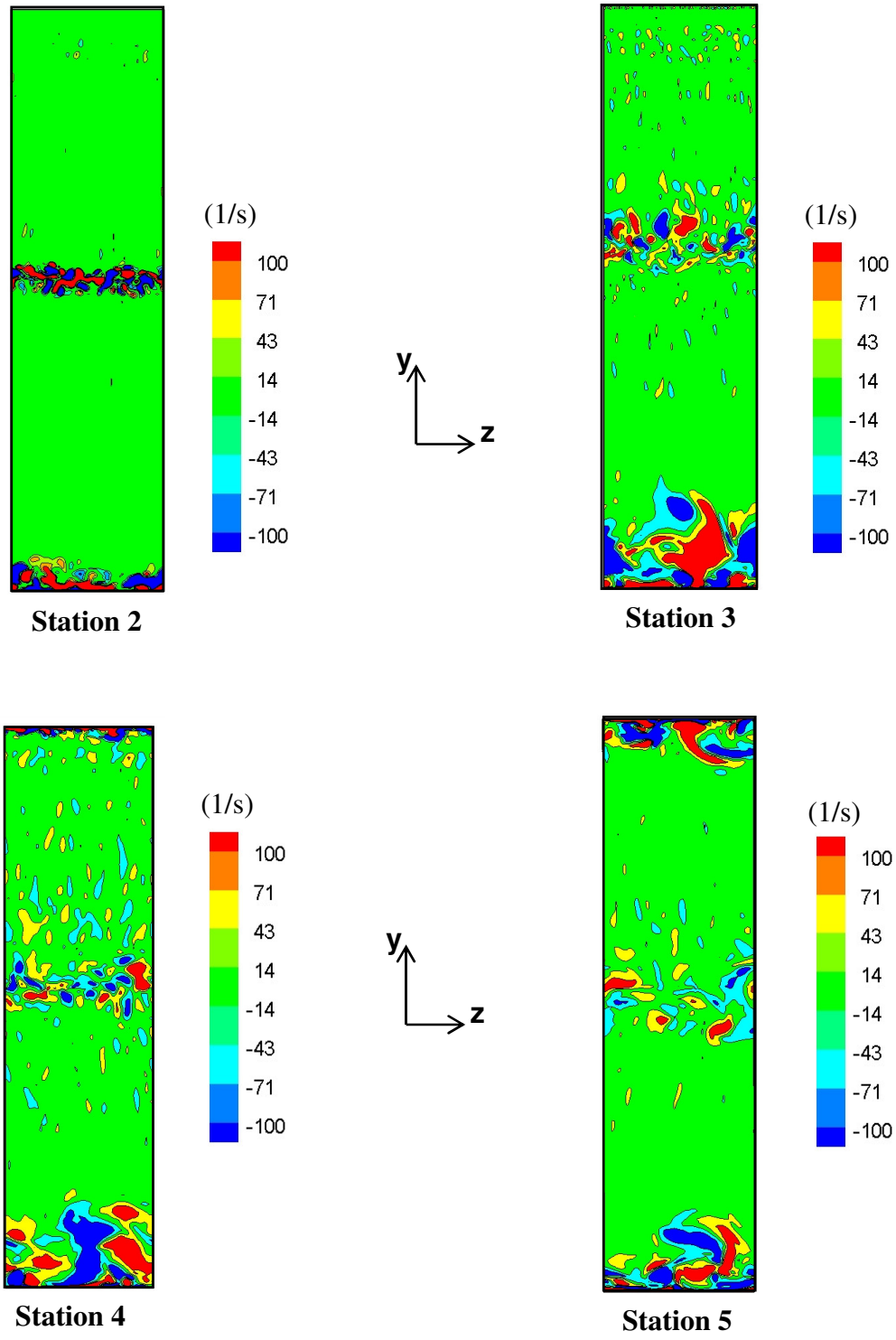

(c) **refinedDSMG**

Figure 7.39: Contours of streamwise vorticity (ω_x) in the *y*-*z* plane, at stations 2 to 5 for the simulations with the DSMG model: (a) coarseDSMG, (b) refinedPiradeepanDSMG, (c) refinedDSMG.

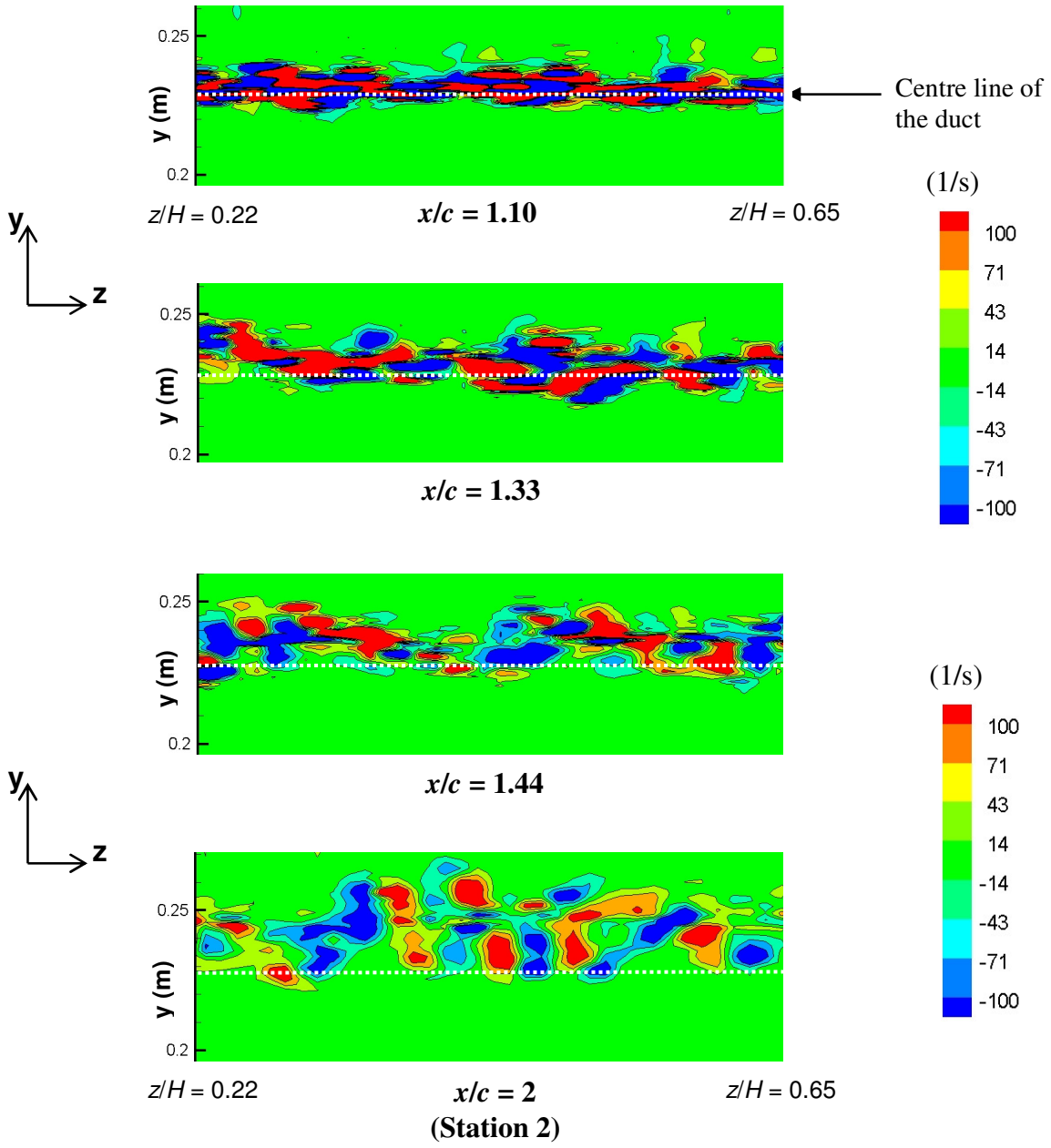

(a) **refinedPiradeepanDSMG**

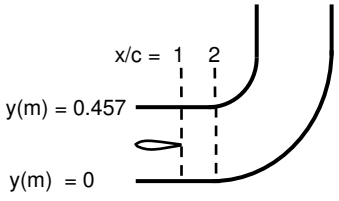

Figure 7.40: For caption see head of figure.

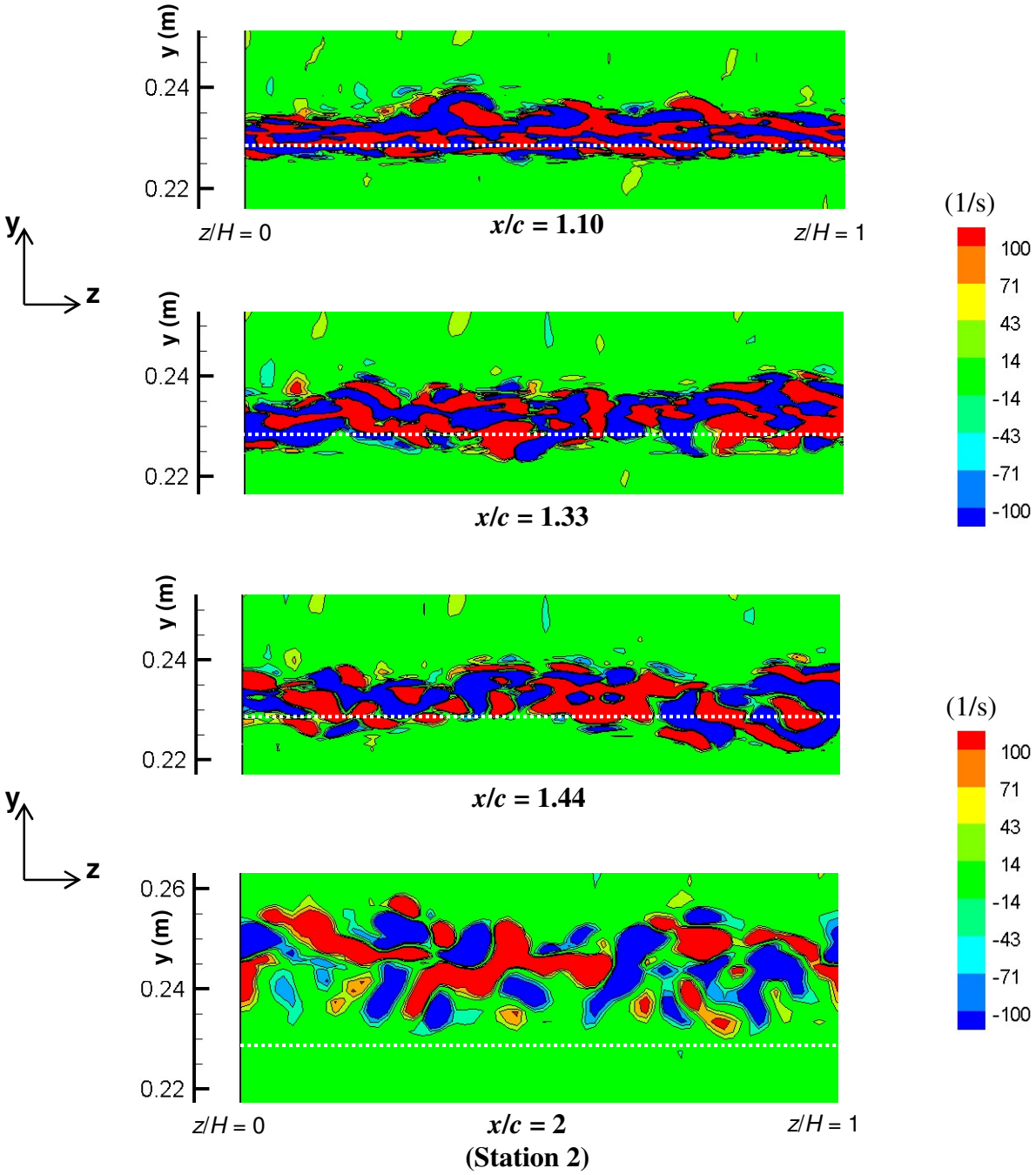

(b) **refinedDSMG**

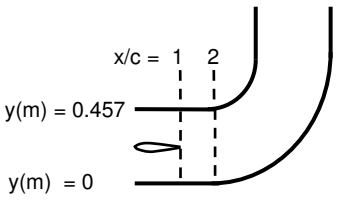

Figure 7.40: Contours of streamwise vorticity (ω_x) in the *y*-*z* plane, at several streamwise locations in the near-wake for: (a) refinedPiradeepanDSMG, (b) refinedDSMG.

Chapter 8

8. CONCLUSIONS AND RECOMMENDATIONS

8.1. Overview

This chapter presents the main conclusions from the experimental and numerical investigations conducted in the boundary layer and wake of an airfoil (NACA 0012) inside a duct with a 90^o bend. In this study the extra rates of strain, namely, curvature and pressure gradient, were imposed by the airfoil angle of attack as well as the curved duct within which the body was placed.

It was stated in Chapter 1 that a better understanding of complex turbulent flows can provide improvements in the design of aerodynamic devices in the aerospace and turbomachinery industries. Often the design of such devices is dependent on numerical modelling techniques that are heavily reliant on experimental data for validation. The broad aim of the present work has been to provide a better understanding of the wake and boundary layer of a symmetrical airfoil in a curved duct. The three-dimensional experimental flow configuration for the airfoil at zero angle of attack in the curved duct with a mainstream velocity of 10 m/s was computed using LES. An experimental investigation, with hot-wire anemometry, was carried out to identify the effects on the wake from the upstream boundary layer, and the dominance of the curvature imposed by the duct. The experimental investigations provided data for the validation of the large eddy simulations. The capability of LES in predicting such complex turbulent flows was assessed by investigating the modelling parameters, to identify weaknesses of the present modelling techniques and suggest improvements that could influence the quality of the results. The conclusions drawn from this work are divided into two main sections; the first section relates to the experimental findings, and the second to the numerical findings, followed by the recommendations for further work.

8.2. Experimental investigation

The experimental static pressure on the upper and lower surfaces of the airfoil, at the nominal condition of zero angle of attack with respect to the horizontal, showed an asymmetric distribution, i.e. adverse pressure gradient on the upper side and a favourable pressure gradient

on the lower side for most of the chord length. For this configuration, the results indicated favourable conditions for separation to occur on the upper surface near the trailing edge, although there was no evidence to suggest flow separated at this angle. With increase in positive angle of attack (clockwise rotation) to $\alpha = 4^o, 6^o$ the results indicated the presence of a separation bubble near the leading edge between x/c = 0.1 and 0.15. For negative angles (anti-clockwise rotations), the distributions of static pressure became more symmetrical, and at $\alpha = -4^o$ profiles of pressure showed distributions that would be expected for an airfoil parallel to the oncoming flow. From these results it was deduced that the approaching flow was not parallel to the airfoil but at an angle. This angle was calculated to be about -2^o in the freestream region at station 1, and -4^o at the leading edge of the airfoil, which suggests that the flow angle imposed by the duct increased (negatively) with streamwise distance.

The airfoil was located in the inviscid region of the flow in the test section, with measured streamwise turbulence intensity levels of 0.5% of the mainstream velocity. A series of verification tests were carried out to confirm consistency with previous work. Considering the relative uncertainties within the experiments, the data was obtained with a good level of accuracy. The experimental error analysis, that considered the changes in ambient conditions, probe alignment, probe calibration and equipment, indicated an uncertainty of 3.3% in the measurement of mean velocity and turbulence intensities (RMS) with a stand alone hot-wire probe, and 5.2% in the measurement of these parameters with the rake of single-wire probes. The estimated uncertainty in the measurement of turbulence shear stress was 6.6%.

The following conclusions were made:

1) At the nominal condition of zero angle of attack, the velocity profiles in the near-wake and at one chord length downstream of the trailing edge were asymmetric about the wake centre line. This was attributed to the effect of curvature from the duct, which caused the inner and outer sides of the wake to develop under varying pressure gradients. The lateral shift of the wake was attributed to the radial pressure distribution in the flow.

2) The results showed two contributory effects on the wake, one as a result of the airfoil angle of attack and the other from the curvature and pressure gradient imposed by the duct. Near the trailing edge, the dominant factor was the airfoil angle of attack, and at one chord length downstream of the trailing edge, the effect of the duct played a more dominant role on the flow. The coupled effect of airfoil angle of attack and curvature from the duct,

resulted in the enhancement of the wake (for positive angles) and the suppression of the wake (for negative angles), which may be an important factor when considering the design of practical devices.

3) As the airfoil angle of attack was varied, the pressure distribution on the airfoil was modified which resulted in changes in the boundary layer and the downstream wake. For positive angles of attack (α = 2°, 4°, 6°) the wake was first shifted downwards and then upwards due pressure gradient imposed by the duct. On the other hand, for the negative angles (α = -2°, -4°, -6°), the wake was always above the centre line of the duct. At α = -4° the profiles in the near-wake were nearly symmetrical about the wake centre line, but the effect of the bend was apparent one-chord length downstream of the trailing edge.

4) The derived wake half-widths for $\alpha = 0^{o}$ in the near-wake, up to station 2, indicated larger magnitudes on the inner side than the outer side. As angle of attack increased positively, the half-width on the inner side increased, especially near the trailing edge of the airfoil, but, further downstream, it became closer to that measured for the nominal test case of $\alpha = 0^{o}$. In general, the results showed that the total wake half-width increased with streamwise distance, but more significantly with angle of attack. The deduced maximum velocity defect increased with positive angle of attack and decreased with negative angle of attack. The results showed that the rate of decay of velocity defect in the streamwise direction was not significantly affected by the airfoil angle of attack.

5) Near the trailing edge, the effect of positive angle of attack resulted in more pronounced profiles of the Reynolds stresses on the inner side of the wake, but further downstream, the profiles on the outer side became more distinguishable. In line with the results for the mean velocity, the effect of negative angle of attack was less influential on the Reynolds stresses, although the alignment of the airfoil with the flow resulted in symmetrical profiles in the near-wake.

6) The streamwise turbulence intensity profiles in the wake were characterised by the presence of a double peak. As the angle of attack was varied, positively or negatively, the peaks moved away from the centre line of the wake resulting in a wider profile. The normal stresses displayed a single peak, which also showed lateral sensitivity to angle of attack. The profiles of turbulence shear stress in the wake were more strongly influenced by the curvature and pressure gradient than the normal stresses. The enhancement of

turbulence on the inner side of the wake, and its suppression on the outer side, were consistent with the theoretical interpretation in transport equations of these quantities.

7) The distributions of mean velocity and turbulence intensity in the wake indicated large spanwise variations, characterized by the presence of peaks and troughs. The amplitude of the variations was more enhanced on the inner side of the wake than the outer side, which was attributed to the effect of streamline curvature on the flow. The peaks and troughs were periodic in the spanwise direction, and the profiles of velocity were out of phase with the profiles of turbulence intensity. These results suggested the presence of streamwise vortical structures in the wake. Further downstream, at station 2, the amplitude of the variations suggested a decrease in streamwise vorticity, although the periodic nature of the variations was still apparent. The effect of positive angle of attack and mainstream velocity was to increase the three-dimensionality in the wake.

8) The experiments in the airfoil boundary layer ($\alpha = 0^o$) indicated significant changes in the mean velocity and turbulence intensity profiles between x/c = 0.83 and 0.93, which were consistent with the features deduced from the pressure distribution on the airfoil. The velocity profiles close to the trailing edge correlated well with the log-law and suggested the development of a turbulent boundary layer in this region.

9) The findings suggested that the location of the boundary layer transition was sensitive to the experimental conditions. For the configuration of a NACA 0012 airfoil at zero angle of attack, with respect to the horizontal, and chord Reynolds number of 1×10^5, the location of transition was close to the trailing edge. This was partly due to the non-zero flow angle caused by the bend. The results for the effect of positive angle of attack and increased mainstream velocity on the wake, suggested that the transition location moved upstream, thus resulting in increased three-dimensionality and turbulence activity in the wake.

8.3. Numerical investigation

In the numerical study with LES, three different grids were tested. The first two grids comprised the entire spanwise extent of the experimental setup and the third grid consisted of a reduced extent equivalent to 0.5c. On the coarsest grid, computations were carried out for three different SGS models, namely, SMG, DSMG and DKET. On the finer grids, simulations were conducted using the DSMG model only. The results from the coarsest grid, also used in

the RSM computations of Piradeepan (2002), were compared to those of refinedPiradeepanDSMG which comprised the same geometry but with improved resolutions in all directions. To further assess the effect of increasing spanwise resolution, but reducing spanwise extent, the results from the full-extent simulations were compared to those from refinedDSMG.

Based on the comparisons between the different LES cases, experimental data from the present research and data from Piradeepan (2002), the following conclusions were made:

1) In the large eddy simulations, the peak flow angle near station 1 was predicted to be -2.5^{o}. The magnitude and location of the peak flow angle was consistent across the large eddy simulations but showed differences with the experiments, in which a peak flow angle of approximately -2^{o} was measured at station 1. These differences were partly responsible for the discrepancy between the simulations and the experiment further downstream.

2) The experimental trends in the static pressure distributions on the upper and lower surfaces of the airfoil were in close agreement with the trends obtained in the simulations. The computations indicated the presence of an adverse pressure gradient near the trailing edge, with the results from refinedDSMG showing the closest agreement to the experiments.

3) The distributions of pressure on the concave and convex walls of the duct were in close agreement with computations, except for the way in which separation was represented in the profiles. The experimental trend on the convex wall was better predicted by LES with the full extent of the duct. The refinedDSMG computations did not compute separation on the convex wall, at the exit of the bend, due to the differences between the model and the experimental setup, i.e. the shortened spanwise extent, and the imposition of periodic boundary conditions in place of the side walls. On the concave wall, coarse LES was prone to predicting spurious separation between stations 1 and 2, as identified by the plateau in the profile of pressure in this vicinity. This feature was attributed to the poor streamwise grid spacing in this region.

4) The quantitative differences between the computed wall friction and those obtained experimentally with the Clauser chart were attributed to the fact that, in the simulations, the boundary layers were close to separation or had separated, and thus lacked the conformity with the law of the wall. The local values of wall friction on the upper surface

of the airfoil computed with LES were lower in magnitude compared to RSM, due to the different ways in which the wall shear stress was calculated. The results indicated the susceptibility of LES on a grid with coarse spanwise resolution to predict artificial separation. On the full-extent grids, a separation region was computed near the trailing edge of the upper surface of the airfoil. However in refinedDSMG the flow remained attached in this region.

5) In general, the computed flow was close to separation on the concave wall of the duct between stations 1 and 2, but only on the coarsest grid a separation bubble was computed. The high turbulence levels computed on the concave wall in this region were attributed to this phenomenon. On the convex wall, the location of separation was found to be sensitive to grid resolution, where flow separated earlier in refinedPiradeepanDSMG than in coarseDSMG, thus resulting in increased turbulence levels in the region of separation, and some discrepancy with the experimental results in this region.

6) With regards to the prediction of the airfoil boundary layer, the effect of grid resolution was more dominant than the SGS model, in that, the boundary layers computed on the refined grids were thinner than those on the coarser grid. The results from refinedDSMG with the finest spanwise grid spacing were closer to the experiments, especially near the trailing edge of the airfoil, whereas the simulations on the coarser grids were susceptible to predicting separation and reversed flow on this surface, characterised by thicker profiles of turbulence intensity with higher magnitudes in the peak value. In spite of the improvements, the velocity profile in refinedDSMG did not become as fully established as in the experiments.

7) The predictions in the wake were consistent with the quality with which the airfoil boundary layers were predicted. The asymmetric structure of the wake was predicted by all computations. However, there were quantitative differences with the experiments. The results from LES on the full-extent grids indicated thicker profiles, whereas those with the dynamic SGS models showed improvements over coarseSMG, although the wake-width was still overpredicted. The results from refinedDSMG indicated vast improvements in the prediction of the wake, in that the profiles, especially in the near-wake on the inner and outer sides, collapsed well with the experimental profiles. However, even on the finest grid the lateral shift of the wake with respect to the duct centre line was computed higher

than that in the experiments, especially at station 2, where the effects of curvature and pressure gradient became dominant.

8) With regards to the wake parameters, the wake half-widths computed in refinedDSMG were the closest to the experiments, in the near-wake and at stations 2 to 4. On the other hand, the maximum velocity defect and its rate of decay, as derived in refinedPiradeepanDSMG, were better matched with the experiments, in comparison to refinedDSMG, due the effect of a larger spanwise extent.

9) The profiles of the Reynolds stresses $\overline{u'^2}$, $\overline{v'^2}$, $\overline{w'^2}$ and $-\overline{u'v'}$ in the wake, obtained by the refinedDSMG simulations resulted in the closest agreement with the experimental profiles. In particular, the peaks on the inner and outer side of the streamwise turbulence intensity profiles were in close agreement with the double-peak structure of the experimental profiles. In general, the computations on the grids with coarser spanwise resolution computed less satisfactory profiles in the wake, and the differences with the experiments correlated with the differences seen in the profiles on the airfoil.

10) The profiles of velocity and Reynolds stresses computed across the whole cross-section of the duct showed sensitivities to the spanwise extent. The grids with the full spanwise extent resolved the correct velocity and turbulence fields near station 5 on the convex wall, which was due to the occurrence of separation. Despite the improvements in the wake, the results of refinedDSMG were similar to RSM in this region, in that, separation from the convex wall was not computed. This effect was demonstrated by the low levels of turbulence computed, and was attributed to the geometrical differences between the computational and experimental domains.

11) In the region near the concave wall, the coarse grids tended to over-predict the enhancement of turbulence due to the concave curvature, especially at stations 2 to 4. The results showed improvements on this wall for the simulations with finer grids, although even with the finest grid, the turbulence levels at station 2 were over-predicted. This was attributed to the way in which the boundary layers were predicted in this region, that is, LES tended to predict a boundary layer that was close to separation. The velocity and turbulence profiles computed by refinedPiradeepanDSMG near the concave wall showed further improvements at stations 4 and 5 due to a better allowance for the formation of a secondary flow in the duct.

12) The computed spanwise distributions of the mean velocity and turbulence quantities in the wake displayed a well organised peak-valley wavy structure in agreement with the experiments. These variations correlated with the periodic streamwise vortices computed in the wake. However, in the experiments, smaller spanwise variations were measured on the outer side of the wake than computed in the large eddy simulations.

13) The velocity contour and vector plots were used to identify the qualitative features from the simulations. The vector plots in the *x-y* plane from coarseDSMG and refinedPiradeepanDSMG indicated the formation of separation bubbles on the upper surface of the airfoil, features of which were absent in refinedDSMG simulations due to the reduced spanwise grid spacing. The velocity vectors from the full-extent simulations displayed the separation and reattachment phenomena on the convex wall, which resulted in the enhancement of turbulence quantities in this vicinity. The vectors in coarseDSMG indicated a small separation bubble between stations 1 and 2, which contributed to the discrepancies in the mean and RMS quantities measured in this region. This feature was not computed on the finer grids, but significant flow retardation was still evident upstream of the concave curvature in these simulations.

14) The results illustrated the sensitivity of the resolved vorticity field to the grid resolution and the SGS model. As expected the dynamic models yielded a better representation of the vortical structures in the wake. The effect of curvature on vortical structures was also evident. On the finer grids, the vortical structures were better resolved, especially near the trailing edge of the airfoil, where the vortex pattern observed indicated the features of a transitional flow, the correct prediction of which was important in resolving the developing wake downstream.

15) The contour plots in the *y-z* plane indicated the formation of secondary flow, characterized by the development of two counter-rotating vortices near the convex wall, which was better resolved in the refinedPiradeepanDSMG simulations. The absence of a developed secondary flow in the reduced spanwise extent simulations was also indicated. On the concave wall, the results showed the formation of Taylor Görtler vortices, which had a contributory effect on the flow statistics. The large discrepancies observed in the profiles of mean and turbulence quantities on the concave wall, especially on the coarser grids, were attributed partly to the incorrect prediction of such features.

8.3.1. Summary

In this section the salient findings from the numerical study are summarised. On the coarse grid, LES displayed advantages over RANS in predicting flow behaviour near the strong convex curvature, but also shortcomings in relation to the prediction of the wake parameters. The dynamic variants of the SGS models were more accurate in predicting the flow near the trailing edge and in the wake of the airfoil. The better prediction of the wake parameters in refinedDSMG was due to the improved simulation of the boundary layers on the upper and lower surfaces of the airfoil, as result of the improved spanwise grid resolution. Furthermore, the effect of curvature, that is, the increase in turbulence on the convex side of the wake and the decrease on the concave side, and the existence of the double peak in the profile of streamwise intensity were better predicted in refinedDSMG. However, the simulation with a reduced spanwise extent also had its disadvantages, in that, the convex wall separation and secondary flow was not computed. The refinedPiradeepanDSMG simulations provided a more accurate depiction of the secondary flow and the development of the concave wall boundary layer in comparison to the experiments, although the predictions of the airfoil boundary layer and the wake did not improve significantly from those obtained with coarse LES.

The results of the present investigation have indicated some quantitative differences between LES and experiments, even for the simulations on the finest grid, in particular, the inaccurate prediction of the location of wake centre, which needs to be investigated further.

8.4. Recommendations for further work

The present study of curved wakes can be extended both numerically and experimentally. In the light of the shortcomings of the present large eddy simulations, further research can be carried out to consider the effect of several modelling adjustments on the results. The following recommendations are made:

1) The present investigation considered LES as the numerical technique. In recent years RANS/LES hybrid methods have been adopted to study complex flows or geometries where the larger scales of flow are dominant. In these methods the flow near the wall is computed using a RANS turbulence model, and the detached part of the flow is resolved, or vice versa. Detached eddy simulation (DES) is a well known example of such a numerical method. The advantage of these hybrid techniques is the reduced mesh density

and computational time required to run a simulation to obtain a statistically stable solution. Therefore, it would be useful to compute a DES of the present flow configuration, especially since this numerical method has been already implemented into the FLUENT code, thus allowing for consistent comparisons with the presents results.

2) The numerical study could be extended by computing the curved wake of an airfoil at various angles of attack. These simulations would present a challenging case for CFD codes due to the extra rate of strain on the wake caused by the airfoil angle of attack, coupled with the streamwise curvature from the duct. The present experimental investigation provides data for the validation of these simulations.

3) In the present study, the Werner and Wengle wall functions were adopted into the simulations. It was concluded that the discrepancies between LES, RANS and experiments with respect to the wall friction was partly due to the way in which the WW wall functions calculated the wall shear stress, and the differences with the standard wall functions. Furthermore, the delayed development towards a fully turbulent boundary layer on the concave wall and the airfoil invalidated the Clauser chart methods in these regions. Therefore, it would be useful to simulate the no-slip wall condition with the grid of reduced spanwise extent; considered suitable for such a simulation, to deduce the effect of the wall functions on the results.

4) With increase in computational power and memory one could in the future conduct a direct numerical simulation (DNS) of the present test case. DNS presents the full simulation of the Navier-Stokes equations, which can provide more detailed information about the effect of the unresolved scales on the flow. It is estimated that a grid size of more than 100 million cells will be required to conduct such a simulation with the present geometry.

5) The present study may be extended experimentally by studying the effect of the curved wake on a downstream airfoil. This would be possible in the present experimental setup, with some modifications to the test section to facilitate a second airfoil further downstream. Experiments of this type would be beneficial to the field of turbomachinery, to understand the effect that the wake of a turbine or compressor blade has on the downstream blades.

6) Further work could include a study of the present test case, but using a more advanced experimental technique that could deduce the qualitative features of the flow field, for example, separation, recirculation and vortical structures. This could be through methods such as particle image velocimetry (PIV) or the use of a triple-wire probe, which could be used to determine two- or three-dimensional graphical representations of the flow field, including the contours of velocity, turbulence and vorticity in the experimental domain.

Appendix I – Farsimadan and Mokhtarzadeh-Dehghan (2008)

INTERNATIONAL JOURNAL FOR NUMERICAL METHODS IN FLUIDS
Int. J. Numer. Meth. Fluids 2008; **56**:1233–1240
Published online in Wiley InterScience (www.interscience.wiley.com). DOI: 10.1002/fld.1746

A large eddy simulation of an airfoil turbulent wake subjected to streamwise curvature

E. Farsimadan and M. R. Mokhtarzadeh-Dehghan*, †

School of Engineering and Design, Brunel University, Uxbridge Middlesex UB8 3PH, U.K.

SUMMARY

This paper presents large eddy simulations (LES) of the curved wake of an airfoil. The wake was generated by placing a NACA0012 airfoil in a uniform stream of air, which is then subjected to an abrupt 90° curvature created by a duct bend. The trailing edge of the airfoil is one chord length upstream of the bend entry. The duct cross-section measures 457 mm × 457 mm, and the bend has radius to height ratio of 1.17. The flow Reynolds number (1.02×10^5) is based on a mainstream velocity of 10 m/s and airfoil chord length 0.15 m. The sub-grid scale models employed are the classical Smagorinsky, its dynamic variant and the dynamic kinetic energy transport. The performance of LES in depicting the experimental flow is assessed and compared with results predicted by the Reynolds stress model (RSM). The results show the advantages of LES over Reynolds-averaged Navier–Stokes methods in predicting convex wall separation in strongly curved ducts on relatively coarse grids. Results from LES on a considerably finer near-wall-resolved grid lead to much improved comparison with the experimental data in the near wake, bettering predictions by RSM and LES on the coarse grid. Copyright © 2008 John Wiley & Sons, Ltd.

Received 22 March 2007; Revised 8 December 2007; Accepted 10 December 2007

KEY WORDS: LES; wake; airfoil; curvature; turbulent; duct

1. INTRODUCTION

Curved wakes occur in numerous industrial applications. Examples are in turbomachines, multi-element airfoils and ducts with guide vanes. It is known that curvature has significant effect on the properties of the wake. Experimental investigations of the curved wake of an airfoil [1] indicated enhancement of turbulence quantities on the inner-side wake and their suppression on the outer side. Steady-state Reynolds-averaged Navier–Stokes (RANS) computations [2] of the same flow field as in [1] with RSM qualitatively depicted the correct effects of curvature on

*Correspondence to: M. R. Mokhtarzadeh-Dehghan, School of Engineering and Design, Brunel University, Uxbridge Middlesex UB8 3PH, U.K.
†E-mail: reza.mokhtarzadeh@brunel.ac.uk

turbulence. However, clear discrepancies were evident in the quantitative comparison of wake profiles and in regions where separation occurred. A main source of discrepancy was a lack of prediction of separation on the convex wall of the 90° duct. The aim of the present work is to carry out large eddy simulations (LES) of the same flow in order to assess the ability of this technique in overcoming previous inaccuracies and to demonstrate the advantages it places over RANS methods. Several interesting features need to be examined; large vortical structures and their development in the near-wake, and flow separation on the convex wall. There have been a number of recent publications concerning LES of strongly curved duct flows, although to the best knowledge of the authors there exist no known publications on LES of curved wakes in the current configuration.

2. NUMERICAL METHOD AND COMPUTATIONAL SETUP

LES is a methodology developed from an understanding that the majority of energy is contained in the large scales of the flow. In LES, the Navier–Stokes equations are fully resolved for larger scales defined by the filter width, whereas the interactions of the resolved scales with the unresolved small scales are modelled using a sub-grid scale (SGS) model. The SGS models used in the present study are the classical Smagorinsky (SMG), its dynamic variant (DSMG) and the dynamic kinetic energy by transport (DKET). These models relate the eddy viscosity to the rates of strain through parameters C_s (SMG), c_s (DSMG) and C_k (DKET). In the SMG model C_s is fixed at 0.1. The parameters c_s and C_k are both dynamically determined, spatially at each point and temporally at each time step, thus providing better adaptation to local flow length scales. The DKET model differs from the DSMG model in that it additionally solves the turbulent kinetic energy transport equation to deduce k_{sgs} (SGS turbulent kinetic energy). Kim [3] provides further details of these models.

Wall functions defined by Werner and Wengle [4] have been adopted into the simulations. This consists of a two-layer approximation based on the viscous sub-layer and the assumption of a one-seventh power law outside the viscous sub-layer. The employed wall method presents advantages over standard wall function models by providing a more accurate representation of the near-wall layers. Mean velocity profiles measured upstream of the airfoil in [1] are used to define the inlet boundary conditions. The random flow generation technique in [5] based on samples of Fourier harmonics is used to generate a non-homogenous anisotropic flow field, representing turbulent inflow conditions. Within the implementation of this technique, the required turbulence quantities from the experimental data were used. The number of Fourier harmonics representing the turbulence spectrum is fixed at $N=50$. A fixed time step (seconds) $t=8.33\times10^{-3}c/U$ is chosen based on the mainstream velocity U and airfoil chord length c. Assessment of the Courant–Friedrichs–Lewy (CFL) number in the most turbulent regions indicated levels of CFL<1, confirming that the selected time step is capable of capturing the characteristic timescales of the flow. For the time integration an explicit four-stage Runge–Kutta scheme was used.

The majority of the simulations were conducted using the grid of [2], the results of which are referred to as coarseLES. This was in line with our initial aim to assess the degree of improvement, if any, which may be achieved using LES. This led to further simulations using a refined grid, the results of which are also included. The flow domain with the superimposed coarse grid is shown in Figure 1. The structured grid is composed of 25 blocks consisting of 676 000 cells, the full spanwise extent of the duct is represented by side walls, with 42 cells spaced evenly in the

DOI: 10.1002/fld

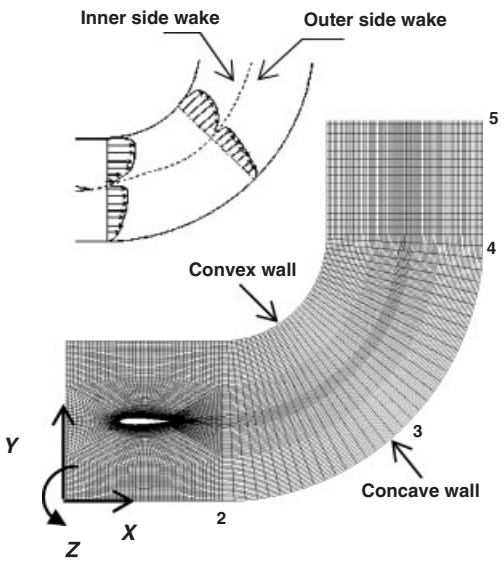

Figure 1. Computational coarse grid [2] and flow domain. Locations of stations 2–5 are indicated.

z-direction. A fine resolution was adopted close to the airfoil surface and the near-wake region. In non-dimensional wall units based on the local value of wall shear stress the near-wall airfoil grid spacings after $x/c=0.1$ are within $140>\Delta x^+>20$, $500>\Delta z^+>100$ and $\Delta y^+<1$ (wall to node distance for the first grid line). The coarse grid distribution in the normal direction on the bend walls ($\Delta y^+=100$) constitutes the reason behind adopting wall functions. The outlet is placed $5.0H$ downstream of station 4, where H is the cross-sectional duct height ($H=0.457$ m). In LES, the coarse spanwise resolution in the grid of [2] was considered to affect the boundary layer growth and the wake development. In response to this a refined grid was set up with a spanwise segment of the tunnel equal to $0.5c$, with periodic conditions defined in this direction. The refined grid has improved wall-normal, streamwise and spanwise resolutions throughout the domain consisting of more than 6.1 million cells and satisfies a near-wall resolution of $\Delta z^+<30$ over most of the airfoil.

The flow solver is based on the finite volume discretization of the governing equations. A bounded central differencing scheme is used to discretize the convection terms; this method is known to remove unphysical oscillations in the flow that are associated with pure central difference schemes, especially on coarser grids. The derivation of pressure is based on the SIMPLEC algorithm. Flow was allowed to develop for substantial computational time so that a statistically steady-state (SSS) condition for turbulence was achieved at station 5 (140 000 time steps or 50 flow through times). A further 40 000 time steps were computed with a sample taken every 10 time steps to obtain turbulence statistics. Simulations were carried out on a COMPUSYS parallel processing cluster. The grids were partitioned on 8 Intel Xeon dual processor nodes running at 3.2 GHz each. On the coarser grid this required an average of 3 s per time step, resulting in approximately 117 central processing unit (CPU) hours to reach SSS. Simulations on the finer grid took 12 s per time step with a running time of 470 CPU hours to reach SSS.

DOI: 10.1002/fld

3. RESULTS AND DISCUSSION

Figure 2 presents the measured and predicted pressure coefficient on the concave and convex walls of the duct. Pressures are relative to the reference value at station 1. There is general agreement between the experiment and the computation for the overall profile and also differences. On the convex wall, the predicted pressure drops to a minimum just before station 3 followed by a period of recovery leading to a distinct plateau. The plateau in the profile that is also seen experimentally was reported in [1] to be due to intermittent flow separation. This feature is not computed by RSM but predicted by coarseLES. However, the SMG model exaggerates this feature, whereas DSMG and DKET present better comparison to experiments. As stated before, the latter model uses an additional transport equation, which describes the physics of turbulence better and provides improved results compared with DSMG. LES also shows closer agreement for the pressure recovery downstream of station 4 and also for the overall pressure loss.

On the concave wall, between stations 1 and 2, coarseLES predicts a small plateau in the pressure profile (Figure 2), a feature not computed in RSM or measured in the experiment. This can be attributed to the occurrence of small flow separation upstream of station 2 as can be seen in Figure 3(a), where the velocity vector field at the midspan is shown. This is believed to be due to the jump in the streamwise grid resolution in this region. In Figure 3(b) the velocity vectors indicate separation from the convex wall just before station 4, where flow is reversed in the vicinity close to the wall. Reattachment is observed at a distance less than the duct height H, downstream of the separation point.

Profiles of streamwise velocity, turbulence intensity and turbulence shear stress at station 5 are presented in Figure 4(a)–(c). LES has computed the velocity and turbulence fields near the convex wall in very good agreement with experiments. All SGS models perform consistently well in this respect. The enhancement of turbulence is attributed to the separation and recirculation resolved by LES, observed in Figure 3(b). Lack of prediction of flow separation on the convex wall by RANS is evident by very low levels of turbulence demonstrated in Figure 4(b). The wake velocity defect and turbulence profiles as predicted by RANS and experiments have reduced considerably

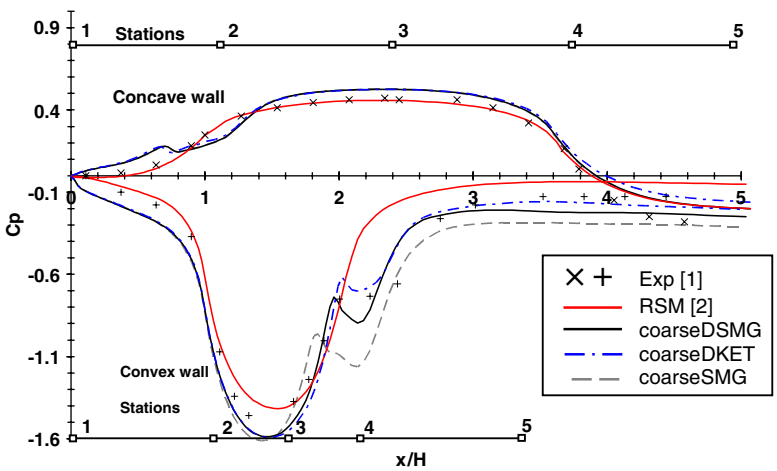

Figure 2. Pressure coefficient along the convex and concave walls of the duct.

Int. J. Numer. Meth. Fluids 2008; **56**:1233–1240
DOI: 10.1002/fld

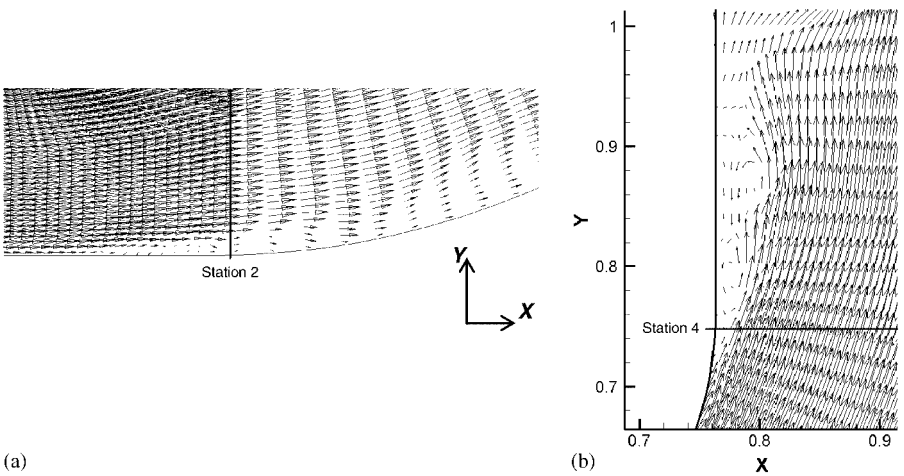

Figure 3. Velocity magnitude vectors plotted at midspan for coarseDSMG: (a) near the concave curvature at station 2 and (b) at the convex wall past station 4.

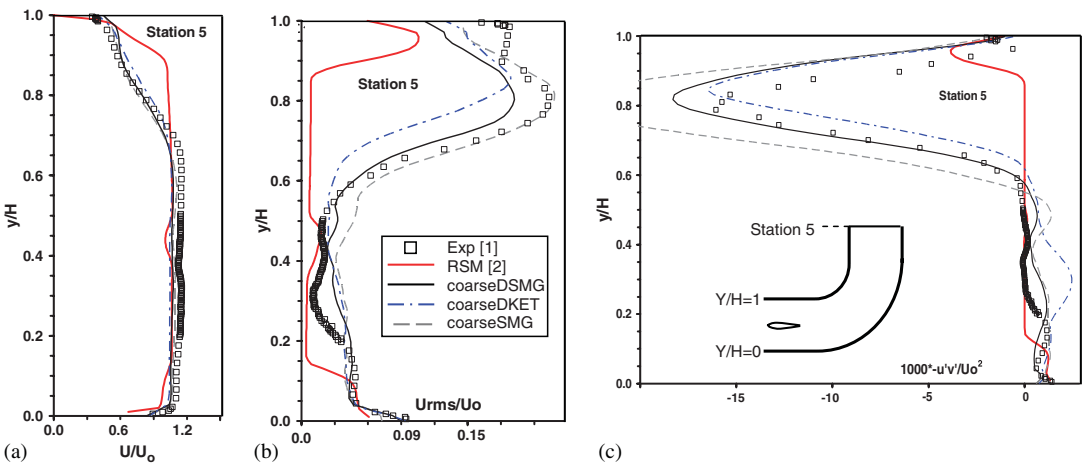

Figure 4. Mean velocity and turbulence quantities predicted by coarseLES across full duct height at station 5: (a) streamwise velocity; (b) streamwise turbulence intensity; and (c) turbulence shear stress.

in magnitude by station 5. In the coarseLES the wake has washed out in this region with less distinguishable features. The results in the highly separated region demonstrate the advantages of LES over RANS in this strongly curved convex curvature.

Figure 5(a), (b) illustrates a comparison of mean streamwise velocity and turbulence intensity in the near wake for $x/c = 1.326$, 1.443 and 2. This figure also presents new experimental data in the wake. The previous studies [1, 2] showed that, relative to the duct centreline, the wake is shifted towards the convex wall at stations 2 and 3, and then towards the concave wall at stations 4 and 5. This was confirmed by the present simulations. In comparison to RSM, coarseLES resolves an

DOI: 10.1002/fld

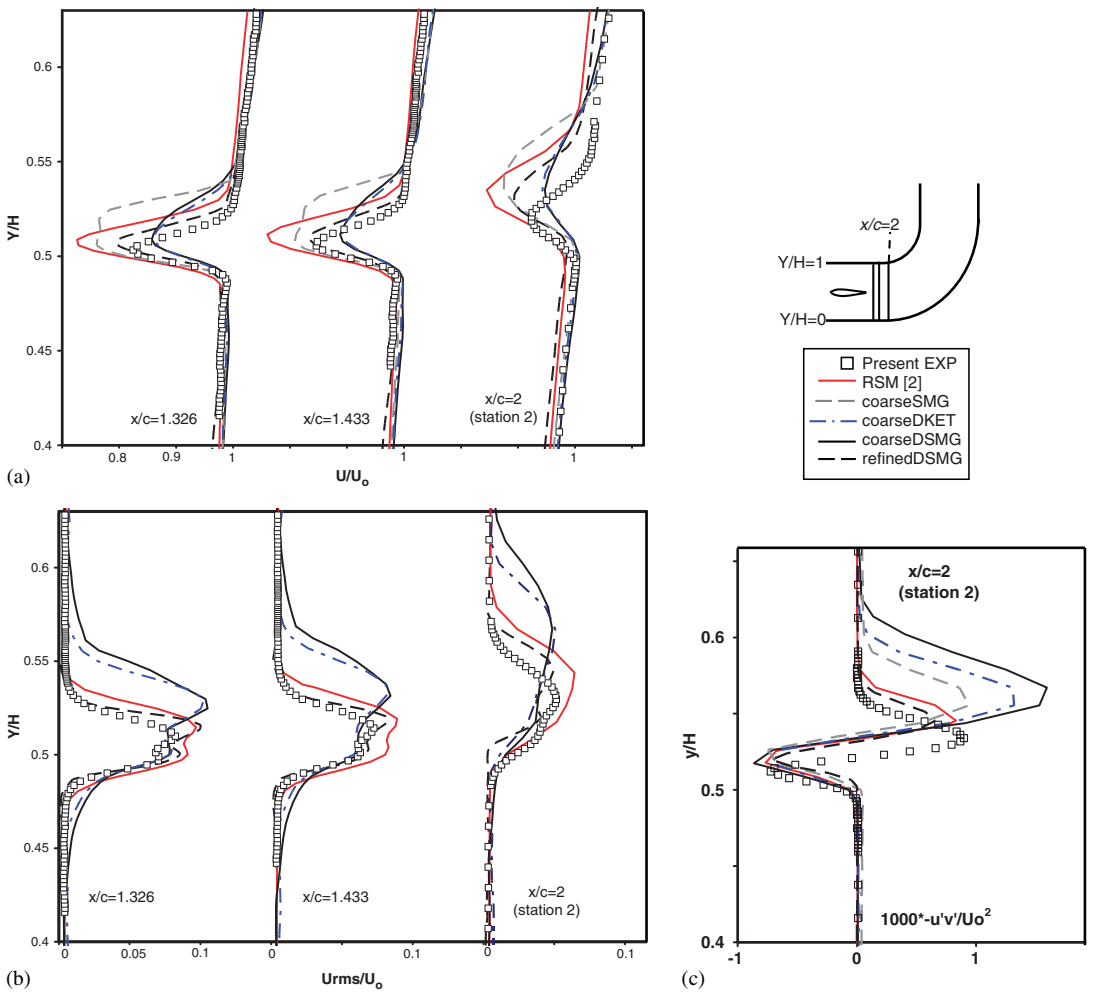

Figure 5. Comparison between coarseLES on the grid of [2] and preliminary results of LES on a refined grid: (a) mean streamwise velocity; (b) streamwise turbulence intensity; and (c) turbulence shear stress.

increased wake width at station 2, a feature that is consistent throughout the downstream stations. CoarseSMG predicts a considerably enhanced profile on the inner side of the wake with larger velocity defect. The dynamic models on the same grid compute a smaller velocity defect. In all computations the centre of the wake is located above the experimental profile. The SMG model resulted in an erroneous streamwise turbulence intensity profile in the wake, results of which are omitted. In Figure 5(b) in comparison to RSM the existence of a double peak in the profile is better depicted by the simulations, but the turbulence intensity is considerably overpredicted on the inner side for the dynamic SGS models in coarseLES. This is believed to stem from the overprediction of turbulence on the upper surface of the airfoil, which was also stated in [2]. The results indicate that the boundary layer predictions on the airfoil have worsened in the case of coarseLES leading

DOI: 10.1002/fld

to larger differences in the curved wake. These differences remain in the profiles at downstream stations 3 and 4 (not shown here). Turbulence shear stress at station 2 in Figure 5(c) is enhanced on the inner side of the wake and suppressed on the outer side. Although this is qualitatively correct, the level of turbulence enhancement in coarseLES is computed too high when compared with RANS and experiments.

In light of the shortcomings of LES on the grid of [2], in the wake, results for the refined grid of reduced spanwise extent are also presented in Figure 5. Results from refinedDSMG indicate vast improvements in the prediction of the wake properties. The wake defect, wake width and, in particular, the presence of a double peak structure in the turbulence intensity profiles are in close agreement with the experiments, surpassing the RSM predictions in Figure 5(b) and (c). We have not included the results for stations 3 and 4, but the improvements noted here remain consistent. Despite the improvements noted in the wake, the results also showed deterioration by predicting a smaller separation region on the convex wall. This is due to the shortened spanwise extent of the flow domain, and in place of the side wall, the imposition of the periodic condition. The inaccurate prediction of the location of the wake centre (Figure 5(a)) still remains consistent with RANS and coarseLES especially at $x/c=2$ when the effect of curvature is more pronounced. This points to a need for further investigations.

Figure 6(a)–(c) presents contours of spanwise vorticity in the near wake as computed by coarseSMG, coarseDSMG and refinedDSMG, respectively. The merging shear layers on the upper and lower surfaces of the airfoil have resulted in the formation of counter rotating vortices in the wake. The effects of curvature on the inner side of the wake compared with the outer side are evident in this figure. As with the velocity and turbulence profiles, the near-wake vorticity is also shifted above the duct centreline. Results from coarseSMG (Figure 6(a)) present a somewhat different pattern compared with the pattern of coarseDSMG (Figure 6(b)), where the latter provides more plausible representation of the dynamic vortical structures on the coarse grid. This is considered to be in response to the limitations of the standard SMG model in representing the local length scale. Results from the classical LES case described by refinedDSMG (Figure 6(c)) indicate a highly resolved vorticity field near the trailing edge, which is in direct response to the increased spanwise, wall-normal and streamwise grid resolutions in the region of the airfoil. The vortex pattern observed in Figure 6(c) on the upper surface of the airfoil near the trailing edge indicates

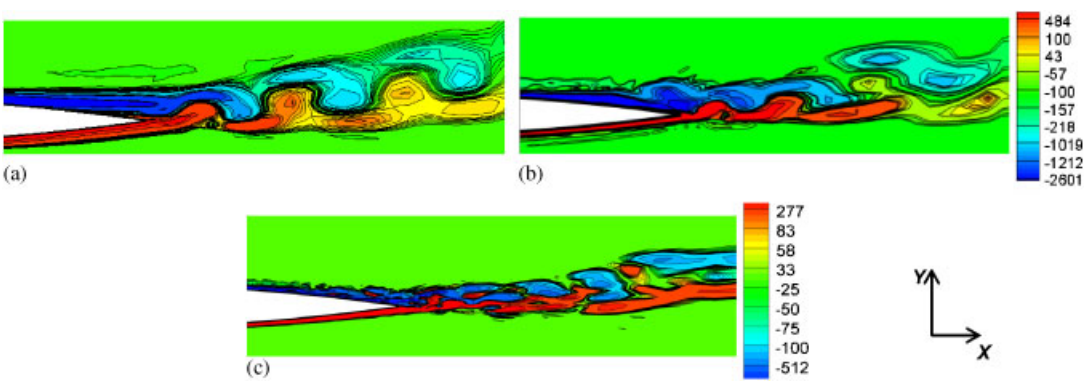

Figure 6. Development of spanwise vorticity (ω_z) in the near wake: (a) coarseSMG; (b) coarseDSMG; and (c) refinedDSMG on the refined grid.

DOI: 10.1002/fld

features of transitional flow, the correct prediction of which is important in resolving the developing wake downstream.

4. CONCLUSIONS

On the coarse grid, LES displayed advantages over RANS in predicting flow behaviour near strong convex curvature, but also shortcomings in relation to the prediction of wake parameters. The dynamic variants of the SGS models were more accurate in predicting flow near the trailing edge and in the wake of the airfoil. The better prediction of wake parameters on the refined grid is due to the improved simulation of the boundary layers on the upper and lower surfaces of the airfoil, as a result of improved grid resolution. The effect of curvature, that is, the increase in turbulence on the convex side of the wake and the decrease in the concave side, and the existence of a double peak in the profile was better predicted by refinedLES. Quantitative differences between refined LES and experiments relate in particular to the inaccurate prediction of the location of wake centre, which needs to be investigated further.

ACKNOWLEDGEMENTS

The study was carried out with FLUENT 6.3.21. Post-processing was conducted with TECPLOT 360.

REFERENCES

1. Piradeepan N, Mokhtarzadeh-Dehghan MR. Measurements of mean and turbulence quantities in the curved wake of an airfoil. *Experimental Thermal and Fluid Science* 2005; **29**:239–252.
2. Mokhtarzadeh-Dehghan MR, Piradeepan N. Numerical prediction of a turbulent curved wake and comparison with experimental data. *International Journal for Numerical Methods in Fluids* 2006; **51**:49–76.
3. Kim S. Large-eddy simulation using an unstructured mesh based finite-volume solver. *Technical Report AIAA-2004-2548*, *American Institute of Aeronautics and Astronautics*, *34th Fluid Dynamics Conference and Exhibit*, Portland, Oregon, 2004.
4. Werner W, Wengle H. Large-eddy simulation of turbulent flow over and around a cube in a plate channel. *Eighth Symposium on Turbulent Shear Flows*, Munich, Germany, 9–11 September 1991; 155–168.
5. Smirnov A, Shi S, Celik I. Random flow generation technique for large-eddy simulations and particle-dynamics modelling. *Journal of Fluids Engineering* 2001; **123**:359–371.

DOI: 10.1002/fld

Appendix II – Wind tunnel schematic

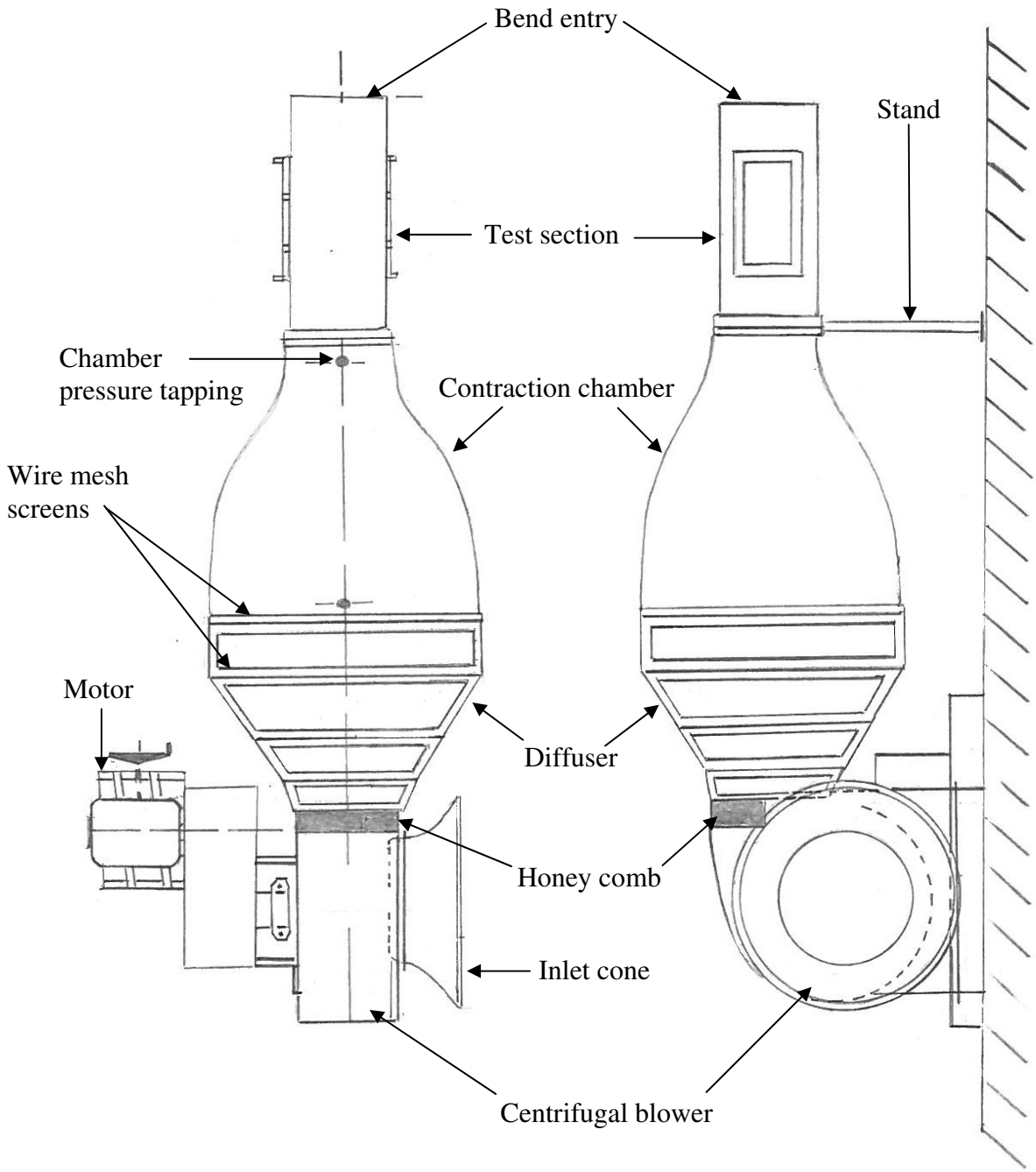

Figure A2.1: A schematic of the wind tunnel

Appendix III – Airfoil geometry

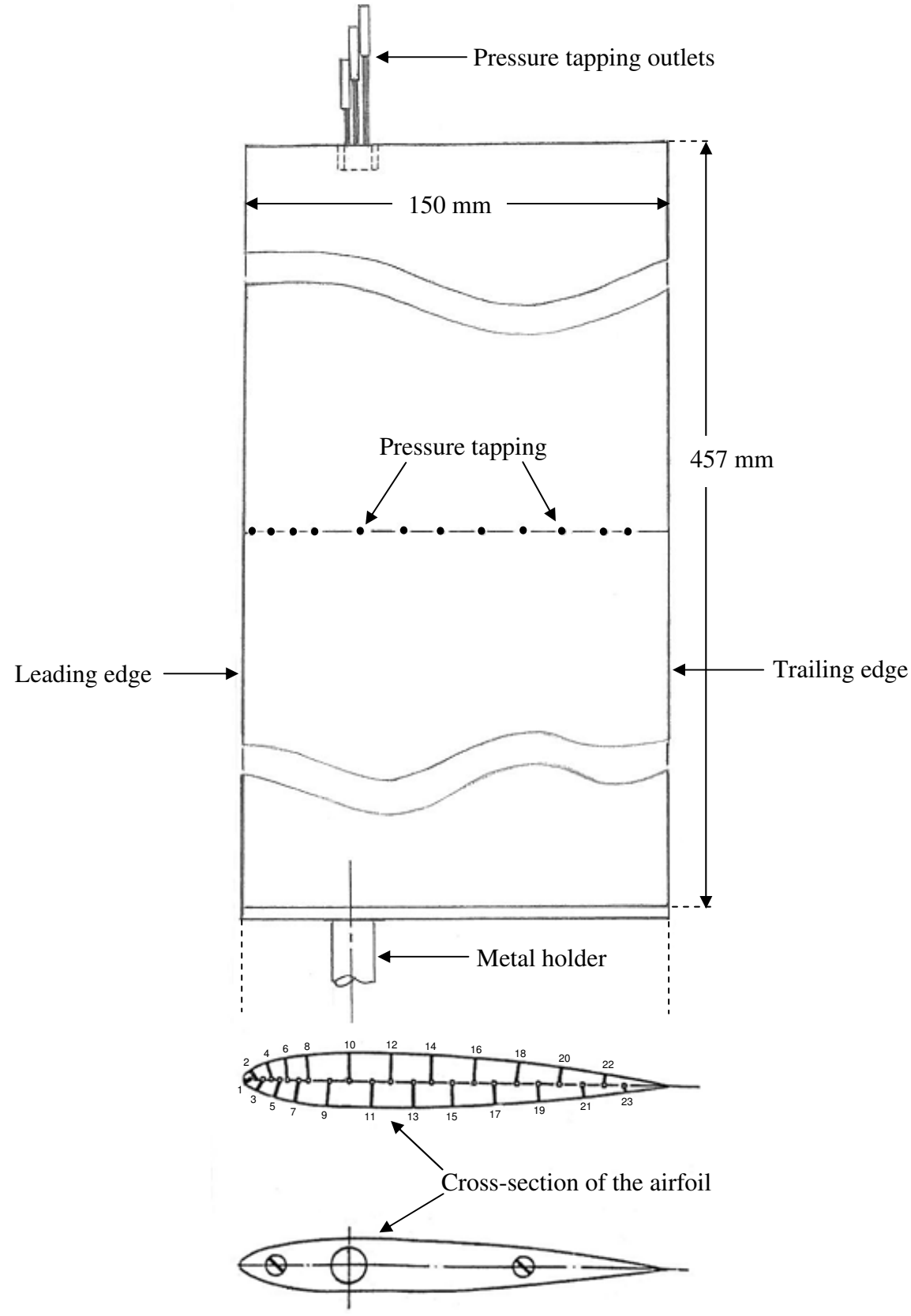

Figure A3.1: A schematic of the airfoil.

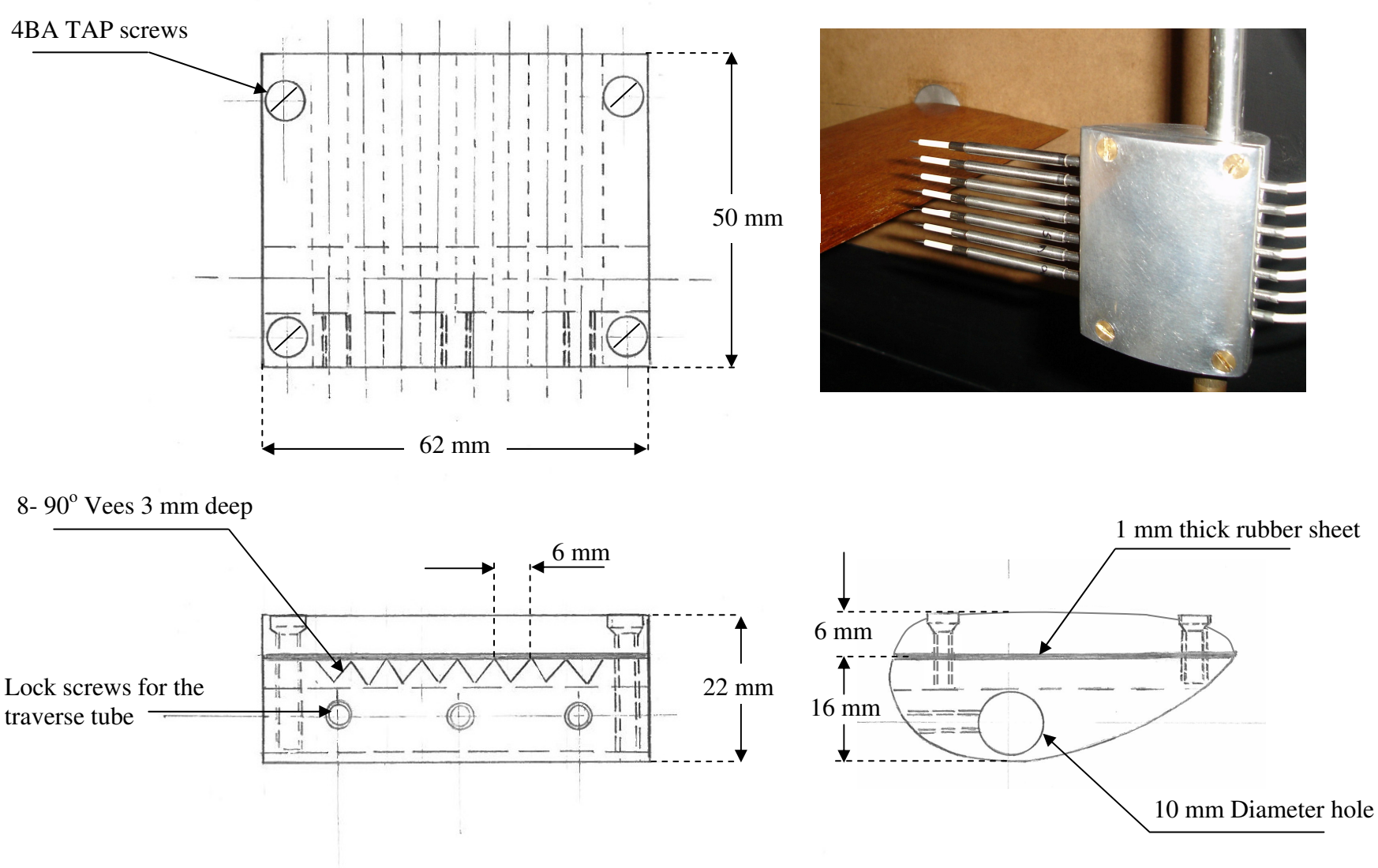

Figure A4.1: A projection drawing and photograph of the multi-probe rake housing.

Appendix V – Sample of experimental results

Mean velocity and turbulence quantities measured in the near-wake and at station 2					
U_o = 9.95 (m/s), P_a = 762 (mm Hg), T_a = 294 (°K), z/H = 0.5, $\alpha = 0^o$					
x/c	**y** (mm)	**Umean** (m/s)	**Urms** (m/s)	**Vrms** (m/s)	$\overline{u'v'}$ (m^2/s^2)
1.05	178.5	10.26	0.036	0.066	-0.001
1.05	183.5	10.22	0.037	0.065	-0.001
1.05	188.5	10.19	0.036	0.063	-0.001
1.05	193.5	10.19	0.038	0.066	-0.001
1.05	198.5	10.18	0.036	0.064	-0.001
1.05	203.5	10.18	0.037	0.060	-0.001
1.05	208.5	10.14	0.036	0.057	-0.001
1.05	213.5	10.06	0.037	0.050	0.000
1.05	214.5	10.04	0.038	0.049	0.000
1.05	215.5	10.02	0.040	0.048	0.000
1.05	216.5	10.00	0.041	0.048	0.000
1.05	217.5	10.01	0.043	0.048	0.000
1.05	218.5	10.01	0.046	0.051	0.000
1.05	219.5	9.99	0.052	0.054	0.000
1.05	220.5	9.97	0.061	0.062	0.000
1.05	221.0	9.99	0.069	0.070	0.000
1.05	221.5	9.95	0.080	0.081	0.000
1.05	222.0	9.94	0.093	0.094	0.000
1.05	222.5	9.93	0.111	0.113	0.000
1.05	223.0	9.91	0.135	0.139	-0.001
1.05	223.5	9.89	0.169	0.176	-0.002
1.05	224.0	9.88	0.214	0.228	-0.003
1.05	224.5	9.82	0.273	0.299	0.001
1.05	224.8	9.77	0.309	0.347	0.014
1.05	225.0	9.63	0.368	0.405	0.049
1.05	225.3	9.33	0.484	0.491	0.132
1.05	225.5	8.88	0.638	0.590	0.249
1.05	225.8	8.29	0.783	0.691	0.373
1.05	226.0	7.52	0.880	0.798	0.467
1.05	226.3	6.79	0.892	0.887	0.454
1.05	226.5	6.16	0.858	0.943	0.339
1.05	226.8	5.69	0.839	0.987	0.134
1.05	227.0	5.38	0.886	1.027	-0.146
1.05	227.3	5.29	1.022	1.058	-0.431
1.05	227.5	5.40	1.142	1.075	-0.620
1.05	227.8	5.62	1.259	1.095	-0.765
1.05	228.0	5.89	1.342	1.100	-0.850
1.05	228.3	6.23	1.382	1.085	-0.869
1.05	228.5	6.60	1.379	1.063	-0.827
1.05	229.0	7.00	1.375	1.026	-0.783
1.05	229.5	7.74	1.289	0.935	-0.630
1.05	230.0	8.18	1.201	0.881	-0.516
1.05	230.5	8.51	1.148	0.840	-0.456
1.05	231.0	8.76	1.093	0.800	-0.397
1.05	231.5	9.05	1.031	0.759	-0.343
1.05	232.0	9.22	0.988	0.731	-0.312
1.05	232.5	9.50	0.880	0.672	-0.243

1.05	233.0	9.65	0.803	0.632	-0.201
1.05	233.5	9.82	0.692	0.571	-0.145
1.05	234.0	9.92	0.620	0.523	-0.119
1.05	234.5	10.02	0.540	0.476	-0.090
1.05	235.0	10.12	0.449	0.415	-0.059
1.05	235.5	10.17	0.376	0.362	-0.039
1.05	236.0	10.21	0.321	0.320	-0.026
1.05	236.5	10.24	0.271	0.278	-0.017
1.05	237.0	10.27	0.226	0.239	-0.009
1.05	237.5	10.31	0.185	0.198	-0.005
1.05	238.0	10.32	0.168	0.179	-0.004
1.05	238.5	10.33	0.149	0.157	-0.003
1.05	239.5	10.37	0.108	0.114	-0.001
1.05	240.5	10.42	0.084	0.095	-0.001
1.05	241.5	10.45	0.071	0.084	-0.001
1.05	242.5	10.48	0.062	0.077	0.000
1.05	243.5	10.52	0.054	0.072	0.000
1.05	248.5	10.66	0.042	0.068	0.000
1.05	253.5	10.77	0.040	0.074	-0.001
1.05	258.5	10.87	0.041	0.075	0.000
1.05	263.5	10.92	0.040	0.079	-0.001
1.05	268.5	11.00	0.041	0.083	0.000
1.05	273.5	11.07	0.041	0.087	0.000
1.05	278.5	11.15	0.040	0.087	0.000
1.05	288.5	11.24	0.042	0.098	-0.001
1.05	298.5	11.34	0.041	0.098	-0.001
1.05	308.5	11.39	0.041	0.110	-0.001
1.05	318.5	11.44	0.039	0.108	-0.001
1.05	328.5	11.49	0.041	0.115	-0.001

U_o = 9.98 (m/s), P_a = 760 (mm Hg), T_a = 295 (^{o}K), z/H = 0.5, $\alpha = 0^o$

x/c	**y** (mm)	**Umean** (m/s)	**Urms** (m/s)	**Vrms** (m/s)	$\overline{u'v'}$ (m^2/s^2)
1.10	165.0	10.02	0.039	N/A	N/A
1.10	166.0	10.01	0.041	N/A	N/A
1.10	167.0	10.01	0.042	N/A	N/A
1.10	168.0	10.02	0.040	N/A	N/A
1.10	169.0	10.01	0.042	N/A	N/A
1.10	170.0	10.02	0.038	N/A	N/A
1.10	171.0	10.03	0.035	N/A	N/A
1.10	172.0	10.03	0.034	N/A	N/A
1.10	173.0	10.03	0.034	N/A	N/A
1.10	174.0	10.03	0.036	N/A	N/A
1.10	175.0	10.03	0.040	N/A	N/A
1.10	176.0	10.02	0.043	N/A	N/A
1.10	177.0	9.99	0.043	N/A	N/A
1.10	178.0	10.00	0.044	N/A	N/A
1.10	179.0	9.99	0.042	N/A	N/A
1.10	180.0	9.99	0.042	N/A	N/A
1.10	181.0	10.00	0.044	N/A	N/A
1.10	182.0	10.01	0.042	N/A	N/A
1.10	183.0	10.01	0.043	N/A	N/A
1.10	184.0	10.00	0.044	N/A	N/A
1.10	185.0	10.00	0.043	N/A	N/A
1.10	186.0	10.02	0.038	N/A	N/A
1.10	187.0	10.00	0.044	N/A	N/A
1.10	188.0	9.99	0.043	N/A	N/A

1.10	189.0	10.00	0.044	N/A	N/A
1.10	190.0	10.00	0.043	N/A	N/A
1.10	191.0	9.97	0.041	N/A	N/A
1.10	192.0	10.00	0.044	N/A	N/A
1.10	193.0	10.00	0.044	N/A	N/A
1.10	194.0	10.01	0.043	N/A	N/A
1.10	195.0	10.02	0.040	N/A	N/A
1.10	196.0	10.02	0.040	N/A	N/A
1.10	197.0	10.03	0.035	N/A	N/A
1.10	198.0	10.01	0.043	N/A	N/A
1.10	199.0	10.02	0.035	N/A	N/A
1.10	200.0	10.02	0.040	N/A	N/A
1.10	201.0	10.02	0.040	N/A	N/A
1.10	202.0	10.01	0.040	N/A	N/A
1.10	203.0	10.00	0.044	N/A	N/A
1.10	204.0	10.01	0.038	N/A	N/A
1.10	205.0	10.00	0.042	N/A	N/A
1.10	206.0	10.00	0.044	N/A	N/A
1.10	207.0	9.99	0.043	N/A	N/A
1.10	208.0	9.99	0.044	N/A	N/A
1.10	209.0	9.98	0.044	N/A	N/A
1.10	210.0	9.97	0.045	N/A	N/A
1.10	211.0	9.96	0.043	N/A	N/A
1.10	212.0	9.97	0.045	N/A	N/A
1.10	213.0	9.95	0.044	N/A	N/A
1.10	214.0	9.95	0.043	N/A	N/A
1.10	215.0	9.95	0.045	N/A	N/A
1.10	216.0	9.95	0.047	N/A	N/A
1.10	217.0	9.95	0.050	N/A	N/A
1.10	218.0	9.94	0.057	N/A	N/A
1.10	219.0	9.94	0.065	N/A	N/A
1.10	220.0	9.95	0.081	N/A	N/A
1.10	221.0	9.95	0.107	N/A	N/A
1.10	221.5	9.96	0.132	N/A	N/A
1.10	222.0	9.96	0.162	N/A	N/A
1.10	222.5	9.97	0.204	N/A	N/A
1.10	223.0	9.98	0.268	N/A	N/A
1.10	223.5	9.96	0.351	N/A	N/A
1.10	224.0	9.86	0.486	N/A	N/A
1.10	224.5	9.64	0.661	N/A	N/A
1.10	225.0	9.24	0.858	N/A	N/A
1.10	225.5	8.68	0.984	N/A	N/A
1.10	226.0	8.09	1.017	N/A	N/A
1.10	226.5	7.52	0.977	N/A	N/A
1.10	227.0	7.15	0.937	N/A	N/A
1.10	227.5	6.99	0.966	N/A	N/A
1.10	228.0	7.02	1.041	N/A	N/A
1.10	228.5	7.20	1.124	N/A	N/A
1.10	229.0	7.49	1.184	N/A	N/A
1.10	230.0	8.11	1.188	N/A	N/A
1.10	230.5	8.42	1.139	N/A	N/A
1.10	231.0	8.64	1.098	N/A	N/A
1.10	231.5	8.88	1.051	N/A	N/A
1.10	232.0	9.09	0.970	N/A	N/A
1.10	232.5	9.29	0.907	N/A	N/A
1.10	233.0	9.45	0.821	N/A	N/A
1.10	233.5	9.60	0.743	N/A	N/A
1.10	234.0	9.71	0.654	N/A	N/A
1.10	234.5	9.79	0.588	N/A	N/A
1.10	235.0	9.88	0.507	N/A	N/A

1.10	236.0	10.01	0.365	N/A	N/A
1.10	237.0	10.05	0.253	N/A	N/A
1.10	238.0	10.09	0.171	N/A	N/A
1.10	239.0	10.12	0.128	N/A	N/A
1.10	240.0	10.15	0.099	N/A	N/A
1.10	241.0	10.17	0.079	N/A	N/A
1.10	242.0	10.19	0.068	N/A	N/A
1.10	243.0	10.20	0.060	N/A	N/A
1.10	244.0	10.23	0.055	N/A	N/A
1.10	245.0	10.26	0.054	N/A	N/A
1.10	246.0	10.27	0.052	N/A	N/A
1.10	247.0	10.29	0.050	N/A	N/A
1.10	248.0	10.32	0.049	N/A	N/A
1.10	249.0	10.33	0.049	N/A	N/A
1.10	250.0	10.34	0.048	N/A	N/A
1.10	251.0	10.36	0.046	N/A	N/A
1.10	252.0	10.39	0.043	N/A	N/A
1.10	253.0	10.38	0.042	N/A	N/A
1.10	254.0	10.40	0.043	N/A	N/A
1.10	255.0	10.42	0.047	N/A	N/A
1.10	256.0	10.42	0.048	N/A	N/A
1.10	257.0	10.45	0.046	N/A	N/A
1.10	258.0	10.48	0.043	N/A	N/A
1.10	259.0	10.49	0.043	N/A	N/A
1.10	260.0	10.50	0.043	N/A	N/A
1.10	261.0	10.51	0.047	N/A	N/A
1.10	262.0	10.51	0.048	N/A	N/A
1.10	263.0	10.53	0.048	N/A	N/A
1.10	264.0	10.54	0.048	N/A	N/A
1.10	265.0	10.56	0.041	N/A	N/A

$\boldsymbol{U_o}$ = 9.98 (m/s), $\boldsymbol{P_a}$ = 760 (mm Hg), $\boldsymbol{T_a}$ = 295 (°K), $\boldsymbol{z/H}$ = 0.5, $\alpha = 0^{\circ}$

x/c	**y** (mm)	**Umean** (m/s)	**Urms** (m/s)	**Vrms** (m/s)	$\overline{u'v'}$ (m^2/s^2)
1.22	177.0	10.07	0.038	N/A	N/A
1.22	178.0	10.06	0.041	N/A	N/A
1.22	179.0	10.06	0.041	N/A	N/A
1.22	180.0	10.07	0.038	N/A	N/A
1.22	181.0	10.06	0.041	N/A	N/A
1.22	182.0	10.07	0.036	N/A	N/A
1.22	183.0	10.08	0.033	N/A	N/A
1.22	184.0	10.09	0.034	N/A	N/A
1.22	185.0	10.09	0.034	N/A	N/A
1.22	186.0	10.08	0.034	N/A	N/A
1.22	187.0	10.08	0.038	N/A	N/A
1.22	188.0	10.07	0.040	N/A	N/A
1.22	189.0	10.05	0.044	N/A	N/A
1.22	190.0	10.06	0.042	N/A	N/A
1.22	191.0	10.05	0.044	N/A	N/A
1.22	192.0	10.05	0.043	N/A	N/A
1.22	193.0	10.06	0.042	N/A	N/A
1.22	194.0	10.07	0.038	N/A	N/A
1.22	195.0	10.07	0.038	N/A	N/A
1.22	196.0	10.07	0.041	N/A	N/A
1.22	197.0	10.07	0.038	N/A	N/A
1.22	198.0	10.09	0.035	N/A	N/A
1.22	199.0	10.07	0.040	N/A	N/A

1.22	200.0	10.06	0.041	N/A	N/A
1.22	201.0	10.07	0.039	N/A	N/A
1.22	202.0	10.08	0.036	N/A	N/A
1.22	203.0	10.06	0.043	N/A	N/A
1.22	204.0	10.08	0.037	N/A	N/A
1.22	205.0	10.08	0.036	N/A	N/A
1.22	206.0	10.09	0.034	N/A	N/A
1.22	207.0	10.10	0.040	N/A	N/A
1.22	208.0	10.10	0.043	N/A	N/A
1.22	209.0	10.12	0.044	N/A	N/A
1.22	210.0	10.10	0.043	N/A	N/A
1.22	211.0	10.12	0.045	N/A	N/A
1.22	212.0	10.12	0.046	N/A	N/A
1.22	213.0	10.12	0.047	N/A	N/A
1.22	214.0	10.13	0.048	N/A	N/A
1.22	215.0	10.12	0.050	N/A	N/A
1.22	216.0	10.13	0.053	N/A	N/A
1.22	217.0	10.13	0.059	N/A	N/A
1.22	218.0	10.14	0.068	N/A	N/A
1.22	219.0	10.14	0.085	N/A	N/A
1.22	220.0	10.15	0.111	N/A	N/A
1.22	221.0	10.15	0.160	N/A	N/A
1.22	222.0	10.15	0.248	N/A	N/A
1.22	223.0	10.07	0.388	N/A	N/A
1.22	224.0	9.83	0.592	N/A	N/A
1.22	225.0	9.32	0.782	N/A	N/A
1.22	226.0	8.76	0.841	N/A	N/A
1.22	227.0	8.32	0.807	N/A	N/A
1.22	228.0	8.14	0.805	N/A	N/A
1.22	229.0	8.20	0.887	N/A	N/A
1.22	230.0	8.48	0.962	N/A	N/A
1.22	231.0	8.83	0.979	N/A	N/A
1.22	232.0	9.20	0.932	N/A	N/A
1.22	233.0	9.53	0.845	N/A	N/A
1.22	233.5	9.71	0.766	N/A	N/A
1.22	234.0	9.82	0.703	N/A	N/A
1.22	234.5	9.92	0.645	N/A	N/A
1.22	235.0	10.03	0.566	N/A	N/A
1.22	235.5	10.10	0.486	N/A	N/A
1.22	236.0	10.14	0.426	N/A	N/A
1.22	236.5	10.20	0.372	N/A	N/A
1.22	237.0	10.23	0.317	N/A	N/A
1.22	237.5	10.25	0.271	N/A	N/A
1.22	238.0	10.27	0.212	N/A	N/A
1.22	238.5	10.28	0.184	N/A	N/A
1.22	239.0	10.28	0.161	N/A	N/A
1.22	239.5	10.28	0.148	N/A	N/A
1.22	240.0	10.30	0.120	N/A	N/A
1.22	240.5	10.30	0.108	N/A	N/A
1.22	241.0	10.31	0.095	N/A	N/A
1.22	242.0	10.33	0.077	N/A	N/A
1.22	242.5	10.32	0.072	N/A	N/A
1.22	243.0	10.32	0.068	N/A	N/A
1.22	243.5	10.32	0.066	N/A	N/A
1.22	244.0	10.33	0.060	N/A	N/A
1.22	244.5	10.34	0.057	N/A	N/A
1.22	245.0	10.33	0.055	N/A	N/A
1.22	245.5	10.34	0.053	N/A	N/A
1.22	246.0	10.34	0.052	N/A	N/A
1.22	246.5	10.34	0.051	N/A	N/A

1.22	247.0	10.36	0.051	N/A	N/A
1.22	248.0	10.39	0.049	N/A	N/A
1.22	249.0	10.38	0.049	N/A	N/A
1.22	250.0	10.39	0.049	N/A	N/A
1.22	251.0	10.41	0.045	N/A	N/A
1.22	252.0	10.43	0.045	N/A	N/A
1.22	253.0	10.44	0.048	N/A	N/A
1.22	254.0	10.46	0.047	N/A	N/A
1.22	255.0	10.46	0.048	N/A	N/A
1.22	256.0	10.49	0.047	N/A	N/A
1.22	257.0	10.51	0.041	N/A	N/A
1.22	258.0	10.51	0.043	N/A	N/A
1.22	259.0	10.52	0.043	N/A	N/A
1.22	260.0	10.54	0.046	N/A	N/A
1.22	261.0	10.54	0.045	N/A	N/A
1.22	262.0	10.55	0.046	N/A	N/A
1.22	263.0	10.56	0.048	N/A	N/A
1.22	264.0	10.59	0.047	N/A	N/A
1.22	265.0	10.58	0.048	N/A	N/A
1.22	266.0	10.59	0.044	N/A	N/A
1.22	267.0	10.60	0.043	N/A	N/A
1.22	268.0	10.60	0.045	N/A	N/A
1.22	269.0	10.62	0.041	N/A	N/A
1.22	270.0	10.64	0.046	N/A	N/A
1.22	271.0	10.65	0.047	N/A	N/A
1.22	272.0	10.65	0.047	N/A	N/A
1.22	273.0	10.67	0.049	N/A	N/A
1.22	274.0	10.67	0.048	N/A	N/A
1.22	275.0	10.68	0.048	N/A	N/A
1.22	276.0	10.68	0.049	N/A	N/A
1.22	277.0	10.70	0.043	N/A	N/A

$\boldsymbol{U_o}$ = 9.98 (m/s), $\boldsymbol{P_a}$ = 760 (mm Hg), $\boldsymbol{T_a}$ = 295 (°K), $\boldsymbol{z/H}$ = 0.5, $\boldsymbol{\alpha} = 0^{o}$

x/c	**y** (mm)	**Umean** (m/s)	**Urms** (m/s)	**Vrms** (m/s)	$\overline{u'v'}$ (m^2/s^2)
1.33	189.0	10.06	0.042	N/A	N/A
1.33	190.0	10.06	0.044	N/A	N/A
1.33	191.0	10.06	0.043	N/A	N/A
1.33	192.0	10.07	0.040	N/A	N/A
1.33	193.0	10.06	0.043	N/A	N/A
1.33	194.0	10.08	0.038	N/A	N/A
1.33	195.0	10.09	0.036	N/A	N/A
1.33	196.0	10.09	0.037	N/A	N/A
1.33	197.0	10.09	0.037	N/A	N/A
1.33	198.0	10.09	0.036	N/A	N/A
1.33	199.0	10.09	0.038	N/A	N/A
1.33	200.0	10.09	0.039	N/A	N/A
1.33	201.0	10.07	0.042	N/A	N/A
1.33	202.0	10.08	0.039	N/A	N/A
1.33	203.0	10.07	0.043	N/A	N/A
1.33	204.0	10.08	0.040	N/A	N/A
1.33	205.0	10.09	0.038	N/A	N/A
1.33	206.0	10.09	0.037	N/A	N/A
1.33	207.0	10.10	0.038	N/A	N/A
1.33	208.0	10.10	0.041	N/A	N/A
1.33	209.0	10.10	0.041	N/A	N/A
1.33	210.0	10.13	0.047	N/A	N/A

1.33	211.0	10.11	0.043	N/A	N/A
1.33	212.0	10.11	0.044	N/A	N/A
1.33	213.0	10.12	0.047	N/A	N/A
1.33	214.0	10.13	0.049	N/A	N/A
1.33	215.0	10.11	0.050	N/A	N/A
1.33	216.0	10.14	0.054	N/A	N/A
1.33	217.0	10.15	0.060	N/A	N/A
1.33	218.0	10.16	0.069	N/A	N/A
1.33	219.0	10.18	0.086	N/A	N/A
1.33	220.0	10.19	0.111	N/A	N/A
1.33	221.0	10.20	0.157	N/A	N/A
1.33	222.0	10.18	0.239	N/A	N/A
1.33	223.0	10.12	0.353	N/A	N/A
1.33	224.0	9.94	0.502	N/A	N/A
1.33	225.0	9.62	0.642	N/A	N/A
1.33	226.0	9.21	0.726	N/A	N/A
1.33	227.0	8.83	0.729	N/A	N/A
1.33	228.0	8.59	0.707	N/A	N/A
1.33	229.0	8.50	0.721	N/A	N/A
1.33	230.0	8.57	0.770	N/A	N/A
1.33	231.0	8.78	0.821	N/A	N/A
1.33	232.0	9.03	0.849	N/A	N/A
1.33	233.0	9.30	0.820	N/A	N/A
1.33	234.0	9.58	0.758	N/A	N/A
1.33	235.0	9.80	0.673	N/A	N/A
1.33	236.0	10.01	0.554	N/A	N/A
1.33	237.0	10.12	0.445	N/A	N/A
1.33	238.0	10.21	0.336	N/A	N/A
1.33	239.0	10.27	0.242	N/A	N/A
1.33	240.0	10.31	0.183	N/A	N/A
1.33	241.0	10.33	0.139	N/A	N/A
1.33	242.0	10.34	0.105	N/A	N/A
1.33	243.0	10.36	0.086	N/A	N/A
1.33	244.0	10.38	0.074	N/A	N/A
1.33	245.0	10.39	0.065	N/A	N/A
1.33	245.5	10.40	0.060	N/A	N/A
1.33	246.0	10.40	0.059	N/A	N/A
1.33	246.5	10.41	0.056	N/A	N/A
1.33	247.0	10.43	0.054	N/A	N/A
1.33	247.5	10.42	0.053	N/A	N/A
1.33	248.0	10.42	0.051	N/A	N/A
1.33	248.5	10.43	0.051	N/A	N/A
1.33	249.0	10.43	0.049	N/A	N/A
1.33	249.5	10.44	0.049	N/A	N/A
1.33	250.0	10.43	0.047	N/A	N/A
1.33	250.5	10.43	0.048	N/A	N/A
1.33	251.0	10.43	0.046	N/A	N/A
1.33	251.5	10.44	0.047	N/A	N/A
1.33	252.0	10.45	0.047	N/A	N/A
1.33	252.5	10.45	0.048	N/A	N/A
1.33	253.0	10.45	0.047	N/A	N/A
1.33	254.0	10.47	0.047	N/A	N/A
1.33	254.5	10.46	0.047	N/A	N/A
1.33	255.0	10.46	0.048	N/A	N/A
1.33	255.5	10.46	0.050	N/A	N/A
1.33	256.0	10.47	0.048	N/A	N/A
1.33	256.5	10.49	0.049	N/A	N/A
1.33	257.0	10.47	0.048	N/A	N/A
1.33	257.5	10.48	0.048	N/A	N/A
1.33	258.0	10.48	0.047	N/A	N/A

1.33	258.5	10.48	0.048	N/A	N/A
1.33	259.0	10.49	0.047	N/A	N/A
1.33	260.0	10.52	0.043	N/A	N/A
1.33	261.0	10.51	0.043	N/A	N/A
1.33	262.0	10.52	0.045	N/A	N/A
1.33	263.0	10.54	0.046	N/A	N/A
1.33	264.0	10.55	0.048	N/A	N/A
1.33	265.0	10.57	0.049	N/A	N/A
1.33	266.0	10.58	0.047	N/A	N/A
1.33	267.0	10.58	0.047	N/A	N/A
1.33	268.0	10.60	0.046	N/A	N/A
1.33	269.0	10.61	0.043	N/A	N/A
1.33	270.0	10.62	0.043	N/A	N/A
1.33	271.0	10.62	0.044	N/A	N/A
1.33	272.0	10.65	0.048	N/A	N/A
1.33	273.0	10.64	0.046	N/A	N/A
1.33	274.0	10.65	0.047	N/A	N/A
1.33	275.0	10.66	0.048	N/A	N/A
1.33	276.0	10.67	0.049	N/A	N/A
1.33	277.0	10.66	0.049	N/A	N/A
1.33	278.0	10.68	0.049	N/A	N/A
1.33	279.0	10.69	0.047	N/A	N/A
1.33	280.0	10.68	0.049	N/A	N/A
1.33	281.0	10.70	0.044	N/A	N/A
1.33	282.0	10.72	0.043	N/A	N/A
1.33	283.0	10.72	0.044	N/A	N/A
1.33	284.0	10.73	0.045	N/A	N/A
1.33	285.0	10.73	0.044	N/A	N/A
1.33	286.0	10.73	0.045	N/A	N/A
1.33	287.0	10.74	0.045	N/A	N/A
1.33	288.0	10.74	0.046	N/A	N/A
1.33	289.0	10.76	0.049	N/A	N/A

$\boldsymbol{U_o}$ = 9.98 (m/s), $\boldsymbol{P_a}$ = 760 (mm Hg), $\boldsymbol{T_a}$ = 295 (°K), $\boldsymbol{z/H}$ = 0.5, $\boldsymbol{\alpha} = 0^{\circ}$

x/c	**y** (mm)	**Umean** (m/s)	**Urms** (m/s)	**Vrms** (m/s)	$\overline{u'v'}$ (m^2/s^2)
1.44	201.0	10.07	0.040	N/A	N/A
1.44	202.0	10.06	0.038	N/A	N/A
1.44	203.0	10.07	0.040	N/A	N/A
1.44	204.0	10.08	0.042	N/A	N/A
1.44	205.0	10.07	0.042	N/A	N/A
1.44	206.0	10.09	0.045	N/A	N/A
1.44	207.0	10.10	0.045	N/A	N/A
1.44	208.0	10.12	0.044	N/A	N/A
1.44	209.0	10.12	0.043	N/A	N/A
1.44	210.0	10.12	0.045	N/A	N/A
1.44	211.0	10.12	0.046	N/A	N/A
1.44	212.0	10.12	0.047	N/A	N/A
1.44	213.0	10.10	0.047	N/A	N/A
1.44	214.0	10.11	0.048	N/A	N/A
1.44	215.0	10.11	0.050	N/A	N/A
1.44	216.0	10.11	0.051	N/A	N/A
1.44	217.0	10.13	0.056	N/A	N/A
1.44	218.0	10.14	0.062	N/A	N/A
1.44	219.0	10.15	0.072	N/A	N/A
1.44	220.0	10.16	0.091	N/A	N/A
1.44	221.0	10.17	0.118	N/A	N/A

1.44	222.0	10.19	0.161	N/A	N/A
1.44	223.0	10.15	0.236	N/A	N/A
1.44	224.0	10.08	0.333	N/A	N/A
1.44	225.0	9.93	0.450	N/A	N/A
1.44	226.0	9.68	0.562	N/A	N/A
1.44	227.0	9.35	0.632	N/A	N/A
1.44	228.0	9.07	0.650	N/A	N/A
1.44	229.0	8.84	0.637	N/A	N/A
1.44	230.0	8.72	0.633	N/A	N/A
1.44	231.0	8.74	0.661	N/A	N/A
1.44	232.0	8.86	0.700	N/A	N/A
1.44	233.0	9.03	0.733	N/A	N/A
1.44	234.0	9.23	0.749	N/A	N/A
1.44	235.0	9.48	0.722	N/A	N/A
1.44	236.0	9.71	0.667	N/A	N/A
1.44	237.0	9.89	0.592	N/A	N/A
1.44	238.0	10.03	0.520	N/A	N/A
1.44	239.0	10.14	0.425	N/A	N/A
1.44	240.0	10.22	0.329	N/A	N/A
1.44	241.0	10.28	0.228	N/A	N/A
1.44	242.0	10.31	0.181	N/A	N/A
1.44	243.0	10.32	0.138	N/A	N/A
1.44	244.0	10.33	0.108	N/A	N/A
1.44	245.0	10.34	0.092	N/A	N/A
1.44	246.0	10.34	0.074	N/A	N/A
1.44	247.0	10.35	0.065	N/A	N/A
1.44	248.0	10.37	0.060	N/A	N/A
1.44	249.0	10.36	0.057	N/A	N/A
1.44	250.0	10.37	0.053	N/A	N/A
1.44	251.0	10.38	0.051	N/A	N/A
1.44	252.0	10.40	0.050	N/A	N/A
1.44	253.0	10.41	0.050	N/A	N/A
1.44	254.0	10.41	0.051	N/A	N/A
1.44	255.0	10.43	0.050	N/A	N/A
1.44	256.0	10.45	0.049	N/A	N/A
1.44	257.0	10.46	0.047	N/A	N/A
1.44	257.5	10.47	0.046	N/A	N/A
1.44	258.0	10.47	0.048	N/A	N/A
1.44	258.5	10.48	0.047	N/A	N/A
1.44	259.0	10.49	0.049	N/A	N/A
1.44	259.5	10.49	0.048	N/A	N/A
1.44	260.0	10.48	0.047	N/A	N/A
1.44	260.5	10.50	0.048	N/A	N/A
1.44	261.0	10.50	0.048	N/A	N/A
1.44	261.5	10.50	0.049	N/A	N/A
1.44	262.0	10.50	0.049	N/A	N/A
1.44	262.5	10.50	0.049	N/A	N/A
1.44	263.0	10.49	0.048	N/A	N/A
1.44	263.5	10.50	0.049	N/A	N/A
1.44	264.0	10.51	0.048	N/A	N/A
1.44	264.5	10.51	0.049	N/A	N/A
1.44	265.0	10.52	0.049	N/A	N/A
1.44	266.0	10.53	0.048	N/A	N/A
1.44	266.5	10.52	0.050	N/A	N/A
1.44	267.0	10.52	0.050	N/A	N/A
1.44	267.5	10.52	0.051	N/A	N/A
1.44	268.0	10.53	0.049	N/A	N/A
1.44	268.5	10.54	0.048	N/A	N/A
1.44	269.0	10.53	0.049	N/A	N/A
1.44	269.5	10.53	0.048	N/A	N/A

1.44	270.0	10.53	0.047	N/A	N/A
1.44	270.5	10.53	0.048	N/A	N/A
1.44	271.0	10.54	0.049	N/A	N/A
1.44	272.0	10.57	0.047	N/A	N/A
1.44	273.0	10.56	0.046	N/A	N/A
1.44	274.0	10.57	0.048	N/A	N/A
1.44	275.0	10.58	0.049	N/A	N/A
1.44	276.0	10.60	0.049	N/A	N/A
1.44	277.0	10.61	0.050	N/A	N/A
1.44	278.0	10.61	0.049	N/A	N/A
1.44	279.0	10.62	0.048	N/A	N/A
1.44	280.0	10.64	0.049	N/A	N/A
1.44	281.0	10.65	0.047	N/A	N/A
1.44	282.0	10.65	0.046	N/A	N/A
1.44	283.0	10.66	0.047	N/A	N/A
1.44	284.0	10.68	0.049	N/A	N/A
1.44	285.0	10.67	0.048	N/A	N/A
1.44	286.0	10.68	0.048	N/A	N/A
1.44	287.0	10.68	0.049	N/A	N/A
1.44	288.0	10.70	0.050	N/A	N/A
1.44	289.0	10.69	0.049	N/A	N/A
1.44	290.0	10.70	0.049	N/A	N/A
1.44	291.0	10.71	0.049	N/A	N/A
1.44	292.0	10.70	0.050	N/A	N/A
1.44	293.0	10.72	0.048	N/A	N/A
1.44	294.0	10.74	0.046	N/A	N/A
1.44	295.0	10.74	0.047	N/A	N/A
1.44	296.0	10.75	0.049	N/A	N/A
1.44	297.0	10.75	0.046	N/A	N/A
1.44	298.0	10.75	0.045	N/A	N/A
1.44	299.0	10.76	0.046	N/A	N/A
1.44	300.0	10.76	0.047	N/A	N/A
1.44	301.0	10.77	0.047	N/A	N/A

$\boldsymbol{U_o}$ = 9.90 (m/s), $\boldsymbol{P_a}$ = 764 (mm Hg), $\boldsymbol{T_a}$ = 292 (^{o}K), $\boldsymbol{z/H}$ = 0.5, $\boldsymbol{\alpha} = 0^o$

x/c	**y** (mm)	**Umean** (m/s)	**Urms** (m/s)	**Vrms** (m/s)	$\overline{u'v'}$ (m^2/s^2)
2	150.0	9.39	0.032	0.064	-0.001
2	155.0	9.42	0.032	0.067	-0.001
2	160.0	9.44	0.033	0.072	-0.001
2	165.0	9.49	0.032	0.067	0.000
2	170.0	9.52	0.033	0.066	-0.001
2	175.0	9.58	0.032	0.067	-0.001
2	180.0	9.59	0.033	0.068	-0.001
2	185.0	9.63	0.034	0.068	-0.001
2	190.0	9.65	0.034	0.070	-0.001
2	195.0	9.69	0.035	0.069	-0.001
2	200.0	9.70	0.034	0.068	-0.001
2	205.0	9.75	0.034	0.065	-0.001
2	210.0	9.79	0.036	0.062	-0.001
2	215.0	9.83	0.039	0.065	-0.001
2	220.0	9.86	0.052	0.074	-0.001
2	221.0	9.88	0.058	0.081	-0.001
2	222.0	9.89	0.067	0.090	-0.001
2	223.0	9.90	0.080	0.109	-0.001
2	224.0	9.90	0.103	0.140	0.000
2	225.0	9.92	0.127	0.177	0.002

2	226.0	9.92	0.159	0.221	0.006
2	227.0	9.88	0.199	0.273	0.013
2	228.0	9.82	0.242	0.321	0.022
2	229.0	9.74	0.289	0.374	0.033
2	230.0	9.66	0.331	0.419	0.043
2	231.0	9.58	0.360	0.458	0.048
2	232.0	9.44	0.381	0.495	0.048
2	233.0	9.34	0.396	0.516	0.039
2	234.0	9.23	0.400	0.535	0.022
2	235.0	9.19	0.416	0.545	0.000
2	236.0	9.15	0.424	0.549	-0.026
2	237.0	9.15	0.441	0.556	-0.052
2	238.0	9.16	0.465	0.552	-0.071
2	239.0	9.23	0.487	0.546	-0.091
2	240.0	9.31	0.504	0.534	-0.102
2	241.0	9.41	0.510	0.527	-0.109
2	242.0	9.52	0.506	0.503	-0.110
2	243.0	9.62	0.493	0.481	-0.105
2	244.0	9.70	0.480	0.456	-0.100
2	245.0	9.81	0.451	0.434	-0.090
2	246.0	9.90	0.410	0.388	-0.075
2	247.0	9.97	0.374	0.362	-0.062
2	248.0	10.02	0.337	0.326	-0.052
2	249.0	10.07	0.295	0.292	-0.040
2	250.0	10.11	0.256	0.257	-0.029
2	251.0	10.14	0.219	0.228	-0.022
2	252.0	10.18	0.174	0.193	-0.013
2	253.0	10.19	0.142	0.165	-0.008
2	254.0	10.20	0.119	0.145	-0.006
2	255.0	10.20	0.096	0.122	-0.003
2	256.0	10.24	0.084	0.108	-0.002
2	257.0	10.23	0.072	0.101	-0.002
2	258.0	10.24	0.060	0.087	-0.001
2	259.0	10.26	0.057	0.086	-0.001
2	260.0	10.23	0.053	0.085	-0.001
2	265.0	10.28	0.043	0.077	-0.001
2	270.0	10.33	0.041	0.080	-0.001
2	275.0	10.38	0.040	0.087	-0.001
2	280.0	10.41	0.040	0.087	-0.001
2	285.0	10.49	0.040	0.096	-0.001
2	290.0	10.53	0.042	0.095	-0.001
2	295.0	10.58	0.040	0.095	-0.001
2	300.0	10.63	0.042	0.102	-0.002
2	305.0	10.68	0.041	0.101	-0.002
2	310.0	10.73	0.043	0.112	-0.002
2	315.0	10.76	0.043	0.117	-0.002
2	320.0	10.84	0.042	0.108	-0.002

Table A5.1: Measurements of mean and turbulence quantities in the normal direction (y) in the near-wake and at station 2. Data for the normal turbulence intensity and turbulence shear stress are only available in locations where tests were conducted with a cross-wire probe.

Appendix VI – Coordinate transformation in the bend

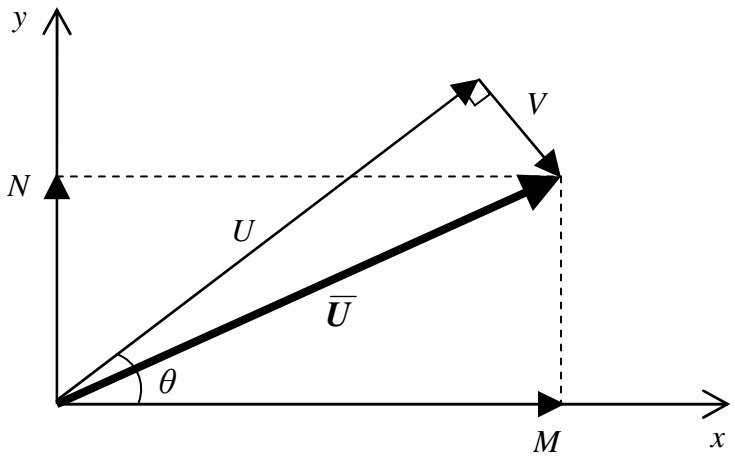

Consider a velocity of magnitude $\overline{U}$, where U and V are the streamwise and radial velocity components, respectively. M and N are the horizontal and vertical velocity components, respectively.

Note that $\theta = 45^{o}$ at station 3.

Expressing U and V in terms of M and N, gives,

$$U = M\cos\theta + N\sin\theta \qquad \text{(A6.1)}$$

$$V = M\sin\theta - N\cos\theta \qquad \text{(A6.2)}$$

Similarly,

$$U = aM + bN \qquad \text{(A6.3)}$$

$$V = cM - dN \qquad \text{(A6.4)}$$

where $a = d = \cos\theta$ and $b = c = \sin\theta$. The instantaneous velocities can be written in terms of the time-averaged and fluctuating components as

$$M = \overline{M} + m' \;,\; N = \overline{N} + n' ,\; U = \overline{U} + u' ,\; V = \overline{V} + v' \qquad \text{(A6.5)}$$

The time-average of the square of equations (A6.3) and (A6.4) can be written in the form,

$$\overline{U^2} = \overline{(aM + bN)^2} = \overline{a^2 M^2} + \overline{b^2 N^2} + \overline{2\,abMN} \tag{A6.6}$$

$$\overline{V^2} = \overline{(cM - dN)^2} = \overline{c^2 M^2} + \overline{d^2 N^2} - \overline{2\,cdMN} \tag{A6.7}$$

Substituting the expressions of equation (A6.5) into (A6.6) and (A6.7), and collecting the appropriate terms using the identities $\overline{U^2} = \overline{U}^2 + \overline{u'^2}$ and $\overline{V^2} = \overline{V}^2 + \overline{v'^2}$, yields:

$$\overline{u'^2} = a^2\,\overline{m'^2} + b^2\,\overline{n'^2} + 2\,ab\,\overline{m'n'} \tag{A6.8}$$

$$\overline{U}^2 = a^2\overline{M}^2 + b^2\overline{N}^2 + 2\,ab\overline{M}\,\overline{N} \tag{A6.9}$$

$$\overline{v'^2} = c^2\,\overline{m'^2} + d^2\,\overline{n'^2} - 2\,cd\,\overline{m'n'} \tag{A6.10}$$

$$\overline{V}^2 = c^2\overline{M}^2 + d^2\overline{N}^2 - 2\,cd\overline{M}\,\overline{N} \tag{A6.11}$$

In a similar way,

$$\overline{UV} = \overline{(aM + bN)(cM - dN)} = \overline{acM^2} + \overline{(bc - ad)MN} - \overline{bdN^2} \tag{A6.12}$$

Therefore, substituting equation (A6.5) into (A6.12) and gathering the appropriate terms using the identity $\overline{UV} = \overline{U}\,\overline{V} + \overline{u'v'}$, yields:

$$\overline{u'v'} = ac\,\overline{m'^2} + (bc - ad)\overline{m'n'} - bd\,\overline{n'^2} \tag{A6.13}$$

$$\overline{U}\,\overline{V} = ac\overline{M}^2 + (bc - ad)\,\overline{M}\,\overline{N} - bd\overline{N}^2 \tag{A6.14}$$

Appendix VII – Statistically steady state (SSS) condition for turbulence

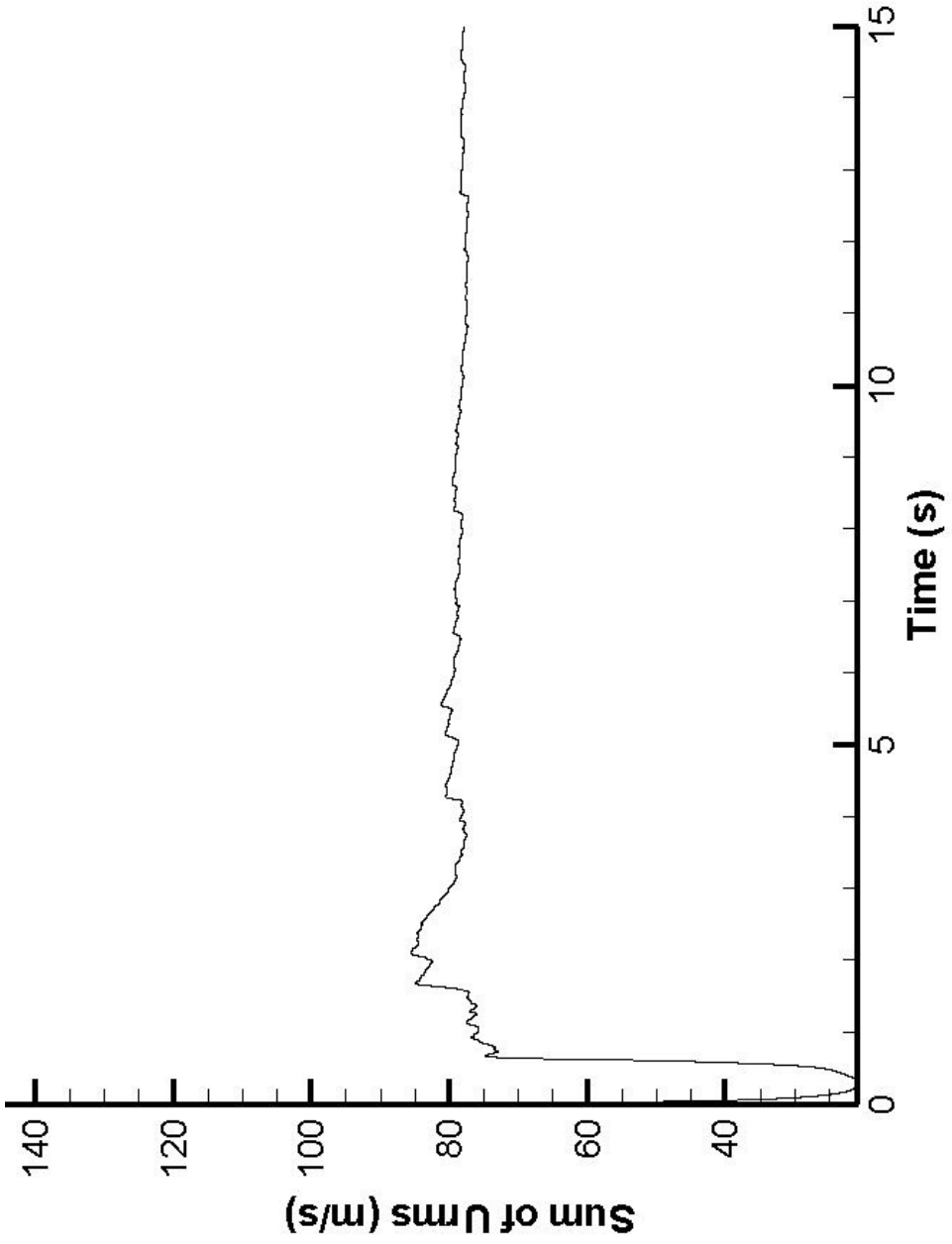

Figure A7.1: Plot of the sum of streamwise turbulence intensity (RMS) at station 5 versus computational flow time. Data is shown from the starting flow to t = 15 seconds.

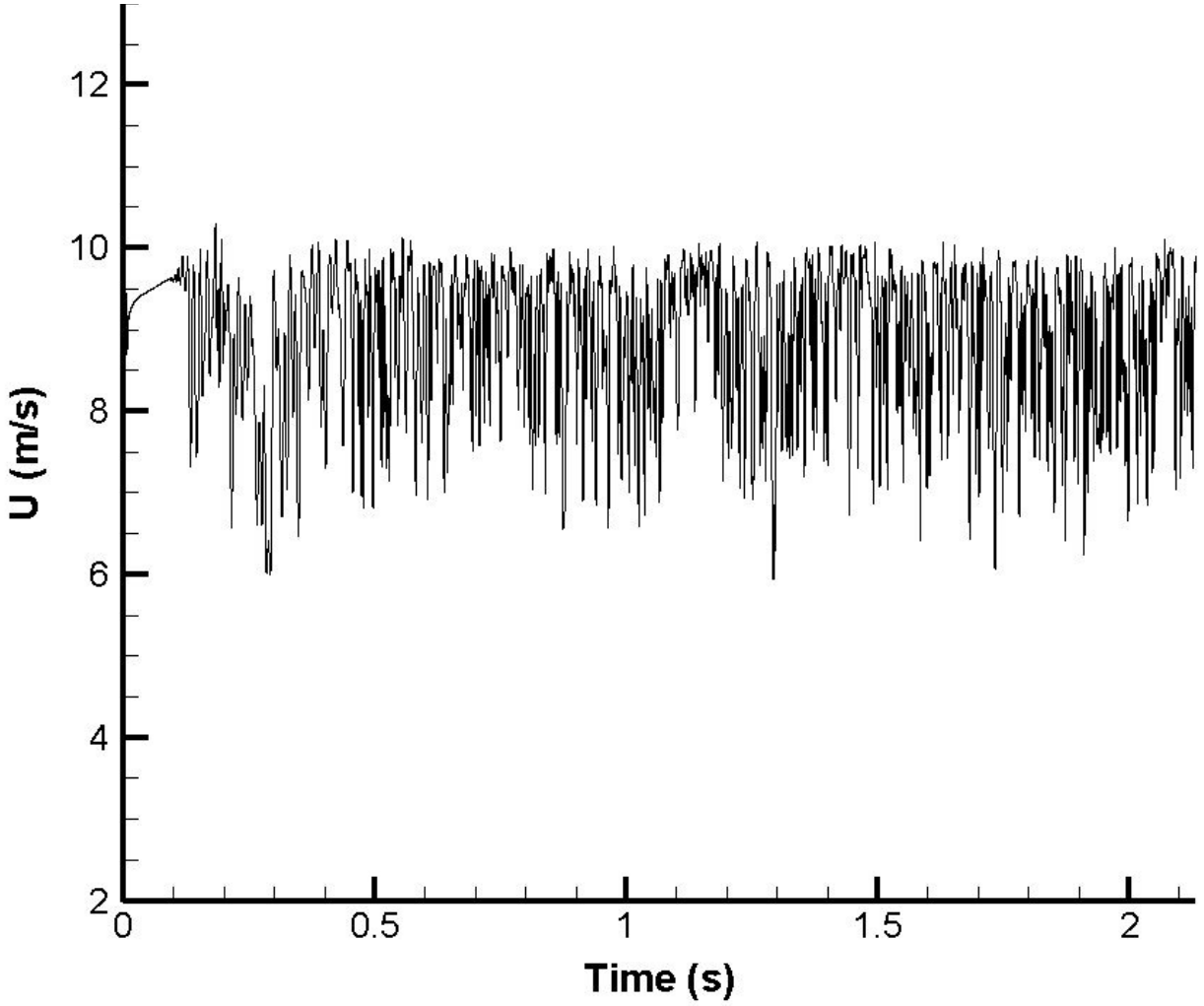

Figure A8.1: A plot of instantaneous streamwise velocity U versus time t, from the large eddy simulations. The data is collected in the near-wake at $x/c = 1.33$ and $y/H = 0.52$, where x is the streamwise distance measured from the trailing edge of the airfoil, and y is the normal distance from the lower wall of the tunnel.

REFERENCES

Abbott, I.H. and Von Doenhoff, A.E., (1959), Theory of wing sections, Dover Publications, pp. 462.

Absil, L.H.J. and Passchier, D.M., (1994), Experiments in the trailing edge flow of an NLR 7702 airfoil, A selection of experimental test cases for the validation of CFD codes, *AGARD-AR-303*, Vol. 2, pp. A7-1.

Alam, M. and Sandham N.D., (2000), Direct numerical simulation of short laminar separation bubbles with turbulent reattachment, *Journal of Fluid Mechanics*, Vol. 410, pp. 1-28.

Alber, I.E., (1980), Turbulent wake of a thin flat plate, *AIAA Journal*, Vol. 18, pp. 1044-1051.

Bandyopadhyay, P.R. and Ahmed, A., (1993), Turbulent boundary layers subjected to multiple curvatures and pressure gradients, *Journal of Fluid Mechanics*, Vol. 246, pp. 503-527.

Barlow, R.S. and Johnston, J.P., (1988), Structure of a turbulent layer on a concave surface, *Journal of Fluid Mechanics*, Vol. 191, pp. 137-176.

Barths, T.J. and Jespersen, D., (1989), The design and application of upwind schemes on unstructured meshes, *Technical Report AIAA-89-0366*, AIAA 27th Aerospace Sciences Meeting, Reno, Nevada.

Blake, W.K., (1975), A statistical description of pressure and velocity fields at the trailing edge of a flat strut, David Taylor Naval Ship Research and Development Centre, Report. 4241, Bethesda, MD, December.

Bradshaw, P., (1973), Effects of streamline curvature on turbulent flow, *AGARDograph* No. 169.

Bradshaw, P., (1976), Complex turbulent flows, Theoretical and Applied Mechanics, W.T. Koiter, ed. North-Holland Publishing Company.

Brendel, M. and Mueller, T.J., (1988), Boundary layer measurements on an airfoil at low Reynolds numbers, *Aeronautical Research Council Current Papers*, CP 1073, University of London.

Breuer, M. and Rodi, W., (1994), Large eddy simulation of turbulent flow through a straight square duct and a 180 degree bend, Fluid Mechanics and its Applications, Selected papers from the first ERCOFTAC Workshop, Guilford, Surrey, United Kingdom, 27-30 March, Voke, Kleiser, Chollet (Eds.), Direct and large eddy simulation I, Vol. 26, pp. 273-285, Kluwer Academy Publisher.

Brunn, H.H., (1995), Hot-wire Anemometry: Principles and signal analysis, *Oxford University Press*.

Castro, I.P. and Epik, E., (1998), Boundary layer development after a separated region, *Journal of Fluid Mechanics*, Vol. 374, pp. 91-116.

Champagne, F.H. and Sleicher, C.A., (1976b), Turbulence measurements with inclined hot-wires, part II, Hot-wire response equations, *Journal of Fluid Mechanics*, Volt. 28, pp. 177-182.

Champagne, F.H, Sleicher, C.A. and Wehrmann, O.H., (1976a), Turbulence measurements with inclined hot-wires, part I, Heat transfer experiments with inclined hot-wires, *Journal of Fluid Mechanics*, Vol. 28, pp. 153-175.

Chasnov, J.R., (1990), Simulation of the Kolmogorov inertial subrange using an improved subgrid model. *Physics of Fluids*, Vol. 3, pp. 188-200.

Cheah, S.C., Iacovides, H., Jackson, D.C., Ji, H., Launder, B.E., (1996), LDA investigation of the flow development through rotating U-ducts, *Journal of Turbomachinery*, Vol. 118(3), pp. 590-596.

Chen, H.C., and Patel, V.C, (1988), Near wall turbulence models for complex flows including separation, *AIAA Journal*, Vol. 26(6), pp. 641-648.

Chevray, R. and Kovasznay, L.S.G., (1969), Turbulence measurements in the wake of a thin flat plate, *AIAA Journal*, Vol. 7, pp. 1641-1643.

Choi, H. and Moin, P., (1994), Effects of the computational time step on numerical solutions of turbulent flow, *Journal of Computational Physics*, Vol. 113, pp. 1-4, July.

Clark, R.A., Ferziger, J.H. and Reynolds, W.C., (1979), Evaluation of subgrid scale models using an accurately simulated turbulent flow, *Journal of Fluid Mechanics*, Vol. 91, pp. 1-16.

Coles, D. and Wadcock, A. J., (1979), Flying hot-wire study of two-dimensional mean flow past an NACA 4412 airfoil at maximum lift, *AIAA Journal*, Vol. 17, pp. 321-329, April.

Conway, S., Caraeni, D. and Fuchs, L., (2000), Large eddy simulation of flow through the blades of a swirl generator, *International Journal of Heat and Fluid Flow*, Vol. 21, pp. 664-673.

Dahlström, S. and Davidson, L., (2002), Large eddy simulation of the flow around an Aerospatiale A-airfoil, *ECCOMAS*, European Congress on Computational Methods in Applied Sciences and Engineering, 11-14 September, Barcelona, Spain.

Davidson, L., Cokljat, D., Fröhlich, J., Leschziner, M.A., Mellen, C. and Rodi, W., (eds.), (2003), LESFOIL: Large Eddy Simulation of Flow Around a High Lift Airfoil*, Notes on Numerical Fluid Mechanics*, Vol. 83, Springer Verlag.

Deardorff, J.W., (1970), A numerical study of three-dimensional turbulent channel flow at large Reynolds numbers, *Journal of Fluid Mechanics*, Vol. 41, pp. 453-465.

Deardorff, J.W., (1973), The use of subgrid transport equations in a three-dimensional model of atmospheric turbulence, *ASME Journal of Fluids Engineering*, Vol. 95, pp. 429-438

El-Gammal, M. and Hangan, H., (2008), Three-dimensional wake dynamics of a blunt and divergent trailing edge airfoil, *Experiments in Fluid*, Vol. 44, pp. 707-717.

Farsimadan, E. and Mokhtarzadeh-Dehghan, R., (2008), A large eddy simulation of an airfoil turbulent wake subjected to streamwise curvature, *International Journal for Numerical Methods in Fluids*, Vol. 56, pp. 1233-1240.

FLUENT 6.3 User's Guide, (2005), Fluent Incorporated Worldwide Corporate Headquarters, Centerra Park, 10 Cavendish Court, Lebanon, NH 03766-1442, USA

Fröhlich, J. and Mellen, C.P., (2001), Transition in LES of bluff body flows and airfoils, In Geurts, B.J., Friedrich, R. and Metais, O., (eds.), *Direct and large eddy simulation IV*, pp. 145-156, Kluwer Academic.

Gad-el-Hak, M. and Bushnell, D.M., (1990), Separation Control: Review, *ASME Journal of Fluids Engineering*, Vol. 113, pp. 5-30.

Germano, M., Piomelli, U., Moin, P. and Cabot, W.H., (1991), A dynamic subgrid scale eddy viscosity model, *Physics of Fluids*, Vol. 3, pp. 1760-1765.

Gleyzes, C., (1989), Opération décrochage-résultats de la 2ème campagne d'essais à F2–mésures de pression et vélocimétrie laser, ONERA, TR RT-DERAT 55/5004, Paris.

Gregory, N. and O'Reilly, C.L., (1970), Low speed aerodynamic characteristics of NACA 0012 section, Including the effect of upper surface roughness simulation hoarfrost, National Physical Laboratory, Teddington, England, Aero Rept. 1308.

Guleren, K. M. and Turan, A., (2007), Validation of large eddy simulation of strongly curved stationary and rotating U-duct flows, *International Journal of Heat and Fluid Flow*, Vol. 28, Issue 5, pp. 909-921, October.

Goldstein, R.J., (1983), Fluid Mechanics measurements, Hemisphere Publication Corporation.

Hah, C. and Lakshminarayana, B., (1982), Measurement and prediction of mean velocity and turbulent structure in the near-wake of an airfoil, *Journal of Fluid Mechanics*, Vol. 115, pp. 251-282.

Hébrard, J., Métais, O. and Salinas-Vasquez, M., (2004), Large eddy simulation of turbulent duct flow: heating and curvature effects, *International Journal of Heat and Fluid Flow*, Vol. 25, pp. 569-580.

Hinze, J.O., (1975), Turbulence, 2nd Edition, McGraw-Hill, New York.

Hoffmann, P.H., Muck, K.C. and Bradshaw, P., (1985), The effect of concave surface curvature on turbulent boundary layers, *Journal of Fluid Mechanics*, Vol. 161, pp. 371-403.

Horton, H.P., (1967), A semi-empirical theory for the growth and bursting of laminar separation bubbles, *Aeronautical Research Council Current Papers*, CP 1073, University of London.

Huang, R.F. and Lin, C.L., (1995), Vortex shedding and shear-layer instability of wing at low Reynolds numbers, *AIAA Journal*, Vol. 33(8), pp. 1398-1403.

Huddeville, R., Piccin, O. and Cassoudesalle, D., (1987), Opération décrochage–mesurement de frottement sur profiles AS 239 et A 240 à la soufflerie F1 du CFM, ONERA, TR RT-OA 19/5025 (RT-DERAT 19/5025 DN), Paris.

John, J. and Schobeiri, M.T., (1996), Development of a two-dimensional turbulent wake in a curved channel with a positive streamwise pressure gradient, Transactions of the ASME, *Journal of Fluids Engineering*, Vol. 118, pp. 292-298.

Jovičić, N. and Breuer, M., (2004), High performance computing in turbulence research: separated flow past an airfoil at high angle of attack*, High performance computing in science and engineering*, Munich, Transaction of the second joint HLRB and KONWIHR status and result workshop, March 2-3, Technical University of Munich, Germany, eds. S. Wagner, W. Hanke, A. Bode, F. Durst, pp. 93-105, Springer Verlag, Berlin Heidelberg New York, ISBN 3-540-44326-6, (2004).

Jørgensen, F.E., (2005), How to measure turbulence with hot-wire anemometers-a practical guide, Dantec Dynamics, Denmark.

Kerho, M.F. and Bragg, M.B., (1997), Airfoil boundary layer development and transition with large leading edge roughness, *AIAA Journal*, Vol. 35, pp. 75-84.

Kim, S.E., (2004), Large eddy simulation using unstructured mesh based finite volume solver, *Technical Report AIAA-2004-2548*, AIAA 34th Fluid Dynamics Conference and Exhibit, June.

Kim, W.W. and Menon, S., (1997), Application of the localized dynamic subgrid-scale model to turbulent wall bounded flows. Technical Report *AIAA-97-0210*, AIAA 35th Aerospace Sciences Meeting, Reno, NV, January.

Kindler, K., Kreplin, H.P. and Ronneberger, D., (2003), Experimentelle Untersuchung kohärenter Strukturen in kritischen Tragfugelströmungen, Interner Bericht, IB 224-2003 A 11, *Inst. f. Aerodynamik und Strömungstechnik*, DLR Göttingen.

Kolmogorov, A.N., (1941a), The local structure of turbulence in incompressible viscous fluid at very large Reynolds number, *Dokl. Akad. Nauk SSSR*, Vol. 30, pp. 301-305.

Kolmogorov, A.N., (1941*b*), On the degeneration of isotropic turbulence in an incompressible viscous fluid, *Dokl. Akad. Nauk SSSR*, Vol. 31, pp. 538-541.

Komurasaki, S. and Kuwahara, K., (2004), Implicit large eddy simulation of a subsonic flow around NACA 0012 airfoil, *Technical Report AIAA-2004-594*, AIAA 42nd Aerospace Sciences Meeting and Exhibit, Reno, Nevada.

Koyama, H.S., (1983), Effects of streamline curvature on laminar and turbulent wakes, *Proc of Forth Symp. On Turbulent Shear Flows*, University of Karlsruhe, Karlsruhe, Germany, pp. 141-155.

Kraichnan, R.H, (1970), Diffusion by a random velocity field, *Physics of Fluids*, Vol. 13, pp. 22-31.

Kraichnan, R.H, (1976), Eddy viscosity in two and three dimensions, *Journal of Atmospheric Sciences*, Vol. 33, pp. 1521-1536.

Launder, B.E. and Spalding, D.B., (1974), The numerical computation of turbulent flows, *Computer Methods in Applied Mechanics and Engineering* 3, pp. 269-289.

LeBlanc, P., Blackwelder, R. and Liebeck, R., (1987), A comparison between boundary layer measurements in a laminar separation bubble flow and linear stability theory calculations, *Perspectives in Turbulence Studies*, edited by H.U. Meier and P. Bradshaw, Springer-Verlag, New York, pp. 189-205.

Lee, H.K., and Kang, S.H., (1998), Flow characteristics of a transitional boundary layer on the NACA 0012 airfoil in wakes, *Proceedings of FEDSM'98*, Washington DC.

Leonard, A., (1974), Energy cascade in large eddy simulations of turbulent fluid flows, *Advances in Geophysics A*, Vol. 18, pp. 237-248.

Leonard, B.P., (1979), A stable and accurate convective modelling procedure based on quadratic upstream interpolation, *Computer Methods in Applied Mechanics and Engineering*, Vol. 19, pp. 59-98.

Leonard, B.P., (1991), The ULTIMATE conservative difference scheme applied to unsteady one-dimensional advection, *Computer Methods in Applied Mechanics and Engineering*, Vol. 88, pp. 17-74.

Leschziner, M.A., (1993), Two-equation models for high-Reynolds number flow, *Introduction to the modelling of turbulence*, Lecture Series 1993-02, von Karman Institute for Fluid Dynamics, pp. TM2-TM41.

Lesieur, M., Métais, O. and Comte, P., (2005), Large Eddy Simulations of Turbulence, Cambridge University Press, New York.

Lilly, D.K., (1967), The representation of small-scale turbulence in numerical simulation experiments, *Proceedings of the IBM Scientific Computing Symposium on Environmental Sciences*, Yorktown Heights, USA.

Lilly, D.K., (1992), A proposed modification of the Germano subgrid-scale closure method, *Physics of Fluids A*, Vol. 4(3), pp. 633-635.

Lin, J.C.M. and Pauley, L.L., (1996), Low Reynolds number separation on an airfoil, *AIAA Journal*, Vol. 34(8), pp. 1570-1577.

Liu, S., Meneveau, C. and Katz, J., (1994a), On the properties of similarity subgrid scale models as deduced from measurements in a turbulent jet, *Journal of Fluid Mechanics*, Vol. 275, pp. 83-119

Liu, S., Meneveau, C. and Katz, J., (1994b), Experimental study of similarity subgrid scale models of turbulence in the far-field of a jet, *Direct and Large Eddy Simulation I*, pp. 37-48, Kluwer.

Lomas, C.G., (1986), Hot-wire Anemometer, Cambridge University Press.

Lopes, A.S., Piomelli, U. and Palma, J.M.L.M., (2006), Large eddy simulation of flow in an S-duct, *Journal of Turbulence*, Vol. 7(11), pp. 1-24.

Lund, T.S. and Moin, P., (1996), Large eddy simulation of a concave wall boundary layer, *International Journal of Heat and Fluid Flow*, Vol. 17, pp. 290-295.

Marsden, O., Bogey, C. and Bailly, C., (2006), Direct noise computation around a 3-D NACA 0012 airfoil, *AIAA-2006-2503*, 12th AIAA/CEAS Aeroacoustics Conference (27th AIAA Aeroacoustics Conference) 8 - 10 May 2006, Cambridge, Massachusetts.

Mary, I. and Sagaut, P., (2002), Large eddy simulation of flow around an airfoil near stall, *AIAA Journal*, Vol. 40, pp. 1139-1145.

Mason, P.J. and Callen, N.S., (1986), On the magnitude if the subgrid-scale eddy coefficient in large-eddy simulations of turbulent channel flow, *Journal of Fluid Mechanics*, Vol. 162, pp. 439-462.

McMillan, J.O., Ferziger, J.H. and Rogallo, R.S., (1980), Tests of new subgrid-scale models in strained turbulence, *AIAA-80-1339*, in AIAA 13th Fluid and Plasma Dynamics Conference, Snowmass, Co.

Mellen, C.P., Fröhlich, J. and Rodi, (2003), Lessons from the European LESFOIL project on LES of flow around an airfoil, *AIAA Journal*, Vol. 41, pp. 573-581.

Meneveau, C., (1994), Statistics of turbulence subgrid-scale stresses: Necessary conditions and experimental tests, *Physics of Fluids*, Vol. 6(2), pp. 815-833.

Moin, P. and Kim, J., (1982), Numerical investigation of turbulent channel flow, *Journal of Fluid Mechanics*, Vol. 118, pp. 341-377.

Mokhtarzadeh-Dehghan, M.R. and Piradeepan, N., (2006), Numerical prediction of a turbulent curved wake and comparison with experimental data, *International Journal for Numerical Methods in Fluids*, Vol. 51, pp. 49-76.

Mokhtarzadeh-Dehghan, M.R. and Yuan, Y.M., (2002), Measurements of turbulence quantities and bursting period in developing turbulent boundary layers on the concave and convex walls of a 90^{o} square bend**,** *Experimental Thermal and Fluid Science*, Vol. 27, pp. 59-75.

Multichannel® CTA / MiniCTA® Installation & user's guide, DANTEC Measurement Technology A/S, Denmark, (2004).

Nakayama, A, (1987), Curvature and pressure-gradient effects on a small-defect wake, *Journal of Fluid Mechanics*, Vol. 175, pp. 215-246.

Narasimhan, J.L., Ramjee, V., Diwakar, Philip. M. and Tulapurkara, E.G., (1991), Prediction of wake in a curved duct, *International Journal for Numerical Methods in Fluids*, Vol. 13, pp. 907-916.

Patankar, S.V. and Spalding, D.B., (1972), A calculation procedure for heat, mass and momentum transfer in three-dimensional parabolic flows, *Journal of Heat and Mass Transfer*, Vol. 15, pp. 1787.

Pauley, L.L, Moin, P. and Reynolds, W.C., (1990), The structure of two-dimensional separation, *Journal of Fluid Mechanics*, Vol. 220, pp. 397-411.

Perry, A.E., (1982), Hot-wire Anemometry, Oxford, Clarendon.

Piomelli, U., (1988), Moin, P. and Ferziger, J.H., (1988), Model consistency in large eddy simulation of turbulent channel flows, *Physics of Fluids*, Vol. 31(7), pp. 1884-1891.

Piomelli, U., (1993), High Reynolds number calculations using the dynamic subgrid-scale stress model, *Physics of Fluids A*, Vol. 5(6), pp. 1484-1490.

Piradeepan, N., (2002), An experimental and numerical investigation of a turbulent airfoil wake in a 90^{o} curved duct, Ph.D. Thesis, Department of Mechanical Engineering, Brunel University.

Piradeepan, N. and Mokhtarzadeh-Dehghan, M.R., (2005), Measurements of mean and turbulence quantities in the curved wake of an airfoil, *Experimental Thermal and Fluid Sciences*, Vol. 29, pp. 239-252

Pope, S.B., (2005), Turbulent Flows, Cambridge University Press, New York.

Prandtl, L., (1904), Uber Flussigkeits bewegung bei sehr kleiner Reibung, *Verhandlungen des dritten internationalen Mathematiker-Kongresses*, Heidelberg, pp. 484-491; Also available in English translation as: Motion of fluids with very little viscosity, *NACA Technical Memorandum-452*, March 1928.

Ramaprian, B.R., Patel, V.C. and Sastry, M.S., (1981), Turbulent wake developed behind streamlined bodies, Institute of Hydraulic Research, University of Iowa, IIHR Report No. 231.

Ramaprian, B.R., Patel, V.C. and Sastry, M.S., (1982), The symmetric turbulent wake of a flat plate, *AIAA Journal*, Vol. 20, pp. 1228-1235.

Ramjee, V. and Neelakandan, D., (1989), Development of wake of a rectangular cylinder in a curved stream, *Experiments in fluids*, Vol. 7, pp. 395-399.

Ramjee, V. and Neelakandan, D., (1990), Curvature effects on the wake of an airfoil and other bodies, *Fluids Dynamic Research*, Vol. 6, pp. 1-13.

Ramjee, V., Tulapurkara, E.G. and Rajasekar, R., (1988), Development of airfoil wake in longitudinally curved stream, *AIAA Journal*, Vol. 26, pp. 948-953, August.

Reynolds, A.J., (1974), Turbulent flows in Engineering, John Wiley & Sons, London.

Rhie, C.M. and Chow, W.L., (1983), Numerical study of the turbulent flow past an airfoil with trailing separation, *AIAA Journal*, Vol. 21 , pp. 1525-1532

Ripley, M.D. and Pauley, L.L., (1993), The unsteady structure of two-dimensional steady laminar separation, *Physics of Fluids A*, Vol. 5, No. 12, pp. 3099-3106.

Sagaut, P., (2006), Large Eddy Simulation of Incompressible flows: An Introduction, Third edition, Springer Berlin Heidelberg, New York.

Saric, W.S., (1994), Görtler vortices, Annual Review in Fluid Mechanics, Vol. 26, pp. 379.

Savill, A.M., (1983), The turbulence structure of a highly curved two-dimensional wake, *Proceeding of the IUTAM symposium on complex turbulent flows*, edited by R. Dumas, and F. Fulachier, Springer-Verlag, Berlin, pp. 185-197.

Schobeiri, M.T., John, J. and Pappu, K., (1996), Development of two-dimensional wakes within curved channels: Theoretical framework and experimental investigation, Transactions of the ASME, *Journal of Turbomachinery*, Vol. 118, pp. 506-518.

Schobeiri, M.T., Pappu, K. and John, J., (1995), Theoretical and experimental study of development of two-dimensional steady and unsteady wakes within curved channels, *Journal of Fluids Engineering*, Vol. 117, pp. 593-598.

Schumann, U., (1975), Subgrid-scale model for finite difference simulations of turbulent flows in plane channels and annuli, *Journal of Computational Physics*, Vol. 18, pp. 376-404.

Sergent, E., (2002), Vers une methodologie de couplage entre la Simulation des Grandes Echelles et les modeles statistiques, PhD thesis, L'Ecole Centrale de Lyon, Lyon, France.

Shan, H., Jiang, L. and Liu, C., (2005), Direct numerical simulation of flow separation around a NACA 0012 airfoil, *Computers and Fluids*, Vol. 34(9), pp. 1096-1114.

Shih, T.H., Liou, W.W., Shabbir, A. and Zhu, J., (1995), A new $k-\varepsilon$ Eddy-viscosity model for high Reynolds number turbulent flows- Model development and validation, *Computers Fluids*, Vol. 24(3), pp. 227-238.

Smagorinsky, J., (1963), General Circulation Experiments with the Primitive Equations. I. The Basic Experiment. *Monthly Weather Review*, Vol. 91, pp. 99-164.

Smirnov, R., Shi, S. and Celik, I., (2001), Random flow generation technique for large eddy simulations and particle-dynamics modeling, *Journal of Fluids Engineering*, Vol. 123, pp. 359-371.

Subaschandar, N., (2005), Measurements in the turbulent near-wake behind an infinitely swept flat plate, *Experimental Thermal and Fluid Sciences*, Vol. 29(4), pp. 415-423.

Suga, K., (2003), Predicting turbulence and heat transfer in 3-D curved ducts by near-wall second moment closures, *International Journal of Heat and Mass Transfer*, Vol. 46, pp. 161-173.

Stark, A.R., Henkes, R.A.W.M. and Tummers, M.J., (1999), Effects of curvature and pressure gradient on a turbulent near wake, *Journal of Experimental Thermal and Fluid Sciences*, Vol. 19, pp. 49-56.

StreamLine® / StreamWare® Installation & user's guide, Vol. 1-3, DANTEC Measurement Technology A/S, Denmark, (2000).

Temmerman, L., Leschziner, M., Mellen, C.P. and Fröhlich, J., (2003), Investigation of subgrid models and wall function approximations in large eddy simulation of separated flow in a channel with streamwise periodic constrictions, *International Journal of Heat and Fluid Flow*, Vol. 24, pp. 157-180.

Tulapurkara, E.G., Ramjee, V. and Jacob, G., (1994), Development of wake in presence of both curvature and pressure gradient, FED-Vol. 184, *Boundary Layer and Free Shear Flows*, ASME 1994, pp. 195-202.

Tulapurkara, E.G., Ramjee, V. and Jacob, G., (1995), Development of a bluff body wake under the combined influence of curvature and pressure gradient, *Experiments in Fluids*, Vol. 18, pp. 311-318.

Tulapurkara, E.G., Ramjee, V. and Jacob, G., (1996), Prediction of airfoil wake subjected to the effects of curvature and pressure gradient, *International Journal for Numerical Methods in Fluids*, Vol. 22, pp. 29-41.

Tulapurkara, E.G., Vengadesan, S. and Lakshminarasimhan, J., (1993), Computation of turbulent asymmetric wake, *International Journal for Numerical Methods in Fluids*, Vol. 16, pp. 239-248, February.

Uzun, A., Blaisdell, G. and Lyrintzis, A., (2003), Sensitivity to the Smagorinsky constant in turbulent jet simulations, *AIAA Journal*, Vol. 41(10), pp. 2077-2079.

Versteeg, H.K. and Malalasekara, W., (1995), An introduction to Computational Fluid Dynamics, The finite volume method, Longmans Scientific and Technical books.

Viswanath, P.R., Cleary, J.W., Seegmiller, H.L. and Horstman C.C., (1980), Trailing-edge flows at high Reynolds number, *AIAA Journal*, Vol. 18, No. 9, pp. 1059-1065.

Wang, M. and Moin, P., (2000), Computation of trailing-edge flow and noise using large-eddy simulation, *AIAA Journal*, Vol. 38, No. 12, pp. 2201-2209.

Wang, M. and Moin, P., (2002), Dynamic wall modelling for large-eddy simulation of complex turbulent flows, *Physics of Fluids*, Vol. 14, No. 7, pp. 2043-2051.

Weber, C. and Ducros, F., (2000), Large eddy and Reynolds-averaged Navier-Stokes simulations of turbulent flow over an airfoil, *International Journal of Computational Fluid Dynamics*, Vol. 13, pp. 327-355.

Werner, H. and Wengle, H., (1991), Large eddy simulation of turbulent flow over and around a cube in a plate channel, *Eighth Symposium on Turbulent Shear Flows*, Munich, Germany.

Weygandt, J.H. and Mehta, R.D., (1995), Three-dimensional structure of straight and curved plane wakes, *Journal of Fluid Mechanics*, Vol. 282, pp. 279-311.

Wolfstein, M., (1969), The velocity and temperature distribution of one dimensional flow with turbulence augmentation and pressure gradient, *International Journal of Heat and Mass Transfer*, Vol. 12, pp. 301-318.

Yakhot, V., Orszag, S.A., Thangam, S., Gatski, T.B. and Speziale, C.G., (1992), Development of turbulence models for shear flows by a double expansion technique, *Physics of Fluids A*, Vol. 4, No. 7, pp. 1510-1520.

Yang, Z. and Voke, P.R., (2001), Large-eddy simulation of boundary-layer separation and transition at a change of surface curvature, *Journal of Fluid Mechanics*, Vol. 439, pp. 305-333.

Yarusevych, S., Sullivan, P.E. and Kawall, J.G., (2004), Investigation of airfoil boundary layer and wake development at low Reynolds numbers, *AIAA-2004-2551*, 34th AIAA Fluid Dynamics Conference and Exhibit, 28th June-1st July, Portland, Oregon.

Yuan, Y.M., (1991), An experimental study of coherent structures in turbulent boundary layers, Ph.D. Thesis, Department of Mechanical Engineering, Brunel University.

Zhang, Q., Lee, S.W. and Ligrani, P.M., (2004), Effects of surface roughness and freestream turbulence on the wake turbulence structure of a symmetric airfoil, *Physics of Fluids*, Vol. 16, No. 6, pp. 2044-2053.

Zhang, Q. and Ligrani, P.M., (2004), Mach number/surface roughness effects on symmetric transonic turbine airfoil aerodynamic losses, *AIAA Journal of Propulsion and Power*, Vol. 20, No. 6, pp. 1117-1125.

Zhang, Q. and Ligrani, P.M., (2006), Wake turbulence structure downstream of a cambered airfoil in transonic flow: Effects of surface roughness and freestream turbulence intensity, *International Journal of Rotating Machinery*, Article ID 60234, pp. 1-12.